Experimentele en numerieke studie van verschillende testsystemen voor de uitvoering en opvolging van vermoeiingsproeven op vezelversterkte thermoplasten

Experimental and Numerical Study of Different Setups for Conducting and Monitoring Fatigue Experiments of Fibre-Reinforced Thermoplastics

Ives De Baere

Promotoren: prof. dr. ir. W. Van Paepegem, prof. dr. ir. J. Degrieck
Proefschrift ingediend tot het behalen van de graad van
Doctor in de Ingenieurswetenschappen: Werktuigkunde-Elektrotechniek

Vakgroep Mechanische Constructie en Productie
Voorzitter: prof. dr. ir. J. Degrieck
Faculteit Ingenieurswetenschappen
Academiejaar 2007 - 2008

UNIVERSITEIT GENT

ISBN 978-90-8578-196-7
NUR 971, 978
Wettelijk depot: D/2008/10.500/15

Promotors:

Prof. dr. ir. Wim Van Paepegem
Ghent University
Faculty of Engineering
Department of Mechanical Construction and Production

Prof. dr. ir. Joris Degrieck
Ghent University
Faculty of Engineering
Department of Mechanical Construction and Production

Examination Committee:

Prof. L. Taerwe (Chair)	Ghent University, Belgium
Prof. W. De Waele (Secretary)	Ghent University, Belgium
Prof. W. Van Paepegem (Promotor)	Ghent University, Belgium
Prof. J. Degrieck (Promotor)	Ghent University, Belgium
Prof. G. De Schutter	Ghent University, Belgium
Prof. H. Sol	Vrije Universiteit Brussel, Belgium
Prof. M. Quaresimin	University of Padova, Italy
Prof. C. Hochard	Université Aix Marseille, France
Dr. ir. S. Wijskamp	Ten Cate Advanced Composites, The Netherlands

Research Institute:

Ghent University
Department of Mechanical Construction and Production
Mechanics of Materials and Structures
Sint-Pietersnieuwstraat 41
B-9000 Gent
Belgium
Tel. +32 (0)9 264 32 55
Fax. +32 (0)9 264 35 87
Ives.DeBaere@UGent.be

This research was funded by the Special Research Fund
(BOF, Bijzonder OnderzoeksFonds)

Some lessons can be taught, others must be lived…

ACKNOWLEDGEMENTS

A colleague once said that a doctoral thesis is not about having a job, it is about personal enrichment. Throughout the research, when encountering various types of problems, a person really gets to know himself. After hours, weeks and even months of research on that one obstacle that prevents the experiments from working, the relief is great when the solution finally arrives. And this experience, of course, cannot be taught.

Of course, there are a number of people who have played an important role throughout this research. Therefore, I would also like to thank, in a random order,

- Prof. dr. ir. Wim Van Paepegem for his continuous guidance and support through rough times, the proof reading of this and other documents and for all the suggestions to further improve my research. This research would not have been the same without him.
- Prof. dr. ir Joris Degrieck for the interesting subject and the valuable ideas during the various meetings we have had. Every time I was a little out of ideas, prof. Degrieck was there with suggestions and possibilities.
- Luc van den Broecke, for transforming my designs and ideas into working tools, for teaching me valuable things I had not seen during my mechanical engineering education, for his typical jokes and of course for the very important wisdom ‘with time and sandwiches, everything is possible’.
- Chris Bonne, for his help with the instrumentation of the specimens and with the development of the electrical resistance measurement technique. Without him, I would have been both blind and deaf during most of the experiments.
- Prof. dr. ir. Danny van Hemelryck and prof. dr. ir. Hugo Sol for their help with the determination of the elastic properties of the material with the ‘resonalyser’ method.
- Prof. dr. ir. Andre van Calster, for his suggestions that further improved the electrical resistance measurement.

- Eli Voet and Stief Goetschalckx, both from FOS&S, for their help with the optical fibre measurements.
- Veerle Cnudde and Bert Masschaele from the department of Subatomic and Radiation Physics for their help with the X-ray micro-tomography.
- All the other friends and colleagues of IR04 for their ideas and their help and for brightening up the day when things seemed a little dark.
- Steven Derycke, for his input while performing his master thesis.

In my personal life, I may not forget my parents, for giving me the opportunity of studying for mechanical engineer and for everything else they have already done for me. Without them, I would not be where I am now. I would also like to thank my friends and family (in law), for their support during the making and writing of this thesis.

And last but not least, my lovely wife Pascale, for her mental support during these past four years of my doctoral study, but mainly for just being there for me when it was necessary. You make me complete.

Since I would not have been able to do this research all by myself, a word of gratitude is in order for the following supporting organisations and companies. First, I would like to thank the Special Research Fund (BOF, Bijzonder OnderzoeksFonds) for the grant that made this thesis possible, the research group IR04 in general for the possibility of making this doctoral thesis and the Belgian Institute for Welding (BIL) for allowing me to use their servo-hydraulic tensile machine. I would also like to express my gratitude to Ten Cate Advanced Composites for supplying the composite material used during this research, to De Beleyr nv. for manufacturing the clamps of the tensile and rail shear experiments and the company FOS&S, for supplying the material necessary for the optical fibre measurements and for their support during the experiments.

And for the persons I might have forgotten, my sincere apologies, …

Ives De Baere
Gent, 06-02-2008

NEDERLANDSTALIGE SAMENVATTING

Vezelversterkte thermoplasten worden alsmaar meer gebruikt in de industrie. Zo zal elk nieuw vliegtuig van het type Airbus A380 ongeveer zes ton vezelversterkte thermoplasten bevatten. Deze materialen hebben echter een vrij complex mechanisch gedrag, dat nog niet volledig begrepen is. Het doel van dit doctoraatsonderzoek is enerzijds meer informatie te verschaffen over hoe deze materialen zich gedragen onder vermoeiingsbelasting en anderzijds om nieuwe technieken aan te reiken om structuren, gemaakt met vezelversterkte thermoplasten, op te volgen gedurende hun levensduur. Aangezien deze materiaalfamilie redelijk omvangrijk is, wordt er slechts één materiaal geselecteerd om deze familie te vertegenwoordigen, met name een koolstofweefsel versterkt polyfenyleen sulfide.

In eerste instantie wordt het CETEX materiaal gekarakteriseerd door middel van uni-axiale quasi-statische trekproeven. De afgeleide waarden van E_{11}, E_{22} and ν_{12} worden vergeleken met de resultaten van de 'resonalyser' methode, die eruit bestaat om de elastische eigenschappen van een materiaal te bepalen op basis van hun eigenfrequenties door een combinatie van experimenten en numerieke simulaties. De resultaten komen heel goed overeen en de lage waarde van de Poissoncoëfficient die werd afgeleid uit de statische proeven, wordt bevestigd. Bovendien worden tijdens deze statische testen de nieuwe observatietechnieken geïntroduceerd, die zullen worden benut in dit doctoraat. Dit zijn enerzijds het gebruik van optische vezelsensoren met een 'Bragg grating' en anderzijds het meten van de elektrische weerstand van het materiaal.

Voor de optische vezelsensoren wordt er eerst geverifieerd of ze het productieproces van de vezelversterkte thermoplast overleven. Deze sensoren zijn reeds succesvol ingebed in epoxies, maar voor het productieproces van thermoplasten zijn doorgaans veel hogere temperaturen en drukken vereist. Echter, de optische vezelsensoren doorstaan deze beproeving zonder al te veel problemen en de eerste (statische) experimenten zijn alvast veelbelovend. Om de ingebedde vezel te visualiseren wordt gebruikt gemaakt van 'X-ray micro-tomografie'.

Er wordt bovendien ook geëxperimenteerd met het extern verlijmen van de optische vezelsensor, om te zien of de sensor ook op deze manier bruikbaar is. Deze werkwijze heeft immers het voordeel dat reeds bestaande componenten toch nog geïnstrumenteerd kunnen worden, aangezien inbedden bij een bestaand onderdeel geen optie meer is. Opnieuw zijn de resultaten veelbelovend.

Voor de elektrische weerstandsmeting wordt een nieuwe manier getest om contact met het proefstuk te maken, namelijk door middel van rivetten. Er zijn twee mogelijke configuraties, met twee contacten of met vier contacten. Die laatste geeft de beste resultaten met betrekking tot de gevoeligheid van het meetsysteem en de stabiliteit van het signaal in de tijd. Bijgevolg wordt de methode met vier contacten geselecteerd voor alle volgende proeven.

Vervolgens worden hysteresisproeven uitgevoerd. Uit de resultaten ervan kan worden afgeleid dat de stijfheid van het materiaal niet vermindert en dat er slechts heel weinig permanente verlenging optreedt. Het verloop van de Poissoncoëfficient daarentegen is veel gevoeliger voor schade dan de twee reeds vermelde parameters, maar het verloop van ν_{12} in functie van de rek ε_{xx} kent een eigenaardige evolutie. Verscheidene proeven worden vervolgens uitgevoerd om uit te zoeken of dit fenomeen te wijten is aan de gebruikte sensoren, maar uiteindelijk kan worden besloten dat dit gedrag inherent is aan de schademechanismen van het materiaal en een analytische verklaring hiervoor wordt aangereikt. Verder geven zowel de optische vezelsensoren als de elektrische weerstandsmeting veelbelovende resultaten onder deze belastingsvorm, zodat beiden ook worden beschouwd voor de vermoeiingsproeven.

Vooraleer echter aan te vangen met deze vermoeiingsproeven, wordt een ontwerp van een stel mechanische klauwen voorgesteld die geschikt zijn voor vermoeiing in trek en druk. In de ontwerpsfase worden een aantal vergelijkingen afgeleid die betrekking hebben op de contactdruk tussen de klauwen en het proefstuk. Met behulp van deze formules kan het probleem van breuk in de tabs worden bekeken. Zowel de "ASTM D3039/D3039M *Standard Test Method for Tensile Properties of Polymer Matrix Composite Materials"* als de "ISO 527-1 *International standard for the determination of tensile properties"* beschrijven het gebruik van tabs voor de proefstukken en beide geven ook een aantal suggesties met betrekking tot tabmateriaal en -geometrie. Desondanks gebeurt het nog vaak dat het proefstuk voortijdig breekt in de klauwen, tussen de tabs, met een onderschatting van levensduur en breuksterkte tot gevolg. De werkelijke spanningsverdeling in het proefstuk tussen en net naast de klauwen wordt met behulp van de eerder afgeleide vergelijkingen gesimuleerd in een eindige-elementenpakket en verschillende combinaties van tabmaterialen en -geometrieën worden beschouwd. Uiteindelijk kunnen een aantal besluiten getrokken worden met betrekking tot het materiaal dat hier bestudeerd wordt.

Vervolgens worden de uni-axiale vermoeiingsproeven uitgevoerd. Net als bij de hysteresisproeven is ook hier geen stijfheidsdegradatie noch permanente vervorming merkbaar, zelfs niet voor een grote variatie aan opgelegde spanningen. De Poissoncoëfficient daarentegen blijkt opnieuw heel wat gevoeliger, maar het is onmogelijk om de evolutie ervan tot het einde van de vermoeiingsproef op te meten, aangezien de dwarse rekstrookjes, nodig voor de meting van de Poissoncoëfficient, loskomen van het proefstuk voordat de breuk optreedt.

De elektrische weerstandsmeting werkt ook heel goed onder de vermoeiingsbelasting, de weerstand volgt duidelijk elke belasting en ontlasting, maar desondanks lijkt hij niet heel gevoelig voor de optredende schade. De optische vezelsensoren, zowel de ingebedde als de externe, overleven de vermoeiingsbelasting en de rekken, bekomen met de sensoren, komen heel goed overeen met de referentierek, afgeleid van de extensometer.

Behalve de reeds vermelde uni-axiale testen horen buigbelastingen en afschuiving ook tot het onderzochte pakket. De spanningstoestand die ontstaat in een buigproef is immers heel interessant: (i) meestal is de werkelijke belastingstoestand ook een vorm van buiging, (ii) de combinatie van trek en druk is een pluspunt voor de validering van eigen materiaalmodellen en (iii) de experimenten op zich zijn redelijk eenvoudig, er kan reeds heel wat afgeleid worden uit het verloop van de kracht en de verplaatsing. Er is echter een nadeel verbonden aan deze opstelling wanneer ze gebruikt wordt om dunne laminaten te beproeven, zoals het materiaal voor deze studie. Hierbij is een vrij grote verplaatsing mogelijk, die de bruikbare frequenties in een vermoeiingsproef beperkt. Voor deze studie wordt er getracht een optimum te vinden tussen enerzijds de experimentele opstelling, zodat grote krachten voor kleine verplaatsingen kunnen worden bekomen en anderzijds de modellering in een eindige-elementenpakket, zodat een eenvoudige simulatie met beperkte rekentijd mogelijk wordt. Daarom worden eerst de standaard driepunts-buigopstelling en een aangepaste versie ervan met roterende opleggingen besproken. Daarna wordt de vierpunts-buigopstelling beschouwd, maar geen van de reeds vernoemde opstellingen lijkt echt de gezochte oplossing te bieden. Daarom wordt er geëxperimenteerd met het inklemmen van de uiteinden van het proefstuk. Dit blijkt geen interessante optie voor de vierpuntsopstelling, maar het was wel de oplossing voor de driepunts-buigopstelling. Er worden hoge krachten bereikt voor kleine verplaatsingen en in een vermoeiingsproef zijn frequenties tot 5 Hz geen enkel probleem, daar waar het maximum bij de standaard driepuntsopstelling reeds ligt bij 2 Hz. Bovendien kan de opstelling eenvoudig in een eindige-elementenpakket geïmplementeerd worden en kost een simulatie niet veel rekentijd.

Voor de belasing in afschuiving worden zowel de ‘three-rail shear test’ als een trektest op een $[(+45°,-45°)]_{ns}$ stapeling beschouwd. De rail shear test wordt normaal gezien enkel gebruikt voor statische proeven, dus een nieuw ontwerp dat ook geschikt is voor vermoeiingsbelasting wordt voorgesteld. Dit nieuwe ontwerp houdt het proefstuk vast door middel van wrijving en een vorm van geometrisch inklemmen. Bijgevolg is er niet langer de noodzaak om gaten te maken in het proefstuk, wat uiteraard voordelig is. Aangaande het proefprogramma worden allereerst een reeks experimenten besproken die nagaan of de door de klemmen geïnduceerde belasting enerzijds symmetrisch is en anderzijds of er geen buiging of knik optreedt, overigens met goed resultaat. Hierna worden verscheidene statische, cyclische en vermoeiingsproeven uitgevoerd om een inzicht te krijgen in het materiaalgedrag. De beschouwde belastingen worden ook opgelegd aan de $[(+45°,-45°)]_{ns}$ stapeling en de resultaten tussen beide testopstellingen komen heel goed overeen. Het materiaal ondervindt een stijfheidsdegradatie en ontwikkelt heel wat permanente vervorming en tijdens de vermoeiingsproeven is er een opmerkelijke temperatuursstijging merkbaar net voor het einde van de proef, de temperatuur wordt zelfs hoger dan de verwekingstemperatuur van de thermoplast.

Hierna wordt een reeds bestaand materiaalmodel, gebaseerd op stijfheidsdegradatie en de opbouw van permanente glijding, herbekeken. Met behulp van de gegevens die kunnen worden afgeleid uit de experimenten worden de vier materiaalconstanten geoptimaliseerd en vervolgens wordt het model geïmplementeerd in het eindige-elementenpakket. Daarna worden de statische proeven gesimuleerd en de resultaten blijken heel goed overeen te komen met de experimenten. Als laatste validatie van het materiaalmodel wordt een driepuntsbuigproef op een $[(+45°,-45°)]_{4s}$ proefstuk uitgevoerd en gesimuleerd, en opnieuw vertonen de resultaten een goede overeenkomst.

Ten slotte worden dan de belangrijkste conclusies nog eens herhaald en worden suggesties voor verder onderzoek voorgesteld.

ENGLISH SUMMARY

Fibre-reinforced thermoplastics are finding more and more applications in the industry. For example, each new commercial aircraft Airbus A380 has 6 tons of fibre-reinforced thermoplastics. However, the mechanical behaviour of these materials is not yet well understood, especially under fatigue loading conditions. It is the purpose of this doctoral thesis to investigate the behaviour of these types of materials under fatigue loading conditions and to provide new techniques to monitor structures made of fibre-reinforced thermoplastics. Since this family of materials is quite large, only one material is selected to represent its family, namely a carbon fabric reinforced polyphenylene sulphide.

First, the material is characterised using uni-axial quasi-static tensile tests. The values of E_{11}, E_{22} and ν_{12} are derived and compared with the results from 'resonalyser' experiments. The latter is a combined experimental-numerical method for the estimation of elastic properties of a material and the principle is based on determining the resonance frequencies of the test specimen. It could be concluded that the results correspond well and the low value of the Poisson's ratio, derived from the static tests, was confirmed. These static tests are also used to experiment with the monitoring techniques, which will be used in this doctoral research: (i) optical fibre sensors with Bragg gratings and (ii) electrical resistance measurement.

With respect to the optical fibre sensors, it was first established whether they survive the embedding process in the reinforced thermoplastics. These sensors had already been embedded in epoxies, but the production processes used for processing thermoplastics usually require higher pressures and temperatures. However, the optical fibre sensors survive the embedding process and the first experiments yield very promising results. The embedded optical fibre was visualised using X-ray micro-tomography.

Experiments were also conducted on bonding an optical fibre externally to a specimen, to verify whether the sensor could also be used in this way. This has the advantage that if a strain measurement is required, but the part is already manufactured, meaning that embedding a fibre is no longer an option, the optical fibres can still be used. Again, promising results were achieved.

With respect to the electrical resistance measurement, a new way of establishing contact is attempted: the use of rivets. Two setups were assessed, the two-probe and the four-probe method. The latter had the most promising results with regards to sensitivity and time-stability, so this was chosen for future tests.

Next, hysteresis experiments are conducted, from which it can be concluded that the chosen material exhibits no stiffness degradation and only limited permanent deformation. The evolution of the Poisson's ratio is much more sensitive to damage than the two previous parameters, but the ν_{12}-ε_{xx} curve has a peculiar shape.

Various experiments were performed to verify whether this was caused by the material itself or by the used sensors. Eventually, it was concluded that this was inherent to the damage mechanics of the material and an analytical explanation is given. Both the optical fibre sensors and the electrical resistance measurement yield very promising results with respect to fatigue loading conditions, so both are considered for the fatigue experiments.

Prior to performing fatigue experiments, a set of mechanical grips was designed, suited for tension and compression fatigue. During this design, formulations with respect to the contact pressure inside the grips were derived. Using these, the problem of end tab failure is discussed. Both the "ASTM D3039/D3039M *Standard Test Method for Tensile Properties of Polymer Matrix Composite Materials"* and the "ISO 527-1 *International standard for the determination of tensile properties"* prescribe the use of end tabs for fatigue experiments and give certain recommendations, but still the specimen fails quite often in the grips, leaving an underestimation of the failure stress and fatigue lifetime. The occurring loading condition of the specimen near the end tabs is simulated using finite element software and various combinations of materials and geometries are considered. Conclusions with respect to the chosen material for this research are drawn.

Then, the uni-axial tension-tension fatigue experiments were conducted. Similar to the hysteresis experiments, no stiffness degradation was found and only limited permanent deformation occurred for a wide range of stresses. The Poisson's ratio was more sensitive, but it proved impossible to measure this parameter until failure, since the transverse strain gauges, necessary for this measurement, de-bonded prior to failure. The electrical resistance measurement works excellently under these loading conditions, it can clearly follow the loading cycles, but apparently it is not very sensitive to the occurring damage during these tests. With respect to the optical fibre sensors, both the embedded and the externally bonded survive the fatigue loading conditions and the derived strain corresponds very well with the strain measurement, done with the extensometer.

Besides the already described uni-axial tests, bending and in-plane shear loading conditions were also investigated. The loading conditions in a bending test are very interesting: (i) the in-service loading conditions are usually bending, (ii) the combination of tension and compression is interesting for validating self-defined material models and (iii) the experiments are fairly easy, the evolution of the force and displacement can already give a lot of information. However, for the thin laminates, such as the material under study, the large midspan displacements that can be reached, tend to limit the frequency range that can be used for fatigue experiments. Here, it was attempted to optimise both the experimental setup, to have high forces for low midspan displacements, and the finite element model of the setup, to have an easy and fast calculating simulation.

As such, first the standard three-point bending setup and a modified version with rotating supports are discussed. Then four-point bending is considered, but none of the above really provided the solution which was looked for. Therefore, experiments were done with clamping the ends of the specimen. This did not work for the four-point setup, but proved a promising solution for the three-point setup; high forces for low midspan displacements were found, fatigue frequencies till 5 Hz were no problem, while 2 Hz was the maximum for the standard three-point setup and the finite element model was both simple and required limited computation time.

For the in-plane shear loading conditions, both the three-rail shear test and the $[(+45°,-45°)]_{ns}$ tensile test were considered. Since the three-rail shear test is normally only used under quasi-static conditions, a new design of this setup, suited for fatigue loading conditions, is presented. This new design uses frictional and geometrical clamping and as such rules out the need for drilling holes through the specimen. First, a series of experiments were conducted to verify whether this new setup induced a symmetrical load distribution, without bending or buckling the specimen, with good results. Then, various quasi-static, cyclic and fatigue experiments were performed to determine how the chosen material behaves under these in-plane shear loading conditions. All of these results were compared with corresponding $[(+45°,-45°)]_{ns}$ tensile tests, with good agreement. The material exhibits stiffness degradation and a significant amount of permanent deformation occurs. During the fatigue experiments, a significant temperature increase, exceeding the softening temperature of the matrix, was noted just prior to failure of the specimen.
Then, an existing damage model, based on the stiffness degradation and permanent deformation, is presented. This is implemented in the finite element software and using the data obtained from the static and cyclic in-plane shear tests, the four material constants could be optimised. Next, the static tests are simulated, with very good results. For a final validation of the material model, a three-point bending experiment on a $[(+45°,-45°)]_{4s}$ specimen is considered. Again, both the experimental and numerical results show good agreement.
Finally, the most important conclusions are repeated and some ideas for future research are given.

TABLE OF CONTENTS

LIST OF SYMBOLS

E_{11}	Stiffness of the lamina in the warp (0°) direction
E_{22}	Stiffness of the lamina in the weft (90°) direction
E_{xx}	Stiffness along the longitudinal axis of the specimen
E_{yy}	Stiffness along the transverse axis of the specimen
F	Measured force obtained from the tensile machine
G_{12}	Shear stiffness of the composite
h	Height of the three-rail shear specimen
S_T	Ultimate shear strength of the composite
t	Thickness of the specimen
w	Width of the tensile specimen
X_T	Ultimate tensile strength of the composite in the warp (0°) direction
Y_T	Ultimate tensile strength of the composite in the weft (90°) direction
ε_i	Strain obtained from strain gauge i in the three-rail shear test
ε_{xx}	Longitudinal strain in the tensile specimen
ε_{yy}	Transverse strain in the tensile specimen
ε_{11}	Strain along the warp (0°) direction
ε_{22}	Strain along the weft (90°) direction
ε_{33}	Strain perpendicular to the lamina
ε_{11}^{ult}	Ultimate strain in the warp (0°) direction
ε_{22}^{ult}	Ultimate strain in the weft (90°) direction
γ_{12}	Shear strain
ν_{12}	Poisson's ratio of the lamina
ν_{xy}	Poisson's ratio of the laminate
σ_{11}	Stress along the warp (0°) direction
σ_{22}	Stress along the weft (90°) direction
σ_{33}	Stress perpendicular to the lamina
σ_{xx}	Stress along the longitudinal axis of the tensile specimen
σ_{yy}	Stress along the transverse axis of the tensile specimen
σ_{zz}	Stress perpendicular to the laminate
τ_{12}	Shear stress

Chapter 1

INTRODUCTION

In this chapter, it is explained what the reader could expect in this doctoral thesis. First, a general introduction is given on the material family of which the studied material is part of, namely the fibre-reinforced polymers. This is followed by the scope of this research, after which a brief overview of the manuscript is given. Finally, the industrial relevance of the research is commented on.

1. 1. COMPOSITE MATERIALS & FIBRE-REINFORCED MATERIALS

Composite materials are materials that consist of two or more clearly distinctive phases. They are as such heterogeneous materials and in most cases they are also non-isotropic. In everyday life, composite materials are all around us, for example in car tires, in floor panels in an airplane, in casings of our computers… Figure 1-1 illustrates other examples of where these materials are used. Composite materials, however, are not 20th century inventions; all over the world, natives have been using straw and twine to reinforce the walls of huts and houses for as long as they can remember.

Figure 1-1 A selection of applications for composite materials.

Which materials to combine, depends on the application that one has in mind. Higher thermal or electrical conductance or resistance, a smaller density, better strength properties, a different colour or appearance…

A subgroup of this material family is formed by the fibre-reinforced plastics, where reinforcement fibres are embedded in a plastic matrix. The goal is a material which has a lower density combined with better strength and stiffness properties. These materials are in general no longer isotropic and the orientation of the fibres determines the mechanical behaviour. Furthermore, these composites often have a layered lay-up and each layer may have a different fibre orientation, depending on its application.

The materials that are mostly used for the reinforcing fibres are glass, carbon and aramid, although other materials such as steel or cotton are possible.
For the matrix, there are two classes of materials: the thermosetting polymers, such as epoxy, unsaturated polyester, vinylester …, and the thermoplastic polymers, such as polypropylene (PP), polyether-ether ketone (PEEK), polyphenylene sulphide (PPS) … One of the main differences between the two is their thermal behaviour. If the temperature is raised, the solid thermoplastic melts again, whereas the solid thermosetting polymer disintegrates.

Finally, Figure 1-2 shows a typical lay-up for a pultruded profile. In the centre of the profile, continuous fibres are used for strength. These are surrounded by a woven mat, which inhibits splitting of the profile and of course, the entire profile is impregnated with an epoxy matrix.

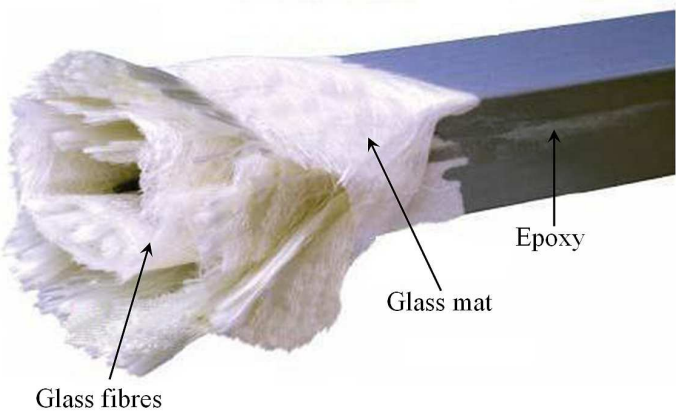

Figure 1-2 Illustration of the typical composition of a pultruded composite profile [1].

For more information on composite materials and fibre-reinforced materials, the author refers to [2, 3].

1. 2. AIM AND SCOPE OF THIS RESEARCH

Until recently, thermosetting polymers reinforced with carbon or glass fibres were often chosen for heavy duty construction parts, since they have a high stiffness combined with a low weight.
One important disadvantage of this type of composites is their sensitivity for delaminations and as a result, their low resistance against impact damage. This is due to the low fracture toughness of the thermosetting matrix: the energy needed for the nucleation and growth of cracks is relatively low [4, 5].
Therefore, in the last few years, better thermoplastic materials have been developed as matrix for the fibre-reinforced materials, which have higher fracture toughness than the thermosetting materials. The sensitivity for delaminations and impact damage is therefore much lower than for the classical thermosetting polymers.
Other aspects in favour of thermoplastic matrices are [6, 7]:

- They are easier to recycle than the thermosetting materials, although for composites this is only a theoretical advantage. It remains complicated to separate the fibres from the matrix. In most cases, a composite part is crushed and grinded into small granulates, which can be re-used in injection moulding techniques. The remark needs to be made that the re-melting and re-solidifying tends to decrease the quality of the thermoplastic. So the recycled material should be used for specifications with lesser demands for strength, stiffness and quality in general than the pre-recycle application.
- Thermoplastics can withstand higher temperatures than the thermosetting polymers [4].
- The production processes with thermoplastics are better suited for automation than the ones with thermosetting materials.
- The weldability of thermoplastics.
- Their very long (infinite) storage life.
- Their high chemical inertness.

Still, the use of fibre-reinforced thermoplastics in load bearing structural applications is very limited. The conservatism of the technical community is large because of the complex mechanical behaviour of these materials, for example under long duration or fatigue loading conditions [5, 8]. The material has a visco-elastic nature and shows some unwanted aspects. For instance, under long duration loading, the material is susceptible to creep, especially at elevated temperature and under cyclic loading conditions, the temperature of the specimen can rise significantly, up to 100 ºC and more [9, 10], depending on the loading amplitude and frequency.

It is the aim of this doctoral research to increase the technical community's confidence in the use of fibre-reinforced thermoplastics for cyclic-load bearing parts. In order to do so, this dissertation has the following objectives:

(i) To modify existing test rigs and develop new setups, better suited for fatigue experiments on fibre-reinforced composites.

(ii) To find better finite element implementations of the boundary conditions, when simulating experiments on composite components.

(iii) To find one or more monitoring techniques which are applicable not only to the material chosen for this thesis, but for a broad group of carbon-reinforced thermoplastics. These monitoring techniques should provide a higher confidence in the (failure) behaviour so that structural parts could be used closer to their limits, without the risk of unexpected problems or failures.

(iv) To gain a better understanding of the macroscopic mechanical behaviour of the selected material for this thesis under various fatigue loading conditions.

Hence, this doctoral study is about conducting and monitoring of different types of quasi-static and fatigue experiments on continuous fibre-reinforced thermoplastics, used for load-bearing parts in structural applications, as well as about the developing of better test setups and the accurate finite element modelling of those setups. There is a growing necessity for this kind of research since currently, a lot of research has been done on the chemical behaviour of the thermoplastic composites, such as the effect of temperature, pressure and cooling speed on the crystallinity, the chemical composition, the adhesion with the fibres … [11-14]. However, very little is known about the dynamic behaviour and more specifically about the behaviour under fatigue loading conditions [5, 9] of these continuous fibre-reinforced thermoplastics. Since the family of fibre-reinforced thermoplastics is quite large, only one material was selected as test material, namely a carbon fabric-reinforced polyphenylene sulphide. It was chosen because of its industrial relevance. This material is already quite commonly used for applications in the aeronautical industry, both by Boeing and Airbus [15, 16]. However, it is attempted to design such experimental setups, both for monitoring as for testing, that they are applicable to other reinforced thermoplastics as well.

It should be mentioned that developing constitutive equations to model the material behaviour under fatigue loading conditions is not the main focus and therefore, techniques such as C-scan, SEM and microscopy to evaluate microscopic damage in detail, are not considered. The emphasis lies on a thorough understanding of different test setups and monitoring systems, applicable for a large family of reinforced thermoplastics, rather than studying the (micro-)mechanical behaviour of one specific material. Therefore, no micro-mechanical research is presented here.

1. 3. INNOVATIVE ASPECTS OF THIS RESEARCH

When discussing fatigue behaviour in literature, it appears that damage usually starts already at the very beginning of the experiment and shows a gradual increase up to failure [17-21], contrary to what happens in metals.
Also, with thermoplastic matrices, heat generation at elevated loading frequencies may occur [8, 10]. With this in mind, the author considers a number of experimental setups so that different load distributions can be imposed separately or combined. As such, the relation between, for instance shear loading and temperature increase, can be established.

The following experimental setups are considered in this research:

- The uni-axial tensile test
- The bending test
- The three-rail shear test

The uni-axial tensile test is quite common and test procedures are well documented in the ASTM standards D3039/3039M "*standard test method for tensile properties of polymer matrix composite materials*" and D3479/D 3479M "*standard test method for tension-tension fatigue of polymer matrix composite materials*" so that no real difficulties with the setup itself are expected. However, this doctoral study pays special attention to a correct introduction of the loads in the specimen and therefore presents a new design of a set of mechanical clamps, suited for both tension and compression fatigue. This design has extra long wedge grips, which allow the use of long tabs or any other fixtures at the end of the specimen, e.g. optical fibres or contact electrodes for electrical resistance measurement. To the author's best knowledge, such a mechanical design with those features has not been presented yet. Furthermore, the stress concentrations in the tabbed ends of the specimen are investigated. Although similar studies exist [22-24], the implemented loads are usually based on equilibrium of the part under consideration, whereas here, the actual occurring grip pressure is calculated and verified.

Bending experiments are not widely excepted as a standard, although they are used quite commonly for research purposes [25-27]. Therefore, this setup is considered here as well. There are, however, some known problems when using the bending setup for thin composite laminates [28]. This thesis discusses both the three-point and the four-point bending setup and pays special attention to the correct finite element implementation of the setup and the corresponding boundary conditions in order to find a solution for these known problems.

A combined optimization of both the experimental setup and its numerical implementation results in a new design of a three-point bending setup with clamped ends, suited for fatigue testing and modelling.

The three-rail shear test is normally only used for quasi-static experiments, such as described in the ASTM D4255/D 4255M "*standard test method for in-plane shear properties of polymer matrix composite materials by the rail shear method*". The current research presents a new design of this setup, which no longer needs drilling holes through the specimen and which is suited for conducting fatigue experiments. To the author's best knowledge, such a design has not yet been presented.

In developing and interpreting the above-mentioned setups, the finite element modelling plays an important role. First, this study assesses each test rig numerically to verify whether it can withstand the highest fatigue loading conditions possible, with respect to the used materials. Second, finite element simulations will also be used here to simulate an actual test, to see how the material will react in the given test setup. As such, the experimental setup can be adjusted during the design in order to obtain an optimum concerning (i) imposed loading conditions, (ii) easy measurable and significant experimental parameters and (iii) easy and fast finite element simulations. The last point is quite important if the setup is simulated with user defined material models. Indeed, what is the point of a very interesting load distribution for validating damage models, when the corresponding finite element model is very complicated and requires a lot of computation time for a converging solution? Furthermore, this research emphasises the correct implementation of boundary conditions.

Since monitoring experiments and material behaviour is another issue of this research, a wide variety of sensors is used. Of course, the commonly used sensors, such as load cells, extensometers, strain gauges and thermocouples are not omitted.
By interpreting the data given by these sensors, this thesis will already give some insight in the material behaviour. Effects such as stiffness degradation, permanent deformation, hysteresis loops and temperature increase are commented on. However, there is still more to explore and therefore, other sensors, of which some are fairly new (with respect to the material under investigation), are used to gain a better understanding of the material behaviour and to determine how they can be further improved with respect to the used material.

These monitoring systems include:

- The Poisson's ratio: its evolution is known to be more sensitive to damage than the degradation of Young's modulus or the growth of permanent elongation [29-33]. Therefore, it is assessed whether this conclusion still holds (i) for the material under study and (ii) under fatigue loading conditions. Measuring the Poisson's ratio till failure under these loading conditions is quite cumbersome. Therefore, new ways of measuring the (small) transverse strain are presented and assessed. Furthermore, the evolution of the Poisson's ratio as function of the longitudinal strain has a peculiar shape. To the author's knowledge, this has not been published before and normally, only the value of the Poisson's ratio at maximum elongation is monitored during cyclic and fatigue experiments. This doctoral study not only offers an explanation for this peculiar behaviour, but studies the effects of fatigue on the entire evolution of the Poisson's ratio as function of the longitudinal strain.
- Optical fibre sensors with Bragg grating: they are already commonly used for strain measurements in reinforced epoxies [34-37], but only one study was found which uses optical fibres with Bragg gratings embedded in a thermoplastic matrix under fatigue loading conditions, and in this case, the sensor was used for temperature monitoring, rather than strain monitoring [38]. This research investigates whether the optical fibre sensors with Bragg grating can be used for strain measurements in reinforced thermoplastics under fatigue loading conditions. First of all, it is examined whether the fibres survive the harsh conditions of the production process of the test samples (higher pressure and temperature than with epoxies). Then, the behaviour of the combination sensor-material under static and fatigue loading conditions is assessed and recommendations for improving the sensors and their data acquisitions system will be suggested.
- Electrical resistance measurement: since carbon fibres conduct electricity, the electrical resistance of a specimen can be used to quantify the level of damage in a carbon-reinforced composite [39-42]. The latter has already been done successfully, but only for unidirectional reinforced polymers and occasionally for cross-ply laminates, since the sensitivity of this technique decreases if more transverse current paths are present [43]. Therefore, this thesis investigates whether the measurement of the electrical resistance can supply valuable information on the state of damage in the fabric-reinforced composite under study, first under static loading conditions and then, under fatigue loading conditions. Special attention is given to the experimental setup to achieve high sensitivity and time-stability.

This work has resulted in 16 accepted SCI publications. For a complete list of all publications, please see the section "About the author" at the end of this thesis.

1. 4. OVERVIEW OF THIS MANUSCRIPT

In chapter 2, an overview is given on all the tools used for conducting, monitoring and simulating the (fatigue) experiments. The material chosen for this doctoral research, a carbon fabric-reinforced polyphenylene sulphide, is commented on. For some damage monitoring techniques, it was more convenient to test it first on another material, namely a unidirectional glass fabric-reinforced epoxy. Therefore, this material is also documented in chapter 2.

The following three chapters describe all uni-axial experiments with the loads applied along the fibre direction. In chapter 3, the material is characterised by means of quasi-static loadings till failure. The mechanical properties are determined by tensile tests and verified with the 'resonalyser' technique, which uses the resonance frequencies of the test samples and finite element modelling in order to predict the mechanical properties. Next, all monitoring techniques, used for the following two chapters, are introduced and assessed. These sensors include standard strain gauges and an extensometer for strain measurement, optical fibre sensors with Bragg gratings and since the reinforcement is carbon, the principle of electrical resistance measurement is also introduced.

Preliminary tests have shown that the standard extensometer has some drawbacks, so a number of improvements are suggested and used for the remainder of the research. For the optical fibres, both embedded and externally bonded fibres are considered and experimented with. In order to visualise the correct location and alignment of the embedded fibre, X-ray micro-tomography is used. Finally, two different setups for measuring the electrical resistance are assessed, after which only one is deemed suited for monitoring fatigue experiments.

In chapter 4, the next step towards fatigue loading conditions is taken. Cyclic quasi-static tests are performed up to a certain load level in order to induce a certain level of damage. Then, it is assessed whether the proposed monitoring techniques are able to detect the possible damage and their sensitivity is determined. Besides the commonly used damage characterisation parameters such as the degradation of Young's modulus and the development of permanent deformation, special attention is given to the evolution of the Poisson's ratio. This parameter is determined using strain gauges, external optical fibre sensors and a transversely mounted modified extensometer.
Of course, the electrical resistance measurement is also assessed during these hysteresis tests.

Finally, the uni-axial fatigue experiments with the load applied along the fibre direction are described in chapter 5. A similar order as in chapter 4 is maintained, but first, some known difficulties which occur when conducting tensile fatigue experiments are dealt with. Since a good introduction of the fatigue load begins with the correct gripping, a new design of a set of mechanical grips, suited for both tension and compression fatigue is presented. The next issue is the use of end tabs on the specimen for the load introduction. The purpose is not to repeat everything that has already been done on the subject of end tabs, but because of the difficulties with adhesive bonding of PPS, a good understanding of the behaviour of the end tab section of the specimen is necessary. Using some of the equations derived during the design of the grips, the problem of end tab failure of the specimen is examined with finite element models. Then, the conducted experiments are discussed.
First, the commonly used procedure of monitoring stiffness degradation and the development of permanent deformation is assessed. During these experiments, boundaries for the loading frequencies and stress ranges, which seem the most promising for the purpose of this research, are determined.
Because of the promising results of the evolution of the Poisson's ratio during hysteresis loadings, this parameter is again considered under fatigue loading conditions. For the optical fibre sensors, both embedded and externally bonded, it is investigated whether they can survive the numerous fatigue loading cycles, which would mean that they are an interesting alternative for the strain gauges under these conditions. Finally, the electrical resistance of the specimen is monitored throughout the entire fatigue test to evaluate whether it is able to detect the occurring fatigue damage.

In chapter 6, a bending setup is investigated for conducting fatigue experiments on the thin composite laminate. Both experimental and numerical advantages and disadvantages are discussed. Most of these problems are related with the fact that the thin laminate can withstand very large displacements, while yielding only a small reaction force. First, both the standard three-point bending setup and a modified version with rotating supports are presented.
Due to various disadvantages, all caused mainly by the low bending stiffness of the used material, rather than the experimental setup itself, improvement is sought in a four-point bending setup. However, this does not seem to solve all problems, so a different approach is presented: clamping the ends of the specimen in a bending setup. Although this solves a number of experimental problems of the four-point setup, it now induces failure at the clamped edges.
However, for the three-point setup, this approach seems to be the right one. Various disadvantages of the standard three-point setup, both experimentally and numerically, are solved, although still some small issues need to be dealt with.

Chapter 7 summarises all experiments related to in-plane shear loading conditions. A modified design of the standard three-rail shear test setup is presented. With respect to the loading conditions, a similar approach as for the uni-axial tests is used. First quasi-static experiments were performed to evaluate the modified design and to assess whether the introduced load is pure shear, meaning that the setup induces a symmetrical load without bending or buckling. This is followed by hysteresis tests, which will be used to model the material behaviour under shear loading conditions. Finally, fatigue loads are imposed, both to assess the behaviour of the grips and to study the material behaviour under these loading conditions. In order to validate all results obtained with the three-rail shear test, all loading conditions were also implemented for uni-axial tensile tests with a $[(+45°,-45°)]_{ns}$ stacking sequence, which are commonly used to study the in-plane shear behaviour; all results were compared with those from the three-rail shear test.
Chapter 8 handles the modelling of the in-plane shear behaviour. First, it is explained how to perform simulations with user defined models in the used finite element software. Then, the quasi-static loading conditions are modelled. Rather than developing a new model, a previously derived model, which was developed for modelling the in-plane shear behaviour of a unidirectional glass fibre-reinforced epoxy, is implemented. This model uses the shear stiffness degradation and the development of permanent shear strain and it is proven in this chapter that such approach may be considered applicable to a wide range of materials.
Indeed, simply by optimising the four material constants, very good agreement between the experiments and the finite element simulations is achieved.

The data necessary for the optimisation of the material model and the comparison with the finite element simulations are derived from chapter 7. For a final validation, a three-point bending test is done and simulated, using the material model.

Finally, chapter 9 summarises the most important facts that could be remembered after reading this doctoral study. Based on the various encountered problems and the conclusions, a number of suggestions are made for future research. Also, the theme for the author's intended post-doctoral research, which is closely related to the subject of this research, is introduced.

1. 5. INDUSTRIAL RELEVANCE

The significance of composites in aircraft structures continues to increase. In 1980, only 8% of the materials used for the A300/A310 were composites, both thermosetting and thermoplastic materials. Twenty years later, this share has almost doubled to 15% for the A340 500/600. For the Airbus A380, 20% is now composite material and by 2010, this share is expected to have doubled [15].
Currently, the share of continuous fibre-reinforced thermoplastics is growing in aircraft structures. Figure 1-3 illustrates some of the 'high-performance' parts in the A340-500/600 for which fibre-reinforced thermoplastics where chosen, for instance stiffeners, the leading edge of the wing, pylons of the turbines …

Figure 1-3 CETEX® applications in the A340-500/600 (courtesy of Ten Cate Advanced Composites).

In the following years, even more thermoplastics will be used, as is shown by the composite programs for the Airbus A380 and A350 [44]. Figure 1-4 illustrates for which applications thermoplastic composites can be used.

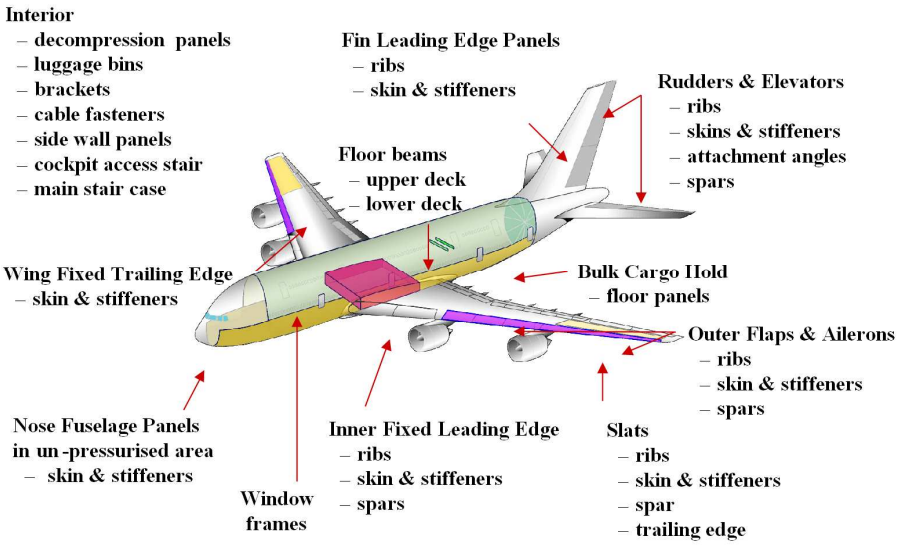

Figure 1-4 Applications of thermoplastics in aircraft structures (courtesy of Ten Cate Advanced Composites).

Bernd Räckers, leader of the research team at Airbus Deutschland, reports that in each new civil aircraft Airbus A380 there are around six tons carbon fibre-reinforced thermoplastics incorporated in elements such as stiffeners in the wings, the fuselage, … but due to the lack of better design methods, the fatigue characteristics are very conservative [16]. Each part is designed using static methods, but with a very large safety factor, so that an import advantage of composites, namely low weight, is lost. This emphasises the need to better understand the material behaviour, so that the safety factors in the design can be chosen more in relation with the actual risk. In this research, various fatigue experiments under several load cases, such as uni-axial tension-tension, bending and in-plane shear are illustrated in order to gain a better understanding of the failure behaviour of the used material.

Another aspect that could reduce the safety factors, without reducing the safety, is to constantly evaluate the (damage) state of the material. Of course various non-destructive evaluation methods, such as ultrasound, radiography, thermography … are available, but they cannot be done real-time, while the structure is in use, for instance on a flying airplane. Therefore, if adequate real-time (damage) monitoring systems are at hand, the composite materials could be used closer to their limits, without loosing confidence in the structural behaviour. If anything should go wrong, it could be detected in time, and adequate precautions for further use of the structure till the next (obligatory) maintenance could be taken.

In this research, it is attempted to provide such real-time sensors, namely the electrical resistance measurement, used mainly for monitoring structural health and the optical fibre sensors, used mainly for monitoring the deformation of the structure.

With respect to the use of embedded optical fibres, both the Airbus Company and FOS&S, the company which has given its full support for all experiments concerning the optical fibre sensors, are very interested in using the optical fibre sensors as embedded strain sensors for the new Airbus airplanes [45].

1. 6. REFERENCES

[1] http://www.gdpkoral.cz/what-are-composite-materials/w15, 30/01/2008

[2] Degrieck, J. (2003) Composites I , Faculty of Engineering, Ghent University.

[3] Degrieck, J. (2003) Composites II , Faculty of Engineering, Ghent University.

[4] Brent Strong, A. (1993). High performance and engineering thermoplastic composites. Lancaster, Technomic Publishing Company.

[5] Lee, C.-H. and Jen, M.-H.R. (2000). Fatigue response and modelling of variable stress amplitude and frequency in AS-4/PEEK composite laminates. Part 1: Experiments. JOURANL OF COMPOSITE MATERIALS, 34(11), 906-929.

[6] Cogswell F.N. Thermoplastic aromatic polymer composites. A study of the structure, processing and properties of the carbon fibre reinforced polyetheretherketone and related materials. Oxford: Butterworth-Heineman; 1992;

[7] Johnston N.J. Towel T.W. and Hergenrother P.M. Physical and mechanical properties of high-performance thermoplastic polymers and their composites. In: Carlsson L.A., editor. Thermoplastic composite materials. Amsterdam: Elsevier Science Publishers B.B.: 1991. p. 27-71.

[8] Lowe, A.C., Moore, D.R. and Robinson, I.M. (1994). Data for designing with continuous-glass-fibre-reinforced polypropylene. COMPOSITES SCIENCE AND TECHNOLOGY, 52, 205-216

[9] Kenny, J.M. and Marchetti, M. (1995). Elasto-plastic behavior of thermoplastic composite laminates under cyclic loading. COMPOSITE STRUCURES, 32, 375-382.

[10] Xiao, X.R. (1999). Modeling of load frequency effect on fatigue life of thermoplastic composites. Journal of Composite Materials, 33(12), 1141-1158.

[11] Blundeu, D.J. and Osborn, B.N. (1985). Crystalline morphology of the matrix of PEEK-carbon fiber APC-2 crystallization behaviour", SAMPE Quarter, 17(1), p. 420.

[12] Lee, Y. and Porter, R.S. (1986). Crystallization of PEEK in carbon fiber composites", POLYMER ENGINEERING SCIENCE, 26, p. 633.

[13] Cebe, P., Hong, S.-D., Chung, S. and Gupta, A. (1987). Mechanical properties and morphology of Poly(etheretherketone). In: Johnson, N.J. (ed.). Toughened composites. ASTM STP 937, Philadelphia, American Society for Testing and Materials, p. 342.

[14] Beehag, A. and Ye, L. (1996). Role of cooling pressure on interlaminar fracture properties of commingled CF/PEEK composites. COMPOSITES PART A, 27, p.175.

[15] Private communication with Van Dreumel W, former CEO of Ten Cate.

[16] Raeckers, B. (2002). Application of advanced composites in the aeronautical industry. Proceedings of the Tenth European Conference on Composite Materials (ECCM-10), Brugge, Belgium, 3-7 June 2002.

[17] Schulte, K., Baron, Ch., Neubert, H., Bader, M.G. , Boniface, L., Wevers, M., Verpoest, I. and de Charentenay, F.X. (1985). Damage development in carbon fibre epoxy laminates : cyclic loading. In : Proceedings of the MRS-symposium "Advanced Materials for Transport", November 1985, Strassbourg, 8 p.

[18] Schulte, K., Reese, E. and Chou, T.-W. (1987). Fatigue behaviour and damage development in woven fabric and hybrid fabric composites. In : Matthews, F.L., Buskell, N.C.R., Hodgkinson, J.M. and Morton, J. (eds.). Sixth International Conference on Composite Materials (ICCM-VI) & Second European Conference on Composite Materials (ECCM-II) : Volume 4. Proceedings, 20-24 July 1987, London, UK, Elsevier, pp. 4.89-4.99.

[19] Schulte, K. (1984). Stiffness reduction and development of longitudinal cracks during fatigue loading of composite laminates. In : Cardon, A.H. and Verchery, G. (eds.). Mechanical characterisation of load bearing fibre composite laminates. Proceedings of the European Mechanics Colloquium 182, 29-31 August 1984, Brussels, Belgium, Elsevier, pp. 36-54.

[20] Highsmith, A.L. and Reifsnider, K.L. (1982). Stiffness-reduction mechanisms in composite laminates. In : Reifsnider, K.L. (ed.). Damage in composite materials. ASTM STP 775. American Society for Testing and Materials, pp. 103-117.

[21] Masters, J.E. and Reifsnider, K.L. (1982). An investigation of cumulative damage development in quasi-isotropic graphite/epoxy laminates. In : Reifsnider, K.L. (ed.). Damage in composite materials. ASTM STP 775. American Society for Testing and Materials, pp. 40-62.

[22] Kulakov VL, Tarnopol'skii YM, Arnautov AK, Rytter J, Stress-strain state in the zone of load transfer in a composite specimen under uniaxial tension. MECHANICS OF COMPOSITE MATERIALS 40 (2): 91-100 MAR-APR 2004.

[23] Portnov, G. G., Kulakov, V. L., Arnautov, A. K., A refined stress-strain analysis in the load transfer zone of flat specimens of high-strength unidirectional composites in uniaxial tension - 1. Theoretical analysis. MECHANICS OF COMPOSITE MATERIALS 42 (6): 547-554 NOV-DEC 2006.

[24] Portnov, G. G., Kulakov, V. L., Arnautov, A. K., A refined stress-strain analysis in the load transfer zone of flat specimens of high-strength unidirectional composites in uniaxial tension - 2. Finite element parametric analysis. MECHANICS OF COMPOSITE MATERIALS 43 (1): 29-40 JAN-FEB 2007.

[25] Sedrakian, A., Ben Zineb, T., Billoet, J.L., Sicot, N. and Lardeur, P. (1997). A numerical model of fatigue behaviour for composite plates: application to a three point bending test. In : Degallaix, S., Bathias, C. and Fougères, R. (eds.). International Conference on fatigue of composites. Proceedings, 3-5 June 1997, Paris, France, La Société Française de Métallurgie et de Matériaux, pp. 415-423.

[26] Sidoroff, F. and Subagio, B. (1987). Fatigue damage modelling of composite materials from bending tests. In : Matthews, F.L., Buskell, N.C.R., Hodgkinson, J.M. and Morton, J. (eds.). Sixth International Conference on Composite Materials (ICCM-VI) & Second European Conference on Composite Materials (ECCM-II) : Volume 4. Proceedings, 20-24 July 1987, London, UK, Elsevier, pp. 4.32-4.39.

[27] Caprino, G. and D'Amore, A. (1998). Flexural fatigue behaviour of random continuous-fibre-reinforced thermoplastic composites. COMPOSITES SCIENCE AND TECHNOLOGY, 58, 957-965.

[28] Van Paepegem, W., De Geyter, K., Vanhooymissen, P. and Degrieck, J. (2006) Effect of friction on the hysteresis loops from three-point bending fatigue tests of fibre-reinforced composites. COMPOSITES STRUCTURES, Volume 72 issue 2, 212-217.

[29] Gao F., Boniface L., Ogin S.L., Smith P.A. and Greaves R.P., Damage accumulation in woven-fabric CFRP laminates under tensile loading: Part 1. Observations of damage accumulation. COMPOSITES SCIENCE AND TECHNOLOGY 59 (1): 123-136 1999.

[30] Surgeon M., Vanswijgenhoven E., Wevers M. and Van der Biest O., Transverse cracking and Poisson's ratio reduction in cross-ply carbon fibre-reinforced polymers. JOURNAL OF MATERIALS SCIENCE 34 (22): 5513-5517 NOV 1999.

[31] Gao F., Boniface L., Ogin S.L., Smith P.A. and Greaves R.P., Damage accumulation in woven-fabric CFRP laminates under tensile loading: 2. Modelling the effect of damage on macro-mechanical properties. COMPOSITES SCIENCE AND TECHNOLOGY 59 (1): 137-145 1999.

[32] Smith P.A. and Wood J.R., Poisson ratio as a damage parameter in the static tensile loading of simple crossply laminates. COMPOSITES SCIENCE AND TECHNOLOGY 38 (1): 85-93 1990.

[33] Parlevliet P.P., Bersee H.E.N. and Beukers A.. Residual stresses in thermoplastic composites – a study of the literature. Part III: Effects of thermal residual stresses. COMPOSITES PART A: APPLIED SCIENCE AND MANUFACTURING., VOLUME 38, ISSUE 6, JUNE 2007, PAGES 1581-1596.

[34] De Waele V, Degrieck J, Moerman W, Taerwe L, De Baets P, Feasibility of integrated optical fibre sensors for condition monitoring of composite structures - Part I: Comparison of Bragg-sensors and strain gauges, INSIGHT 45 (4): 266-271 APR 2003.

[35] Degrieck J, De Waele W, Verleysen P, Monitoring of fibre reinforced composites with embedded optical fibre Bragg sensors, with application to filament wound pressure vessels, NDT & E INTERNATIONAL 34 (4): 289-296 JUN 2001.

[36] Shin C. S. and Chiang C. C., Embedded fibre Bragg grating sensors for internal fatigue damage monitoring in polymeric composites, ADVANCED NONDESTRUCTUVE EVALUATION I, PTS 1 AND 2, PROCEEDINGS KEY ENGINEERING MATERIALS 321-323: 230-233 2006.

[37] Shin CS and Chiang CC, Fatigue damage monitoring in polymeric composites using multiple fiber Bragg gratings, INTERNATIONAL JOURNAL OF FATIGUE 28 (10): 1315-1321 OCT 2006.

[38] Facchini, M., Botsis, J. and Sorensen, L. Measurements of temperature during fatigue of a thermoplastic polymer composite using FBG sensors. SMART MATERIALS & STRUCTURES 16 (2): 391-398 APR 2007.

[39] Abry JC, Choi YK, Chateauminois A, Dalloz B, Giraud G, Salvia M, In-situ monitoring of damage in CFRP laminates by means of AC and DC measurements, COMPOSITES SCIENCE AND TECHNOLOGY 61 (6): 855-864, 2001.

[40] Seo DC, Lee JJ, Damage detection of CFRP laminates using electrical resistance measurement and neural network, COMPOSITE STRUCTURES 47 (1-4): 525-530 DEC, 1999.

[41] Angelidis N, Wei CY, Irving PE ,The electrical resistance response of continuous carbon fibre composite laminates to mechanical strain, COMPOSITES PART A-APPLIED SCIENCE AND MANUFACTURING 35 (10): 1135-1147, 2004.

[42] Park JB, Okabe T, Takeda N, Curtin WA, Electromechanical modelling of unidirectional CFRP composites under tensile loading condition, COMPOSITES PART A-APPLIED SCIENCE AND MANUFACTURING 33 (2): 267-275, 2002.

[43] Xia Z, Okabe T, Park JB, Curtin WA, Takeda N, Quantitative damage detection in CFRP composites: coupled mechanical and electrical models, COMPOSITES SCIENCE AND TECHNOLOGY 63 (10): 1411-1422 AUG, 2003.

[44] Van Barschot J. Airbus en Boeing vliegen met Ten Cate. In: NRC Handelsblad, Rotterdam, 5 January 2005. p. 17.

[45] Private communication with Voet M., CEO and Vlekken J. Head of research department, from the company FOS&S.

Chapter 2

COMPOSITE MATERIAL, EQUIPMENT AND USED SOFTWARE

In this chapter some information is given on the tools, necessary for the fatigue research. First, the material is presented on which the experiments are conducted. Second, the used tensile machines, the instrumentation and data acquisition are discussed. Finally, the choice of finite element software is motivated.

2. 1. THE USED COMPOSITE MATERIALS

For this research, two materials were taken under consideration. The material on which the emphasis of the research lies, is a carbon fabric-reinforced polyphenylene sulphide (PPS), called CETEX. This material is supplied to us by Ten Cate [1]. For some aspects, comparisons were made between the CETEX material and a unidirectional glass fabric-reinforced epoxy. The latter is shortly discussed first and then, a more detailed overview of the carbon fabric-reinforced PPS is given.

2. 1. 1. Unidirectional glass fabric-reinforced epoxy

The glass reinforcement was a unidirectional E-glass fabric (Roviglas R17/475). In the fibre direction $\vec{e}_{11}$, the reinforcement was 475 g/m^2, while in the direction $\vec{e}_{22}$, the reinforcement was 17 g/m^2. The epoxy matrix was Araldite LY 556.

Three stacking sequences were manufactured: $[0°]_8$, $[90°]_8$ and $[0°/90°]_{2s}$ with the angle referred to the direction $\vec{e}_{11}$.

All specimens were manufactured by vacuum assisted resin transfer moulding with a closed steel mould, which is illustrated in Figure 2-1. The vacuum pump (1) creates a vacuum in the closed steel mould (2), which is heated (3). Since vacuum alone is not enough to transfer the resin, an extra transfer pump (4) is used.

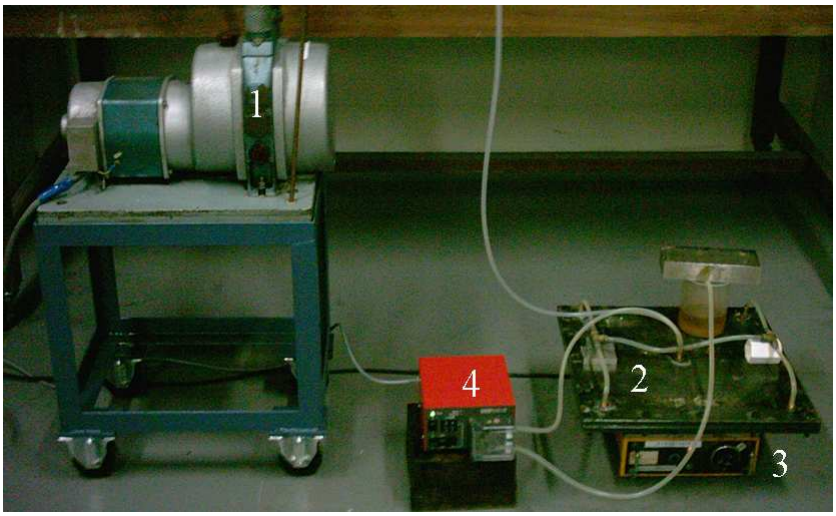

Figure 2-1 Illustration of the vacuum assisted resin transfer moulding.

The nominal thickness of all specimens was 3.0 mm and the fibre volume fraction was between 48 % and 50 %. The samples were cut to dimensions on a water-cooled diamond tipped saw.

The in-plane elastic properties of the individual glass/epoxy lamina were determined by the dynamic modulus identification method (see chapter 3) and are listed in Table 2-1.

Table 2-1 In-plane elastic properties of the individual glass/epoxy lamina.

E_{11} [GPa]	38.9
E_{22} [GPa]	13.3
ν_{12} [-]	0.25
G_{12} [GPa]	5.13

Apart from the dynamic modulus identification method, static tensile tests on the $[0°]_8$ and $[90°]_8$ lay-ups have been performed to check the values of the elastic properties and to determine the static strengths. It is important to mention that the mechanical behaviour in the $\vec{e}_{11}$ and $\vec{e}_{22}$ direction is linear until failure.

The tensile strength properties were determined from the $[0°]_8$ and $[90°]_8$ stacking sequence and are listed in Table 2-2.

Table 2-2 Tensile strength properties of the individual glass/epoxy lamina.

X_T [MPa]	901.0
ε_{11}^{ult} [-]	0.025
Y_T [MPa]	36.5
ε_{22}^{ult} [-]	0.0025

Since there is a little difference between the notations of the stacking sequences for fabric and unidirectional reinforcement in this manuscript, some more information is provided. For the unidirectional reinforcement, the following notations are applied:

- $[0^o]_8$ This means that the material consists of eight layers of reinforcement and all of them have the same orientation, namely zero degrees with respect to the loading direction of the specimen. This means that $[0^o]_8$ is short for $[0^o/0^o/0^o/0^o/0^o/0^o/0^o/0^o]$.
- $[0^o/90^o]_{2s}$ This material also consists of eight layers. The 's' means that the lay-up is symmetrical with respect to the mid plane. The '2' means that what is between the brackets, is repeated two times. Therefore, this notation is short for $[0^o/90^o/0^o/90^o]_s$ or $[0^o/90^o/0^o/90^o/90^o/0^o/90^o/0^o]$.

2. 1. 2. Carbon fabric-reinforced polyphenylene sulphide

2. 1. 2. a. The fibres

The fibre type is the carbon fibre T300J 3K which has the properties listed in Table 2-3.

Table 2-3 Properties of the carbon fibre.

Specific mass [kg/m^3]	1,760
Tensile strength [MPa]	3,600
Ultimate strain [-]	0.014
Young's Modulus [MPa]	231,000

The weaving pattern is a 5-harness satin weave (Figure 2-2) with a mass per surface unit of 286 g/m^2. The 5-harness satin weave is a fabric with high strength in both directions and excellent bending properties.

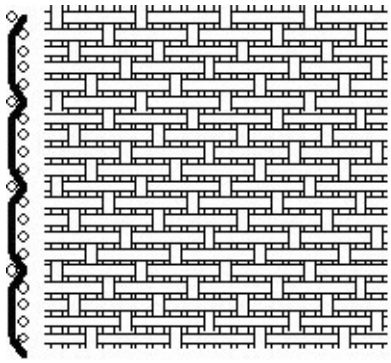

Figure 2-2 Close-up of the 5-harness satin weave pattern [2].

The term '5-harness' means that a fibre bundle in the warp (0º) direction goes over four fibre bundles in the weft (90º) direction before going underneath one. The advantage of this pattern is that the fibre is less bent than in a plain weave (Figure 2-3) and the fabric is more deformable and allows better draping on curved surfaces.

The strength in the warp direction (0º) is a little higher than the strength in the weft direction (90º). A possible explanation lies in the fact that warp fibres are not bent, contrary to the weft fibres. 'Satin' means that crossing moves one or more fibre bundles. This increases the uniformity of the strength.

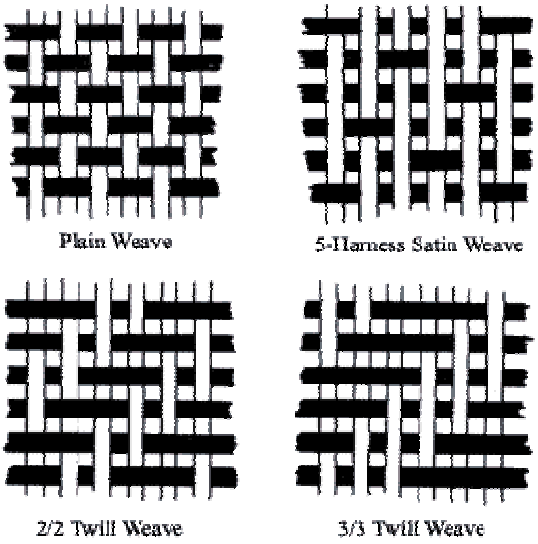

Figure 2-3 Comparison of different weave patterns [3].

2. 1. 2. b. The matrix

The fibres are embedded in polyphenylene sulphide (PPS). The structural formula is shown in Figure 2-4 (a) where the hexagon represents benzene (Figure 2-4 (b)).

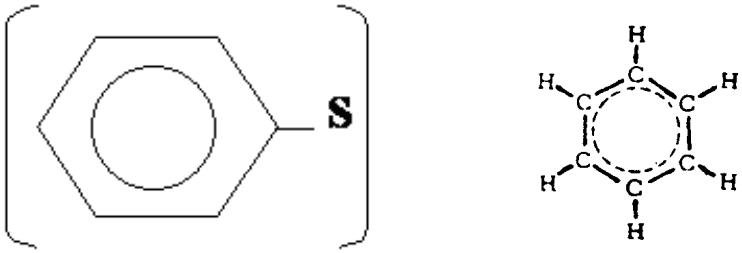

(a) PPS (b) benzene

Figure 2-4 Structural formula of polyphenylene sulphide (PPS) and benzene.

PPS is a thermoplastic polymer matrix with a semi-crystalline structure, a high chemical resistance and good weldability. There are multiple types of this polymer commercially available, but for CETEX the linear variant is used. It has a long chain structure with limited branching resulting in a low viscosity and a faster crystallisation than for the strongly branched polymers.
The linear variant has the properties listed in Table 2-4.

Table 2-4 Properties of the PPS matrix [4].

Melting temperature [ºC]	280
Glass transition temperature [ºC]	90
Optimal crystallisation temperature [ºC]	150 – 160
Specific mass	
Amorphous [kg/m^3]	1.30
Crystallised [kg/m^3]	1.35
Tensile strength [MPa]	75
Shear strength [MPa]	130
Ultimate strain [-]	0.08
Young's modulus in tension [MPa]	3,700
Young's modulus in compression [MPa]	3,800

PPS is a semi-crystalline thermoplastic, which means that the amorphous and the crystalline phase coexist. The proportion between both phases is determined by the preceding temperature cycle. In general, the higher the cooling rate, the more amorphous the structure becomes.

The temperature cycle of PPS consists of different stages, as is illustrated in Figure 2-5 and is discussed below.

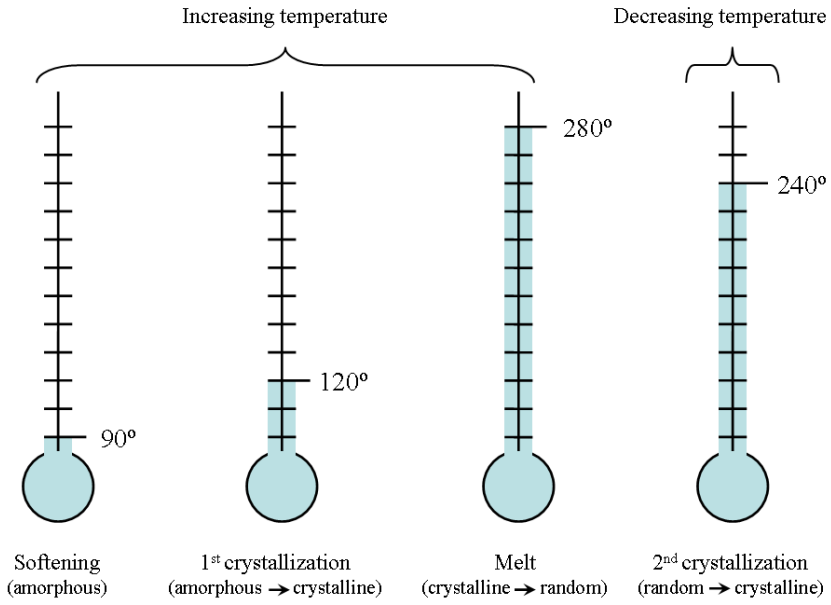

Figure 2-5 Characteristic temperatures for PPS [4].

Amorphous PPS starts to soften at a temperature of 90 ºC. This state of slightly altered viscosity lasts until the material starts to crystallise at 120 ºC. This crystallised material does not soften; the structure is stable and can only be broken by melting.

Melting starts at a temperature of 280 ºC, the material is completely liquid at 300 ºC. This material structure is highly disordered and the molecules have a high mobility. Since the molecular forces are very low, the melted material has a very low viscosity.

The cooling of the melt results in a second crystallisation. The number of crystals being formed depends on the cooling rate. Since crystallisation takes time, the lower the cooling rate, the higher the fraction of crystals. If the material is cooled down very fast, the disordered structure is ‘frozen’ and the resulting material is amorphous.

2. 1. 2. c. Field of application

Composites are used more and more as surfaces in aeronautical applications since they combine high strength and stiffness with low density. They are also more and more preferred over aluminium for structural applications.

CETEX has a number of advantages when compared to other advanced composite materials, namely its weldability, chemical inertness and the possibility of energy absorption at impact. CETEX is the first thermoplastic composite to be used in structural airline applications, for example the 'J nose' part of the leading edge of an airplane wing (Figure 2-6 (a)), reinforcement profiles for the wings (Figure 2-6 (b)) and the 'heavy duty' sandwich floor panels (Figure 2-6 (c)).

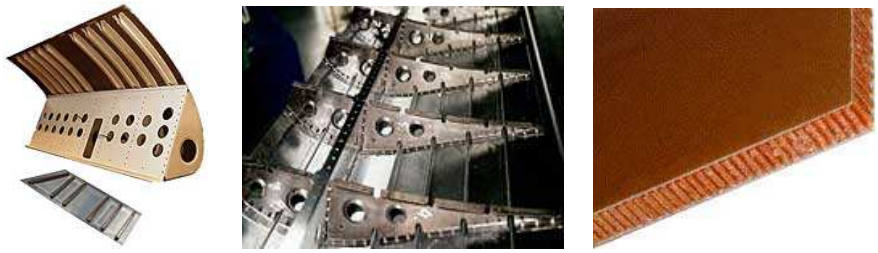

(a) J-nose (b) reinforcement profiles (c) Sandwich panels

Figure 2-6 Structural CETEX parts in aeronautics.

That the confidence in thermoplastic composites for structural applications is growing, may appear from the fact that in the Airbus A340-500/600 there is more than 1000 kg of CETEX and in the new Airbus A380, there is about 6000 kg of CETEX [1].

2. 1. 2. d. Production process

Since PPS weakens at elevated temperatures (see paragraph 2. 1. 3), it is excellent for hot pressing. This is a fast and flexible method for producing plates from semi-pregs on one hand, and parts from blanks on the other hand (see Figure 2-7).

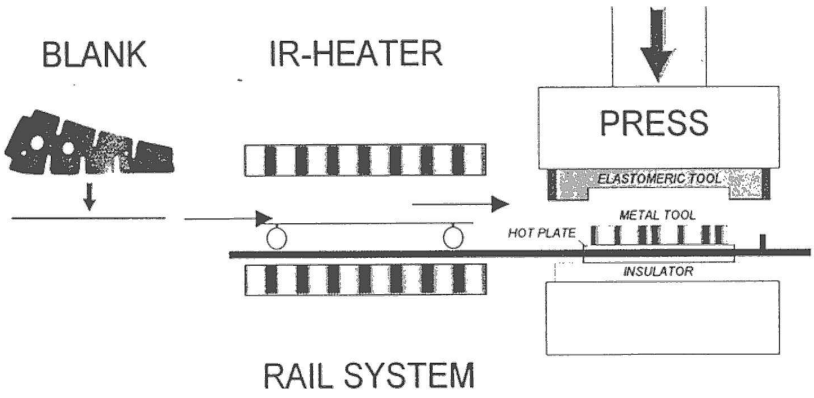

Figure 2-7 Illustration of hot pressing.

A semi-preg consists of two layers: (i) a layer of fabric, for instance the carbon fabric and (ii) a thermoplastic film, for instance a PPS film. The two layers are bonded to each other simply by heating the two, so that the thermoplastic melts and bonds to the fabric. A semi-preg differs from the well known pre-preg, because for the former, the two layers can still be distinguished, whereas for the latter, the fabric is already completely impregnated with the (thermoplastic) matrix.
A plate is then formed by hot pressing a number of semi-pregs together, allowing the films of thermoplastic to fully impregnate the fabric reinforcement, before hardening again. From these plates, blanks can be made, which are no more than flat panels with dimensions fit for the final product. By reheating the blank and pressing it into a mould, such as illustrated in Figure 2-7, a part can be realised.

PPS has the advantage that it can be produced in an easy manner, but because of the shrinkage during (re)crystallisation, internal stresses are introduced. When the bonding between carbon fibre and matrix is insufficient, fracture will occur at the fibre-matrix interface and will cause an early failure. However, by varying parameters such as cooling speed and sizing of the fibres, adhesion between fibre and matrix could be optimised.

2. 1. 2. e. Test specimens

Ten Cate has supplied us with a number of plates of 45 cm by 48 cm (see Figure 2-8 (a)). Some of the plates were manufactured on a small laboratory press and others were pressed on their industrial press, meaning that there is a slight difference in thickness of the plates. Some of the plates have a thickness of 2.4 mm and others are 2.5 mm thick. A detailed image of the structure of the carbon-PPS is shown in Figure 2-8 (b)

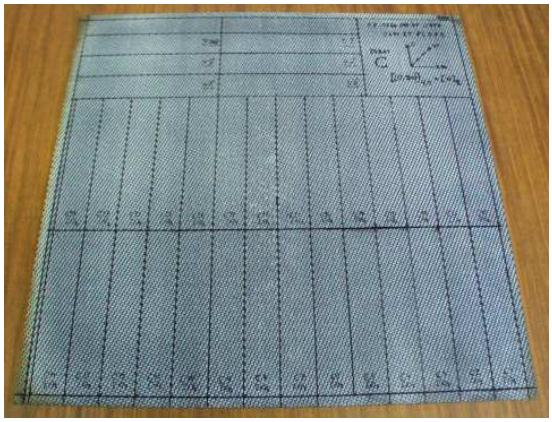

(a) A CETEX plate, with the lines to cut the coupons.

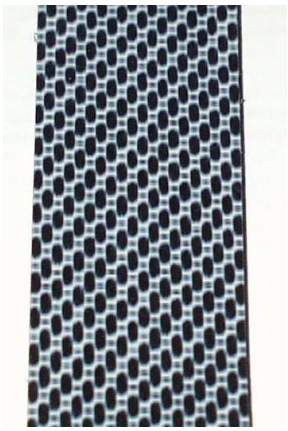

(b) Detail of the structure

Figure 2-8 An example of a CETEX plate, with the lines to cut the coupons.

The stacking sequences used for this doctoral thesis are $[(0^o,90^o)]_{4s}$, $[(0^o,90^o)/(90^o,0^o)]_{2s}$ and $[(+45^o,-45^o)]_{4s}$. The last is the same as the first, but cut under a 45° angle.

As can be noticed, another type of notation is used to define the stacking sequences of fabric reinforcement. The notation used for this manuscript, according to the European norm, is suggested by Ten Cate and has the following meaning: $(0^o,90^o)$ represents one layer of reinforcement, the 0° corresponds with the warp direction of the weaving process. Therefore, the $[(0^o,90^o)]_{4s}$ is again an eight-layer laminate which is symmetrical with respect to the mid-plane. The latter, however, is not the same as a $[(0^o,90^o)]_8$. For the latter, all fabric layers have the same top to bottom orientation, meaning that all warp fibres are on top and all weft fibres are at the bottom. For the $[(0^o,90^o)]_{4s}$ lay-up, the four top layers have the warp side on top and the four bottom layers have the warp side at the bottom, resulting in a symmetrical laminate; if it is turned upside down, no difference will be seen whereas with the $[(0^o,90^o)]_8$, the fibre orientation will change. For uni-axial testing, this will not give different results, but for example for bending experiments, where there is a stress gradient over the thickness, different results will be obtained because of the different strength properties for the warp and the weft direction. Therefore, this modified notation is used.

Of course, the other conventions stay the same, the $[(0^o,90^o)/(90^o,0^o)]_{2s}$ stacking sequence is also an eight layer symmetrical laminate and it is short for:
$[(0^o,90^o)/(90^o,0^o)/(0^o,90^o)/(90^o,0^o)/(90^o,0^o)/(0^o,90^o)/(90^o,0^o)/(0^o,90^o)]$.

The test coupons were sawn on a water-cooled diamond tipped saw. The dimensions of the coupons and the corresponding experiment are listed in Table 2-5.

Table 2-5 Dimensions of the used specimens.

Type of experiment	Dimensions (length x width)
Tensile test	250/270 mm x 30 mm
Bending test	160 mm x 30 mm
Three-Rail Shear Test	230 mm x 100 mm

2. 2. TESTING EQUIPMENT

2. 2. 1. The tensile testing machines

During this doctoral research, a new testing machine was acquired, so tests were done both on the INSTRON 1342 and the INSTRON 8801.

2. 2. 1. a. The INSTRON 1342

The servo-hydraulic INSTRON 1342 Tensile testing machine is equipped with a FastTrack 8800 digital controller (Figure 2-9). The machine is excellently suited for fatigue testing and it can reach displacement velocities up to 75 mm/s.

Figure 2-9 The servo-hydraulic INSTRON 1342 Tensile machine, equipped with the FastTrack 8800 digital controller.

This machine can work displacement-controlled, force-controlled or strain-controlled. The machine's outputs are:

- The absolute displacement of the hydraulic actuator, which has a range of ± 50 mm.
- The force, which is measured by a load cell with a dynamic range of 100 kN.
- The longitudinal strain, which is measured by an extensometer. The latter is discussed in more detail in section 2. 3. 4.

2. 2. 1. b. The INSTRON 8801

The servo-hydraulic INSTRON 8801 Tensile testing machine is also equipped with a FastTrack 8800 digital controller (Figure 2-10).

Figure 2-10 The servo-hydraulic INSTRON 8801 Tensile machine, equipped with the FastTrack 8800 digital controller.

The machine is excellently suited for fatigue testing and it can reach higher displacement velocities than the INSTRON 1342, because of a different hydraulic valve. This machine can also work in a displacement-controlled, a force-controlled or a strain-controlled manner. The machine's outputs are:

- The absolute displacement of the hydraulic actuator, which has a range of ± 70 mm.
- The force, which is measured by a load cell with a dynamic range of 100 kN.
- The longitudinal strain, which is measured by an extensometer. It is discussed in more detail in section 2. 3. 4.

2. 3. INSTRUMENTATION

While performing experiments, the more information that can be gathered, the better. As mentioned in the previous paragraphs, the tensile machines already provide the load, displacement and strain data. The specimen itself could also be instrumented with different sensors, such as strain gauges, thermocouples, … providing extra data. Of course, all this data should be registered, preferably on the same time basis. In the next paragraphs, the used data acquisition systems are discussed. This is followed by a short overview of the more general sensors used for this research. The more specific sensing techniques will be addressed in more detail in the corresponding chapters.

2. 3. 1. NI-DAQ data acquisition card for fireWire

One of the used data acquisition cards is the National Instruments DAQpad 6052E for fireWire, IEEE 1394 (see Figure 2-11). It is equipped with 16 single-ended or 8 differential analogue inputs and 2 analogue outputs. The input and output resolution is 16 bits. It has 8 digital input/output channels and 2 timers. The maximum sampling rate is 333,000 samples per second. The input range goes from ± 0.05 V up to ± 10 V, the output range is ± 10 V. It has both analogue and digital triggers and it works with traditional NI-DAQ measurement service software. For more information about this card, the author refers to the National Instruments™ website [5].

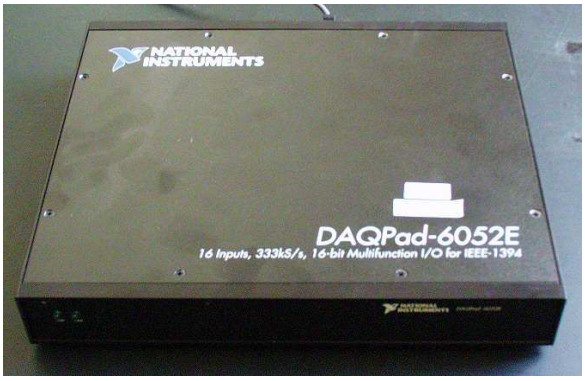

Figure 2-11 The used NI-DAQpad 6052E.

2. 3. 2. NI-DAQ data acquisition card for USB

The second data acquisition card is the NI-USB-6251, also from National Instruments. The features of this card are very much the same as for the DAQpad 6052E, with the main difference that this card uses USB instead of FireWire for its communication with the pc.

It also has 16 single-ended or 8 differential analogue inputs and two analogue outputs with 16 bit resolution. The maximum sample rate is even higher, 1,250,000 samples per second. This card only works with the NI-DAQxm software, the traditional NI-DAQ measurement service software is no longer supported. For more information about this card, the author refers to the National Instruments™ website [6].

Figure 2-12 The NI-USB 6251 data acquisition card.

2. 3. 3. SCB-68 connector.

The used connector block is a SCB-68 (Figure 2-13). It is a connector block with 68 screw terminals for easy signal connection to a National Instruments 68 DAQ device. The SCB-68 features a general breadboard area for custom circuitry and sockets for interchanging electrical components. These sockets or component pads allow RC filtering, 4 to 20 mA current sensing, open thermocouple detection and voltage attenuation. The open component pads allow signal conditioning to be easily added to the analogue input and output signals [7].

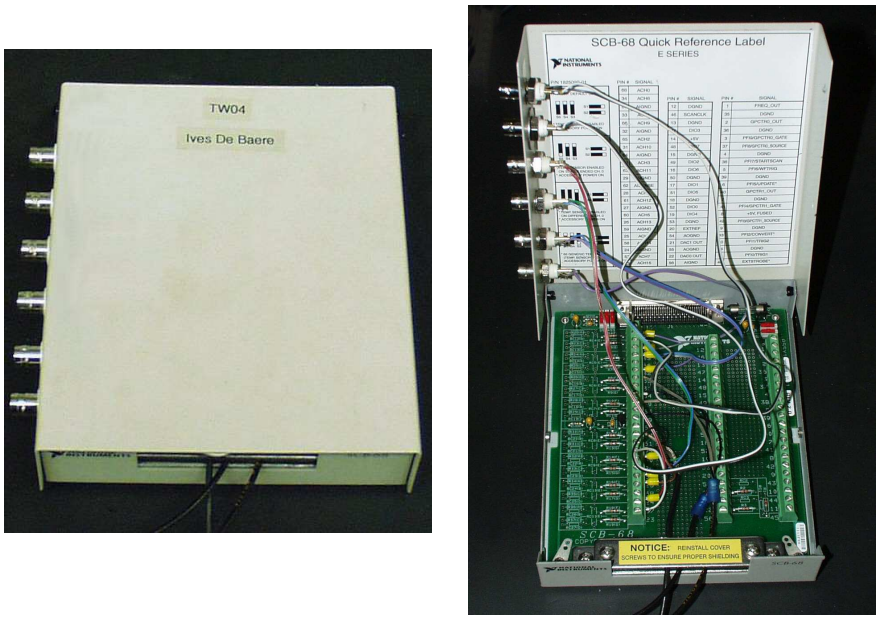

Figure 2-13 The SCB-68 pin shielded connector block.

The SCB-68 can be used for single-ended and for differential measurements. The former has as advantage that more channels can be measured, but with a common ground. The latter has half the number of channels, but it has a better noise immunity. However, after some preliminary testing, it was noticed that the noise immunity was equal for both configurations, so it was chosen to connect all channels in single-ended mode, so extra channels could be monitored.

As mentioned in paragraph 2. 2. 1. a, the outputs given by the tensile machine are force, displacement and strain, which yield three channels. For the temperature reading, two channels are necessary (see paragraph 2. 3. 6) Since these signals are necessary for the correct interpretation of any test, they are wired to the inside of the SCB (see Figure 2-13). Five of the remaining channels are wired to BNC connectors on the outside, which makes an easy change of input signal possible.

The software used for the data acquisition, is LABVIEW 7.1. It allows a very intuitive programming style, although programming in C++ is also possible, and it works with two terminals. One is the block diagram, of which a screenshot is given in Figure 2-14 and on this terminal, the actual programming is done by wiring together functional ‘blocks’. These blocks may represent data input, output, calculations…

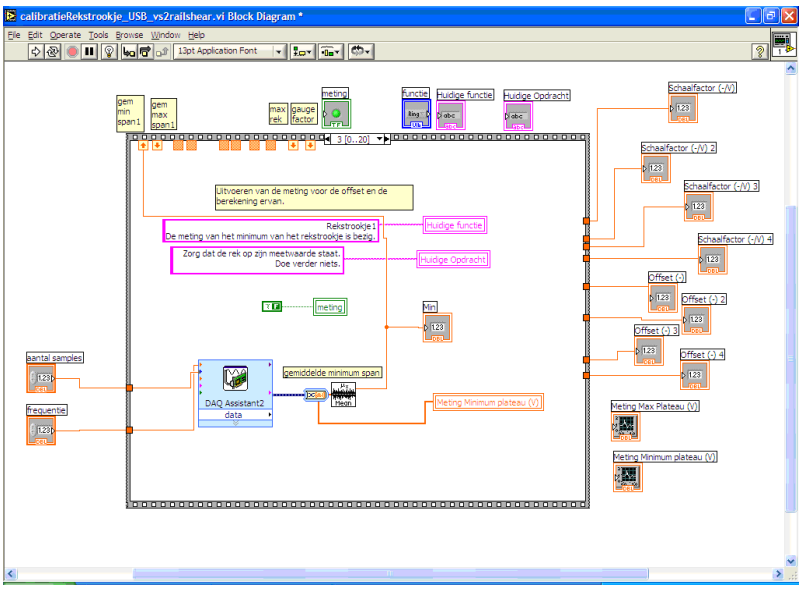

Figure 2-14 Illustration of a block diagram in LABVIEW.

Once the programming is done, this screen is no longer needed for the measurement. The actual user-interface is the so called ‘front panel’ which can be given a similar lay-out as for example an oscilloscope. An image of such a front panel is illustrated in Figure 2-15. For more information on this software, the author refers to the user manual, which can be found on the internet [8].

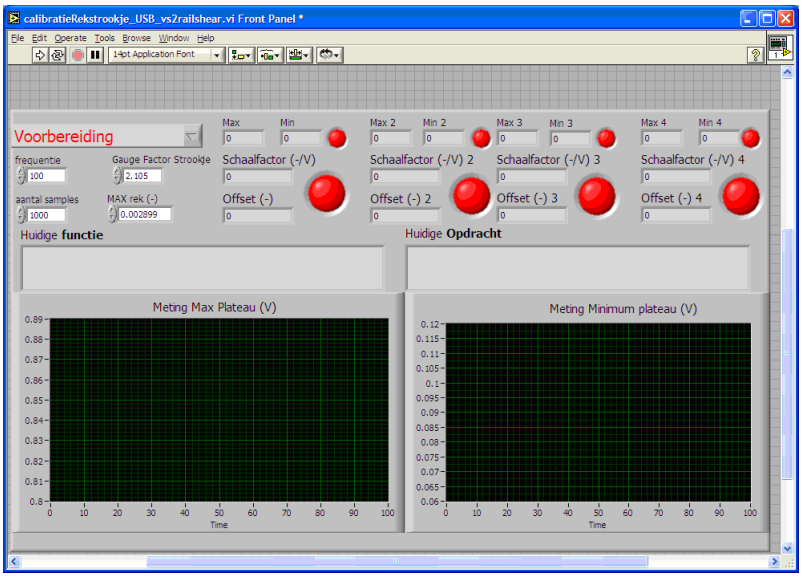

Figure 2-15 Illustration of a front panel in LABVIEW.

2. 3. 4. The extensometer

For longitudinal strain measurements, an extensometer is used rather than a strain gauge, since the latter tends to de-bond after a few thousand cycles during a fatigue test, even if the strains are low. The INSTRON test machine is capable of reading the data directly from the extensometer, which is not possible when using a strain gauge. The machine can also work in strain-controlled mode, as mentioned above in paragraph 2. 2. 1. a. The used extensometer is from INSTRON (see Figure 2-16), catalogue nr. 2620-603, which is suited for dynamic measurements and it is calibrated electronically. The device is mounted on the specimen using elastic rubber bands.

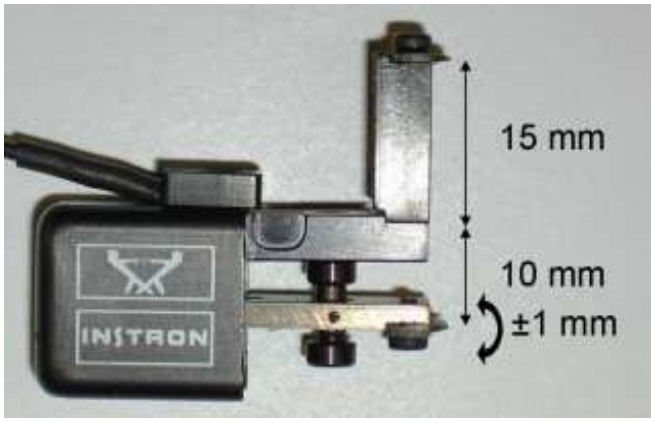

Figure 2-16 The extensometer, used for longitudinal strain measurements.

The extensometer has an absolute travel of 1 mm in both directions, as is depicted in the picture above. There are three different gauge lengths possible: 10 mm, 25 mm and 50 mm. 10 mm is the standard distance, without any attachment. For 25 mm, an end-piece of 15 mm is added, as shown on Figure 2-16 and for 50 mm, an end-piece of 40 mm is mounted. Thus, strain can be measured within three ranges of accuracy:

Travel	Range
1 mm over 10 mm	10%
1 mm over 25 mm	4%
1 mm over 50 mm	2%

For tensile testing on our composite material, the setup will be used as shown in Figure 2-16, giving a range of 4% in tension as well as in compression. Ranges of 10% will never be reached in our fibre reinforced material and 2% may be a bit tight, since one never knows for sure that, after mounting the extensometer, the movable pin is still in the neutral position.

For example, if after mounting the movable pin is 0.5 mm out of centre, there is only 0.5 mm left of travel, giving a range of only 1%, which is too small. If the travel is exceeded, the extensometer may be damaged beyond repair.

2. 3. 5. The strain gauges

In order to measure the transverse strain, a strain gauge is mounted on the test specimen. Together with the longitudinal strain Poisson's ratio can be calculated:

$$\nu_{12} = -\frac{\varepsilon_{22}}{\varepsilon_{11}} \tag{2.1}$$

The used strain gauges are "*general purpose Strain Gauges*" from VISHAY micro-measurements. The grid resistance is 350.0 ± 0.3% Ω and they have a gauge factor of 2.105. An image is given in Figure 2-17 and for the given orientation, the horizontal strain is measured.

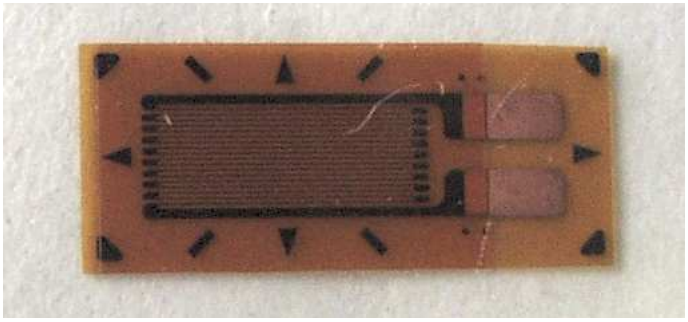

Figure 2-17 Image of the used strain gauges.

The strain gauges are bonded using the M-BOND 200 adhesive from Vishay Micro-Measurements. For the actual measurement, a stabilised 350 Ω Wheatstone bridge, type SGA 503 from CIL is used; each strain gauge has its own amplifier to which the gauge is attached using a three-wire connection.

2. 3. 6. The thermocouple

A thermocouple (Figure 2-18) is created when two dissimilar metals touch and the contact produces a small voltage that changes as a function of temperature. By measuring the voltage of a thermocouple, it is possible to determine the temperature using a nonlinear equation that is unique to each thermocouple type [7]. The type used for our experiments is K. The equation is a sixth degree polynomial of the voltage.

Figure 2-18 The used thermocouple, type K.

The voltage, generated by a thermocouple as a function of the temperature is a relative measurement, which means that it gives the temperature, relative to the temperature of the surroundings. In order to get an absolute temperature reading, a reference temperature is necessary. This is called a Cold-Junction Compensation (CJC).

The SCB-68 is equipped for the use of thermocouples. It has an extra signal conditioning circuit, which is necessary, since the voltage produced by a thermocouple is typically only a few millivolts. Channel zero of the SCB-68 functions as the CJC, so no inputs can be mounted on this channel.

Within LABVIEW, the easiest way of measuring the temperature is by using either the 'Measurement and Automation Explorer' (MAX) or the NI-DAQ assistant, depending on the type of data-acquisition card and the required software. In both cases, different analogue channels can be configured. If the option 'temperature measurement' is tagged and the type of sensor, which in this case is a type K thermocouple, is selected, the NI-DAQ automatically gives the value of the temperature instead of a voltage, when this channel is being read.

2. 4. FINITE ELEMENT SOFTWARE

2. 4. 1. Choice of software

For this study, ABAQUS™ is used, which has two calculation methods available: ABAQUS/Standard and ABAQUS/explicit. The difference between the two is the way they calculate the information for the next time step. Standard uses an implicit integration method, which means that for the values at time T , the routine not only uses the information gathered in previous time steps, for t < T, but it also uses the values at T. This means that for each time step, ABAQUS needs to run a few iterations before it reaches its convergence criteria for that step, but since it is self correcting, the time steps can be bigger than in ABAQUS/Explicit.
Indeed, ABAQUS/Explicit uses an explicit integration method, which means that for the calculation of the values at time T, it only uses the values at times t<T. Therefore, it does not need to run multiple iterations for a single step, but since its not self correcting, the time steps need to be a lot smaller than in ABAQUS/Standard.

ABAQUS/Explicit is best suited for dynamic problems, where speed, acceleration and inertia are key elements in the problem, as is the case with impact. ABAQUS/Standard does not take these parameters in consideration.

2. 4. 2. Used computers

For this research, two computers have been used.

1. A Dell Inspiron 8200 with a Mobile Intel® Pentium® 4-m CPU with a clock frequency of 2.00 GHz and 1.00 Gb of RAM was used to generate the input files and perform the less time consuming simulations.
2. A Linux workstation with an AMD Athlon64 CPU with a clock frequency of 1.8 GHz and 4096 Mb of DDR400 RAM was used for the implementation of the material model and all other simulations which have higher demands with respect to the amount of RAM memory.

2. 5. REFERENCES

[1] http://www.Ten Cate.com, 10/10/2007.

[2] http://www.tech.plym.ac.uk/sme/MATS324/MATS324C2%20fabrics.htm, 04/08/2005.

[3] http://www.fibermaterialsinc.com/2Dws.htm, 04/08/2005.

[4] CETEX – PPS Guide Lines, Ten Cate Advanced Composites.

[5] http://sine.ni.com/nips/cds/view/p/lang/en/nid/10931, 10/10/2007.

[6] http://sine.ni.com/nips/cds/view/p/lang/en/nid/202597 10/10/2007.

[7] SCB-68 68-Pin Shielded Connector Block User Manual, National Instruments, December 2002 edition.

[8] http://www.elis.ugent.be/ELISgroups/tfcg/student/lvuser.pdf 10/10/2007.

[9] ASTM D3518-76, standard practice for in-plain shear stress-strain response of unidirectional reinforced plastics, 1982.

[10] W. Van Paepegem, Mechanics of Materials, Faculty of Engineering, Ghent University, 2005.

Chapter 3

QUASI-STATIC TESTING

This chapter first discusses a few principles which are not only necessary for the quasi-static testing, but which will also be used in the following chapters. Further, it presents two monitoring systems, namely the electrical resistance measurement and optical fibre with fibre Bragg gratings. The mechanical properties of the used carbon fabric-reinforced polyphenylene sulphide are also derived, both from the quasi-static experiments, as from the 'resonalyser' method.

3. 1. INTRODUCTION

In this chapter, a number of general principles which will be used in further chapters are commented on. First, some information is given on the use of end tabs on the specimen. The necessity of this feature, as well as different ways to achieve it and the pitfalls that may occur, are discussed. Then, the determination of the mechanical properties of the carbon fabric-reinforced polyphenylene sulphide is illustrated. These properties are not only derived by conducting the standard quasi-static tensile tests, as described in the standards, but also by a different method, namely the 'resonalyser' method.

This is followed by the introduction of two types of sensors, used to monitor the experiments. The first is the use of optical fibre sensors with Fibre Bragg Gratings (FBGs) and the second is the electrical resistance measurement. Although only quasi-static tests are discussed here, both monitoring principles will also be applied for fatigue testing.

3. 2. THE USE OF TABS ON THE SPECIMEN

3. 2. 1. The necessity of end tabs

When performing quasi-static tests on fibre-reinforced materials, the use of end tabs is often necessary to prevent clamp failure. The "*ASTM D3039/D3039M Standard Test Method for Tensile Properties of Polymer Matrix Composite Materials"*, states that tabs are not required, but the need to use tabs should be determined by the experiments themselves. If acceptable failure modes occur with reasonable frequency, then there is no need to change the gripping method. However, if grips are required, the standard gives some recommendations considering the tab dimensions.

Summarized, a continuous glass fibre-reinforced polymer with $[\pm 45^o]_{ns}$ laminate configuration should be used, the length should be about 50 mm and the bevel angle should be 7 or 90 degrees, depending on the stacking sequence of the test material. When gripping the specimen, the grips should overhang the bevelled portion of the tab by approximately 10 to 15 mm. For the tab material, the same material as the one being tested or aluminium can also give good results. It is also stated that 'sufficient' lateral pressure should be used to avoid slipping.

The ISO 527-1 *International standard for the determination of tensile properties* gives similar recommendations: the tabs should have a length larger than or equal to 50 mm, the angle should be 90 degrees and the jaws should overhang the tabbed section. For the material, a cross-ply glass fibre-reinforced polymer with the fibres at $\pm 45^o$ to the tensile direction is suggested.

When performing uni-axial fatigue tests, clamp failure is even more likely to occur. The "*ASTM D3479/D3479M Standard Test Method for Tension-Tension Fatigue of Polymer Matrix Composite Materials"* states that end tabs should always be used, using the same geometry recommendations as in the ASTM D3039/D3039M Standard.

As may be concluded from the paragraphs above, the ASTM and ISO standards can only give recommendations. The ASTM D3039/D3039M even mentions that '*Design of mechanical test coupons remains to a large extent an art rather than a science*'.
Of course, a choice of tab material and geometry still has to be made. The end tabs can be made of aluminium, a fibre-reinforced thermosetting or thermoplastic polymer. Furthermore, there are a few possible ways of attaching the end tabs to the specimen (i) using an adhesive, (ii) co-consolidating them during production of the test plates and (iii) fusion bonding.

Preliminary tests have shown that PPS is not easily bonded to any material, because of its chemical inertness, so an extensive test program has been conducted to search the best way of bonding another material to the PPS, but first, it is examined whether tabs are really necessary. Then, the options of co-consolidation and fusion bonding are examined and finally, the use of an adhesive is discussed.

3. 2. 1. a. Dog-bone specimen

Fist, it was attempted to perform tests without end tabs, to verify if the end tabs are necessary for (static) tensile testing. However, the specimen kept failing in the gripped section, so a different kind of solution without tabs was tested.

The tensile specimen was given a ‘dog-bone’ shape (see Figure 3-1), which is very common when testing aluminium.

Figure 3-1 ‘Dog-bone’ shaped specimen.

Although the stresses are much higher in the middle section, because of the smaller cross section, the specimen failed in the curvature (Figure 3-2) with an ultimate stress of 699 MPa.

Figure 3-2 ‘Dogbone’ shaped specimen, which failed in the curved section.

A three-dimensional finite element simulation yielded that, due to the orthotropic nature of the material, stress concentrations exist at the end of the curvature, causing the failure. Furthermore, the milling of such a specimen is a very intensive process and the tools have a high abrasion because of the carbon fibres in the composite. Moreover, it is very likely that the milling induces damage at the sides of the specimen, resulting in early failure. It also needs to be remarked that this type of specimens is not allowed by the ASTM Standard or by the ISO norm. Therefore, this method is no longer considered.

3. 2. 2. Co-consolidation of the tabs during the production of the plate

If the tabs could be mounted during the production of the plates, the problem of bonding the tabs would be solved. The used production process is hot pressing, as has been described in chapter 2. If the tabs are to be formed during production, a new mould needs to be designed. There are, however, a few obstacles.

When hot pressing a composite part, the gaps between the upper and lower mould have a very important function. If the gaps are too large, then too much PPS can flow out of the mould, leaving naked fibres. If the gaps are too narrow, there is a pressure build up inside the mould because too much PPS remains inside. This may damage the mould and will also result in a badly formed composite. Of course, the amount of PPS that needs to be disposed, depends on the number of semi-pregs that are placed inside the mould.

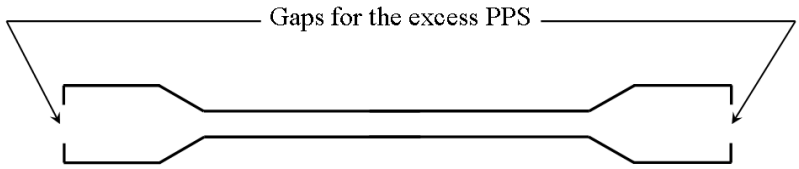

Figure 3-3 Example of a design for a mould for tensile test specimens with integrated chamfered tabs.

The same problem will occur when a mould is designed for the tabs. The gaps on the sides need to have the exact size, or there will be problems underneath the chamfered area. The design of such a mould is usually a process of trial and error, and therefore very expensive and time consuming.
Furthermore, once the mould is designed, the dimensions of the specimens or the tabs can no longer be altered. Because of these disadvantages, this method is no longer considered

The CETEX can also be produced with the autoclave technique, but similar problems as with the hot pressing technique occur. The tabs can easily be mounted on the top side, since the top mould in the autoclave technique is no more than a set of breathers, bleeders, a release film and a vacuum bag. For the bottom mould however, the same problems as mentioned above occur. The design depends on the number of semi-pregs and the amount of excess PPS and therefore, it is again trial and error. Therefore, this method is not an option either.

3. 2. 3. Fusion bonding

This type of bonding uses the property of thermoplastic matrices to flow when heated above their glass transition temperature T_g (for amorphous polymers) or the crystalline melting point T_m (for semi-crystalline polymers). The interface of the bond is heated to that temperature and the two parts are then pressed together. The heat source is removed and the bond is cooled under pressure (consolidated).
There are multiple choices on how to heat the interface: friction of the two surfaces, using the electrical resistance of an insertion, using the conductive properties of carbon fibre for induction welding, an external heat source for ‘hot-tool’ welding … Two of them are taken into consideration, namely resistance welding and hot-tool welding.

3. 2. 3. a. Resistance welding

The principle of resistance welding is quite simple and is illustrated in Figure 3-4. A metal mesh with certain dimensions is placed between the two parts which need to be bonded; this mesh is often impregnated with the thermoplastic material, since it needs to be electrically isolated from the other parts [1].

A current is injected through the mesh, which causes heating due to Joule's law. Once the melting temperature of the thermoplastic material at the interface is reached, pressure is applied and the current is removed. The interface cools down under pressure and a bond is formed; the metal mesh is left inside the bond. It should be mentioned that for the heating element, carbon fibres could also be used. However, the use of a metal mesh has a number of advantages: the welding process is generally easier to perform compared with the carbon heating element, it produces welds with better consistency and higher average strength and the welds are less sensitive to variations of the welding parameters, thus they have a larger processing window [2]. Therefore, the principle is explained only for the metal mesh.

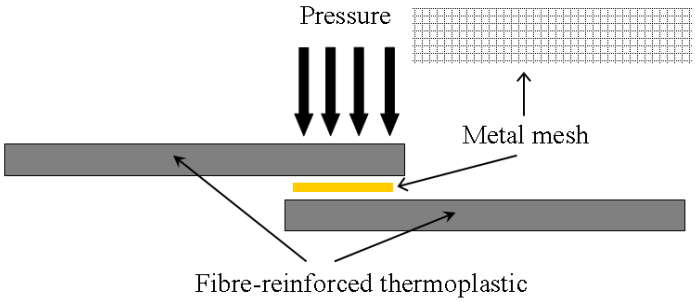

Figure 3-4 The principle of resistance welding of fibre-reinforced thermoplastics.

The advantages of this principle are low cost tooling and no surface treatment [2-4]. For this process, multiple parameters need to be optimized (Figure 3-5).

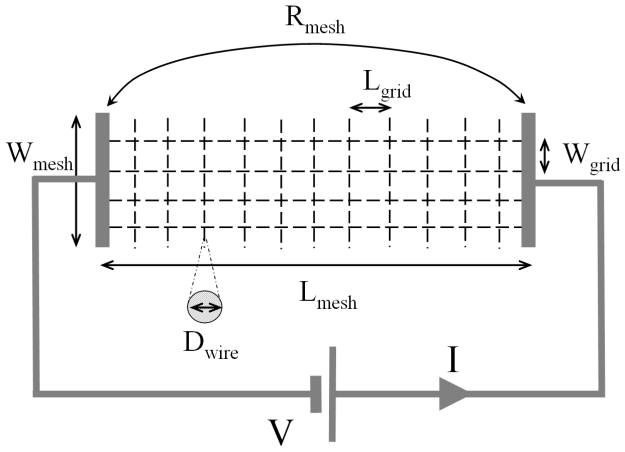

Figure 3-5 Schematic of the parameters that must be optimized for resistance welding.

- The diameter of the wire of the metal mesh D_{wire}. This determines the thickness of the mesh and also has its influence on the total resistance of the mesh R_{mesh} and the way the heat is dispersed in the thermoplastic material.
- The length of one grid, L_{grid}, which has its influence on the heat dispersion in the matrix.
- The width of one grid, W_{grid}, which also determines the heating of the surrounding material.
- The total length, L_{mesh}, and total width, W_{mesh}, of the mesh, which determine the total resistance of the mesh.
- The voltage V that is placed over the mesh or the current I which flows through it. Together with the total resistance and the total time t, they determine the heat input:

$$Q = R_{mesh} I^2 \mathrm{t} \qquad [J] \tag{3. 1}$$

  The necessary amount of heat, can be calculated if the total dimensions of the mesh are known, together with the glass transition temperature T_g (for amorphous polymers) or the crystalline melting point T_m (for semi-crystalline polymers) of the thermoplastic matrix.

$$P = \frac{RI^2}{L_{mesh} W_{mesh}} \qquad \left[\frac{W}{m^2}\right] \tag{3. 2}$$

  Although the power levels P, used for different combinations of materials and heating elements are different, they are typically divided in three groups: low (10 – 75 kW/m^2), intermediate (75 – 130 kW/m^2) and high power level (from 130 kW/m^2 and more) [2].
- How long the voltage or current is applied (t). The energy input is then given by:

$$E = Pt \qquad \left[\frac{kJ}{m^2}\right] \tag{3. 3}$$

  It is obvious that the same energy input can be given by either a high power level during a short time or a low power level during a long time. The results, however, are not the same. More detailed information can be found in [2].
- The amount of pressure applied during the consolidation.

The optimization of the parameters above is very time consuming and would form a doctoral thesis on its own. Therefore, our research group has contacted the Faculty of Aerospace Engineering, Design and Production of Composite Structures at Delft University of Technology, who already have a lot of expertise concerning this matter [2].

It appeared that the type of bond, more exactly the size of the surface that needs to be welded, posed great difficulty. Usually, the size of the bond is about 10 mm wide, as is the case in the typical lap shear test, used to test these bonds [2]. The tabs, however, are 30 mm wide and 60 mm long. The heating of such a surface would yield great difficulty in reaching a uniform temperature across the bond. Furthermore, the chamfering would give trouble during the consolidation under pressure, since it is not easy to have a uniform pressure underneath the chamfering. This would result in a bad flow of the liquid PPS, which leads to a bad bond. Finally, always a small gap remains near the edges of such a bond.
Therefore, this option of bonding the tabs to the specimen is not explored any further, since it would take too much time before a successful bond is achieved.

3. 2. 3. b. Hot-tool welding

A disadvantage of the electrical resistance welding is that the heating element remains in the bond and therefore may have an influence on the mechanical properties. The question is whether the heating element needs to remain inside the bond.
The 'hot-tool welding' process has already been used successfully to bond plastic battery cases, fuel tanks, fuel pipes and for infrastructure applications, such as gas and water distribution, sewage and effluent disposal pipes [5]. The two surfaces to be welded are pushed against a heating element and once the temperature is high enough, the two parts are pressed against one another with sufficient force.
Of course, a similar process should be applicable for fibre-reinforced thermoplastics, as is illustrated in Figure 3-6.

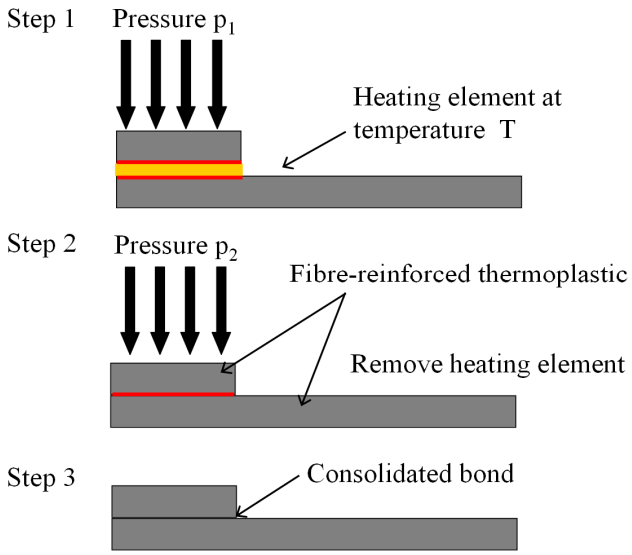

Figure 3-6 The principle of 'hot-tool' welding.

Of course, there are a number of parameters that need to be optimised:

- The pressure p_1 used to press both composite parts against the heater in step 1.
- The temperature T of the heater. This should be higher than the melting point of the thermoplastic matrix, but during the time it takes to remove the heater before going to step 2, the two heated surfaces will have cooled a bit.
- The duration of step 1, to ensure the materials have heated enough.
- The use of a filling material in the bond, for instance a few plies of the matrix, some fibre-reinforcement, or a combination of both.
- The pressure p_2 applied while the bond is curing. This must be high enough to establish good contact between the surfaces, but not too high so that all liquid matrix material flows away.
- The duration of step 2. If the pressure is removed too soon, the bond might not be fully consolidated, but the step should not take too long since this only increases preparation time.

Again, the development of such a welding device, in combination with the optimization would take too long in the extent of this research, so this option is not explored further.

3. 2. 4. The use of an adhesive

In order to find a suitable combination of end tab material, geometry and adhesive, several experiments were performed; different kinds of tab material, adhesive and surface preparation were tested. The different types of fracture that occurred are depicted in Figure 3-7; they are illustrated for chamfered tabs, but the meaning remains the same in the case of straight tabs.

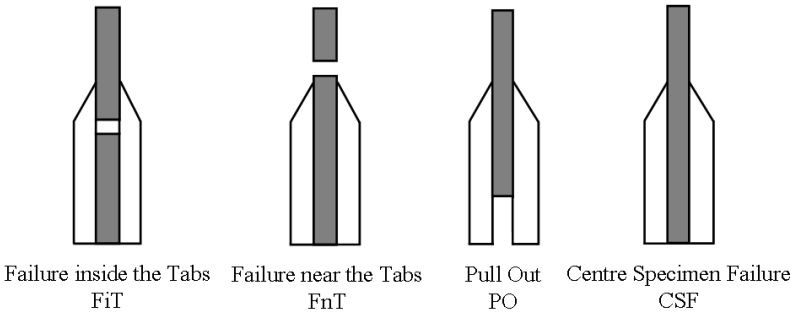

Figure 3-7 Different types of failure that occurred during tensile and compressive testing.

For the chamfering of the tabs, a tool has been designed that can be used on a CNC milling cutter (Figure 3-8). This enables us to mount and chamfer a large plate of 60 mm by 500 mm of which the tabs will be made. These are then attached to the composite plate, before sawing it into coupons.

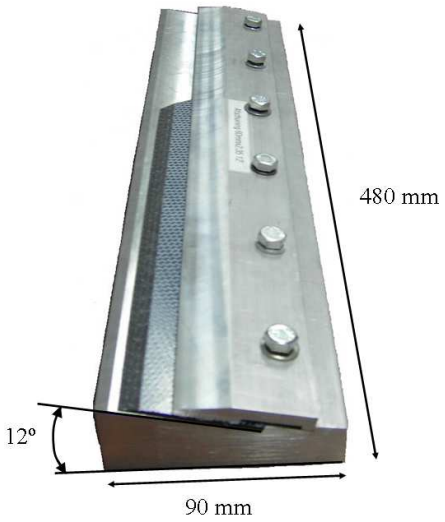

Figure 3-8 Mould for the chamfering of the tabs.

To limit the length of the tabs, a chamfering angle of 12º is used. The dimensions of the tabs, made with the tool mentioned above can be seen in Figure 3-9.

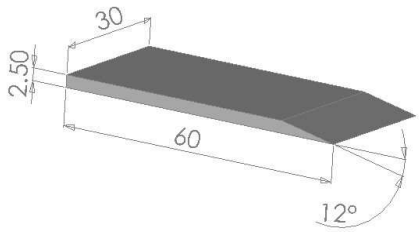

Figure 3-9 Dimensions of the used chamfered tab.

All significant preliminary experiments that were performed are listed in Table 3-1. Some explanations of the used abbreviations are given below the table; the stacking sequence for the tensile coupon was always the same, namely the $[(0°,90°)]_{4s}$.

Table 3-1 Performed experiments on bonding the tabs by means of an adhesive.

Nr.	Tab material	Surface preparation	Used adhesive	Maximum stress [MPa]	Type of fracture
1	Straight aluminium	Sanded + acetone	Loctite 405	671	FnT
2	Straight aluminium	Sanded + acetone	Epofix	610	FnT
3	Straight aluminium	Sanded + acetone	Plexus MA425	631	PO
4	Straight glass-epoxy	Sanded + acetone	Loctite 405	595	FnT
5	Straight glass-epoxy	Sanded + acetone	Epofix	720	FiT
6	Straight glass-epoxy	Sanded + acetone	Hysol EA9394 and glass beads	601	FiT
7	Straight PEI	Sanded + acetone	Hysol EA9394	665	FnT
8	Straight PEI	Sanded + acetone	Hysol EA9394 and glass beads	741	FnT
9	Straight PPS	Sanded + acetone	Loctite 405	650	FiT
10	Straight PPS	Sanded + acetone	Loctite superglue 3	840	FnT
11	Straight PPS	Sanded + acetone + glass-fibres	Epofix	840	FnT
12	Chamfered PPS	Sanded + acetone	MMA 300	270	PO
13	Chamfered PPS	Sanded + acetone	Plexus MA425	323	PO
14	Chamfered PPS	Sanded + acetone	Epofix	780	FnT
15	Chamfered PPS	Sandblasted + acetone	Loctite 406	738	FiT
16	Chamfered PPS	Sandblasted + acetone	Plexus MA420	675	FiT

Figure 3-10 gives a graphical overview of the maximum stress levels. The type of failure is also shown on the illustration.

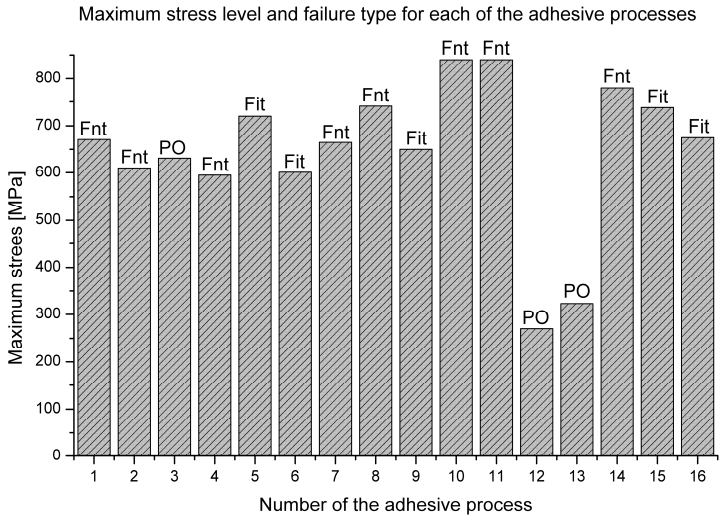

Figure 3-10 The achieved maximum stress level and failure type.

Tab Material

- Straight aluminium: standard aluminium plate of 1.5 mm thick. No chamfer was milled.
- Straight glass-epoxy: a glass fibre-reinforced epoxy with a $[+45°/-45°]_{2s}$ stacking sequence. The reinforcement was a unidirectional E-glass fabric (Roviglas R17/475) and no chamfer was applied.
- Straight PPS: the same carbon fabric-reinforced polyphenylene sulphide as used for the experiments. The used stacking sequence was $[(+45^o,-45^o)]_{4s}$ and no chamfer was milled.
- Chamfered PPS: the same material as the previous, but now the previously discussed chamfer was milled.
- Straight PEI: a glass fibre-reinforced Poly-ethylene Imide. The used stacking sequence was $[(+45^o,-45^o)]_{5s}$.and no chamfer was milled

Surface preparation

- Sanded + acetone: the surfaces of both tabs and specimen were sanded using sandpaper number 80 to have a rough surface. After sanding, both surfaces were degreased using acetone.
- Sanded + acetone + glass fibre: the same as the previous type, but a thin mat of chopped glass fibres was placed between the tabs and the specimen in order to enhance the mechanical adhesion of the adhesive.

- Sandblasted + acetone: both surfaces were sandblasted. This has the advantage over sanding that the roughness is more uniform and the process is slightly faster, especially for large plates although the preparation of the plate takes longer. Furthermore, there is more control on how rough the surface gets, which is an advantage since the fibres at the surface of the specimen are preferably left undamaged.

Adhesives

- Loctite 405: this is a transparent, one-component cyanoacrylate adhesive with low viscosity. It is designed for bonding of metals where very fast fixturing is required. Full functional strength is achieved in maximum ninety seconds, depending on the material combination.
- Loctite 406: this is a transparent, one-component cyanoacrylate adhesive with low viscosity. It is designed for bonding of plastics and elastomeric materials where very fast fixturing is required. Full functional strength is achieved in maximum ninety seconds, depending on the material combination.
- Loctite superglue3: this is a transparent, one component cyanoacrylate adhesive with low viscosity. It is a cheap and simple contact adhesive.
- Epofix: this is a cold-setting resin based on two liquid epoxy components. Epofix is specially developed for mounting of irregularly shaped specimens and for impregnation of porous specimens, where low shrinkage and good mechanical properties in the cured state are required. Owning to its low viscosity, Epofix will penetrate into all porosities and cracks of the specimens. After curing, Epofix can be cut, ground, polished, milled etc. The curing time at room temperature is twenty four hours. No pressure is needed during curing, but it enhances the strength. Therefore, a weight is placed on top of the tabs during curing. Because of the low viscosity, however, the tabs tend to drift away, so they need to be fixed with duck tape.
- Plexus MA 425: this is a two-component methacrylate adhesive designed for structural bonding of thermoplastic, metal and composite assemblies. The white adhesive and blue activator or mixed in a mix ratio by volume of ten to one. The greenish blue mixture has a working time of thirty minutes and a fixture time of eighty minutes, both at room temperature.
- Plexus MA 420: this is a two-component methacrylate adhesive designed for structural bonding of thermoplastic, metal and composite assemblies. The white adhesive and blue activator or mixed in a mix ratio by volume of ten to one. The greenish blue mixture has a working time of one to two minutes and achieves three quarters of its ultimate strength in three to four minutes, both at room temperature.

- MMA300: this is a two-component methyl methacrylate adhesive, which is mixed in a one to one volume ratio. It has a working time of about ten minutes.
- Hysol EA 9394: this is a two-component structural adhesive, which cures at room temperature and possesses excellent strength to 177 ºC and higher. The grey component A and black component B are mixed in a hundred to seventeen weight ratio, resulting in a grey mixture. Both part A and resulting mixture have a high viscosity, which makes it difficult to mix and apply properly. The curing was done under pressure for about one hour and then it was post cured at about seventy degrees Celsius for about one hour. The pressure was realised by placing weights on top of the tabs, about twenty kilograms.

All the tests mentioned above were done on single specimens. However, the objective is to bond a large tab-panel to a large plate and then saw this plate into several specimens. Therefore, some of the more promising tests of Table 3-1 are not suited for the production of large batches.
Both the Loctite 406 and superglue3 give good results, but the working time is too small to allow the bonding of larger plates. The same goes for the insertion of the chopped fibre mat and the Epofix. Because of the low viscosity and the long curing time, both the tabs and the chopped fibres need to be fixed in place. The latter is more easily said than done, since the tabs tend to drift away on the adhesive when the weight is added.

3. 2. 4. a. Chosen adhesive process

Eventually, the two following processes were chosen. The first method was chosen when a large number of specimens were prepared at one time. The PPS-tabs are bonded with Hysol EA 93 94, a two-component structural adhesive, which cures at room temperature and possesses excellent strength to 177 ºC and higher. The mix ratio of the two components is 100 parts A and 17 parts B, by weight.
A small fraction of glass beads, equal to two percent of total weight of the mixed parts is added. The purpose of the beads is to ensure a constant thickness of the layer of epoxy during curing under pressure and to have a better mechanical grip of the adhesive on the PPS.
The tabs are fixed in place using duck tape before curing. The adhesive is then cured for one hour under pressure. The pressure is applied using weights, about 20 kg, on top of the tabs. Afterwards, the epoxy is post-cured for one hour at 70 ºC with a little weight on top of the tabs. Both specimen and tabs are sandblasted to achieve a relatively rough surface, but the surface fibres of the specimen may not be damaged.
This process is chosen because of the limited scatter on the results and the relative ease of the bonding itself. Ten Cate, who uses the same process for their quality control tests, also recommended this process to us.

Since the chamfering of the tabs did not give any improvement, it is no longer done to save preparation time. The edge is polished to remove all protruding fibres, which causes a small radius instead of a straight edge, but no further actions are taken.

The second method was chosen if only small batches of two or three specimens were needed. In this case, the amount of adhesive needed was too low to obtain a homogenous mixture of the Hysol mixed with beads. In this case, the polished or sandblasted specimens and tabs were degreased with acetone and then, the tabs were bonded using the Loctite 406 adhesive.

3. 3. MODIFICATIONS OF THE EXTENSOMETER

While doing the preliminary tests to determine the end tab configuration and bonding process, it was noticed that the original INSTRON blades sometimes lost their grip on the specimen, resulting in a jump in the strain measurement. Such a jump can be very dangerous in a strain-controlled experiment, where the hydraulic machine loads and unloads the specimen up to specified strain levels. A sudden jump will cause an overshoot, possibly resulting in damage to the tensile machine.

The main problem of the loss of grip is explained in Figure 3-11. The force that pulls the blade to the surface of the specimen is F_{blade}. The force in the rubber band is F_{band}. The best case is of course that F_{blade} equals F_{band}. However, since the width of the specimen is larger than the distance between the two mounting points for the elastic rubber, this is not the case for the standard blades.

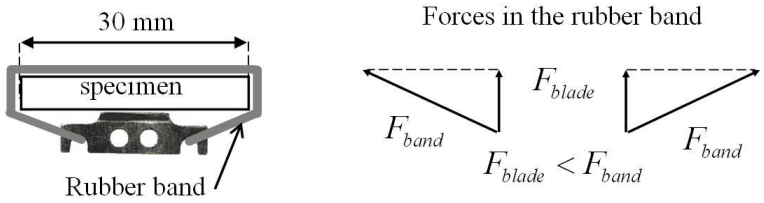

Figure 3-11 The principle of the forces when mounting an extensometer blade on a specimen; original INSTRON blade.

INSTRON did not have wider blades, so a set of our own was made. An example of these blades is also shown in Figure 3-12; for these blades F_{blade} equals F_{band}, which is of course the ideal situation.

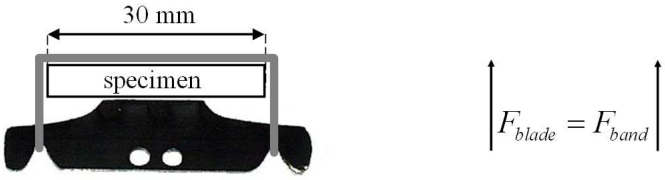

Figure 3-12 The principle of the forces when mounting an extensometer blade on a specimen; newly made blade.

The first tests with these blades were successful, in this way that they no longer lost grip on the specimen. However, when comparing the measured stiffness of these specimens with the stiffness measured in earlier tests, with the original blades, it was noticed that the material suddenly seemed stiffer.

Since it was the same material, the problem should lie in the extensometer. The extensometer was then calibrated, using both the original and the new blades. The calibration setup is shown in Figure 3-13.

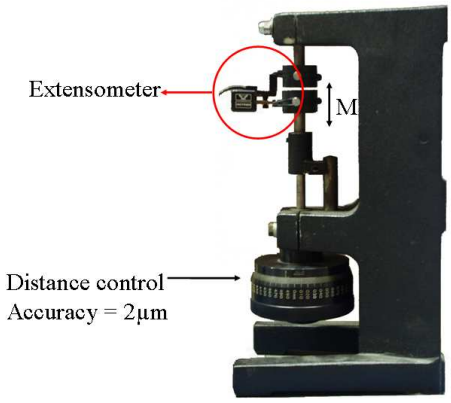

Figure 3-13 Illustration of the setup used for calibrating the extensometer.

Using a special micrometer, a displacement with an accuracy of 2 µm can be imposed on a pseudo-test specimen. Using the strain measurement of the extensometer, the corresponding displacement can be calculated by multiplying the strain with the gauge length. If this measured displacement is depicted as a function of the imposed displacement, the calibration factor can be derived.
For the original blades, a factor of 0.9873 with respect to the strain given by the INSTRON Fasttrack controller was found, where the new blades yielded a factor of 1.1919 (Figure 3-14).

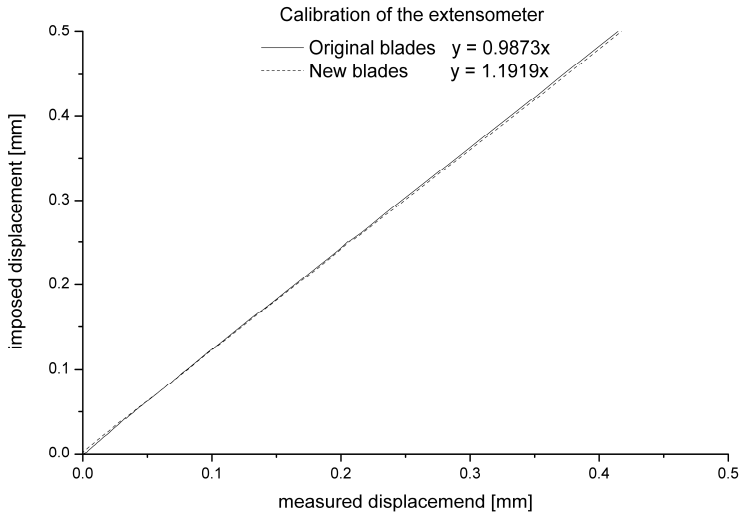

Figure 3-14 Calibration data of the original and new blades of the extensometer.

The difference between the factors can be explained by the combination of the length of the blade and the principle of the extensometer. This is illustrated in Figure 3-15.

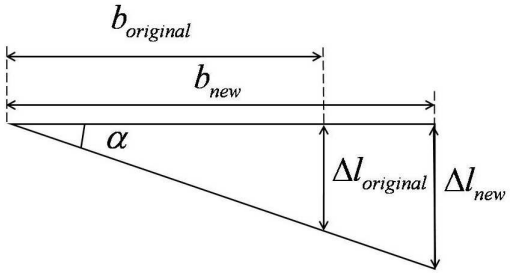

Figure 3-15 Illustration of the difference in calibration factors.

The strain measurement of the extensometer is based on bending, so on the angle α. The signal conditioner then calculates the strain as

$$\varepsilon_{orig} = \frac{\Delta l_{original}}{l_{gauge}} \tag{3.4}$$

This strain corresponds with a blade length of $b_{original}$, which is standard for the INSTRON extensometer. However, if the blades have a different length, for instance b_{new}, the actual strain corresponding with α is

$$\varepsilon_{new} = \frac{\Delta l_{new}}{l_{gauge}} \tag{3.5}$$

which is different than the strain measured.
Since the angle α remains the same, the ratio between the two strains can be easily calculated using the definition of a tangent in a rectangular triangle:

$$\tan\alpha = \frac{\Delta l_{new}}{b_{new}} = \frac{\Delta l_{original}}{b_{original}} \tag{3.6}$$

If the two previous equations are substituted, the following is obtained:

$$\varepsilon_{new} = \frac{\Delta l_{new}}{l_{gauge}} = \frac{b_{new}}{b_{original}} \frac{\Delta l_{original}}{l_{gauge}} = \frac{b_{new}}{b_{original}} \varepsilon_{original} \tag{3.7}$$

This means that if the new blades are longer, which is the case, the measured strain is smaller than the strain that actually occurs. From Figure 3-14 it can be concluded that the relationship between actual and measured strain is linear. Therefore, there is no reason for not to use the new and improved blades, since the effect of the length of the blades can be easily compensated by multiplying the strain with a constant factor.

The fact that the calibration factor of the original blades is not one can also be explained by Equation 3.7. Because of the extensive use of the extensometer in the past, the blades had lost their sharpness. The blades were re-sharpened, causing a reduction in length, which leads to the factor smaller than one.

Even though this new mounting system shows great improvement with respect to the loss of grip, the use of two line contacts does not seem the ideal solution for excellent grip of the blades on the surface. If both edges are not exactly aligned, which is almost always the case, there is one blade which only makes contact on one corner.
During a visit at Ten Cate, this problem was mentioned and they had the perfect solution. Their tensile machine was a Zwick tensile testing machine and they had a different design of extensometer blades, which make contact with the specimen on three discrete points. Since three points fully define a plane in space, the extensometer should always establish a good contact. INSTRON does not have these kinds of blades, and therefore, a new set was made (Figure 3-16).

Figure 3-16 Three-point extensometer blades.

This set of blades was also calibrated, yielding a factor of 1.1773 with respect to the strain given by the Fasttrack controller.
The three-point system, together with the wider gripping of the specimen gave best results with respect to the loss of contact during testing; therefore this principle was used for all further experiments.

3. 4. MATERIAL PROPERTIES

The following mechanical properties (Table 3-2) were received for the carbon fabric-reinforced polyphenylene sulphide from the Technical University of Delft. They were determined according the 'MIL 17 Guidelines for Characterization of Structural Materials' and they apply for a temperature of 23 ºC and an atmospheric humidity of 50 %.

Table 3-2 Mechanical properties of the Carbon 5H CD0286 T300J 3K film stacked.

Tensile strength warp [MPa]	734*
Tensile strength weft [MPa]	754
Tensile modulus warp [MPa]	56,000
Tensile modulus weft [MPa]	57,000
Compression strength warp [MPa]	567
Compression strength weft [MPa]	498
Compression modulus warp [MPa]	52,000
Compression modulus weft [MPa]	50,000
In-plane shear strength [MPa]	110
In-plane shear modulus [MPa]	4,175
Open hole tensile strength [MPa]	274
Open hole compressive strength [MPa]	259
Compression after impact [MPa]	238
Yield bearing strength [MPa]	391
Ultimate bearing strength [MPa]	738

* this value is the most recent and is based on the average value of all static tests conducted during this research.

3. 4. 1. Determining the properties by quasi-static tensile testing

For the static testing, only the $[(0°,90°)]_{4s}$ lay-up was used. The test coupons were sawn with a water-cooled diamond tipped saw, the dimensions of the coupons are shown in Figure 3-17. $[\pm 45^{o}]_{2s}$ glass fibre epoxy tabs were used in order to avoid damage of the specimens by the grips of the tensile machine. These tests were also used for determining the best end tab configuration, hence the used tab-material.

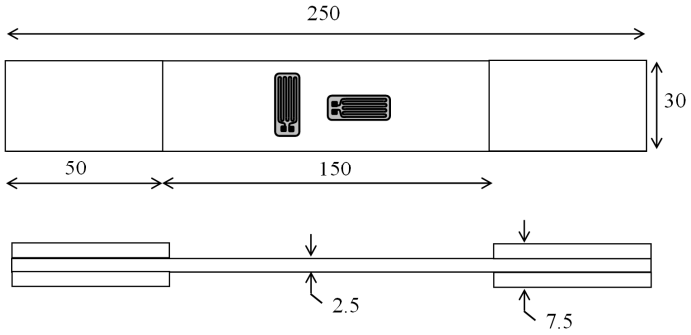

Figure 3-17 Dimensions of the used tensile coupon, equipped with tabs of $[\pm 45^{o}]_{2s}$ glass fibre epoxy.

The strain gauges were mounted in the 0º and 90º directions to measure longitudinal and transverse strain.
Poisson's ratio is then given by:

$$\nu_{12} = -\frac{\varepsilon_{22}}{\varepsilon_{11}} \tag{3.8}$$

An example of an instrumented tensile coupon is depicted in Figure 3-18.

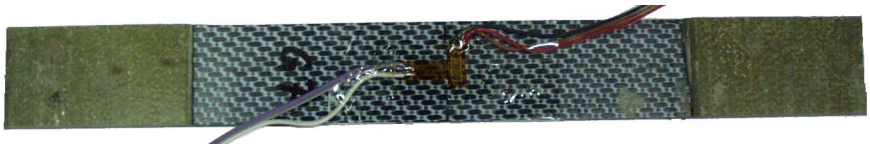

Figure 3-18 An example of a specimen instrumented with the longitudinal and transverse strain gauge.

Figure 3-19 depicts the evolution of both longitudinal and transverse strains for both the $[(0°,90°)]_{4s}$ specimens G4 and G7 as a function of pseudo-time, where 0 corresponds with the start of the experiment and 1 corresponds with failure of the specimen. It can be noticed that the transverse strains remain very small. At failure they reach a value of -0.00039 for G4 and -0.00030 for G7. The ultimate longitudinal strains are 0.0112 and 0.0102 respectively for G4 and G7.

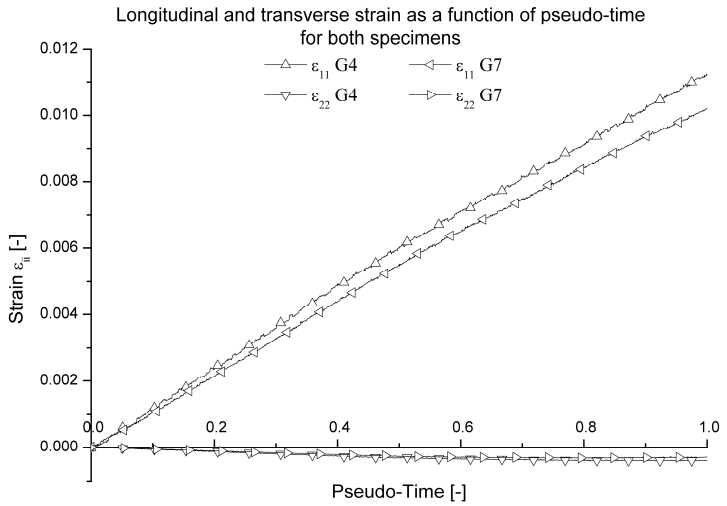

Figure 3-19 ε_{11} and ε_{22} as a function of pseudo-time for both specimens.

In Figure 3-20, the evolution of the stress σ_{11} as a function of the strain ε_{11} is given. It may be concluded that this material has a linear behaviour up to failure when tested along the warp direction. The failure stresses are 643.5 MPa for G4 and 594.3 MPa for G7. These low values, compared to the value in Table 3-2 are the result of the used tab-material and -geometry. Young's modulus can also be derived from these experiments, a value of 57.5 GPa for G4 and 58.4 GPa for G7 are found. These values show good agreement with the values in Table 3-2.

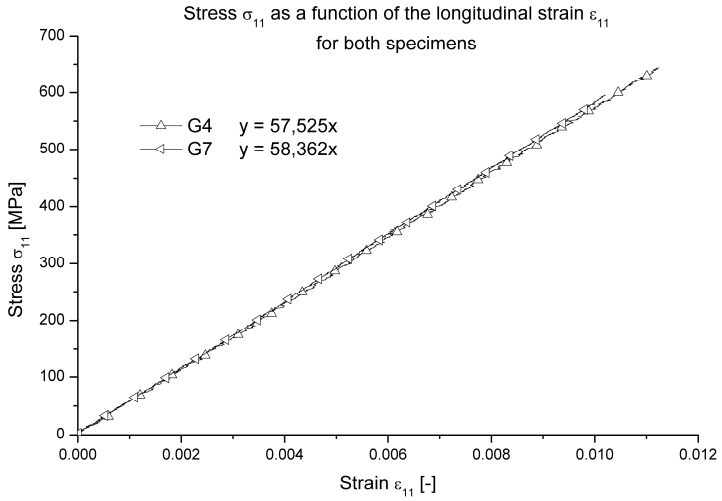

Figure 3-20 σ_{11} as a function of ε_{11} for both specimens.

Finally, Figure 3-21 shows the evolution of Poisson's ratio as a function of the longitudinal strain. An average value of 0.049 and 0.053 is found for G4 respectively G7.

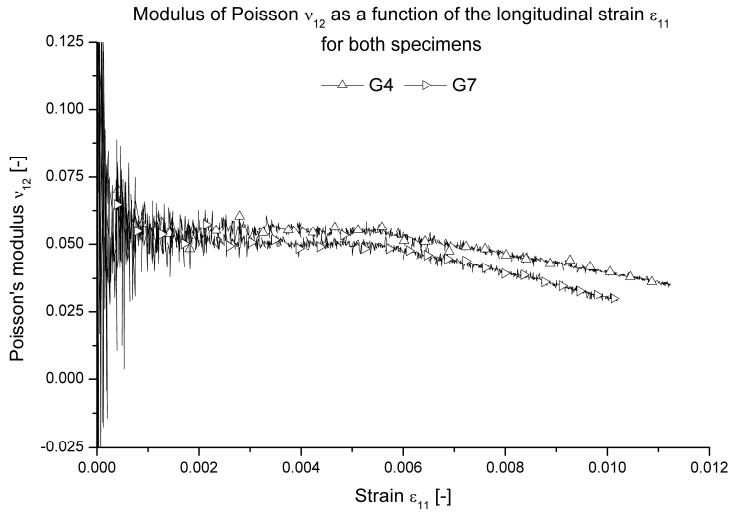

Figure 3-21 ν_{12} as a function of ε_{11} for both specimens.

It may be noted that once the longitudinal strain exceeds about 0.006, the ratio tends to decrease. At fracture, ν_{12} is only about 60% of its original value, namely 0.035 for G4 and 0.03 for G7. This decrease in the Poisson's ratio may present the possibility to use ν_{12} as a means to characterize damage.

3. 4. 2. Determination of the elastic properties using the resonalyser method

3. 4. 2. a. Introduction

When designing constructions with any type of material, the accurate knowledge of the elastic properties of the used materials is very important. Often, the choice of material and type of construction depend on it. Therefore, a large number of experiments are available to determine the various mechanical properties.
The resonalyser method [6, 7] is a material identification technique, which is based on the measurement of resonance frequencies of freely suspended rectangular test plates, combined with numerical simulations. It is an inverse method that identifies the material parameters in such a way that the numerically computed resonance frequencies match the experimental values. The results obtained with this method are then compared with the results from a standard tensile test according to the "*ASTM standard D3039-93 standard test method for tensile properties of polymer matrix composite materials"*, given in the previous paragraph.
In the next paragraphs, the theoretical background and the principle of the resonalyser is discussed.

3. 4. 2. b. Theoretical background of the resonalyser

The elastic behaviour of materials having orthotropic symmetry axes in a state of plane stress can be described by the following relation between strains and stresses:

$$\begin{Bmatrix} \varepsilon_{11} \\ \varepsilon_{22} \\ \gamma_{12} \end{Bmatrix} = \begin{bmatrix} \frac{1}{E_{11}} & -\frac{\nu_{12}}{E_{11}} & 0 \\ -\frac{\nu_{21}}{E_{22}} & \frac{1}{E_{22}} & 0 \\ 0 & 0 & \frac{1}{G_{12}} \end{bmatrix} \begin{Bmatrix} \sigma_{11} \\ \sigma_{22} \\ \tau_{12} \end{Bmatrix} \tag{3.9}$$

In this expression, 1 and 2 are the main material axes of the orthotropic material, (ε_{11}, ε_{22}, γ_{12}) represents the strain components, (σ_{11}, σ_{22}, τ_{12}) the stress components, E_{11} and E_{22} the Young's moduli in the first and second main material direction, ν_{12} and ν_{21} the Poisson's ratios and G_{12} is the shear modulus in the (1,2)-plane. If linear material behaviour is assumed, the elastic properties E_{11}, E_{22}, ν_{12}, ν_{21} and G_{12} are also called the 'engineering constants'. Due to the symmetry of the compliance matrix in Equation 3.9, four independent engineering constants remain: E_{11}, E_{22}, ν_{12} and G_{12}.

The resonalyser procedure is a mixed numerical / experimental method that aims to identify the engineering constants of orthotropic materials using measured resonance frequencies of freely suspended rectangular specimens.

For the identification of the four orthotropic material constants, it is necessary to measure the first three resonance frequencies of a rectangular plate and the first resonance frequency of two beams, one cut along the longitudinal direction and the other cut along the transversal direction of the test plate.

Identification of the Young's modulus by measuring the resonance frequency of a test beam

The first resonance frequency of a test beam with free boundary conditions is associated to a bending mode deformation. From the first resonance it is possible to calculate the Young's modulus E of the material in the longitudinal direction of the beam using the formula [8-11] :

$$E = 0.946 \frac{\rho f^2 L^4}{t^2} \text{ [MPa]} \tag{3.10}$$

Where:

ρ:	specific mass [kg/m^3]
f:	measured resonance frequency [Hz]
t:	thickness of the beam [mm]
L:	length of the beam [mm]

This formula is only valid for sufficiently thin beams. This requires for composite materials a ratio L/t larger than 50.

Identification of the orthotropic stiffness properties by measuring the resonance frequencies of a test plate

The identification of the orthotropic stiffness properties is done by simulation of the rectangular test plate using a numerical model on the computer. The numerical model allows the calculation of the resonance frequencies on the condition that the stiffness properties, the dimensions and the mass of the plate are known. The basic principle of the resonalyser is to compare measured frequencies of the test plate with computed frequencies using a numerical finite element model of the same test plate (Figure 3-22). The engineering constants in the numerical model are considered as unknown material parameters. Starting from an initial guess, the engineering constants are iteratively updated till a series of numerically computed resonance frequencies match the experimentally measured frequencies.

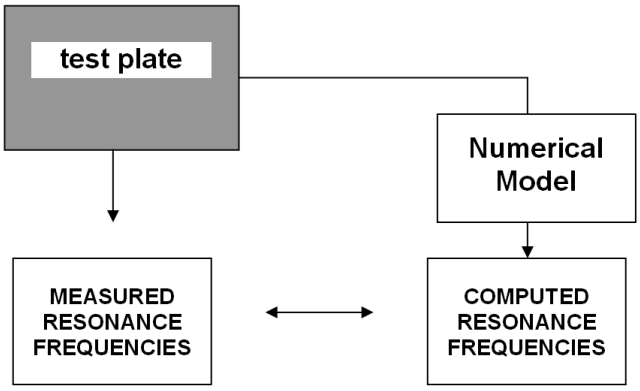

Figure 3-22 Comparison between experimentally measured and computed resonance frequencies of the same test plate.

Such an inverse procedure can only yield good results if the numerical model is controllable and if the elastic properties can be observed through the measured data [12-14]. This requires that in the selected series of frequencies at least one of the frequencies varies significantly for variations of each of the elastic properties. It can be shown [15, 16] that this requirement is fulfilled if the ratio a/b of the length and width of the test plate equals approximately to $\frac{a}{b} = \sqrt[4]{\frac{E_{11}}{E_{22}}}$. A plate with such a ratio is called a 'Poisson test plate' [16]. A Poisson test plate shows a predictable sequence of mode shapes for the first 3 resonances: a torsional, an anticlastic and a synclastic (Figure 3-23). The anticlastic mode is also known as the saddle mode and the synclastic is known as the breathing mode.

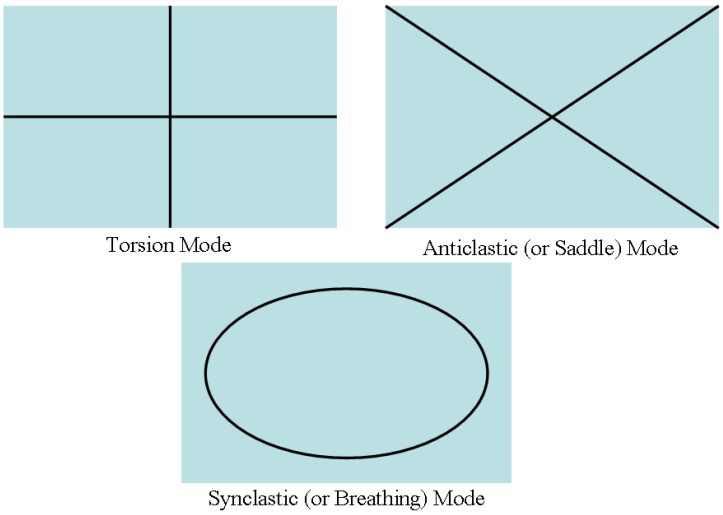

Figure 3-23 The first three mode shapes of a Poisson test plate.

The name 'Poisson test plate' has been chosen based on the observation that the frequencies of the anticlastic and synclastic mode shapes are particularly sensitive for changes of the Poisson's ratio of the plate material. A material with a (hypothetical) zero value for Poisson's ratio would make the frequencies of both modes coincide, which means that the synclastic and anticlastic modes become pure bending modes in respectively the 1 and the 2-direction. As such, the plate can be considered as a beam in the length direction, giving a value for E_{11} using Equation 3.10, but also as a beam in the transverse direction, yielding a value for E_{22} using the same equation. Since the resonance frequencies of both modes are equal, the ratio of $\frac{a}{b} = \sqrt[4]{\frac{E_{11}}{E_{22}}}$ can easily be derived. The values E_{11} and E_{22} necessary to compute the plate dimensions a and b can be found by cutting two test beams, one along the first principal material direction and a second along the second principal direction. By measuring the first resonance frequencies of the freely suspended test beams, the values of E_{11} and E_{22} can be computed using Equation 3.10. The obtained values of E_{11} and E_{22} are also used as initial values for the resonalyser procedure. Good initial values for the other elastic constants G_{12} and ν_{12} can be obtained with empirical formulas [16]. The determination of these values will be discussed in the next section. Starting with these initial values, the engineering constants in a finite element model of the test plate are iteratively updated till the three first computed resonance frequencies match the measured frequencies associated with the mode shapes shown in Figure 3-23. In the finite element model, the plate dimensions and mass are considered as known and fixed values. The four engineering constants are stored in a parameter column **p**. The updating of **p** is realised by minimising a cost function C(**p**):

$$C(\boldsymbol{p}) = \left[m_r - y_r(\boldsymbol{p})\right].W^m_{rs}.\left[m_s - y_s(\boldsymbol{p})\right] + (p_r^{(0)} - p_r).W^p_{rs}.(p_s^{(0)} - p_s) \quad (3.11)$$

In Equation 3.11 $C(\boldsymbol{p})$ is a $\Re^{NP} \rightarrow \Re$ cost function yielding a scalar value, $\boldsymbol{p}$ is a *(NP x 1)* column containing the *NP=4* material parameters E_{11}, E_{22}, ν_{12} and G_{12}, $\{p^{(0)}\}$ contains the initial estimates for the material parameters, *{y}* is a *(NM x 1)* output column containing the *NM=3* computed frequencies using parameter values *{p}*, *{m}* contains the *(NM x 1)* measured frequencies, $[W^{(m)}]$ is a *(NM x NM)* weighing matrix applied on the difference between the measured column and the output column, and $[W^{(p)}]$ is a *(NP x NP)* weighing matrix for the difference between the initial parameter column $\{p^{(0)}\}$ and the parameter column *{p}*.

The cost function $C(\boldsymbol{p})$ has a minimal value for the optimal parameter values column $\{p^{(opt)}\}$. The choice of the weighing matrices is discussed, among others, in [12, 17, 18].

The updating of the initial parameter column toward $\{p^{(opt)}\}$ by minimization of the cost function is given by the following recurrence formula in iteration step (j+1):

$$p_k^{(j+1)} = p_k^{(j)} + [W_{km}^{p} + S_{rk}^{j}.W_{rs}^{(m)}.S_{sm}^{j}]^{-1} .\left[S_{rm}^{j}.W_{rs}^{(m)}.(m_s - y_s^{(j)}) + W_{ms}^{(p)}.(p_s^{(0)} - p_s^{(j)})\right] \quad (3.12)$$

In Equation 3.12 S^J is the sensitivity matrix containing the partial derivatives of the output column to the parameter column.

The measurement of the three resonance frequencies of the test plate can be performed simple, fast and accurate with a PC equipped with a data acquisition card. An accelerometer is fixed on the freely suspended test plate which is impacted with a small hammer. The generated time domain signal in the accelerometer is digitised by the data acquisition card and stored in the computer's memory. Next the signal is transformed by a Fast Fourier Transformation [19] to the frequency domain in which the resonance frequencies occur as sharp peaks and can easily be identified. The numerical model of the test plate is based on the Love-Kirchhoff theory for thin plates. The model is sufficiently accurate if the length/thickness ratio of the plate exceeds a factor of about 50 [20]. Very accurate eight order polynomial Lagrange functions are taken as the shape functions in the used numerical finite element model of the test plate [16]. The stiffness matrix of the test plate is evaluated in each iteration cycle using standard finite element procedures with the values of the parameter column **p** at that moment. The computed resonance frequencies are obtained by the solution of a generalised eigenvalue problem composed with the constant mass matrix and the evaluated stiffness matrix. The iteration procedure using Equation (3.12) ends if convergence of **p** is reached. The value of the engineering constants in **p** in the last iteration cycle is considered as the result of the Resonalyser procedure.

Determination of the initial values of the orthotropic stiffness properties used by the numerical model

The measurement of the resonance frequencies of two test beams (which was necessary to establish the correct test plate ratio), also supplies us with good initial values of E_{11} and E_{22}, via the Equation 3.10.

For the determination of the initial values of the Poisson's ratio and the shear modulus G_{12}, a further study of the mode shapes of the rectangular plate is required. As mentioned above (Figure 3-23), the first mode of the test plate is a torsion mode.

The magnitude of the eigenvalue belonging to this mode is almost exclusively determined by the shear modulus G_{12}, and can be approximated by the formula [16]:

$$\lambda_T = 41.75\frac{G_{12}t^3}{Mab} \tag{3.13}$$

where:

$\lambda_T = (2\pi f_T)^2$: eigenvalue corresponding to the torsion mode [Hz^2]
t: thickness of the test plate [mm]
f_T: resonance frequency corresponding to the torsion mode [Hz]
a: length of the test plate [mm]
b: width of the test plate [mm]
M: mass of the test plate [kg]

The eigenvalues belonging to the saddle and breathing modes coincide when the Poisson's ratio is equal to zero. A value of Poisson's ratio different from zero makes the eigenvalue of the saddle mode decrease and the eigenvalue of the breathing mode increase. So, the bigger the Poisson's ratio, the bigger becomes the difference between the eigenvalues of the saddle and breathing modes. Using an empirical formula it is possible to express the relation between the Poisson's ratio and the two eigenvalues [15, 16]:

$$\nu_{12} = C_1\frac{\lambda_A - \lambda_z}{\lambda_A + \lambda_z} \tag{3.14}$$

where:

$\lambda_A = (2\pi f_A)^2$ eigenvalue corresponding to the breathing mode [Hz^2]
$\lambda_Z = (2\pi f_Z)^2$ eigenvalue corresponding to the saddle mode [Hz^2]
f_A: resonance frequency corresponding to the breathing mode [Hz]
f_Z: resonance frequency corresponding to the saddle mode [Hz]
C_1: a constant [-]

3. 4. 2. c. Stacking sequences and experimental setup

Two stacking sequences were used for this study, namely a $[(0°,90°)]_{4s}$ and a $[(0°,90°)/(90°,0°)]_{2s}$. The latter was considered to have confirmation of the results, obtained with the first stacking sequence, with respect to the low Poisson's ratio.
The thickness of each layer is about 0.3 mm, the density of the lamina is 1555 kg/m^3 and the fibre volume fraction is 50%.

For the resonalyser method, two different test plates were used:

(i) Plate 1: $[(0°,90°)]_{4s}$

One plate and eight beams, four along the warp and four along the weft direction, were cut out of the master plate.

(ii) Plate 2: $[(0°,90°)/(90°,0°)]_{2s}$

Again, one test plate and eight test beams, four along the warp and four along the weft direction, were cut.

The exact geometry, mass and specific mass of each test specimen are given in Table 3-3.

Table 3-3 Geometry, mass and specific mass of the test specimens.

Specimen	Length [m]	Width [m]	Thickness [m]	Mass [kg]	Specific Mass [kg/m^3]
Plate $[(0°,90°)]_{4s}$	0.149	0.14904	0.00241	0.08350	1560.200
Plate $[(0°,90°)/(90°,0°)]_{2s}$	0.14934	0.14993	0.00241	0.08314	1543.939
Beam 1: $[(0°,90°)]_{4s}$	0.1488	0.02153	0.00235	0.01189	1579.309
Beam 2: $[(0°,90°)]_{4s}$	0.1482	0.0222	0.00241	0.01238	1561.358
Beam 3: $[(0°,90°)]_{4s}$	0.14854	0.0234	0.00237	0.01290	1565.965
Beam 4: $[(0°,90°)]_{4s}$	0.14904	0.0235	0.00239	0.01319	1575.710
Beam 5: $[(0°,90°)]_{4s}$	0.14823	0.02365	0.00242	0.01305	1538.253
Beam 6: $[(0°,90°)]_{4s}$	0.14875	0.02288	0.00236	0.01269	1579.926
Beam 7: $[(0°,90°)]_{4s}$	0.14848	0.02405	0.00236	0.01329	1576.994
Beam 8: $[(0°,90°)]_{4s}$	0.14809	0.02346	0.00238	0.01308	1581.893
Beam 9: $[(0°,90°)/(90°,0°)]_{2s}$	0.14948	0.02207	0.00241	0.01237	1555.848
Beam 10: $[(0°,90°)/(90°,0°)]_{2s}$	0.14936	0.02409	0.00240	0.01340	1551.752
Beam 11: $[(0°,90°)/(90°,0°)]_{2s}$	0.14926	0.02315	0.00242	0.01283	1534.323
Beam 12: $[(0°,90°)/(90°,0°)]_{2s}$	0.14915	0.02341	0.00243	0.01304	1536.904
Beam 13: $[(0°,90°)/(90°,0°)]_{2s}$	0.14913	0.02320	0.00239	0.01286	1555.214
Beam 14: $[(0°,90°)/(90°,0°)]_{2s}$	0.14926	0.02355	0.00239	0.01297	1543.859
Beam 15: $[(0°,90°)/(90°,0°)]_{2s}$	0.14941	0.023	0.00236	0.01271	1567.206
Beam 16: $[(0°,90°)/(90°,0°)]_{2s}$	0.149	0.02349	0.00239	0.01300	1554.090

Experimental setup for the Resonalyser method

The experimental setup includes a suspension frame for the rectangular test plate, a loudspeaker for the excitation, a laser velocity vibrometer, a signal conditioning unit, a data acquisition unit and a personal computer (see Figure 3-24).
The test plate is suspended on the frame with thin wires. This configuration simulates completely free boundary conditions. The test plate is excited by a periodic chirp signal with a desired bandwidth through a loudspeaker. As a result of this excitation, the test plate will start to vibrate on its resonance frequencies inside the frequency band of the signal. The vibration amplitude of the plate as a function of time is picked up by the laser vibrometer and stored in the memory of PC by a data acquisition system. The resonance frequencies of the plate in the band of interest are detected by taking the Fast Fourier transform of the signal.

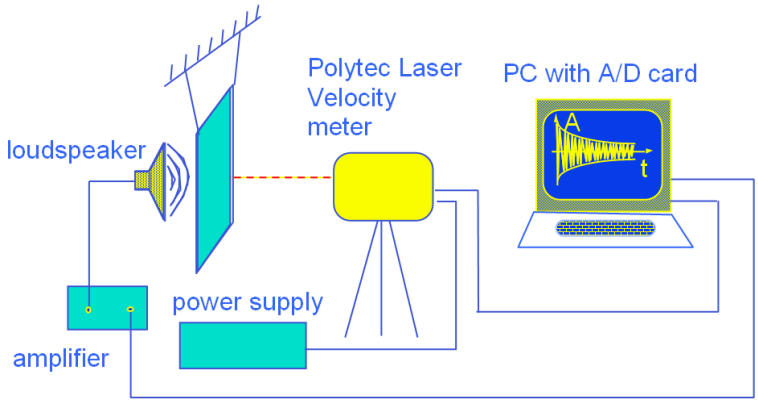

Figure 3-24 The resonalyser setup.

3. 4. 2. d. Resonalyser results

Identification of the material properties using the resonalyser procedure

The first three resonance frequencies of the plates, as well as the first resonance of each beam were measured with the setup. Next the material properties in the numerical model in the resonalyser procedure were tuned iteratively, as described in paragraph 3. 4. 2. b, till the computed frequencies match the measured frequencies as closely as possible. The values of the four orthotropic stiffness properties in the last iteration cycle of this procedure were identified, and the final results are listed in Table 3-4.
The values of E_{11} and E_{22} measured from the resonance frequencies of the beam specimens using Equation 3.10 are also listed in Table 3-4.

Table 3-4 Measured resonance frequencies and identified material properties via the resonalyser technique.

Specimen	Resonance Frequency [Hz]	E_{11} [GPa]	E_{22} [GPa]	G_{12} [GPa]	ν_{12} [-]
Plate $[(0°,90°)]_{4s}$	201.96 625.91 687.02	61.19	51.52	4.82	0.023
Plate $[(0°,90°)\ /(90°,0°)]_{2s}$	193.49 636.87 660.34	55.37	55.77	4.48	0.040
Beam 1: $[(0°,90°)]_{4s}$	662,02	58.14	-	-	-
Beam 2: $[(0°,90°)]_{4s}$	666,02	54.44	-	-	-
Beam 3: $[(0°,90°)]_{4s}$	666,38	57.04	-	-	-
Beam 4: $[(0°,90°)]_{4s}$	664,27	56.84	-	-	-
Beam 5: $[(90°,0°)]_{4s}$	615,95	-	45.53	-	-
Beam 6: $[(90°,0°)]_{4s}$	606,96	-	48.42	-	-
Beam 7: $[(90°,0°)]_{4s}$	611,93	-	48.78	-	-
Beam 8: $[(90°,0°)]_{4s}$	617,18	-	48.42	-	-
Beam 9: $[(0°,90°)\ /(90°,0°)]_{2s}$	640,97	52.00	-	-	-
Beam 10: $[(0°,90°)\ /(90°,0°)]_{2s}$	642,95	52.45	-	-	-
Beam 11: $[(0°,90°)\ /(90°,0°)]_{2s}$	639,27	50.29	-	-	-
Beam 12: $[(0°,90°)\ /(90°,0°)]_{2s}$	644,10	50.57	-	-	-
Beam 13: $[(0°,90°)\ /(90°,0°)]_{2s}$	637,79	-	51.84	-	-
Beam 14: $[(0°,90°)\ /(90°,0°)]_{2s}$	633,88	-	51.01	-	-
Beam 15: $[(0°,90°)\ /(90°,0°)]_{2s}$	631,20	-	52.87	-	-
Beam 16: $[(0°,90°)\ /(90°,0°)]_{2s}$	634,37	-	51.07	-	-

In this table, the difference between the warp (0°,90°) and the weft (90°,0°) direction can again (see Table 3-2) be noticed. This difference is due to the weaving process. The warp fibres are pre-stressed during the weaving process, but the weft fibres are shot through and then cut at the ends. As such, these fibres bend around the stressed warp fibres. When load is applied, the warp fibres are immediately loaded, whereas for the weft fibres, first all the bends are stretched, resulting in a lower stiffness.

Visualisation of the mode shapes

The mode shapes of a typical test beam (Figure 3-25) and the mode shapes of both test plates (Figure 3-26 and Figure 3-27) are visualised using the laser vibrometer.

Figure 3-25 Bending mode of a typical test beam.

The mode shapes corresponding to the measured resonance frequencies for both plates are given in the following pictures (Figure 3-26 and Figure 3-27). Here, it can be noticed that the synclastic and anticlastic mode (second and third mode) are very much alike and are practically bending modes.

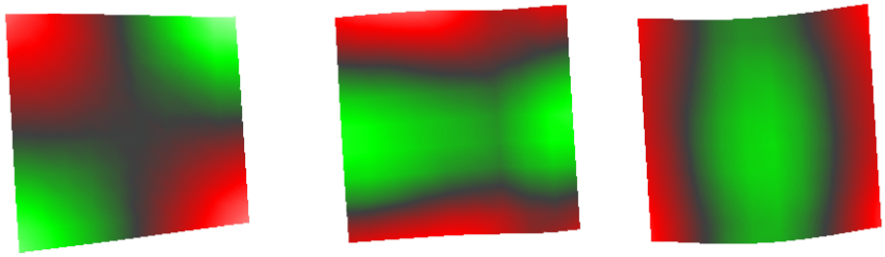

Figure 3-26 Mode shapes of plate 1: $[(0^{o},90°)]_{4s}$ corresponding to the first three resonance frequencies, measured with the laser velocity vibrometer.

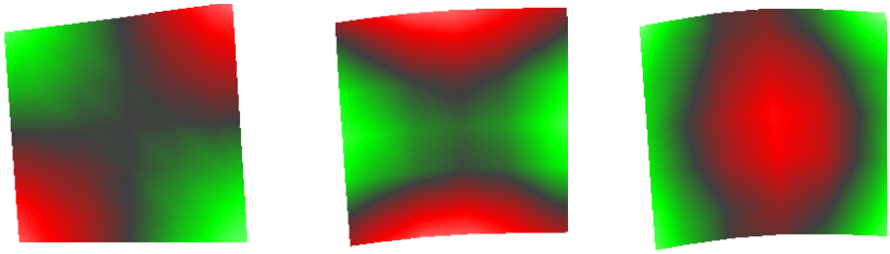

Figure 3-27 Mode shapes of plate 2: $[(0^{o},90°)/(90^{o},0°)]_{2s}$ corresponding to the first three resonance frequencies, measured with the laser velocity vibrometer.

3. 4. 2. e. Conclusions

The resonalyser technique is well suited for the accurate identification of the elastic properties of an orthotropic composite material. The values determined with this method show good correspondence with the values derived from the static uni-axial tests. However, the advantage of the resonalyser technique over the uni-axial test is the little preparation time needed for the experiments, once the resonalyser setup is acquired, since the technique does not require strain gauges, extensometers or end tabs.

The Poisson's ratio of the plate $[(0°,90°)]_{4s}$ is very small. An average value of 0.033 was found. For the resonalyser technique, this causes the second and third mode shapes to be almost two bending mode shapes instead of saddle and breathing mode-shapes. The low ν_{12} is also confirmed by the $[(0°,90°)/(90°,0°)]_{2s}$ experiments.

3. 5. OPTICAL FIBRE SENSORS

3. 5. 1. Introduction

The classical methods for periodical maintenance of composite structures, for example airplanes, use many NDE techniques (e.g. ultrasound, radiography and thermography). However, these techniques require extensive human involvement and expensive procedures. Moreover, this kind of periodical inspection cannot give any information concerning accidents or failures occurring between two successive overhauls. In order to overcome such shortcomings it is now possible to use 'sensitive' materials, which means the material includes sensors providing real-time information about the material itself, e.g. embedded optical fibres [21, 22].

Continuous health monitoring of materials would result in improved durability and safety of structures. On-line health monitoring sensors must meet three requirements: (i) they must be small in size (with no damage to the structure), (ii) they must offer the possibility of being located in remote and inaccessible areas of the structure and (iii) they must be able to transmit information to a central processor. This information must be in direct relation with the physical process being monitored and the properties and performances that have to be maintained. Evidently they must compete in sensitivity with conventional NDE techniques and be able to monitor a sufficient area of the structure.

As mentioned, the optical fibre sensors can be used to obtain a sensitive material. These fibres are embedded together with the other reinforcement fibres and are capable of carrying loads. An average optical fibre is about 125 microns in diameter, which is about ten times as much as the average carbon fibre (10 microns). Because of the load carrying capability however, they have limited influence on the mechanical behaviour. The feasibility of optical fibre sensors for monitoring the mechanical behaviour is already studied in [23, 24] for a thermosetting matrix, with good result.

It was even concluded that optical fibre Bragg sensors were more reliable than classical strain gauges [23]. Doyle et al. [25] experimented on the use of fibre optic sensors for tracking the cure reaction of a fibre-reinforced epoxy, with success. They also successfully demonstrated the feasibility of these sensors for monitoring the stiffness reduction due to fatigue damage, but for thermosetting matrix. The latter was also done by Shin and Chiang for a carbon fibre-reinforced epoxy [26, 27].

The polyphenylene sulphide matrix, which is considered for this research, is known for its chemical inertness, which means that de-bonding of the optical fibre may be a problem. Therefore, extra attention is given to the embedding of the fibre.

Furthermore, the optical fibre needs to endure far worse circumstances during the hot pressing of the plates (high pressure and high temperature) than it is the case for the previously mentioned reinforced epoxies, which were manufactured by autoclave or vacuum assisted resin transfer moulding. As such, the question will be if the fibre even survives the hot pressing process.
In order to visualize the embedded fibre, X-ray micro-tomography is used. The feasibility of the latter is also assessed for visualizing fatigue damage.

3. 5. 2. An introduction on optical fibres

The principle of an optical fibre sensor with a Bragg grating is illustrated in Figure 3-28.

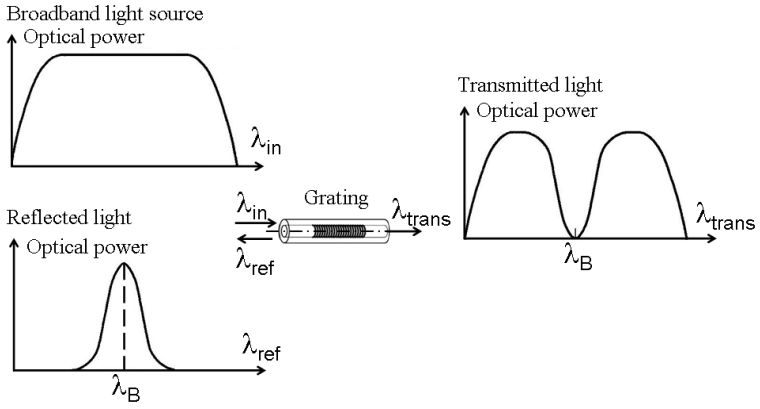

Figure 3-28 The principle of a optical fibre Bragg grating (FBG).

Broadband light is transmitted into the optical fibre. At a specific point in this fibre, there is a Bragg grating, which acts as a wavelength selective mirror. For each grating only one wavelength, the Bragg wavelength, λ_B is reflected with a Full Width at Half Maximum of typically 100 pm, while all other wavelengths are transmitted. As a result, an optical fibre can be read out from both ends of the fibre.
A fibre Bragg grating is actually no more than an area in the core of the fibre with successive zones with an alternating refractive index. If Λ is the period of the grating, then the Bragg wavelength of the grating is given by:

$$\lambda_B = 2 n_{eff} \Lambda \tag{3.15}$$

where n_{eff} is an averaged refractive index over the length L of the grating.
To better understand the strain sensing principle of an FBG (Fibre Bragg Grating), we first have to derive the basic Bragg condition (Equation 3.15). Taking the differential yields:

$$d\lambda = 2\left[\frac{\partial n_{eff}}{\partial \varepsilon}\Lambda + n_{eff}\frac{\partial \Lambda}{\partial \varepsilon}\right]d\varepsilon + 2\left[\frac{\partial n_{eff}}{\partial T}\Lambda + n_{eff}\frac{\partial \Lambda}{\partial T}\right]dT \tag{3.16}$$

By using the Bragg condition (Equation 3.15) on all four terms of Equation 3.16, this equation can be rewritten as:

$$d\lambda = \lambda_B \left[\frac{1}{n_{eff}} \frac{\partial n_{eff}}{\partial \varepsilon} + \frac{1}{\Lambda} \frac{\partial \Lambda}{\partial \varepsilon} \right] d\varepsilon + \lambda_B \left[\frac{1}{n_{eff}} \frac{\partial n_{eff}}{\partial T} + \frac{1}{\Lambda} \frac{\partial \Lambda}{\partial T} \right] dT \qquad (3.17)$$

Since $\partial\Lambda / \Lambda = \partial\varepsilon$ and assuming the strain and temperature variations are small, the differentials in Equation 3.17 can be replaced by differences.

By defining:

$$\begin{cases} P = -\dfrac{1}{n_{eff}} \dfrac{\partial n_{eff}}{\partial \varepsilon} = \dfrac{{n_{eff}}^2}{2} (p_{12} - \nu(p_{11} + p_{12})) \\ \alpha_n = \dfrac{1}{n_{eff}} \dfrac{\partial n_{eff}}{\partial T} \\ \alpha_f = \dfrac{1}{\Lambda} \dfrac{\partial \Lambda}{\partial T} \end{cases} \qquad (3.18)$$

with P the effective photo-elastic coefficient or strain-optic coefficient, p_{11} and p_{12} the elasto-optic coefficients of the strain-optic tensor, ν the Poisson's ratio, α_n the thermo-optic constant and α_f the thermal expansion coefficient of the fibre. Substituting these coefficients in Equation 3.17 yields:

$$\Delta\lambda / \lambda_B = (1 - P)\Delta\varepsilon + (\alpha_n + \alpha_f)\Delta T \qquad (3.19)$$

Some material constants used to calculate the strain-sensitivity of GeO_2 doped silica glass-fibre are:

Effective refractive index	$n_{eff} = 1.45$
Poisson's ratio:	$\nu = 0.16$
Elasto-optic constants:	$p_{11} = 0.113$
	$p_{12} = 0.252$
The thermo-optic constant	$\alpha_n = 5.9\ 10^{-6}\ K^{-1}$
The thermal expansion coefficient	$\alpha_f = 0.55\ 10^{-6}\ K^{-1}$

Together with the FBG-wavelength, these coefficients determine the linear strain and temperature sensitivities:

$$\begin{aligned} s_S &= (1 - P) \cdot \lambda_B = 0.796 \cdot \lambda_B \\ s_T &= (\alpha_n + \alpha_f) \cdot \lambda_B = 6.45 \cdot 10^{-6} \cdot \lambda_B \end{aligned} \qquad (3.20)$$

With this, the linear approximation becomes:

$$\Delta\lambda = s_S \Delta\varepsilon + s_T \Delta T \qquad (3.21)$$

Typical values for S_S and S_T for an FBG in the C-band region, which means the wavelength is between 1520 nm and 1560 nm, are 1.2 pm/με and 10 pm/°C respectively. It should be noted that these sensitivities are in fact wavelength dependent – they are directly proportional to the FBG-wavelength λ_B – but for small wavelength changes they are normally approximated as being constant.
Since an FBG is sensitive for both strain and temperature, two FBGs are needed, one to measure strain and one to measure temperature. This latter is necessary to compensate for wavelength shifts due to temperature fluctuations. A relatively easy method to achieve this is to use a capillary or a ferrule design where the second FBG is kept strain-free. This is illustrated in Figure 3-29. Both the strain and the temperature of the surrounding composite affect grating 1, whereas grating 2 only sees the temperature, because the fibre ends in the capillary and therefore is not strained. By subtracting the shift in wavelength in grating 2 from the shift in grating 1, the strain measurement is realised and the shift in grating 2 represents the temperature.

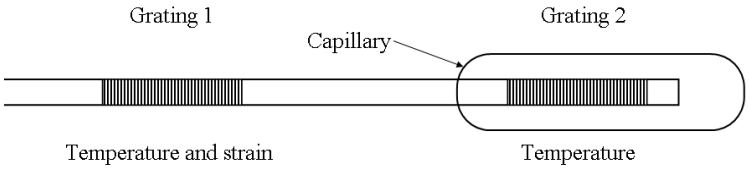

Figure 3-29 Illustration of the use of a capillary for the compensation of temperature effects.

If no significant temperature increase during the experiment occurs, then no capillary needs to be embedded.
If the temperature during the experiment is constant, then the second term in Equation 3.21 can be omitted and a measurement of the strain is achieved: the difference between the wavelength of the strained and the unstrained grating increases linearly with the imposed strain (Equation 3.21) and the sensitivity is 1.2 picometer per microstrain at the operating wavelength of 1.5 micrometer.

This is an absolute value, since it only depends on the geometry of the grating and the elasto-optic constants of the glass, and not on any form of electronic manipulation such as filtering or amplifying. Furthermore, it has to be noticed that a fibre Bragg grating written in hydrogenated fibres will notice a decrease of refractive index modulation of approximately 15% [28] hence a drift of Bragg wavelength and decrease of reflection of about 9% in the first few weeks after fabrication of the grating. However, this is not the case for gratings written in non-hydrogenated fibres [29], such as for the fibre Bragg gratings employed for the experiments described in this thesis.

Therefore, the Bragg wavelength of these sensors does not drift away in time as may occur with strains, derived from strain gauge measurements. The used data acquisition system has an accuracy of 5 pm and it is constant in time. Therefore, this system also does not cause a drift of the measurement.

The choice of the characteristic wavelength λ_B depends on the type of experiment and the data acquisition unit. The latter will be able to register only a certain range of wavelengths and has a certain bandwidth in the C-band region (1520 nm - 1560 nm) that is determined by the optical source of the interrogator.
If the experiment is pure tension, λ_B should be chosen near the lower boundary of that range and if the experiment is pure compression, λ_B should be chosen near the upper boundary of that range. The outer boundary should not be chosen, since hot pressing of the plates introduces unknown stresses and as a result, a small shift in λ_B [23, 30-32].

The fibre optic sensors used for these embedding experiments are uniform Draw Tower fibre Bragg gratings (DTGs), provided by FBGS-Technologies GmbH, Jena (Germany). Such gratings are manufactured during the fabrication process of the optical fibre and are coated just after the inscription of the Bragg grating [33]. These draw tower fibre Bragg gratings (manufactured by FBGS-technologies) have a uniform index profile (i.e. not chirped or tapered) and are fabricated during the drawing of the fibre. They have a reflectivity of typically 15-20 % with nominal wavelengths typically in the range of 1520 nm -1575 nm. The method employed for inscribing gratings over such a wide wavelength range is a technology based on a Talbot interferometer which makes it possible to change the design wavelength by changing the angle of the two mirrors which unite the diffracted laser beams at the centre of the fibre [33]. Due to the combination of these two first order laser bundles an interference pattern with a defined length is induced and thus a fibre Bragg grating with a specific Bragg wavelength is created at that exact spot.
The FBGs are written in a (special) Single Mode optical fibre with core- and cladding-diameter of 6 µm and 125 µm, respectively. Such a special Single Mode fibre is made of fused Silica (SiO_2) with a highly Ge-doped (GeO_2) core (approximately 18 mol%) for high photosensitivity, necessary for inducing the periodic refractive index pattern with a single laser shot during the draw tower process and thus creating the Bragg grating sensor.
Fibre draw tower gratings have a core diameter of 6 µm, a cladding diameter of 125 µm and an outer diameter, with ORMOCER coating (ORganic MOdified CERamic), of 195 µm; for comparison, the diameter of a carbon fibre bundle is approximately 320 µm.

The ORMOCER coating material provides excellent mechanical properties such as an ultimate strain value between 5-6%. It should be noted that the ORMOCER has good bonding properties with the glass surface of the optical fibre and as such this optical fibre has very good sensor properties for strain measurements. Also a good adhesion with the PPS matrix is found, even after half a million cycles the FBG-sensors showed no signs of de-bonding (see chapter 5).

3. 5. 3. Optical data acquisition systems

For the registration of the optical data, two different systems were used. The first is the SLI 1000, which is discussed next and the second is the FBG-scan interrogator. Both systems were supplied to us by FOS&S, the company who also supplied the optical fibre gratings.

3. 5. 3. a. The Swept Laser Interrogator (SLI)

This system uses a tuneable laser as light-source which is swept across a broad spectrum at 100 Hz with a bandwidth of approximately 38 nm in the C-Band range (1520 nm – 1558 nm). The reflected wavelength was measured during quasi-static loading at a frequency of 100 Hz. However, an important remark about the sampling frequency must be made. The SLI has a sampling frequency of 100 Hz, but it does not use a sample and hold principle, it reads continuously. The difference between the two is illustrated in Figure 3-30 where the illustrated sinusoidal signal has a frequency of 5 Hz.

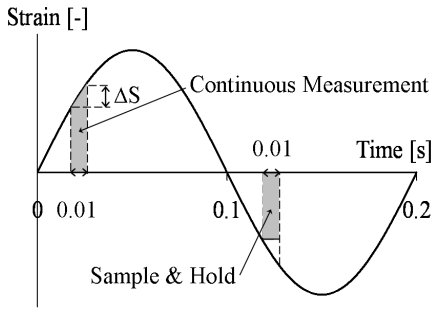

Figure 3-30 Illustration of the difference between a sample and hold and a continuous measurement.

The ‘sample & hold’ principle freezes the registered value until the data acquisition unit has finished processing it. For the continuous measurement, the registration takes 1/f seconds, f being the sample frequency, to gather the data. Since the SLI samples at 100 Hz, it takes 0.01 seconds for the measurement. For quasi-static tests with a displacement speed of 2 mm/min, the difference in the occurring strain at time t and at t + 0.01 seconds is small enough and will be maximum 2.22 μstrain.

As such, the error is very small, in the order of a few micro-strain, and can be neglected in further calculations.
For fatigue loadings, however, this will be a problem, since the loading frequency during the fatigue tests can be 5 Hz. The 100 Hz sampling rate is too low, since there is already a large difference in the occurring strain at time t and t+0.01 seconds. To overcome this problem, the fatigue experiment should be paused after a certain number of cycles and a quasi-static tensile test should be performed with a displacement speed of 2 mm/min.
A small disadvantage is that afterwards, the data needs to be sampled manually on the same time basis as the other data, obtained from the tensile machine.

3. 5. 3. b. FBG-scan interrogator

The FBG-scan interrogator is a compact, low-cost and completely intelligent, portable device that can monitor up to 16 different optical lines. The core of the device is a state-of-the-art Fabry-Pérot tuneable filter.
It features a wavelength accuracy of 10 pm and a scan range of 40 nm, from 1527 nm till 1567 nm. The wavelength repeatability is 1 pm, and the scan and report time is 1 s, representing a sampling rate of 1 Hz in total. The latter means that it takes one second to scan one channel, so if two gratings are read, the sampling frequency of each channel is 0.5 Hz.
The low sampling rate of this device is of course a serious disadvantage with respect to the SLI for registering quasi-static tests. For quasi-static tests with a displacement speed of 2 mm/min, the difference in the occurring strain at time t and at t + 1 seconds will be too large. As such, the quasi-static test should be performed in discrete load steps, and after each step, while the load is kept constant, the strain should be registered. This process is very intensive unless it can be automated.

As previously mentioned, if the SLI is used for fatigue measurements, the fatigue test needs to be stopped after a certain number of cycles to perform a quasi-static test. The latter has to be done manually, since the SLI cannot be controlled by a computer. The FBG-scan interrogator, however, can be controlled by a pc. As such, the optical data acquisition can be combined with the control of the tensile testing machine. Using the ‘Wavemaker’ and ‘Waverunner’ software from INSTRON™, the user is able to specify any waveform, or successive waveforms. For a fatigue experiment, the waveform should be composed out of a static test and a fatigue test, both load controlled. For the fatigue test, the only parameters are the average load, the amplitude and the frequency. The static test is implemented as a multistage evolution of the load, which is illustrated in Figure 3-31. The user has to implement the step-height and -time and the number of steps (500 N, 150 s and 10 steps in the presented figure).

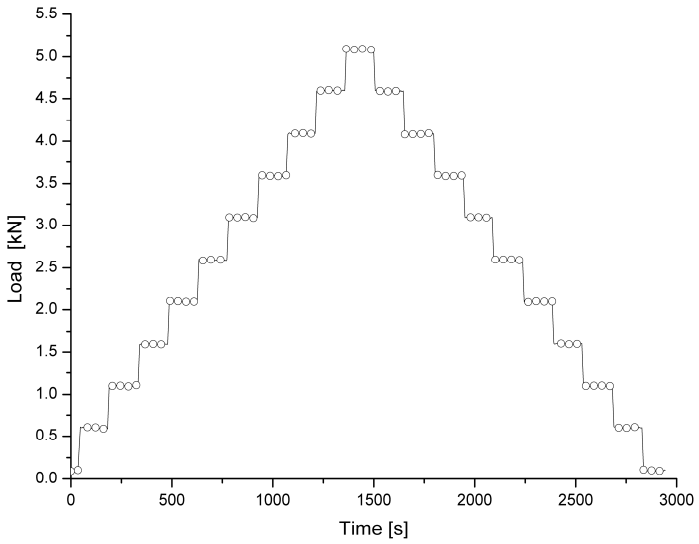

Figure 3-31 Illustration of the evolution of the force during the optical data acquisition.

The optical data is registered by the FBG-scan interrogator, which is monitored by a computer. This computer also monitors the strain, load and displacement given by the tensile machine. If the load remains constant for a certain period of time, which is the case in the multistage static test, but not in the fatigue test, all of the data, both from the FBG-scan as from the tensile machine, are written to file. As such, all static tests are automated and registered without the necessity of further human intervention and all data are written on the same time basis.
If only a quasi-static test is performed, then the same principle as illustrated in Figure 3-31 can be implemented, using the same software. As such, again no extensive human involvement is necessary.

3. 5. 3. c. Preparing a fibre

After production of the fibre, a connector, which is called a ‘pigtail’ (see Figure 3-32) should be mounted on the end of the fibre, so that the light can be transmitted through the fibre.

Figure 3-32 Illustration of a pigtail. On the left, the connector is shown and the fibre on the right is spliced to the optical fibre with the grating.

Connecting such a pigtail to a fibre is called splicing and consists of a number of steps and requires specialised equipment, as illustrated in Figure 3-33.

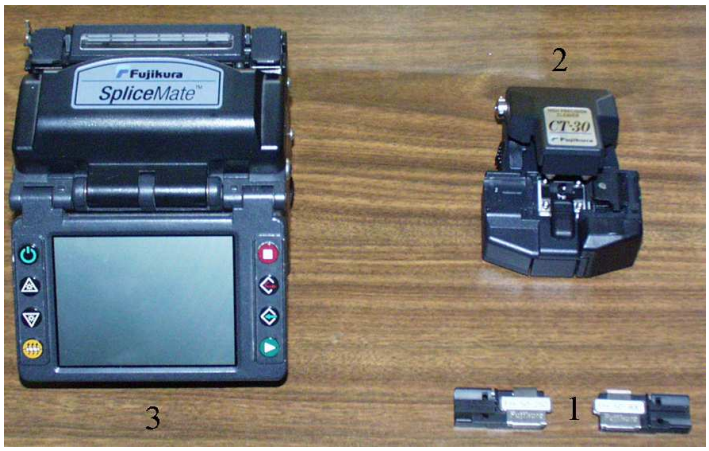

Figure 3-33 Equipment used for splicing a fibre and a pigtail.

First, the coating of the glass fibre is removed over a small length from both the glass fibre and the end of the pigtail, after which the ends of the glass fibres are placed in special holders (1).
Next, the fibres are cut, using a special machine (2), which yields a very clean and straight fracture plane of the fibre. Both the fibre and the pigtail, still in the special clamps (1), are now placed in the splicer (3), which first positions the two fracture planes exactly opposite to each other at a well determined distance. Next, these two planes are melted together by means of a laser burst, after which the splicer tests the connection for power losses. Finally, a new protective coating is melted around the splice and the fibre is ready for use.

3. 5. 4. The embedded fibres

3. 5. 4. a. The embedding of the fibre

As mentioned in chapter 2, the composite plates are manufactured by hot pressing a number of pre-pregs. The optical fibres can be put in between two layers of semi-preg and can be fixed in any orientation simply by using an ultrasonic welding device and a small piece of PPS-sheet to fix the fibre at the semi-preg layer.
Of course, the fragile optical fibre needs to be protected where it exits the specimen. This was achieved by mounting Kapton tape on the sides of the semi-pregs where the fibre exited the specimen. The fibres were also fixed by taping them with an extra piece of Kapton tape on the underlying layer of tape. Both systems are illustrated in Figure 3-34; Figure 3-35 shows how the protection of the Kapton tape on the exiting fibre after the plate is cured.

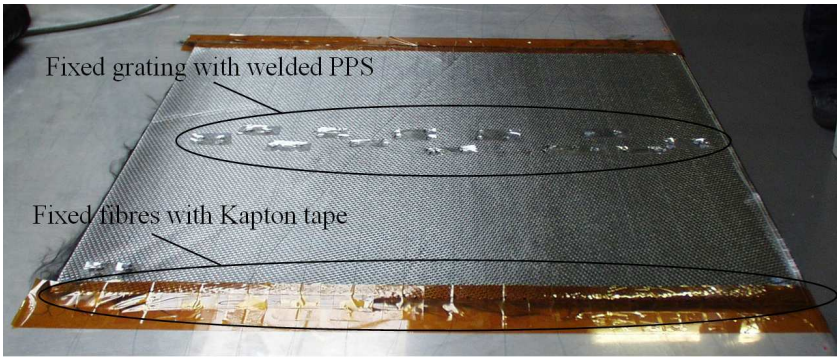

Figure 3-34 Illustration of how both gratings and fibres can be fixated.

Figure 3-35 A fibre, protected by the Kapton tape, exiting the specimen.

While making a few test samples using the $[(0^o,90^o)]_{4s}$ stacking sequence, it was noticed that multiple peaks around the expected wavelength occurred in the reflected spectrum during curing of the laminate.

Figure 3-36 illustrates the reflected spectrum of a fibre before it is embedded, which looks like the expected spectrum (see Figure 3-28). As can be seen, there is one single peak around 1548 nm. Even after zooming in on the peak, only one maximum is registered.

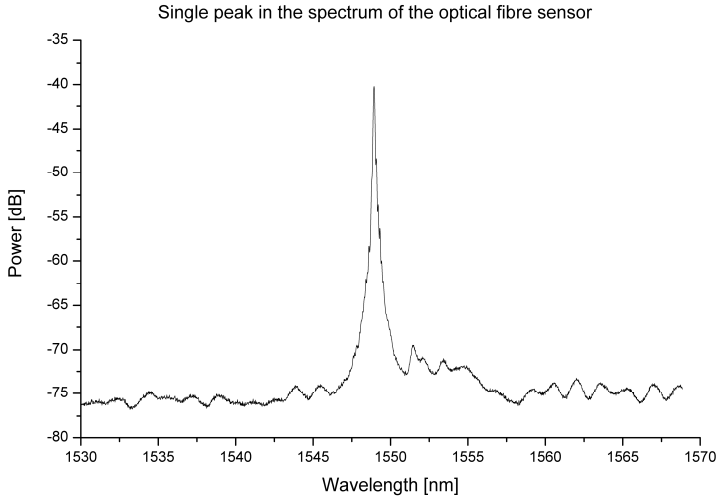

Figure 3-36 Illustration of a measured spectrum of an optical fibre sensor with one single peak.

However, after embedding, usually a spectrum as illustrated in Figure 3-37 is measured on the reflected side. As can be noticed from this spectrum around the central wavelength of 1550, multiple small peaks occur.

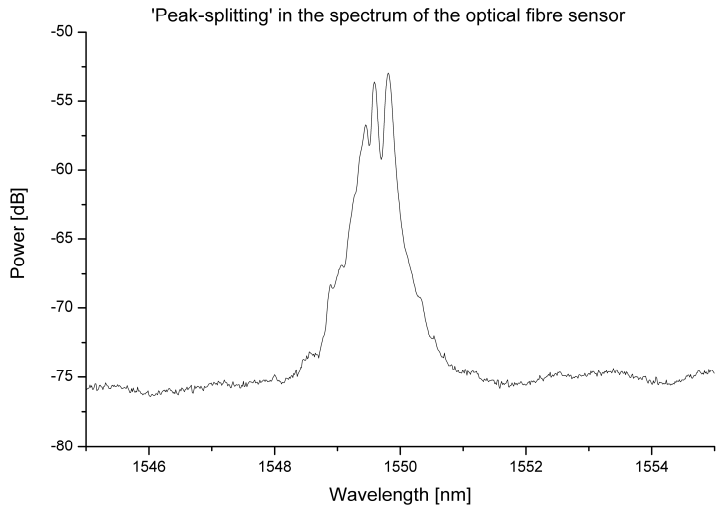

Figure 3-37 Illustration of a measured spectrum of an optical fibre sensor with 'peak-splitting' around the expected value.

Both the SLI and the FBG-scan interrogator are able to detect and register multiple peaks, when there is a sufficient difference in central wavelength. However, for the peak-splitting, both acquisition systems cannot distinguish the different peaks and tend to register only the maximum peak. Furthermore, it is very hard to determine the occurring strain from such a spectrum. This can no longer be done by monitoring only one peak, the entire spectrum must be monitored and the evolution of the point of gravity of such a spectrum may give an indication of the occurring strain. FOS&S, the company who supplied the optical fibres, as well as the optical data acquisition systems, is currently investigating how strain can be measured accurately when peak-splitting occurs, but for this research, such spectra could not be used.
The splitting of the central peak is due to an in-homogenous stretching of the grating. As was discussed earlier, stretching of the grating results in a shift in the reflected wavelength. If only part of the grating is stretched, then this part will reflect a wavelength which differs only slightly from the wavelength, reflected by the unstrained part. As was mentioned earlier, the splitting occurred during the curing of the plates. Of course, many processes take place during the hot pressing and curing, but one of the reasons for this peak-splitting is due the fact that the reinforcement is a fabric. This is illustrated in Figure 3-38; the embedded fibre is aligned with for instance the warp fibres of the fabric, but it still crosses the weft fibres.

Due to the pressure applied during the hot pressing, the optical fibre sensor is bent around these fibres, resulting in a non-uniform straining of the grating. As such, multiple peaks are formed around the Bragg wavelength λ_B. A similar explanation can be found in [34].

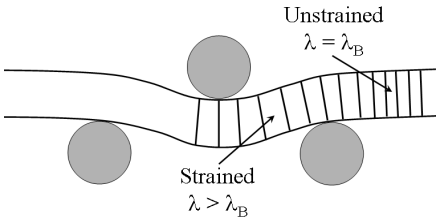

Figure 3-38 Illustration of the bending of a fibre Bragg grating in a fabric-reinforcement.

Therefore, thin plates compiled of only 4 lamina $([(0^o,90^o)]_{2s}$ stacking sequence) were used to investigate if the optical fibre showed any significant influence on the material properties, whether it has a large disturbance on the micro-structure and to investigate why the multiple peaks in the spectrum tend to occur and how it can be avoided. The latter is currently under investigation by FOS&S and until now, no real solution can be given. The fibres were placed between lamina 1and 2 or between lamina 2 and 3.

Considering the dimensions of such semi-preg layers (thickness approximately 320 µm) one would say optical fibres with a coating diameter of 195 µm could induce local disturbance in the matrix and influence the structural behaviour of the composite. However, fatigue tension tests showed positive results indicating that the fibre optic sensor has little or no effect on the mechanical properties of the composite plate (see chapter 5).

In addition the coating of the optical fibre should have a good adhesion with the matrix-material, so strain inside the composite is transmitted well. The ORMOCER coating has proven to be a well suited coating for embedding in CETEX material.

Finally, Figure 3-39 shows the change in spectrum resulting from a successful embedding process. As can be noted, there is a shift to the right from 1548.577 nm to 1549.47 nm, yielding a strain of 744 microstrain. Furthermore, losses in power have occurred due to macro-bending on entrance of the plate and micro-bending inside the plate.

Changes in reflected spectra after consolidation are known to happen in epoxy-matrices [35-37], but have also been documented for the thermoplastic matrix PPS in [34].

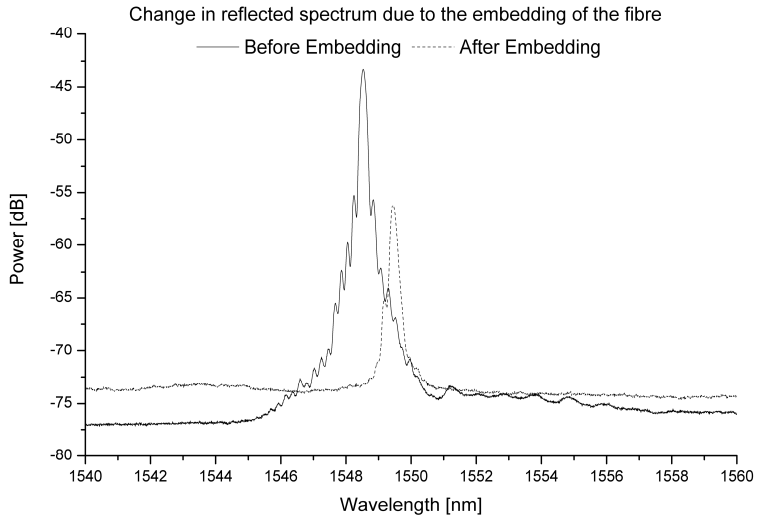

Figure 3-39 Illustration of the reflected spectrum prior and after the embedding process.

3. 5. 4. b. Visualising the fibre with Micro-tomograpy

Introduction

High-resolution 3D X-ray micro-tomography or micro-CT is a relatively new technique which allows scientists to investigate the internal structure of their samples without actually opening or cutting them. Without any form of sample preparation, 3D computer models of the sample and its internal features can be produced with this technique. The physical parameter, providing the information about the structure, is the X-ray attenuation coefficient μ. This coefficient is the product of the photon mass attenuation coefficient μ/ρ (cm^2/g) and the chemical mass density ρ (g/cm^3). The attenuation coefficient μ depends on the local composition of the material of the sample.

Further more, the mass attenuation coefficient depends on the energy of the X-rays: the higher the energy of the photon, the smaller the attenuation in the sample. Portable X-ray sources are producing the X-rays, while X-ray detectors are used to record the attenuation information along lines through the object and register the image as a radiograph. In order to perform tomography, digital radiographs of the sample are made from different orientations by rotating the sample along the scan axis from 0 to 360 degrees. After collecting all the projection data, the reconstruction process is producing 2D horizontal cross-sections of the scanned sample. These 2D images can then be rendered into 3D models, which enable to virtually look into the object. Special 3D software, Morpho+ [38] is developed in order to obtain 3D data of the internal features, including volume distributions, porosity, pore sizes, etc.

The high power directional tube of the dual head 160 kV Feinfocus® open-type tube X-ray source was used. This tube attenuates most of the X-rays below 10 keV and is equipped with a conical tungsten anode and an aluminium exit window. With a maximum power of 150 W and a high X-ray power output, the directional tube is perfectly suited to penetrate the thermoplastic composites. The X-ray detector, a remote Radeye EV CMOS flat panel (http://www.rad-icon.com) was applied. This detector provides a high contrast for micro-focus CT, with X-ray tube voltages up to 160 kV. Its active area is 24.6 mm by 49.2 mm and consists of a 512 by 1024 matrix of silicon photodiodes on 48 µm centres. A thin straight fibre optic coupling is used to transport the visible light from the phosphor to the CMOS. The samples are positioned on a highly sensitive sample manipulator, consisting of seven motor stages. The samples are positioned between the X-ray tube and the X-ray detector with an XYZ-translation stage with Berger Lahr stepper motors (IcIA IFS). To reach the high precision CT-scan, a rotation stage with air bearing (MICOS, UPR160F-AIR) is used.
A standard air compressor and a series of filters provide 4.5 bar air pressure for the stage. Additionally, a XY-piezo stage with 50 nm resolution and 20 mm travel range is fixed on the rotation platform to centre the sample on the rotation axis.
Previous experiments with this method on a glass fabric-reinforced epoxy yielded very good results. Figure 3-40 shows an image of this material, but the epoxy matrix was removed with the software, in order to visualise only the fibres. It should be noted that even the individual fibre filaments can be distinguished.

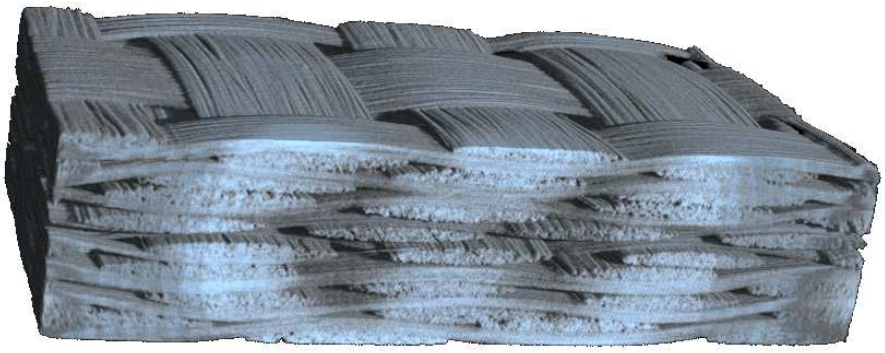

Figure 3-40 Micro-tomography of a glass fabric-reinforced epoxy.

All micro-tomographies were done in cooperation with the X-ray and CT-facility of the department of Subatomic and Radiation Physics (SSF) at the Faculty of Sciences, Ghent University.

Visualising the fibres

Because of the high level of detail achieved with the glass fabric-reinforced epoxy (Figure 3-40), the micro-tomography should be able to visualize the optical fibre. Since the thickness of the four layer stacking sequence is only 1.25 mm, it is hard to machine a beam-like test sample for the micro-tomography. Therefore, a few samples were machined and then taped together. The orientation of the top and bottom specimen differed ninety degrees with the centre one, to have a clear view of the fibres, both longitudinal as transverse. The taped specimens are shown in Figure 3-41. The optical fibre is clearly visible between the first and second layer.

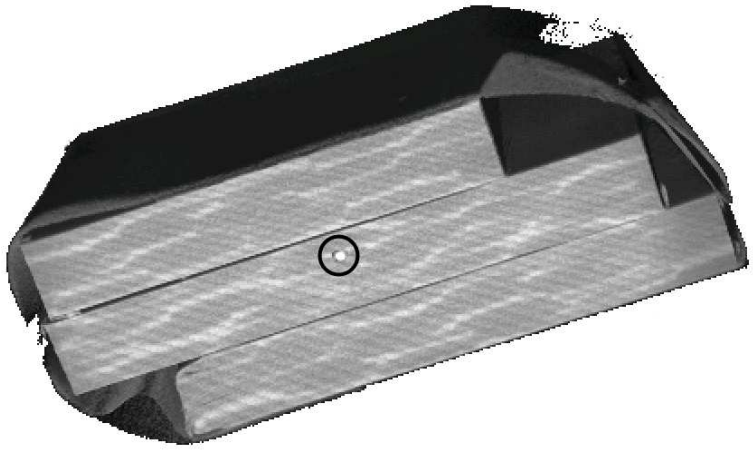

Figure 3-41 3D-image of the three samples (taped together) of $[(0^o,90^o)]_{2s}$ carbon-PPS with optical fibre.

The CT data was reconstructed with Octopus (http://www.xraylab.com) and for the 3D rendering, the software VGStudiomax (www.volumegraphics.com) was used. The 3D volume can be cut in different sections. The position of the cut was chosen so that all three fibres were visible. This is shown in Figure 3-42. All three fibres are clearly visible. Again, the accuracy of this method is illustrated; the coating of the optic fibre can be distinguished.

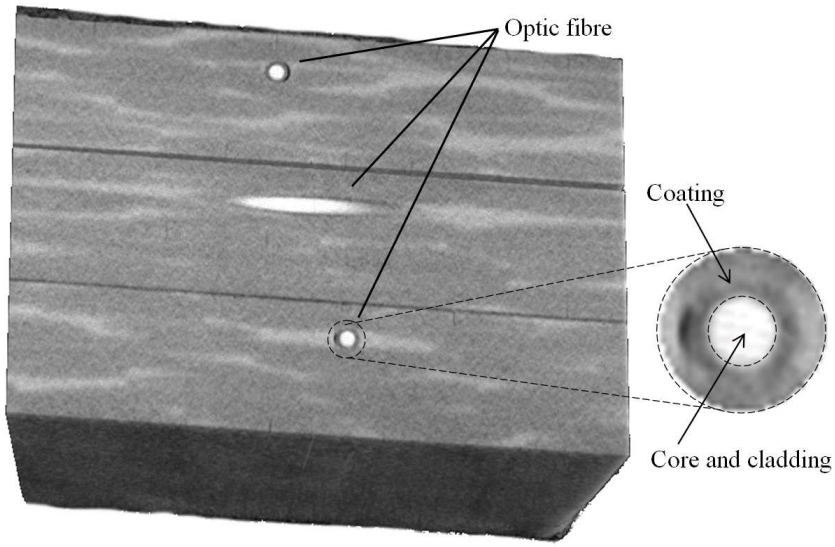

Figure 3-42 Cut of the 3D image of the taped $[(0^o,90^o)]_{2s}$ carbon-PPS samples.

Damage assessment

It was also assessed whether damage could be visualised, using the micro-tomography. However, the achieved resolution proved insufficient to accurately verify whether micro-cracks occurred in the PPS. Furthermore, the preparation of the specimens, sawing and grinding to the exact size, may generate sufficient heat to melt the matrix and as such, the micro-cracks may be closed. Moreover, grinding itself may also generate cracks on the surface of the specimen.

3. 5. 4. c. A first experiment

During the production of a number of laminates with embedded fibres, for the investigation of the peak-splitting, there were a number of fibres that did not have this effect, possibly because the grating is located somewhere on the fabric where it is not bent too much. From these plates, test coupons containing these fibres were cut to perform both quasi-static tests, of which an example is shown here, and fatigue tests (see chapter 5). The dimensions of the coupons are shown in Figure 3-43. It was attempted to have the grating of the fibre somewhere in the middle of the gauge length and specimen width.

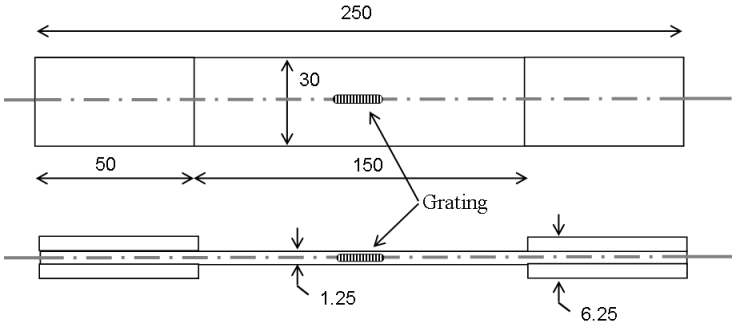

Figure 3-43 Dimensions of the used tensile coupon, equipped with tabs.

For these preliminary experiments, the Swept Laser Interrogator was used, which means that the tests could be done displacement-controlled with a speed of 2 mm/min. All experiments were stopped once the maximum detectable wavelength of the SLI was reached, so that the specimens remained intact for further investigation with respect to the peak-splitting and the disturbance of the microstructure. The Bragg wavelength λ_B of both used fibres was 1555 nm, which leaves about 3 nm for strain measurement. This corresponds with a longitudinal strain of 0.0025. λ_B was chosen so high since its original purpose was to measure the effects during curing of the plate, during which crimp was expected. Therefore, the wavelength was chosen near the upper boundary of the SLI, rather than near the lower boundary which is more applicable for tensile testing.

Figure 3-44 shows the evolution in time of the longitudinal strain, measured with both the extensometer and the fibre Bragg grating for two experiments. It can be noticed that the correspondence is very good.

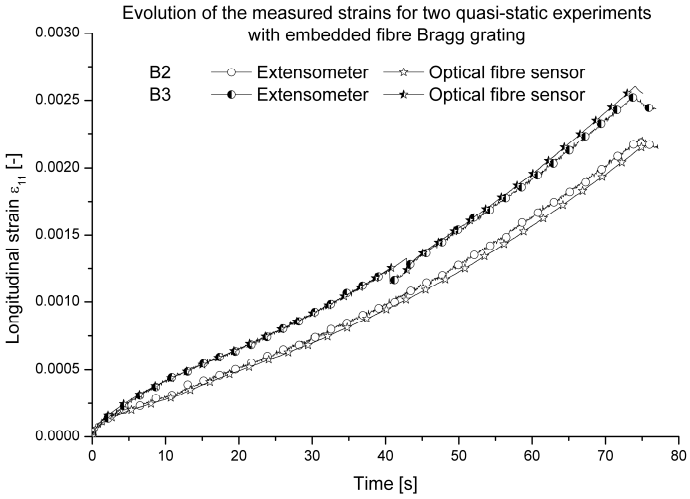

Figure 3-44 Evolution of the strain, measured by both the extensometer and the fibre Bragg grating.

Finally, Figure 3-45 shows the longitudinal stress-strain evolution of both specimens. There is a little more scatter on the stiffness as with all previous quasi-static experiments, but this might be due to the fact that the plates from which the specimens were cut were made on the small laboratory press, whereas most of the other specimens came from plates manufactured on the industrial press of Ten Cate. It can be noted that specimen B3 behaves a lot stiffer than B2, and this is also the reason why the increase in strain in Figure 3-44 is higher for B3 than for B2, since the displacement speed was the same.

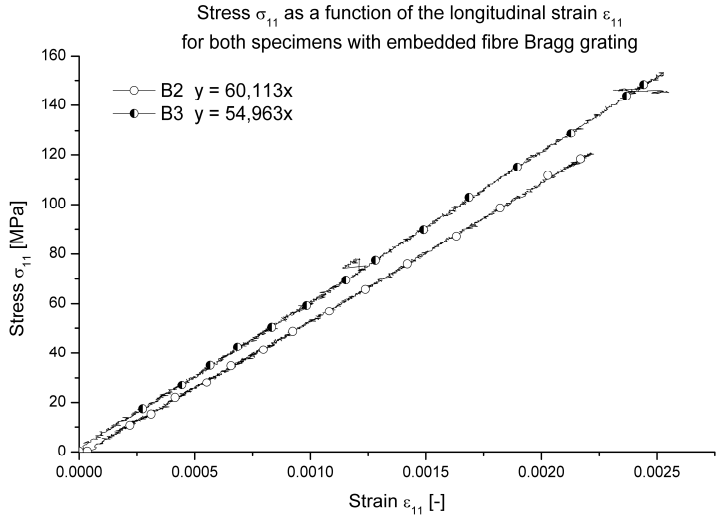

Figure 3-45 σ_{11} as a function of ε_{11} for the specimens with the embedded grating.

3. 5. 5. External optical fibres

3. 5. 5. a. Introduction

Since there were problems with multiple peaks arising during the curing of the plate with the embedding process, it was attempted to bond the fibre on the surface of the composite specimens. As such, the grating is not compressed or damaged and no peak-splitting occurs.

The externally bonded grating also has the advantage of being attached after fabrication of a composite part. Normally, fibres are embedded in the composite part at locations where measurements are deemed necessary. If it is decided afterwards that extra sensors are needed at specific locations, they can no longer be embedded in the already cured part.

Possible problems of course may arise due to the chemical inertness of the PPS matrix, which makes it difficult to bond to. This will be even more a problem under fatigue loading conditions (see chapter 5).

3. 5. 5. b. Bonding the external fibre to the surface

If the external fibre is bonded on the surface, then no disturbance of the composite will occur. The followed procedure is the same as for bonding strain gauges. First, the surface of the specimen was polished in order to have a smooth surface, after which it was degreased with acetone. Then, the fibre was accurately positioned and pre-strained, before being fixed to the specimen by means of duck tape. The pre-strain caused a shift of about 100 to 200 pm corresponding with a strain of 80 to 160 microstrain. This was done to avoid buckling of the fibre when the specimen is unloaded.

Finally, the fibre was bonded over the entire length of the grating, using a Z70 cyanide-acrylate adhesive, designed for bonding strain gauges. Extra pressure for the curing of the adhesive was applied, using a piece of soft rubber that morphs around the fibre and a Teflon film to avoid the rubber from bonding to the specimen and the fibre. An image of an externally bonded fibre is given in Figure 3-46.

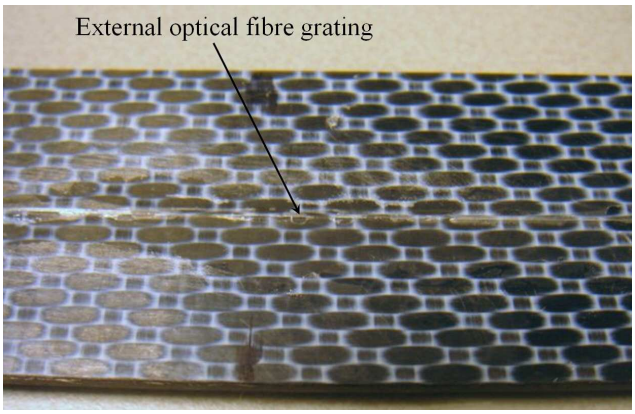

Figure 3-46 Detailed image of an externally bonded optical fibre.

3. 5. 5. c. Quasi-static experiment

For this experiment, the FBS-scan interrogator was used, which means that the quasi-static test had to be done load-controlled with a stepwise increase of the load. The test was done until a stress of 300 MPa was reached and then the specimen was unloaded, also with a stepwise decrease of the load, to verify whether the optical fibre would still yield accurate results. The Bragg wavelength was 1550 nm, which was low enough to measure the expected strain corresponding with 300 MPa.

Figure 3-47 illustrates the evolution of the strains, measured with both the extensometer and the optical fibre sensor. Again, the correspondence is very good, both for the loading and unloading of the specimen. The stepwise evolution of the force and therefore the strain can also be seen.

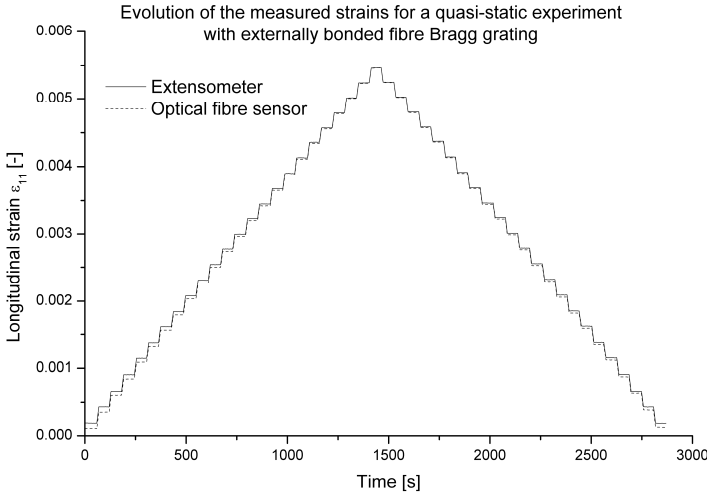

Figure 3-47 Evolution of the strain, measured by both the extensometer and the fibre Bragg grating for the specimen with the external grating.

Finally, Figure 3-48 shows the stress-strain evolution of the specimen. The derived stiffness from the loading part of the curve again corresponds very well with the other values, mentioned in this chapter.

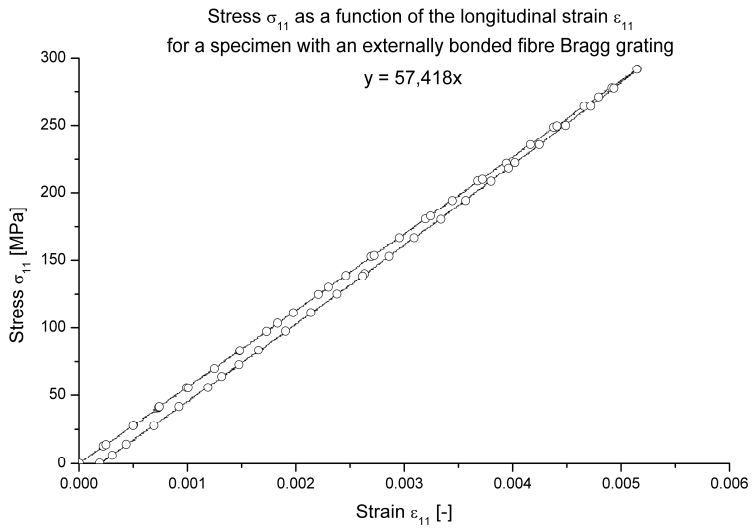

Figure 3-48 σ_{11} as a function of ε_{11} for the specimen with the external grating.

3. 5. 6. Conclusions

It may be concluded that the optical fibre sensors with fibre Bragg gratings are suited for measuring the longitudinal strain during quasi-static experiments. Two setups have been discussed: the optical sensor can either be bonded to the surface or embedded. Embedding often resulted in peak-splitting, making it difficult to measure strain, but the external fibre is more fragile, since the grating lies at the surface and is only protected by a thin layer of adhesive. However, the strain measured with both configurations corresponded very well with the strain derived from the extensometer.

Two data acquisition systems were illustrated: the Swept Laser Interrogator and the FBG-scan interrogator. Both of them can be used for quasi-static measurements, although the nature of the test is different. Because of the high sampling frequency of the SLI, a displacement-controlled test with a speed of 2 mm/min is possible. This however is not possible with the FBG-scan, since its maximum sampling rate is only 1 Hz. For the latter, the experiments must be done load-controlled with a stepwise increase (or decrease) of the load. However, the FBG-scan has the advantage over the SLI that is controllable by a PC, so that fatigue experiments may be registered without human intervention, whereas for the SLI, the fatigue experiment has to be paused to manually perform a quasi-static experiment. The latter will be discussed in detail in chapter 5.

3. 6. ELECTRICAL RESISTANCE MEASUREMENT

3. 6. 1. Introduction and principle

The introduction on the optical fibre sensors mentioned the so-called ‘sensitive’ materials, which meant the material includes sensors providing real-time information about the material itself. The use of embedded optical fibres was one example, but the use of electrical resistance measurement also creates a sensitive material. The most natural way to obtain a ‘sensitive’ material is to use the material itself (or a part of it) as sensor. Of course, this is possible in the case of carbon fibre-reinforced polymers, since carbon fibres are electrical conductors embedded in an insulating matrix [39]. Furthermore, in some industries, for instance in the aeronautical industry, composites are attached using rivets. Therefore, it is investigated whether these rivets can be used for the purpose of electrical resistance measurement.

The principle of electrical resistance measurement is illustrated in the following pictures. Since carbon fibres conduct electricity, they can be represented by resistors. For a fabric, one can imagine the following symbolic lay-out (Figure 3-49). The total resistance of the composite is R_{tot}.

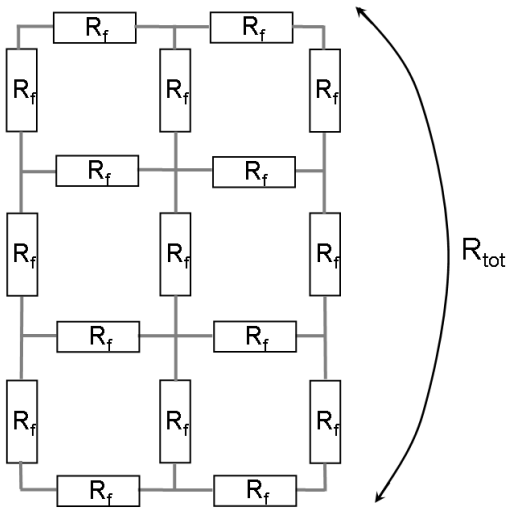

Figure 3-49 Electric network of resistors, representing a fabric of carbon fibres in an insulating matrix.

If a fibre breaks, then the current can no longer travel through that fibre and needs to find another path. This means that the corresponding resistor disappears, leading to a situation as depicted in Figure 3-50.

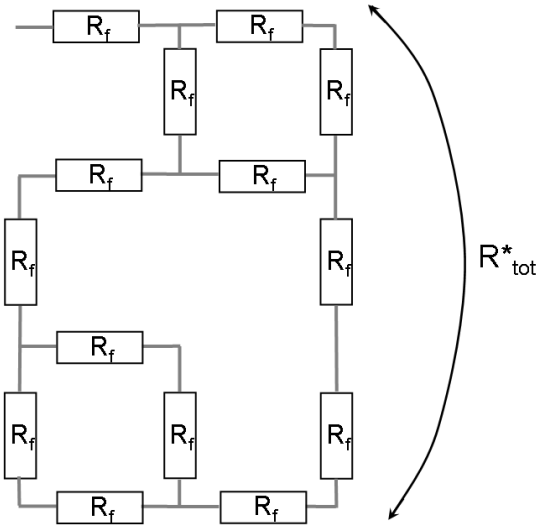

Figure 3-50 Representation of the result of damage in carbon fibre resistor-network.

The more carbon fibres are broken, the fewer paths are available for the electric current, so the higher the total resistance R^*_{tot} becomes. This ends with fracture of the specimen, giving infinite resistance. This conclusion may also be found in various articles about this subject [39-47].

While doing the literature study, it was noticed that most authors concentrated their work on polymers with unidirectional fibre-reinforcement [40-49]. Occasionally, cross-ply laminates are studied [39-41, 47, 49], but materials reinforced with fabrics were never closely observed using this technique. A possible reason may be that the sensitivity of resistance measurement tends to decrease if there are more transverse fibre contacts, which is already the case with cross-ply laminates, but will be even more apparent in fabrics. The latter has been proven theoretically by Xia et al. [46]. Nevertheless, it was attempted to use this method to observe damage in the used carbon fabric-reinforced PPS. An advantage of cross-ply laminates is that the potential distribution on the surface of the laminate is much more uniform than with unidirectional samples even when point surface introduction of the current is used, because the transverse current is carried by the off-axis plies [41]. This is an important effect for establishing contact.

In the next paragraph, the used materials and experimental setups are discussed. This is followed by the discussion of the conducted experiments and finally, some conclusions are drawn.

3. 6. 2. Measuring the resistance

3. 6. 2. a. Introduction

In order to measure the resistance, a current is introduced in the specimen and the voltage is measured. There are various ways to do so [39-47], but in general, there are two types of configurations: (i) the two-probe technique, which means that the voltage is measured on the same electrodes where the current is introduced and (ii) the four-probe technique, where the first two contacts are needed for the current injection and the voltage is measured with the remaining two.
Both setups have advantages and disadvantages. The four-electrode technique is said to be more accurate [42, 43], but is more complicated as experimental setup. Furthermore, it may not represent sub-surface behaviour if all probes are mounted on the same surface [41]. The two-probe technique is easier but the measurement unit needs a high input impedance, to assure that the injected current goes through the specimen and not through the voltmeter. The latter is the case with the used SCB-68 connector block of the data acquisition card. It is said that the surface conditions have a greater influence in the two-probe method [43]. Sanding or polishing the specimen surface enhances the electrode-fibre contact, but it may induce small surface cracks, influencing fatigue life or tensile strength and therefore corrupting the data.

For the current, both AC and DC can be used. The difference between the two is that the DC technique is mainly sensitive to fibre failures and the measurement is longitudinal, whereas the AC measurements provide information essentially on the development of matrix cracks but the measurement is done perpendicular to the fibres [39]. The latter can be explained since an AC measurement not only measures the resistance, but also the capacitance of the specimen. Most authors use DC measurements [40-45, 49] which also have the advantage of an easier measurement, since there is no need to divide the measured impedance into a resistance and a capacitance, as is the case with AC. Values of the DC current tend to vary between 5 mA and 50 mA, but most authors use 10 mA.

The measured resistance between the two clamps of the tensile testing machine is approximately 0 Ω, which means a short circuit.
If a current is injected using the two electrodes, it will choose the path of least resistance, meaning through the testing machine. In order to prevent this, the test specimen needs to be insulated from the machine. This can easily be achieved by using end tabs which do not conduct electricity. This means that the fibre-reinforcement has to be glass or aramid.

Todoroki et al. [42] have proven that a poor electrical contact of the electrodes leads to inadequate results. This has also been reported by Angelidis et al. [41]. However, due to the effect, mentioned above, that in a cross-ply laminate, the transverse current is carried by the off-axis plies, even a point current injection will lead to a uniform potential distribution. The reinforcement fibres for the material being used here are a fabric, so the conduction of the transverse current will not be a problem since longitudinal and transverse fibres contact one another in each ply. Therefore, establishing good electric contact should not pose any difficulties.

3. 6. 2. b. Used setup and geometry

The dimensions of the coupons used for the electrical resistance measurement are shown in Figure 3-51.

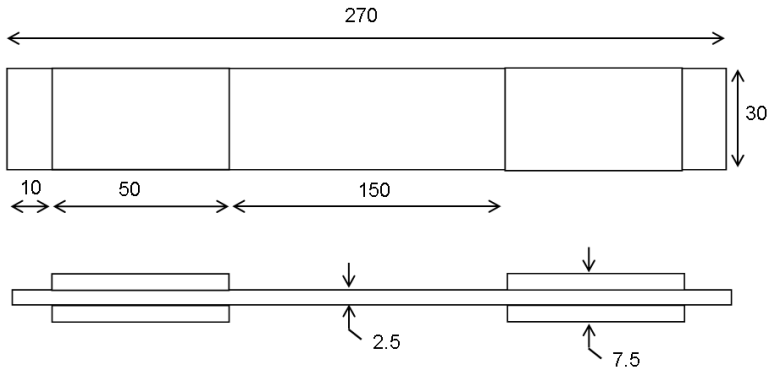

Figure 3-51 Dimensions of the used tensile coupon, equipped with isolating tabs of $[\pm 45^{o}]_{2s}$ glass fibre epoxy.

In order to mount the rivets, holes must be drilled through the specimen. This damages and therefore weakens the material locally.

To avoid that these holes influence the mechanical behaviour of the material, the rivets need to be mounted in a zone that is not loaded. Therefore, the tabs are not attached at the end of the specimen, but a small zone is left uncovered (Figure 3-51). The holes are drilled in this area and the rivets are mounted. Since no stresses occur beyond the tabs, the electrodes are in strain-free zones which should prevent contact loss of the probe.

Figure 3-52 represents the used setup. A two-probe technique is used and a DC current of 100 mA is injected through the rivets. DC is considered rather than AC because of the easier measurement, as previously mentioned, and the value of 100 mA is a compromise for achieving a high signal-to-noise ratio while not generating Joule's heat.

The same rivets are used to measure the voltage. In order to isolate the specimen from the tensile machine, a unidirectional glass fibre-reinforced epoxy with a $[\pm 45^{o}]_{2s}$ stacking sequence is used.

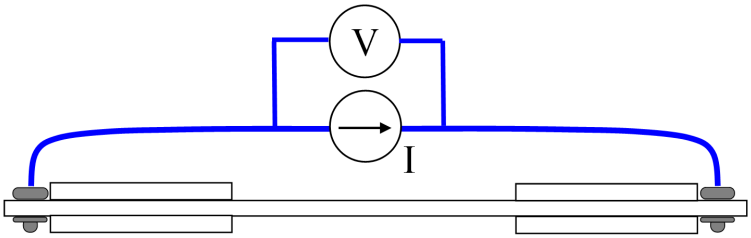

Figure 3-52 Symbolic representation of the used two-probe method for electrical resistance measurement.

Figure 3-53 shows in more detail how a rivet is mounted. A small hole is drilled on each side of the specimen and a rivet with a wire attached to it, is inserted and riveted. The surfaces under the rivets are sanded for better contact with the fibres.

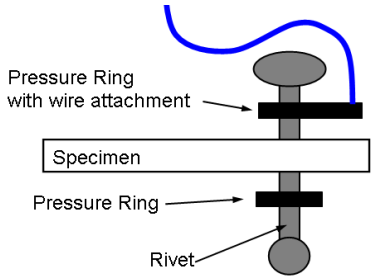

Figure 3-53 Mounting a rivet through the specimen.

An example of a specimen can be seen in Figure 3-54, a detail of the riveting is depicted in Figure 3-55.

Figure 3-54 Specimen prepared with rivets for electrical resistance measurement.

(a) top view (b) bottom view (c) side view

Figure 3-55 Detailed pictures of the rivet.

The rivets must not exceed the thickness of the tabs, because they would make contact with the clamps of the tensile machine.

Since the influence of the extensometer on the resistance measurement needed to be assessed, some specimens were instrumented with both extensometer and strain gauge and others were only equipped with the extensometer. The strain gauges were mounted in the 0º direction to measure longitudinal strain.
The current needed for the electrical resistance measurement was given by an ILX lightwave LDX-3412 precision current source.

3. 6. 3. Discussion of the conducted experiments

3. 6. 3. a. A preliminary test

All the experiments were done displacement controlled with a displacement speed of 2 mm/min. To assess the proposed method, a first test on specimen F1 was done. For this test, rivets of 10 mm length and 3 mm in diameter were mounted. The longitudinal strain was not measured.
In Figure 3-56, the evolution of the relative resistance is plotted against a pseudo-time, where 0 corresponds with the start of the experiment and 1 corresponds with fracture of the specimen. The relative resistance change ρ is calculated as:

$$\rho = \frac{\Delta R}{R_0} = \frac{R_t - R_0}{R_0} \tag{3.22}$$

Where R_0 is the resistance of the unloaded specimen and R_t is the resistance of the loaded specimen. Because of the large amount of noise on the signal, a filtered curve was fitted on the original signal, to show the trend of the measurement.

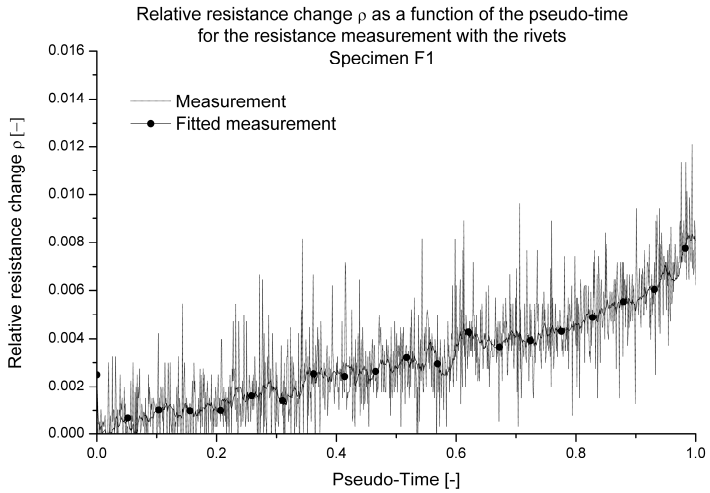

Figure 3-56 The evolution of ρ as a function of the pseudo-time for the specimen F1.

For specimen F1, the starting resistance R_0 was 1.24 Ω and the failure stress of the specimen was 694.5 MPa. The value of the relative resistance change at failure, ρ^{ult} was 0.00699. This value is low when compared to literature, but of course, only unidirectional or cross-ply reinforcement was considered. For instance, for unidirectional reinforcement, a relative change of 2 was found in [44] and of 1 in [43] at failure in a quasi-static test. For the cross-ply reinforcement, a change of 0.02 in [47] and of 0.3 was found in [49]. As can be noted, the relative change is significantly lower for the cross-ply than for the UD, because of the better current distribution due to contacting transverse fibres. Furthermore, differences in the used matrix and production method will also have an influence on the current distribution in the material. As such, it is not unexpected that the values for a fabric could be even lower.

The relative resistance increases, which means that a good contact is achieved [41, 42]. The evolutions can be divided in two separate phases; a 'steady state phase', where the increase of ρ is constant, and an 'end-of-life' phase, where the growth suddenly increases (from t = 0.8 and onward). This suggests that this method can be used for predicting the end-of-life of carbon reinforced composites.

Because of the promising results of the previous test, two more specimens, G1 and G2, were tested to see if the results are reproducible. To further increase the contact conditions, new rivets were used which are 4 mm in diameter and 100 mm in length. The increase in diameter gives a larger contact surface of the rivet. Furthermore, silver paint (RS components) was added around the mounted rivet (see Figure 3-55). The strain was measured with an extensometer, in order to have an evolution of the relative resistance change as a function of the longitudinal strain. An extensometer was chosen rather than strain gauges, because we would like to use this technique for fatigue testing. Under these loading conditions, strain gauges only survive a few thousand cycles and then the adhesive fails.

However, the question is whether the extensometer influences the electrical resistance measurement. To investigate this possible influence, two more specimens, G4 and G7, were tested. Both specimens were instrumented with strain gauges. These strain gauges are isolated from the specimen, because otherwise, they would not function properly. Therefore, they will not have any influence on the measured resistance.

All four specimens were subjected to two loading cycles.
For the first experiment, the extensometer was mounted and the specimens were loaded until about half the ultimate stress (see Table 3-2). These experiments were used to determine any influence of the extensometer on the electrical resistance measurement. This is discussed in paragraph 3. 6. 3. c.
For the second experiment, the extensometer was removed to avoid any interference of the extensometer on the resistance measurement. The specimen was loaded till fracture to assess the possibility of failure predictability. This is discussed in paragraph 3. 6. 3. d.

In Figure 3-57, the evolution of the stress as a function of the longitudinal strain is shown for all four specimens. Both loading and unloading curves are given. Each curve is given a certain strain-offset to have a clear image. The used strain for this picture is from the extensometer, since all four specimens were instrumented with the extensometer.
Table 3-5 gives an overview of the stiffness moduli of all four specimens. These values show good agreement with the values previously determined with the dynamic modulus identification method and the quasi-static testing.

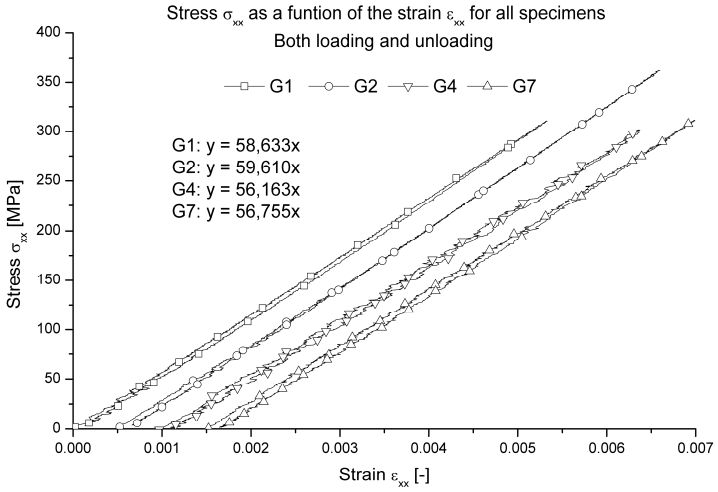

Figure 3-57 Stress as function of the strain for all specimens.

Table 3-5 Stiffness moduli derived from the static testing on the specimens.

Specimen	Stiffness [GPa]
G1	58.6
G2	59.6
G4	56.2
G7	56.8

It may be noted from the stress-strain curves above that the reached load level (350 MPa for G2, 300 MPa for the others) does not cause any stiffness degradation or permanent strain. Furthermore, no hysteresis loops are observed. Therefore, it is assumed that these load levels do not induce damage in the specimen and that the secondary loading of the specimen is representative for the loading of an undamaged specimen.

3. 6. 3. b. Assessment of the method

Figure 3-58 shows the evolution of the relative resistance change ρ as a function of the pseudo-time for all four experiments. Table 3-6 gives an overview of the initial resistance, failure stress and relative resistance change at failure.

Table 3-6 Overview of the measured values for the four experiments.

Specimen	R_0 [Ω]	ρ^{ult} [-]	$\sigma_{xx}{}^{ult}$ [MPa]
G1	0.705	0.0125	655.2
G2	0.569	0.0122	632.9
G4	0.560	0.0131	643.5
G7	0.563	0.0114	594.3

If these initial resistances are compared with the starting value of F1 (1.24 Ω), the effect of the larger rivets and the silver paint cannot be missed. The failure stresses show good agreement with the values obtained from TUDelft (Table 3-6) and from the quasi-static tests. Finally, the values of the ultimate resistance change are higher than the one obtained for F1 (0.00699). This is probably due to the better contact established with the larger rivets and the silver paint.

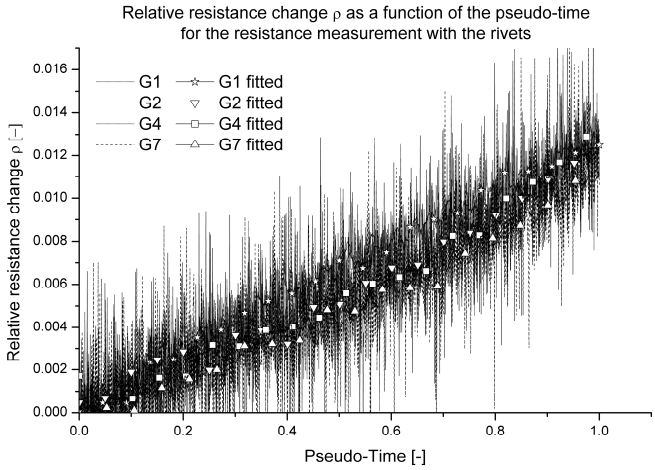

Figure 3-58 The evolution of ρ as a function of the pseudo-time for specimens G1, G2, G4 and G7.

It must be noted that the 'end-of-life' and 'steady growth' phases, that were clearly distinctive for F1, are no longer visible for any of the specimens. On the other hand, ρ^{ult} is a lot higher. Furthermore, the curves for G2, G4 and G7 are almost identical. G1 deviates slightly. The reason is probably a reduced contact of the rivets in comparison with G2, G4 and G7. The initial resistance is also a little higher.

It must be remarked that there is still a lot of noise on the measurement. This noise is present because no form of filtering (through software or hardware) was applied; the original raw data are shown. One reason for this noise on the relative resistance is the fact that the absolute increase in resistance is very low, about 7 mΩ which corresponds with an increase of only 0.7 mV, but this is within the range of the used data acquisition system.
This noise will always be present, but most authors present only the filtered signals. The signal to noise ratio may greatly be improved by increasing the current, as is illustrated in Figure 3-59. For this measurement, the specimen was kept unloaded and first a current of 100 mA was injected for a small period of time. Then, a current of 1000 mA was injected. For both cases, first, the average resistance was calculated and then ρ was determined. Should the rivets be the cause of this noise, because of bad contact or alternating contact resistance, then the noise should increase similarly with the signal when the current is increased, since voltage is equal to resistance times current and the contact resistance is also measured in the two-probe setup. It can clearly be seen that this is not the case in Figure 3-59, so the rivets do not cause the noise. In fact, increasing the current decreases the noise.
It is also common knowledge that any resistor generates white noise and that carbon film resistors generate more noise than metal film resistors. Therefore, this noise does not pose a problem, since it is most likely to be inherent to the carbon fibres and it can easily be filtered away.
Of course, higher currents may introduce heating of the specimen, so for now, this solution is not yet considered.

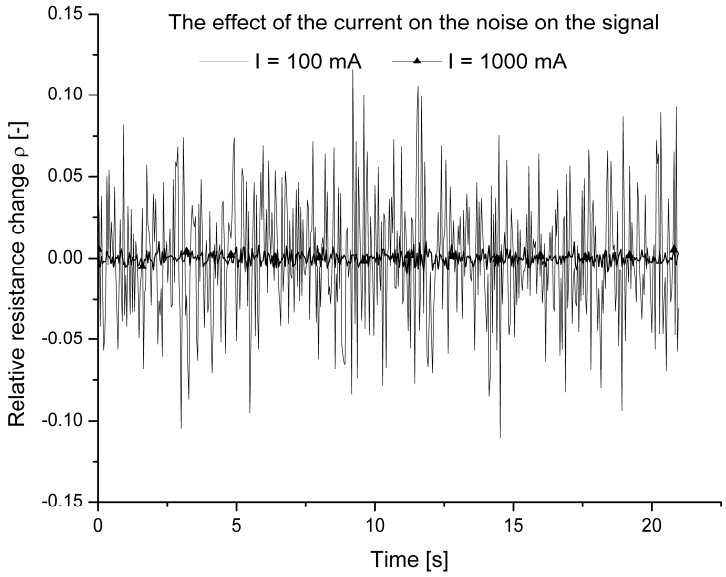

Figure 3-59 Illustration of the effect of higher current on the signal to noise ratio.

3. 6. 3. c. Influence of the extensometer

It is unclear how large the influence of the extensometer is on the electrical resistance measurement. If the current is able to flow through the device, it creates a conductive bridge over the stressed and possibly damaged zone and therefore corrupts the data.

Figure 3-60 shows the used extensometer for the strain measurements. The movable blade runs over a small cylinder (indicated by the white circle) that is connected with the rigid blade. If contact occurs at the cylinder, the two blades form a short circuit over the specimen, excluding a large area with possible damage from the resistance measurement.

When measuring the resistance between the fixed and the movable blade, a value of 20.3 Ω is registered. This is certainly not high enough to be considered infinite with respect to the resistance of the specimens. Therefore, the extensometer will influence the resistance measurements on the specimen.

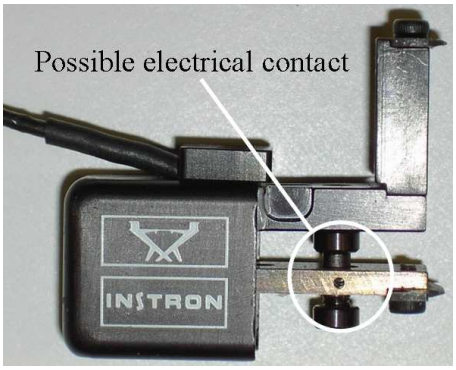

Figure 3-60 Illustration of the used extensometer. The possibility of electrical contact is highlighted.

Consider the theoretical resistor model in Figure 3-61 where the specimen is divided in two parts, one which represents the part of the specimen with the extensometer as a parallel resistor, illustrated by R_E, and another part which represents the rest of the specimen. The total resistance of the sample is R and a < 1.

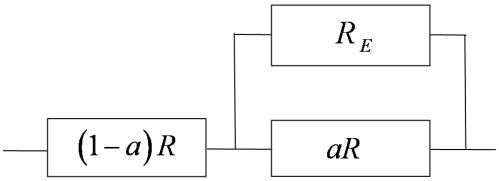

Figure 3-61 Theoretical illustration of the effect of the extensometer on the resistance measurement.

If no extensometer is mounted, then the total resistance becomes R and the relative resistance change becomes:

$$\rho = \frac{R_t - R_0}{R_0} \tag{3.23}$$

With R_t the resistance of the loaded and R_0 the resistance of the unloaded specimen, as previously mentioned. If the extensometer is mounted, then the relative resistance change at time t, using the same initial resistance, becomes:

$$\rho_E = \frac{\left((1-a)R_t + \frac{aR_tR_E}{aR_t + R_E}\right) - R_0}{R_0} \tag{3.24}$$

This can be rewritten as

$$\rho_E = \rho - \frac{a^2R_t^2}{R_0} \tag{3.25}$$

This means that the relative resistance change will be higher without the extensometer than when it is mounted. However, when the extensometer is mounted, the initial resistance will not be R_0 but:

$$R_0^E = (1-a)R_0 + \frac{aR_0R_E}{aR_0 + R_E} \tag{3.26}$$

If this initial value is used, the following is derived for ρ_E.

$$\rho_E^* = \frac{aR_0 + R_E}{(1-a)aR_0 + R_E}\rho - \frac{a^2R_t^2(aR_0 + R_E)}{R_0[a(1-a)R_0 + R_E)]} \tag{3.27}$$

It is now very difficult to estimate the exact influence, because the multiplier of ρ is slightly higher than one, but from this product, a small value is subtracted. The main conclusion, however, is that the extensometer will have an influence.

To investigate the influence of the extensometer on the resistance measurement experimentally, the extensometer was mounted and the specimens were loaded until about half the ultimate stress (see Table 3-6) and then unloaded. Next, the extensometer is removed and the specimen was loaded again. Figure 3-62 shows the evolution of ρ as a function of the strain ε_{xx} for both these loadings. Only the data points from the fitted curves are plotted for a clear overview. The strain in the abscissa is the one from the strain gauge, to exclude any influence of the difference between the extensometer and the strain gauge.
It can be seen that at larger strains (>0.0035) the relative resistance change increases more when the extensometer is mounted than otherwise; the open symbols systematically lie above the filled symbols for the higher strains. So it may be concluded, both from experimental and theoretical point of view, that the extensometer has an influence on the electrical resistance measurement.

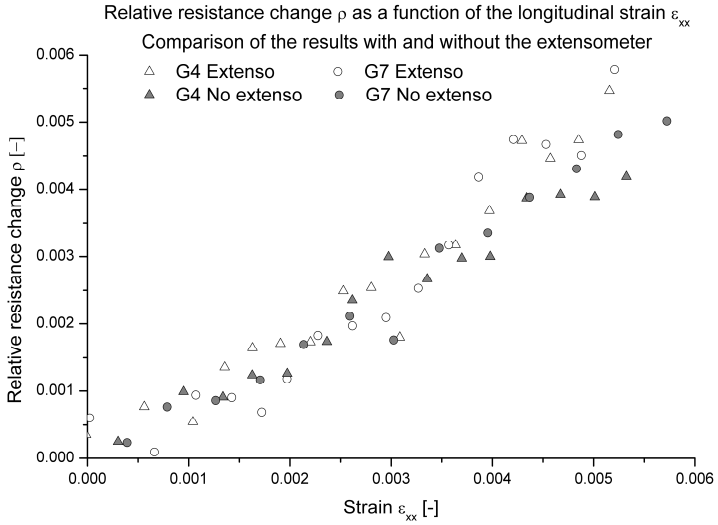

Figure 3-62 The evolution of ρ as a function of the longitudinal strain ε_{xx} for the specimens G4 and G7. Only the filtered curves are plotted for a clean image.

Finally, Figure 3-63 illustrates the evolution of the relative resistance change as a function of the longitudinal strain for G4 and G7, measured by the strain gauges until fracture.

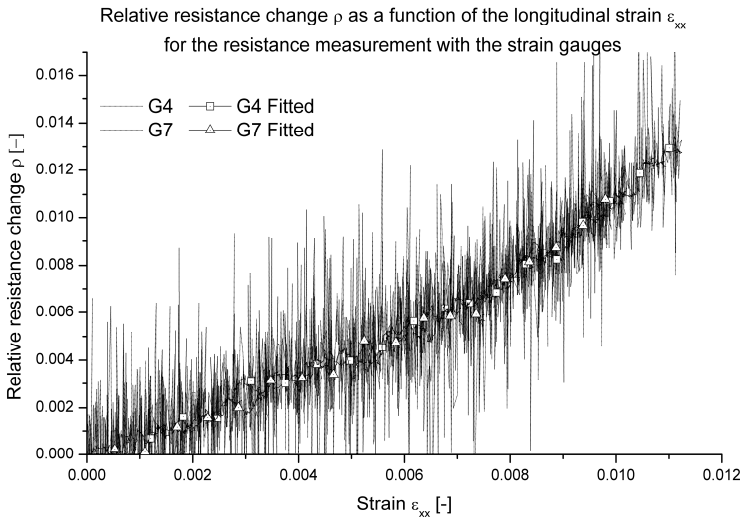

Figure 3-63 The evolution of the relative resistance change as a function of the longitudinal strain, measured by the strain gauges until fracture for specimens G4 and G7.

It must be noted that both measurements are almost identical, which illustrates the reproducibility of the results.

3. 6. 3. d. Failure predictability

From the previous paragraphs, it has become clear that the resistance increases with increasing strains (or loads). The question remains whether this increase can be used for damage modelling or to predict failure.

Figure 3-56 and Figure 3-58 show the evolution of ρ for all experiments. Only for F1 the 'end-of-life' phase can be seen. However, all other experiments tend to have an ultimate relative resistance change of about 0.0012, regardless of the initial resistance. This can also be seen in Table 3-6. When comparing the experiments with the 4 x 10 rivets, it must be noted that the curves for G2, G4 and G7 are very much alike. Only G1 has a slightly different form. Since the R_o of G1 is slightly higher than the others, this is probably due to an inferior contact.

As such, a failure criterion in the form of a maximum allowable value of ρ could be proposed.

3. 6. 3. e. Further modifications to the extensometer

As was proven in paragraph 3. 6. 3. c the standard extensometer influences the electrical resistance measurement, since it conducts electricity. This problem can be solved for quasi-static and hysteresis experiments, simply by using longitudinal strain gauges. However, longitudinal strain gauges could not be used for fatigue testing, since they will de-bond after a few hundred cycles.

So if longitudinal strain is to be measured while the electrical resistance measurement is used, a new approach of strain measurement needs to be applied.

A first option is to use embedded optical Bragg fibres. This is documented extensively in paragraph 3. 5, but it has a small set back: it is very useful if the specimens are yet to be fabricated, but for the existing material, it is impossible to insert a fibre. It may, however, be possible to use externally bonded fibre gratings, but in general optical fibres are more expensive then the second option.

This second option is to modify the existing extensometer. If the two blades are electrically isolated, then there is no problem with the electrical resistance measurement. This can be done in two ways: (i) the blades are made from an isolating material or (ii) the blades are mounted on an isolating base.

The first option is not easily achieved, since the only materials that (i) are hard enough so that the sharp points for the three point principle can be made and (ii) are electrical isolators, are ceramics. These materials, however, are not easily milled and therefore, the section option was chosen. Two small supports, on which the blades can be mounted, are made in polyvinyl chloride (PVC). Two new three-point blades are made and glued in the PVC, making sure that the blades do not make contact with the two bolts which mount the blade on the extensometer. This design can be seen in Figure 3-64

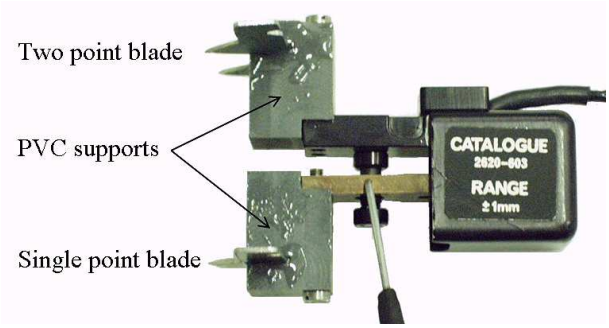

Figure 3-64 Isolating blades on the extensometer.

For the calibration of this new device, the same setup as previously mentioned is used. A calibration factor of 1.27 was found with respect to the strain data given by the tensile machine. From now on, this isolated extensometer is used for all experiments with electrical resistance measurement.

3. 6. 4. Four-probe method

The resistance of the specimen is measured by injecting a known current through two electrical contacts on the specimen and measuring the voltage between two electrodes. In the previous paragraphs, a two-probe technique was used, which means that the voltage is measured on the same electrodes where the current is introduced.

This principle worked excellent for the quasi-static tests, but an extra parameter is introduced when conducting fatigue experiments: time.

Therefore, the time-stability of this setup was first tested by measuring the resistance of an unloaded specimen for an extended period of time, corresponding with an average fatigue test.

Several of these tests have been performed in order to have reproducible results; they are shown in Figure 3-65. For specimen I7, a current of 1000 mA was injected and three successive measurements (I7-1 till I7-3) were done. After a certain period of time, the current was removed and the specimen was left untouched for a few hours. Afterwards, the current was injected again and the measurement was redone to see if the increase in resistance was reversible. It can clearly be noticed that the resistance change is irreversible, since the initial resistance of I7-2 differs from the starting resistance of I7-1. Also, should this be a reversible phenomenon, one would expect coincident curves for all three tests and this is definitely not the case. The same experiment was done on specimen I8 (I8-1 and I8-2), but with a current of 100 mA, to assess whether the high current may cause the increase. Again, there is an irreversible increase in resistance, since the initial value of I8-2 is higher than the initial value of I8-1.

To assess whether this effect is due to the data acquisition unit, a reference resistor was also measured using the same setup. It can be noted that the measured value is constant, which rules out the data acquisition unit.

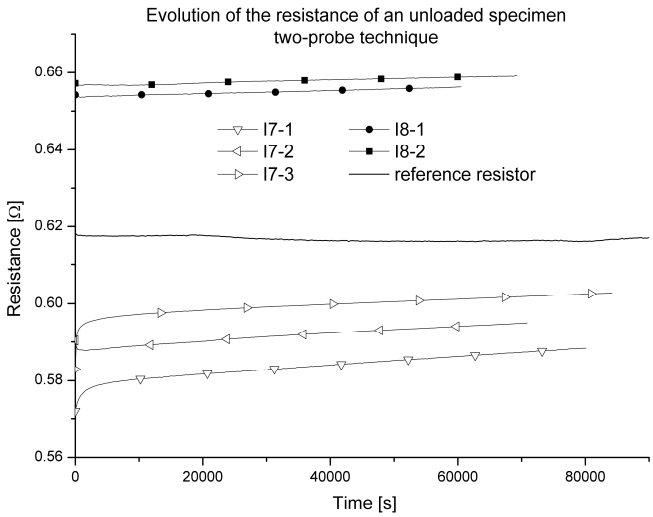

Figure 3-65 Evolution of the resistance of an unloaded specimen, measured with the two-probe technique.

It must be remarked that during the experiments described above, the temperature was monitored. There was no significant increase or decrease of the temperature, which rules out the temperature as possible influence. Furthermore, this means that the higher current of 1000 mA may be used without the risk of generating Joule's heat.

For the quasi-static tests, this increase did not have any influence on the measurement, since the total time needed for the experiment was too short for any significant increase to occur. For the fatigue experiments, however, this could be a major problem, since the value of the increase due to fatigue damage may be of the same order as the increase measured above.
The main reason for this increase is that in the two-probe method, the contact resistance of the electrodes is also measured. The principle of the two-probe method is illustrated in Figure 3-66.

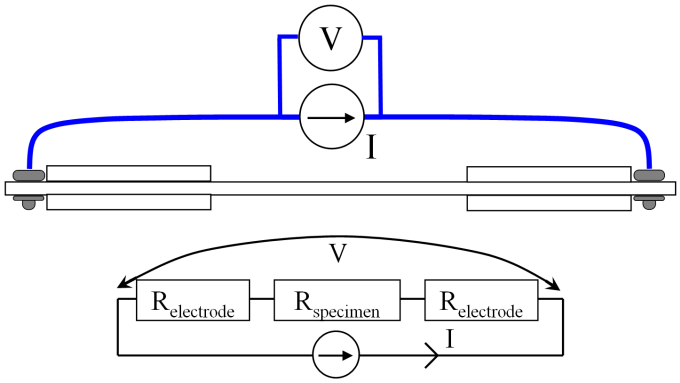

Figure 3-66 The two-probe system for resistance measurement.

The voltage measured by the system is given by:

$$V = R_{tot}.I = (2R_{electrode} + R_{specimen}).I \tag{3.28}$$

Therefore, if the resistance of the contact electrodes varies in time, this variation is also measured by the system and this is the reason why the measurements depicted in Figure 3-65 are not stable. The variation of the contact resistance may have various reasons, such as creep of the composite around the rivets or electrochemical reactions of the Sn in the soldered connection between rivet and wire, which is a well known problem in the electronics industry [50-52]. It is impossible to model all these effects on the total resistance, so the best solution is to avoid measuring the contact resistance.

Therefore, a four-probe method is considered. This setup is also used in [41-43, 48, 49, 53, 54]. This technique is said to be more accurate [42, 43] than the two-probe technique, but is more complicated as experimental setup. Furthermore, it may not represent sub-surface behaviour if all probes are mounted on the same surface [41]. The used setup for this research is illustrated in Figure 3-67. The two electrodes for current injection are the same as for the two-probe method, but for the voltage electrodes, rivets are no option since this would require drilling holes in the loaded part of the specimen. Therefore, a special conductive copper tape is wound around the specimen and the wires for the voltage measurement are then attached to this tape. By winding the electrode around the specimen, subsurface behaviour is represented. The area underneath the tape is degreased with acetone, but it is not polished, since this would damage the surface and induce premature fatigue failure.

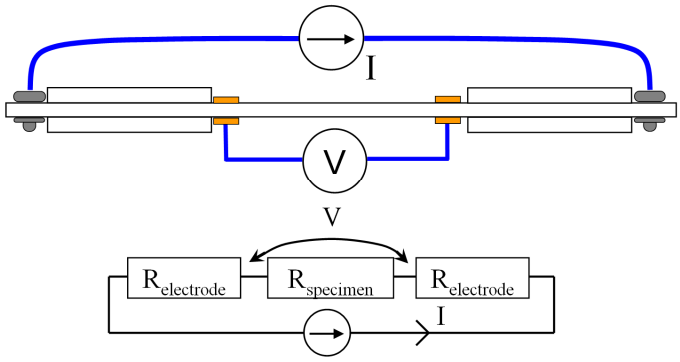

Figure 3-67 The four-probe system for resistance measurement.

As for the two-probe method, the current still travels through the contact electrodes $R_{electrode}$, but the measured voltage is now given by:

$$V = R_{specimen}.I \tag{3.29}$$

Normally, the voltage measurement unit has a very high input impedance, so no current travels through the wires from the specimen to the unit and therefore, the contact resistance of the copper conductive tape has no influence. However, some say the quality of the electrodes tends to have a small influence [55].
Figure 3-68 shows the end of a specimen, instrumented with the four-probe method. On the right of the tab, the rivet which is used for current injection can be seen and the copper tape, used to measure the voltage is mounted on the left of the tab.

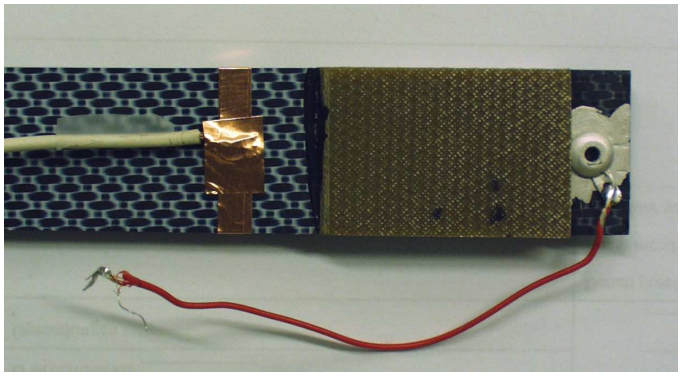

Figure 3-68 Illustration of the two electrodes, the copper tape on the left of the tab and the rivet on the right of the tab.

Of course, the time-stability of this method should still be tested. Again, a current of 1000 mA was injected through the specimen and the resistance was measured for an extended period of time. The result was also depicted in Figure 3-69 and as can be seen, no increase occurs.

In fact, the signal is even more stable than the reference resistor measurement, which proves that the four-probe method is definitely an improvement.

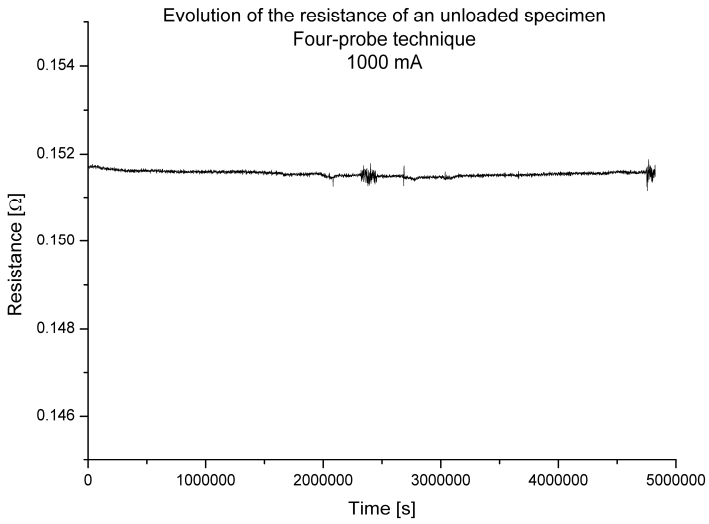

Figure 3-69 Evolution of the resistance of an unloaded specimen, measured with the four-probe technique.

Furthermore, the low value of the resistance should be noted. The voltage, given by the current source, was about 0.7 V, while the actual resistance of the specimen is only 0.1518 Ω, meaning that the contact resistance of each of the rivets is about 0.275 Ω. As a result, the sensitivity of the setup should have increased.
The choice of 1000 mA was made to further increase the signal to noise ratio. Of course, this current could cause heating of the specimen due to Joules heating, but temperature was monitored for all the four-probe experiments and no significant increase in temperature was noted. The increase in current however did have a significant effect on the noise on the signal, as was illustrated in Figure 3-59. It must be noted that the measured noise is white noise, the average value of both signals is 0 and this noise can be easily filtered away by using a low band pass filter.

3. 6. 4. a. Experiments with the four-probe method

Of course, before using this method for the quasi-static cyclic testing (chapter 4) or fatigue testing (chapter 5) the conclusions from the two-probe method should first be validated using this four-probe method. Therefore, a few static tests have been performed, of which the results are shown in Figure 3-70; both the measurement and the filtered signal are presented. The tests were displacement controlled at a speed of 2 mm/min.

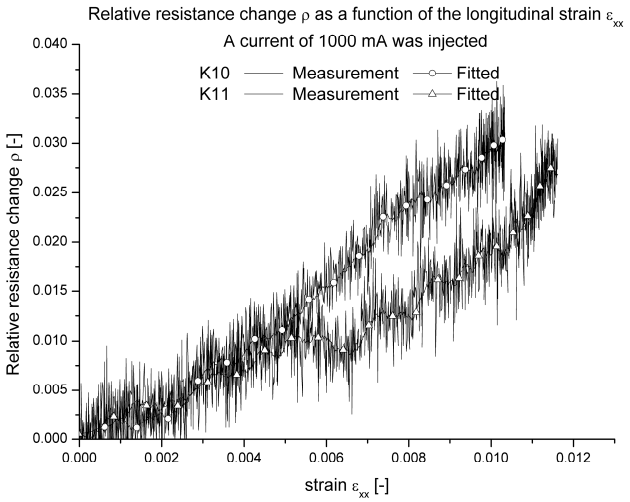

Figure 3-70 Quasi-static tests of the four-probe method for resistance measurement.

When comparing these static results to the ones in paragraph 3. 6. 3, it should be noted that the value of ρ at failure is more than double. Here, values of 0.0304 for K10 and 0.028 for K11 are found, compared to values of 0.011 and 0.013 found in paragraph 3. 6. 3. b. This illustrates the increase in sensitivity of the four-probe over the two-probe method. On the other hand, the higher sensitivity might be the reason why the reproducibility is not as high as in the previous study. The increase of both signals is very similar, apart from the dip in the curve of K11.

Figure 3-71 shows the longitudinal stress-strain relationship. Again, the derived Young's modulus shows good agreement with the values obtained with the resonalyser method and with the values obtained form TUDelft (Table 3-2).

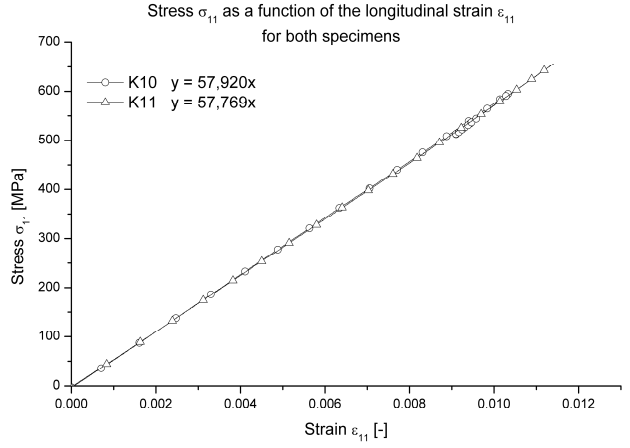

Figure 3-71 σ_{11} as a function of ε_{11}.

Specimens K10 and K11 failed at respectively 596 MPa and 668 MPa.

3. 6. 5. Conclusions

Rivets can be used as contact electrodes for electrical resistance measurement with reproducible results. The measured resistance increases with increasing strain, which indicates that good contact is achieved by using rivets. The contact can be improved by using rivets with a larger diameter and by adding silver paint on the contact zone.
The extensometer certainly has a negative influence on the resistance measurement, the evolution of ρ is wavier and the values are higher than when the extensometer is not mounted. Therefore, an extra modification has been made to the extensometer; for all further experiments which involve the electrical resistance measurement, the extensometer with the electrically isolated three-point blades is used.
The two-probe setup works fine for quasi-static testing, but unfortunately, the method lacks stability in time; there is an unpredictable drift on the signal. As such, this method cannot be used for fatigue experiments. Therefore, a four-probe setup has been proposed, which is stable in time and is even more sensitive to changes in the resistance than the two-probe method. As such, the four-probe method will be used for all further testing involving the resistance measurement.

3. 7. REFERENCES

[1] Ageorges C, Ye L, Hou M, Advances in fusion bonding techniques for joining thermoplastic matrix composites: a review. COMPOSITES PART A-APPLIED SCIENCE AND MANUFACTURING 32 (6): 839-857 2001.

[2] Stavrov D, Bersee HEN, Resistance welding of thermoplastic composites - an overview, COMPOSITES PART A-APPLIED SCIENCE AND MANUFACTURING 36 (1): 39-54 2005.

[3] X. R. Xiao, S. V. Hoa and K. N. Street, Composites Bonding, ASTM STP 1227 (1994) 30.

[4] C. L. T. Lambing, R. C. Don, S. M. Andersen, S. T. Holmes, B. S. Leach and J. W. Gillespie Jr, in Proc. ANTEC '91, 1991, p2527

[5] Yousefpour A, Hojjati M, Immarigeon JP, Fusion bonding/welding of thermoplastic composites. JOURNAL OF THERMOPLASTIC COMPOSITE MATERIALS 17 (4): 303-341 JUL 2004.

[6] Sol, H., Hua, H., De Visscher, J., Vantomme, J., De Wilde, W.P., "A Mixed Numerical/Experimental technique for the nondestructive identification of the Stiffness Properties of fibre-reinforced Composite Materials", Journal of NDT&E International, Vol. 30, N°2, pp.85-91, Elsevier Science Ltd, 1997.

[7] T. Lauwagie, H. Sol, G. Roebben, W. Heylen and Y. Shi. Validation of the resonalyser method: an inverse method for material identification, Proceedings of ISMA 2002, International Conference on Noise and Vibration Engineering, Leuven, 16-18 Sept. 2002, pp. 687-694.

[8] F. Förster. Ein neues Messverfahren zur Bestimmung des Elastizitätsmoduls und der Dämpfung. Z. Metallkd., Vol. 29:109–115, 1937.

[9] G. Pickett. Equations for computing elastic constants from flexural and torsional resonant frequencies of vibrating prisms and cylinders. Proceedings ASTM, Vol. 45:846–865, 1945.

[10] S. Spinner and W. E. Teft. A method for determining mechanical resonance frequencies and for calculating elastic moduli from these frequencies. Proceedings ASTM, Vol. 61:1209–1221, 1961.

[11] H. Sol, T. Lauwagie, W. Heylen, G. Roebben. Simultaneous identification of the elastic and damping properties of composite materials as a function of temperature. Second International workshop on damping technologies, Materials and devices for the next decade, Stellenbosch, South Africa, 24-26 mar. 2003.

[12] Hua, H., 1993. "Identification of Plate Rigidities of Anisotropic Rectangular Plates, Sandwich Panels and Orthotropic Circular Disks using Vibration Data". Ph.D. Thesis presented at the Vrije Universiteit Brussel, Belgium.

[13] Kreindler, E & Sarachik, P.E., 1964. "On the concepts of Controllability and Observability of linear Systems", IEEE trans., A.C., Vol. AC-9.

[14] T. Lauwagie, W. Heylen. A Multi-Model Updating Routine For Layered Material Identification, Proceedings of the International Modal Analysis Conference, IMAC XXI, Kissimmee, 3-6 Feb. 2003.

[15] Sol, H. et al., 1996, “La procedure resonalyser”, La revue des laboratoires d'Essais, n° 46, pp.10-12.

[16] Sol,H., 1986, “Identification of anisotropic plate rigidities using free vibration data”, Ph.D.Thesis presented at the vrije Universiteit Brussel, Belgium.

[17] Collins, J.D. & Hart, G.C. & Hasselman, T.K. & Kennedy B., 1974. “Statistical Identification of Structures”, AIAA Journal, 12(2), pp.185-190.

[18] Sol, H. & Oomens, C. 1997. “Material Identification Using Mixed Numerical Experimental Methods”, Kluwer Academic Publishers.

[19] Brigham, E. Oren, 1988, “The Fast Fourier Transform and Its Applications”, Englewood Cliffs, NJ: Prentice-Hall, Inc., 448 pp.

[20] Vinson, Jack R., 2005, “Plate and Panel Structures of Isotropic, Composite and Piezoelectric Materials, Including Sandwich Construction”, SOLID MECHANICS AND ITS APPLICATIONS, Vol. 120, Springer;

[21] De Waele W, Degrieck J, De Baets P, Moerman W, Taerwe L, Feasibility of integrated optical fibre sensors for condition monitoring of composite structures - Part II: Combination of Bragg-sensors and acoustic emission detection. INSIGHT 45 (8): 542-+ AUG 2003.

[22] De Waele W, Degrieck J, Baets R, Moerman W, Taerwe L, Load and deformation monitoring of composite pressure vessels by means of optical fibre sensors. INSIGHT 43 (8): 518-525 AUG 2001.

[23] De Waele V, Degrieck J, Moerman W, Taerwe L, De Baets P, Feasibility of integrated optical fibre sensors for condition monitoring of composite structures - Part I: Comparison of Bragg-sensors and strain gauges, INSIGHT 45 (4): 266-271 APR 2003.

[24] Degrieck J, De Waele W, Verleysen P, Monitoring of fibre-reinforced composites with embedded optical fibre Bragg sensors, with application to filament wound pressure vessels, NDT & E INTERNATIONAL 34 (4): 289-296 JUN 2001.

[25] Doyle C, Martin A, Liu T, Wu M, Hayes S, Crosby PA, Powell GR, Brooks D, Fernando GF, In-situ process and condition monitoring of advanced fibre-reinforced composite materials using optical fibre sensors, SMART MATERIALS & STRUCTURES 7 (2): 145-158 APR 1998.

[26] Shin C. S. and Chiang C. C., Embedded fibre Bragg grating sensors for internal fatigue damage monitoring in polymeric composites, ADVANCED NONDESTRUCTUVE EVALUATION I, PTS 1 AND 2, PROCEEDINGS KEY ENGINEERING MATERIALS 321-323: 230-233 2006.

[27] Shin CS and Chiang CC, Fatigue damage monitoring in polymeric composites using multiple fiber Bragg gratings, INTERNATIONAL JOURNAL OF FATIGUE 28 (10): 1315-1321 OCT 2006.

[28] Malo B, Albert J, Hill K O, Bilodeau F and Johnson D C, Effective index drift from molecular hydrogen diffusion in hydrogen-loaded optical fibres and its effect on Bragg grating fabrication, ELECTRONICS LETTERS. 30 442–3, 1994.

[29] Patrick H J, Gilbert S L, Lidgard A and Gallagher M D, Annealing of Bragg gratings in hydrogen-loaded optical fiber, JOURNAL OF APPLIED PHYSICS 78 2940–5, 1995.

[30] K.T.V. Grattan, B.T. Meggitt, Optical fibre sensor technology: Fundamentals, Kluwer academic publishers, Boston/Dordrecht/London, 2000.

[31] Parlevliet P.P., Bersee H.E.N. and Beukers A.. Residual stresses in thermoplastic composites – a study of the literature. Part III: Effects of thermal residual stresses. COMPOSITES PART A: APPLIED SCIENCE AND MANUFACTURING., VOLUME 38, ISSUE 6, JUNE 2007, PAGES 1581-1596.

[32] Parlevliet P.P., Bersee H.E.N. and Beukers A., Residual stresses in thermoplastic composites—A study of the literature—Part I: Formation of residual stresses. Composites Part A: Applied Science and Manufacturing, Volume 37, Issue 11 , November 2006, Pages 1847-1857.

[33] C. Chojetzki, M. Rothhardt, H.-R. Müller, H. Bartelt, Large Fibre Bragg Grating Arrays for monitoring applications – Made by Drawing Tower Inscription, IPHT, Jena, Germany & FOS&S, Geel, Belgium, 2005.

[34] Sorensen L, Gmur T, Botsis J, Residual strain development in an AS4/PPS thermoplastic composite measured using fibre Bragg grating sensors. COMPOSITES PART A-APPLIED SCIENCE AND MANUFACTURING 37 (2): 270-281 2006.

[35] Colpo F., Humbert L. and Botsis J., Characterisation of residual stresses in a single fibre composite with FBG sensor. COMPOSITES SCIENCE AND TECHNOLOGY 67 (9): 1830-1841 JUL 2007.

[36] Montanini, R., D'Acquisto, L., Simultaneous measurement of temperature and strain in glass fiber/epoxy composites by embedded fiber optic sensors: I. Cure monitoring. SMART MATERIALS & STRUCTURES 16 (5): 1718-1726 OCT 2007.

[37] Colpo F, Humbert L, Glaccari P, Botsis J., Characterization of residual strains in an epoxy block using an embedded FBG sensor and the OLCR technique. COMPOSITES PART A-APPLIED SCIENCE AND MANUFACTURING 37 (4): 652-661 2006.

[38] Vlassenbroeck, J., Cnudde, V., Dierick, M., Masschaele, B., Van Hoorebeke, L., Jacobs, P. Software tools for quantification of X-ray microtomography at the UGCT. 10th International Symposium on Radiation Physics, Coimbra, Portugal, 17-22 September 2006.

[39] Abry JC, Choi YK, Chateauminois A, Dalloz B, Giraud G, Salvia M, In-situ monitoring of damage in CFRP laminates by means of AC and DC measurements, COMPOSITES SCIENCE AND TECHNOLOGY 61 (6): 855-864, 2001.

[40] Seo DC, Lee JJ, Damage detection of CFRP laminates using electrical resistance measurement and neural network, COMPOSITE STRUCTURES 47 (1-4): 525-530 DEC, 1999.

[41] Angelidis N, Wei CY, Irving PE ,The electrical resistance response of continuous carbon fibre composite laminates to mechanical strain, COMPOSITES PART A-APPLIED SCIENCE AND MANUFACTURING 35 (10): 1135-1147, 2004.

[42] Todoroki A, Yoshida J, Electrical resistance change of unidirectional CFRP due to applied load, JSME INTERNATIONAL JOURNAL SERIES A-SOLID MECHANICS AND MATERIAL ENGINEERING 47 (3): 357-364 , JUL 2004.

[43] Park JB, Okabe T, Takeda N, New concept for modeling the electromechanical behavior of unidirectional carbon-fiber-reinforced plastic under tensile loading, SMART MATERIALS & STRUCTURES 12 (1): 105-114 FEB, 2003.

[44] Park JB, Okabe T, Takeda N, Curtin WA, Electromechanical modelling of unidirectional CFRP composites under tensile loading condition, COMPOSITES PART A-APPLIED SCIENCE AND MANUFACTURING 33 (2): 267-275, 2002.

[45] Abry JC, Bochard S, Chateauminois A, Salvia M, Giraud G, In situ detection of damage in CFRP laminates by electrical resistance measurements, COMPOSITES SCIENCE AND TECHNOLOGY 59 (6): 925-935, 1999.

[46] Xia Z, Okabe T, Park JB, Curtin WA, Takeda N, Quantitative damage detection in CFRP composites: coupled mechanical and electrical models, COMPOSITES SCIENCE AND TECHNOLOGY 63 (10): 1411-1422 AUG, 2003.

[47] Irving PE, Thiagarajan C, Fatigue damage characterization in carbon fibre composite materials using an electrical potential technique, SMART MATERIALS & STRUCTURES 7 (4): 456-466 AUG, 1998.

[48] Wang XJ, Chung DDL, Real-time monitoring of fatigue damage and dynamic strain in carbon fiber polymer-matrix composite by electrical resistance measurement, SMART MATERIALS & STRUCTURES 6 (4): 504-508, AUG 1997.

[49] Wang XJ, Chung DDL, Self-monitoring of fatigue damage and dynamic strain in carbon fiber polymer-matrix composite, COMPOSITES PART B-ENGINEERING 29 (1): 63-73 ,1998.

[50] Moon K.S., Liong S, Li H.Y. and Wong C.P., Stabilizing contact resistance of isotropically conductive adhesives on various metal surfaces by incorporating sacrificial anode materials. JOURNAL OF ELECTRONIC MATERIALS 33 (11): 1381-1388 NOV 2004.

[51] Chen Z.G. and Kim Y.H.,Characteristics of the interfacial microstructure of chip-on-plastic joints under thermal cycling and aging treatment, JOURNAL OF ELECTRONIC MATERIALS 36 (1): 45-55 JAN 2007.

[52] Benhenda S., Benjemaa N., Perrin C. and Simon D., Corrosion behaviour of TiN and Sn coatings deposited onto brass substrates for electrical contact interfaces, SURFACE & COATINGS TECHNOLOGY 56 (3): 249-255 MAR 10 1993.

[53] Todoroki A, Omagari, K, Shimamura Y, and Kobayashi H, Matrix crack detection of CFRP using electrical resistance change with integrated surface probes, Composites Science and Technology, Volume 66, Issues 11-12 , September 2006, Pages 1539-1545.

[54] J. B. Park, T. K. Hwang, H. G. Kim and Y. D. Doh, Experimental and numerical study of the electrical anisotropy in unidirectional carbon-fiber-reinforced polymer composites, Smart Materials and Structures Volume 16 February 2007 pages 57-66.

[55] D.D.L. Chung, Shoukai Wang, Discussion on paper "The electrical resistance response of continuous carbon fibre composite laminates to mechanical strain" by N. Angelidis, C.Y. Wei and P.E. Irving, Composites: Part A 35, 1135-1147 (2004), Composites Part A: Applied Science and Manufacturing, Volume 37, Issue 9, pages 1490-1494.

Chapter 4

QUASI-STATIC CYCLIC TESTING

This chapter describes the quasi-static cyclic experiments, which are an intermediate step between the static tensile experiments from chapter 3 and the fatigue experiments in chapter 4. The sensor types, introduced in chapter 3 will be considered here for the cyclic loadings and the use of the Poisson's ratio for damage monitoring is discussed.

4. 1. INTRODUCTION

In the previous chapter, the mechanical properties of the carbon fabric-reinforced PPS were determined and a number of methods were introduced for monitoring tensile experiments. The use of these measurement methods for monitoring quasi-static tensile tests till failure was assessed. In this chapter, the next step towards fatigue loading is taken. A large number of quasi-static hysteresis tests were performed and the presented monitoring techniques are investigated. Such a quasi-static hysteresis test consists of a number of successive tensile tests: the specimen is loaded until a certain stress level is reached, after which the specimen is unloaded. This is repeated a number of times, during which the maximum stress level can remain the same, be increased or decreased, although the last option is not considered here. The general idea is that during the loading, certain damage processes take place and it is assumed that during the unloading, no extra damage growth occurs. The effects of the damage mechanics are then visualised by unloading the specimen and determining certain parameters, such as Young's modulus, permanent deformation, electrical resistance …

In the next paragraph, the general approach, consisting of measuring stiffness degradation and permanent deformation is discussed. Then, the evolution of the Poisson's ratio is assessed for its damage predictability. Finally, the electrical resistance measurement is used to monitor possible damage growth during the cyclic experiments.

4. 2. HYSTERESIS TESTS

The first hysteresis experiments were performed with an increasing maximum load level for each cycle. The specimen was loaded till 100 MPa and then unloaded to 0 MPa. For all following cycles, the maximum load was increased with 50 MPa with respect to the previous maximum load and this was repeated till failure. All experiments were displacement-controlled with a speed of 2 mm/min. Figure 4-1 shows three of those experiments.

For I2, 13 cycles were performed; the cycle at 550 MPa was omitted and the specimen failed in the last cycle at 720 MPa. For I3, 14 cycles were performed, the specimen failed in the last cycle at 685 MPa, although it had reached 700 MPa the cycle before. Finally, for I5, only 11 cycles could be performed, at 600 MPa of the last cycle, which supposed to reach 650 MPa, the tabs de-bonded.
The three curves are given an offset of 0.003 in the longitudinal strain, in order to have a clear image.

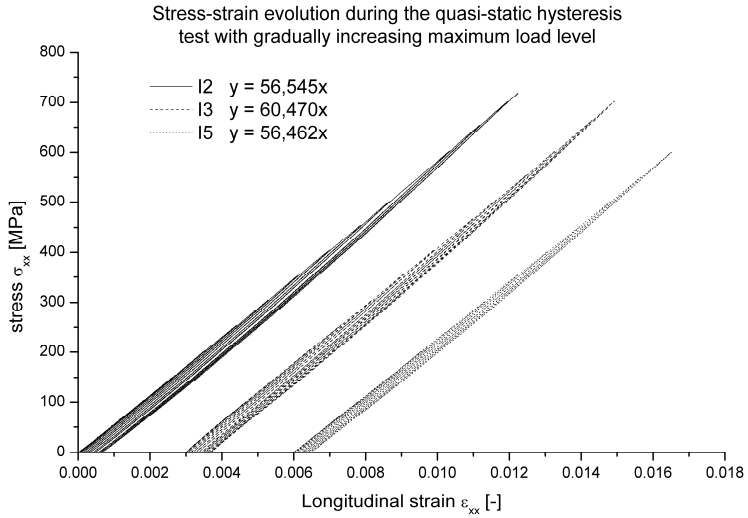

Figure 4-1 Stress as function of the strain for the quasi-static hysteresis test with increasing load level.

It can be noticed that there is a gradual increase in permanent deformation, but there is no stiffness degradation. In fact, the material has a slight increase in stiffness, but this is quite common for carbon reinforced polymers, as reported in [1]. The derived stiffness, calculated from the slope of the tangent of the first loading cycle in the origin corresponds well with the results from chapter 3.

A second series of hysteresis tests was done at a constant loading level. It was attempted to have ten loading cycles up to a certain maximum, after which the specimen was loaded until failure. The purpose is to see whether under these loading conditions, the stiffness degrades and whether the permanent deformation continues to grow.
Considering the high failure stresses of the previous experiments, a first test was done with a maximum load level of 575 MPa. Because of the success of this test and its high failure stress, the second test illustrated was done with a maximum load level of 625 MPa.

Again both experiments were done displacement-controlled with a speed of 2 mm/min and the extensometer was removed before the final test till failure, since it was noted from the previous experiments that the shockwave in the specimen, caused by the failure, sometimes resulted in strains that might damage the extensometer.
The stress-strain curves of these experiments are shown in Figure 4-2; again the curves have been given a longitudinal strain offset of 0.003. Specimen G11 failed at 761 MPa and specimen G9 failed at 725 MPa.

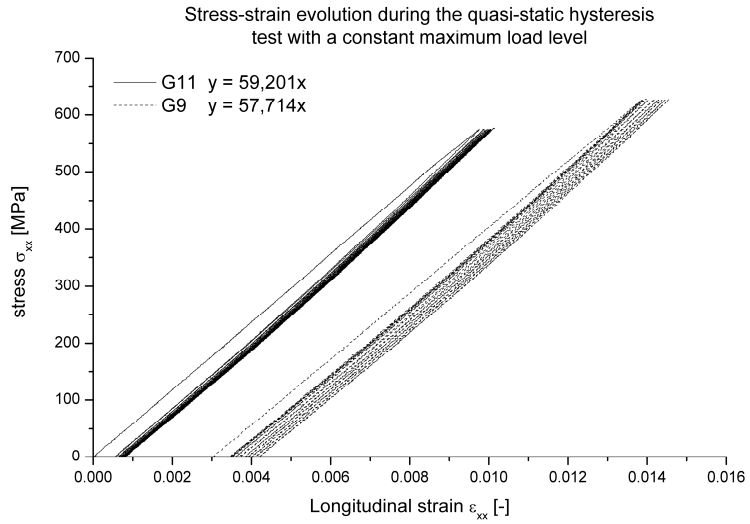

Figure 4-2 Stress as function of the strain for the quasi-static hysteresis with constant load level.

Again, the stiffness tends to gradually increase instead of decrease. With regard to the permanent deformation, the largest increase happens in the first cycle and for the following cycles, only very limited increase occurs, although the effect of a higher maximum load cannot be missed.

As a result from both types of measurement, it appears that monitoring stiffness degradation to predict failure or model damage will not be an option, since there is no decrease for this parameter. Using the permanent deformation may be an option, but the sensitivity seems to be limited, only a very limited increase was noticed.
Therefore, it is investigated whether another mechanical property of the material, namely the Poisson's ratio could be used for this purpose.

4. 3. MEASUREMENT OF THE POISSON'S RATIO

4. 3. 1. Introduction

There are a number of articles in literature which mention the fact that generally, the Poisson's ratio is more sensitive to damage than Young's modulus or residual (or permanent) deformation [1-5]. Also, in his master thesis, the author has seen a gradually decreasing Poisson's ratio as a function of the longitudinal strain [6]. Therefore, it is assessed whether this parameter can be used to monitor any damage degradation under quasi-static cyclic loading conditions.
Since the Poisson's ratio of the carbon fabric-reinforced PPS is quite low, around 0.033 (see chapter 3), first a number of experiments were conducted on a unidirectional fabric-reinforced-epoxy, which has a larger Poisson's ratio of 0.25 (see chapter 2). This material also has the advantage of being transparent, so cracks are more visible.

4. 3. 2. Discussion of the results

4. 3. 2. a. Unidirectional glass fabric-reinforced epoxy

The dimensions of the used coupons are shown in Figure 4-3; the used stacking sequence is $[0°/90°]_{2s}$.

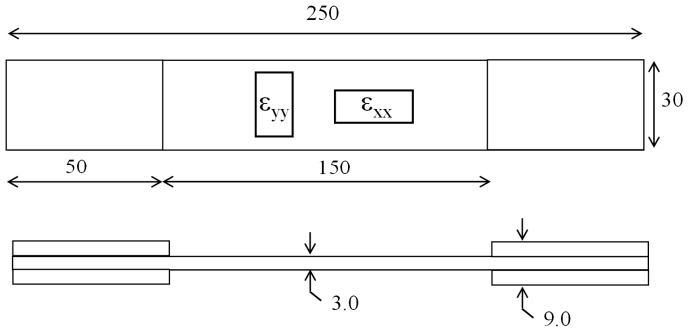

Figure 4-3 Dimensions of the used specimen for the measurement of Poisson's ratio for the UD glass fabric-reinforced epoxy.

For these first tests, both longitudinal strain ε_{xx} and transverse strain ε_{yy} were measured with strain gauges. Figure 4-4 illustrates the specimen IF6 mounted in the tensile machine before testing (a) and after failure (b).

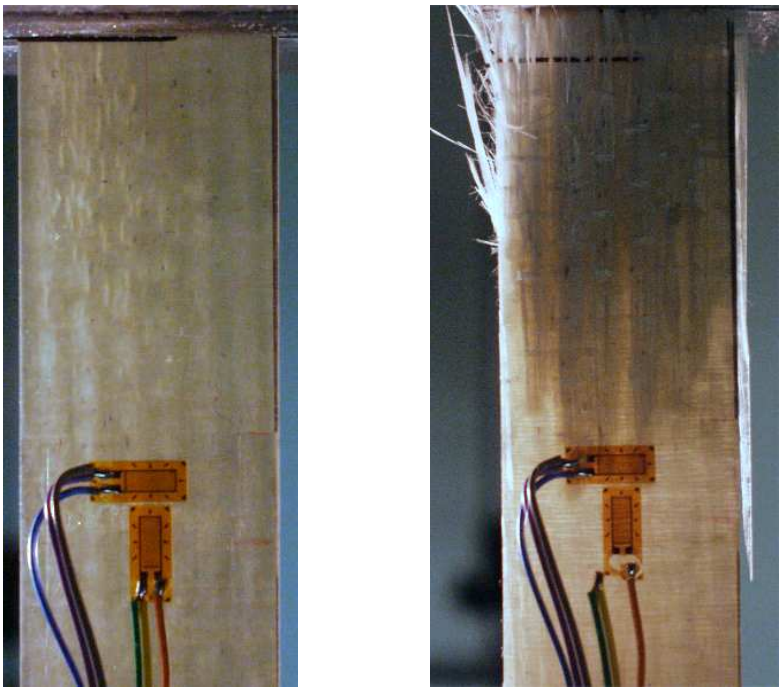

(a) Specimen before testing (b) Specimen after Failure

Figure 4-4 Images of the UD glass fabric-reinforced epoxy specimen, equipped with strain gauges.

First, two quasi-static tests are performed, to determine the Poisson's ratio of the $[0°/90°)]_{2s}$ stacking sequence.

Figure 4-5 shows the stress-strain evolution of two quasi-static tests. These curves are shown until the longitudinal strain gauge failed, which happened at ε_{xx} equal to 0.00987 for IF4 and equal to 0.0226 for IF6. Failure stresses were 446.7 MPa for IF4 and 465.5 MPa for IF6, which corresponds with the failure strain of 0.0226.

At a load level of about 100 MPa axial stress, there is a small change in slope of the stress-strain curve. The corresponding strain is slightly higher than 0.0025 which is the fracture strain of the 90º plies in the cross-ply laminate (see chapter 2).

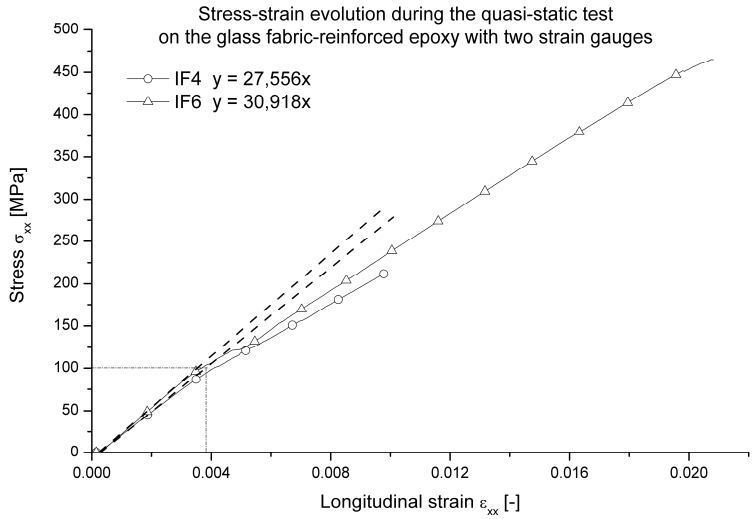

Figure 4-5 Stress as function of the strain for the quasi-static test with two strain gauges.

The evolution of Poisson's ratio as a function of the longitudinal strain ε_{xx} is depicted in Figure 4-6. An initial value of 0.15 can be derived. Furthermore, a significant decrease in Poisson's ratio can be seen, from 0.15 to 0.05 just before failure of IF6. Similar decreases were mentioned in [1-4].

Finally, a sudden drop can be seen in the evolution of Poisson's ratio around a longitudinal strain ε_{xx} of about 0.004, which corresponds with the knee-point in Figure 4-5 at about 100 MPa.

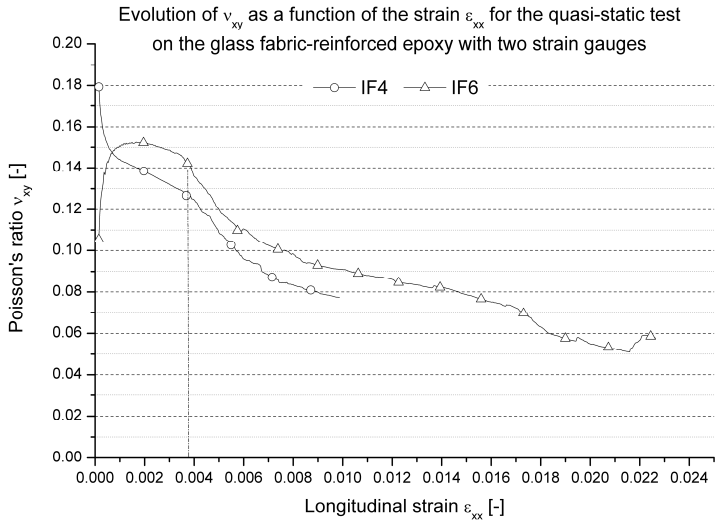

Figure 4-6 Poisson's ratio ν_{xy} as function of ε_{xx} for both measurements.

The decrease in the Poisson's ratio is usually explained by the occurring transverse cracking, causing elongation in the longitudinal direction. These transverse cracks originate from failure in the transverse plies, but the cracks remain open, causing the elongation, because of the release of thermal (or residual) stresses, resulting from the curing or production process [7-11].

Next, a quasi-static hysteresis test was performed. The test speed was 2 mm/min and the load cycles were between 1 kN and subsequent load levels of 20, 20, 25, 35, 35, 42, 45, 48 and 54.7 kN (failure load), as shown in Figure 4-7. The small change of the slope in the curve at 10 kN corresponds with a longitudinal stress σ_{xx} of 102.4 MPa. This knee-point could indeed be observed in the stress-strain curves in Figure 4-5.

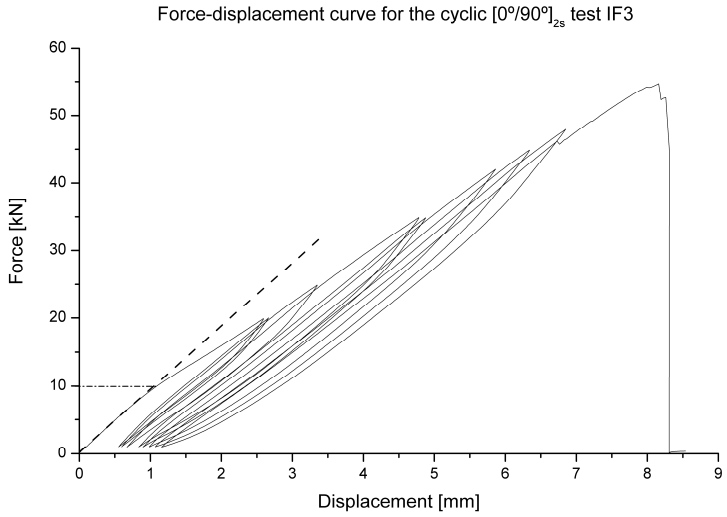

Figure 4-7 Force as a function of the displacement for the $[0°/90°]_{2s}$ specimen IF3.

Of course, our main interest lies in the evolution of the strains and the corresponding Poisson's ratio. The evolution of the longitudinal and transverse strain is shown in Figure 4-8. It can be remarked that the transverse strain ε_{yy} becomes slightly positive after each unloading, which would result in a negative Poisson's ratio.

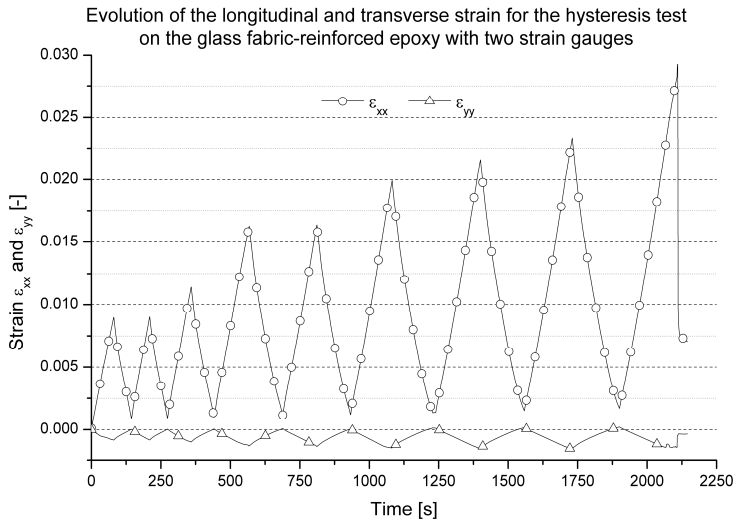

Figure 4-8 Evolution of ε_{xx} and ε_{yy} as a function of time for the hysteresis test on IF3.

Indeed, as depicted in Figure 4-9, the Poisson's ratio becomes negative after unloading. For illustration purposes, the quasi-static test IF6, where both strain gauges measured till failure of the specimen, is also depicted. It can be noted that this quasi-static curve forms an envelope of the cyclic curve. Furthermore, the value of ν_{xy} at maximum load of each cycle decreases with the number of cycles, as has been reported in [1-4].

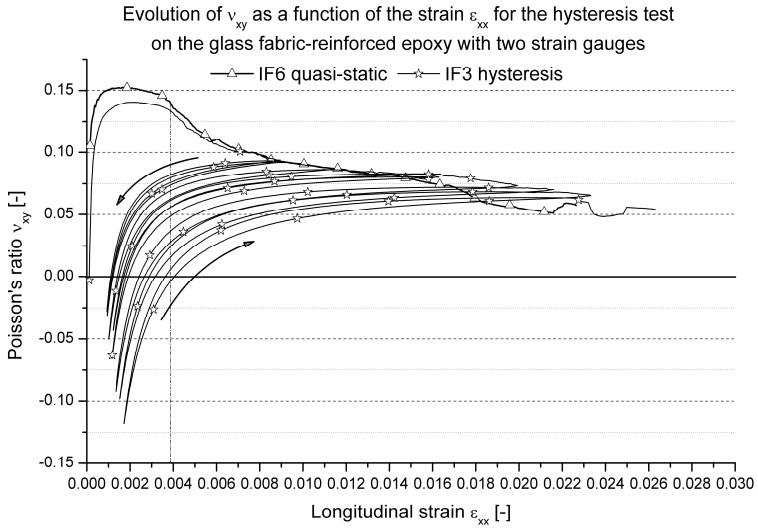

Figure 4-9 The evolution of Poisson's ratio as function of the longitudinal strain for both a quasi-static and the cyclic experiments.

Of course, the very peculiar evolution of Poisson's ratio cannot be neglected. After a certain longitudinal strain, which lies approximately around the previously mentioned knee-point for the first few loading cycles, the Poisson's ratio drastically decreases. For the later loading cycles, the drop occurs earlier and earlier in the unloading (meaning at higher strain levels). It should also be noted that the unloading curve always lies higher than the next loading curve.
However, in all mentioned articles, [1-4] this behaviour was not mentioned. In fact, to the author's best knowledge, this has never been reported in open literature. As such, no real explanation can be found in open literature for this peculiar shape of the curve.
When modelling the evolution of the Poisson's ratio, it is always plotted as a function of (transverse) crack density [1-4]. Of course, for fibre-reinforced epoxies, this approach may work just fine, for instance for the material considered here, the evolution of cracks can be easily visualised, even without the need for penetrant enhanced radiography, as could be seen in Figure 4-4. However, if the Poisson's ratio is to be used to monitor and model damage during fatigue experiments, it would seem more convenient to model this behaviour as function of the occurring stress or strain state.

4. 3. 2. b. Carbon fabric-reinforced PPS

In the previous paragraph, the existence of thermal or residual stresses was already mentioned. For the carbon fabric-reinforced polyphenylene sulphide, these stresses will be even higher, because of the following factors: (i) the reinforcement is carbon, which has a negative thermal expansion coefficient in the fibre direction and therefore is more likely to shrink on the elevated temperature during hot pressing; (ii) the polyphenylene sulphide is a semi-crystalline polymer.
The difference in thermal stresses between the amorphous and the semi-crystalline matrices is due to the following: the amorphous matrix is in a visco-elastic state between the processing temperature and the glass transition temperature (T_G), meaning that possible stress build-up due to thermal shrinkage can still be relaxed. Once T_G is reached, the amorphous polymer becomes glassy (thermo-elastic state) and residual stresses are formed.
For the semi-crystalline matrix, the stress build-up can only be relaxed until the crystallisation temperature, since then crystals are formed, which can carry load. As such, it is more difficult to relax the stress build-up. The residual thermal stresses are the consequence of a larger temperature difference, since the crystallisation temperature is higher than the glass transition temperature and therefore, the stresses are a lot higher. In fact, they are known to cause micro-cracking simply by cooling the plate to room temperature [5, 9].

However, the reinforcement here is a balanced fabric, compared to the unidirectional fabric-reinforcement previously considered. For the first, the strengths in warp and weft direction are very much alike (see chapter 3), which is certainly not the case for the UD reinforcement. For the latter, a significant drop was visible for stresses in the range of the failure stress of the transverse plies (the 'knee-point'). As such, it is uncertain whether the higher residual stresses will increase the decrease in Poisson's ratio, since it is counteracted by the absence of a 'knee-point'.

The first experiments were also done with an increasing maximum load level for each cycle. The specimen's geometry is depicted in Figure 4-10 and the experiments were done displacement-controlled with a speed of 2 mm/min.

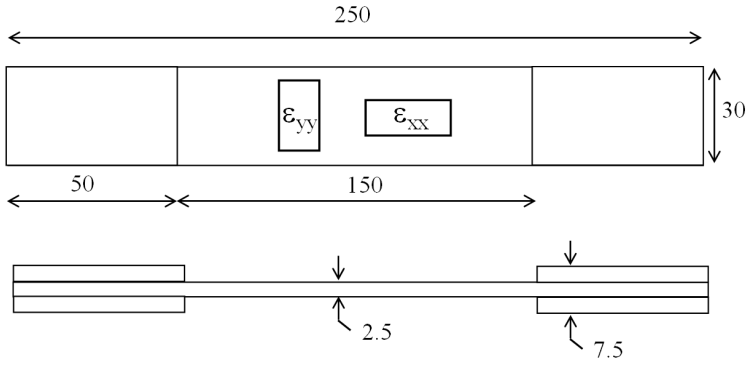

Figure 4-10 Dimensions of the used specimen for the measurement of Poisson's ratio for the carbon fabric-reinforced PPS.

Various experiments were done, all with similar results, so only a few are illustrated here. Figure 4-11 shows the stress-strain evolution for three specimens H8, H13 and H15. For a clear image, the different curves are given a longitudinal strain offset of 0.003.

For specimen H13, 14 cycles were done and the specimen failed during the fourteenth cycle at 730 MPa. Specimen H8 endured 15 cycles and failed during the last cycle at 741 MPa and Specimen H15 lasted 13 cycles, the cycle of 650 MPa was omitted, and failed at 760 MPa. Again, there is no stiffness degradation and only very limited permanent deformation, which corresponds with the previous results. It should be noted that the derived stiffness corresponds well with the values obtained in chapter 3.

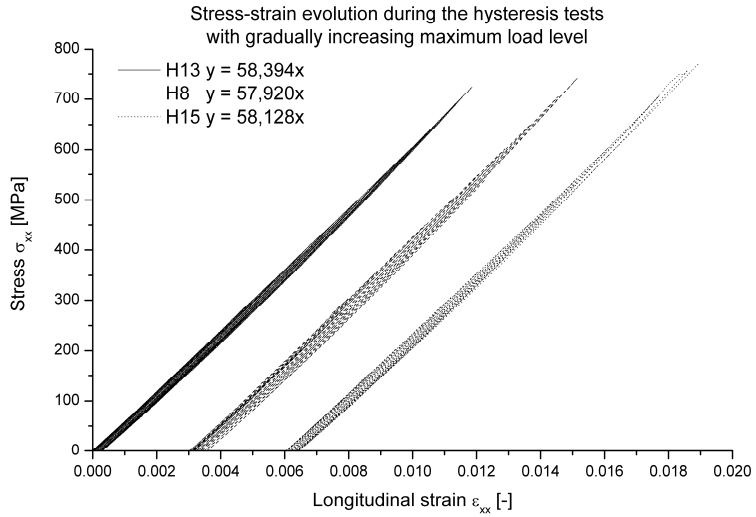

Figure 4-11 Stress as function of the strain for the quasi-static hysteresis test with increasing load level.

The longitudinal and transverse strain for the test on specimen H15 are shown in Figure 4-12; similar results were found for all other experiments.

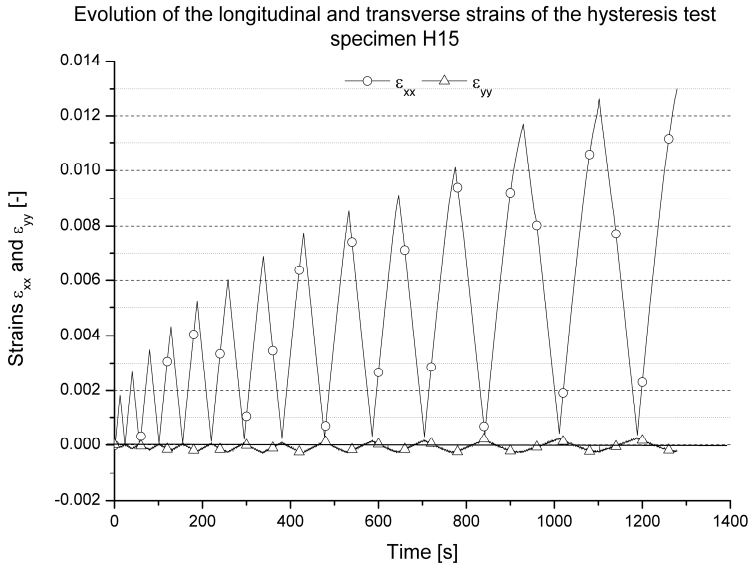

Figure 4-12 Evolution of ε_{xx} and ε_{yy} as a function of time for the hysteresis test on H15.

It should be noted that, similar to the hysteresis experiment on the UD glass-epoxy material, the transverse strain ε_{yy} becomes positive after unloading, which would result again in a negative value of the Poisson's ratio.

This can be verified in Figure 4-13, where the evolution of Poisson's ratio is depicted for the same specimen.

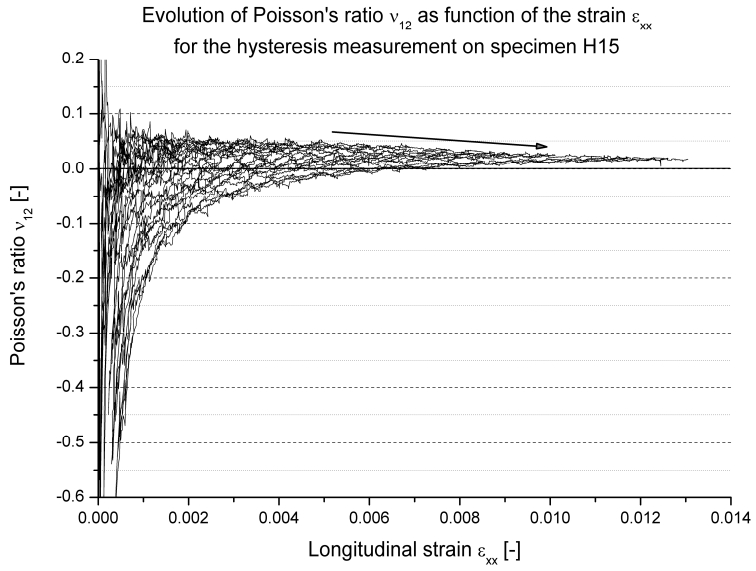

Figure 4-13 The evolution of Poisson's ratio as function of the longitudinal strain.

Again, the typical diving of the Poisson's ratio, meaning the large decrease upon unloading, cannot be missed, although the initial value is a lot lower than for the UD glass-epoxy. However, the difference between the loading and the unloading curve is a lot less for this material than for the UD glass fabric-reinforced epoxy, where the loading curve was always clearly below the unloading curve. Furthermore, the value of the Poisson's ratio at maximum load decreases, as illustrated by the arrow. An initial value of about 0.05 is found, which corresponds well with the previously derived values and at failure, the Poisson's ratio has decreased to 0.02. Therefore, this is a promising parameter for monitoring damage.

In order to assess whether this behaviour is due to the use of strain gauges, a few tests were conducted where prior to the hysteresis loadings, starting from 100 MPa with increasing maximum load level, four cycles to 100 MPa were performed. This value should be low enough not to induce any damage in the material, so if the effect is the result of the strain gauges, it should be visible. Again, various experiments were performed, all with similar results, so only one is depicted. The evolution of the Poisson's ratio as function of the longitudinal strain for such an experiment (specimen H13) is shown in Figure 4-14. Of course, there is some scatter on the Poisson's ratio for very small strains, but once the signal is stabilized, the diving effect does not occur and for the four cycles, the value of the Poisson's ratio does remain constant at a value of about 0.05, which corresponds with the previously derived values.

This constant value also confirms that the maximum stress level of 100 MPa is low enough not to induce damage.

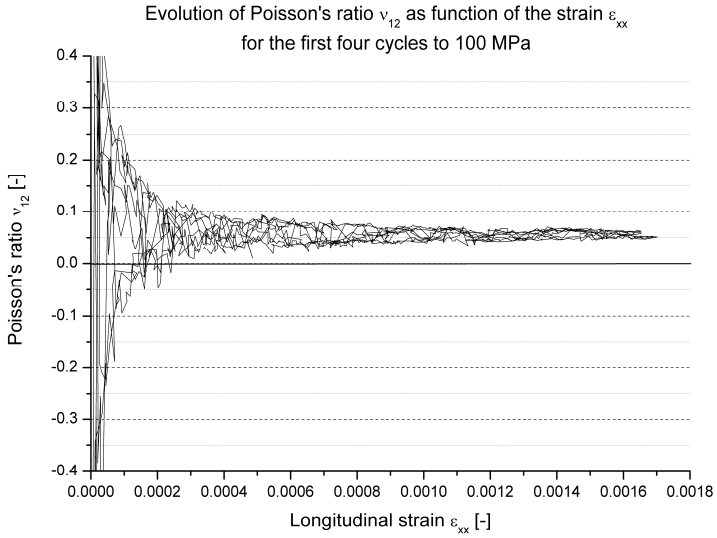

Figure 4-14 The evolution of Poisson's ratio as function of the longitudinal strain for the first four cycles to 100 MPa.

For this specimen, Figure 4-15 shows the evolution of the Poisson's ratio for the successive hysteresis test with increasing maximum load and again, the typical behaviour is present.

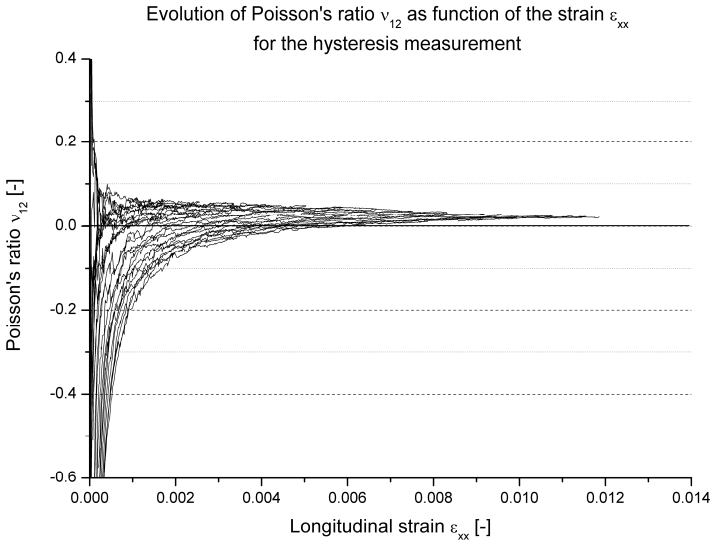

Figure 4-15 The evolution of Poisson's ratio as function of the longitudinal strain for the 14 hysteresis loops with increasing maximum load.

Another possible cause of the 'diving' effect may be the testing speed. All previous test, including the ones on the UD glass fabric-reinforced epoxy were done with a displacement speed of 2 mm/min. To rule out any possible visco-elastic effects of the matrix, the next experiment was done at 0.1 mm/min. Furthermore, two transverse strain gauges were used, one on each side of the specimen, to rule out the effects of torsion or buckling due to misalignment of the clamps. Because of the low testing speed, only three cycles till 100 MPa were done, after which the maximum load of each cycle was increased with 100 MPa. This resulted in five cycles and a maximum stress of 600 MPa, because then the tabs started to de-bond.
The evolution of the strains for the first three cycles is shown in Figure 4-16. There is a very good correspondence between both transverse strain gauges, meaning no buckling or torsion due to misalignment of the clamps is present. Furthermore, the transverse strain does not become positive.

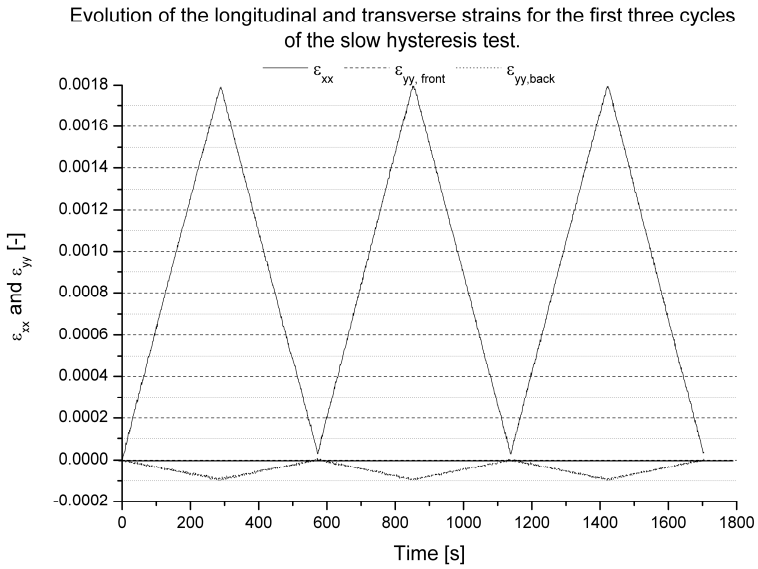

Figure 4-16 Evolution of ε_{xx} and ε_{yy} as a function of time for the first cycles of the slow hysteresis test.

The corresponding evolutions of the Poisson's ratio, for both transverse strain gauges, are shown in Figure 4-17. Apart from the scatter, due to the very low strain levels, no diving is present; an initial value of 0.05 is found, in accordance with the previously determined values.

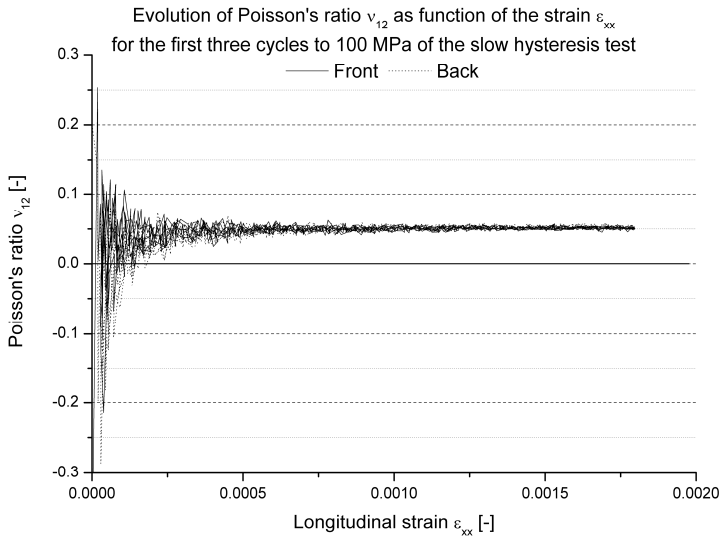

Figure 4-17 The evolution of Poisson's ratio as function of the longitudinal strain for the first three cycles to 100 MPa.

The evolution of the strains for the cycles with increasing maximum load is depicted in Figure 4-18. Again, there is a very good correspondence between the two transverse strain gauges, except for the last cycle. This may be explained by the de-bonding of the tabs, which also causes the nonlinear behaviour of the longitudinal strain ε_{xx} for the last cycle.

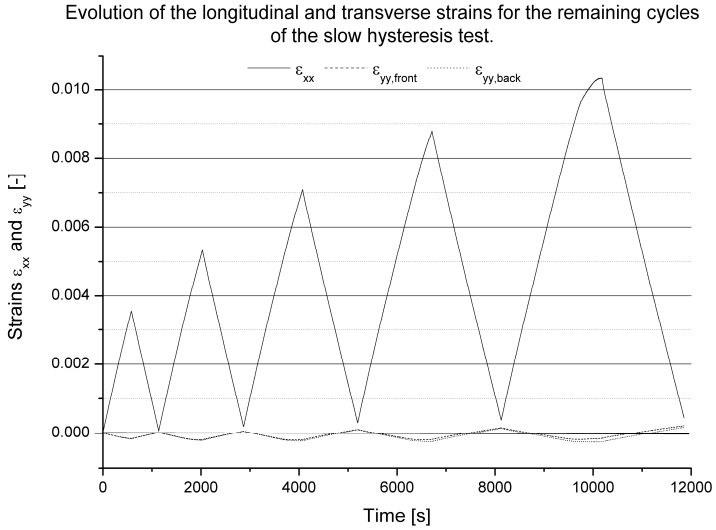

Figure 4-18 Evolution of ε_{xx} and ε_{yy} as a function of time for the remaining cycles of the slow hysteresis test.

Despite the slow displacement speed, the transverse strain still becomes positive for both strain gauges, which would mean that the typical diving also occurs for this testing speed. This can be verified from Figure 4-19, which shows the evolution of the Poisson's ratio for both the transverse strain gauges. It should be noted that both curves correspond well, except for the last cycle, because of the de-bonding of the tabs.

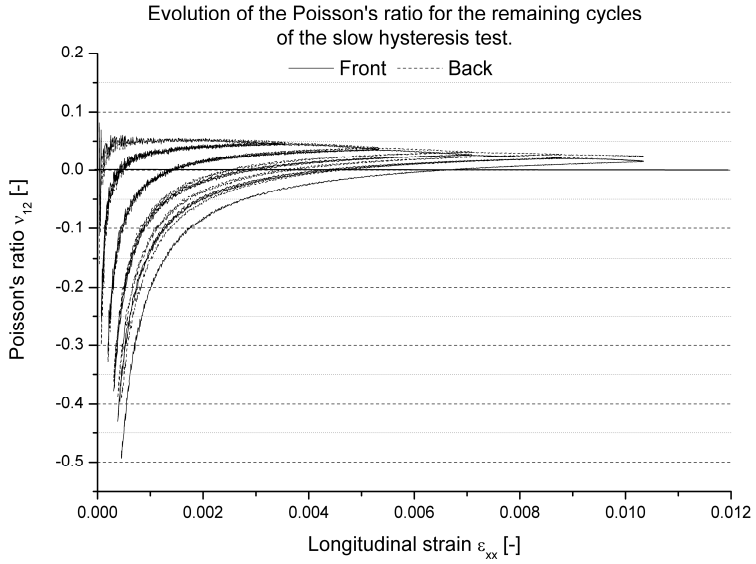

Figure 4-19 The evolution of Poisson's ratio as function of the longitudinal strain for the remaining cycles.

Finally, a number of experiments were performed with a constant maximum load, not so much to find an explanation for the diving effect of the Poisson's ratio, but to assess the behaviour of the Poisson's ratio under these loading conditions, which are more closely related to the fatigue loading conditions with constant stress amplitude, discussed in the next chapter.

Since the displacement speed did not seem to have a significant effect, all experiments were done at 2 mm/min. Various experiments were performed, again all yielding similar results, so only a few are shown here. Figure 4-20 shows the stress-strain relationship of two of such tests. For both, again four cycles till 100 MPa were done to assess the behaviour of the Poisson's ratio at low stress levels, but similar results as in Figure 4-14 and Figure 4-17 were obtained, so these results are not shown here. Then, ten cycles were imposed on each specimen, after which the specimen was tested till failure. Specimen F15 endured ten cycles with a maximum load of 550 MPa and failed at 640 MPa and specimen H7 was tested at a maximum load of 600 MPa and failed at 770 MPa. Both curves are given an offset in longitudinal strain of 0.003 for a clear image.

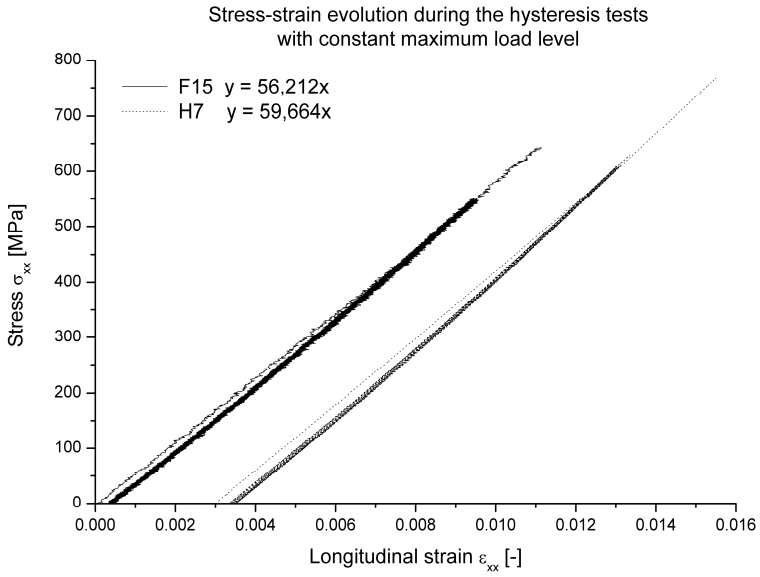

Figure 4-20 Stress as function of the strain for the quasi-static hysteresis with constant load level.

Similar evolutions as in paragraph 4. 2 are found. No stiffness degradation occurs and only limited permanent deformation is present. This permanent deformation is formed mainly during the first cycle. The evolution of the Poisson's ratio is shown in Figure 4-21 for specimen F15 and in Figure 4-22 for specimen H7.

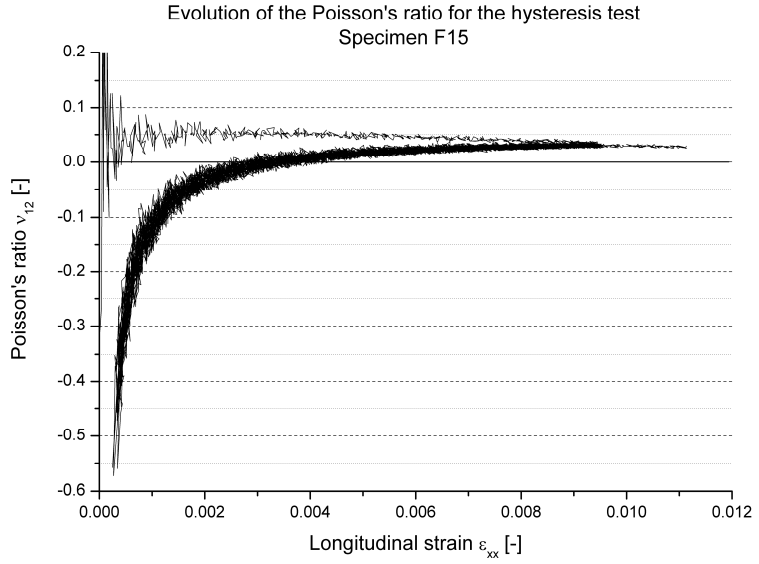

Figure 4-21 The evolution of Poisson's ratio as function of the longitudinal strain.

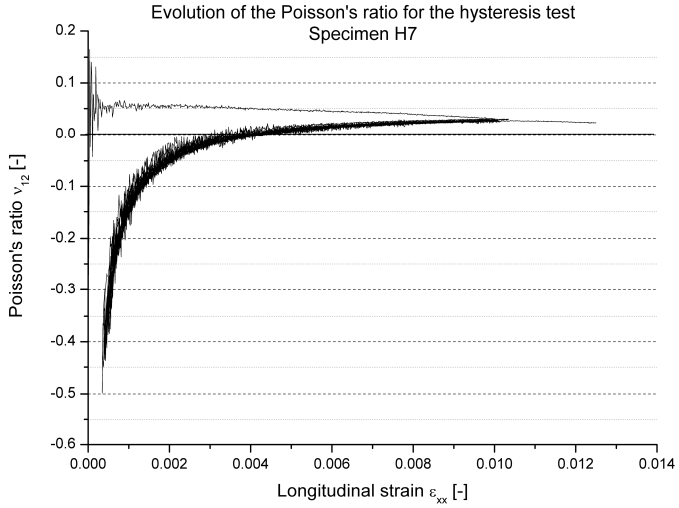

Figure 4-22 The evolution of Poisson's ratio as function of the longitudinal strain.

The difference between these results and the results from the hysteresis tests with gradually increasing maximum load cannot be missed. For the latter, a gradual increase in Poisson's ratio could clearly be seen, whereas here, the curves for the different loading cycles overlap. This is even more the case for higher load levels (specimen F7). It appears that all changes to which the Poisson's ratio is sensitive, happen during the first loading, similar to the permanent deformation. Only a very slight decrease can be seen if the evolution of the Poisson's ratio is plotted against time. These evolutions are shown in Figure 4-23 for specimen F15 and in Figure 4-24 for specimen H7.

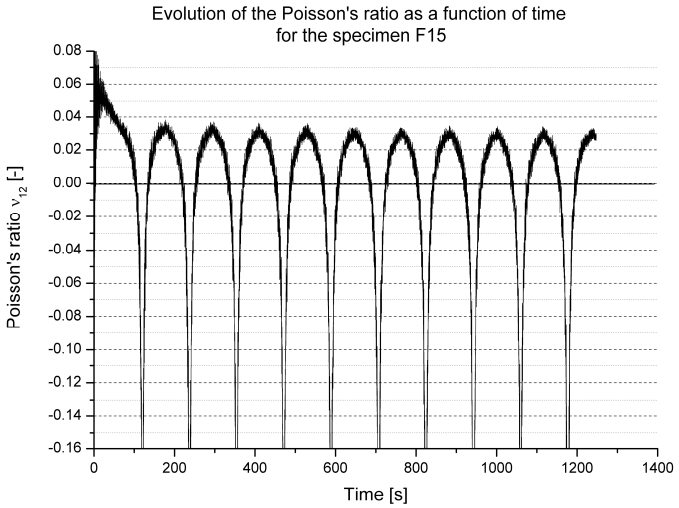

Figure 4-23 The evolution of Poisson's ratio as function of time.

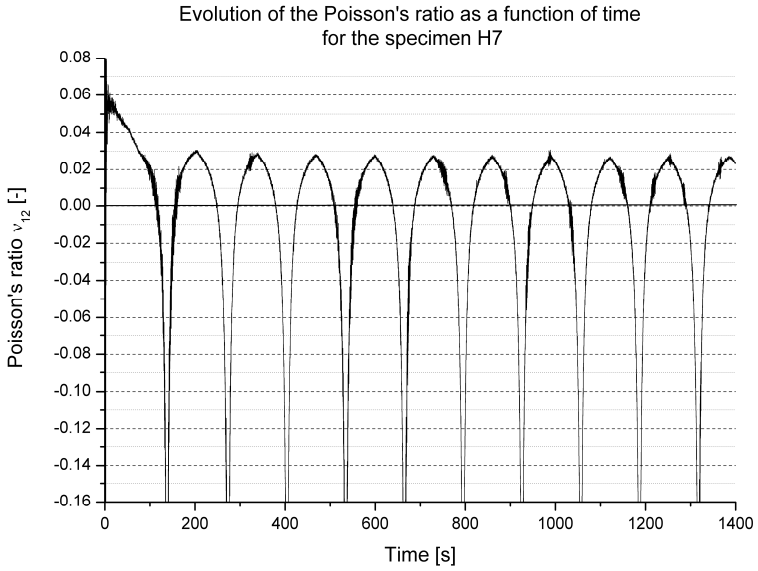

Figure 4-24 The evolution of Poisson's ratio as function of time.

Before attempting to find an explanation for this behaviour, first it is assessed whether this behaviour does not come from the used sensor to measure the transverse strain. Therefore, in the next paragraph, the transverse strain is measured using an externally bonded optical fibre.

4. 3. 3. Transverse external optical fibre

4. 3. 3. a. Unidirectional glass fabric-reinforced epoxy

In the previous paragraph, it was investigated whether the typical shape of the ν_{xy} - ε_{xx} curve was due to the displacement speed or to a possible misalignment of the grips, with negative result. However, this shape may also result from the used sensor, being a strain gauge. Therefore, a similar experiment was performed, but with a transverse optical fibre bonded to the surface of the specimen. For comparison purposes, a transverse train gauge was also used for the transverse strain measurement. The instrumentation is illustrated in Figure 4-25. It should be noted that a different adhesive is used than mentioned in chapter 3. Normally, the longitudinal optical fibres are bonded with Z70, an adhesive used for bonding strain gauges. However, the behaviour the Poisson's ratio may also be caused by the adhesive. Therefore, the optical fibre is bonded here with a two-component epoxy, which is a different type of adhesive than the cyanide-acrylate adhesive used for bonding the strain gauge.

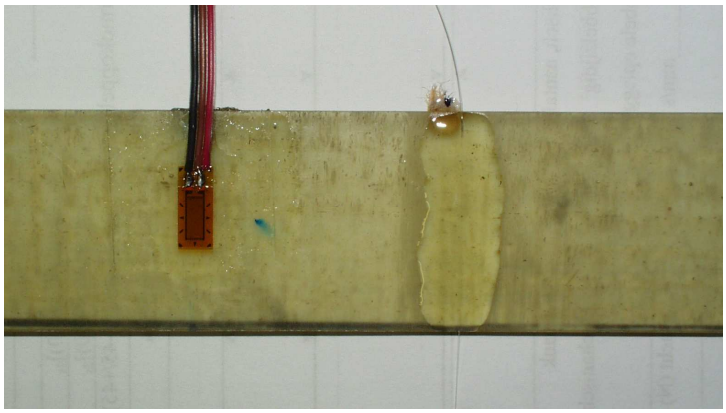

Figure 4-25 Illustration of the external optical fibre and strain gauge for the transverse strain measurement.

For this measurement, the FBG-scan interrogator was used, meaning that the quasi-static tests were performed with block loading in load control, as explained in chapter 3. For the load levels between 0 MPa and the maximum value of the cycle, different levels were chosen for loading and unloading, so that the measurements would not coincide on the graphs and different strain levels were measured.

For the hysteresis test, first four cycles till 50 MPa were done to verify (i) if the optical fibre measured accurately, since the values of the strain are quite low and (ii) if the peculiar 'diving' of the Poisson's ratio occurs for such low strain levels. The evolution of the strain for these loading cycles is illustrated in Figure 4-26. It can be seen that the signals from both sensors correspond very well.

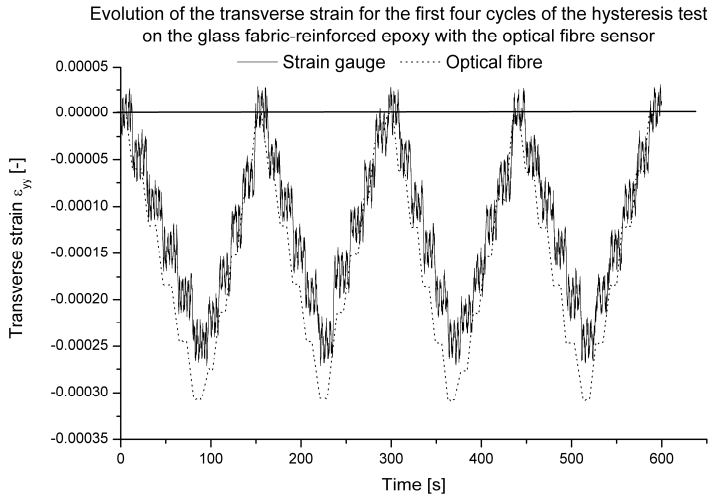

Figure 4-26 Evolution of ε_{yy} for both the optical fibre and strain gauge measurement, as a function of time for the first four cycles.

The corresponding evolution of the Poisson's ratio is depicted in Figure 4-27, where only the strain gauge measurement is illustrated. The optical fibre is sampled on a different time basis than the longitudinal strain, since a different data acquisition system is used and therefore, it is difficult to calculate the Poisson's ratio. This however, does not pose a problem, since our main interest lies in the shape of the evolution and since there is very good agreement between the transverse strains obtained with both sensors, the Poisson's ratio will also be alike.
It can be noted that for these low stress (and strain) levels, the typical diving does not occur. Moreover, a value for the Poisson's ratio of 0.165 is found, which corresponds well with the previously derived values. Again there is some scatter for the low strain levels, but this disappears for longitudinal strains higher than 0.0002, which is about five times lower than the strain at which the diving occurs for this material (see Figure 4-9, diving till $\varepsilon_{xx} = 0.001$).

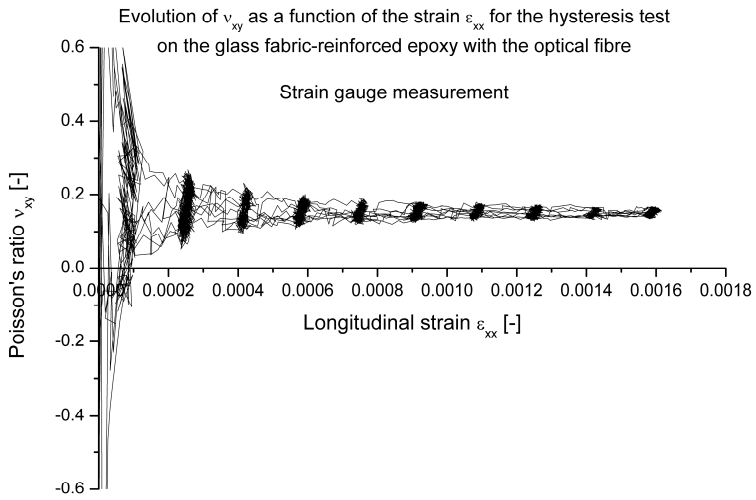

Figure 4-27 The evolution of Poisson's ratio as function of the longitudinal strain for the strain gauge measurements for the first four loading cycles till 50 MPa.

Next, the maximum load of each loading was increased with 50 MPa until 350 MPa was reached, after which the experiment was stopped. Figure 4-28 illustrates the evolution of the strain as function of time. Again, there is a good correspondence between the strain gauge and the optical fibre, although the optical fibre tends to give strain values which are lower. The latter can be explained by the fact that the layer of adhesive is quite thick (see Figure 4-25) resulting in a complicated load transfer. Besides the desired axial load, transferred from the specimen, the fibre will also endure transverse loads, causing extra shifts in the wavelength. For higher load levels, they even induce peak-splitting, which corresponds with the interruption in the optical fibre curve in Figure 4-28.

The latter is also the reason why the experiment was stopped after 350 MPa. However, in the unloaded state, these transverse effects will be a lot less dominant, and then it can be seen that the transverse strain becomes positive, causing the sub zero decrease of the Poisson's ratio.

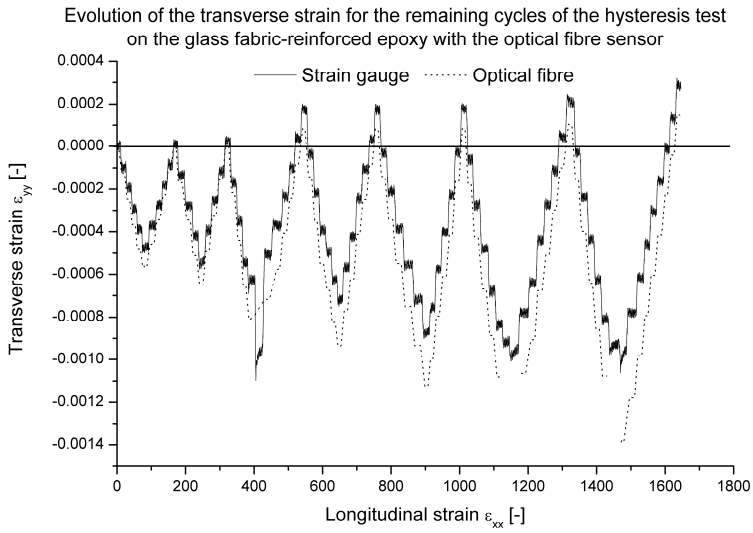

Figure 4-28 Evolution of ε_{yy} for both the optical fibre as strain gauge measurement, as a function of time.

Finally, the evolution of the Poisson's ratio as a function of the longitudinal strain is depicted in Figure 4-29 for the strain gauge measurement.

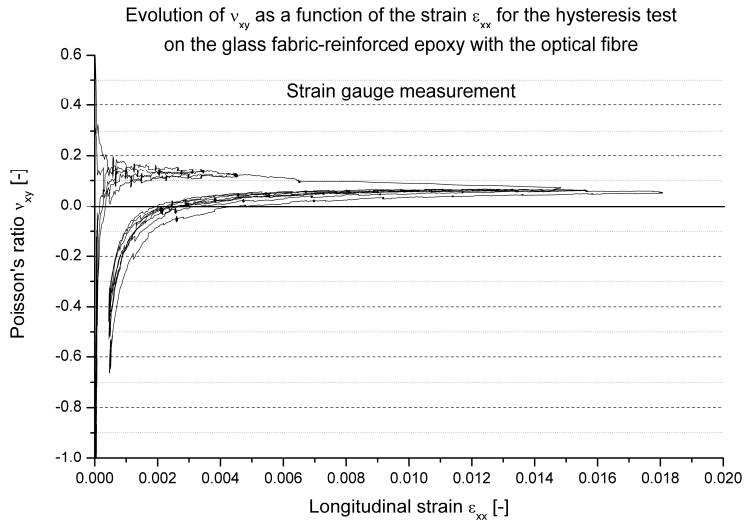

Figure 4-29 The evolution of Poisson's ratio as function of the longitudinal strain for the strain gauge measurement.

As expected, the typical behaviour occurs. The sudden drop after the stress of 100 MPa, corresponding with failure in the transverse plies is less visible here, but this may be due to the fact that the experiment was done with stepwise loadings, rather than a continuous and constant displacement speed.
Finally, Figure 4-30 shows the specimen after the test was stopped. The transverse cracks, which cause the decrease in Poisson's ratio can clearly be distinguished.

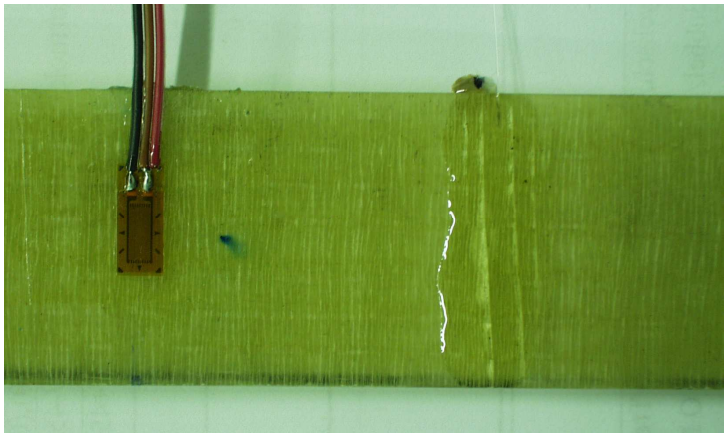

Figure 4-30 Illustration of the transverse cracks after the experiment was stopped.

4. 3. 3. b. Carbon fabric-reinforced PPS

Of course it could already be expected that using a transverse optical fibre will also yield the typical behaviour of the Poisson's ratio. However, this sensor is still considered here, since now it can be assessed whether it is capable of measuring the small transverse strains under the quasi-static cyclic loading conditions.
Various experiments were performed, yielding similar results, so again, only one is illustrated here. For this test, the optical fibre was bonded using the Z70 adhesive, as described in chapter 3 and the optical data acquisition system was the FBG-scan interrogator, as was the case in the previous paragraph. This means that the experiment was done load-controlled with stepwise loadings. First, three loading cycles till 100 MPa were performed and then the maximum stress was gradually increased with 50 MPa for each cycle.
Figure 4-31 illustrates the evolution of the transverse strain, measured with both the strain gauge and the optical fibre sensor. It can be seen that the correspondence is very good.

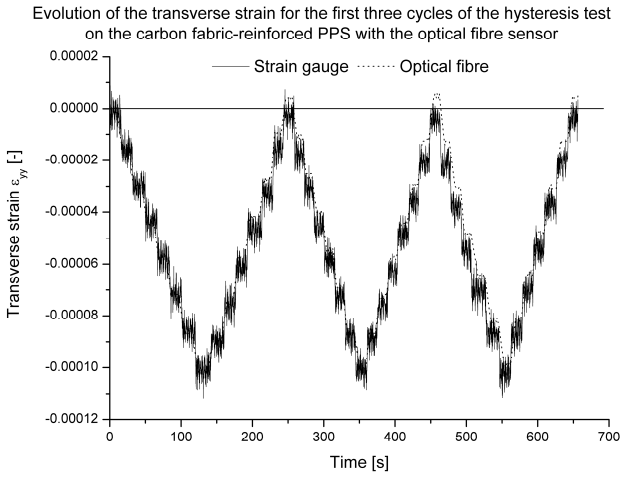

Figure 4-31 Evolution of ε_{yy} for both the optical fibre as strain gauge measurement, as a function of time for the first three cycles.

The corresponding evolution of the Poisson's ratio as function of the longitudinal strain is illustrated in Figure 4-32, where only the strain gauge measurement is illustrated. Again, because of the different data acquisition systems, the signals from longitudinal strain and optical fibre are sampled on different time bases and it is difficult to calculate the Poisson's ratio from the optical fibre measurement. However, because of the good correspondence of the transverse strains, the correspondence in Poisson's ratio will also be good.
An initial value of 0.06 is found, which is in good agreement with the previously derived values.

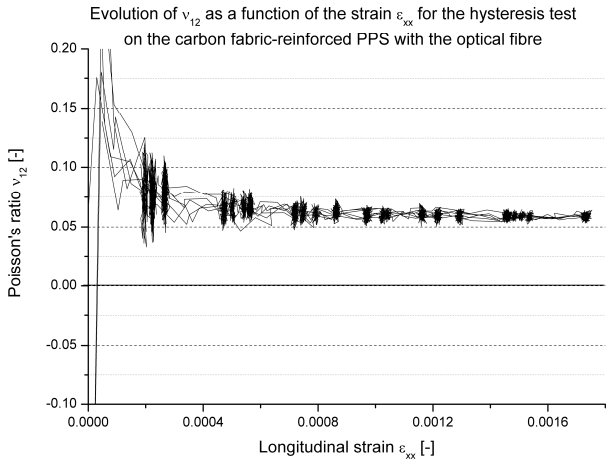

Figure 4-32 The evolution of Poisson's ratio as function of the longitudinal strain for the strain gauge measurements for the first four loading cycles till 100 MPa.

While performing the cyclic loading with increasing maximum stress level, it was noted that for the higher strain levels, the optical fibre measurement started to peak. This is illustrated in Figure 4-33, which illustrates the transverse strains for the cycles from 150 MPa till 250 MPa. It should be noted that despite this 'peaking' the correspondence still is very good.

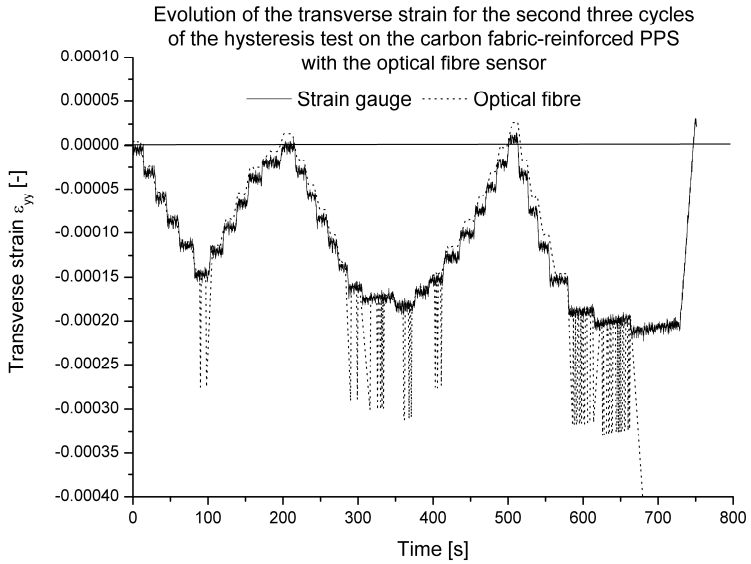

Figure 4-33 Evolution of ε_{yy} for both the optical fibre as strain gauge measurement, as a function of time for the second three cycles.

The 'peaking' effect is due to the occurrence of multiple peaks in the reflected spectrum, which is caused by inhomogenous straining of the grating, as explained in chapter 3 for the embedded fibres. If the bond between the fibre and the specimen's surface is not perfect, as is the case here, then this will result in a varying strain field, causing 'peak-splitting'. This was experimentally verified for this specimen and is shown in Figure 4-34. The specimen was loaded till a certain stress level and a screenshot of the entire spectrum was taken. For the lower stress levels, only one peak was seen, but for higher stress levels, multiple peaks occurred.
The peak used for the strain measurement in Figure 4-33 is the one to the right in Figure 4-34. Since it is shifted to the right, this explains the sudden 'increase' in strain in Figure 4-33.

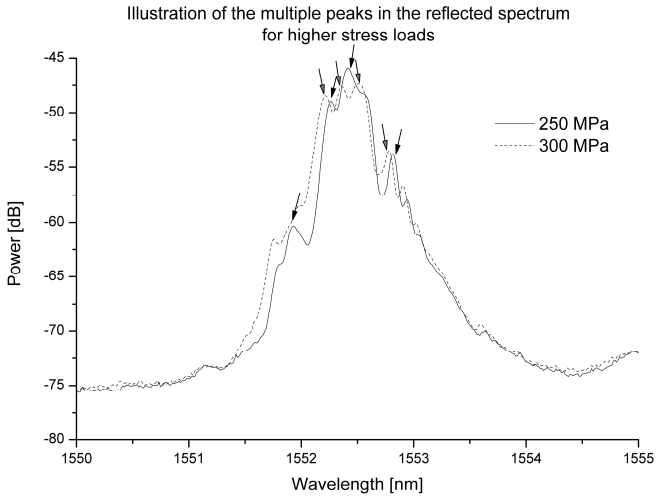

Figure 4-34 Reflected spectra of the externally bonded optical fibre for higher stress levels.

However, the purpose of this test was mainly to verify if the transverse strain becomes positive after cyclic loadings and since the 'peak-splitting' does not occur for low stress levels, the experiment was continued and the optical fibre was only read when the stress was equal to zero. The resulting evolution of the transverse strains for the remaining cycles from 250 MPa to 600 MPa is depicted in Figure 4-35. Considering the fact that the measured strains are very low, there is a good agreement between the strain gauge and the optical fibre in the unloaded condition.

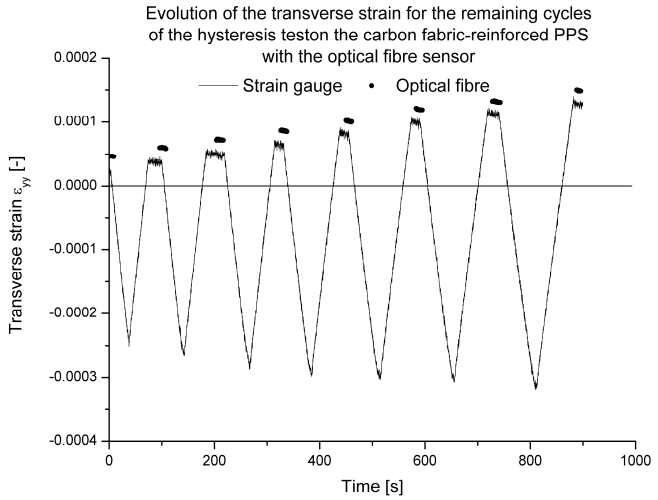

Figure 4-35 Evolution of ε_{yy} for both the optical fibre as strain gauge measurement, as a function of time for the remaining cycles.

Finally, Figure 4-36 shows the evolution of the Poisson's ratio as function of the longitudinal strain for the strain gauge measurement. As could be expected, again the peculiar behaviour is visible.

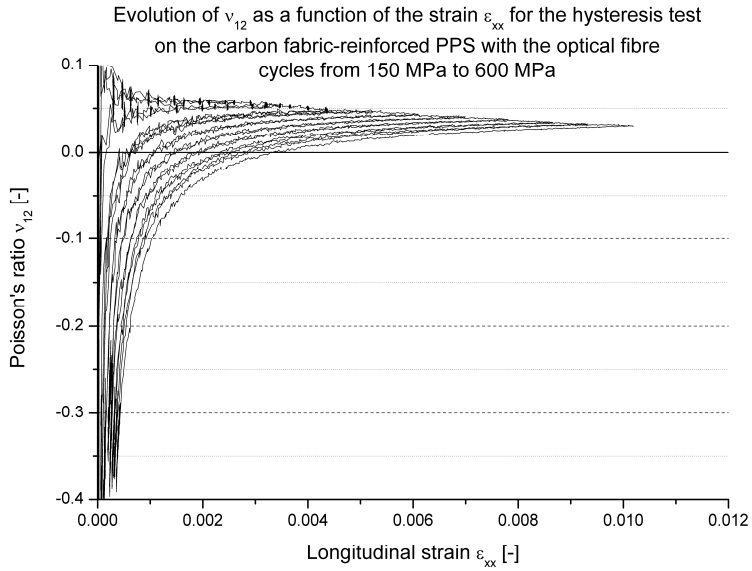

Figure 4-36 The evolution of Poisson's ratio as function of the longitudinal strain for the strain gauge measurements for the loading cycles between 150 MPa and 600 MPa.

An important remark must be made. The occurrence of multiple peaks in the spectrum for higher stress levels does not render this method useless for measuring the longitudinal strain under fatigue loading conditions, but it emphasises that the preparation of the specimen and the bonding of the fibre needs to be done extremely carefully, if the measurement is to be a success.

4. 3. 4. Transverse extensometer

The two previously used sensors have one thing in common. They are both bonded to the surface, using an adhesive. Of course, the origin of this peculiar evolution of the Poisson's ratio may be due to the adhesive. Therefore, the standard extensometer was adjusted, so it can measure the transverse strain. This of course requires some adjustments for the extensometer, which are discussed next.

4. 3. 4. a. Modifications to the existing extensometer

Two U-shaped pieces are used to mount the extensometer around the specimen. Two pointy bolts are used to press the extensometer blades against the specimen. Since preliminary tests yielded that the standard blades, which make a line contact, tend to slide, two new blades were made which each make contact with the surface on two discrete points, similar to the three-point blades described in the previous chapter for the longitudinal strain measurements. These modifications can be seen in Figure 4-37.

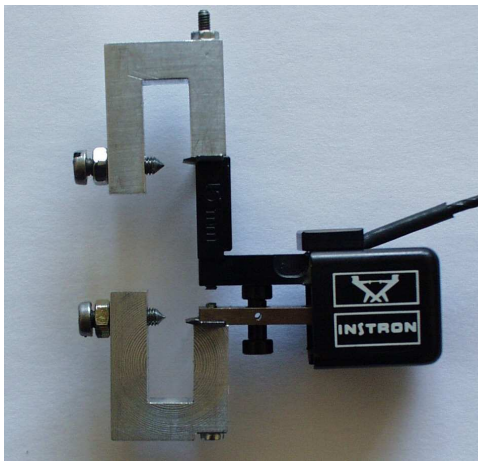

Figure 4-37 The standard INSTRON extensometer, modified to measure transverse strain.

4. 3. 4. b. Unidirectional glass fabric-reinforced epoxy

Figure 4-38 illustrates how the extensometer is mounted on a specimen. Also, the two extra strain gauges can be seen. Indeed, the transverse strain gauge is to verify whether the transverse strains correspond and the longitudinal strain gauge is necessary to measure the longitudinal strain, so that Poisson's ratio can be calculated.

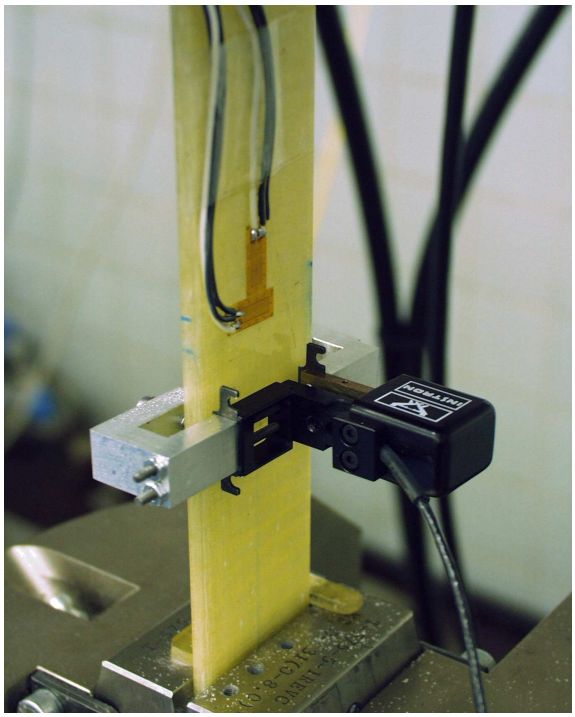

Figure 4-38 The transverse extensometer, mounted on a glass-epoxy specimen.

Then, a hysteresis test was performed and similar to the previous experiment, first four loadings until 100 MPa were done, to verify if the 'diving' of Poisson's ratio occurs. The value of 100 MPa corresponds with the previously mentioned 'knee-point' in the curve, corresponding with failure in the transverse plies. Next, the maximum load of each loading was increased with 50 MPa until 450 MPa was reached, after which the experiment was stopped. The specimen was not loaded till failure since the fracture of the specimen might damage the extensometer.
Figure 4-39 shows the evolution of the stress as a function of the longitudinal strain, measured with the strain gauge for all performed cycles; a stiffness of 25.06 GPa was found. Again, the knee-point, corresponding with failure in the transverse plies, can be seen.

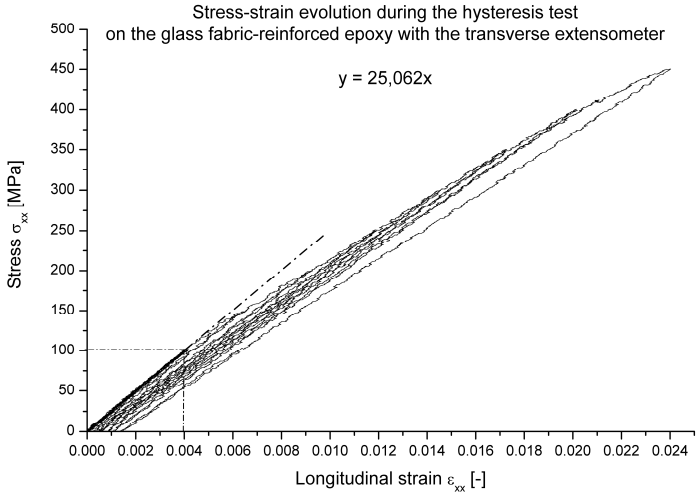

Figure 4-39 Stress as function of the strain for the hysteresis test with the transverse extensometer.

The evolution of the transverse strain, measured with both the transverse extensometer and the strain gauge is given in Figure 4-40 for all cycles. It can be noted that, despite a small difference, both signals correspond very well and more important, even for the extensometer signal, the strain becomes positive after a few cycles. This proves that the typical behaviour of Poisson's ratio is due to the material, rather than to the adhesive, since no adhesive is present when using the extensometer.

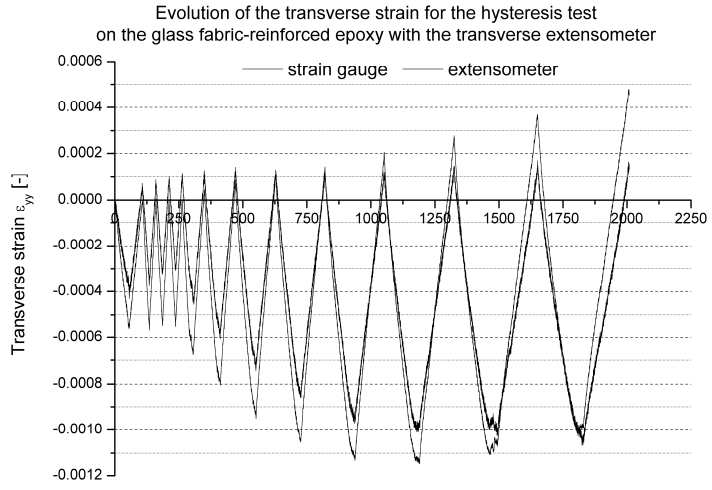

Figure 4-40 Evolution of ε_{yy} for both the extensometer as strain gauge measurement, as a function of time.

The results of the first four loading cycles till 100 MPa are depicted in Figure 4-41. The Poisson's ratio found with the strain gauge is equal to 0.15 and corresponds very well with the previously found values; the value derived from the extensometer measurement is slightly lower, around 0.1. This could be expected from the evolution of the transverse strains, illustrated in Figure 4-40. It should be noted for both measurements, that the significant dip, corresponding with failure of the transverse plies does not occur, so the choice of 100 MPa was not too high.

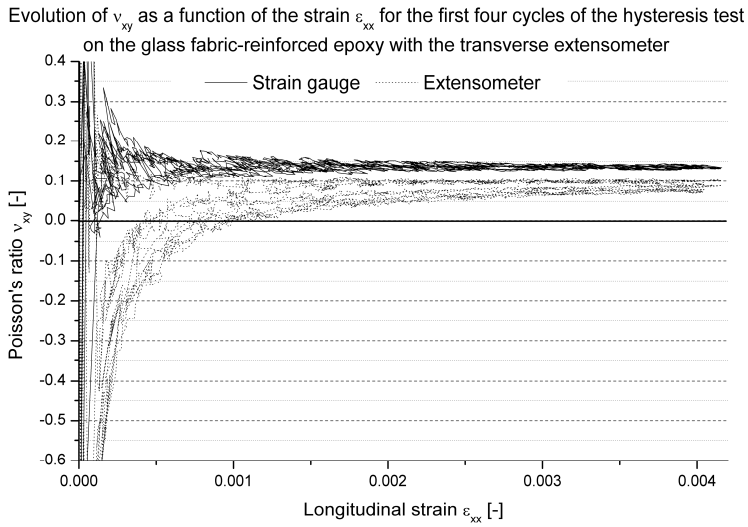

Figure 4-41 The evolution of Poisson's ratio as function of the longitudinal strain for both measurements for the first four loading cycles till 100 MPa.

Furthermore, it can be seen that the typical diving is not present for the strain gauge measurement but on the other hand, it is unexpected that the extensometer measurement does show the 'diving' effect. This however, could be explained by the fact that the extensometer blades may have shifted slightly during these first loadings, which would also explain the lower value of the Poisson's ratio. Moreover, in Figure 4-40 it can be seen that for the first four loadings, the strain derived from the strain gauges evolves between the same outer limits, as expected since the load level is lower than the one which causes failure to the transverse plies, whereas the strain derived from the extensometer, tends to have a gradual increase to higher values.

Finally, Figure 4-42 shows the evolution of Poisson's ratio as a function of the longitudinal strain, for both transverse strain measurements. As could be expected from the evolution of the transverse strain (see Figure 4-40) the typical behaviour occurs for both ν_{xy} calculated with the strain gauge signal and for ν_{xy} calculated with the extensometer signal.

The initial ratio is a little higher with the strain gauge as with the extensometer, but in general, the signals correspond well and now for both measurements, the typical shape of the ν_{xy}-ε_{xx} is visible.

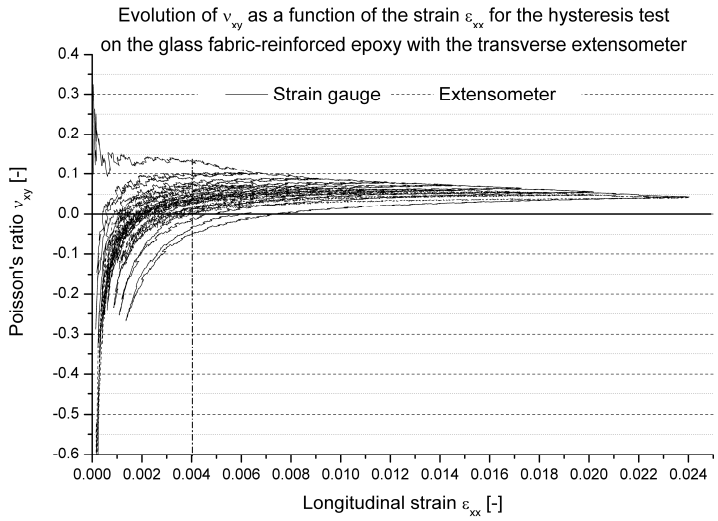

Figure 4-42 The evolution of Poisson's ratio as function of the longitudinal strain for both measurements.

4. 3. 4. c. Carbon fabric-reinforced PPS

Again, it has already been confirmed that the typical behaviour for the Poisson's ratio will also occur using a transverse extensometer, but this method is still assessed since it would be a very interesting tool to measure transverse strains during fatigue experiments.

A few experiments were done, again with similar results, so only one is illustrated here. This test was done starting at 100 MPa and for each next cycle, the maximum stress was increased with 50 MPa; the displacement speed was 2 mm/min. As such, 13 cycles were done, reaching a stress level of 700 MPa and during the fourteenth cycle, the tabs de-bonded around 600 MPa. Figure 4-43 shows the evolution of the transverse strain, measured with both the transverse extensometer and the strain gauge. It can clearly be seen that the signals do not correspond at all. Although the strain gauge gives the expected evolution of the strain which gradually shifts to positive values, the extensometer has a continuous shift to negative strains and a sudden jump also occurs (circle).

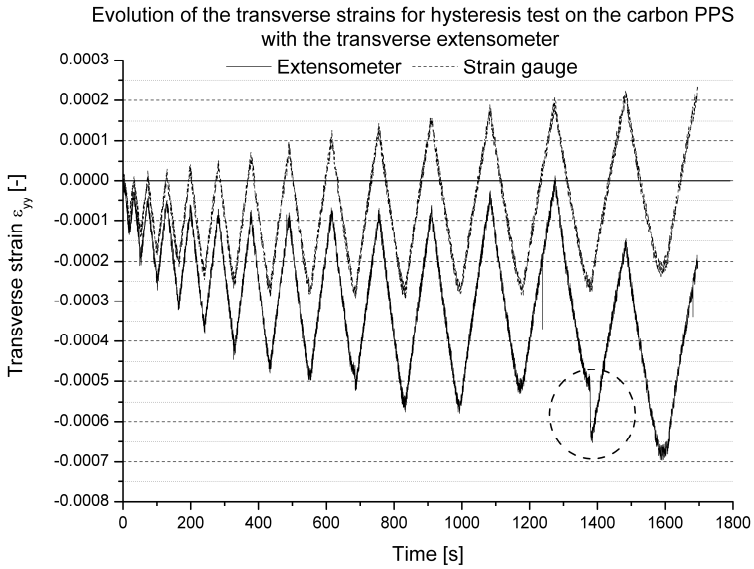

Figure 4-43 Evolution of ε_{yy} for both the extensometer as strain gauge measurement, as a function of time.

As previously mentioned, multiple experiments were performed and various precautions were taken: (i) both the original straight edge blades and the pointy blades were used; (ii) the bolts that grip the specimen were extra tightened; (iii) after mounting the extensometer, an hour passed before starting the test in order to let the blades settle. In general, similar effects as illustrated in Figure 4-43 kept occurring, no matter what precautions were taken and only few experiments yielded a good correspondence with the transverse strain gauge.

This could probably be explained by (i) the fact that the surface of the PPS is a lot smoother than the epoxy, making it a lot easier for the blades to shift and (ii) the transverse strains are a lot lower for the carbon-PPS than for the glass-epoxy, making any shift of the blades much easier to visualise.

This, however, means that this principle of measuring transverse strains, although very promising at first, cannot be used for fatigue measurements.

4. 3. 5. Discussion and conclusion

From all experiments discussed above, it can be concluded that the carbon fabric-reinforced polyphenylene sulphide shows no stiffness degradation and only limited permanent deformation occurs. When cyclic loadings with increasing maximum stress are applied, the permanent deformation also increases with each load. However, when cyclic loadings with constant maximum stress are applied, the permanent deformation tends to form in the first loading cycles and for the following cycles, it only grows very little.

With respect to the Poisson's ratio, a decreasing Poisson's ratio is found. Similar to the permanent deformation, ν_{12} continuously decreases with increasing maximum load cycles and the different cycles can clearly be distinguished, but when the maximum load in the hysteresis remains constant, the ν_{12}-ε_{xx} curves are almost coincident and very little decrease can be noted.

When the Poisson's ratio is plotted versus the longitudinal strain, a very peculiar evolution is found. From the different types of experiments conducted, it can be concluded that this behaviour is not caused by misalignment of the grips, nor by visco-elastic effects, since the shape of the curve remained the same for both 2 mm/min and 0.1 mm/min displacement speed. The effect is not caused by the strain gauge, since it also occurred when using optical fibre sensors. Both strain gauge and optical fibre are bonded to the surface, but the adhesive is not the driving force either, since the behaviour was also noted when using a (modified) transverse extensometer, for which no adhesive is necessary. For the latter, the remark must be made that for most experiments on the carbon-PPS, sudden shifts in transverse strain occurred due to shifting of the blade. However, for the glass-epoxy, good correspondence was found, supporting the fact that the typical behaviour is not caused by the sensor.

As such, it may be concluded that the typical shape from the curve is caused by the material itself.

In all curves, the Poisson's ratio was calculated by dividing the total strains:

$$\nu_{12}^{dam} = -\frac{\varepsilon_{22}^{total}}{\varepsilon_{11}^{total}} \tag{4.1}$$

As well known, the total strain consists of an elastic strain and a permanent strain.

$$\nu_{12}^{dam} = -\frac{\varepsilon_{22}^{elas} + \varepsilon_{22}^{perm}}{\varepsilon_{11}^{elas} + \varepsilon_{11}^{perm}} \tag{4.2}$$

The definition of the Poisson's ratio is given in Equation 4.3, meaning that the ratio is found by dividing elastic strains:

$$\nu_{12}^{0} = \lim_{\varepsilon_{11} \to 0} \left(-\frac{\varepsilon_{22}}{\varepsilon_{11}} \right) \tag{4.3}$$

Considering this definition and the fact that the evolution of Poisson's ratio remained constant for the experiments with a constant low maximum stress of 100 MPa, it may be assumed that Equation 4.4 is valid:

$$\nu_{12}^{0} = -\frac{\varepsilon_{22}^{elas}}{\varepsilon_{11}^{elas}} \tag{4.4}$$

As such, Equation 4.2 can be rewritten as:

$$\nu_{12}^{dam} = -\frac{-\nu_{12}^{0}\varepsilon_{11}^{elas} + \varepsilon_{22}^{perm}}{\varepsilon_{11}^{elas} + \varepsilon_{11}^{perm}} \tag{4.5}$$

During the loading of the specimen, a permanent deformation will occur, as could be seen in the various experiments described, meaning that both ε_{11}^{perm} and ε_{22}^{perm} can be complicated functions of both stress and strain and the pre-loading history.
However, it is very unlikely that both permanent strains will decrease significantly during the unloading of a cycle, meaning they can be considered as constants, corresponding to a certain stress level. As such, Equation 4.5 can be considered as the following function during unloading:

$$\nu_{12}^{dam}(x) : x \rightarrow \frac{\nu_{12}^{0}x + \varepsilon_{22}^{perm,\sigma_{MAX}^{cycle}}}{x + \varepsilon_{11}^{perm,\sigma_{MAX}^{cycle}}} \tag{4.6}$$

This is no more than a hyperbolic function with a horizontal asymptote for y equal to ν_{12}^{0} and a vertical asymptote for x equal to $-\varepsilon_{11}^{perm,\sigma_{MAX}^{cycle}}$. As such, the typical behaviour is explained for the unloading part of the cyclic loading.

During the various experiments with constant maximum load level, it was noted that the permanent deformation had a significant increase for the first cycle, but for all the following cycles at the same load level, the permanent deformation virtually did not grow. This might be explained as follows. By applying tension in one direction, the actual local tensile stresses of the matrix will be much higher than the applied stress, because of the residual compression of the fibres. As such damage (matrix cracks, de-bonding of the fibres,…) will occur once a certain global stress level is reached, allowing the compressed fibres to relax, causing permanent elongation, and form a new equilibrium in stresses and strains. Since the thermal stresses will not be uniformly distributed along the entire plate, because of non uniform cooling of the plate (some zones will cool faster than others), some fibres will be stressed more and are therefore allowed to relax sooner than other fibres.
The next loading cycle with the same stress level will only cause a very limited amount of damage, since at this maximum stress level, there already was an equilibrium. It is only for higher stress levels that new damage develops and a new equilibrium in stresses is formed.
Of course, a similar process will happen in the transverse direction. Due to damage of the matrix, the transverse fibres are allowed to relax the residual stresses, causing transverse elongation, which results in positive transverse strains.

A small remark can be made considering these thermal stresses and the preparation of the test samples. After sawing the specimens, some of the specimens tended to twist around their longitudinal axis; even some large plates had a slight saddle-like shape. Both phenomena prove that these residual stresses were present.

Going back to the explanation on the Poisson's ratio, this means that Equation 4.6 is also valid for the loading of the next cycle until the stress level in this cycle is about the same as the maximum stress from the previous cycle. From that point on, both ε_{11}^{perm} and ε_{22}^{perm} will continue to increase, which causes a different, slower evolution towards the horizontal asymptote, since ε_{11}^{perm} grows faster than ε_{22}^{perm} because the specimen is loaded along the warp direction. This and the fact that ν_{12}^{0} is smaller than one causes the denominator to increase more than the numerator, yielding a decreasing Poisson's ratio.
The vertical asymptote (for x equal to $-\varepsilon_{11}^{perm,\sigma_{MAX}^{cycle}}$) will shift to the left, which can also be seen in the experiments with increasing maximum load level. When the specimen is unloaded, the slope of the tangent in this point is steeper for the cycle with a lower maximum load level.
This is illustrated in Figure 4-44, which is no more than a detailed image of one of the results depicted in Figure 4-19, with tangent lines added. This effect is more visible for this experiment than for the others, since the difference in maximum load levels is 100 MPa, causing the curves to be more apart and probably because of the lower testing speed, which seemed to decrease the noise on the signal.

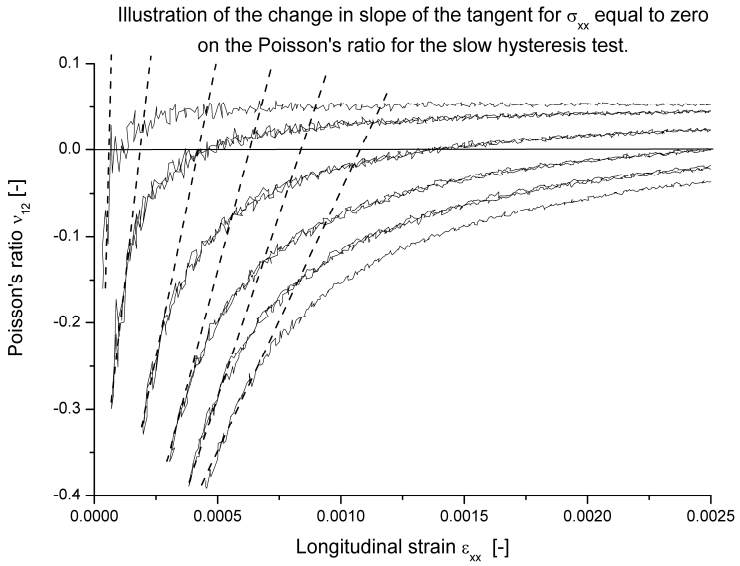

Figure 4-44 Illustration of the decrease in slope of the tangent line for higher loading cycles.

Of course, if multiple loadings at the same stress level are applied, processes such as crack initiation and crack growth will occur, gradually damaging the material and eventually leading to failure. As such, for the fatigue loadings discussed in the next chapter, a decrease in Poisson's ratio is also expected.
At this point, no validated explanations for the occurrence of this permanent deformation can be given, only assumptions can be made. In order to determine whether this deformation is due to plastic deformation of the matrix, the occurrence of micro-cracks along or perpendicular to the fibres or other phenomena, a profound study of the micro-mechanical behaviour of this specific material is required.

The explanation given above can also be confirmed numerically. In Figure 4-45, a theoretical evolution of the longitudinal and transverse strain is illustrated. An increasing permanent deformation was simulated both for the longitudinal and the transverse strain after each unloading. It should be remarked that these values of the permanent deformation are chosen arbitrary, just to illustrate the explanation above. This is not a model of the damage mechanics of the material under study.

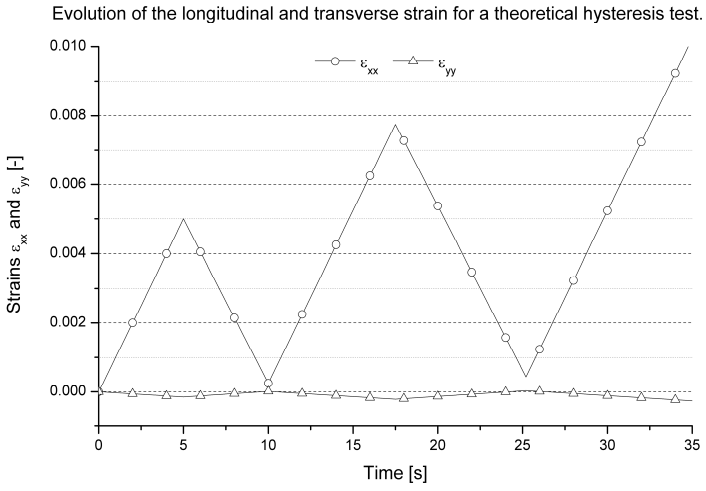

Figure 4-45 Theoretical evolution of the ε_{xx} and ε_{yy}.

The corresponding evolution of the Poisson's ratio as a function of the longitudinal strain is shown in Figure 4-46. It can be remarked that the typical hyperbolic shape is visible, validating the derivation above. Also, the effect of the permanent deformation after each loading cycle can be seen on the evolution towards the horizontal asymptote. For this theoretical case, the horizontal asymptote occurs for y = 0.03 and each loading evolves slower towards this asymptote then the previous, creating the decrease in the Poisson's ratio at maximum load of each loading cycle.

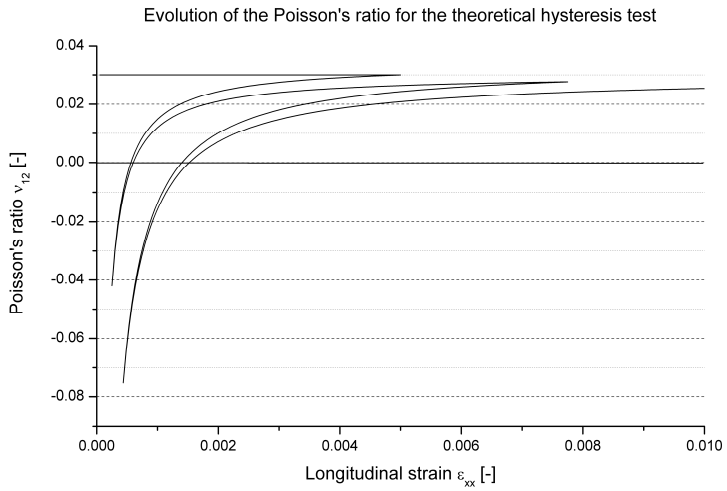

Figure 4-46 Theoretical evolution of ν_{12} as function of ε_{xx}.

4. 4. ELECTRICAL RESISTANCE MEASUREMENT

Because of the promising results for the quasi-static tensile tests till failure, described in the previous chapter, this method is also considered for monitoring cyclic tests. Since the two-probe method showed a drift in time, this setup is no longer considered and all experiments discussed here were done using the four-probe setup. A number of hysteresis tests are performed to assess whether the resistance has an irreversible growth, with corresponding results.

As was shown in [12, 13] the resistance should increase if the specimen elongates, but as long as no damage occurs, the resistance should decrease to its original value if the load is removed. Therefore, a number of successive loading cycles were imposed on the specimen, starting from 100 MPa and then increasing with 50 MPa per cycle until fracture occurred. The tests were done displacement-controlled using a speed of 2 mm/min, similar to all previous experiments. The corresponding stress-strain curves are shown in Figure 4-47. The different tests are given an offset of 0.0015 along the strain-axis for a clear picture. Similar to all previous experiments, there is no stiffness degradation and only very limited permanent deformation occurs. Premature failure in the tabs occurred for specimen L1 at 600 MPa, which corresponds with 11 cycles and both L5 and L6 failed at 500 MPa, corresponding with 9 cycles. The latter was due to bad bonding quality on PPS. H14 on the other hand failed outside the tabs at 753 MPa (=14 cycles).

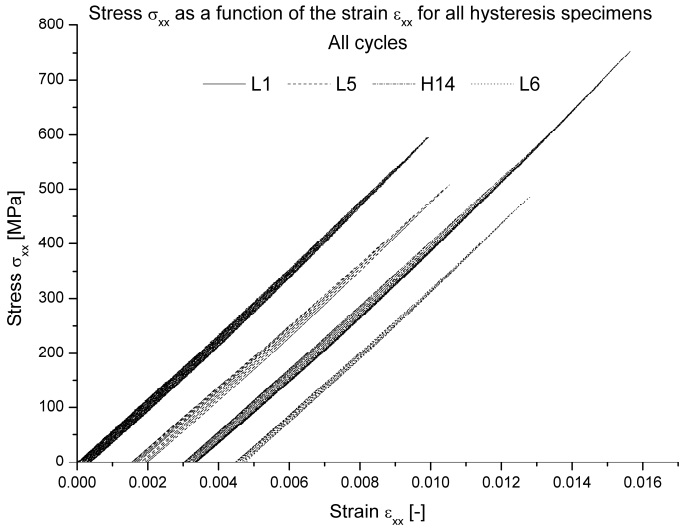

Figure 4-47 Stress as function of the strain for the hysteresis tests.

The evolution of the relative resistance, as well as the corresponding strain is given in Figure 4-48 and Figure 4-49 for specimen L5 and H14 respectively. The tests on specimens L1 and L6 gave a similar image as L5.
As a reminder, the relative resistance change is given by:

$$\rho = \frac{\Delta R}{R_0} = \frac{R_t - R_0}{R_0} \tag{4.7}$$

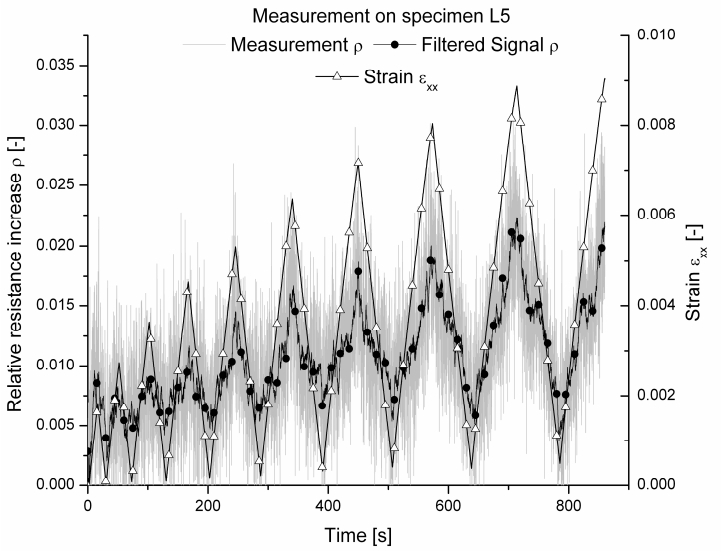

Figure 4-48 Relative resistance change and strain as a function of time for specimen L5.

It must be noted that there is a lot more (white) noise present on the signal L5 than on the static tests. Investigation yielded that a power converter, which generates large electromagnetic fields was working close by. This system was shut down before conducting the test on H14, resulting in a lot less noise.

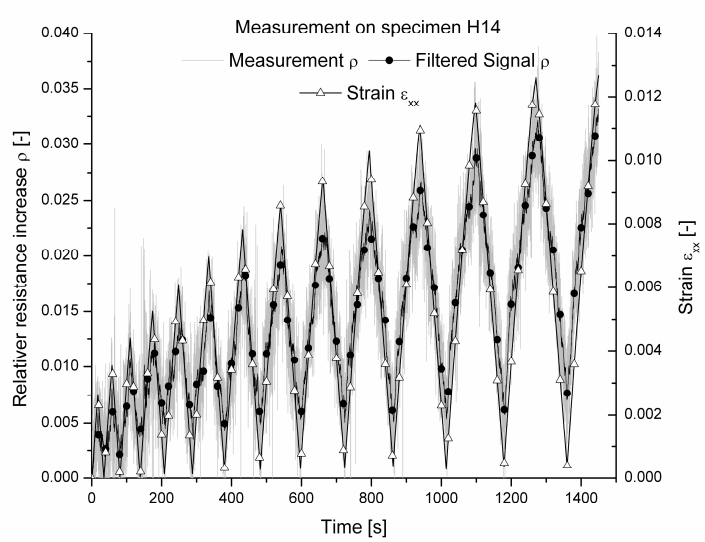

Figure 4-49 Relative resistance change and strain as a function of time for specimen H14.

It was noticed from all the tests that the relative resistance change follows the evolution of the strain as it is supposed to, meaning the rivets and copper conductive tape establish a good constant contact [12, 13]. During the higher loading cycles, it can be seen that the relative resistance no longer returns to zero, which means that this method is sensitive to the occurring damage. As such, this method will also be considered for monitoring fatigue experiments, described in the next chapter.

4. 5. CONCLUSIONS

In this chapter, the next step towards fatigue loading conditions was studied, namely quasi-static hysteresis tests. From all experiments on the carbon fabric-reinforced PPS, it can be concluded that this material does not show significant stiffness degradation, so this parameter cannot be used for monitoring or modelling fatigue experiments. Permanent deformation does occur, but only very limited. If cyclic loadings are applied with gradually increasing maximum load, then the permanent deformation also increases gradually. However, if all cycles have the same maximum stress level, then the permanent deformation only occurs in the first cycle; for all successive cycles, very little permanent deformation occurs. Since fatigue loading conditions are no more than cycles with the same maximum stress level, a similar behaviour is expected. Various fatigue experiments will be necessary to assess whether the permanent deformation growth is large enough to monitor the fatigue test.

In literature, the Poisson's ratio is often used for damage modelling, since it is said to be a lot more sensitive to damage than Young's modulus or permanent strain development. The experiments conducted here indeed showed a large decrease in Poisson's ratio during the cyclic tests with increasing maximum stress level. However, similar to the permanent deformation, there is only a limited decrease during cyclic experiments with constant load level. As such, several fatigue tests will be necessary to assess the usefulness of this parameter.

In order to measure the transverse strain, necessary for the calculation of Poisson's ratio, strain gauges, external optical fibres and a (modified) transverse extensometer were considered. From all these sensors, the strain gauge still remains the best option for the material under study, since the optical fibre sometimes suffers from 'peak-splitting' at higher load levels and the transverse extensometer showed too much drifting and shifting for an accurate measurement, because of the smooth surface of the PPS.

When the Poisson's ratio is plotted as a function of the longitudinal strain, a peculiar shape was noticed. From the experiments with the different sensors, it could be concluded that this behaviour was not caused by the used sensor, so it is inherent to the material. A mathematical explanation, based on the development of permanent strains, was suggested for this peculiar shape.

Finally, the use of electrical resistance measurement was assessed for monitoring quasi-static cyclic tests. It could be concluded that the resistance follows the loadings and that for higher stress levels, the relative resistance did not return to zero upon unloading, making it sensitive for damage. As such, this method will also be considered for the fatigue experiments, discussed in the next chapter.

4. 6. REFERENCES

[1] Gao F., Boniface L., Ogin S.L., Smith P.A. and Greaves R.P., Damage accumulation in woven-fabric CFRP laminates under tensile loading: Part 1. Observations of damage accumulation. COMPOSITES SCIENCE AND TECHNOLOGY 59 (1): 123-136 1999.

[2] Surgeon M., Vanswijgenhoven E., Wevers M. and Van der Biest O., Transverse cracking and Poisson's ratio reduction in cross-ply carbon fibre-reinforced polymers. JOURNAL OF MATERIALS SCIENCE 34 (22): 5513-5517 NOV 1999.

[3] Gao F., Boniface L., Ogin S.L., Smith P.A. and Greaves R.P., Damage accumulation in woven-fabric CFRP laminates under tensile loading: 2. Modelling the effect of damage on macro-mechanical properties. COMPOSITES SCIENCE AND TECHNOLOGY 59 (1): 137-145 1999.

[4] Smith P.A. and Wood J.R., Poisson ratio as a damage parameter in the static tensile loading of simple crossply laminates. COMPOSITES SCIENCE AND TECHNOLOGY 38 (1): 85-93 1990.

[5] Parlevliet P.P., Bersee H.E.N. and Beukers A.. Residual stresses in thermoplastic composites – a study of the literature. Part III: Effects of thermal residual stresses. COMPOSITES PART A: APPLIED SCIENCE AND MANUFACTURING., VOLUME 38, ISSUE 6, JUNE 2007, PAGES 1581-1596.

[6] De Baere I. Studie van het afschuifgedrag van composieten. Graduate thesis 2003-2004, Faculty of Engineering, Ghent University.

[7] DiLandro L., Pegoraro M., Evaluation of residual stresses and adhesion in polymer composites. COMPOSITES PART A-APPLIED SCIENCE AND MANUFACTURING 27 (9): 847-853 1996.

[8] Bassa F. , Boniface L., Jones K. and Ogin S.L., On the behaviour of the residual strain produced by matrix cracking in cross-ply laminates. Composites Part A 29 A (1998) 1425-1432.

[9] Parlevliet P.P., Bersee H.E.N. and Beukers A., Residual stresses in thermoplastic composites—A study of the literature—Part I: Formation of residual stresses. Composites Part A: Applied Science and Manufacturing, Volume 37, Issue 11 , November 2006, Pages 1847-1857.

[10] Senel M., Akbulut H., Toparli M., Residual stress analysis in symmetric thermoplastic laminated plates under thermal loads: Analytic solution. JOURNAL OF THERMOPLASTIC COMPOSITE MATERIALS 17 (6): 481-507 NOV 2004.

[11] Filiou C., Galiotis C., In situ monitoring of the fibre strain distribution in carbon-fibre thermoplastic composites 1. Application of a tensile stress field. COMPOSITES SCIENCE AND TECHNOLOGY 59 (14): 2149-2161 1999.

[12] Angelidis N, Wei CY, Irving PE ,The electrical resistance response of continuous carbon fibre composite laminates to mechanical strain, COMPOSITES PART A-APPLIED SCIENCE AND MANUFACTURING 35 (10): 1135-1147, 2004.

[13] Todoroki A, Yoshida J, Electrical resistance change of unidirectional CFRP due to applied load, JSME INTERNATIONAL JOURNAL SERIES A-SOLID MECHANICS AND MATERIAL ENGINEERING 47 (3): 357-364 , JUL 2004.

Chapter 5

TENSION-TENSION FATIGUE

In this chapter, tension-tension fatigue is discussed. First, a design for a set of clamps, suited for both tension and compression fatigue is presented. Then, the issue of the use of end tabs is reconsidered for fatigue. Next, the fatigue experiments are discussed. All types of sensing, introduced in chapters 3 and 4 are used to monitor possible fatigue damage.

5. 1. INTRODUCTION

This chapter is the first of three in which fatigue experiments are discussed. Here, all uni-axial fatigue experiments are documented, whereas in chapter 6 bending fatigue is handled and in chapter 7 shear fatigue. As it turned out, performing valid tension-tension fatigue experiments is not as easy as it seems. In order to induce a uni-axial stress state in a specimen, without bending or torsion loads, accurate gripping devices are necessary. Therefore, first the design of a set of mechanical clamps, suited for both tension as compression fatigue is discussed, during which some interesting equations concerning the contact pressure of the tabbed section of the specimen are derived. Using these equations, the stress state of the clamped ends of the specimen can be simulated accurately and as such, the problem of end tab failure is readdressed numerically.

Next, some standard fatigue experiments are discussed, during which it appeared that the material hardly shows any stiffness degradation or permanent deformation. Because of the promising results on monitoring the Poisson's ratio for the quasi-static cyclic testing, mentioned in the previous chapter, the use of this parameter for damage characterization in fatigue experiments is assessed, again first for a glass fabric-reinforced epoxy, with a higher Poisson's ratio and then for the carbon fabric-reinforced PPS.

In chapters 3 and 4, the use of optical fibre gratings for strain measurement has been successfully introduced. Now, it is assessed whether these sensors can be used for monitoring fatigue experiments.

Finally, the electrical resistance measurement is used to verify whether it can detect damage and whether the resistance is suited as a parameter for damage characterisation.

5. 2. DESIGN OF A NEW SET OF CLAMPS

5. 2. 1. Introduction

The reasons for developing a new set of clamps evolved from the research described in the previous chapters, for instance when the specimen requires extra space at the ends for special fixtures or sensors. If the longitudinal strain is measured with the optical fibre sensor [1-4], this fibre comes out of the specimen at the end (Figure 5-1) (see chapter 3 for more details on the use of optical fibre sensors). Since this fibre breaks off very easily, it requires some space so it can be bent with a relatively large radius. Often, this space is not available with standard grips.

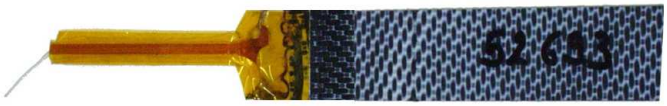

Figure 5-1 An optical fibre at the end of a test specimen. To protect the fibre during production and handling of the specimen, a kapton tape was added.

Another type of in-situ monitoring for composites is the use of the carbon fibre-reinforcement for electrical resistance measurement. If the contact electrodes are placed outside the tabs in the strain free area, as described in [5-8] and as is the case in this doctoral study (see chapter 3), then there needs to be sufficient space.
Figure 5-2 illustrates the gripping of a specimen, instrumented for resistance measurement with the method used in this research. The end of the specimen may not touch the clamps, because the specimen should be electrically isolated from the tensile machine. It is clear that more space should be available, since with these clamps, only 35 mm of the available 50 mm of tab-length is gripped.

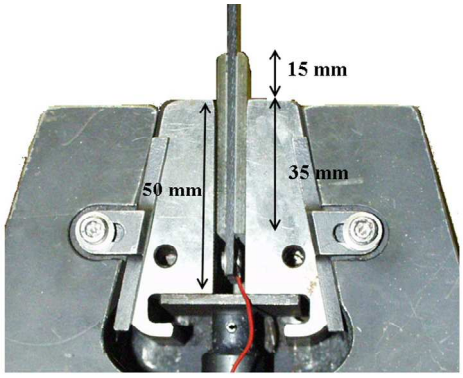

Figure 5-2 The gripping of a specimen, instrumented for electrical resistance measurement as described in chapter 3.

Another problem is that uni-axial testing of composite specimens usually requires tabs on the ends, especially when performing off-axis tests [9-13]. This is also described in the *"ASTM D3039/D 3039M Standard Test Method for Tensile Properties of Polymer Matrix Composite Materials"*, as well as in the *"ASTM D 3479/D 3479M Standard Test Method for Tension-Tension Fatigue of Polymer Matrix Composite Materials"*. However, some composites or plastics are not easily bonded, resulting in low ultimate shear stress of the adhesive. By increasing the surface area of the tabs, the fracture load of the specimen can be reached before ultimate shear stress of the adhesive is reached. But these large tabs still need to fit inside the grips.

All problems above are related with the dimensions of the clamps. In Figure 5-3, two types of standard tensile machine fixtures are shown, with the dimensions of the grips.

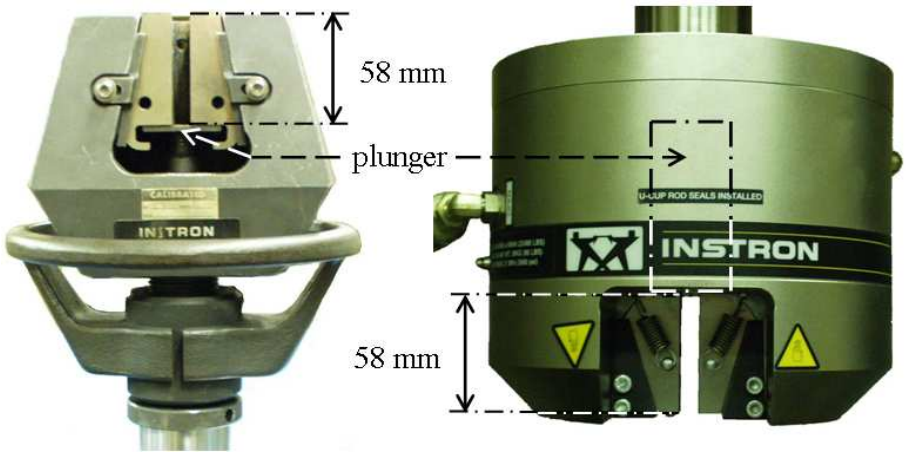

Figure 5-3 An illustration of the grip-dimensions of a standard set of mechanical and hydraulic clamps (INSTRON™).

Concerning mechanical grips, the following remarks could be made. If a set of mechanical wedge grips is used, it is usually only suited for either tension or compression testing, but rarely for both. For the gripping, the principle of a wedge is used (Figure 5-4). It is obvious that this only works in one direction. If the wedges are pulled down, which is the case in a tensile test, the grips move inwards, increasing contact pressure. But if the wedges are pushed up, as in a compressive test, the wedges open and the contact pressure decreases. Of course, it is possible to have mechanical grips for compressive tests, simply by putting the wedges upside down, but then they will no longer function under tensile conditions.

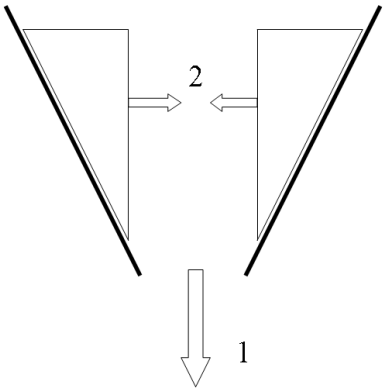

Figure 5-4 Illustration of the wedge principle.

The problem mentioned above is also present in fatigue loading. Both tension-tension and compression-compression fatigue are possible, using only wedges, but without any other fixture, tension-compression fatigue is impossible. Usually, hydraulic grips, such as shown in Figure 5-3, are used for fatigue. These clamps use the wedge principle for tensile mode, whereas the hydraulic plunger supports the grips in compressive mode.
However, these clamps still have the problem of insufficient space for extra fixtures and they are expensive. Furthermore, extra hydraulics for the clamps may not always be at hand.
In the next paragraphs, the design of a set of mechanical clamps is presented that can be used for quasi-static and fatigue testing in tension and compression. Furthermore, there is sufficient space for specific fixtures at the ends, e.g. optical fibres, contact electrodes or large tabs.

5. 2. 2. Design of the clamps

For the design of the clamps, the following specifications must be met:

- The clamps must be mounted on a servo-hydraulic testing machine to accommodate for fatigue testing.
- The gripping range of the clamps is 0 – 12 mm. The average thickness of the composite plates that should be tested on this machine is about 3 mm, but when tabs are mounted on the specimen, the thickness may be 9 mm or thicker, depending on the thickness of the tabs.
- The load range which the clamps should resist is the same as the load cell, 100 kN in tension and compression, under dynamic loading conditions.

For testing in tension, the principle of a wedge is used (see Figure 5-4) as mentioned in the introduction. This results in the fact that the more the specimen is pulled, the higher the contact pressure becomes and the better the specimen is gripped.

However, the wedge does exactly the opposite when used in compression. An upward motion of the wedge results in a lower contact force. To avoid this, an extra set of horizontal wedges is placed above the wedge-shaped grips (see Figure 5-5).

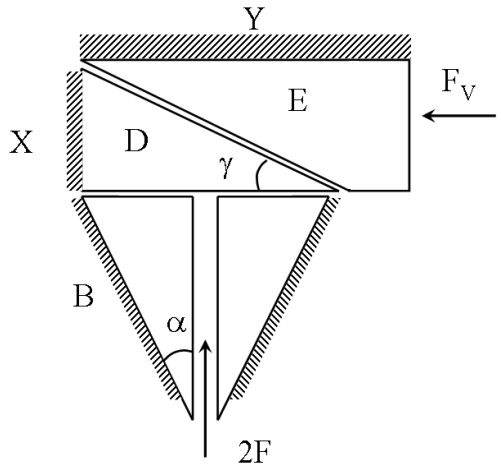

Figure 5-5 The use of a set of horizontal wedges to give a certain amount of pre-stress.

A certain amount of pre-stress F_v is placed on wedge E. This pushes wedge D and both grips downward, to compensate the upward motion of the grips, caused by the compressive load 2F. Thus, this system has the same function as the hydraulic plunger in the hydraulic clamps (Figure 5-3).
The pre-stress F_v is given by a set of disc springs. The latter are chosen rather than twisted springs, because the discs can deliver a higher force for a smaller size.
In the next paragraph, an analysis is made of the influence of the angles α and γ on the relationship between F and F_V.

5. 2. 2. a. Compression after tension

First, the setup in Figure 5-6 is considered. For now, parts D and E are combined in one part (part A), which is considered as a black box. Its function is to deliver a certain downward force on the two grips. The calculation of parts D and E would only complicate the derivation in this stage.
A force of 2F is imposed, so that each grip is loaded with F.

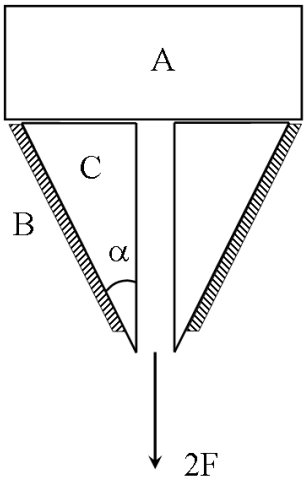

Figure 5-6 Symbolic setup of the design.

For this calculation, the assumption is made that the clamps will first be loaded in tension and then in compression. This assumption is justified by the fact that a normal tension-compression fatigue test starts in tension. This however has an important influence on the calculation, since the loading in tension will put a certain pre-stress in the clamps that will have an effect when loading in compression afterwards.

In Figure 5-7, the situation of one grip is illustrated, with all (reaction) forces that need to be taken into account. The direction of the friction forces T_A and T_B is chosen according the way they work. For the tensile situation, the grips are pulled down and inwards, whereas in the compressive situation, the grips are pushed up and outwards.

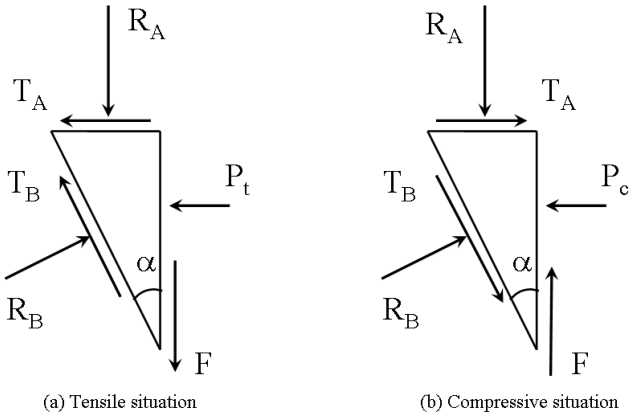

Figure 5-7 The (reaction) forces on one grip.

First, the tensile situation is discussed. The equilibrium of the grip, combined with the friction leads to the following equation:

$$\begin{cases} F + R_A = R_B \sin\alpha + T_B \cos\alpha \\ P_t + T_A + T_B \sin\alpha = R_B \cos\alpha \\ T_A \le \mu_{AC} R_A \\ T_B \le \mu_{BC} R_B \end{cases} \tag{5.1}$$

In this equation, μ_{IJ} is the friction coefficient between part I and part J. The worst case scenario is taken, which means the maximum value of T_A and T_B. This means the situation exactly before there is any movement of the parts.
This leads to:

$$\begin{cases} F + R_A = R_B(\sin\alpha + \mu_{BC}\cos\alpha) \\ P_t + \mu_{AC} R_A + \mu_{BC} R_B \sin\alpha = R_B \cos\alpha \end{cases} \tag{5.2}$$

From the first of these equations, R_B can be calculated:

$$R_B = \frac{F + R_A}{\sin\alpha + \mu_{BC}\cos\alpha} \tag{5.3}$$

With this value, the contact pressure of the grips on the specimen can be calculated:

$$P_t = F\frac{\cos\alpha - \mu_{BC}\sin\alpha}{\sin\alpha + \mu_{BC}\cos\alpha} + R_A\frac{(1-\mu_{AC}\mu_{BC})\cos\alpha - (\mu_{BC} - \mu_{AC})\sin\alpha}{\sin\alpha + \mu_{BC}\cos\alpha} \tag{5.4}$$

In this equation, the effect of the wedge is in the first term and the effect of the pre-stress is in the second.
Now the compressive situation is considered (Figure 5-7 (b)). It is hereby assumed that the force R_B from Equation 5.3 is still present. When the grips are pulled down, the force R_B has a similar but opposite reaction on part B (Figure 5-6) which symbolises the clamp. This reaction causes a small elastic deformation of the clamp. When the force F changes direction (tensile-compressive) this elastic deformation will still be present. Moreover, the friction will inhibit any movement of the parts. Therefore, the reaction R_B will also remain present. The value of R_A will also be the same as in the tensile situation.
Equilibrium of the grip combined with the friction laws in Figure 5-7 (b) yields:

$$\begin{cases} F + R_B \sin\alpha = R_A + T_B \cos\alpha \\ P_c = T_A + R_B \cos\alpha + T_B \sin\alpha \\ T_A \le \mu_{AC} R_A \\ T_B \le \mu_{BC} R_B \end{cases} \tag{5.5}$$

Again, the highest values of T_A and T_B are assumed. Together with the known value of R_B (Equation 5.3), this gives for the contact pressure of the grips on the specimen:

$$P_c = F\frac{\cos\alpha + \mu_{BC}\sin\alpha}{\sin\alpha + \mu_{BC}\cos\alpha} + R_a\frac{(1+\mu_{AC}\mu_{BC})\cos\alpha + (\mu_{AC}+\mu_{BC})\sin\alpha}{\sin\alpha + \mu_{BC}\cos\alpha} \tag{5.6}$$

Furthermore, the required value of R_A can be calculated form the first line of Equation 5.5:

$$R_A = F + R_B(\sin\alpha - \mu_{BC}\cos\alpha) \tag{5.7}$$

Since R_B is known as a function of F and R_A (Equation 5.3), the amount of pre-stress R_A required for a tension-compression test with amplitude 2F (Figure 5-6) can be determined as a function of F:

$$R_A = \frac{\tan\alpha}{\mu_{BC}}F \tag{5.8}$$

It is hereby assumed that the value of R_A is the same in the tensile and compressive situation. This assumption is justified by the fact that all calculations are done in the situation just before there is any movement of the parts. Since there is no movement, there will be no change in R_A.

At this point in the calculation, part A which represents the two horizontal wedges, can be examined in more detail. A symbolic representation is given in Figure 5-8. The objective is to find a value of F_V as a function of F.

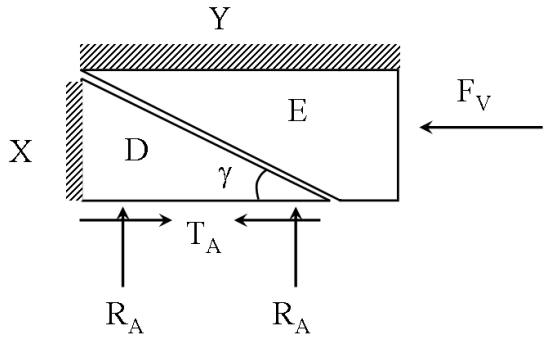

Figure 5-8 Symbolic representation of the part that imposes the pre-stress R_A.

In Figure 5-9, the friction and reaction forces on both horizontal wedges are given. By writing equilibrium, a relationship between R_A and F_V can be found and since the relationship between R_A and F is known, an equation for F_V as a function of F can be derived.

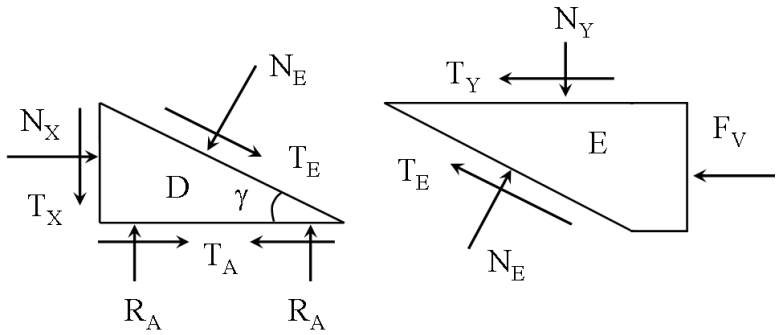

Figure 5-9 The (reaction) forces on the horizontal wedges.

The equilibrium of part D yields:

$$\begin{cases} 2R_A = T_X + N_E\cos\gamma + T_E\sin\gamma \\ N_X + T_E\cos\gamma = N_E\sin\gamma \\ T_E \le \mu_{DE} N_E \\ T_X \le \mu_{DX} N_X \end{cases} \tag{5.9}$$

As before, the situation just before movement is considered, which means the maximum values of T_E and T_X are chosen. Thus, a value for R_A can be calculated:

$$R_A = \frac{1}{2} N_E[(1-\mu_{DE}\mu_{DX})\cos\gamma + (\mu_{DE}+\mu_{DX})\sin\gamma] \tag{5.10}$$

The equilibrium of part E gives:

$$\begin{cases} F_V + T_Y + T_E\cos\gamma = N_E\sin\gamma \\ N_Y = N_E\cos\gamma + T_E\sin\gamma \\ T_E \le \mu_{DE} N_E \\ T_Y \le \mu_{EY} N_Y \end{cases} \tag{5.11}$$

Again with the maximum values of T_E and T_Y, the formula for F_V can be derived:

$$F_V = N_E[(1-\mu_{DE}\mu_{EX})\sin\gamma - (\mu_{DE}+\mu_{EX})\cos\gamma] \tag{5.12}$$

The expression for N_E can be calculated using Equation 5.10. Combining this with the previous equation and Equation 5.8, the following relation between the load F and the needed pre-stress F_V is found:

$$F_V = 2\tan\alpha \frac{1}{\mu_{BC}} \frac{(1-\mu_{DE}\mu_{EX})\sin\gamma - (\mu_{DE}+\mu_{DX})\cos\gamma}{(1-\mu_{DE}\mu_{EX})\cos\gamma + (\mu_{DE}+\mu_{DX})\sin\gamma} F \tag{5.13}$$

In this equation, μ_{IJ} is the coefficient of friction between part I and part J.

Since these friction coefficients are only known within a relatively large margin, all coefficients are chosen equal to 0.1.Normally the friction coefficient between steel and steel is about 0.6, but to avoid micro-welding of the metal surfaces, a special coating is used and some parts are greased.

Both precautions lower the friction coefficient. With these values of μ_{IJ}, the equation becomes:

$$f = \frac{F_V}{2F} = \tan\alpha \frac{990\sin\gamma - 200\cos\gamma}{99\cos\gamma + 20\sin\gamma} \tag{5.14}$$

This ratio is depicted in Figure 5-10 and is further noted as f.

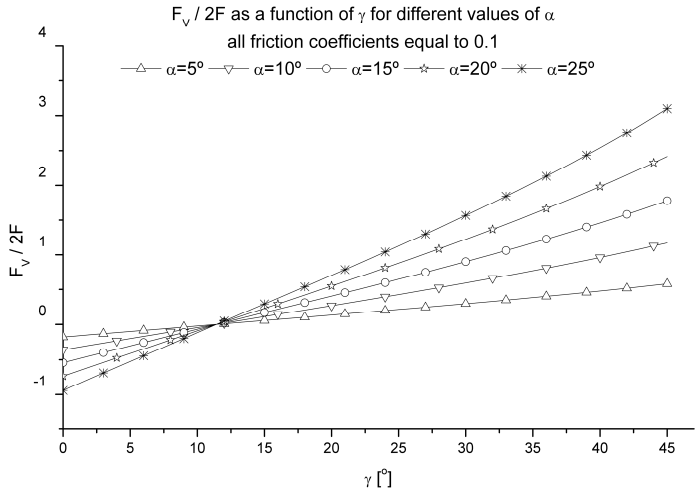

Figure 5-10 $F_V/2F$ as a function of the angle γ for different values of α. Friction coefficients of 0.1.

It can be concluded that an increase in γ or in α gives an increase in f, which means a stronger spring will be necessary. So a low value of both angles is preferred.
It may also be noticed that the ratio becomes zero for a value of γ of 11.4°. A negative value means that F_V changes direction in Figure 5-5. This is actually a consequence of the used model. In the deduction of Equation 5.13, the maximum values of the tangential forces (T_A, T_B, T_E, …) were chosen. In reality, when the model predicts a negative value for F_V this would mean that the friction between all parts is large enough to carry the load.
A higher friction should be able to compensate higher loads, which means that the value of γ for which the ratio becomes zero should increase. For instance, using friction coefficients of 0.5, the value of γ for which the ratio becomes zero is 53.1°.

In order to choose the values of α and γ, not only the force F_v but also the gripping of the specimen itself needs to be taken under consideration. Figure 5-11 gives an overview of the movement of all parts in the design. ΔE is the displacement of the pre-stress setup which is imposed by the user and ΔC is the narrowing of the grips as a consequence of ΔE. The purpose is to have a relatively large ΔC with a relatively small ΔE in order to keep the dimensions of the parts reasonable.

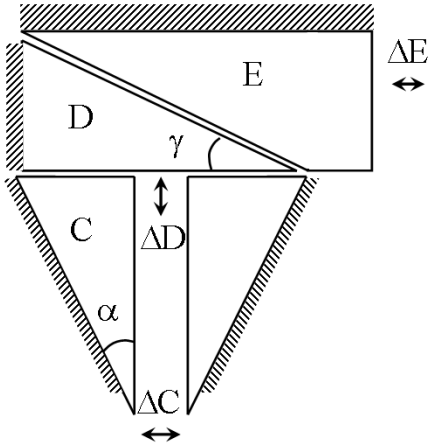

Figure 5-11 Movement of the different parts in the design.

Some simple trigonometry gives:

$$\begin{cases} \Delta D = \Delta E.\tan\gamma \\ \Delta C = 2.\Delta D.\tan\alpha \end{cases} \Rightarrow \Delta C = 2.\Delta E.\tan\alpha.\tan\gamma \qquad (5.15)$$

$$\Leftrightarrow \frac{\Delta C}{\Delta E} = 2.\tan\alpha.\tan\gamma$$

The evolution of this ratio is given in Figure 5-12.

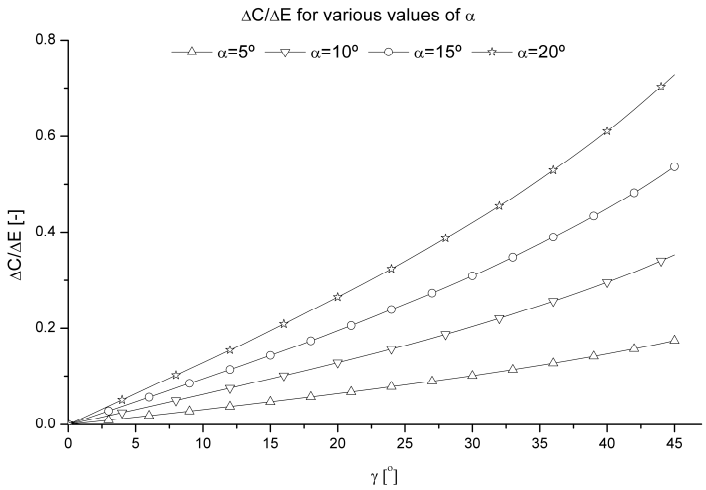

Figure 5-12 The evolution of ΔC/ΔE for various values of α, plotted as a function of γ.

It can be concluded that an increase in α or γ gives an increase in the displacement ratio. This means that a high value of the angles is preferable, because otherwise, a lot of horizontal space is necessary inside the clamps for part E to move (Figure 5-11).

Both α and γ also have an effect on the geometry of the clamps. The smaller α is, the longer the grips become, resulting in more space for extra fixtures on the specimen. The larger γ becomes, the higher the wedge system (parts D and E in Figure 5-11), which increases the height of clamps and as a result the total weight of the clamps. The latter results in higher inertia forces during a test, but also gives more difficulty in mounting the clamps. Therefore, the angles should be chosen sufficiently small.

Finally, a compromise was chosen between a high value for the displacement and a low value for the springs, taking the effect of the angles on the geometry into account. Values of $\alpha = 10^o$ for the grips and $\gamma = 20^o$ for the wedges were chosen. With these angles, it is possible to calculate the force F_v necessary to compensate a total compressive force F_{tot} equal to 2F, using Equation 5.13.

$$F_v = 0.266 F_{tot} \tag{5.16}$$

The clamps should resist a dynamic load of 100 kN, resulting in an F_v of 26.6 kN. Two disc springs of 15 kN are placed in series (Figure 5-13 (a)), resulting in a total force of 30 kN. Six of these sets are placed in parallel (Figure 5-13 (b)), in order to regulate the pre-stress. One set of discs reaches 30 kN after an indentation of 1.05 mm. With six sets of discs, there is 6.3 mm of displacement (ΔE) available to reach the 30 kN.

Figure 5-13 Illustration of what is meant by ‘series’ and ‘parallel’ for disc springs.

5. 2. 2. b. Clamps only loaded in compression

In the paragraph above, compression after tension is considered. But what happens with tests in compression-compression, where there is no tension to pre-load the clamps? In this paragraph, the calculation is done for the worst-case scenario: compression without any form of pre-loading of the clamps.

A few things change when the clamps are immediately loaded in compression, which is the case with a quasi-static compression test or compression-compression fatigue. In this worst-case scenario, all pre-stress of the clamps is lost and the wedges need to compensate the entire load.

This gives the following formula instead of Equation 5.8:

$$R_A = F \tag{5.17}$$

Which means that:

$$\frac{\tan\alpha}{\mu_{BC}} = 1 \tag{5.18}$$

Substituting this in Equation 5.13 gives:

$$\frac{F_V}{2F} = \frac{(1-\mu_{DE}\mu_{EX})\sin\gamma - (\mu_{DE}+\mu_{DX})\cos\gamma}{(1-\mu_{DE}\mu_{EX})\cos\gamma + (\mu_{DE}+\mu_{DX})\sin\gamma} \tag{5.19}$$

With the values of μ_{IJ} equal to 0.1, α equal to 10º and γ equal to 20º, this ratio becomes:

$$F_V = 0.151F_{tot} \tag{5.20}$$

This means that the pre-load, given by the disc springs is even lower in this case than it was in tension-compression. This can be explained by the absence of the effect of R_B on R_A. Therefore, the disc springs, selected in the paragraph above, suffice.

5. 2. 2. c. Space for extra fixtures

Given the principle illustrated in Figure 5-5, it is clear that the only location were extra space can be created, is between the grips. Therefore, the grips are chosen extra long, which also ensures that long end tabs can be gripped. The housing of the grips (part B in Figure 5-5) is therefore widened. This is illustrated in Figure 5-14. If the housing is broadened over a distance d, the length of the grips increases from ℓ to L.

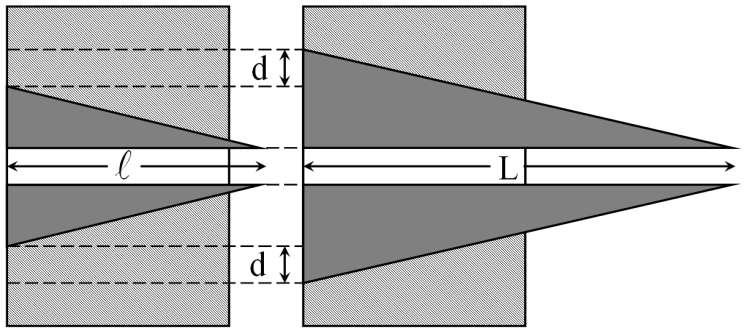

Figure 5-14 Illustration of the effect of the widening of the housing of the grips.

Since the sandwich load cell of our servo-hydraulic testing machine has 6 M20 holes in a circle with a diameter of 150 mm, the clamps were designed as a cylinder with a diameter of 200 mm, with holes so large that long M20 bolts can be mounted through the cylinder.

It is known that long slim bolts are better suited for fatigue loading conditions than short bolts, because of the effect of pre-loading them.
The final design of the clamps is given in Figure 5-15.

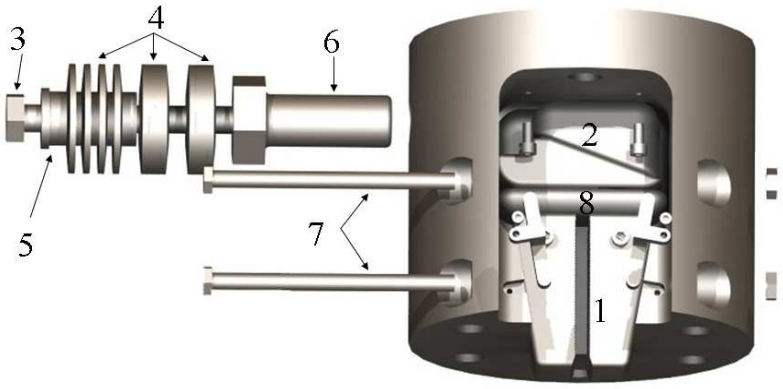

Figure 5-15 Exploded view of the clamps for tension and compression fatigue loading.

The wedge system (2), which represents parts D and E in Figure 5-10, pushes the two long grips (1) down. The top wedge is connected with the pre-load system (4, 5 and 6) by a bolt (3). The pre-load is delivered by six sets of disc springs (4), which were discussed in a previous paragraph (for illustration purposes, only the two left sets are drawn apart, the other four sets are drawn in contact). These springs are able to move between the head of bolt (6) and the head of bolt (3). To guide the springs over the bolt (3), a small cylinder (5) is used. This cylinder can also regulate the pre-load: a different length gives a different indentation of the springs and as a result a different pre-load. A hollow bolt (6) screws in the cylinder and runs over bolt (3). Its head makes contact with the last disc spring. Two long bolts (7) are there to prevent the bottom from opening when large loads are applied. Finally, discs with different thicknesses (8) are used to regulate the distance between the grips. For the range 0 – 10 mm, there are five setups (Table 5-1). There is a small overlap between the ranges, to make it user-friendly.

Table 5-1 Used setups to regulate the distance between the grips.

Height of the disc [mm]	Range [mm]		
31.2	0.00	–	2.20
23.4	1.75	–	4.95
15.6	4.50	–	7.70
7.8	7.25	–	10.45
No disc	10.00	–	13.20

Once the correct disc is chosen, a specimen can be mounted: bolt (6) is screwed out of the cylinder, which causes parts (3), (4) and (5) and the top wedge to move to the left. This results in the downward motion of the bottom wedge and both grips (1). Once these grips make contact with the specimen, the pre-load is placed on the system by further screwing out bolt (6). This causes a certain indentation of the disc springs, resulting in the pre-load.

5. 2. 2. d. Finite element modelling of the cylinder

For the design, the drawing package 'Solidworks 2003' was used. In this package, there is also a finite element module, 'COSMOS Express' which was used to determine the stress distribution in the cylinder.
In order to ensure an infinite fatigue life under loading of 100 kN, a safety factor of 3 with respect to the yield stress was taken into account when designing the cylinder. Because of the high loads, a high-strength steel was chosen. For the simulation, done with the COSMOS Express package, the following material constants were used:

Table 5-2 The used material constants in COSMOS express.

Elastic modulus [GPa]	210
Poisson's ratio [-]	0.28
Yield strength [MPa]	620
Mass density [kg/m^3]	7700

Applying a load of 100 kN in tension results in Figure 5-16, where the values of the Von Mises criterium are illustrated, the deformation is scaled with a factor of 598. The two bolts ((7) in Figure 5-15) are not simulated, meaning the worst case scenario is considered.

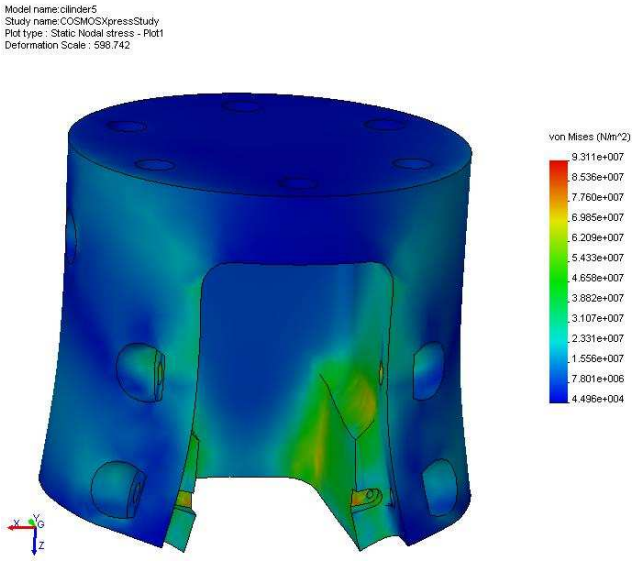

Figure 5-16 Von Mises stress distribution in the cylinder when applying a load of 100 kN. Deformation factor is 598; maximum stress level is 93.1 MPa.

The minimum factor of safety is 6.66, which means a maximum stress of 93.1 MPa when applying the maximum load of 100 kN. This should ensure infinite fatigue life.

The mechanical clamps were made out of two steels: the THYROPLAST 2311 and the THYROPLAST 3344 EFS. The first is a quenched and tempered plastic mould steel with a supplied hardness of 280-325 HB.

However, hardness and strength can still be modified by thermal treatment. This was done in order to achieve a material with a hardness of 51 HRC and a tensile strength of 1730 MPa. The material has no yield strength; the behaviour is linear till fracture. The DIN material number is 1.2311 and it is referred to as 40 CrMnMo 7. The chemical composition is listed in Table 5-3.

Table 5-3 Chemical composition for the THYROPLAST 2311, typical analysis in %.

C	Mn	Cr	Mo
0.40	1.5	1.9	0.2

The THYROPLAST 3344 EFS is also a quenched and tempered mould steel, but with a different chemical composition (Table 5-4), resulting in a better toughness and tensile strength. After quenching, the material has a hardness of 54 HRC and a tensile strength of 1910 MPa. The DIN material number is 1.2344 and is referred to as X 40 CrMoV 5 1. This material was recommended for the highest demands.

Table 5-4 Chemical composition for the THYROPLAST 2344 EFS, typical analysis in %.

C	Si	Cr	Mo	V
0.40	1.0	5.3	1.4	1.0

The cylinder, the grips, the hollow bolt (item (6) in Figure 5-15) and the fixing medium for the tensile machine have been produced with the THYROPLAST 2344, since these parts are subjected to the highest (fatigue) loads. All other parts have been manufactured in THYROPLAST 2311.
After production, the cylinders were nitrated for a higher surface hardness, since thermal hardening would result in large, intolerable deformations. The other parts are coated with a (black) nitrate layer with a 'niblox' treatment to avoid micro-welding of the surfaces. A detailed image of the clamp is shown in Figure 5-17; bolts (7) are omitted for a better view on the mechanism.

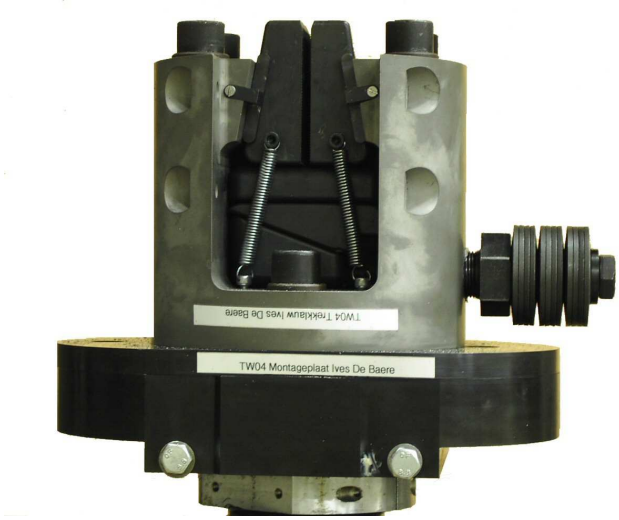

Figure 5-17 Detail of the clamp.

With these clamps, several static and fatigue experiments were performed in tension and compression. The clamps do not seem to have any demonstrable influence on the derived results, such as in-plane elastic properties and fatigue lifetime. Furthermore, the manufacturing of the clamps cost about one third the price of commercial hydraulic clamps.

5. 2. 3. Finite element verification of the contact pressure

In order to have a verification of the theoretical deduction in the previous paragraphs, a simulation of a part of the mechanism has been done in ABAQUS™/Standard v6.6-2. The purpose of this simulation is to verify if Equation 5.4 is accurate.

Figure 5-18 illustrates the simulated parts in the finite element model. Because of symmetry, only half of the clamps is modelled, which reduces calculation time. The corresponding symmetry boundary conditions have been imposed on the specimen. To further reduce computation time, a rigid body constraint is placed on part of the cylinder, only the area where the cylinder makes contact with the grip is left deformable. Furthermore, a part that models the wedge is added, also with a rigid body constraint to reduce calculation time. The reference point of this part is given a certain downward displacement. This part represents item 2 in Figure 5-15, although it could also represent the hydraulic plunger in the hydraulic clamps (Figure 5-3).

It must be noted that this part could be omitted and replaced by a downward force on top of the grip. This force would be equal to R_A in the deduction in the previous paragraphs. However, when doing so, the simulation required a lot of calculation time and often did not converge to a solution. Therefore, this model was used and a corresponding value of R_A was derived from the reaction force in the reference point of the wedge.

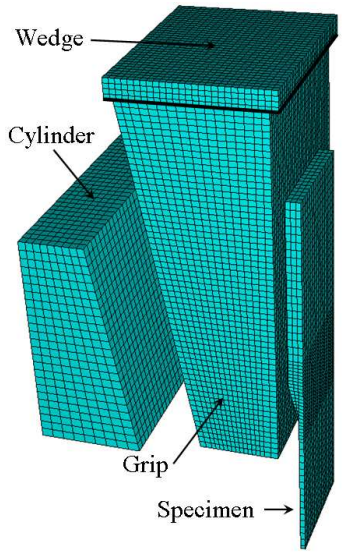

Figure 5-18 The simulated clamps in the finite element model.

Two time steps were implemented: in the first, the wedge was given a downward motion of 0.75 mm, simulating the tightening of the grips; in the second, the bottom of the specimen was pulled down over 1 mm, simulating a tensile test.
Contact conditions were imposed between the surfaces of the specimen and the grip, the grip and the cylinder and the grip and the wedge. Since the grip first follows the movement of the wedge and then the movement of the specimen, the slave surfaces of all contact conditions mentioned, were placed on the grips. Between specimen and grip, the tangential behaviour 'rough' was implemented, which means that no slip occurs once nodes make contact. For the other contact conditions, the 'lagrange' condition was used, which means that the tangential force is μ times the normal force, μ being the friction coefficient. The same friction coefficient was used for both conditions.
The grip was meshed with a C3D8R element, a linear brick element with reduced integration, whereas all other parts were meshed with C3D20R, a quadratic brick element with reduced integration. The C3D8R of the grip is required instead of the C3D20R, since the slave surfaces require midface nodes and the C3D20R do not have one.
For the grip, the wedge and the cylinder, steel was implemented with a Young's modulus of 210,000 MPa and a Poisson's ratio of 0.3. The specimen was modelled in a composite material with the following elastic properties (Table 5-5).

Table 5-5 The implemented engineering constants in the finite element model for the specimen.

E_{11} [MPa]	E_{22} [MPa]	E_{33} [MPa]	ν_{12} [-]	ν_{13} [-]	ν_{23} [-]	G_{12} [MPa]	G_{13} [MPa]	G_{23} [MPa]
56,000	57,000	9000	0.033	0.3	0.3	4175	4175	4175

Two simulations were performed, one with μ equal to 0.1 and one with μ equal to 0, which means no friction occurred. A value for R_A is derived from the reaction force of a reference point on top of the wedge and a value for F is calculated from the longitudinal stress in the specimen. With both values, an average contact pressure p_t can be calculated using Equation 5.4 and the following equation, with A_{tab} the surface of the contact area between tab and specimen:

$$p_t = \frac{P_t}{A_{tab}} \tag{5.21}$$

For comparison, an average contact pressure for the ABAQUS™ simulation is calculated by integrating the local contact pressure over the surface, yielding a resultant force, and dividing this resultant force by the surface of the tab A_{tab}.

An overview of both simulations is given in Table 5-6. Each simulation took about 33 hours of calculation time.

Table 5-6 Results of both the ABAQUS™ simulation and the prediction with the derived model (Equation 5.21).

Friction coefficient μ	[-]	0.0	0.1
Force F	[kN]	17.89	16.43
Force R_A	[kN]	3.78	18.09
Averaged p_t (ABAQUS™)	[MPa]	**67.33**	**66.97**
Predicted p_t (Equation 5.21)	[MPa]	**68.26**	**68.45**

It may be concluded that the theoretical model predicts the actual value very well. Finally, Figure 5-19 illustrates the actual contact stress distribution for the simulation with a friction coefficient equal to 0 together with the analytical prediction mentioned above. The simulations with μ equal to 0.1 yielded a similar contact stress distribution.

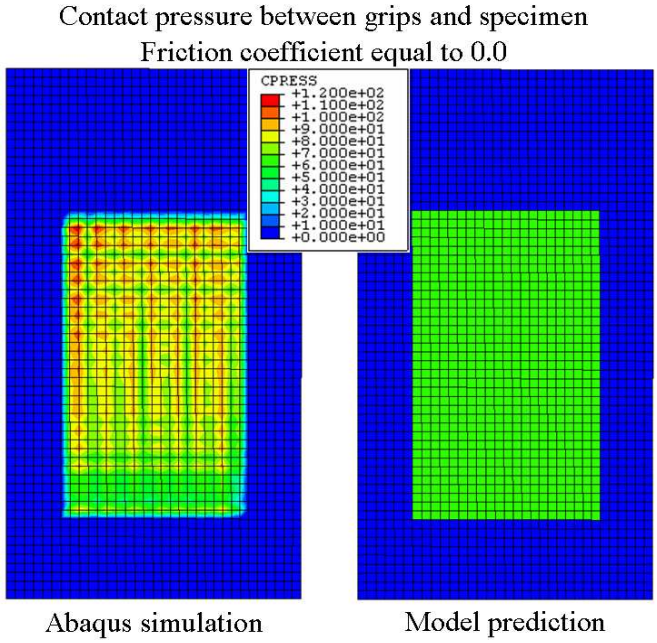

Figure 5-19 Illustration of the contact-stress distribution, calculated with μ = 0.0 for both the ABAQUS™ simulation and the prediction with the derived analytical model.

It may be noted that in the ABAQUS™ simulation, the contact pressure is not evenly distributed, but seems to have stress concentrations.
This, however, is a result of the combination of the used C3D8R elements for the grip and the 'Rough' contact condition.

The ‘Rough’ contact condition was implemented because it is the most accurate description of the real conditions, where the grips have a serrated surface and once the teeth penetrate the specimen surface, no slip occurs. Figure 5-20 shows the contact pressure between the grip and the cylinder (see Figure 5-18) where the contact condition ‘Rough’ was replaced by a ‘Lagrange’ law with a friction coefficient of 0.1. It can be seen that the pressure is evenly distributed.

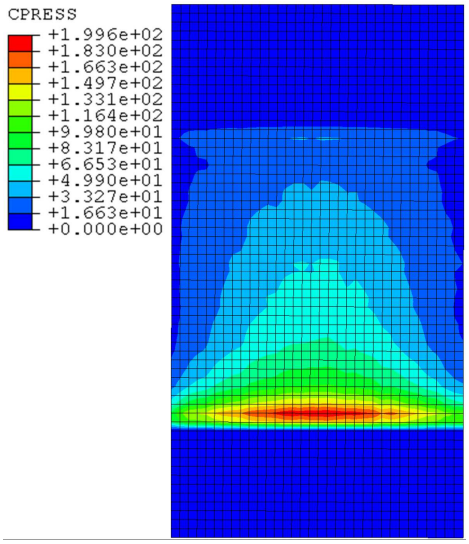

Figure 5-20 Distribution of the contact-stress between the grip and the cylinder. The contact condition was ‘Lagrange’ with μ equal to 0.1.

5. 2. 4. Conclusions

Based on the results obtained in the previous paragraphs, the following conclusions may be drawn:

- It is possible to design a set of mechanical clamps with extra long wedge grips, used for tension-compression fatigue.
- The design allows the use of long tabs or any other fixtures at the end of the specimen, e.g. optical fibres or contact electrodes for electrical resistance measurement.
- The proposed setup does not have any influence on the mechanical and tensile properties of the tested material in static tensile testing.
- The clamps are also suited for compressive testing. The obtained fracture is as expected.
- The mechanical design does not have a demonstrable influence on fatigue lifetime.
- The contact pressure, predicted by the derived model corresponds excellently with the results from the ABAQUS™ simulation of the clamps.

5. 3. THE USE OF END TABS

5. 3. 1. Introduction

It was already mentioned in chapter 3 that it is often necessary to use end tabs when performing quasi-static tests on fibre-reinforced materials, to prevent clamp failure. In chapter 3, the suggestions made in both the "*ASTM D3039/D3039M Standard Test Method for Tensile Properties of Polymer Matrix Composite Materials"* and the "*ISO 527-1 International standard for the determination of tensile properties"* were summarised. However, the ASTM and ISO standards only gave recommendations. The ASTM D3039/D3039M even mentions that '*design of mechanical test coupons remains to a large extent an art rather than a science*'.

While performing preliminary fatigue tests, regardless which norm was followed, usually failure occurred in the tabbed section of the specimen. Hence, a more extensive study on the use of end tabs was deemed necessary.
In open literature, there are very few articles on this subject. In most cases, end tab design is just a small remark when discussing experimental results, such as in [14, 15]. There are a few studies on the gripping of tubular specimens [16-18], but the occurring stress states are too different from the ones in tensile coupons. Ming Xie and Donald Adams have performed a study on tab configuration, but for compression testing of composite materials [19]. Kulakov et al. [20-22] have already done a similar study such as the one which will be described next, but on unidirectional reinforced epoxies. In their study, they consider different tab geometries, the effect of the adhesive and a few tab materials. They also present two loading schemes, based on a normal and tangential force and a friction coefficient, but no analytical formula to calculate the grip pressure for a given clamp geometry is given.

The emphasis of this section lays on different tab geometries presented in Figure 5-21, combined with four different materials (or composite lay-up) for the end tabs, by means of finite element modelling. The effect of the tabs being completely inside or partly outside the grips is examined, as well as the effect of the magnitude of the grip pressure. The latter cannot be controlled with mechanical clamps (Figure 5-3 on the left) but can be adjusted when using hydraulic clamps (Figure 5-3 on the right). In [19-22], a simplified load case, consisting of a normal and tangential frictional force, both derived from equilibrium equations, is considered whereas in this study, the occurring grip pressure in a tensile grip, of which the deduction is given in paragraph 5. 2. 2. a is used.

Four load cases are considered here:

- Bevelled end tabs, mounted with the grips 10 mm over the tab edge.
- Straight end tabs, mounted with the grips 10 mm over the tab edge.
- Bevelled end tabs, mounted with the tabs 10 mm outside of the grips.
- Straight end tabs, mounted with the tabs 10 mm outside of the grips.

These configurations are illustrated in Figure 5-21.

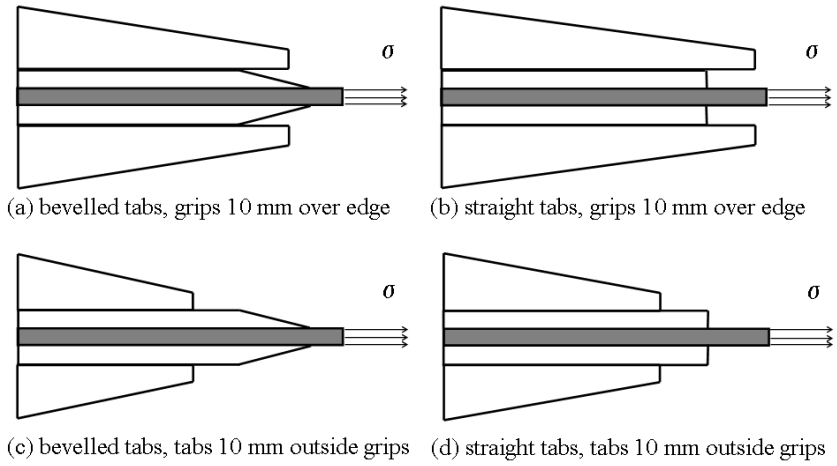

Figure 5-21 Different tab and clamping setups, discussed in this paragraph.

5. 3. 2. Finite element modelling

5. 3. 2. a. Introduction

In paragraph 5. 2. 2. a, a formula has been derived for the setup illustrated in Figure 5-22 that describes the interaction between the load F on the specimen, the force R_A of the plunger (see Figure 5-3) represented by part A and the contact force P on the specimen.

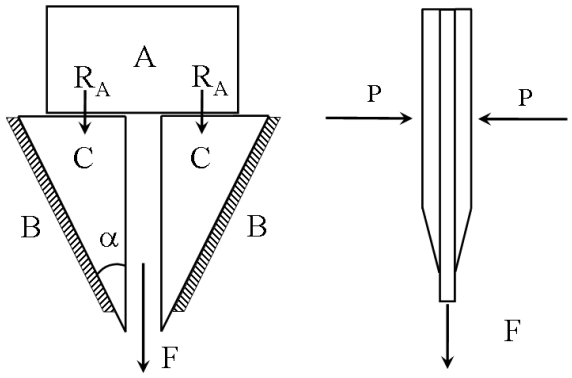

Figure 5-22 Symbolic representation of the gripping principle of a clamp.

The following equation was derived, with μ_{IJ} the coefficient of friction between parts I and J (I,J=A,B,C):

$$p = \frac{1}{A_{tab}}\left(\frac{F}{2}\frac{\cos\alpha - \mu_{BC}\sin\alpha}{\sin\alpha + \mu_{BC}\cos\alpha} + R_A \frac{(1-\mu_{AC}\mu_{BC})\cos\alpha - (\mu_{BC}-\mu_{AC})\sin\alpha}{\sin\alpha + \mu_{BC}\cos\alpha} \right) \quad (5.22)$$

For both grips displayed in Figure 5-3, the angle α is equal to 10 degrees.
Since Equation 5.22 is accurate enough to predict the contact pressure (see paragraph 5. 2. 3), there is no need to model the entire clamp to investigate the different setups proposed in Figure 5-21. For a given load in the specimen and a given force from the plunger, the contact pressure can be estimated by Equation 5.22. Therefore, a simplified model can be used.
For this simplified model, first a choice must be made concerning the dimensions of the tabs. The first possibility is to have equal tab length for all the setups in Figure 5-21. As a result, it would be very easy to compare the stress distributions along the tabbed section for the different geometries, for instance the location of possible stress concentrations. However, since the surface area of the gripped zone varies (tabs inside the grips or 10 mm outside the grips) this would result in different contact pressures, given by Equation 5.22 for a given grip force P and therefore, stresses resulting from different load cases are compared.
The second possibility is to have an equal contact pressure for all the setups. This gives more meaning to the comparison of stress distributions and stress concentrations, since they are the result of the same original loads. Of course, this results in different tab lengths, depending on the gripping setup. The author has chosen for the second option because the comparison of the stress distributions is more valid in this case.

According to the standards mentioned earlier, the clamped section was always chosen 50 mm. Depending on the gripping setup (Figure 5-21) this leads to simulated tab lengths of 60 mm for setup a, 50 mm for setup b, 70 mm for setup c and 60 mm for setup d. Since the thickness of the tabs is 2.4 mm, this results in a bevelled angle of 13.5º for the chamfered tabs in setups b and c.
The final configurations are depicted in Figure 5-23.

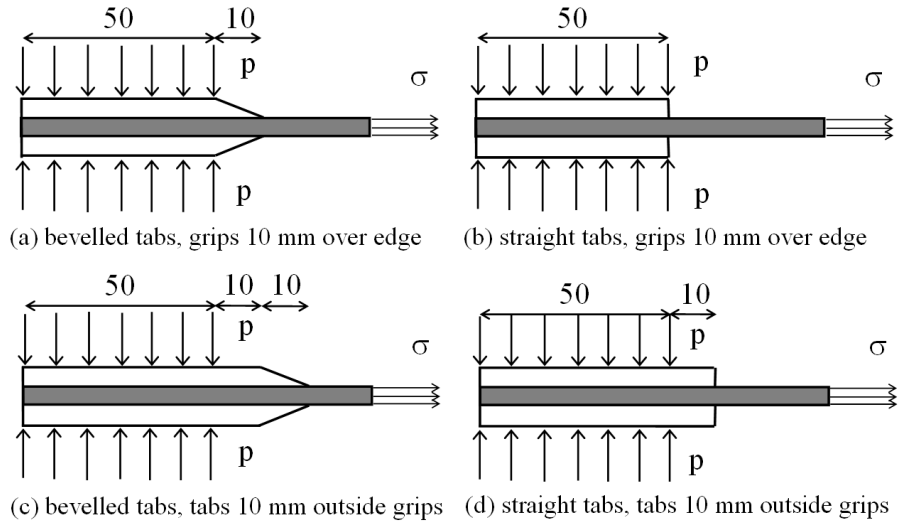

Figure 5-23 Different gripping setups, simplified model.

5. 3. 2. b. Finite element simulation of a simplified model

The finite element models of the four setups are similar to each other; the specimen for setup c is discussed. Figure 5-24 shows the model of this setup, both mesh and boundary conditions are illustrated.

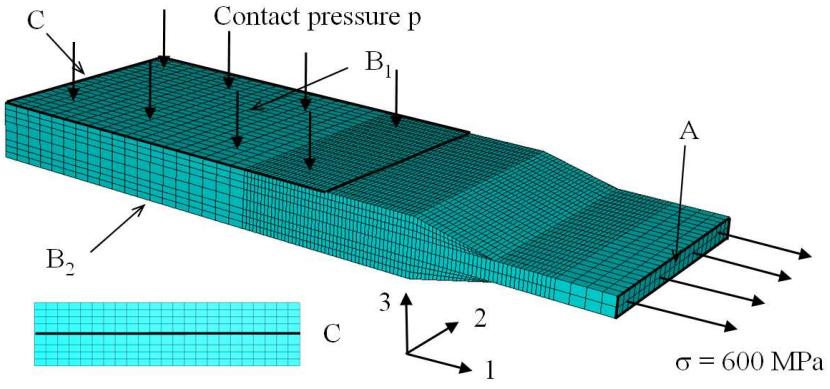

Figure 5-24 Illustration of the model for specimen type c.

The specimen is meshed using C3D20R elements using a global element size of 2 mm. Where stress concentrations were expected, the element size was reduced to 0.5 mm. The thickness of the specimen was 2.4 mm, which is also the thickness of the tabs, as has already been mentioned. The material properties for the composite specimen were already given in Table 5-5.

For the boundary conditions, the displacement along the 1- and 2-axis was inhibited for planes B_1 (on top) and B_2 (at the bottom), simulating the 'rough' boundary condition from the previous paragraph. Since contraction of the specimen is possible in the 3-direction due to the Poisson effect, the movement along the 3-axis was allowed for both planes. In order to prevent movement of the entire sample along the 3-axis, the central line of plane C (at the back) was fixed. This contraction may decrease the contact pressure under real circumstances, but the wedge effect of the grips should assure that only a small decrease is possible, so for the simulation, the contact pressure is kept constant.
Two time steps were modelled. In the first, the contact pressure p, calculated with Equation 5.22, was imposed. In the second, a tensile stress of 600 MPa was applied on surface A. The exact value of the stress does not matter, since the stress concentration factors will be compared. This value was chosen, since most of the experiments ended at about 600 MPa. The low fracture stress compared to the one given in chapter 3 (X_T = 734 MPa) is due to preliminary failure inside or under the edge of the tabs. This would mean that there is a stress concentration factor of about 1.25.

For the contact pressure, two series of calculations were done. The first represents the mechanical clamps in Figure 5-3, which corresponds with R_A equal to zero and the contact pressure p equal to 51.19 MPa. The second corresponds with the hydraulic clamps. For these clamps, INSTRON suggests a gripping pressure that is correlated with the applied load, because in a fatigue experiment, the grips should be pre-stressed so that the grips themselves are not fatigued. For the given load level of 600 MPa tension, INSTRON suggests a pressure level of 68 bar in the grips. As a result, R_A becomes about 10 kN and p is equal to 76.52 MPa.

Concerning the tab material, the following setups were tested.
(i) Carbon fabric-reinforced PPS, using a $[(+45^o,-45^o)]_{4s}$ setup, which is suggested by the standards. The mechanical properties are the same as in Table 5-5.
(ii) Glass fabric-reinforced epoxy, using a $[(+45^o,-45^o)]_{4s}$ setup, which is also suggested by the standards. The mechanical properties are given in Table 5-7.

Table 5-7 The implemented engineering constants in the finite element model for the glass-epoxy tabs.

E_{11} [MPa]	E_{22} [MPa]	E_{33} [MPa]	ν_{12} [-]	ν_{13} [-]	ν_{23} [-]	G_{12} [MPa]	G_{13} [MPa]	G_{23} [MPa]
24,000	24,000	6000	0.153	0.153	0.153	4830	4830	4830

(iii) Aluminium tabs, mentioned in the standards. The stiffness is equal to 70,000 MPa and Poisson's ratio is 0.3.

(iv) Carbon fabric-reinforced PPS, using a $[(0^o,90^o)]_{4s}$ setup, with the same mechanical properties as the sample. In this setup, there is no sudden change in the elastic properties between the specimen and the tab in the xyz coordinate system (x being the tension direction and z the through-thickness direction). The author expects that this would result in lower stress concentrations.

(v) Finally, the stress concentrations may also be the result of the used geometry of the specimen instead of the orthotropic nature of the composite and the combination of different materials. For example, it is well known that a sudden change in cross-section of a structure causes stress concentrations. To assess if this also occurs here, the entire setup has also been modelled in isotropic material, in this case steel, with a stiffness of 210,000 MPa and a Poisson's ratio of 0.3.

It must be noted that in this study, it was decided not to model the adhesive layer. As is mentioned in [21, 22], the adhesive will soften the occurring stress concentrations, so in this section, the worst case scenario is considered for all the setups. If the adhesive is modelled, then extra parameters will come into play, since an accurate model of the adhesive would require a damage law for the adhesive. One can choose a though adhesive, but with a low bonding strength to the surface, or a brittle adhesive with a high bonding strength. Also, the thickness of the layer has its influence. The effect of all these parameters for all mentioned setups has not been investigated.

A preliminary examination of the results yielded that the stress concentrations were the highest at the surface of the specimen. This was also reported in [21]. Therefore, the longitudinal stress σ_{xx} was plotted along a path central on the surface of the specimen. A typical result of this evolution is given in Figure 5-25 for the setup with the straight end glass epoxy tabs, mounted inside the grips. Both the simulation with $R_A = 0$ (mechanical grips, no pre-stress) and $R_A = 10$ kN (hydraulic grips with pre-stress) are depicted.

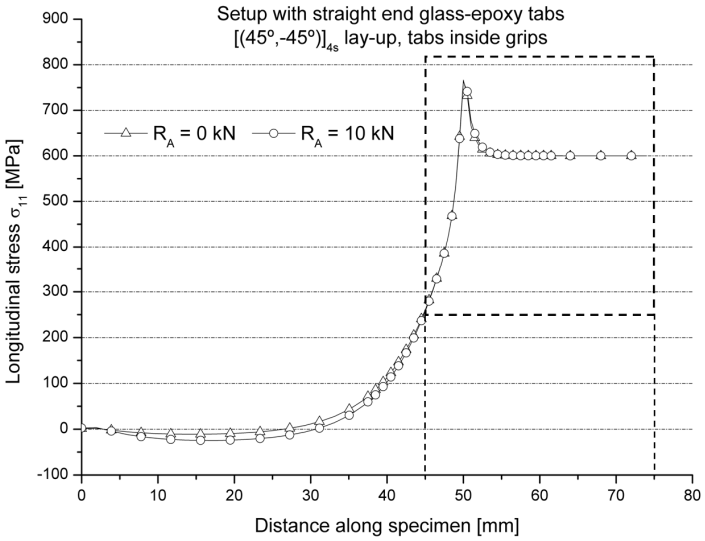

Figure 5-25 Evolution of the longitudinal stress along the surface of the specimen for setup b.

It may be remarked that the value of R_A has only a minor influence, although the contact pressure is fifty percent higher for R_A equal to 10 kN. Only underneath the tab, it seems to have some influence. Furthermore, it was noted that all of the graphs of the different setups showed an evolution similar to the one depicted. Since we are only interested in the zone around the peak stress, only the evolution inside the indicated rectangle in Figure 5-25 is considered. For an easier comparison of the different setups, the stress concentration factor is plotted instead of the absolute stress value, since the latter depends on the load in the specimen. This factor SCF is given by:

$$SCF = \frac{\sigma_{11}}{600MPa} \tag{5.23}$$

Another important load that needs to be considered is the peel stress between the end tab and the composite specimen. This stress gives an idea on how large the bonding strength of the adhesive should be, and considering the fact that PPS is not bonded very easily, this value should not be too high.

The peel stress σ_{33} was plotted along the same path as for the longitudinal stress. For the straight end glass epoxy tabs, mounted inside the grips, this yields the evolution depicted in Figure 5-26. Both the simulation with $R_A = 0$ and $R_A = 10$ kN are depicted.

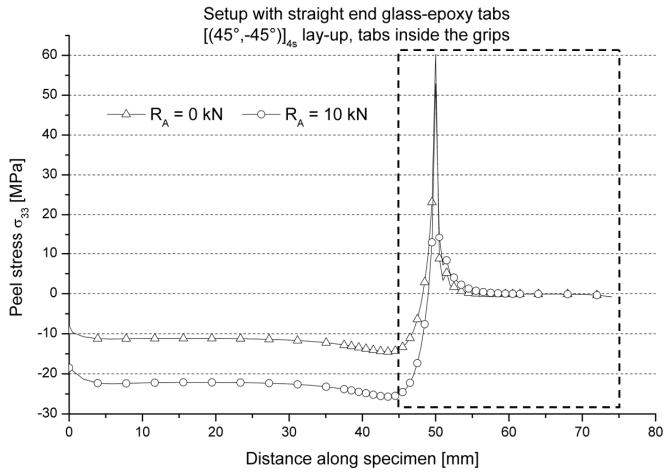

Figure 5-26 Evolution of the peel stress along the surface of the specimen for setup b.

It may be remarked that the value of R_A does not seem to have a very large influence on the maximum value, although the contact pressure is fifty percent higher for R_A equal to 10 kN. The latter can be seen underneath the tab (from 0 to 40 mm). Furthermore, it was noted that all graphs of the different setups showed an evolution similar to the one depicted. Since we are only interested in the zone around the peak stress, where the peel stress becomes positive and may lead to de-bonding of the tab, only the evolution inside the indicated rectangle in Figure 5-25 is considered.

5. 3. 3. Discussion of the simplified model simulations

Figure 5-27 till Figure 5-30 give the evolution of SCF for the different setups. It may be remarked that the value of R_A does not seem to have any influence on the values of the stress concentration factor, although the contact pressure is fifty percent higher for R_A equal to 10 kN. Only in Figure 5-28, a small difference between the curves of two corresponding setups may be distinguished. The position of the highest stress is always just left of the left end of the tab. All maximum stress concentration factors are summarised in Table 5-8 for the calculations with $R_A = 0$ and in Table 5-9 for $R_A = 10$ kN.

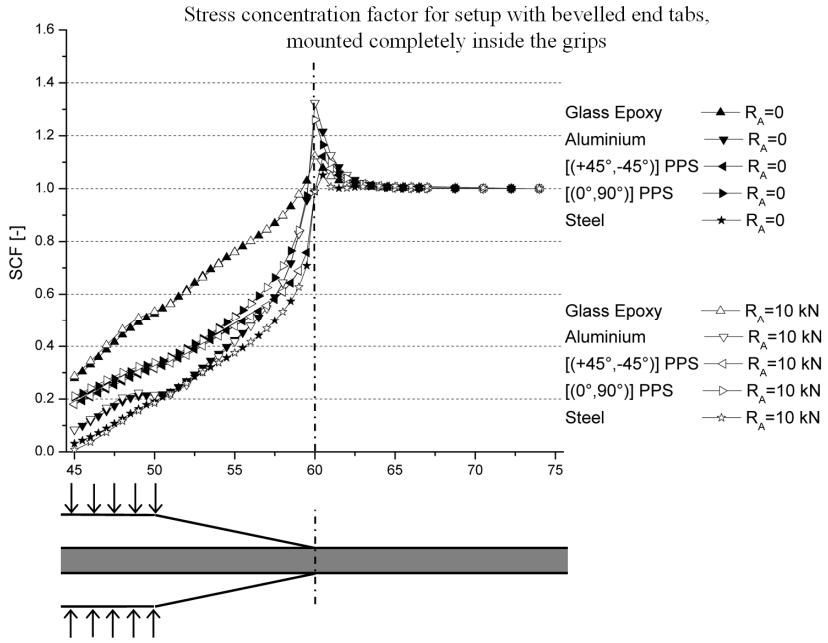

Figure 5-27 Detail of the evolution of the stress concentration factor along the surface of the specimen for geometry a.

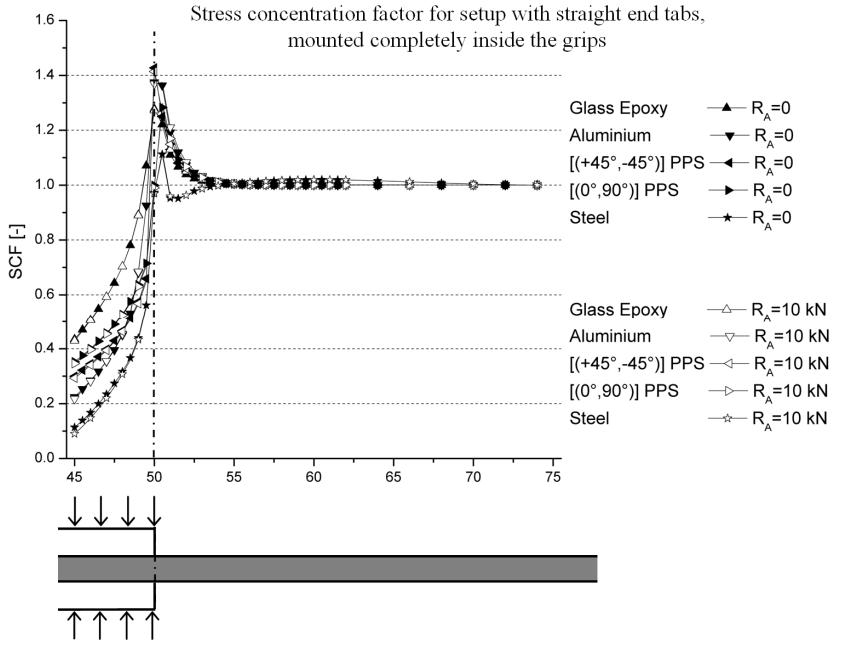

Figure 5-28 Detail of the evolution of the stress concentration factor along the surface of the specimen for geometry b.

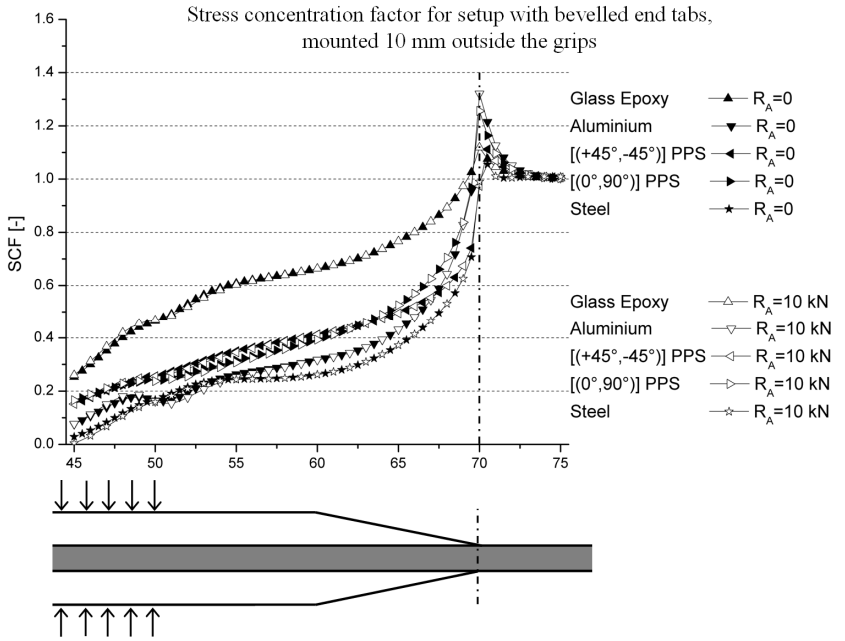

Figure 5-29 Detail of the evolution of the stress concentration factor along the surface of the specimen for geometry c.

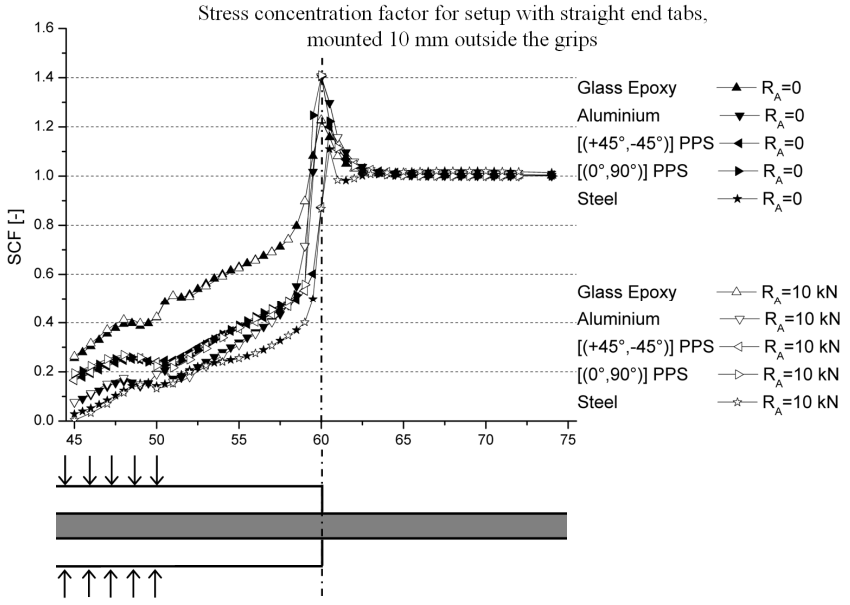

Figure 5-30 Detail of the evolution of the stress concentration factor along the surface of the specimen for geometry d.

Table 5-8 Maximum stress concentration factors for the mechanical clamps (R_A = 0 N).

R_A = 0 N	Glass-epoxy	Aluminium	C-PPS [(45º,-45º)]	C-PPS [(0º,90º)]	Isotropic
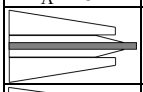	1.12	1.32	1.12	1.26	1.05
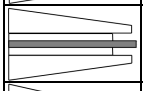	1.28	1.37	1.43	1.28	1.11
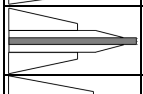	1.12	1.32	1.11	1.26	1.06
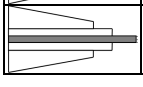	1.23	1.40	1.20	1.41	1.11

Table 5-9 Maximum stress concentration factors for the hydraulic clamps (R_A = 10 kN).

R_A = 10 kN	Glass-epoxy	Aluminium	C-PPS [(45º,-45º)]	C-PPS [(0º,90º)]	Isotropic
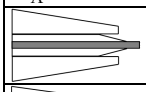	1.12	1.32	1.12	1.26	1.05
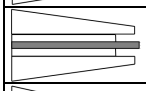	1.27	1.37	1.41	1.30	1.12
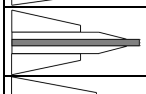	1.12	1.32	1.11	1.26	1.06
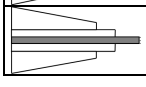	1.23	1.41	1.20	1.41	1.11

As could be expected, the stress concentration factors are the lowest for the isotropic material. It can also be seen that the contact pressure has very limited effect on these factors. In general, it may also be concluded that the bevelled tabs have lower stress concentration factors than the straight end tabs. From these tables, it can be concluded that the best setup for the presented material is to use either chamfered glass fabric-reinforced epoxy or carbon fabric-reinforced PPS tabs with the $[(+45º,-45º)]_{4s}$ lay-up.

It should however be noted that if the stresses are observed five to ten mm away from the end tab, the desired stress state (uni-axial loading) is achieved, as could be expected (principle of Saint-Venant). The orthotropic nature has of course a large influence on the stress state in the tabbed section, but is not the main reason for the stress concentrations. This can be derived from the fact that the stress concentration is still present in simulations with the isotropic material although lower than with the orthotropic material. This proves that it is not only the orthotropic nature that causes this stress state, but also geometry has its influence. Apparently, it is not the fact that the material is orthotropic, but rather a combination of the orthotropic constants and fibre orientation, which causes the stress concentration.

Changing the stacking sequence for the carbon-PPS tabs from $[(0°,90°)]_{4s}$ to $[(+45°,-45°)]_{4s}$ already gave a large decrease in stress concentration factor.

Figure 5-31 till Figure 5-34 give the evolution of the peel stress for the different setups. It may be remarked that the value of R_A does not seem to have any influence on the maximum values of the peel stress, although the contact pressure is fifty percent higher for R_A equal to 10 kN. Of course, underneath the tab, there is a large influence, as already mentioned, but since the peel stress is negative underneath the tab, this will not lead to de-bonding of the tab and as such does not pose a problem.
All maximum values of the peel stress are summarised in Table 5-10 for the calculations with $R_A = 0$ and in Table 5-11 for $R_A = 10$ kN.

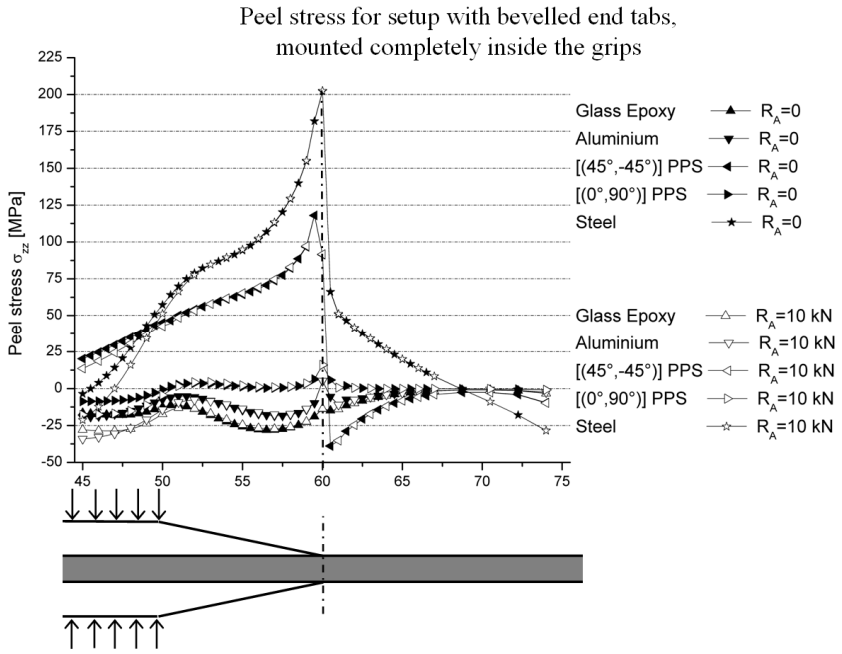

Figure 5-31 Detail of the evolution of the peel stress along the surface of the specimen for geometry a.

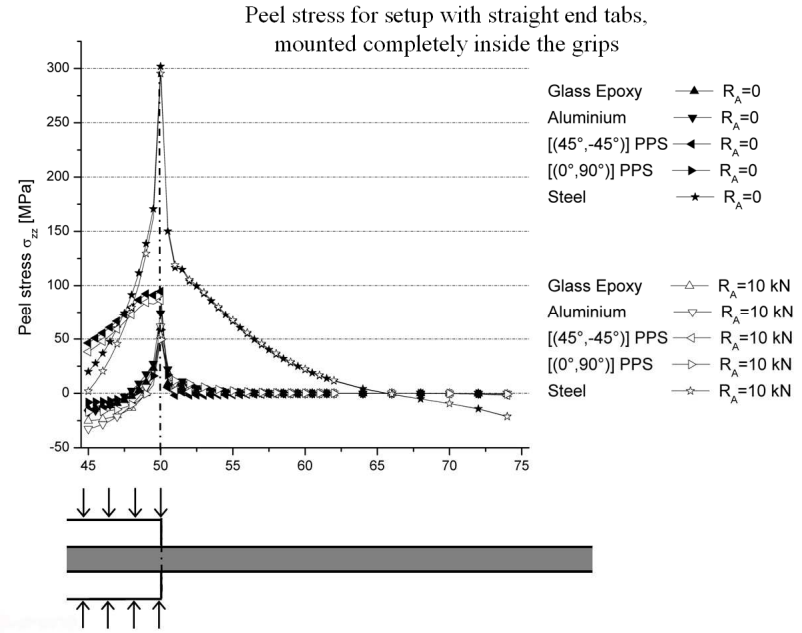

Figure 5-32 Detail of the evolution of the peel stress along the surface of the specimen for geometry b.

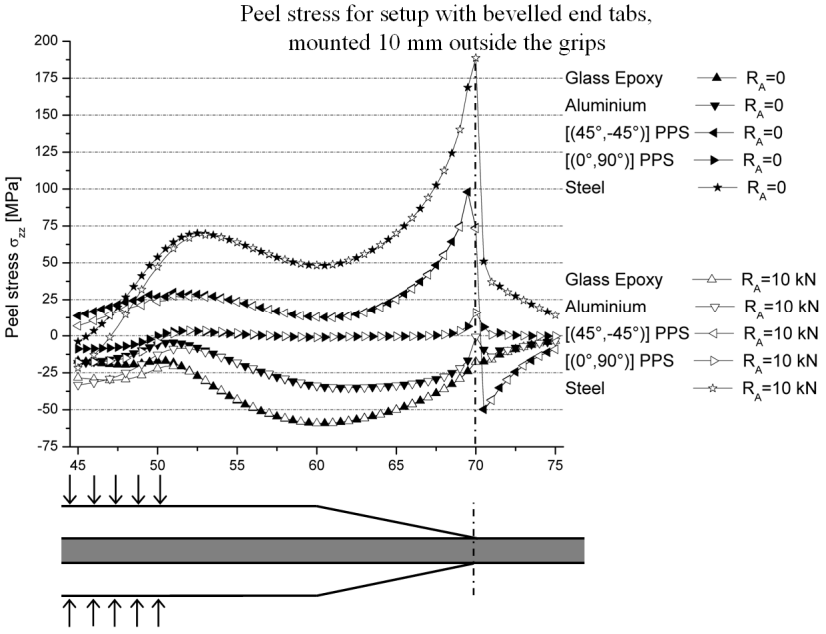

Figure 5-33 Detail of the evolution of the peel stress along the surface of the specimen for geometry c.

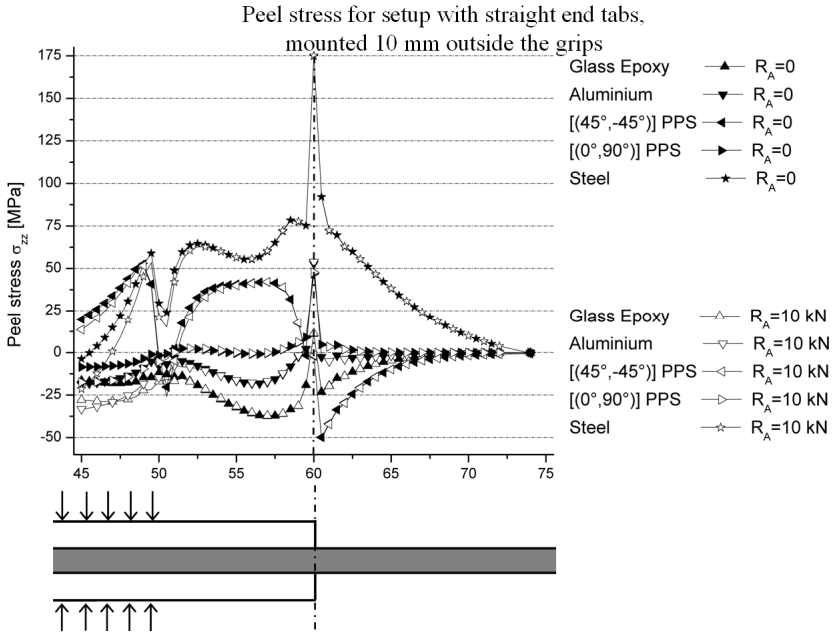

Figure 5-34 Detail of the evolution of the peel stress along the surface of the specimen for geometry d.

Table 5-10 Maximum peel stress [MPa] for the mechanical clamps (R_A = 0 N).

R_A = 0 N	Glass-epoxy	Aluminium	C-PPS [(+45º,-45º)]	C-PPS [(0º,90º)]	Isotropic
	60.31	74.27	94.60	58.44	301.89
	11.07	52.84	52.49	46.86	174.82
	-0.94	4.95	117.99	15.90	202.17
	0.004	-0.55	97.99	16.01	188.70

Table 5-11 Maximum peel stress [MPa] for the hydraulic clamps (R_A = 10 kN).

R_A = 10 kN	Glass-epoxy	Aluminium	C-PPS [(+45º,-45º)]	C-PPS [(0º,90º)]	Isotropic
	52.90	61.65	86.38	49.52	295.29
	11.35	53.81	51.64	47.70	175.16
	-2.76	5.20	118.39	15.99	202.53
	-0.03	-0.59	97.53	15.97	188.72

The maximum peel stress does not change significantly when the contact pressure increases, with exception of the setup with bevelled tabs inside the grips. An increase in pressure decreases the peel stress. With respect to the material combination, the glass-epoxy tabs have the lowest peel stress, with exception of setup a, where the carbon-PPS with $[(0^o,90^o)]_{4s}$ stacking sequence has a slightly lower value. Changing the stacking sequence from $[(+45^o,-45^o)]_{4s}$ to $[(0^o,90^o)]_{4s}$ drastically reduces the peel stress for the carbon-PPS tabs.
It should also be remarked that the values for the isotropic calculation are very high. This is probably due to numerical problems in the solver; when looking at the evolution of the peel stress for the isotropic simulation, it does not drop to zero immediately after the end of the tab, which is of course expected since this is an unloaded surface, where σ_{33} is zero. Refining the mesh did not solve this problem. Furthermore, for the straight end tabs, there will always be a singularity due to the 90° angle between tab and specimen. This will also cause a stress concentration due to numerical problems in the solver and refining the mesh will only make things worse.
With respect to the peel stress, again the glass-epoxy tabs are the best choice for the material and with respect to the setup, straight end tabs mounted 10 mm outside the grips tends to be the best choice, except for the $[(0°,90°)]_{4s}$ carbon-PPS and isotropic simulation, where the straight tabs should be mounted inside the grips.

Of course, what is mentioned above is only theoretical. An important remark must be made about the bonding of the tabs on the specimen, which of course relates to the peel stress. It is well known that thermoplastics do not bond easily and because of the chemical inertness of the polyphenylene sulphide, the latter surely is no exception. After numerous tests with different types of adhesives (see chapter 3), the author has come to the conclusion that, from all the combinations mentioned, PPS is bonded best to PPS. And even in this case, problems occur. Figure 5-35 illustrates the failure of the bond between the tabs and the specimen. In order to visualise this, both specimen and tabs were first painted white and afterwards, horizontal lines were drawn. This bond-failure already occurs at stresses lower than a third of the ultimate stress. In this figure, it is illustrated for the setup with straight end carbon-PPS $[(0°,90°)]_{4s}$ tabs, mounted outside the grips, but it also occurs for the other three setups. A similar fracture was also reported in [14] for a unidirectional-reinforced epoxy, so this problem also occurs for matrices that are more easily bonded.

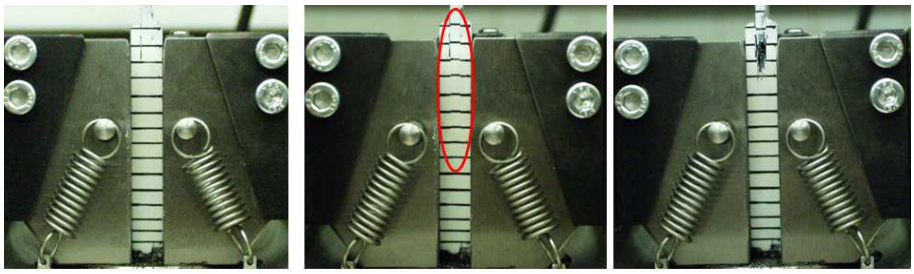

Figure 5-35 Illustration of the breaking of the bond between the tabs and the specimen, resulting in tab failure.

When performing a quasi-static test, sometimes the fracture occurs outside the tabs, but in a fatigue test, the breaking of the bond has a second effect. Since tab and specimen are no longer attached, the specimen is able to move inside the tabs. Because of the contact pressure applied by the grips, friction occurs, resulting in both wear and heating of the specimen. Since softening of the PPS already occurs at 90 ºC, it is no exception that the specimen breaks inside the tabs after very few cycles, not because fatigue life is reached, but because of the friction.

Another consequence of the lack of bonding is that theoretically, setups a, c and d become setup b once the bond is broken over a certain length. If this is considered, together with the fact that only PPS is bonded relatively well to PPS, than it may be concluded from both Table 5-8 and Table 5-9 that a straight $[(0^o,90^o)]_{4s}$ carbon fabric-reinforced PPS tab gives best results.

5. 3. 4. Conclusions

Based on the excellent correspondence between the simulated and the predicted contact pressure, given in paragraph 5. 2. 3, a simplified finite element model was developed to investigate which end tab geometry gives best results for tension (fatigue) tests on the material under study. Four different geometries and four different material combinations were examined. From these simulations, it could be concluded that a chamfered glass-epoxy or carbon-PPS with a $[(+45^o,-45°)]_{ns}$ stacking sequence gave lowest stress concentration factors. With respect to the peel stress, the glass-epoxy tabs are the best choice for all geometries.

However, due to the chemical inertness of the used material, resulting in a poor bond between tab and specimen, it is proposed to use straight end tabs with a $[(0^o,90^o)]_{4s}$ lay-up and to mount the specimen in such a way that the end tabs are completely between the grips. This yields higher peel stress but a lower stress concentration than if the tabs are slightly out of the grips. All tension-tension fatigue experiments discussed in this manuscript will be done with this geometry.

5. 4. FATIGUE EXPERIMENTS

5. 4. 1. Specimen geometry

The dimensions of the coupons used for fatigue experiments were chosen according the ASTM D3479 standard and are shown in Figure 5-36. The stacking sequence of specimen and tabs is $[(0^o,90^o)]_{4s}$.

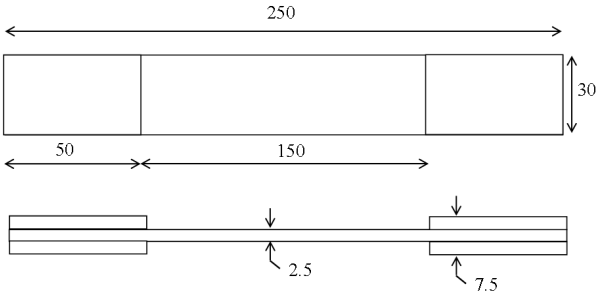

Figure 5-36 Dimensions of the used tensile coupon, equipped with end tabs.

Figure 5-37 illustrates such a specimen, with the dimensions mentioned above and Figure 5-38 shows the mounted specimen, equipped for longitudinal strain and temperature measurement.

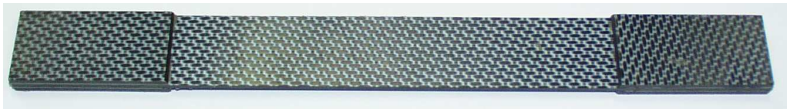

Figure 5-37 Example of a used specimen for fatigue testing.

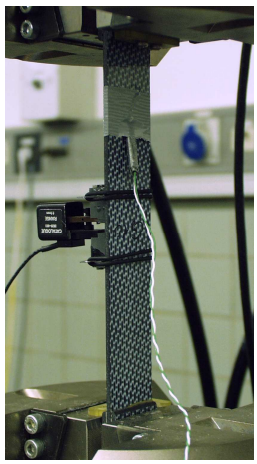

Figure 5-38 Specimen mounted in the tensile machine and equipped with the extensometer and thermocouple.

5. 4. 2. Performing fatigue tests

5. 4. 2. a. Data acquisition

Because of the long duration of a fatigue test, it is not possible to measure continuously at high frequencies. In order to have accurate results, the sampling frequency should be high enough to be able to accurately reproduce the sinusoidal signal. However, measuring continuously with those high frequencies would yield very large data files, which are difficult to process.
Since it is expected that damage grows only slowly throughout the fatigue test, it would suffice to measure a few cycles and then skip a certain number of cycles. The following procedure was implemented: every five minutes, five cycles are registered and written as a single line in a spreadsheet file. The used sample rate depends on the frequency of the signal and the number of columns available in the used spread sheet. For instance, if five cycles are registered for a 5 Hz signal, then the sample rate becomes 250 Hz, which fits the 256 columns available in EXCEL. For a 2 Hz signal, the sample rate becomes 100 Hz.
Furthermore, for each burst, the maximum, minimum and average value of the signal is calculated and stored in a separate file, so a general image of the evolution of a parameter throughout the fatigue experiment is obtained.
The force, displacement and longitudinal strain, given by the tensile machine, are always registered. For some experiments, the transverse strain was also measured, using a strain gauge. Because of the low Poisson's ratio, the transverse strain gauge survives a few hundred thousands of cycles. However, the longitudinal strain was only measured with the extensometer, since an axial strain gauge de-bonds after a few dozen cycles.

5. 4. 2. b. Test control mode

When conducting fatigue experiments, there are three possible choices for the control mode: (i) displacement-control; (ii) strain-control and (iii) load-control. The first option is not so interesting, since there will always be a limited amount of sliding in the grips. As such, it is very difficult to perform two experiments with exactly the same loading conditions, since the amount of sliding will differ. Furthermore, the amplitude and average value of both load and strain will change throughout the fatigue life, making them difficult to interpret. This option is only interesting if one is interested in the evolution of a fatigue parameter for a (guaranteed) constant displacement, for instance the force during a bending experiment. For tension-tension fatigue, this option is not considered.
For a strain-controlled test, the strain will vary between specified minimum and maximum values. As such, the amplitude and average value of the strain will remain the same throughout the fatigue test, making it easier to interpret the load signal.

However, even with the modified blades for the extensometer (see chapter 3), a strain controlled test is risky. If the blades shift over the surface of the specimen, then the tensile machine would compensate for this shift, which corrupts the fatigue load data, since the strain no longer cycles between the desired maximum and minimum value. If the shift is quite large, failure of the specimen and even damage to the tensile machine or extensometer may occur. Finally, it is very dangerous to perform strain controlled tests till failure, since this might damage both the extensometer and the tensile machine. As a result, this control mode is only used, when the advantage of a constant strain range is necessary, but for all other tests, load-control is used.

In a load-controlled test, the load (and as a result, the stress) will vary between specified minimum and maximum values. As a result, the amplitude and average value of the load and stress will remain the same throughout the fatigue test, making it easier to interpret the strain signal, with respect to permanent deformation and the evolution in stiffness. Furthermore, should a sudden shift in load occur, for instance because of sudden limited sliding in the grips, then the tensile machine of course will compensate, but contrary to the strain-controlled test, this will not corrupt the fatigue strain data. Furthermore, if the specimen fails, then the load will remain zero, which can be detected by the tensile machine if all corresponding settings are implemented correctly. As such, fatigue tests can be done until failure in load-control without the risk of damaging the machine.
As result, all fatigue experiments discussed here are done load-controlled, unless specified otherwise. The load range R is equal to zero, meaning that the stress varies between a minimum stress of $\sigma_{min} = 0$ MPa and a certain maximum stress σ_{max}. To avoid that the test would go in compression as result of a possible overshoot of the tensile machine, the specimen was always pre-stressed with a load of 0.5 kN meaning that σ_{min} is not exactly zero, but close to zero (about 6.6 MPa, depending on the actual dimensions of the specimen).

In order to have an estimate of which values of σ_{max} are interesting for studying fatigue damage, a large number of experiments were performed. For the following discussion, only one experiment of each group is shown, but the results were highly reproducible.

5. 4. 3. Experiments

Throughout the fatigue lifetime, damage can take many forms in fibre-reinforced composites [23, 24]: (i) matrix cracks, (ii) fibre-matrix interface failure, (iii) fibre pull-out, (iv) delaminations, (v) fibre fracture.

This damage affects the value of the elastic properties at an early stage. Especially in fatigue, the damage initiation phase can cause a pronounced drop of the elastic modulus of 5 to 10 %. In the next damage propagation phase, the stiffness continues to decrease gradually, ranging from a few percent for unidirectionally reinforced carbon composites to several tens of percents for multidirectional glass laminates [25-29]. Furthermore, most one-dimensional damage models for fibre-reinforced composites only account for the effect of damage on the stiffness [30-38]. As such, the first series of fatigue experiments focussed on the expected stiffness degradation.

A first test was done with a maximum stress of 400 MPa at 5 Hz. This stress is about 55 % of the static failure strain and the frequency is chosen as a compromise between the expected heat generation and the duration of the experiment. Figure 5-39 shows the evolution of the longitudinal strain and the temperature of this experiment. Since it is a load-controlled test, the amplitude of the strain corresponds with possible variations in stiffness and as can be seen, no real stiffness degradation occurs. Furthermore, there is only very limited permanent deformation. It should also be noted that there is no significant change in temperature. The test was stopped after 1,268,688 cycles without failure, or even any visible damage.

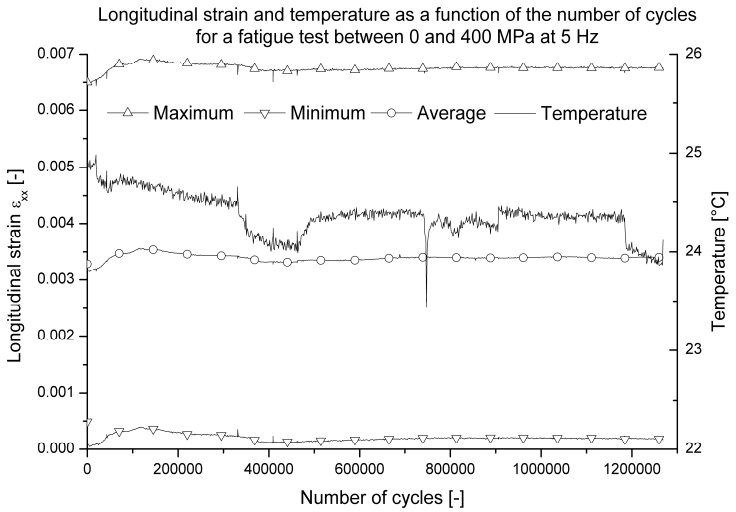

Figure 5-39 Maximum, minimum and mean value of the strain and the temperature during the 400 MPa@5Hz fatigue experiment.

The limited variations of the temperature are due the changes in the room temperature. The room where the experiments were conducted, has a climate control system but the variations in Figure 5-39 are within the range of this system.

In general, for all uni-axial fatigue experiments, no significant variation in temperature occurred, and all changes can be ascribed to variations in room temperature.
In order to evaluate the stiffness degradation, this experiment was paused regularly and displacement-controlled quasi-static tests at 2 mm/min were performed. These results are shown in Figure 5-40 and indeed no stiffness degradation occurs and only very limited permanent deformation can be seen, so higher stress levels are required. It should be noted that the stiffness corresponds quite well with the values derived in chapter 3 (resonalyser method E_{11} = 57 GPa). The small deviations are within the normal scatter of the elastic properties of composite materials.

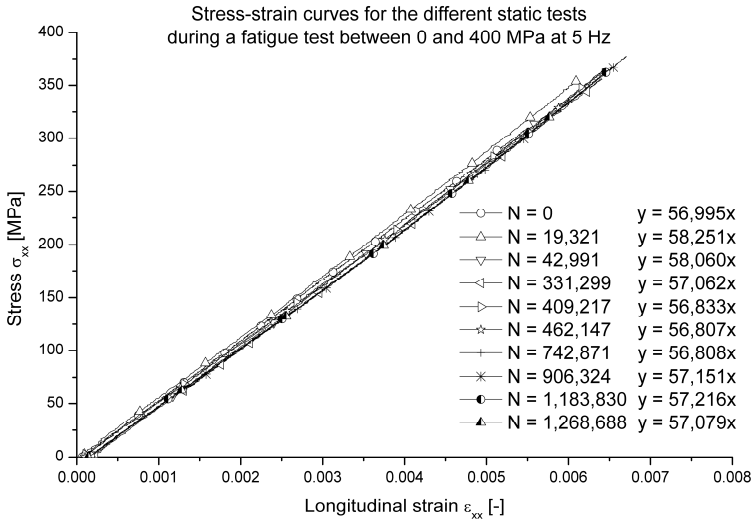

Figure 5-40 Results for the intermediate quasi-static tests from the 400 MPa@5Hz test.

The next experiment has a maximum stress level of 450 MPa also at 5 Hz. The evolution of the longitudinal strain and the temperature are shown in Figure 5-41. Again there is no significant change in temperature and no real stiffness degradation. The general evolution of the strain tends to be slightly increasing, but in general, the evolution does not differ that much from the 0-400 MPa@5Hz test. The experiment was stopped without failure or visible damage after 1,283,421 cycles.

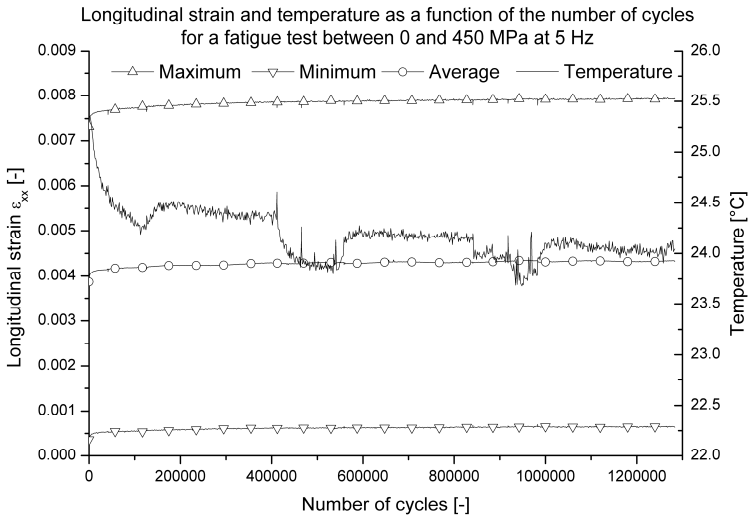

Figure 5-41 Maximum, minimum and mean value of the strain and the temperature during the 450 MPa@5Hz fatigue experiment.

Again, quasi-static tests were performed after a certain number of cycles. These stress-strain curves are shown in Figure 5-42.

It can be noted that again, no stiffness reduction or large permanent deformation occur, even at this higher maximum load level. The stiffness is slightly higher than the values derived in chapter 3 but the small deviations are within the normal scatter of the elastic properties of composite materials.

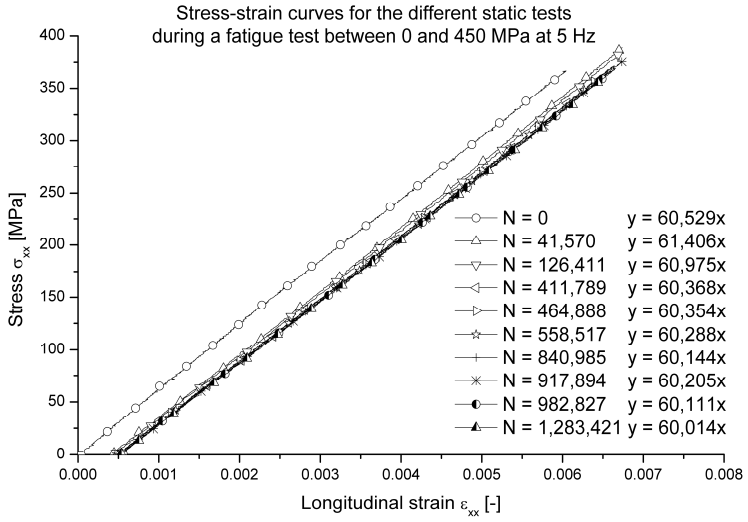

Figure 5-42 Results for the intermediate quasi-static tests from the 450 MPa@5Hz test.

Since the increase of 50 MPa did not yield different results, the maximum stress is now increased to 550 MPa. The results of such a test are shown in Figure 5-43. Yet again, there is no significant temperature change due to fatigue loading, nor does stiffness degradation or permanent deformation occur. The test was stopped after 1,217,500 cycles, again without failure or visible damage.

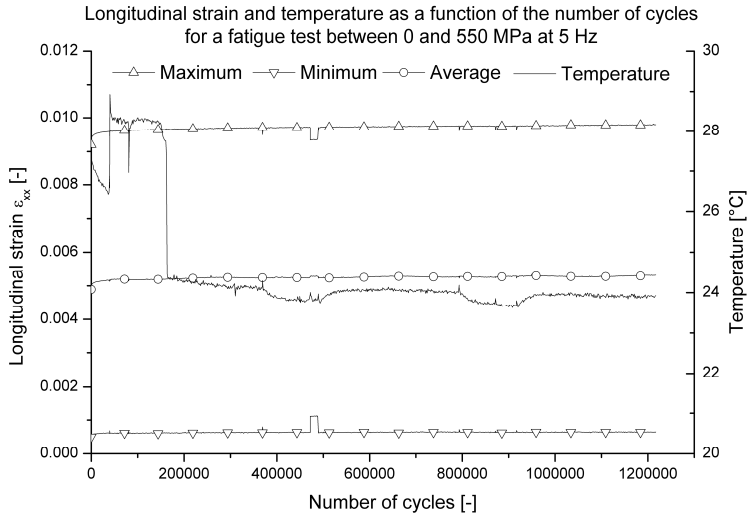

Figure 5-43 Maximum, minimum and mean value of the strain and the temperature during the 550 MPa@5Hz fatigue experiment.

The results of the performed quasi-static experiments are shown in Figure 5-44, but similar conclusions can be drawn: no stiffness degradation or significant permanent deformation occurs. Since the same conclusions with respect to stiffness degradation and permanent deformation can be drawn from the evolution of the strain throughout the fatigue experiment, there is no need for performing the intermediate quasi-static experiments. As such, they are no longer deemed necessary.

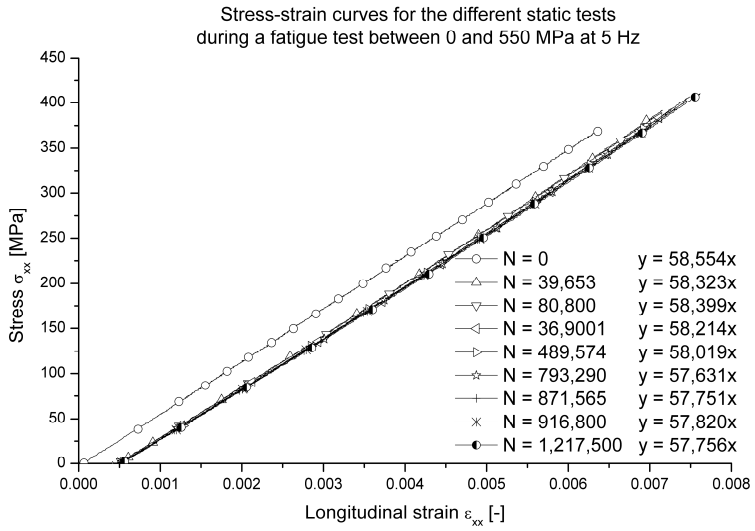

Figure 5-44 Results for the intermediate quasi-static tests from the 550 MPa@5Hz test.

When the intermediate quasi-static experiments are observed more closely, it appears that the limited permanent deformation tends to develop early in fatigue life. For the 450 MPa@5Hz test (Figure 5-42), after 41,570 cycles, the static curves are coincident; for the 550 MPa@5Hz test (Figure 5-44), the same can be said after 39,653 cycles.

Figure 5-45 shows the longitudinal stress-strain relationship of about sixty cycles during the run-in of a 550 MPa@5Hz experiment and as can be seen, the limited permanent deformation tends to develop in these first sixty cycles. This is also the reason why the minimum value of the strain does not start at zero in al fatigue graphics illustrated.

The derived stiffness during the run-in corresponds well with the values determined in chapter 3, although the displacement speed is a lot higher than 2 mm/min, required for quasi-static testing. As such, it can be concluded that the testing speed does not seem to have an influence on the Young's modulus.

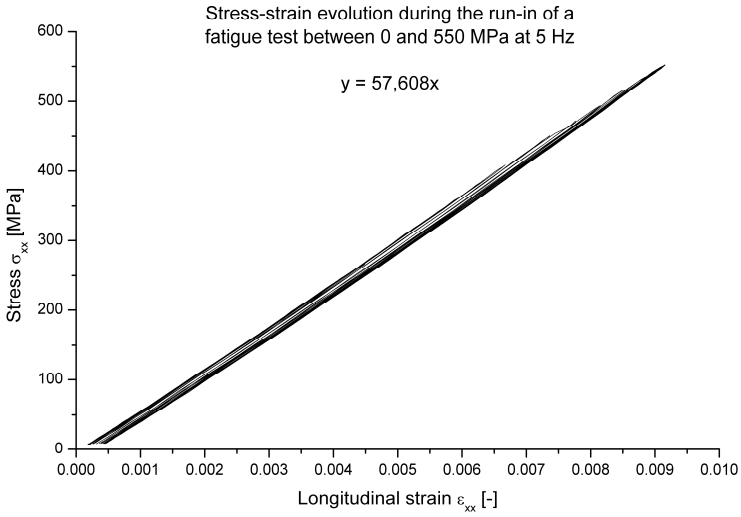

Figure 5-45 Stress as function of the strain for the run-in of a 550 MPa@5Hz experiment.

Almost all experiments with higher maximum stress levels of 575 MPa and 600 MPa failed during or soon after the run-in, so these result are not shown here.

A remark must be made concerning the fatigue test with 550 MPa as maximum stress level. The experiment shown here survived over 1,2 million cycles and a few others also survived one million cycles or failed soon afterwards. However, multiple specimens failed very early in the expected fatigue life, due to tab failure.
The reason was already mentioned in paragraph 5. 3. 3 when discussing the clamp simulations: due to failure of the adhesive over a certain length inside the grips, friction and wear occurs and the generated heat caused the premature failure. Therefore, two options are explored: (i) specimens without end tabs and (ii) a lower test frequency, so that less frictional heat is generated. The latter also allows investigating the effect of the frequency on the fatigue behaviour.
The first option always resulted in very early failure inside the grips, due to the stress concentration of the serrated surfaces of the grips. Therefore, the second option is investigated more thoroughly.
Figure 5-46 illustrates the temperature and strain evolution of a 2 Hz experiment with a maximum stress level of 550 MPa. Yet again, there is no significant stiffness reduction, nor permanent deformation. The specimen failed after 1,898,997 cycles in the vicinity of the end tabs, meaning the lifetime is underestimated, but besides the fracture, no visible damage could be detected.

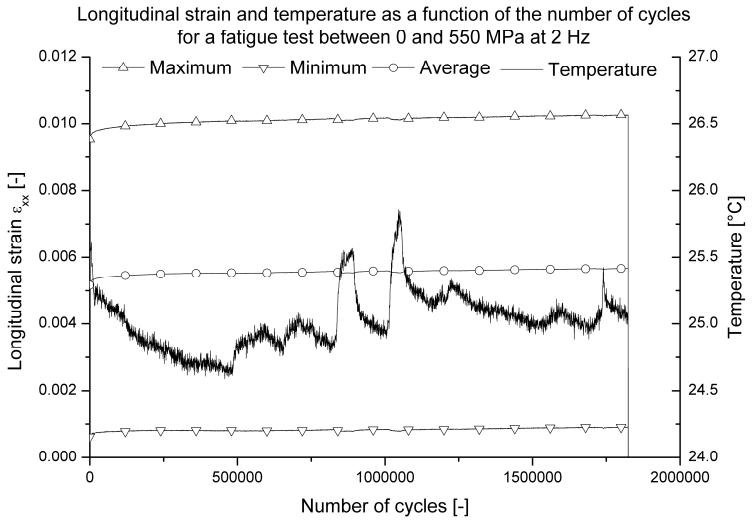

Figure 5-46 Maximum, minimum and mean value of the strain and the temperature during the 550 MPa@2Hz fatigue experiment.

Again it appears that the permanent deformation occurs during the first cycles. To validate this, Figure 5-47 shows about thirty cycles of the run-in of this experiment and as can be seen, most of the permanent deformation indeed forms during these first thirty cycles. The derived stiffness corresponds well with the values determined with quasi-static testing.

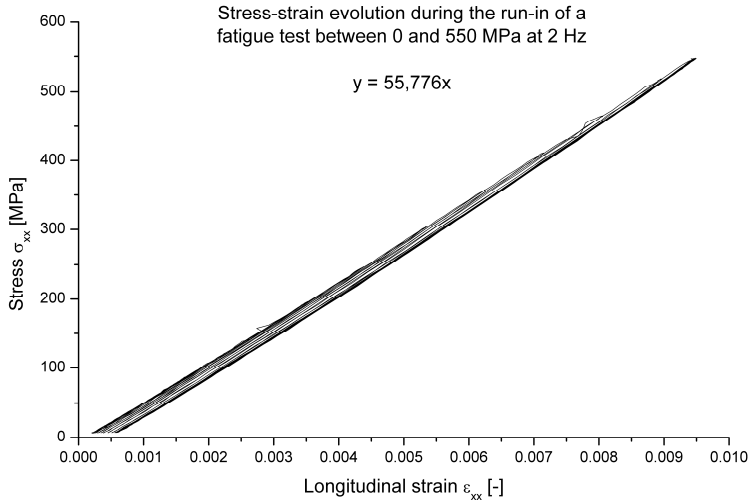

Figure 5-47 Stress as function of the strain for the run-in of a 550 MPa@2Hz experiment

Again, various experiments were performed, but the same conclusions as for the 5 Hz test frequency could be made with respect to the lifetime.

For σ_{max} equal to 550 MPa, a number of specimens survive over one million cycles, but multiple specimens fail very early in the expected fatigue life, due to frictional heating in the tabs. For a higher maximum stress level, the specimen fails during or soon after the run-in.

As previously mentioned, most of the specimens failed inside the tabs, due to frictional heating. However, acceptable failures in vicinity of the centre of the specimen also occurred. Figure 5-48 and Figure 5-49 illustrate such fracture, which occurred halfway the specimen. When visually inspecting the side of the specimen, no delaminations could be detected. It should be mentioned that all fractures, both inside and outside the tab area, were similar to the one depicted.

Figure 5-48 Fatigue fracture outside of the tab area, seen from above the failure.

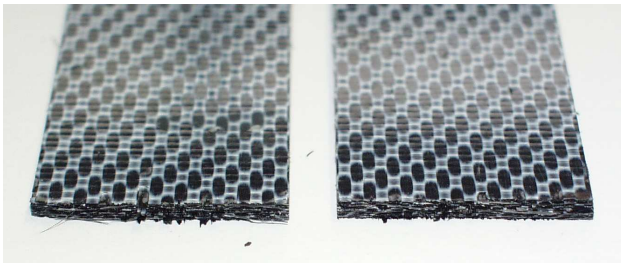

Figure 5-49 Fatigue fracture surface.

5. 4. 4. Conclusions

Figure 5-50 summarises all successful fatigue tests, meaning that the specimen did not fail prematurely, failed inside the tabs or that the end tabs de-bonded. Some of these tests are already discussed and others will be discussed in the remainder of this chapter.

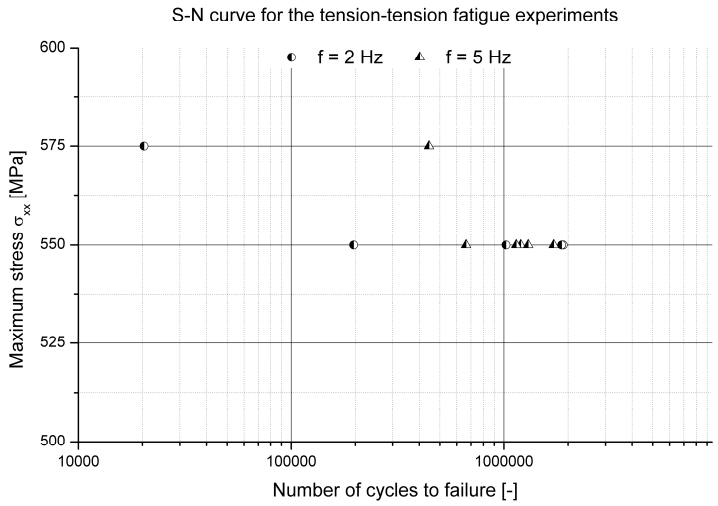

Figure 5-50 S-N curve for all uni-axial fatigue experiments discussed in this chapter

With respect to the stiffness reduction, no significant decrease could be found. In [39] a significant stiffness reduction was found, but for a carbon fibre-reinforced epoxy. This illustrates the differences of fatigue behaviour of thermosetting and thermoplastic matrices.
With respect to the permanent elongation, it may be said that almost no permanent deformation occurs because of the fatigue loads. Only during the first fifty cycles or so, a limited amount of permanent deformation is formed.
Therefore, it can be said that the material itself has a very brittle behaviour. It breaks very sudden without any visible or audible cracks before failure.

It is however still assumed that something must deteriorate in the material due to the fatigue loading conditions. Therefore, other less common parameters are investigated. In the next paragraph, the evolution of Poisson's ratio under fatigue loading conditions is investigated and at the end of this chapter, the electrical resistance measurement is used to monitor the fatigue experiments, due to the promising results obtained in the two previous chapters. In these discussions of course more fatigue results are shown.

5. 5. EVOLUTION OF POISSON'S RATIO

5. 5. 1. Introduction

When discussing the quasi-static hysteresis tests in chapter 4, it was noticed that the decrease in Poisson's ratio was more significant than the stiffness decrease, which is virtually non-existent. Therefore, it is assessed whether the evolution of Poisson's ratio is able to give more information on the damage growth inside the material.
This degradation has already been observed and is not negligible [40, 41]. Bandoh et al. showed that the Poisson's ratio of a carbon/epoxy UD laminate can drop by 50 % under static tensile loading [40], while Pidaparti and Vogt proved that the Poisson's ratio is a very sensitive parameter whilst monitoring fatigue damage in human bone [41].
As was done in chapter 4 for the hysteresis tests, this phenomenon is first assessed by performing some experiments on the unidirectional glass fabric-reinforced epoxy, since this material has a higher Poisson's ratio than the carbon fabric-reinforced PPS and therefore, the decrease may be more easily visualised.
The longitudinal strain is measured with the extensometer, but the transverse strain is measured with strain gauges. As such, measurements till failure are difficult to achieve, since the transverse strain gauge is most likely to de-bond before the specimen fails, given the very large number of cycles to failure at 550 MPa.

The modifications made to the extensometer in order to measure transverse strain as discussed in chapter 4, did not give accurate results for fatigue measurements. Apparently, the higher deformation speed caused the blades to shift more easily, despite the pointed blades; given the very low value of the transverse strain, this made the measurement useless. Since the peculiar behaviour of Poisson's ratio did not seem to be the result of the use of strain gauges, it is expected that if the behaviour occurs during fatigue experiments, it will also not be caused by the strain gauges. As such, only transverse strain gauges were applied for the measurements in this chapter.

Since the Poisson's ratio is no more than the ratio of transverse strain and longitudinal strain, it would be more meaningful to perform these experiments in a strain-controlled manner. As such, any effects of stiffness decrease will not effect the decrease in Poisson's ratio, since the outer strain boundaries will always be the same. Of course, the problems of a shift of the extensometer blades, as mentioned in paragraph 5. 4. 2. b are still present. However, for the unidirectional glass fabric-reinforced epoxy, the surface is fairly rough and such a shift is not so likely to happen.

Therefore, the experiments performed on this material were done strain-controlled. The surface of the carbon fabric-reinforced PPS, however, is much smoother and preliminary tests have shown that such a shift may occur, even with the new three-point blade design. However, since there is virtually no stiffness degradation, the change of the outer strain boundaries of a load-controlled fatigue test will not change that much, thus all experiments on this material are done load-controlled. This has also the advantage of an easier comparison with the results already presented in this chapter.

5. 5. 2. Unidirectional glass fabric-reinforced epoxy

Figure 5-51 illustrates a specimen, mounted in the tensile machine and equipped for temperature, longitudinal and transverse strain measurement.

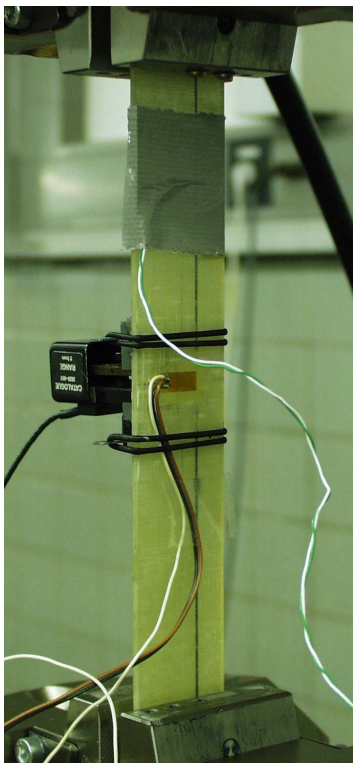

Figure 5-51 Specimen mounted in the tensile machine and equipped with a transverse strain gauge, the extensometer and thermocouple.

A detailed image of the extensometer and strain gauge is shown in Figure 5-52. It was always attempted to measure longitudinal and transverse strain on the same area of the specimen.

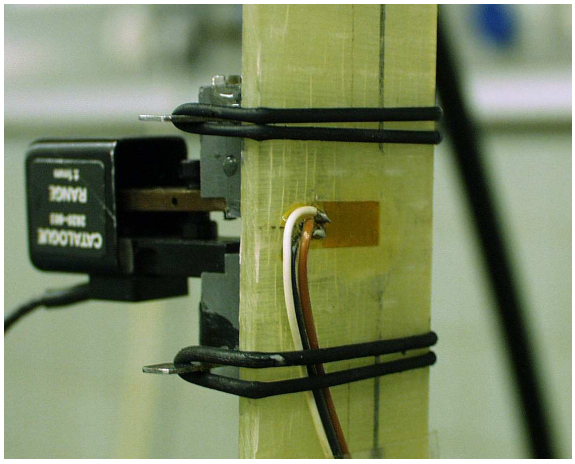

Figure 5-52 Detail of the mounted extensometer and transverse strain gauge for measuring Poisson's ratio.

Several similar fatigue experiments were performed, but all yielded similar results, so only one of these experiments is discussed in detail. The fatigue test was done strain-controlled between $\varepsilon_{xx}^{min} = 0.0006$ and $\varepsilon_{xx}^{max} = 0.006$, yielding a strain ratio of 0.1 (similar to stress ratio $R = \sigma_{min}/\sigma_{max}$) and with a loading frequency of 2 Hz. Before the start of the experiment, a quasi-static tensile test was done to determine the value of the Poisson's ratio. The specimen was loaded only to 0.001 longitudinal strain, because the failure strain of the 90° plies is 0.0025 (see chapter 3). Intermediate quasi-static tests were done after 7,500 and 22,800 cycles in the same strain range as the fatigue experiment.

The results of these three quasi-static tests are shown in Figure 5-53. It can be seen that the initial value of the Poisson's ratio is about 0.15. The scatter is quite large in the initial strain regime, due to the very low axial strains ε_{xx} and even lower transverse strains ε_{yy}. However, at an axial strain ε_{xx} of 0.001, the Poisson's ratio converges to a more or less constant value of 0.15. In the intermediate static tests at cycles 7,500 and 22,800, the same evolution as found for the quasi-static cyclic tests in chapter 4 appears.

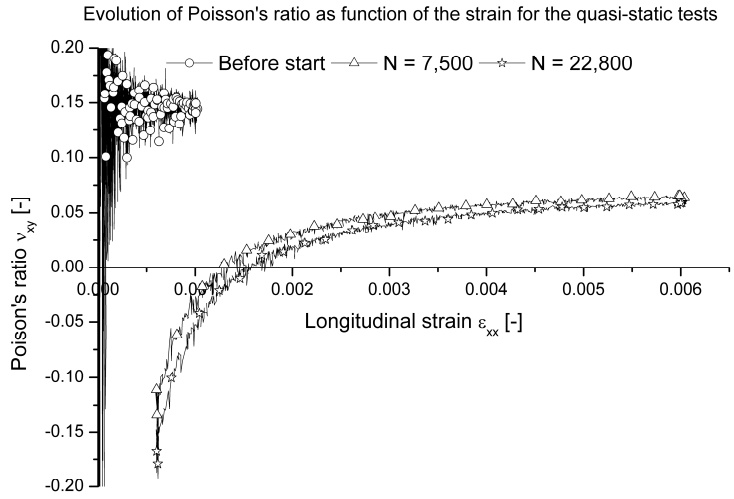

Figure 5-53 Evolution of Poisson's ratio as function of the longitudinal strain for the quasi-static tests.

To verify whether the same shape of the curve occurs during fatigue cycling, the results during a few fatigue cycles are depicted in Figure 5-54. The same shape as during the intermediate quasi-static test appears, meaning that the shape of this curve is not affected by the real-time measurement during fatigue loading.

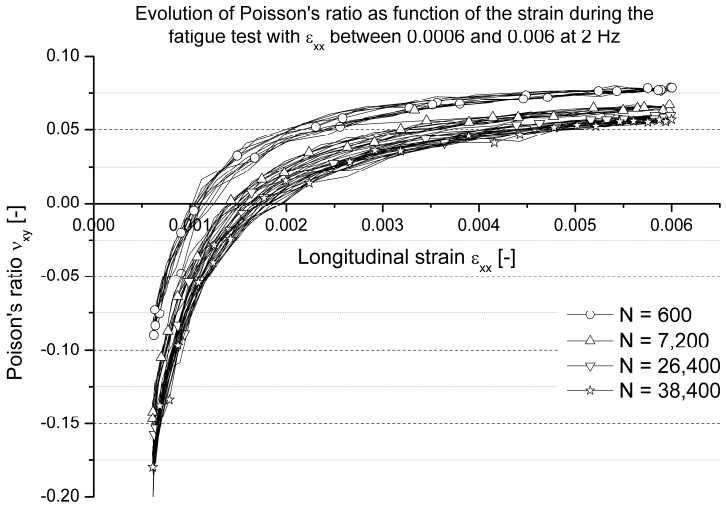

Figure 5-54 Evolution of Poisson's ratio as function of the longitudinal strain during the fatigue test at 2 Hz for ε_{xx} between 0.0006 and 0.006.

As previously mentioned, more fatigue tests have been performed and they all confirm the results mentioned above [42].

Therefore, it is expected that the carbon fabric-reinforced PPS will show a similar behaviour, since the same evolution of the Poisson's ratio as function of the strain was found for the quasi-static cyclic tests, discussed in chapter 4.

5. 5. 3. Carbon fabric-reinforced PPS

Figure 5-55 illustrates a specimen, mounted in the tensile machine and equipped for temperature, longitudinal and transverse strain measurement.

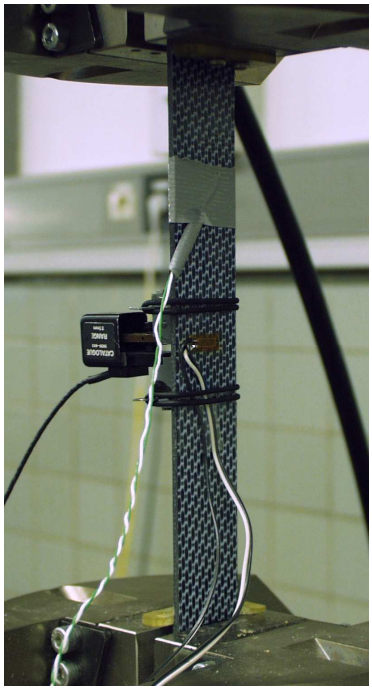

Figure 5-55 Specimen mounted in the tensile machine and equipped with a transverse strain gauge, the extensometer and thermocouple.

A detailed image of the extensometer and strain gauge is shown in Figure 5-56. It was always attempted to measure longitudinal and transverse strain on the same area of the specimen.

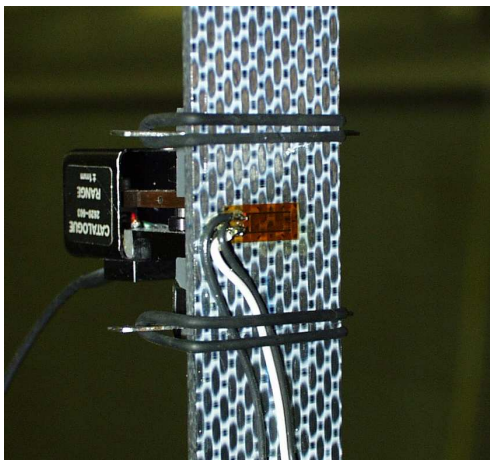

Figure 5-56 Detail of the mounted extensometer and transverse strain gauge for measuring Poisson's ratio.

A first test was done at a frequency of 2 Hz and a maximum stress level of 550 MPa. The evolution of the stress as function of the strain during the run-in is shown in Figure 5-57; the derived stiffness corresponds well with the expected value and the expected amount of permanent strain is developed.

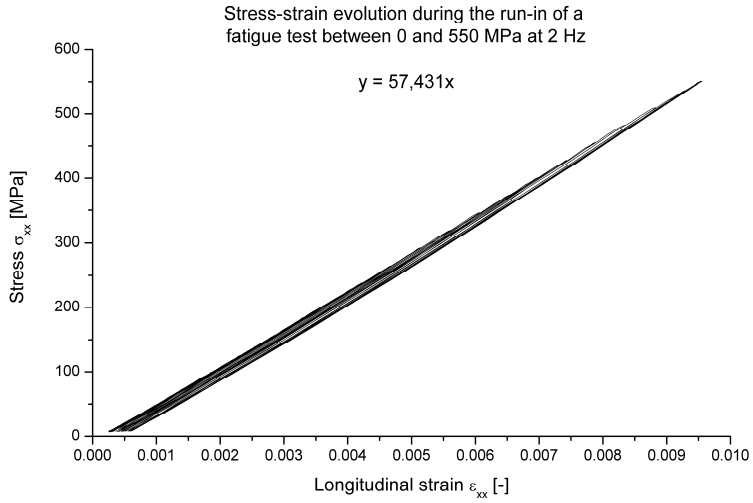

Figure 5-57 Stress as function of the strain for the run-in of a 550 MPa@2Hz experiment.

The corresponding evolution of Poisson's ratio is shown in Figure 5-58; the initial value is slightly higher than the one derived in chapter 3 and 4 ($\nu_{12} = 0.033$).

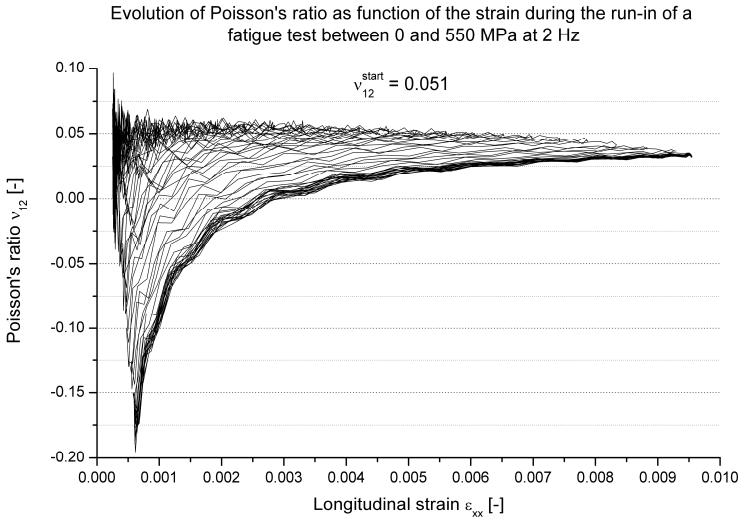

Figure 5-58 Evolution of Poisson's ratio as function of the longitudinal strain for the run-in of the 550 MPa@2Hz test.

Again, the very characteristic evolution, seen with the hysteresis tests in chapter 4, manifests itself. Also, the value is decreasing very rapidly, after about thirty cycles, the Poisson's ratio decreases from the initial 0.051 to about 0.03.

Figure 5-59 illustrates the evolution of the measured strains until the transverse strain gauge de-bonded after 282,280 cycles. For the longitudinal strain, the expected evolution is found and remains the same until failure of the specimen at 1,022,492 cycles. The transverse strain, however, shows a completely different evolution: a significant permanent deformation can be seen.

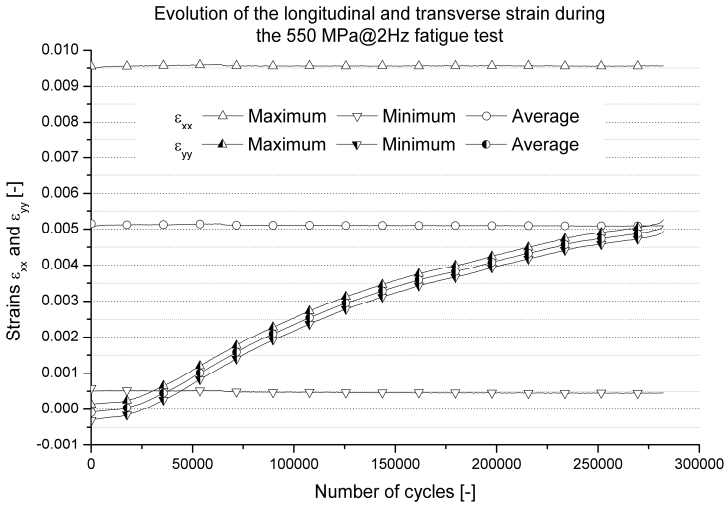

Figure 5-59 ε_{xx} and ε_{yy} during the 550 MPa@2Hz fatigue test.

These evolutions of the strain result in the following evolutions of the Poisson's ratio during the fatigue test (Figure 5-60). It should be noted that very early in fatigue life, the ratio becomes lower than zero and the characteristic form of the evolution, which was seen in chapter 4 for the quasi-static hysteresis experiments and during the run-in of the test, becomes more and more apparent for higher numbers of fatigue cycles.

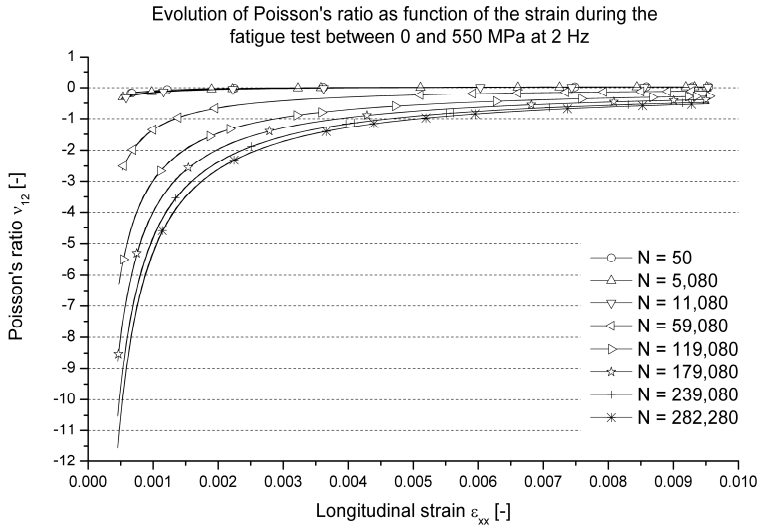

Figure 5-60 Evolution of Poisson's ratio as function of the longitudinal strain during the 550 MPa@2Hz test.

During this experiment, the temperature was recorded, but as expected, no rise in temperature occurred.

For the next experiment, the same load range was chosen, but the test frequency was increased to 5 Hz. Figure 5-61 shows the stress-strain evolution for the run-in of this experiment and again, during the first sixty cycles, the permanent deformation develops and there is no stiffness degradation; the initial stiffness shows good agreement with the expected value, derived with the resonalyser method (chapter 3).

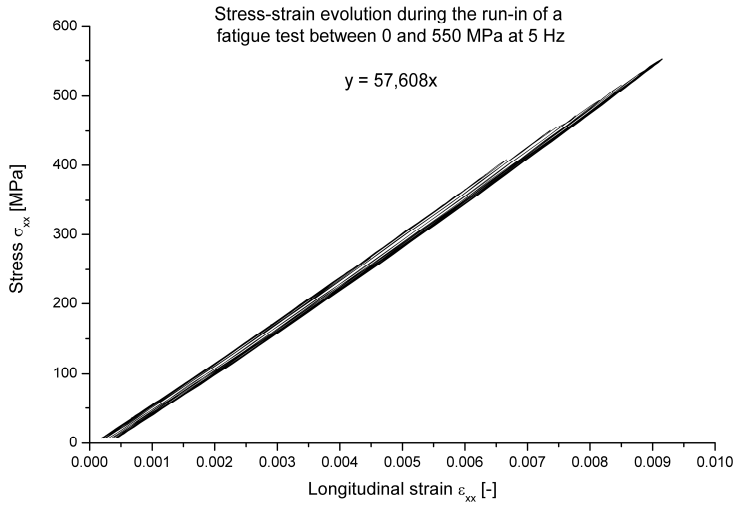

Figure 5-61 Stress as function of the strain for the run-in of a 550 MPa@5Hz experiment.

The evolution of Poisson's ratio during the run-in of this experiment is shown in Figure 5-62. Similar to the 2 Hz experiment, after about sixty cycles, the value tends to go below zero. The initial value corresponds very well to the values derived in chapter 3 and 4.

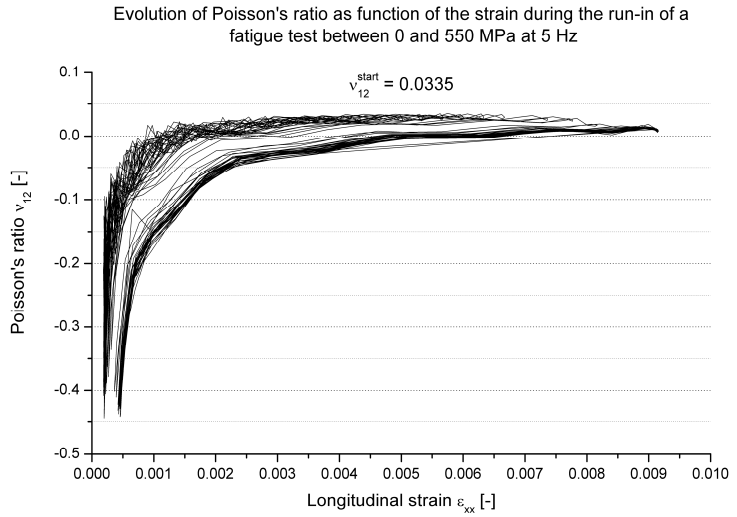

Figure 5-62 Evolution of Poisson's ratio as function of the longitudinal strain for the run-in of the 550 MPa@5Hz test.

Figure 5-63 illustrates the evolution of the measured strains until the transverse strain gauge de-bonded after 265,792 cycles. This value corresponds very well with the 2 Hz test. For the longitudinal strain, again the expected evolution is found and remains the same until failure of the specimen at 1,713,532 cycles.

The evolution of the transverse strain is very similar to the 2 Hz test: a significant permanent deformation can be seen and right before de-bonding, approximately the same value of the strain is found for both the 2 Hz and the 5 Hz experiment, illustrating that the frequency does not seem to have a lot of influence and that the results are reproducible.

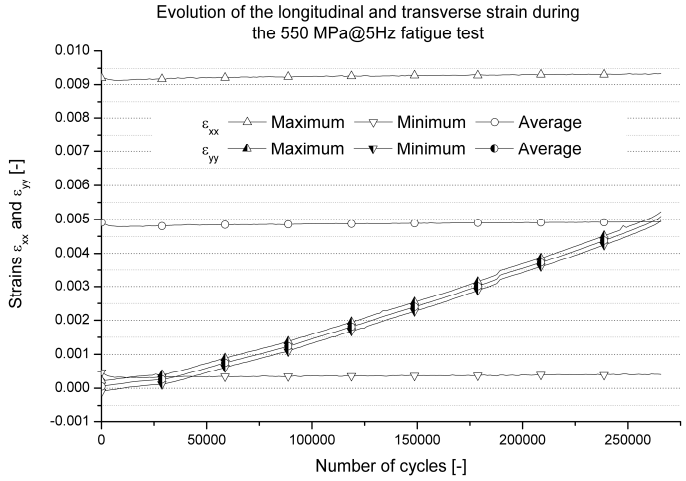

Figure 5-63 ε_{xx} and ε_{yy} during the 550 MPa@5Hz fatigue test.

The corresponding evolution of Poisson's ratio is depicted in Figure 5-64. The same conclusions as for the 2 Hz test can be made: (i) very early in fatigue life, the Poisson's ratio becomes lower than zero and (ii) the characteristic form of the evolution becomes more and more apparent for higher numbers of fatigue cycles.

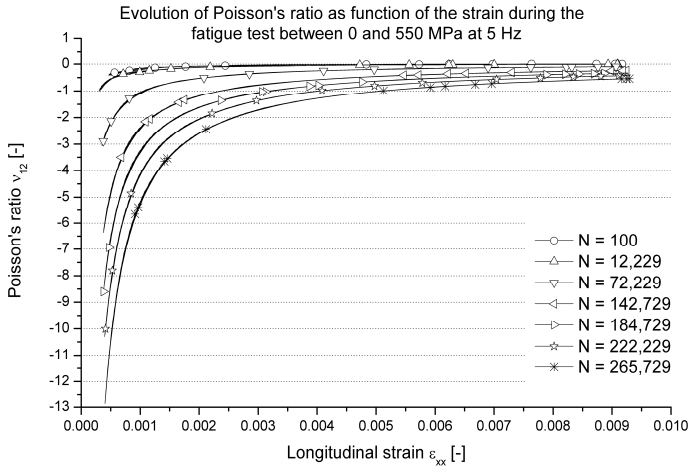

Figure 5-64 Evolution of Poisson's ratio as function of the longitudinal strain during the 550 MPa@5Hz test.

During this experiment, the temperature was recorded, but as expected, no rise in temperature occurred.

Finally, it was attempted to perform a fatigue test with maximum stress level of 575 MPa in order to have an 'acceptable' failure before the transverse strain gauge de-bonded. As such, it could be assessed if the evolution of Poisson's ratio could be used for damage modelling and failure predictability. A test with such an acceptable failure, meaning the specimen did not fail during the run-in or in the tabs due to frictional heating, was achieved at a loading frequency of 5 Hz. The stress-strain evolution during the run-in of this experiment is shown in Figure 5-65. The build-up of permanent deformation can be noted and the derived stiffness corresponds very well with the previously found values.

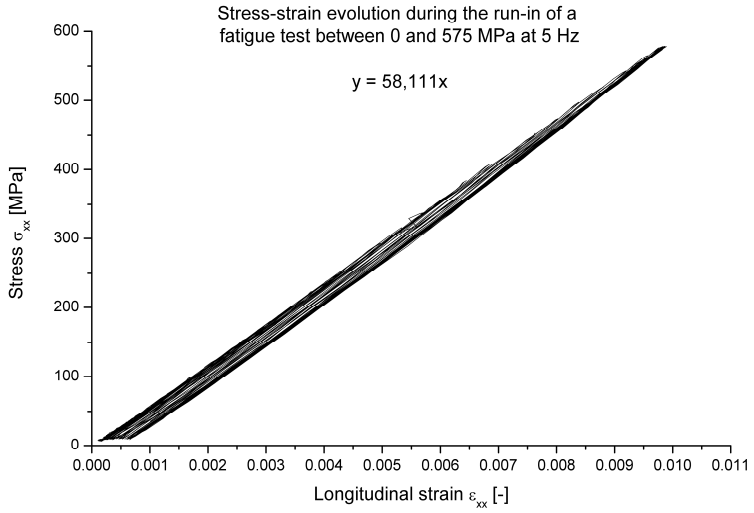

Figure 5-65 Stress as function of the strain for the run-in of a 550 MPa@5Hz experiment.

The evolution of Poisson's ratio during the run-in of this experiment is shown in Figure 5-66 and is very similar to the 550 MPa experiments, although the ratio does not decrease below zero during the run-in. The initial value corresponds very well to the previously found values.

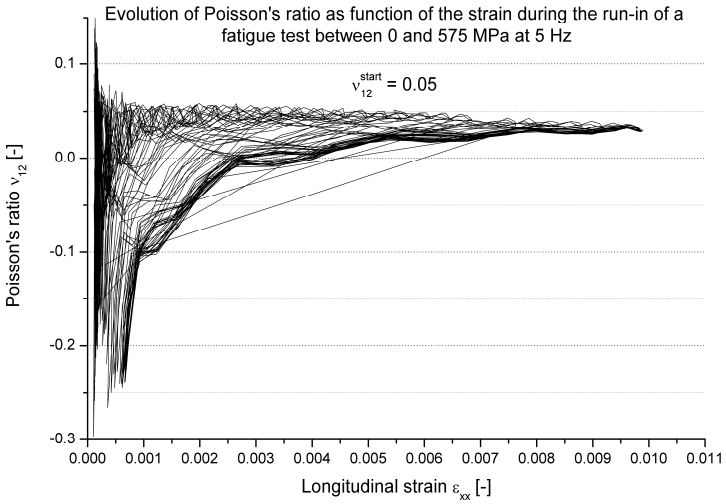

Figure 5-66 Evolution of Poisson's ratio as function of the longitudinal strain for the run-in of the 575 MPa@5Hz test.

Figure 5-67 illustrates the evolution of the measured strains until the transverse strain gauge de-bonded after 183,046 cycles. This time of de-bonding is less than for the 550 MPa tests, which could have been expected, since the strains are a little higher. For the longitudinal strain, a similar evolution is found as for the 550 MPa tests, which means that even for this higher load range, there still is no stiffness degradation, nor large permanent deformation. The specimen failed after 445,546 cycles, which is too far behind the point at which the strain gauge de-bonded in order to draw valid conclusions about failure prediction and damage modelling. The evolution of the transverse strain is similar to the previous tests, although the value tends to be lower. This may suggest that during the fatigue tests at 550 MPa, the transverse strain gauges de-bonded gradually, causing the gradual increase till values of 0.005 for these tests. This again emphasises the need for a better way of measuring the transverse strains during fatigue experiments.

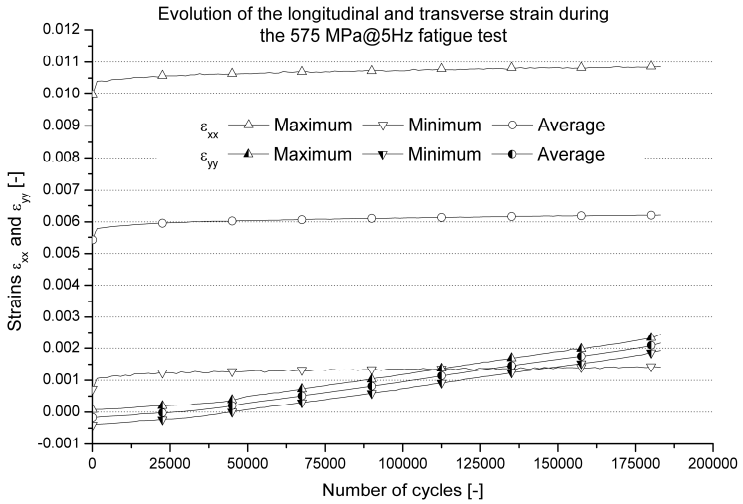

Figure 5-67 ε_{xx} and ε_{yy} during the 575 MPa@5Hz fatigue test.

The corresponding evolution of Poisson's ratio is depicted in Figure 5-68. Again the characteristic form of the evolution is visible and becomes more and more apparent for higher numbers of fatigue cycles, although the minimum value is a lot less than for the two previous tests, but this is of course the result of the higher longitudinal strains, which are in the denominator when calculating the Poisson's ratio; here, the minimum value is about 0.0014, whereas for the experiments at 550 MPa, the minimum value of ε_{xx} is 0.0004, causing the absolute value of ν_{12} to be significantly higher.

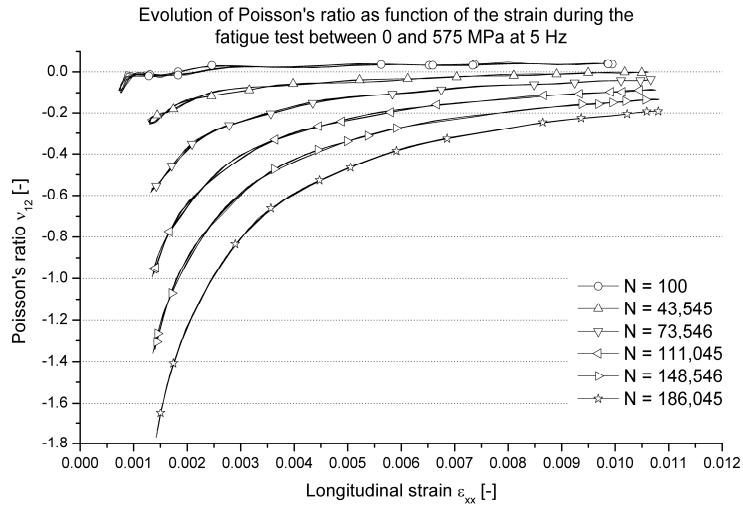

Figure 5-68 Evolution of Poisson's ratio as function of the longitudinal strain during the 575 MPa@5Hz test.

Finally, Figure 5-69 depicts the evolution of the value of the Poisson's ratio at the maximum stress level of each (measured) fatigue cycle, for all three experiments described above. As can be noted, there is a decreasing trend for the ratio, but contrary to what would be expected, a higher maximum stress level causes the Poisson's ratio to decrease less. This can be explained by two reasons. First, the transverse strains in the 550 MPa experiments are significantly higher than for the 575 MPa, possibly due to gradual de-bonding of the strain gauge, causing a lower value of the Poisson's ratio. Second, the values depicted in Figure 5-69, are recorded at the maximum value of the longitudinal strain. This is around 0.015 for the 575 MPa@5Hz test, compared to only 0.0095 for both the 550 MPa experiments. For the 575 MPa@5Hz test, the values of ν_{12} at $\varepsilon_{xx} = 0.0095$ are lower than at $\varepsilon_{xx} = 0.015$, so the corresponding curve in Figure 5-69 will be little lower if all the values are compared at the same strain level.

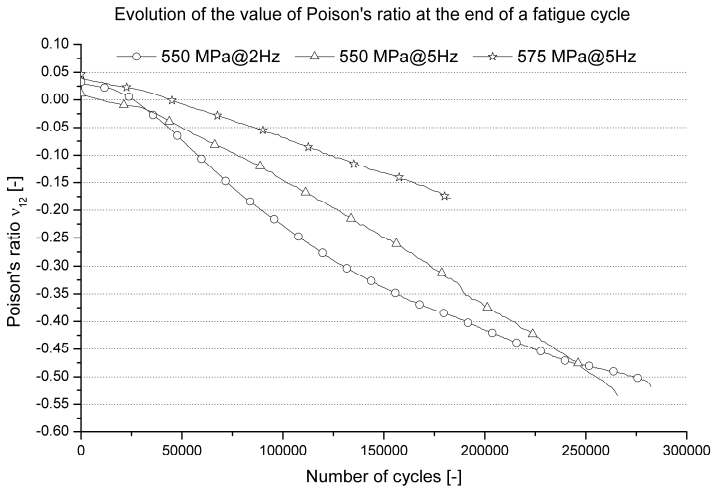

Figure 5-69 Illustration of the decrease of Poisson's ratio during fatigue.

5. 5. 4. Creep testing

In the performed fatigue tests, the stress ratio was zero, meaning that the stress evolves between 0 MPa and a certain maximum σ_{max}. As such, the specimen is subjected to an average stress of half of σ_{max} during the entire fatigue experiment, which may cause the material to creep.

In order to verify whether the drop in Poisson's ratio, depicted in Figure 5-69 is due to fatigue damage, rather than to creep, an extra experiment was performed. The specimen was loaded with 275 MPa over a period of 600,000 seconds. For a 5 Hz fatigue test, this corresponds with three million cycles and for a 2 Hz experiment, it corresponds with 1,200,000 cycles. The evolutions of both longitudinal and transverse strain are shown in Figure 5-70, each on its own scale. It can be noted that little creep is present for both strains.

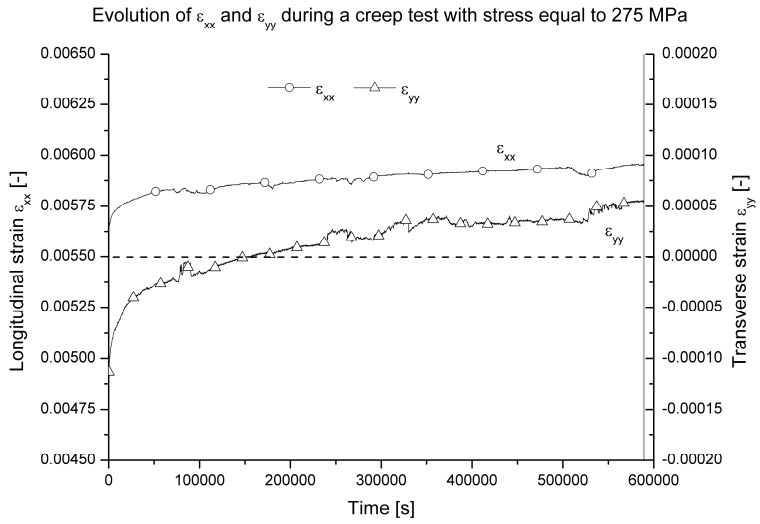

Figure 5-70 Evolution of ε_{xx} and ε_{yy} during the creep experiment.

These strains result in the following evolution of Poisson's ratio (Figure 5-71) and indeed, there is a decrease in ν_{12}. However, this decrease is very small when compared to the decrease that occurred during the fatigue tests (see Figure 5-69; both graphs are on the same scale).

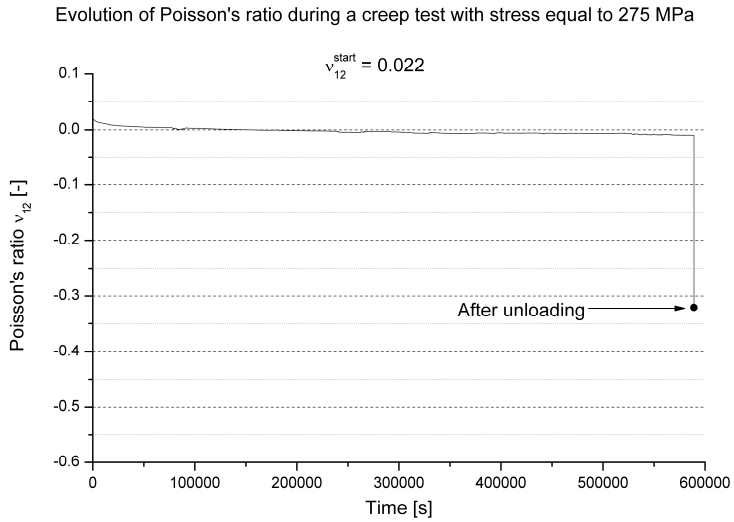

Figure 5-71 Evolution of Poisson's ratio during the creep experiment.

After the creep test was stopped and unloaded, a quasi-static test with a displacement speed of 2 mm/min was performed till failure to determine the stiffness and the evolution of the Poisson's ratio. The longitudinal stress-strain relation is given in Figure 5-72 and the Poisson's ratio as function of the longitudinal strain in Figure 5-73. The stiffness corresponds again very well with the previously derived values in chapter 3.

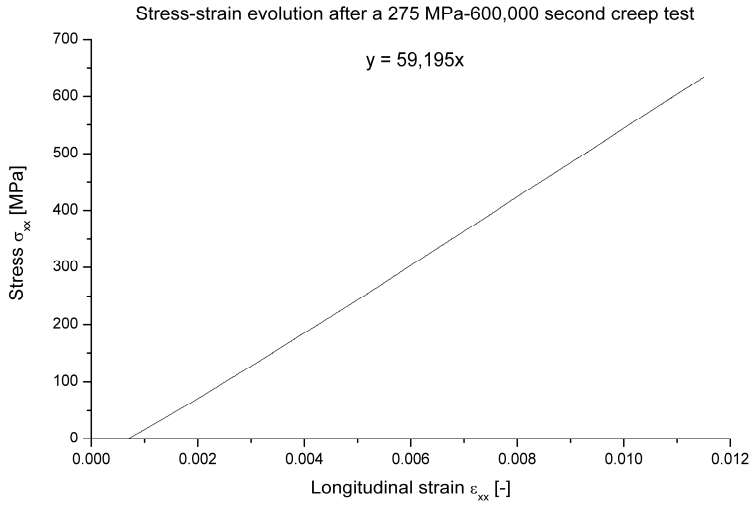

Figure 5-72 Stress as function of the strain for the quasi-static test after the creep experiment.

The evolution of Poisson's ratio already has the same peculiar evolution and remains negative, but its value is still significantly higher than during the fatigue experiments.
At a strain level of 0.006, the same value of the Poisson's ratio (ν_{12} = -0.01) is found as was the case right before the creep test was stopped and unloaded (Figure 5-71). Also, the starting value in the quasi-static test (ν_{12} = -0.3) corresponds with the value after unloading the creep test (Figure 5-71).

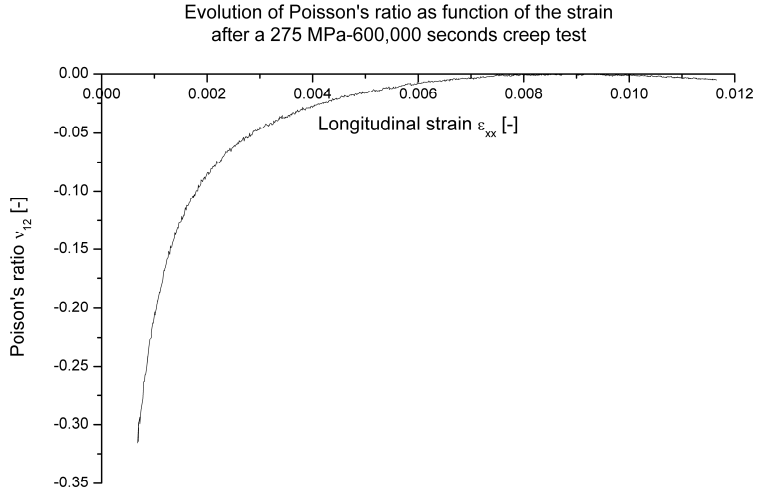

Figure 5-73 Evolution of Poisson's ratio as function of the longitudinal strain after the creep experiment.

5. 5. 5. Conclusions

A number of preliminary fatigue experiments were performed to assess whether the Poisson's ratio can be used for damage modelling or failure predictability. From these experiments, the same conclusion with respect to the stiffness degradation and permanent deformation, which were previously drawn, could be verified. With respect to the Poisson's ratio, a clearly decreasing trend is visible; the change in value is far more greater than the increase in permanent elongation and the decrease in stiffness. A creep test was performed to verify whether the decrease in Poisson's ratio is due to fatigue damage and although the Poisson's ratio decreases due to creep, the decrease in value is significantly lower than during a fatigue experiment.
However, more experiments need to be done to be able to model damage by means of the Poisson's ratio, but in order to do so, first a new way of measuring the transverse strain should be implemented, so the strain could be measured until failure. Only then, valid conclusions with regard to the evolution of Poisson's ratio and its relation to damage modelling and failure predictability can be made. During this research, an attempt was made by modifying the standard extensometer. The latter, however, could only be used for the quasi-static hysteresis measurements on specimens with a rough surface (glass-epoxy) but not on the smooth surface of the carbon-PPS. Therefore, the transverse extensometer was not considered for the fatigue measurements discussed here, since the high deformation rate during 2 Hz and 5 Hz fatigue tests will certainly be too high for the extensometer to measure accurately.

5. 6. OPTICAL FIBRE SENSORS

5. 6. 1. Introduction

As was mentioned in chapter 3, the optical fibre with Bragg grating can be used both as embedded fibre and externally bonded. However, due to the occurrence of multiple peaks in the spectrum of an embedded fibre after curing, most of the produced specimens with embedded sensor could not be used for strain measurement, since the means of deriving strain from the evolution of such a spectrum are not yet sufficiently tested and calibrated. In order to investigate the occurrence of this 'peak-splitting', a few plates were made with specially selected embedded gratings and the evolution of the spectrum during curing was monitored, in order to find a cause and solution for the 'peak-splitting'. This is currently under investigation at FOS&S. Fortunately, some embedded fibre sensors did not have a spectrum with multiple peaks and a few were suited for fatigue testing.

Of course, the option of an externally bonded grating for fatigue strain measurement is also assessed. Since the PPS is difficult to bond, the question remains whether the used adhesive will survive the fatigue loading, in order to accurately transfer the strain from the specimen to the fibre sensor.

As reminder, the linear approximation for the relation between strain, temperature and wavelength is given by :

$$\Delta\lambda = s_S \Delta\varepsilon + s_T \Delta T \tag{5.24}$$

With typical values for S_S and S_T for an FBG in the C-band region (1520 nm-1560 nm) equal to 1.2 pm/με and 10 pm/°C respectively. As was also mentioned in chapter 3, the FBG is sensitive for both strain and temperature, thus two FBGs are needed, one to measure strain and one to measure temperature.

However, since no significant temperature increase was noticed during the other fatigue experiments (see section 5. 4.) no capillary was embedded.

For instance, an increase of about 1ºC yields 10 pm shift in wavelength, whereas the increase in strain for a fatigue experiment with a maximum stress of only 300 MPa maximum is about 5250 microstrain, corresponding with 6300 picometer shift in wavelength. As a result, the influence of the temperature on the optical fibre measurement may be neglected, since the effect of the strain on the Bragg wavelength is dominant over the temperature effect on the wavelength.

With respect to the optical data acquisition equipment, both systems described in chapter 3, namely the Swept Laser Interrogator and the FBG-scan interrogator are considered.

5. 6. 2. Specimen geometry

The dimensions of the coupons with embedded optical fibres used for fatigue experiments were chosen according the ASTM D3479 standard and are shown in Figure 5-74. It was attempted to have the grating of the fibre somewhere in the middle.

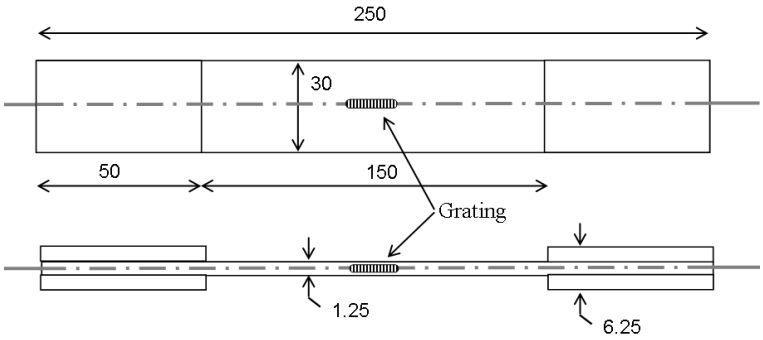

Figure 5-74 Dimensions of the used tensile coupon, equipped with tabs.

For the specimens with the externally bonded grating, the same dimensions as for the general fatigue tests are used (paragraph 5. 4. 1, Figure 5-36).

5. 6. 3. Fatigue experiments

5. 6. 3. a. Embedded Fibres

To assess whether the optical fibre is capable of measuring strains during the entire lifetime of the composite specimen, several fatigue tests were performed using both optical data acquisition systems. As was mentioned in chapter 3, it is not possible to read the optical fibre during the fatigue test with neither of the two systems considered for this research, so the fatigue tests were paused in order to perform quasi-static tensile tests were performed. With the Swept Laser Interrogator (SLI) this had to be done manually, whereas with the FBG-scan, this process was automated.

For the first experiment presented here, the Swept Laser Interrogator was used and seven quasi-static tensile tests were performed. The first static test was done before the fatigue experiment was started and the test was stopped after the seventh static test. The fatigue test was not done till fracture, so that this specimen could still be examined using non-destructive testing.

The optical fibre in the specimen had a starting wavelength of 1556 nm. The latter is relatively high for a tensile test, but as previously mentioned this wavelength was chosen for the monitoring of the production process of the plate.

The quasi-static tests were displacement-controlled with a speed of 2 mm/min, the fatigue tests were force controlled with σ_{max} equal to 300 MPa, which is about 50 % of the ultimate stress (see chapter 3), and σ_{min} equal to 0 MPa and a loading frequency of 5 Hz.
Such low value of the maximum stress was chosen, since the strength of the bond between the ORMOCER coating of the fibre and the polyphenylene sulphide matrix still needed to be assessed. To verify if the optical fibre strain is accurate, the longitudinal strain was also monitored with the extensometer.

Figure 5-75 illustrates the measured strains, both with the extensometer and the optical fibre. The strain is plotted as a function of time; the different curves are given a certain offset with respect to each other, to have a clear image. Underneath each measurement, the corresponding cycle is noted; the first curve corresponds with the initial static test.
The results correspond perfectly. The small plateau at the end of the optical measurement is due to the saturation of the optical data acquisition unit, when the wavelength exceeds the range the SLI is able to detect, so it corresponds with a wavelength of 1560 nm. The extensometer measurement was stopped a little after the SLI saturated.

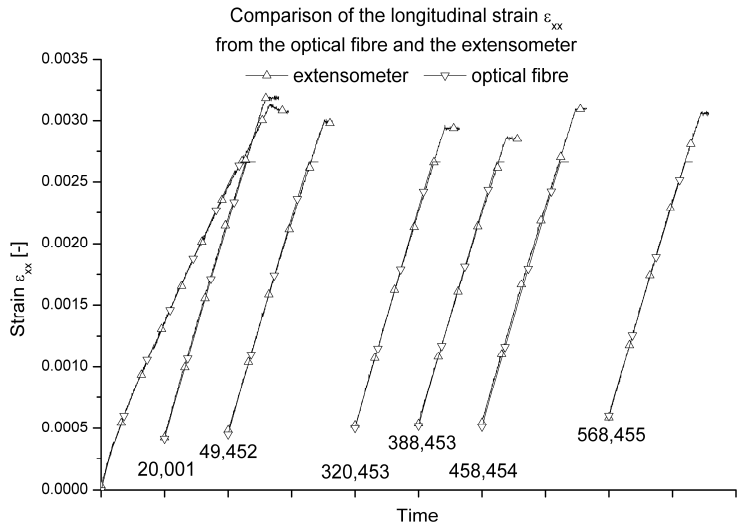

Figure 5-75 Comparison of the different longitudinal strains, as a function of the time.

It may be noticed that the strain for the first static test increases slower than for all the other tests. This is due to slipping and tightening of the clamps.
The stress-strain curves, corresponding with these static tests, are shown in Figure 5-76, together with the corresponding stiffness.

Again, there is no stiffness degradation and only very limited permanent deformation, even after more than half a million cycles, so the embedded fibre does not influence the fatigue behaviour for these loading conditions.

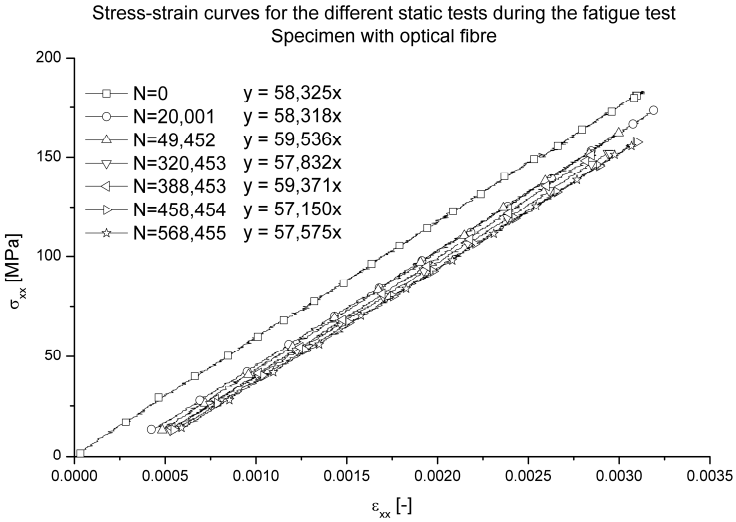

Figure 5-76 Longitudinal stress as a function of the longitudinal strain for the different static tests; specimen with optical fibre.

To verify these results, a similar test was performed using the FBG-scan. This 300 MPa@5 Hz experiment was paused every 40,200 cycles to perform a load controlled static test, as described in chapter 3. In total, fourteen static tests were done and then the specimen was removed from the tensile machine, so it could be examined further; the specimen had not failed. The embedded optical fibre had a starting wavelength of 1549.47 nm.

Figure 5-75 illustrates the measured strains of these static tests, both with the extensometer and the optical fibre. The strain from both loading and unloading is plotted as a function of time [s], the fourteen different curves are given a certain small offset with respect to each other, to have a clear image. Underneath each measurement, the number of the quasi-static test is noted (Table 5-12); the first curve corresponds with the initial static test. It may be remarked that the results correspond perfectly.

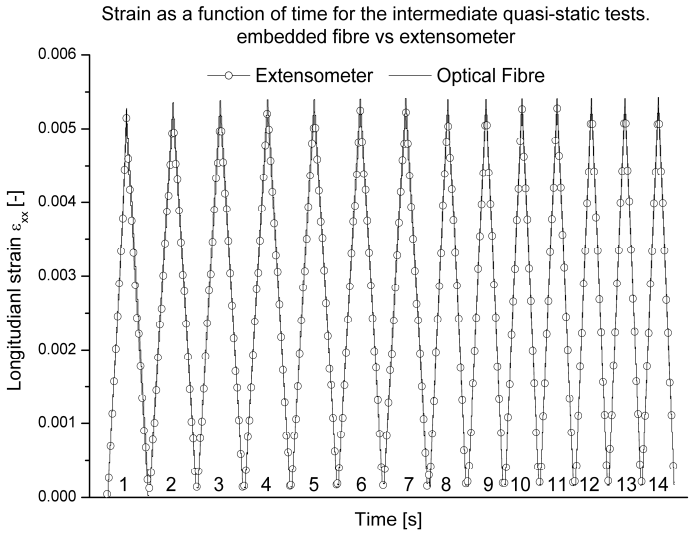

Figure 5-77 Comparison of the different longitudinal strains, as a function of the time for the successive quasi-static tests for the specimen with the embedded optical fibre.

Table 5-12 Corresponding number of fatigue cycles with the quasi-static test.

Number	Number of cycles	Number	Number of cycles
1	0	8	281,400
2	40,200	9	321,600
3	80,400	10	361,800
4	120,600	11	402,000
5	160,800	12	442,200
6	201,000	13	482,400
7	241,200	14	522,600

The stress-strain curves, corresponding with these static tests, are shown in Figure 5-78, together with the corresponding stiffness. Again, there is almost no stiffness degradation and only very limited permanent deformation, even after more than half a million cycles. This permanent deformation was also measured by the optical fibre, as can be seen in Figure 5-77.

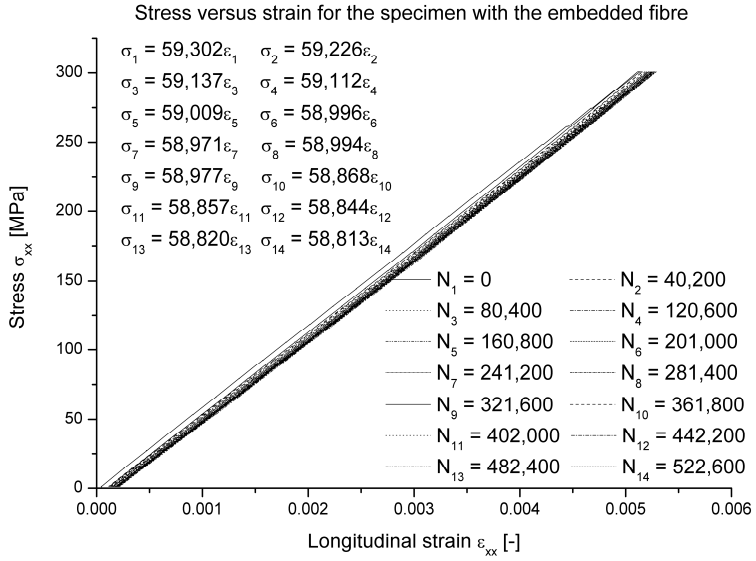

Figure 5-78 Longitudinal stress as a function of the longitudinal strain for the different static tests for the specimen with the embedded optical fibre.

Finally, Figure 5-79 shows the change in spectrum resulting from the embedding process and the fatigue experiment. As can be noted, there is a shift to the right from 1548.577 nm to 1549.47 nm, yielding a strain of 744 microstrain. Furthermore, losses in power have occurred due to macro-bending on entrance of the plate and micro-bending inside the plate. Changes in reflected spectra after consolidation are known to happen in epoxy-matrices [43-45], but have also been documented for the thermoplastic matrix PPS in [46].

The shift in wavelength as a result of the permanent strain, developed during the fatigue test can also be seen.

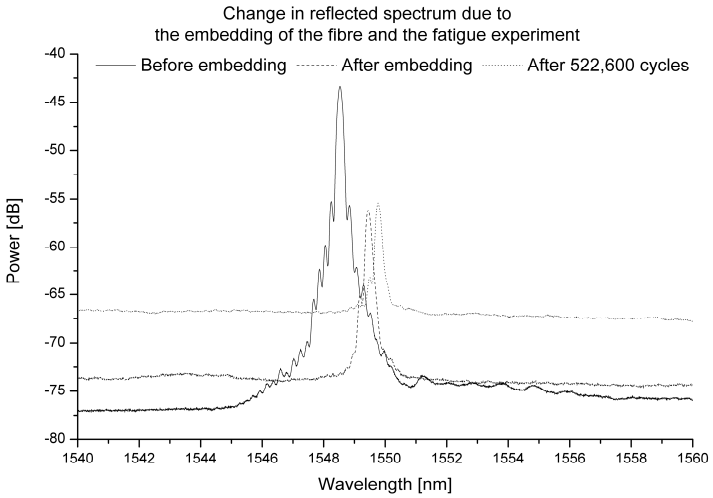

Figure 5-79 Illustration of the reflected spectrum prior and after the embedding process and after 522,600 cycles.

In conclusion, both the experiments done with the SLI and the FBG-scan yield very similar results. In both cases, the correspondence between the strains derived from the embedded fibre and the extensometer is very good, meaning that the strain is transferred excellently from specimen to optical fibre. As such, it may be concluded that the ORMOCER coating is very suitable for embedding in polyphenylene sulphide. Again no stiffness degradation or permanent deformation did occur and the measured stiffness corresponds very well to the one measured with the quasi-static testing and resonalyser method (see chapter 3) meaning that the embedding of the fibre does not have any significant influence on the mechanical properties, nor on the fatigue behaviour of the material.

5. 6. 3. b. Externally bonded fibres

To assess whether an optical fibre grating could also be used as an external sensor for fatigue measurement, a few specimens were prepared with an external optical fibre. The external optical fibre had a starting wavelength of 1540,531 nm. This fatigue test was also done with a maximum tensile stress of 300 MPa with a loading frequency of 5 Hz and the minimum stress was also 0 MPa, for comparison purposes. Five quasi-static tests were done to verify if the external fibre measured accurately. The first was done before the start of the fatigue test and the other four intermediate tests were done every 100,000 cycles. The experiment was stopped without failure after 400,000 cycles. The corresponding strain curves from extensometer and external grating are plotted in Figure 5-80. Both loading and unloading cycles are depicted; the different static tests are given a small offset for a clear image.

It may be remarked that again there is perfect correspondence between the optical fibre and the extensometer.

Table 5-13 Corresponding number of fatigue cycles with the quasi-static test.

Number	Number of cycles	Number	Number of cycles
1	0	4	300,000
2	100,000	5	400,000
3	200,000		

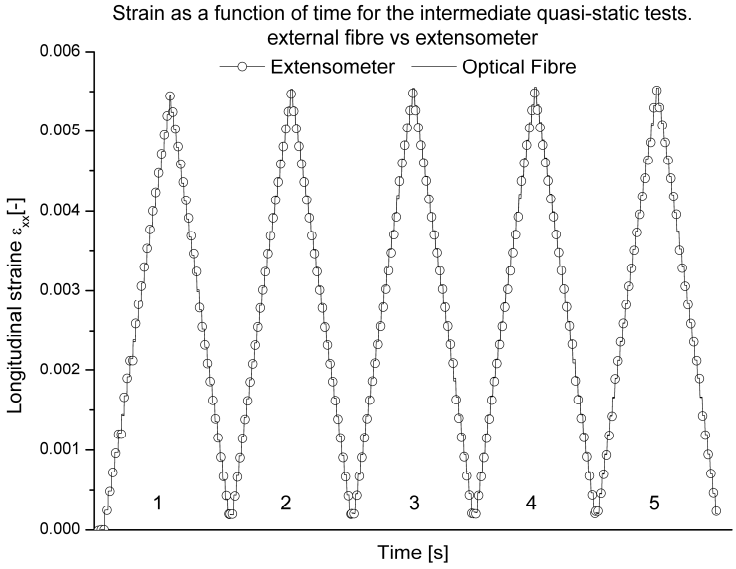

Figure 5-80 Comparison of the different longitudinal strains, as a function of the time for the successive quasi-static tests for the specimen with the external grating.

The corresponding stress-strain curves are plotted in Figure 5-81. Again, only limited permanent deformation and stiffness degradation occurs.

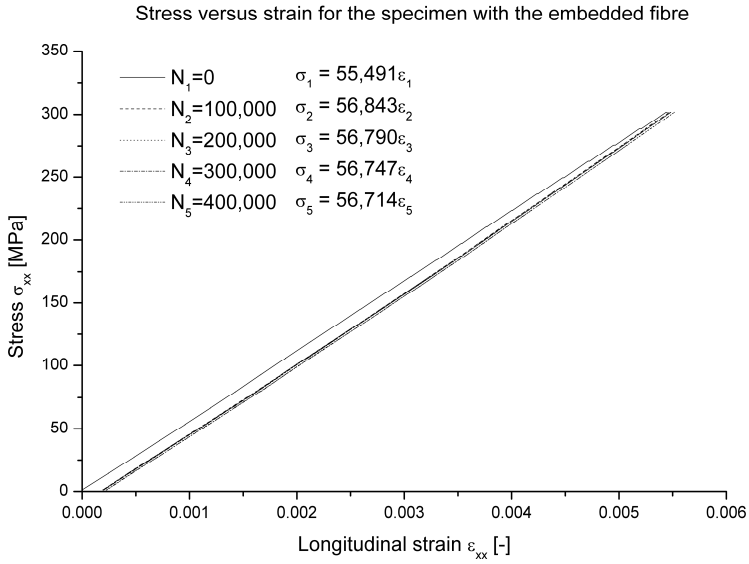

Figure 5-81 Longitudinal stress as a function of the longitudinal strain for the different static tests for the specimen with the external optical fibre.

5. 6. 4. Conclusions

It may be concluded that optical fibres, both embedded as externally bonded, survive over half a million fatigue cycles, which is a lot more than strain gauges which tend to de-bond. Therefore, the ORMOCER coating used on the fibres was the right choice.

Both the SLI 1000 system as the FBG-scan can be used for monitoring fatigue experiments, under the condition that the fatigue test is paused after a certain number of cycles to perform a quasi-static tensile test. The combined setup of INSTRON and FBG-scan interrogator automate the process, which is an advantage over the SLI. However, for both systems, it is not possible to read the optical fibre during fatigue loading with high frequencies and as such, no data during fatigue cycling can be derived from the fibre grating.

For the chosen stress range and frequency, namely 0-300 MPa@5 Hz, the embedded fibre does not influence the mechanical properties or the fatigue behaviour of the carbon fabric-reinforced thermoplastic. There is still no stiffness degradation and only very limited permanent deformation, as was the case for the specimens without embedded fibres; the measured stiffness corresponds very well to the one obtained from the resonalyser method and the quasi-static tests in chapter 3.

However, future research at higher tension levels is necessary for both setups to examine whether the optical fibre does not de-bond and gives accurate measurements under these conditions, but the first results are very promising.

5. 7. ELECTRICAL RESISTANCE MEASUREMENT

5. 7. 1. Introduction

Because of the good results obtained for the quasi-static tests (chapter 3) and hysteresis tests (chapter 4), the method is now used for monitoring fatigue tests. Because of the time stability, the four-probe method is chosen rather than the two-probe method. The higher sensitivity of the former is definitely a plus.

There have already been a few studies on the use of the electrical resistance measurement for monitoring fatigue [5-7, 47, 48], but as previously mentioned in chapter 3 and 4, the focus lies mostly on unidirectional [5-7, 48] or cross-ply reinforcement [6, 47]. Seo et al. [5] have found a very promising correlation between stiffness degradation and relative resistance change, but for a unidirectional carbon fibre-reinforced epoxy.
The order of change tends to vary with the used material. In [5], the resistance increased about 30% for the UD carbon-epoxy, whereas in [47], an increase of 5 % was reached at failure for a cross-ply material.

5. 7. 2. Fatigue experiments

Two types of tests were performed; the first has a loading frequency of 2 Hz and the second of 5 Hz. Two frequencies were chosen to reconfirm that the frequency has no significant influence on the evolution of elastic and fatigue parameters and to see whether the resistance measurement still follows the loading at higher frequencies. Both tests were done between $\sigma_{min} = 0$ and $\sigma_{max} = 550$ MPa (R=0), to compare them with previous the experiments. As such, it is assessed whether some form of damage can be detected by monitoring the electrical resistance. The other experiments described in this chapter already yielded infinite lifetime at stresses below 450 MPa and for stresses higher than 600 MPa, failure occurred after no more than a few hundred cycles.
Figure 5-82 and Figure 5-83 show the evolution of the relative resistance change as a function of time for a few fatigue cycles, as well as the corresponding strain for the test at respectively 2 and 5 Hz. It can be noted that the relative resistance increase ρ clearly follows the loading and unloading of the specimen in both cases.

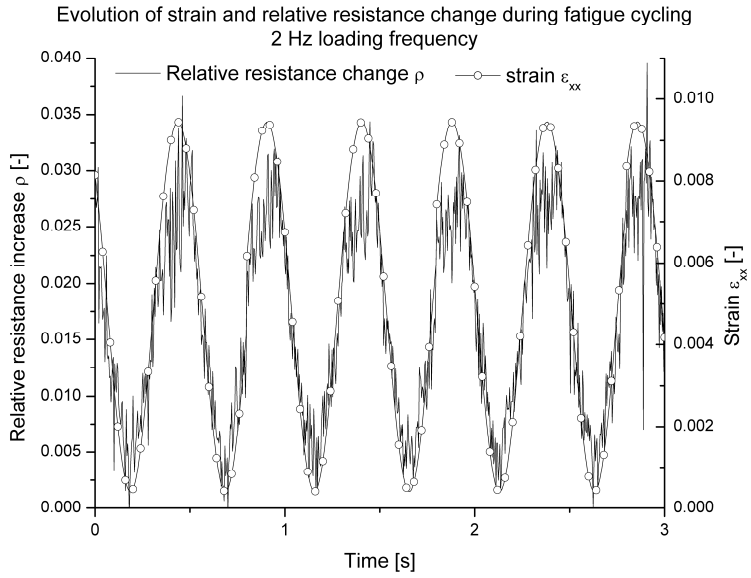

Figure 5-82 Strain and resistance change during fatigue cycling at 2 Hz, specimen K4.

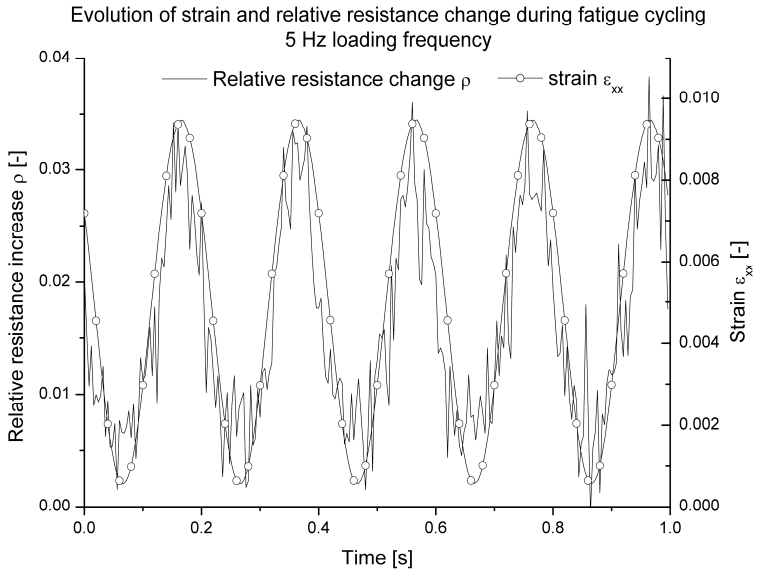

Figure 5-83 Strain and resistance change during fatigue cycling at 5 Hz, specimen M1.

During the fatigue test, every five minutes five cycles are registered by the data-acquisition system and the maximum, minimum and mean value of these measurements (load, displacement, strain and resistance) are calculated. Figure 5-84 shows the evolution of these values for the longitudinal strain for both a 2 Hz and a 5 Hz test until failure of the specimen.

It can be seen that for the two tests, the strain behaviour is much alike. Furthermore, only a very limited increase is registered of about 1E-10 per cycle.

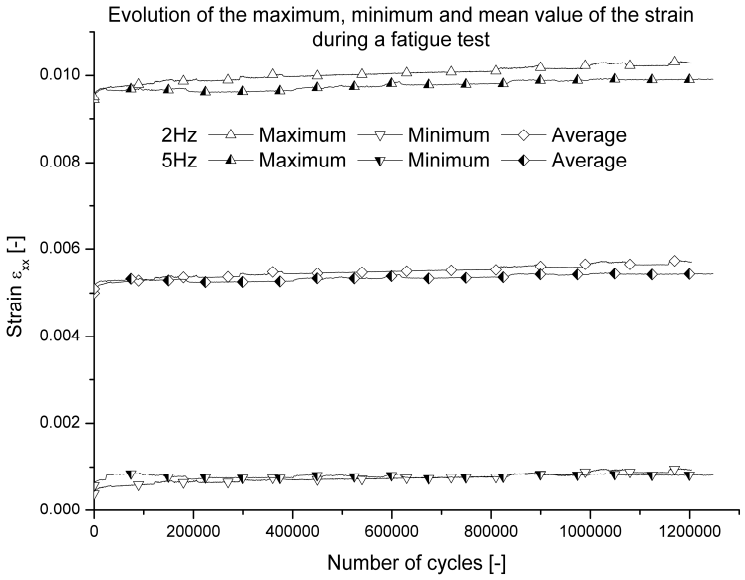

Figure 5-84 Illustration of the evolution of the maximum, minimum and mean value of the strain as a function of the number of fatigue cycles for both a 2 Hz and a 5 Hz test.

To assess whether damage can be visualised by the relative resistance change, the evolution of its average value during cycling is plotted in Figure 5-85 for the 2 Hz test. The corresponding temperature is also added, to evaluate whether there is a temperature increase due to the used 1000 mA and whether the temperature increases near the end of life of the specimen. It should be noted that the temperature remains constant throughout the test.

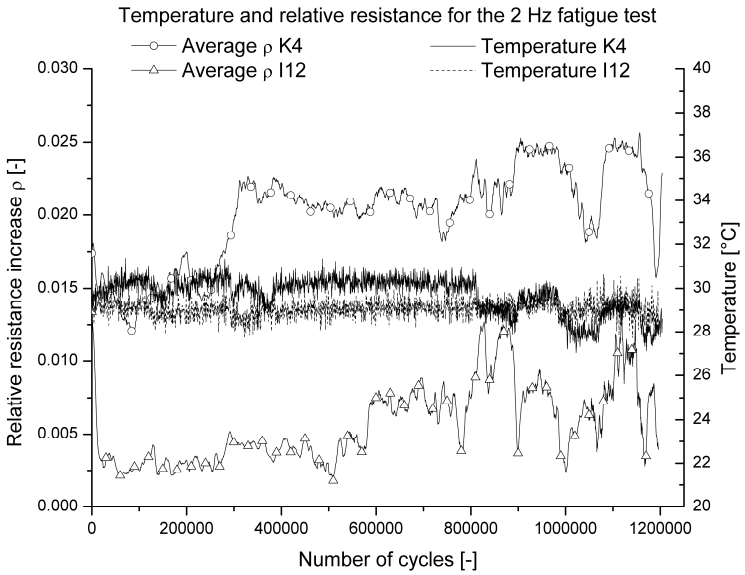

Figure 5-85 Evolution of the relative resistance change and the temperature throughout the 2 Hz fatigue test.

One would expect that the resistance curves for both tests would be coincident, since the relative resistance is plotted instead of the absolute value, but this is not the case. The two specimens were sawn from different plates and maybe this causes the difference in measurements. However, it can be noted that both curves have a similar increase of 6.989E-09 per cycle for K4 and 5.185E-09 per cycle for I12 (the given values are the slopes of fitted linear trend lines). These values, however, are not much higher than the increase in strain, which is of the order 1E-10 per cycle. As such, the evolution of the resistance is no great improvement for monitoring damage.

This could be explained by the fact that the longitudinal resistance is highly influenced by failure of the carbon fibres. Since there is neither real stiffness degradation nor permanent elongation that suggests fibre damage and a very sudden brittle failure, the expected increase of resistance of the specimen is limited. This could also be concluded from the damage model in [5] where a correlation was found between stiffness degradation and the reverse of the relative resistance increase. Since the material used in [5] exhibited a large decrease in stiffness, a large increase (up to 0.3) in relative resistance was measured.

In some cases however, a decrease in resistance is noticed instead of an increase. An example of such a test is shown in Figure 5-86, where the average value of the relative resistance change is depicted. First, there is a significant increase in relative resistance, but then it gradually decreases. Failure occurred after 347,757 cycles.

This phenomenon of a decreasing resistance has already been reported in literature [47, 48] and is due to an increase in the degree of fibre alignment and due to a reduction of residual stress [48]. However, this usually only happens during the first few hundred cycles of the fatigue test, but apparently, it can also happen later in fatigue life.

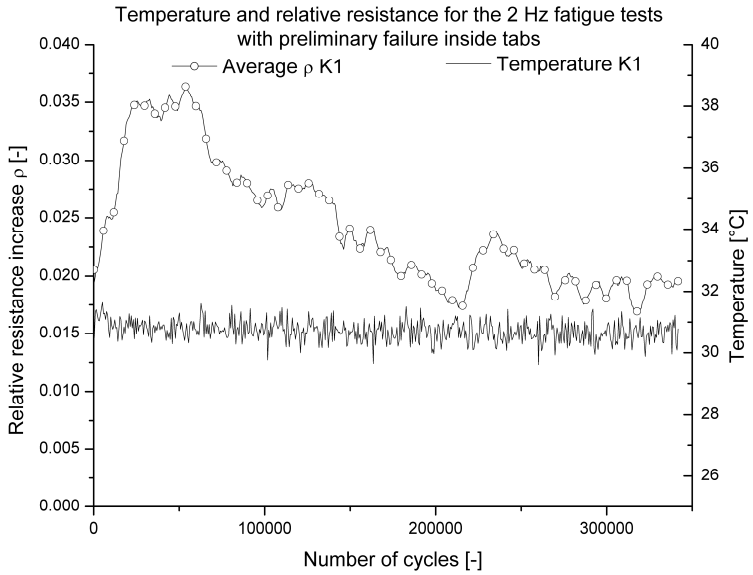

Figure 5-86 Evolution of the relative resistance change and the temperature throughout a 2 Hz fatigue test with a decreasing resistance.

For the 5 Hz test, the problem of tab failure occurred more often. A lot of test samples failed during the first 50,000 cycles due to stress concentration in the tabs, as previously discussed or gradual de-bonding of the adhesive resulting in heating due to friction between tabs and specimen with failure as result. Since the purpose of the resistance measurement is to predict damage and failure, two of these experiments are shown in Figure 5-87. It can be noted that there is no significant increase in temperature. The relative resistance increases about 1.378E-07 per cycle, which still is not suited for damage monitoring, although it is almost 100 times higher than for the 2 Hz samples. Furthermore, there is no significant change in evolution right before failure, so failure predictability does not seem possible.

It should be noted that there is a small decrease for M1 and a large decrease for M2 in resistance for the first 2000 cycles, which may be due to the increase in the degree of fibre alignment and due to a reduction of residual stress [48], as previously mentioned.

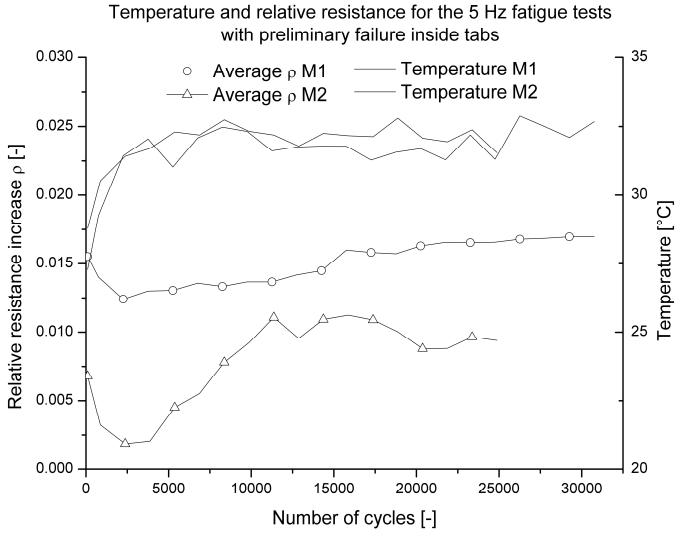

Figure 5-87 Evolution of the relative resistance change and the temperature throughout the 5 Hz fatigue test for the specimens with preliminary failure.

An example of a successful test at 5 Hz is shown in Figure 5-88. Again, the temperature remains constant until failure of the specimen at 1,296,769 cycles. It must be noted that in this case, again, the relative resistance tends to decrease, as was the case with the 2 Hz test in Figure 5-86, so this phenomenon does not depend on the used frequency. Again, this evolution of the relative resistance cannot be used to monitor damage or predict failure.

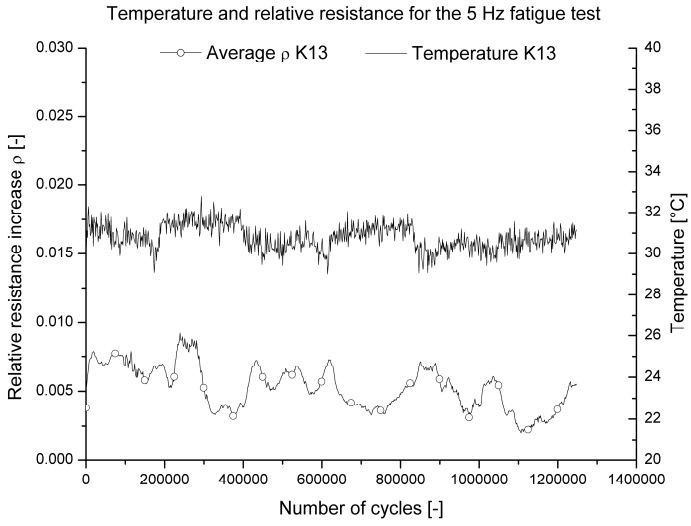

Figure 5-88 Evolution of the relative resistance change and the temperature throughout the 5 Hz fatigue test.

5. 7. 3. Conclusions

The use of electrical resistance measurement was investigated for monitoring fatigue damage in the carbon fabric-reinforced PPS. The four-probe method, as illustrated in chapter 3 was used for these purposes, because of its higher sensitivity than the two-probe method, but especially because of its stability in time.

Several fatigue tests were done to assess the performance of the resistance measurement in damage detection. It was proven that the electrical resistance measurement is capable of monitoring fatigue experiments; the resistance clearly followed the loading and unloading of the specimen during both the 2 Hz and 5 Hz experiments. However, the electrical resistance measurement could not monitor damage growth, since no measurable damage was present. The longitudinal resistance is very sensitive to fibre failure and since neither stiffness reduction nor permanent elongation occurred, fibre fracture is not the dominant mode of damage.

5. 8. CONCLUSIONS

In this chapter, all uni-axial fatigue experiments performed for this doctoral study and the correlated problems were discussed. First, a new design of mechanical wedges, suited for tension and compression fatigue is illustrated; the extra amount of space between the grips proved useful for experiments with electrical resistance measurement and embedded optical fibres. During this design, analytical expressions were derived with respect to contact pressure on the tabbed area of the specimen. As such, the problem of tab failure was re-assessed numerically. Together with some experimental experience, it was concluded that using straight end tabs with a $[(0^o,90^o)]_{4s}$ lay-up and mounting the specimen in such a way that the end tabs are completely inside the grips was the best solution for the carbon fabric-reinforced PPS.

Various fatigue experiments were performed, of which some were discussed here. Two frequencies, 2 Hz and 5 Hz, were chosen to assess the influence of the frequency on the fatigue lifetime and damage growth. While performing these experiments, it was investigated how possible damage could be monitored. It could be concluded that there was no stiffness degradation and only limited permanent deformation occurred. This was concluded from longitudinal strain measurements done with the extensometer, the embedded optical fibre and the externally bonded fibre. The Poisson's ratio is far more sensitive to possible damage, but because of the de-bonding of the strain gauge, it was not possible to evaluate the evolution of Poisson's ratio to failure. It was proven that the electrical resistance measurement is capable of monitoring fatigue experiments, but the expected increase in resistance, as mentioned in the previous section, was not registered. Also, it could be concluded that the frequency does not have any demonstrable influence and it should be mentioned that the material exhibits very brittle fracture behaviour; failure occurs quite sudden, without any preliminary (visible or audible) cracks.

It should be mentioned that no tension-compression or compression-compression fatigue was discussed. The objective of this doctoral research was to develop testing and monitoring setups suited for the entire group of carbon-reinforced thermoplastics and to obtain a thorough understanding of these setups, rather than to study the behaviour of one specific material. Of course, further research under the mentioned loading conditions will be necessary to fully understand the macro-mechanical behaviour of the material, selected for this research.

5. 9. REFERENCES

[1] De Waele W, Degrieck J, De Baets P, Moerman W, Taerwe L, Feasibility of integrated optical fibre sensors for condition monitoring of composite structures - Part II: Combination of Bragg-sensors and acoustic emission detection. INSIGHT 45 (8): 542-+ AUG 2003.

[2] De Waele W, Degrieck J, Baets R, Moerman W, Taerwe L, Load and deformation monitoring of composite pressure vessels by means of optical fibre sensors. INSIGHT 43 (8): 518-525 AUG 2001.

[3] C.S. Shin and C.C. Chiang, Fatigue damage monitoring in polymeric composites using multiple fiber bragg gratings. International Journal of Fatigue, Volume 28, Issue 10, October 2006, Pages 1315-1321, The Third International Conference on Fatigue of Composites.

[4] Larissa Sorensen, Thomas Gmür and John Botsis, Residual strain development in an AS4/PPS thermoplastic composite measured using fibre Bragg grating sensors, COMPOSITES PART A: APPLIED SCIENCE AND MANUFACTURING 37 (2) Feb 2006 270-281.

[5] Seo DC, Lee JJ, Damage detection of CFRP laminates using electrical resistance measurement and neural network, COMPOSITE STRUCTURES 47 (1-4): 525-530 DEC, 1999.

[6] Angelidis N, Wei CY, Irving PE ,The electrical resistance response of continuous carbon fibre composite laminates to mechanical strain, COMPOSITES PART A: APPLIED SCIENCE AND MANUFACTURING 35 (10): 1135-1147, 2004.

[7] Irving PE, Thiagarajan C, Fatigue damage characterization in carbon fibre composite materials using an electrical potential technique, SMART MATERIALS & STRUCTURES 7 (4): 456-466 AUG, 1998.

[8] Park JB, Okabe T, Takeda N, New concept for modeling the electromechanical behavior of unidirectional carbon-fiber-reinforced plastic under tensile loading, SMART MATERIALS & STRUCTURES 12 (1): 105-114 FEB, 2003.

[9] Van Paepegem W. , De Baere I. and Degrieck J. , Modelling the nonlinear shear stress-strain response of glass fibre-reinforced composites. Part I: Experimental results. COMPOSITES SCIENCE AND TECHNOLOGY 66 (2006) 1455-1464.

[10] Sun, C.T. and Chung, I. (1993). An oblique end tab design for testing off-axis composite specimens. COMPOSITES, 24 (8), 619-623.

[11] Pierron, F. And Vautrin, A. (1996). The 10deg off-axis tensile test: a critical approach. COMPOSITES SCIENCE AND TECHNOLOGY, 56, 483-488.

[12] Pierron, F. and Vautrin, A. (1997). New ideas on the measurement of the in-plane shear strength of unidirectional composites. JOURNAL OF COMPOSITE MATERIALS, 31 (9), 889-895.

[13] Pierron, F., Alloba, E., Surrel, Y. and Vautrin, A. (1998). Whole-field assessment of the effects of boundary conditions on the strain field in off-axis tensile testing of unidirectional composites. COMPOSITES SCIENCE AND TECHNOLOGY, 58, 1939-1947.

[14] Andre Lavoie J. , Soutis C. and Morton J., Apparent strength scaling in continuous fiber composite laminates. COMPOSITES SCIENCE AND TECHNOLOGY, Volume 60, Issue 2, 1 February 2000, Pages 283-299.

[15] Odegard G. and Kumosa M., Elastic-plastic and failure properties of a unidirectional carbon/PMR-15 composite at room and elevated temperatures. COMPOSITES SCIENCE AND TECHNOLOGY, Volume 60, Issue 16, December 2000, Pages 2979-2988.

[16] Kim KS, Hahn HT, A stress analysis of a mechanical joint for carbon composite rods. ADVANCED COMPOSITE MATERIALS 7 (2): 137-150 1998.

[17] Miyano Y, Nakada M, Kudoh H, Muki R, Determination of tensile fatigue life of unidirectional CFRP specimens by strand testing. MECHANICS OF TIME-DEPENDENT MATERIALS 4 (2): 127-137 2000.

[18] Liu W, Soden PD, Kaddour AS, Design of end plugs and specimen reinforcement for testing +/- 55 degrees glass/epoxy composite tubes under biaxial compression. COMPUTERS & STRUCTURES 83 (12-13): 976-988 MAY 2005.

[19] Xie M. and Adams, DF., Effect of specimen tab configuration on compression testing of composite materials. JOURNAL OF COMPOSITES TECHNOLOGY AND RESEARCH, JCTRER 17 (2), APRIL 1995, pp77-83

[20] Portnov, G. G., Kulakov, V. L., Arnautov, A. K., A refined stress-strain analysis in the load transfer zone of flat specimens of high-strength unidirectional composites in uniaxial tension - 1. Theoretical analysis. MECHANICS OF COMPOSITE MATERIALS 42 (6): 547-554 NOV-DEC 2006.

[21] Kulakov VL, Tarnopol'skii YM, Arnautov AK, Rytter J, Stress-strain state in the zone of load transfer in a composite specimen under uniaxial tension. MECHANICS OF COMPOSITE MATERIALS 40 (2): 91-100 MAR-APR 2004.

[22] Portnov, G. G., Kulakov, V. L., Arnautov, A. K., A refined stress-strain analysis in the load transfer zone of flat specimens of high-strength unidirectional composites in uniaxial tension - 2. Finite element parametric analysis. MECHANICS OF COMPOSITE MATERIALS 43 (1): 29-40 JAN-FEB 2007.

[23] Mallick, P.K. (1997). Composites Engineering Handbook. New York, Marcel Dekker Inc.

[24] Herakovich, C.T. (1998). Mechanics of fibrous composites. New York, John Wiley & Sons, Inc.

[25] Schulte, K., Baron, Ch., Neubert, H., Bader, M.G. , Boniface, L., Wevers, M., Verpoest, I. and de Charentenay, F.X. (1985). Damage development in carbon fibre epoxy laminates : cyclic loading. In : Proceedings of the MRS-symposium "Advanced Materials for Transport", November 1985, Strassbourg, 8 p.

[26] Schulte, K., Reese, E. and Chou, T.-W. (1987). Fatigue behaviour and damage development in woven fabric and hybrid fabric composites. In : Matthews, F.L., Buskell, N.C.R., Hodgkinson, J.M. and Morton, J. (eds.). Sixth International Conference on Composite Materials (ICCM-VI) & Second European Conference on Composite Materials (ECCM-II) : Volume 4. Proceedings, 20-24 July 1987, London, UK, Elsevier, pp. 4.89-4.99.

[27] Schulte, K. (1984). Stiffness reduction and development of longitudinal cracks during fatigue loading of composite laminates. In : Cardon, A.H. and Verchery, G. (eds.). Mechanical characterisation of load bearing fibre composite laminates. Proceedings of the European Mechanics Colloquium 182, 29-31 August 1984, Brussels, Belgium, Elsevier, pp. 36-54.

[28] Fujii, T., Amijima, S. and Okubo, K. (1993). Microscopic fatigue processes in a plain-weave glass-fibre composite. COMPOSITES SCIENCE AND TECHNOLOGY, 49, 327-333.

[29] Pandita, S.D., Huysmans, G., Wevers, M. and Verpoest, I. (2000). Tensile fatigue behaviour of glass-plain weave fabric composites in the on and off-axis directions. Proceedings of the Fifth International Conference on Textile Composites, Leuven, Belgium, 18-20 September 2000.

[30] Sidoroff, F. and Subagio, B. (1987). Fatigue damage modelling of composite materials from bending tests. In : Matthews, F.L., Buskell, N.C.R., Hodgkinson, J.M. and Morton, J. (eds.). Sixth International Conference on Composite Materials (ICCM-VI) & Second European Conference on Composite Materials (ECCM-II) : Volume 4. Proceedings, 20-24 July 1987, London, UK, Elsevier, pp. 4.32-4.39.

[31] Vieillevigne, S., Jeulin, D., Renard, J. and Sicot, N. (1997). Modelling of the fatigue behaviour of a unidirectional glass epoxy composite submitted to fatigue loadings. In : Degallaix, S., Bathias, C. and Fougères, R. (eds.). International Conference on fatigue of composites. Proceedings, 3-5 June 1997, Paris, France, La Société Française de Métallurgie et de Matériaux, pp. 424-430.

[32] Kawai, M. (1999). Damage mechanics model for off-axis fatigue behavior of unidirectional carbon fiber-reinforced composites at room and high temperatures. In: Massard, T. and Vautrin, A. (eds.). Proceedings of the Twelfth International Conference on Composite Materials (ICCM-12). Paris, France, 5-9 July 1999, pp. 322.

[33] Hwang, W. and Han, K.S. (1986). Fatigue of composites - Fatigue modulus concept and life prediction. JOURNAL OF COMPOSITE MATERIALS, 20, 154-165.

[34] Hwang, W. and Han, K.S. (1986). Cumulative damage models and multi-stress fatigue life prediction. JOURNAL OF COMPOSITE MATERIALS, 20, 125-153.

[35] Whitworth, H.A. (1987). Modelling stiffness reduction of graphite epoxy composite laminates. JOURNAL OF COMPOSITE MATERIALS, 21, 362-372.

[36] Yang, J.N., Jones, D.L., Yang, S.H. and Meskini, A. (1990). A stiffness degradation model for graphite/epoxy laminates. JOURNAL OF COMPOSITE MATERIALS, 24, 753-769.

[37] Brøndsted, P., Andersen, S.I. and Lilholt, H. (1997). Fatigue damage accumulation and lifetime prediction of GFRP materials under block loading and stochastic loading. In : Andersen, S.I., Brøndsted, P., Lilholt, H., Lystrup, Aa., Rheinländer, J.T., Sørensen, B.F. and Toftegaard, H. (eds.). Polymeric Composites - Expanding the Limits. Proceedings of the 18th Risø International Symposium on Materials Science, 1-5 September 1997, Roskilde, Denmark, Risø International Laboratory, pp. 269-278.

[38] Brøndsted, P., Lilholt, H. and Andersen, S.I. (1997). Fatigue damage prediction by measurements of the stiffness degradation in polymer matrix composites. In : Degallaix, S., Bathias, C. and Fougères, R. (eds.). International Conference on fatigue of composites. Proceedings, 3-5 June 1997, Paris, France, La Société Française de Métallurgie et de Matériaux, pp. 370-377.

[39] Shin CS and Chiang CC, Fatigue damage monitoring in polymeric composites using multiple fiber Bragg gratings, INTERNATIONAL JOURNAL OF FATIGUE 28 (10): 1315-1321 OCT 2006.

[40] Bandoh, S., Matsumura, K., Zako, M., Shiino, T. and Kurashiki, T. (2001). On the detection of fatigue damage in CFRP by measuring Poisson's ratio. In: Hui, D. (ed.). Eighth International Conference on Composites Engineering (ICCE/8). Proceedings. Tenerife, Spain, 5-11 August 2001, pp. 55-56.

[41] Pidaparti, R.M. and Vogt, A. (2002). Experimental investigation of Poisson's ratio as a damage parameter for bone fatigue. JOURNAL OF BIOMEDICAL MATERIALS RESEARCH PART A, 59 (2): 282-287.

[42] Van Paepegem W., De Baere I., Lamkanfi E. and Degrieck J., Poisson's ratio as a sensitive indicator of (fatigue) damage in fibre-reinforced plastics, FATIGUE AND FRACTURE OF ENGINEERING MATERIALS AND STRUCTURES, 30 (4): 269-276 APR 2007.

[43] Colpo F., Humbert L. and Botsis J., Characterisation of residual stresses in a single fibre composite with FBG sensor. COMPOSITES SCIENCE AND TECHNOLOGY 67 (9): 1830-1841 JUL 2007.

[44] Montanini, R., D'Acquisto, L., Simultaneous measurement of temperature and strain in glass fiber/epoxy composites by embedded fiber optic sensors: I. Cure monitoring. SMART MATERIALS & STRUCTURES 16 (5): 1718-1726 OCT 2007.

[45] Colpo F, Humbert L, Glaccari P, Botsis J., Characterization of residual strains in an epoxy block using an embedded FBG sensor and the OLCR technique. COMPOSITES PART A-APPLIED SCIENCE AND MANUFACTURING 37 (4): 652-661 2006.

[46] Sorensen L, Gmur T, Botsis J, Residual strain development in an AS4/PPS thermoplastic composite measured using fibre Bragg grating sensors. COMPOSITES PART A-APPLIED SCIENCE AND MANUFACTURING 37 (2): 270-281 2006.

[47] Wang XJ, Chung DDL, Self-monitoring of fatigue damage and dynamic strain in carbon fiber polymer-matrix composite, COMPOSITES PART B-ENGINEERING 29 (1): 63-73 ,1998.

[48] Wang XJ, Chung DDL, Real-time monitoring of fatigue damage and dynamic strain in carbon fiber polymer-matrix composite by electrical resistance measurement, SMART MATERIALS & STRUCTURES 6 (4): 504-508, AUG 1997.

Chapter 6

A BENDING SETUP FOR FATIGUE OF THIN COMPOSITE LAMINATES

In this chapter, it is investigated whether a bending setup is suited for performing fatigue experiments and modelling of thin fibre-reinforced composites with a low bending stiffness such as the carbon-PPS material under study. First, the standard and a modified three-point bending setup are discussed. Next, a four-point bending setup is commented on. Then, clamped outer supports are added to decrease the midspan displacement. For all these topics, both experimental and numerical results are presented.

6. 1. INTRODUCTION

The vast majority of fatigue tests on fibre-reinforced composites is performed in uni-axial tension/tension or tension/compression fatigue [1-5]. These tests are accepted by international standards (ASTM D3479) and provide the S-N data for the tested material.

Although bending fatigue tests are not widely accepted as a standard, they are used a lot for research purposes [6-8]. They do have some important advantages as well: (i) bending loads often occur in in-service loading conditions, (ii) there are no problems with buckling, compared to tension/compression fatigue, and (iii) the required forces are much smaller. The latter results in the fact that simple equipment can suffice for conducting bending fatigue tests, compared to the expensive servo-hydraulic tensile machines, required for tension and compression fatigue. To evaluate the stiffness degradation and damage growth in the fibre-reinforced laminate, the hysteresis loop of one loading cycle can be measured. In case of three- and four-point bending fatigue, the history of bending force versus midspan displacement is recorded.

In this chapter, it is investigated if a bending setup with certain modifications can be used for the validation of (a combination of) damage models for thin composite laminates under static or fatigue loading conditions. First, the standard three-point bending setup is commented on. Next, a modified three-point bending setup with fully-reversed loading is considered. This is followed by the discussion of a four-point bending setup, because its loading conditions should allow for an easy finite element modelling. In order to reduce midspan displacements and to increase the occurring bending forces, the ends of the specimen are clamped. This is considered first for the four-point and then for the three-point setup. During these discussions, both experimental and numerical data are provided, if applicable.

6. 2. THE STANDARD THREE-POINT BENDING SETUP

6. 2. 1. Introduction

The loading conditions in a three-point bending setup are interesting for the validation of damage models. Figure 6-1 shows the resulting transverse force and bending moment in a beam, subjected to three-point bending. For an isotropic material, this bending moment results in the following stresses [9]:

$$\sigma_{xx} = \frac{Mz}{I_{yy}} \tag{6.1}$$

Where I_{yy} is the moment of inertia of the cross section of the beam and z is the position in the beam with respect to the neutral fibre. This means that the upper side of the beam is loaded in compression and the lower side in tension, with a maximum absolute value of:

$$\sigma_{xx,MAX} = \left| \frac{M_{MAX} \frac{h}{2}}{I_{yy}} \right| \tag{6.2}$$

With h being the total height of the beam and M_{MAX} the maximum bending moment in the centre of the beam. The latter is equal to $\frac{FL}{4}$ as is shown in Figure 6-1.

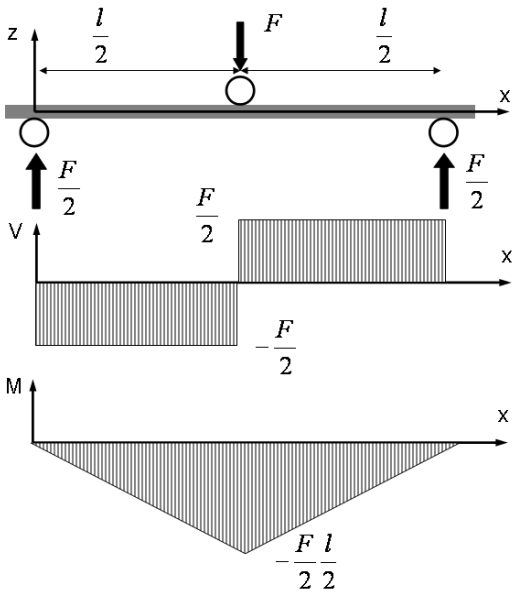

Figure 6-1 Transverse force and bending moment in a three-point bending setup.

Therefore, this loading setup already imposes both tension and compression in the specimen, but at different locations.
This setup could be used for the validation of (i) a static damage model that implicates both tensile and compressive damage; (ii) a combination of a tension-tension and a compression-compression fatigue damage model.
Although the setup itself has some very promising aspects with regards to the load conditions, the standard setup also has some negative aspects, both experimental and numerical.

6. 2. 2. Experimental results

6. 2. 2. a. Specimen geometry

The dimensions of the coupons used for the three-point bending experiments are shown in Figure 6-2, all dimensions are in millimetres. The used material was the carbon fabric-reinforced PPS and the stacking sequence was $[(0^o,90^o)]_{4s}$ with respect to the longitudinal axis of the specimen.

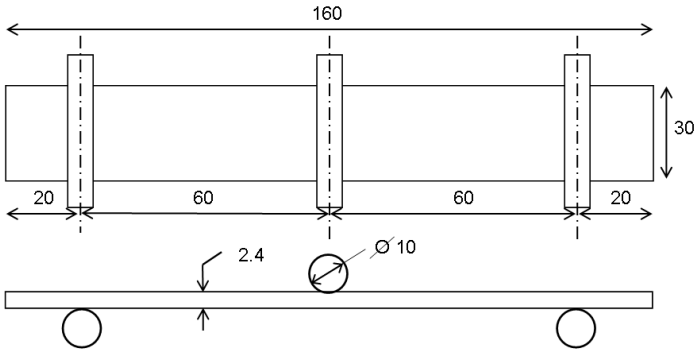

Figure 6-2 Dimensions of the used bending coupon in millimetres.

The dimensions of the bending coupons are 160 mm x 30 mm, as previously mentioned. The length of the specimen is chosen so large to assure that the out of plane shear stresses τ_{13} will be negligible compared to the in-plane stresses. As a result, the damage behaviour of the composite will be controlled by the in-plane stresses. The coupons are sawed with a water cooled diamond tipped disc, but the width cannot be adjusted very accurately, the width of the coupon tends to vary between 29 mm and 31 mm. In order to be able to compare the results, the force is scaled to a width of 30 mm. This can be done without corrupting the results, as illustrated below. The same coordinate system as in Figure 6-1 is used for the theoretical deduction of the scaling law.

The displacement as function of the force can be written as [9]:

$$u(x) = \frac{F}{EI} f(x) \tag{6.3}$$

Where $f(x)$ is just a function of x. The influence of the dimensions lies in the factor I

$$I = \frac{1}{12} bh^3 \tag{6.4}$$

This leads to

$$F = \frac{1}{12} bh^3 \frac{u(x)}{f(x)} \tag{6.5}$$

which means that the force F is a linear function of the width b. So to scale the force in the experiment, it must be divided by the original width and then multiplied by 30 mm, the standard width.

6. 2. 2. b. Quasi-static hysteresis tests

In the introduction, it was mentioned that the hysteresis loop can be used to quantify the damage during bending. However, not all of the occurring hysteresis in the force-displacement evolution is due to damage. To prove this, some quasi-static hysteresis tests were performed. These experiments were done in a displacement-controlled manner with a displacement speed of 2 mm/min. Specimen C10 was loaded until 15 mm midspan displacement was reached and specimen C19 was unloaded after 14 mm of midspan displacement. The resulting force-displacement curves are depicted in Figure 6-3, the loading and unloading directions are illustrated.

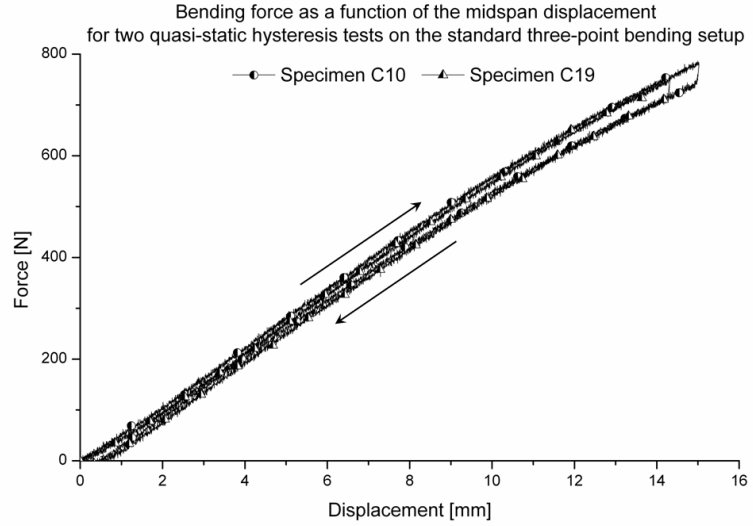

Figure 6-3 Force-displacement curve for the quasi-static hysteresis test on the single-sided three-point bending setup.

The occurring hysteresis can clearly be seen, but it should be remarked that at the turning point, there is a sudden drop in the bending force. This can be seen more clearly in Figure 6-4, where the evolution of the bending force in time is illustrated.

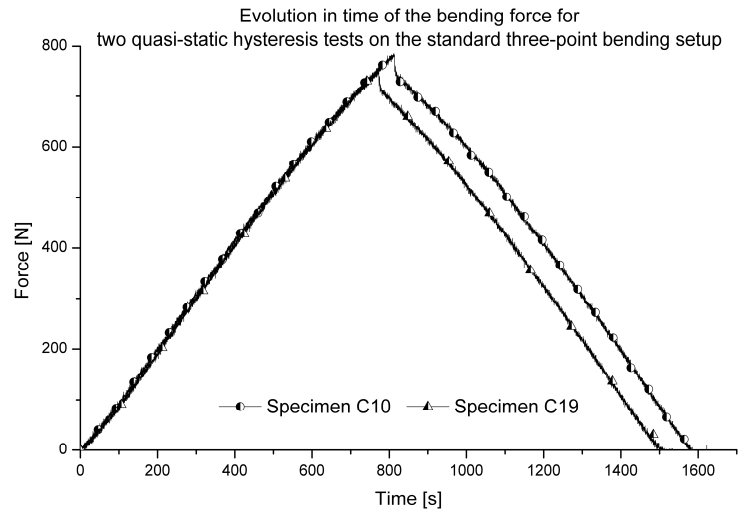

Figure 6-4 Bending force as a function of time for quasi-static hysteresis test on the single-sided three-point bending.

The sudden drop in bending force is due to the friction between the specimen and the supporting rolls. This is illustrated in Figure 6-5.

Since the tested specimens are quite thin, the midspan deflections become so large that the reaction forces of the supports are no longer vertical. This results in tangential friction forces F_S which always point opposite to the direction of movement. For a given midspan displacement, the specimen itself yields a certain bending force F_B, which is independent of the direction of movement.
If the central indenter moves down (Figure 6-5 (a)) then the specimen slides inward over the supports, yielding outward pointing frictional forces. Their resultant force points upward, increasing the bending force F_B to $F_{B,T}$ which is registered by the load cell.

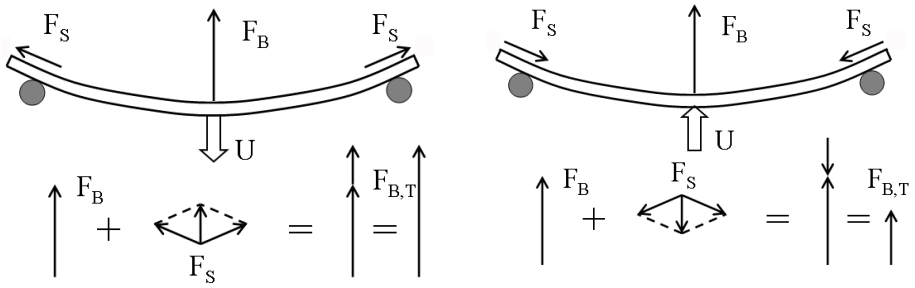

(a) Downward movement (b) Upward movement

Figure 6-5 Illustration of the effect of friction on the supports on the resulting bending force.

If the central indenter moves upward (Figure 6-5 (b)) then the specimen slides outward over the supports, yielding inward pointing frictional forces. Their resultant force points downward, decreasing the bending force F_B to $F_{B,T}$ which is registered by the load cell.
This can be verified experimentally by artificially changing the coefficient of friction between the specimen and the supports. Three situations were considered: (i) a sheet of Teflon is placed on the supports, so a low coefficient of friction is achieved; (ii) nothing is added, just plain composite-steel contact and (iii) a high coefficient of friction is achieved by bonding some emery paper on the supports. The results of these quasi-static hysteresis tests are given in Figure 6-6, the tests were done in a displacement controlled manner with a displacement speed of 2 mm/min and the point of return was 10 mm midspan displacement.

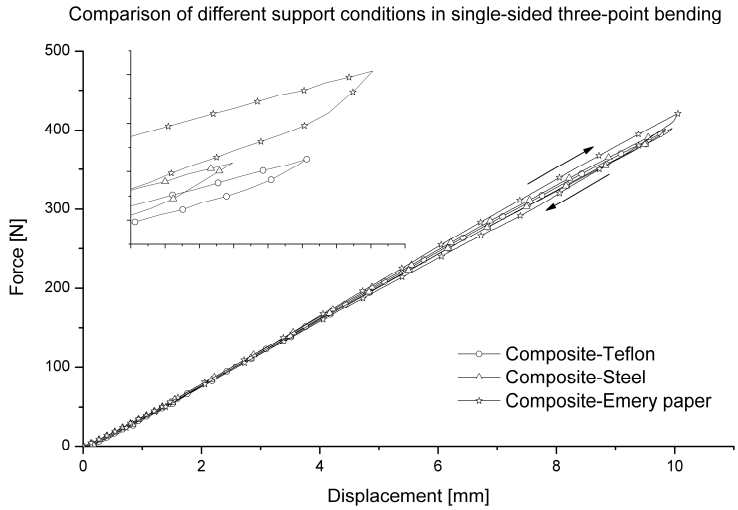

Figure 6-6 Force-displacement curves for the three different contact situations.

From the enlarged view, it can clearly be verified that the higher the friction, the larger the jump in bending force, as was expected.
Of course, this can also be verified by performing finite element calculations, which will be discussed in paragraph 6. 2. 3.
It should be mentioned that for these experiments, no strain gauges were considered. Because of the large midspan displacements, the strain gauge itself would also be bent significantly, influencing the actual strain measurement. Furthermore, in the new design, which is discussed in paragraph 6. 3, there is no space to mount the strain gauges, so there is no possibility of comparing strain measurements.
For the fatigue experiments, the strain gauges would de-bond very early, again because of the large midspan displacements.

6. 2. 2. c. Fatigue experiments

While conducting some preliminary fatigue tests, another negative aspect of the occurring friction conditions between specimen and supports was noticed. Because of the sliding of the specimen over the supporting rolls, wear occurs of both specimen and rolls. The surface-damage of the specimen is illustrated in Figure 6-7. It is obvious that this should be avoided if possible.

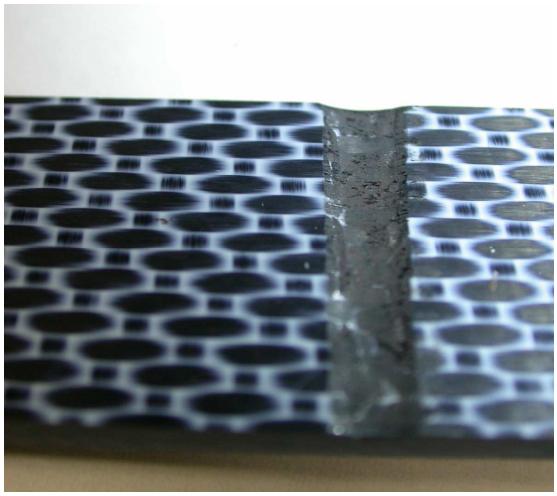

Figure 6-7 Illustration of the wear pattern on the specimen due to the contact with the supporting rolls.

6. 2. 3. Finite element simulations

6. 2. 3. a. General

The used finite element software was ABAQUS™/Standard 6.7-3, as mentioned in chapter 2. The modelling of the three-point bending setup in general has some difficulties. Figure 6-1 illustrates the loading conditions in a beam that is subjected to three-point bending. As can be seen, there is a transverse force V, equal to half of the loading force F, over the entire beam and the bending moment grows linearly until the centre of the beam.
These loading conditions cannot be modelled by equivalent loads and boundary conditions, meaning that the supports need to be modelled. The latter requires contact conditions with friction, which has its effect on the calculation time. A friction coefficient for friction between the carbon-PPS and steel was determined in [10]. If friction is omitted, then the force will be underestimated, because the resultant of the friction on the supports is not taken into account. Furthermore, the influence of the friction on the hysteresis loops, which is well proven in [11] should not be neglected. Finally, because of the large deformations, a geometrically nonlinear analysis must be performed.

6. 2. 3. b. Three-point bending with rigid supports

In order to save calculation time, symmetry is used to model the setup, so only a quarter of the setup is implemented. This is illustrated in Figure 6-8.

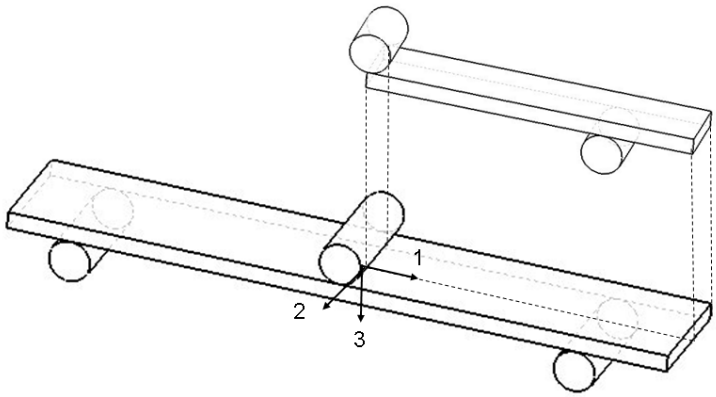

Figure 6-8 Modelling only a quarter of the total setup.

The dimensions of the modelled specimen are 2.4 mm x 15 mm x 80 mm and the rolls have a diameter of 10 mm and a length of 20 mm. The specimen is partitioned eight times, each partition representing one layer. Three more partitions are made for the contact surfaces. The rolls are also partitioned for a better mesh. The boundary conditions as well as the used mesh are illustrated in Figure 6-9.

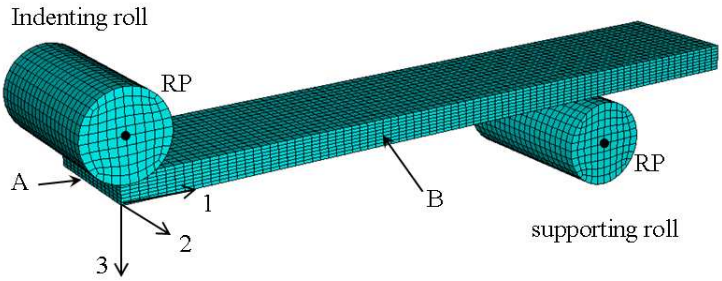

Figure 6-9 Illustration of the mesh and the boundary conditions for the three-point bending setup with rigid supports.

To model symmetry, the following boundary conditions are applied.
On plane A: $U_1 = 0$.
On plane B: $U_2 = 0$.
Since 3D elements do not have rotational degrees of freedom, no rotational boundary conditions are used. The reference point of the supporting role is completely fixed. For the indenting roll, the movement along the 1-axis and 2-axis is inhibited and a downward displacement of 20 mm is imposed on the reference point in the case of a displacement-controlled test.
For the specimen, a quadratic brick element with reduced integration, C3D20R, is used. For the material, a linear elastic orthotropic material model with the following properties (Table 6-1) is used.

The values of G_{13} and G_{23} are assumed to be equal to G_{12} since these values are very difficult to determine experimentally and will have only very limited influence on the results.

Table 6-1 Engineering constants implemented in ABAQUS™.

E_{11} [MPa]	E_{22} [MPa]	E_{33} [MPa]	ν_{12} [-]	ν_{13} [-]	ν_{23} [-]	G_{12} [MPa]	G_{13} [MPa]	G_{23} [MPa]
56000	57000	9000	0.033	0.3	0.3	4175	4175	4175

The supports are meshed with a linear brick element with reduced integration, C3D8R. The mesh size is approximately 1 mm for both the rolls and the specimen. To further reduce calculation time, a rigid-body constraint is enforced on the areas of the roll that do not make contact with the specimen. For these area's, ABAQUS™ assumes it is analytically rigid and does not calculate stresses nor strains.

As was previously mentioned, friction must also be modelled if the simulation is to be as realistic as possible. For the indenting roll, no tangential movement is expected. Therefore, a 'hard normal contact' is defined for this region.
For the supporting roll, there is a tangential movement, since the specimen slides over the roll as the displacement grows. In order to determine the friction coefficient, a number of simulations were performed, using different coefficients of friction (Figure 6-10).
Since damage was not taken into account for these simulations, the calculated force should be an overestimation of the experimental force at higher displacements. Therefore, a coefficient between 0.2 and 0.3 is chosen. This also is in good agreement with the measurements done in [10]. For the ABAQUS™ friction formulation, friction with a Lagrange multiplier and finite sliding is chosen. With these conditions, an average simulation takes about six hours on the used computer.

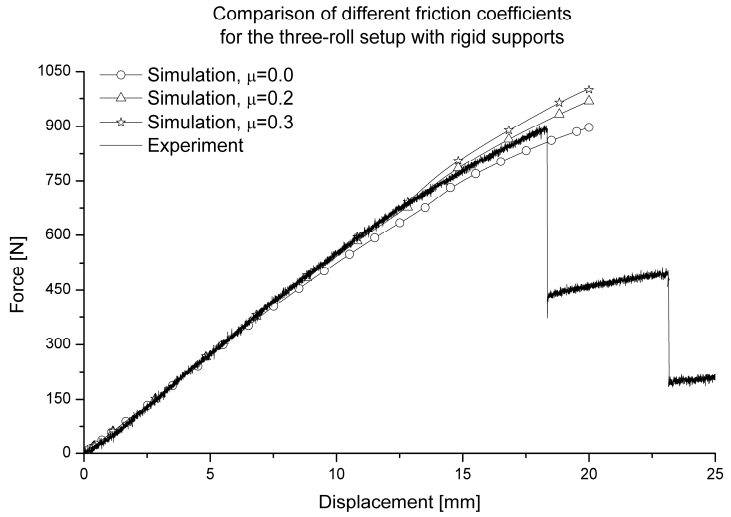

Figure 6-10 Comparison of the experiment with simulations using different friction coefficients for the three-point bending setup with rigid supports.

Finally, the effect of friction on the hysteresis loops can also be proven, as mentioned in paragraph 6. 2. 2. b. Three simulations were performed, each with a different coefficient of friction. These results are shown in Figure 6-11.

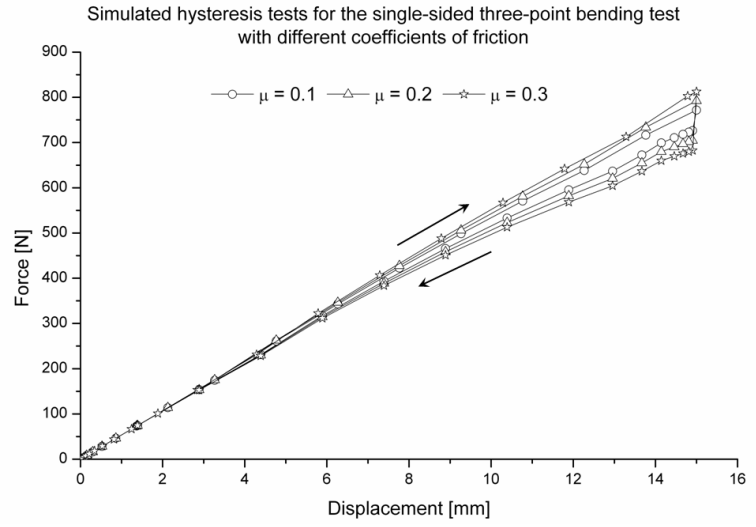

Figure 6-11 Simulated hysteresis loops with different coefficients of friction.

6. 2. 3. c. Stress distribution results

It could already be noted that there is a very good correspondence in the evolution of the force as a function of the midspan displacement (see Figure 6-10).
The average midspan deflection, at which fracture occurs for the single-sided setup, is about 17 mm (see Figure 6-10). For this deflection, Figure 6-12 shows the longitudinal stresses for the simulation with μ equal to 0.2 which gave best correspondence in the force-displacement curve.

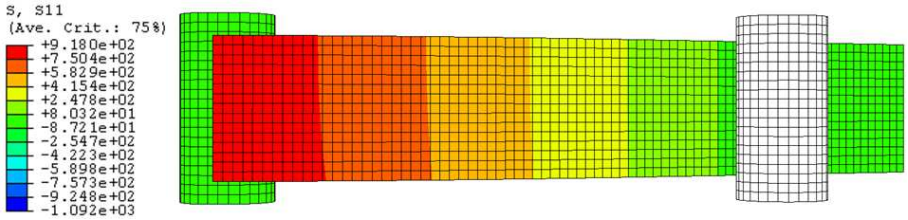

Figure 6-12 The longitudinal stress distribution (σ_{11}) at 17 mm midspan deflection for the single-sided setup.

It may be remarked that, despite the excellent agreement in the force-displacement curve (Figure 6-10), the longitudinal stresses are higher than the ultimate stress (See Chapter 3; X_T = 734 MPa). However, this simulation only includes linear elastic material behaviour. Implementing an accurate material model should only improve the agreement of both stresses and force-displacement curve, since the stresses are only caused by the elastic part of the strain. In these linear simulations, the total strain is equal to the elastic strain, but once a material model, which takes permanent deformations into account, is implemented, the elastic strains will be less than the total strains, resulting in lower stress levels for equal midspan displacements.

6. 3. THREE-POINT BENDING SETUP WITH ROTATING SUPPORTS

When single-sided three-point bending is used (see Figure 6-13), the deflection of the centre of the specimen evolves between zero and a certain value u_{max} (displacement-controlled).

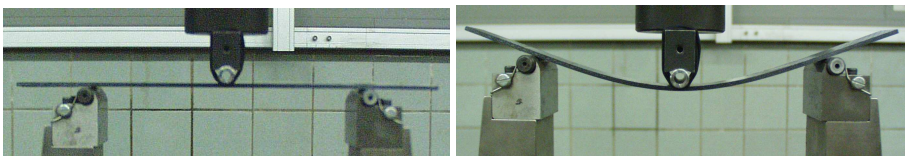

0 mm deflection 17 mm deflection

Figure 6-13 Single-sided three-point bending test.

This value of u_{max} may be very large for thin composites with low bending stiffness, 17 mm was reached for the $[(0^o,90^o)]_{4s}$ carbon-PPS in Figure 6-13. Another negative aspect of the single-sided setup is that at large midspan displacements, the friction on the outer supports influences the shape of the hysteresis loops, as has been mentioned in paragraph 6. 2.

Moreover, in fatigue testing, depending on the stacking sequence, the specimens can show permanent deflection after a few thousands of cycles. When performing a displacement-controlled test, the latter results in the loss of contact of the indenter when its displacement is smaller than the permanent deflection. In the next cycle, the indenter impacts on the surface of the specimen, causing impact damage and as a result, the fatigue data is corrupted. Furthermore, the small sliding of the specimen over the supporting rolls causes large wear of the composite surface (see Figure 6-7). The first issue can be solved if the permanent deflection is kept symmetrically, which means it is kept at zero deflection. This can easily be obtained by fully-reversed bending, where the displacement of the indenter varies between $- u_{max}$ and $+ u_{max}$. If the test is performed in load-control, then this 'loss of contact' problem does not occur. However, a load-controlled bending test requires a very accurate PID controller and the test should be performed at lower frequencies than under displacement control. Furthermore, the load-controlled simulation resulted in a lot more convergence problems. Therefore, load-control has not been considered here. When fully-reversed bending is used, each side of the specimen is successively loaded in tension as well as in compression. As a result, the material in the beam sees alternating tension and compression, which makes this setup ideal for the validation of tension-compression fatigue models.

Of course, fully-reversed bending is not possible with the standard three-point bending setup (Figure 6-13). Some adjustments must be made to this setup to allow for the upward motion. These modifications are discussed in the next paragraph.

6. 3. 1. Design of the fully-reversed setup

If fully-reversed bending is considered, some changes must be made to the original setup as illustrated in Figure 6-13: (i) for the central indenter as well as the outer supports, two contact cylinders are required, one for the upward and one for the downward motion. Since the centre of the specimen remains horizontal (see Figure 6-13, the right), no additional modifications are needed for the central indenter; (ii) because the specimen rotates at its ends (see Figure 6-13, the right), the outer supports need to allow for this rotation. Otherwise, this would induce unwanted reaction forces in the specimen, corrupting the fatigue data.

The design of the central indenter is shown in Figure 6-14. This part is the easiest, since the only modification is that there need to be two supporting rolls. These rolls are fitted in a rectangular aluminium frame; the rolls themselves are hardened steel, to limit the wear of the supports. One roll is fixed in the frame and the other can move vertically, guided between four guidance bars; the distance between the two rolls can be adjusted by two bolts to fit the thickness of the specimen. Because of the two rolls, strain gauges can no longer be mounted on the specimen, since they would be damaged by these rolls.

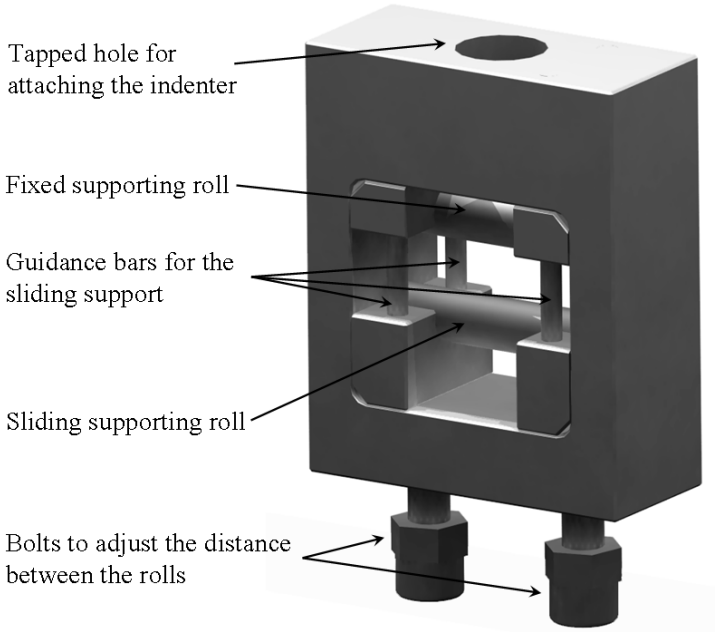

Figure 6-14 Design of the central indenter.

The two outer supports have an extra difficulty, they should allow for rotation. This was solved by the following concept: an outer aluminium frame is designed, which holds a slightly modified design of the central indenter.

For the latter, the tapped hole at the top is omitted and two axes are mounted on the sides of the frame. These two axes are then supported by the outer frame by means of ball bearings and as such, the rotation is allowed. Both supporting rolls, which again are made of hardened steel to limit wear of the supports, are adjustable by bolts. The inner frame of the outer support is shown in Figure 6-15.

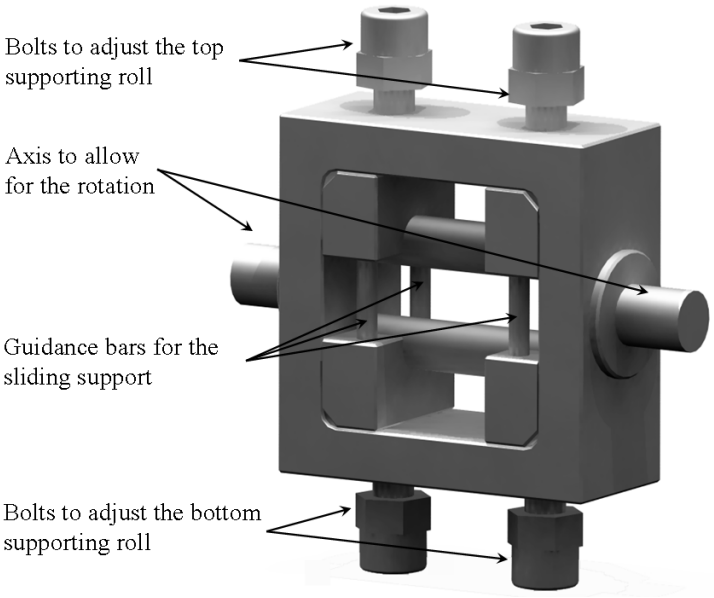

Figure 6-15 Illustration of the inner frame of the outer supports.

The outer support has two central spaces for the ball bearings. For maintenance purposes, such as lubricating, these bearings need to be accessible, but during experiments, it is best they are shielded to avoid dust and debris to penetrate the bearings. Therefore, cover plates are provided. An extra fixture at the bottom of the outer support is foreseen to mount it on the standard INSTRON rail. The design of the outer frame is depicted in Figure 6-16.

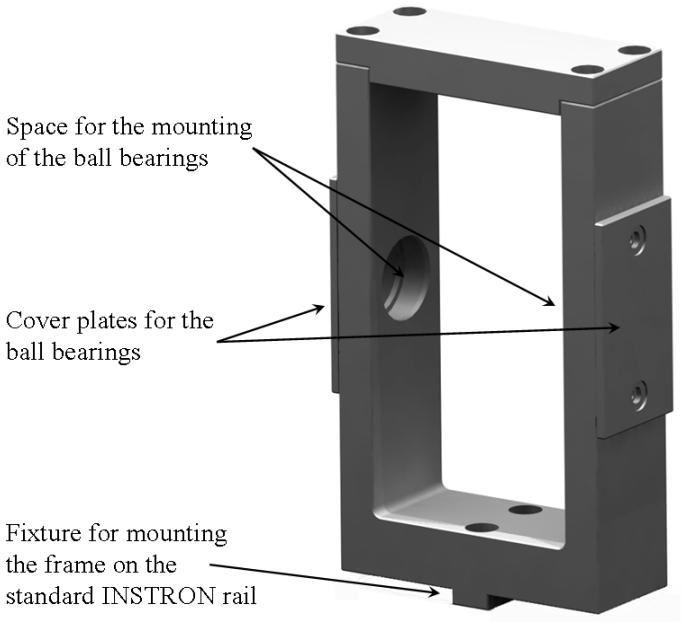

Figure 6-16 Illustration of the outer frame of the outer supports.

The final design of both the support and the indenter is shown in Figure 6-17 and the total setup is illustrated in Figure 6-18. The central indenter is already mounted on an extra fixture which can be fitted to the servo-hydraulic tensile machine. It should also be remarked that although the outer frame of the outer support was originally designed in two parts (see Figure 6-16) it was possible to mill it in one piece, which of course increases stiffness and fatigue resistance.

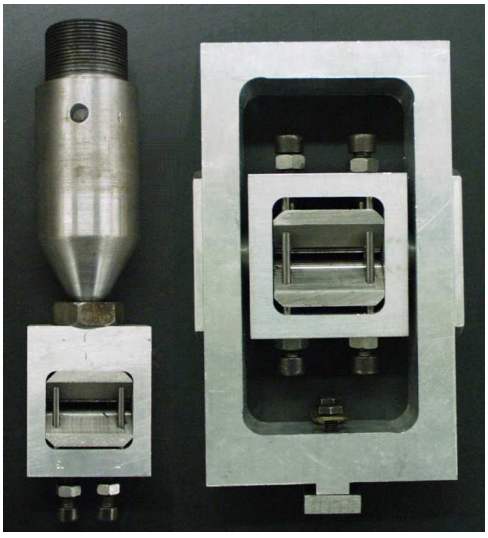

Figure 6-17 The rotating outer support (right) and the central roll (left).

Figure 6-18 The fully-reversed three-point bending setup.

Details and drawings of this setup can be found in [12]. Figure 6-19 illustrates the described setup at maximum deflection, the rotation of the supports can be seen.

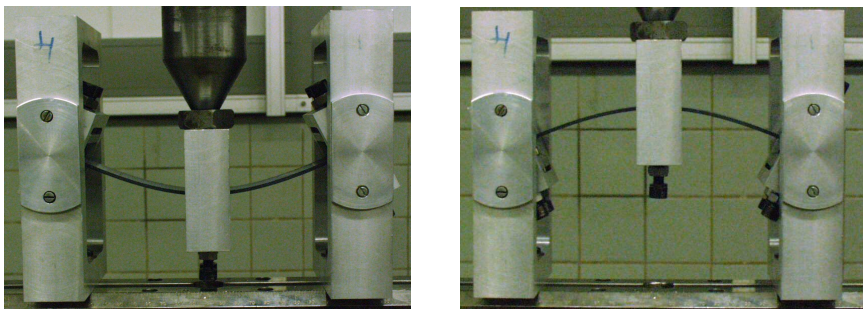

-17 mm deflection +17 mm deflection

Figure 6-19 Illustration of the fully-reversed three-point bending with the described setup.

A problem that occurred during fatigue testing was the drifting of the specimen in the clamps. Tightening the outer supports is not an option, since this would induce membrane stresses in the specimen. Tightening the centre rolls may not be done either, because this pressure compresses the specimen through the thickness and makes the propagation of cracks more difficult. This corrupts the lifetime of the specimen.

To prevent the drifting of the specimen, a small U shaped object was mounted on the side of the outer support as illustrated in Figure 6-20. If the specimen is mounted, the supporting rolls should make contact without applying any extra pressure.

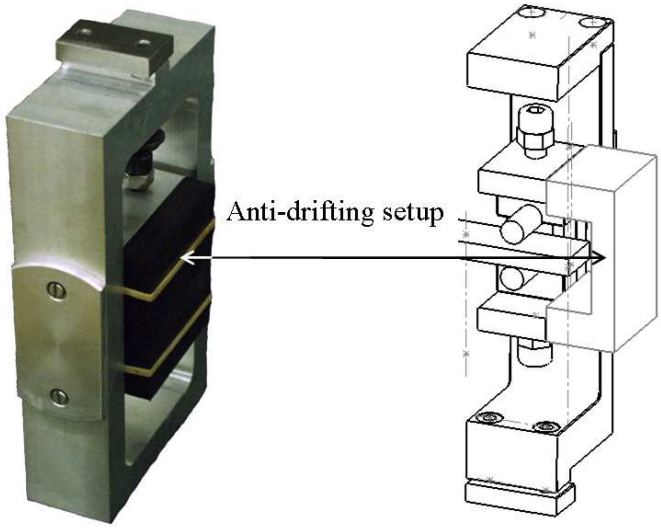

Figure 6-20 The anti-drifting setup.

6. 3. 2. Experiments and Discussion

6. 3. 2. a. Testing Speeds

The preliminary static tests were done at different speeds, to verify whether the loading velocity has any influence on the bending stiffness and strength.
The first speed selected is 2 mm/min, for a quasi-static test. The other speeds are chosen with the fatigue tests in mind (Figure 6-21).

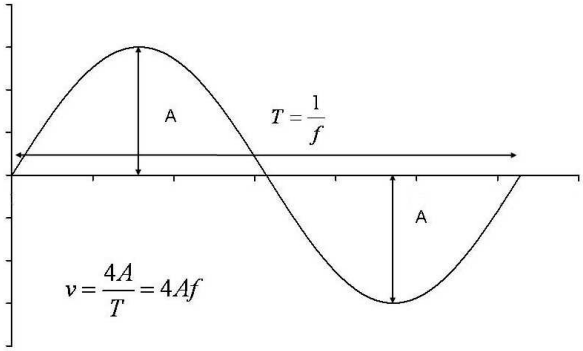

Figure 6-21 Determination of the displacement speed in a fatigue test.

A fatigue test with a displacement-amplitude of 7.5 mm (total displacement 15 mm) and a frequency of 0.5 Hz means an average speed of 15 mm/s or 1200 mm/min. Given the same amplitude, but at a frequency of 2.5 Hz results in a speed of 75 mm/s or 4500 mm/min.

Taking the limits of the machine into account, speeds of 2400 mm/min and 4500 mm/min (= 75 mm/s) are chosen to characterise the material at deformation speeds that occur during fatigue testing. Since the interval between 2 mm/min and 2400 mm/min is quite large, a fourth speed of 300 mm/min is chosen.

6. 3. 2. b. Experiments

When discussing the experiments, the standard three-point bending setup with rigid supports will be referred to as the single-sided or 3ROLL setup, whereas the setup with the rotating supports will be referred to as the fully-reversed or 6ROLL setup.
Figure 6-22 shows the results of a few bending experiments at the mentioned speeds, performed on the setup with the rotating outer supports. It must be noted that the speed has no influence on the bending stiffness, nor on the ultimate bending force. The small deviation in ultimate force is due to scatter in the results. All the specimens break at approximately 20 mm displacement at a corresponding force of approximately 900 N.

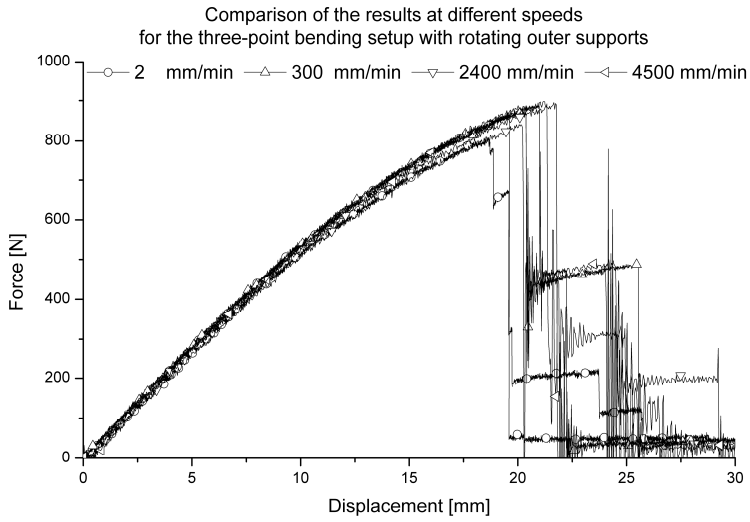

Figure 6-22 Force as a function of the displacement at different speeds.

However, there is a difference in the results for the single-sided bending setup with rigid supports (3ROLL) and the fully-reversed bending setup with rotating supports (6ROLL), as is illustrated in Figure 6-23. It can clearly be seen that for an equal displacement, the force is lower if the rotating outer supports are used. The bending stiffness and ultimate bending force are higher when the single-sided setup without rotating supports is used. This effect is entirely due to the setup, as will be proven in the next paragraph, where the finite element modelling of the setup is discussed.
It may be noticed that for the bending setup with the rigid supports, the influence of the speed on bending stiffness and ultimate bending force is also negligible.

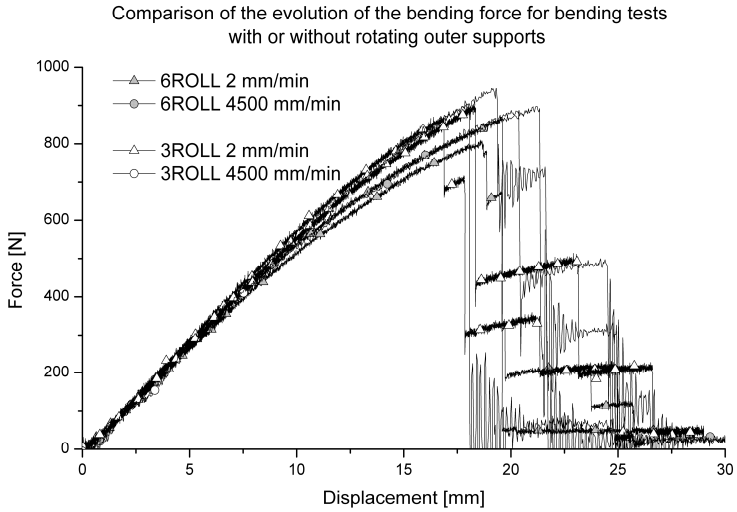

Figure 6-23 Illustration of the influence of the rotating outer supports in three point bending.

6. 3. 3. Finite element simulations

6. 3. 3. a. Fully-reversed three-point bending with rotating supports

As previously done for the standard three-point bending setup with rigid supports, the setup is modelled using symmetry.

Since the central indenting rolls do not require any rotation, they are modelled by two separate rolls (Figure 6-24). To reduce calculation time, rigid body conditions are applied on all areas that do not make contact with the specimen. The element type is the same linear brick element with reduced integration, C3D8R and the element size is 0.5 mm.

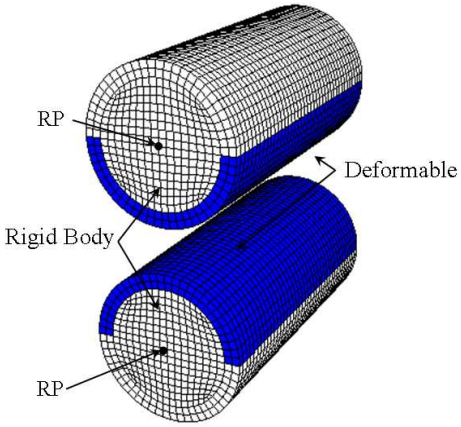

Figure 6-24 The model of the central indenter as two separate rolls.

The easiest way to model the rotating support is by modelling it as a single part, which is depicted in Figure 6-25. The rolls are slightly longer than the width of the specimen, so that the specimen does not make contact with the connecting part between the two rolls. Extra partitions are created (Figure 6-25 on the left) resulting in a better mesh. The distance between the two rolls is equal to the thickness of the specimen and the rolls have a diameter of 10 mm, as was the case in the experimental setup.

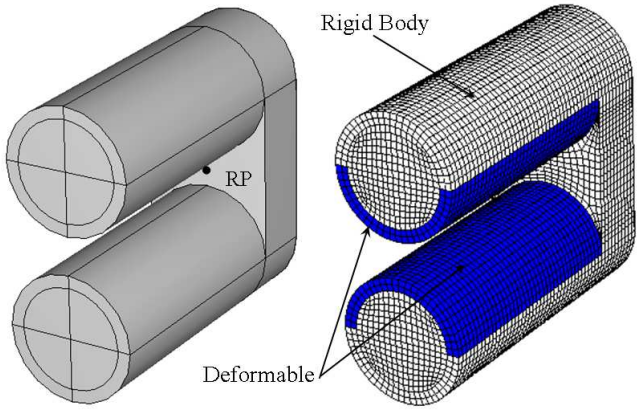

Figure 6-25 The model of the rotating support as one part.

Again there is a rigid-body constraint on all partitions that do not make contact with the specimen, in order to save calculation time (Figure 6-25 on the right). The part is meshed with C3D8R elements; the element size is also 0.5 mm. The latter is done to assure that the calculation does not diverge as a result of contact problems and therefore, the mesh size is smaller than with the rigid supports.

For the boundary conditions of the rotating support, only the rotation of the support around its 'natural axis' is allowed, all other movement is constrained.

For the contact conditions, the slave surface is put on the support and the master surface is on the specimen. The latter helps the rotating of the support, since normally, the slave surface follows the movement of the master surface.

The symmetry conditions are the same as with the three-roll setup (Figure 6-26):

On plane A: $U_1 = 0$

On plane B: $U_2 = 0$

Of course, the symmetry conditions are also applied on the supports.

For the indenting support the boundary conditions are applied on both reference points. The movement along the 1- and the 2-axis is restricted and along the 3-direction, a downward displacement of 20 mm is imposed.

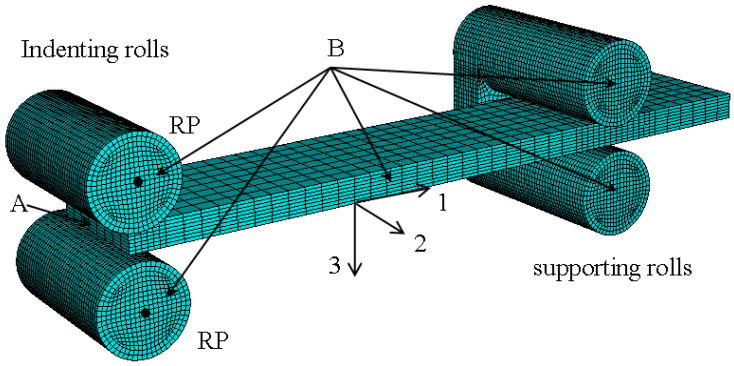

Figure 6-26 Illustration of the mesh and the boundary conditions for the three-point bending setup with rotating supports (6ROLL).

The specimen is a beam with dimensions 2.4 mm x 15 mm x 80 mm and it is meshed with quadratic brick element with reduced integration, C3D20R. The global size of the elements is 3 mm. However, in the zones of contact, the size is 1 mm to ensure that no convergence problems occur due to the contact conditions. The material model is the same as in the previous paragraph (see Table 6-1).

Friction is modelled in the same way as with the three-roll setup. Taking into account that damage was not modelled, a friction coefficient between 0.2 and 0.3 gives a good correspondence (Figure 6-27), although the correspondence is less than with the three-roll setup. No explanation could be found for the waviness of the simulation with μ equal to 0.2. Even with a denser mesh, it still occurred. Possibly it is the result of numerical instability due to the contact.

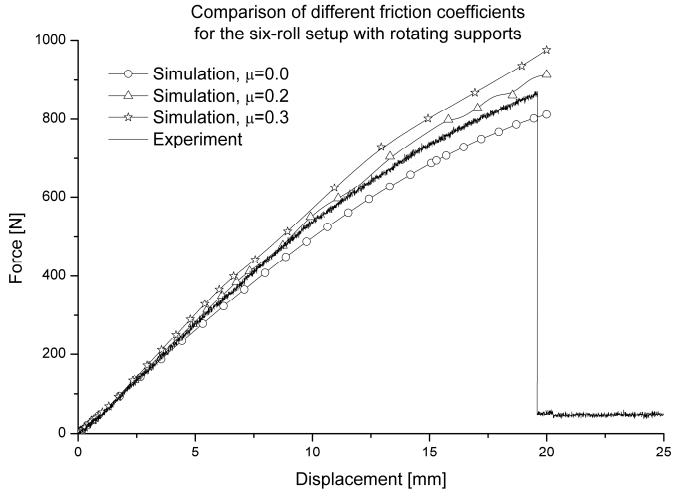

Figure 6-27 Comparison of the experiment with simulations using different friction coefficients for the fully-reversed (6ROLL) setup.

In paragraph 6. 3. 2. a, it was mentioned that the higher bending stiffness and ultimate bending force for the single-sided setup was due to the setup. In Figure 6-28, it can clearly be seen that, for higher displacements, the necessary bending force for a given displacement is higher for the single-sided setup, for al implemented friction coefficients. As such, the influence of the used setup on bending stiffness and force is proven. This effect is most likely caused by the increasing span width due to the rotation of the supports during the experiment with the fully-reversed setup.

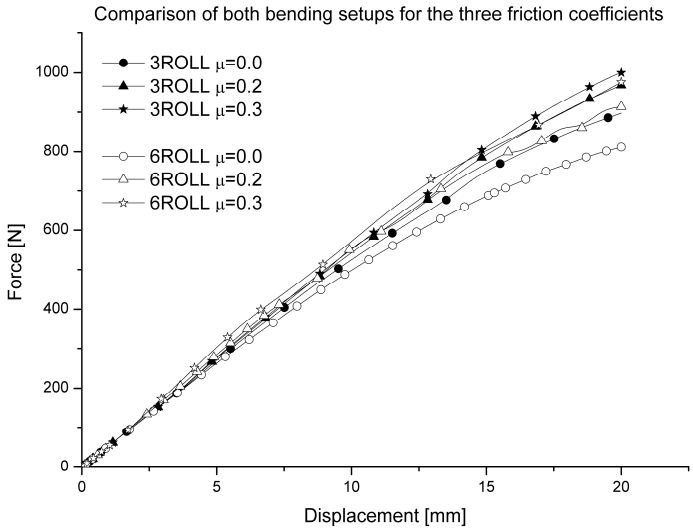

Figure 6-28 Illustration of the effect of the used bending setup on the bending stiffness and ultimate force.

This way of modelling leads to a converging calculation, but the calculation of the rotation of the support takes a lot of time. A simulation with a simple linear elastic orthotropic material model takes about thirty six hours to finish for a friction coefficient of 0.3. Adding a user-defined material model will only increase the time, so it is obvious that this model cannot be used for fatigue damage modelling. For the latter, multiple successive runs of this model are required, since each run only represents one fatigue cycle and damage growth can only be predicted accurately if sufficient fatigue cycles are simulated.

In Figure 6-29, the calculated rotation of the support is plotted against a pseudo-time, where zero corresponds with the start of the simulation and one with the end. Two things can be noted: (i) the assumed friction between supports and specimen has a significant influence on the rotation and (ii) if friction is modelled, the coefficient of friction does not have a large influence on the angle reached at the end of the simulation corresponding with a midspan displacement of 20 mm, nor on its evolution.

The dip that occurs at the beginning (t=0.1) is a result of the numerical implementation of the contact. ABAQUS/Standard requires a number of nodes to be connected numerically and as a result, the rotation of the support lags a little. This phenomenon was also seen during the experiments, because there was a very small gap (< 0.1 mm) between the rolls and the specimen, to assure that no extra pressure was induced through the contact. The numerical implementation of the contact is the mathematical equivalent of that very small gap.

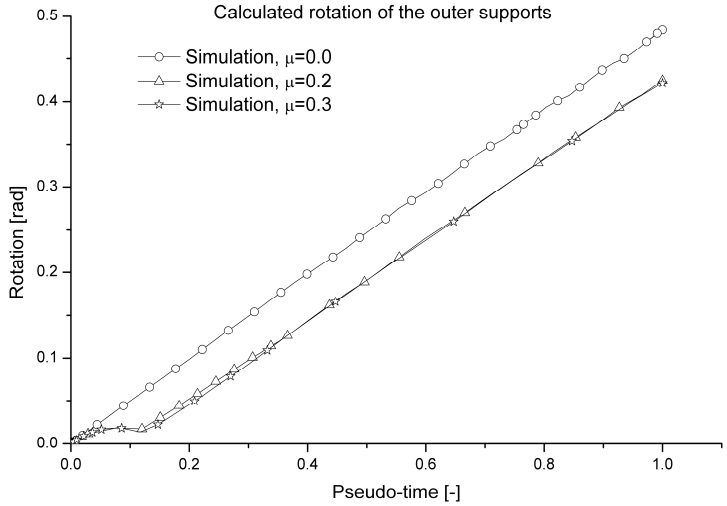

Figure 6-29 The rotation of the support as a function of the pseudo-time.

Now, the calculation is redone, but with a linear rotation, similar to the ones depicted in Figure 6-29, added as a boundary condition on the reference point of the outer supports (Figure 6-25). As such, ABAQUS™ no longer needs to calculate the angle. The simulation was done for a friction coefficient of 0.2 and 0.3, with the corresponding final angles of 0.425 and 0.422 respectively (Figure 6-29).
Under these circumstances, it only takes three hours and the corresponding force-displacement curve corresponds very well with the simulation with the normal boundary conditions (see Figure 6-30). However, it must be noted that for a given displacement, the force is a little larger than when the rotation is calculated, especially for the simulation with μ equal to 0.3.

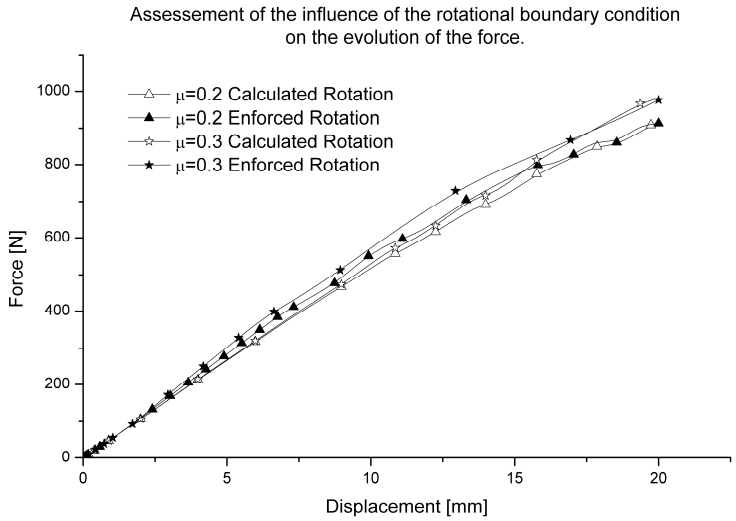

Figure 6-30 Comparison of the force-displacement curve for the simulations with different rotational boundary conditions.

As such, the computing time can be reduced drastically by enforcing the rotation on the outer supports, but unfortunately, it cannot be implemented for the validation of material models, since the angle of the rotational supports reached at full midspan displacement will depend on the stiffness of the specimen. Once damage occurs, this angle will change and the original boundary conditions will no longer be correct.

6. 3. 3. b. Results

It could already be noted that there is a very good correspondence in the evolution of the force as a function of the midspan displacement, both for the single-sided (Figure 6-10) and the fully-reversed bending setup (Figure 6-27).

The average midspan deflection, at which fracture occurs for the fully-reversed setup, is about 20 mm (see Figure 6-22). For this deflection, Figure 6-31 shows the stress along the fibres for the simulation with μ equal to 0.2. The bottom centre support has been removed for a better view on the stresses.

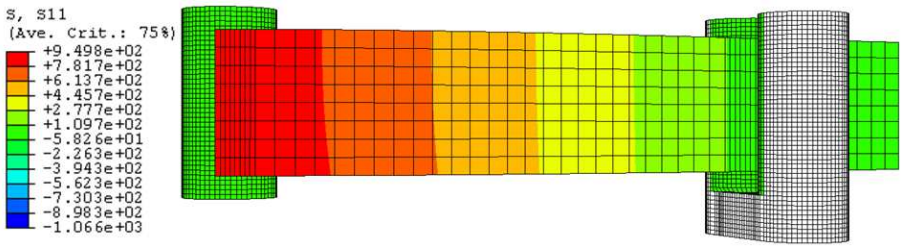

Figure 6-31 The longitudinal stress distribution (σ_{11}) at 20 mm midspan deflection for the fully-reversed setup.

It can be noted that the occurring stresses in the centre of the specimen are again higher than the ultimate tensile strength (see chapter 3; X_T = 734 MPa). Similar to the standard three-point bending simulations, this is due to the fact that no material model, which accounts for permanent deformations, was implemented.

6. 3. 4. Conclusions

The loading conditions in three-point bending are quite interesting for validating fatigue damage models for thin composite laminates with low bending stiffness, since they combine both tensile stresses on one side and compressive stresses on the other. Single-sided bending has the advantages of being easily modelled. The disadvantage of this setup is found in the experiments. After a few thousand cycles, the permanent deflection of the specimen causes the indenter to impact on the surface and therefore corrupting the fatigue data. Furthermore, due to the friction, wear damage occurs on the specimen in the contact area between specimen and supports.

Fully-reversed (symmetrical) bending does not have such a disadvantage. Furthermore, tension-compression fatigue is possible. However, the modelling in finite elements is problematic with long calculation times, due to the rotating of the supports.

Therefore, it may be concluded that despite of the interesting loading conditions of the setup, three-point bending in this configuration is not ideally suited for validating damage models for thin composite materials, because of the large midspan displacements which are reached.

6. 4. THE FOUR-POINT BENDING SETUP

Contrary to the three-point bending setup presented in the previous paragraph, a four-point bending setup has a more interesting load distribution for modelling (Figure 6-32).

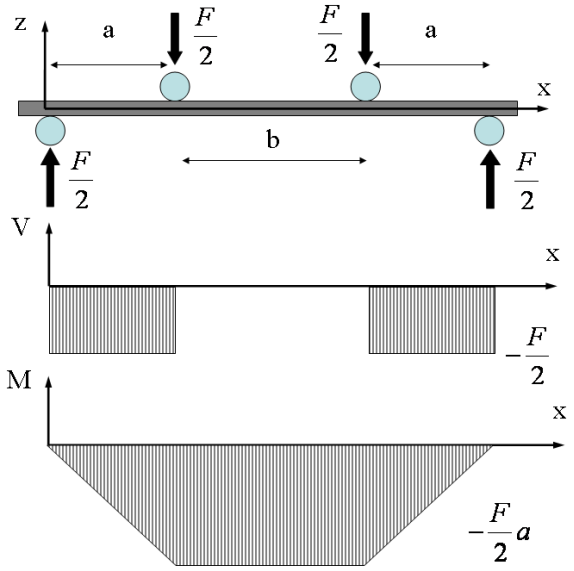

Figure 6-32 Illustration of the occurring loads in a four-point bending setup.

The area between the two indenting rolls has a constant bending moment equal to $-\frac{F}{2}a$ and no transverse force. As a result, the finite element modelling of a load controlled test is very straightforward, only the section between the two indenting rolls must be modelled and a corresponding moment must be applied.

However, problems arose during the experimental assessment of this setup. Figure 6-33 shows the used geometry for these bending experiments; for the span, values of 30, 40 and 50 mm were chosen to see its effect on the force-displacement curves.

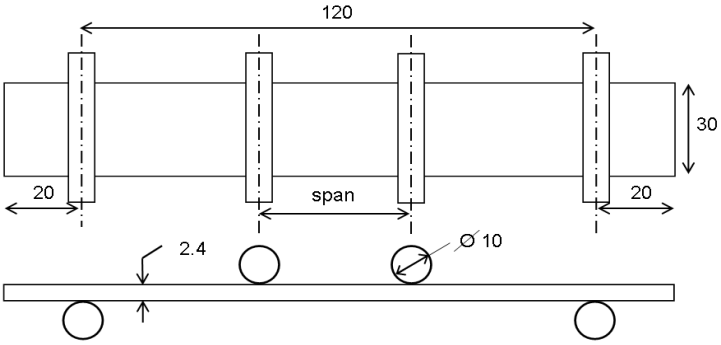

Figure 6-33 Dimensions of the used four-point bending coupon in millimetres.

However, for the experiments with a span of 40 and 50 mm, the specimen could not be bent until fracture, because of limitations in the setup. This is illustrated in Figure 6-34. Because of the large midspan displacements, the mounting mechanism of the indenting rolls makes contact with the specimen, instead of the indenting rolls.

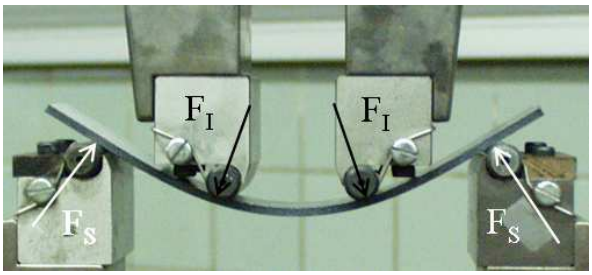

Figure 6-34 Illustration of the problems with the four-point bending setup.

For a 30 mm span, failure was reached right before the unwanted contact established. For comparison purposes, another loading and unloading experiment was done on the 30 mm span setup with a maximum load of 90% of the failure load from the previous test. The force-displacement curves for the three setups are shown in Figure 6-35. It must be noticed that, even for the 30 mm span, the loads are relatively low and the midspan displacements are quite high, again limiting the maximum frequency of a fatigue test. Further, it must be noted that quite large hysteresis loops are visible, but very limited permanent deformation manifests itself. The hysteresis loops, however, are entirely due to the friction on the supports, as was documented earlier. This can be seen in the evolution of the force as a function of time in Figure 6-36, where the sudden drop in force becomes visible when the displacement changes direction.

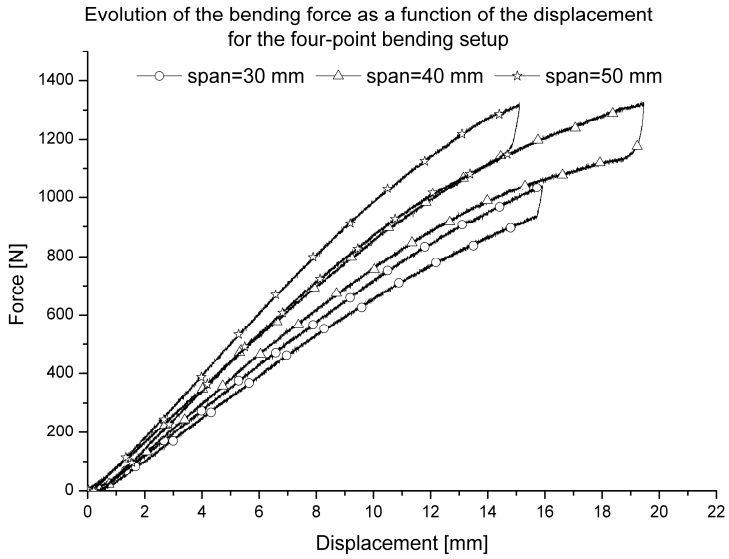

Figure 6-35 Force-displacement hysteresis loops in the four-point bending experiments.

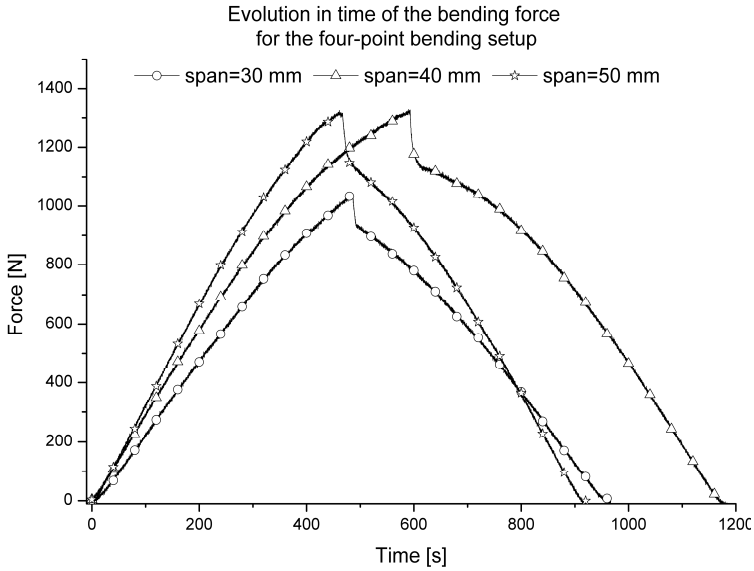

Figure 6-36 Force-time curves for the hysteresis loops in the four-point bending experiments.

Another major set back is illustrated in Figure 6-34. Since thin laminates are tested, the midspan displacements become so large that the occurring loads are no longer given by Figure 6-32. Since F_S and F_I are perpendicular to the (bent) surface of the specimen, they are no longer vertical, introducing normal forces in the specimen.

Therefore, the simple finite element model described above is no longer valid and the entire setup must be modelled and a geometrically nonlinear calculation must be performed. As a result, the main advantage of this setup over the standard three-point bending, namely the straight-forward numerical modelling, is lost because the midspan displacement of the thin laminates under study is too large.

6. 4. THE CLAMPED FOUR-POINT BENDING SETUP

In order to have higher forces for lower displacements in the four-point bending setup, the specimen is now clamped at both ends, inducing membrane stresses. However, this compromises the easy modelling in finite element software, since the membrane stresses cannot be determined in an analytical formula and hence, the entire setup (using symmetry) must be modelled. A first experiment, however, yielded another problem: the specimen failed at the clamped ends. This, however, could be expected, since simple beam theory also yields that the bending moment at the clamps, using the dimensions from Figure 6-32, is given by [13]:

$$M = F\frac{l^2 - b^2}{4l} \tag{6.6}$$

Where l equals $2a+b$. The (constant) moment in the area between the indenters is given by [13]:

$$M^* = F\frac{(l-b)^2}{4l} \tag{6.7}$$

Solving $M^* > M$ yields $b > l$, which of course is impossible. However, the experiment indeed yielded a higher bending load for a lower midspan displacement; the specimen failed at 2636 N with corresponding midspan displacement of 8.3 mm, illustrating the effect of clamping the specimen's ends.

6. 5. THE CLAMPED THREE-POINT BENDING SETUP

6. 5. 1. Introduction

Because of the promising results of the clamped edges in the previous paragraph, the same principle is used on a three-point bending setup. The used setup is illustrated in Figure 6-37.

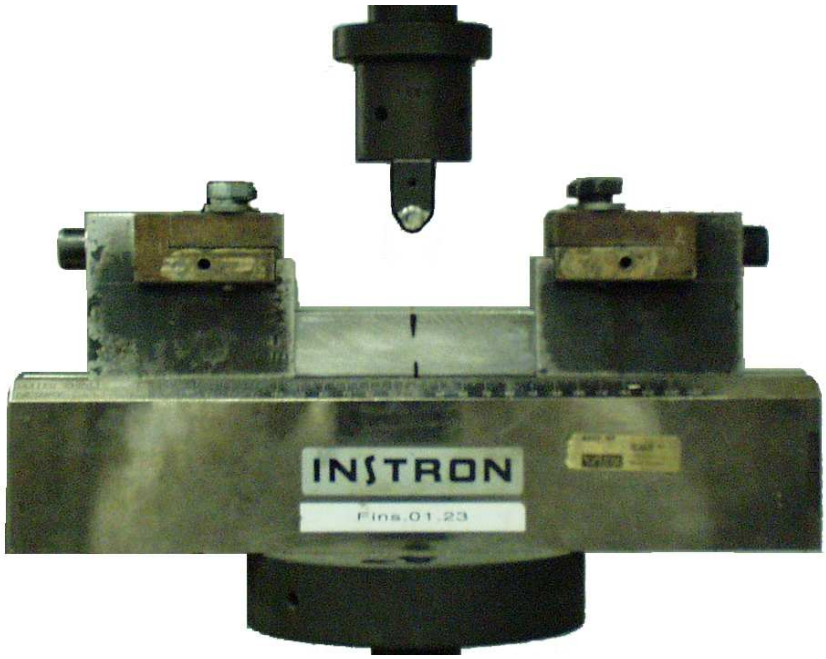

Figure 6-37 The clamped three-point bending setup with anti-sliding block.

The two grips which clamp the specimen's ends are mounted on a supporting steel fixture with a T-sleeve connection. Preliminary tests had shown that the two clamps can slide towards each other during the test, due to the large membrane stresses, even if the maximum torque is applied on the bolts that clamp the grips on the supporting fixture. Therefore, a massive block of aluminium was placed between the two grips, at the exact width, preventing them from sliding inwards, as shown in Figure 6-37. This observation indicates, however, that the induced membrane stresses due to geometric nonlinearity, must be very large.

6. 5. 2. Quasi-static experiments

The dimensions of the coupons used for these bending experiments are shown in Figure 6-38, all dimensions are in millimetres.

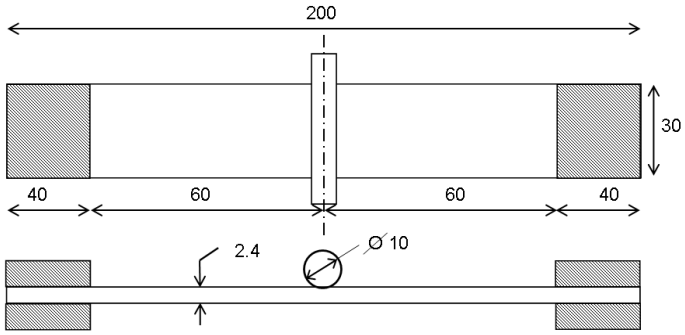

Figure 6-38 Dimensions of bending coupon in millimetres.

The results of a few quasi-static tests are shown in Figure 6-39, the corresponding displacement speed was 2 mm/min. It may be remarked that the results are very reproducible, there is only a limited difference, due to scatter on the results. Furthermore, high forces for low displacements are achieved; the loads are four times higher at failure, for less than half the displacement when compared with the standard three-point bending setup (see paragraph 6. 3. 2. b).

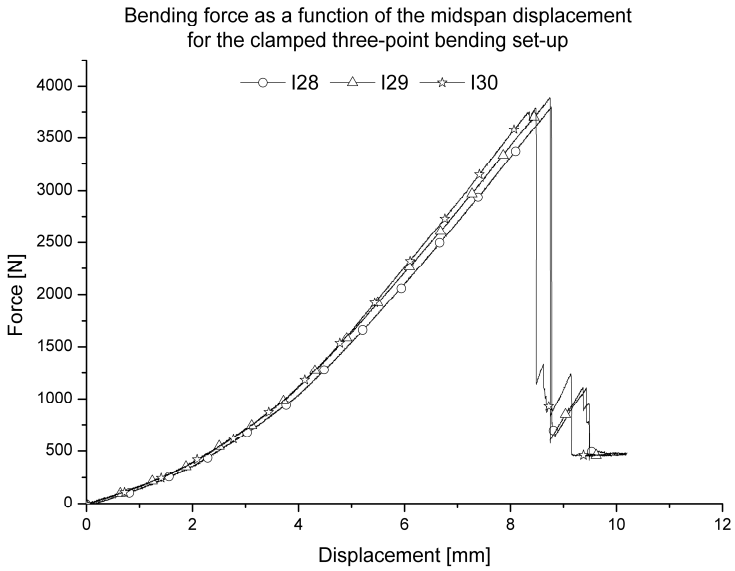

Figure 6-39 Force-displacement curves of the quasi-static test with the clamped three-point bending setup.

6. 5. 3. Finite element modelling

To investigate in which relative proportion the membrane stresses and bending stresses contribute to the resultant bending force, finite element simulations have been done using ABAQUS™/Standard. Further, the setup was modelled both with 3D continuum elements and 1D beam elements, to investigate if a much faster 1D model could accurately describe the stress state in the specimen. The 3D model is illustrated in Figure 6-40.

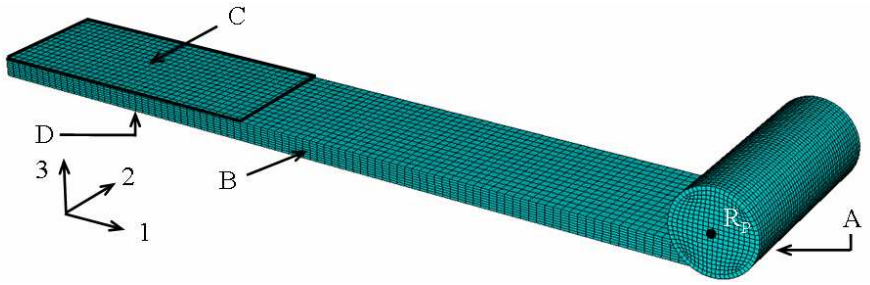

Figure 6-40 Finite element model of the clamped three-point bending setup.

Using the symmetry of the set-up, only a quarter was modelled in 3D quadratic brick elements with reduced integration, C3D20R; the size of the elements was 1 mm to have a dense mesh. In a first simulation, the gripped section of the specimen was not allowed to move inwards (3D clamped-fixed). In a second simulation, the gripped section could slide freely (3D clamped-sliding). This second simulation was done to investigate the influence of the membrane stresses, since for this simulation only the rotation of the clamped end is inhibited, but longitudinal displacement is allowed and therefore, the membrane stresses should be a lot smaller than for the first simulation, where both longitudinal displacement and rotation of the clamped end are not allowed.

The implementation of the boundary conditions for these simulations is given in Table 6-2; since 3D elements are used, there are no rotational degrees of freedom. For the bending load, a displacement U_3 = 10 mm was enforced on the reference point of the indenting roll, RP.

Table 6-2 Used boundary conditions for the three-dimensional simulations.

Simulation	Face A	Face B	Face C	Face D
3D clamped-fixed	$U_1 = 0$	$U_2 = 0$	$U_1 = U_2 = 0$	$U_1 = U_2 = U_3 = 0$
3D clamped-sliding	$U_1 = 0$	$U_2 = 0$	$U_2 = 0$	$U_2 = U_3 = 0$

Figure 6-41 shows the 1D finite element model. For this simulation, no symmetry was used, so the entire specimen was modelled, using a three-node quadratic beam element in space, B32 with a size of 2 mm. For points A and C, all movement was restricted, which means that $U_1 = U_2 = U_3 = 0$; $\alpha_1 = \alpha_2 = \alpha_3 = 0$; a vertical displacement $U_3 = 10$ mm was enforced on point B. As for the 3D case, a 1D clamped-fixed and a 1D clamped-sliding simulation were done.
Of course, for both the 3D and 1D simulation, a geometrically nonlinear analysis was performed. The implemented material data are the same as in Table 6-1.

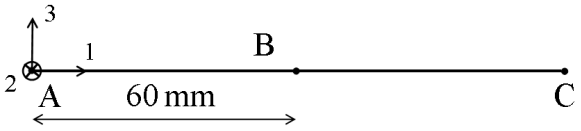

Figure 6-41 Illustration of the one-dimensional model of the clamped setup. No symmetry is used.

From the 1D model, it is very easy to obtain values of bending moments, longitudinal and transverse forces for both the clamped-fixed and clamped-sliding calculation, whereas for the 3D simulations, these values need to be calculated manually from the stress distributions. Figure 6-42 and Figure 6-43 give an overview of the values of the bending moment, the transverse force and the longitudinal force for the clamped-fixed setup and the clamped-sliding setup respectively, derived from the one-dimensional analysis, for a displacement of 9 mm, corresponding to final fracture in the static experiments. The forces have been rescaled to have a clear image; the scaling factor differs for both graphs.

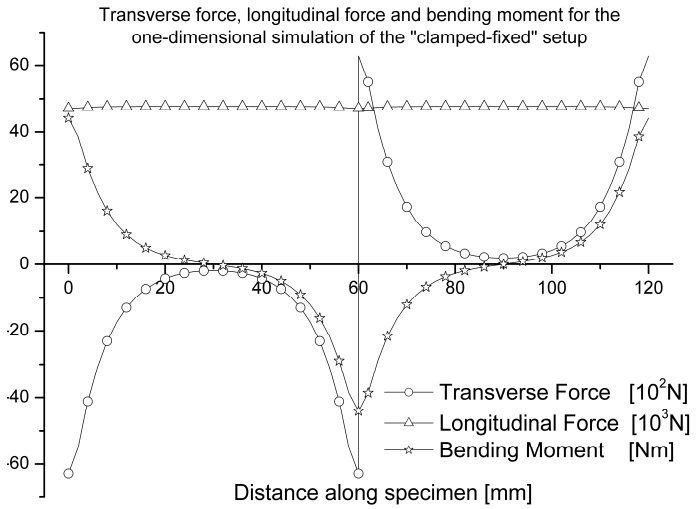

Figure 6-42 Evolution of the longitudinal force, transverse force and bending moment along the specimen for the clamped-fixed setup.

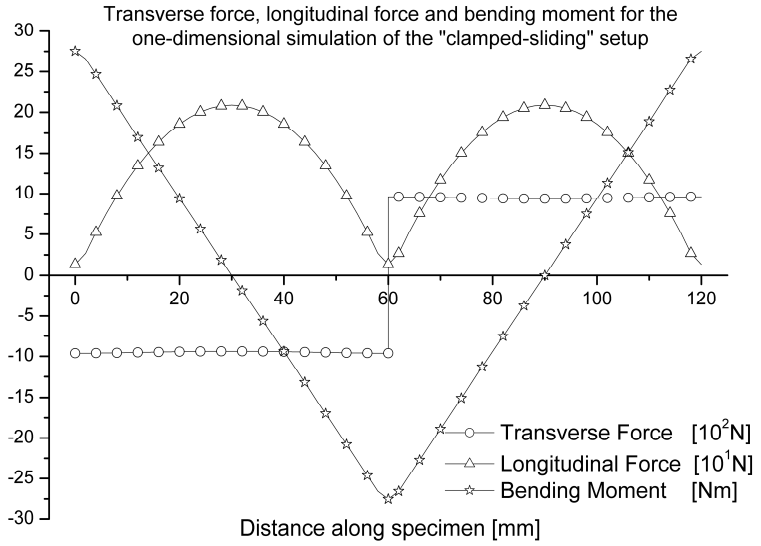

Figure 6-43 Evolution of the longitudinal force, transverse force and bending moment along the specimen for the clamped-sliding setup.

Because of the fixing of the clamped end, very high longitudinal forces are imposed. For the clamped-sliding setup, the force only becomes 200 N, whereas for the clamped-fixed specimen, the force is about 47800 N, which is almost 250 times higher. For the clamped-sliding setup, the evolution of the transverse force is about the same as with the standard three-point bending setup. By preventing the ends of the specimen from sliding inwards, the maximum bending moment almost doubles, whereas the transverse force in the centre of the specimen increases from 962 N to 6280 N.

In Figure 6-44, the evolution of the longitudinal stress across the height of the specimen is compared for both the 1D and 3D analysis in the centre of the specimen at the same corresponding midspan displacement. It must be remarked that there is an excellent correspondence, except near the top of the specimen, where the 3D analysis predicts a higher compressive stress than the 1D analysis. This is probably due to the local indentation of the load striking edge which is modelled in the 3D analysis. This again proves that the one-dimensional simulation is very useful for the validation of fatigue damage models, since there is only a limited deviation in the longitudinal stresses.

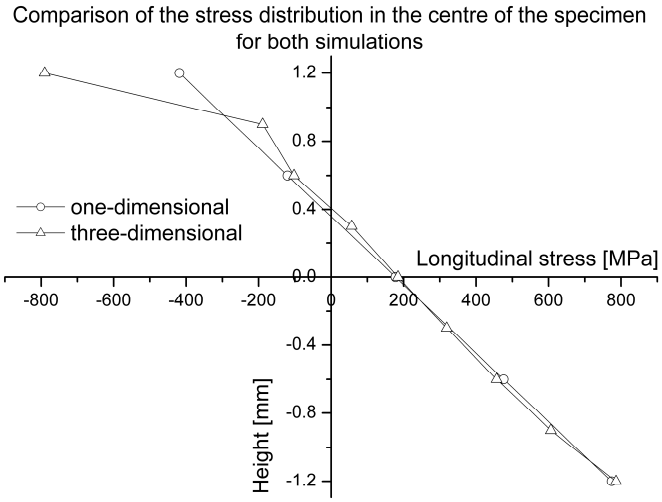

Figure 6-44 Height distribution of the longitudinal stress in the centre of the specimen.

Finally, the force-displacement curves calculated from the 3D and 1D analysis are compared with the experimental results from the static tests (see Figure 6-39). The results are shown in Figure 6-45. First of all, it must be noted that if sliding in the grips is allowed, the force decreases significantly for a given displacement. It can also be remarked that the prediction of the simple elastic beam theory corresponds very well with the 3D analysis. This is very interesting for fatigue simulations with damage models, since a one-dimensional calculation is done in a matter of seconds, whereas the three-dimensional analysis takes a few hours to complete because of the dense mesh needed for accurate results.

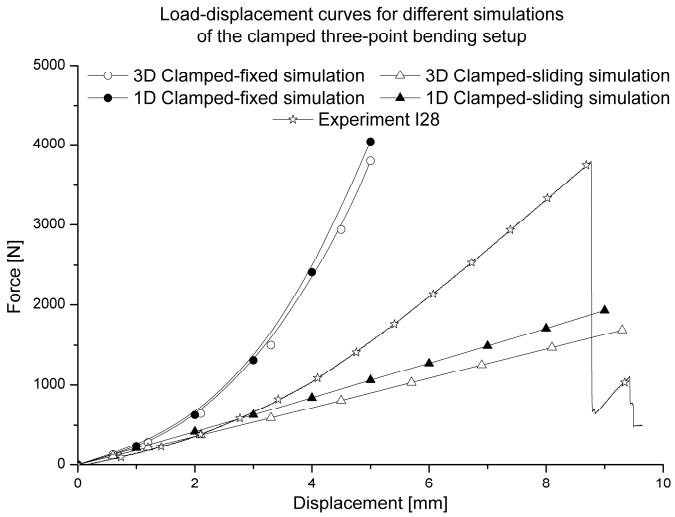

Figure 6-45 Different force-displacement curves for the simulations of the clamped setup.

Unfortunately, the experimental curve from the static test I28 lies in between the two extremes (clamped and sliding), so this indicates that little sliding must be present in the experiments. This is investigated further during the fatigue experiments.

6. 5. 4. Fatigue experiments

Because of the promising results in the quasi-static tests, some fatigue tests with the clamped three-point bending setup have been done. During those tests, it was noticed that after a few hundred cycles, the indenter lost contact over a certain period of time during every loading cycle. This is illustrated in Figure 6-46, which shows the evolution of the bending force and the displacement as a function of time for cycle N = 1 and cycle N = 1,015,011 from a displacement-controlled test with amplitude of 6 mm and a frequency of 2 Hz.

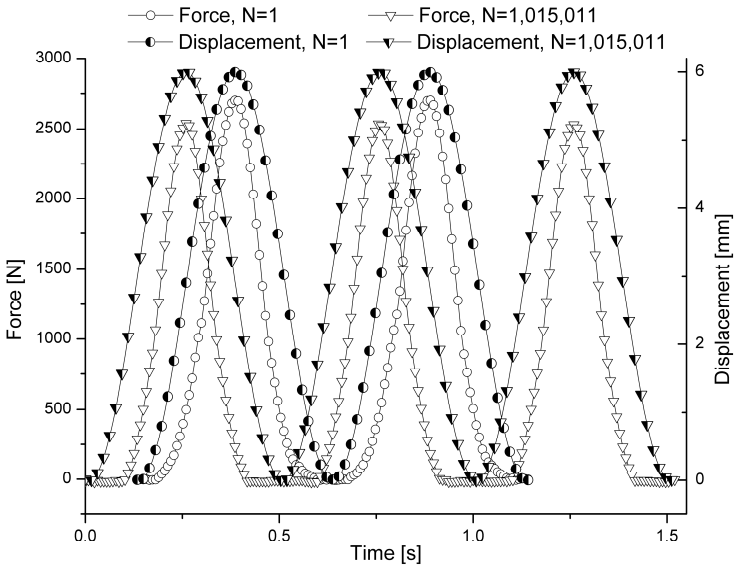

Figure 6-46 Force and displacement as a function of time for the first and last measurement.

For the last depicted cycle (N = 1,015,011 cycles) the load F remains zero for a certain period of time, although the displacement D varies. This means that the indenter loses contact during cycling. The latter may be caused by permanent deformation or slipping inside the grips. Therefore, small markings were placed on the specimen next to the clamps to verify if the specimen slips out of the grips. It was noticed that the specimen indeed slipped over a very limited distance, circa 0.5 mm, because of the very high membrane stresses. This would explain the loss of contact in Figure 6-46, although permanent deformation may not be neglected. Therefore, extra precautions must be developed to avoid this sliding.

Possibilities are to use an additional actuator to compensate the gripping or to use bolts through the specimen, ensuring that this does not advance preliminary failure. Further efforts are now undertaken to optimize this clamped three-point bending set-up for fatigue testing of thin composite laminates with a low bending stiffness, since the accurate 1D modelling is very promising. Special attention is given to stop the sliding from happening, since this is virtually impossible to model accurately.

Despite the little sliding, already a few fatigue tests were performed to establish the outer boundaries, varying from failure after a few dozen cycles to infinite fatigue life. All these preliminary tests were done with a loading frequency of 2 Hz in displacement-controlled mode. The tests had a displacement amplitude of 6 mm, 7 mm and 7.5 mm. The first experiment was stopped after 1,015,010 cycles and it was considered to be infinite life, the specimen did not break and showed very limited permanent deformation. Since the load distribution in the bending setup is pure tension or compression along the fibre, but no shear, this amount of permanent deformation is consistent with the results from the uni-axial fatigue tests on the $[(0^o,90^o)]_{4s}$ stacking sequence. The latter also showed only very limited permanent deformation. The run-in of this test is shown in Figure 6-47; it should be noted that hysteresis loops occur and that the indenter makes contact during the entire cycle, since the force does not remain zero over a certain range of the displacement. This means that sliding in the grips accumulates slowly during fatigue cycling, rather than suddenly during the run-in. It should be mentioned that in the quasi-static tests sliding did happen, but the static displacements at failure were 50 % higher than the displacement amplitudes in fatigue (9 mm at failure versus 6 mm after the run-in). This would mean that sliding starts either after a certain number of cycles at low amplitude or after one cycle with a larger amplitude.

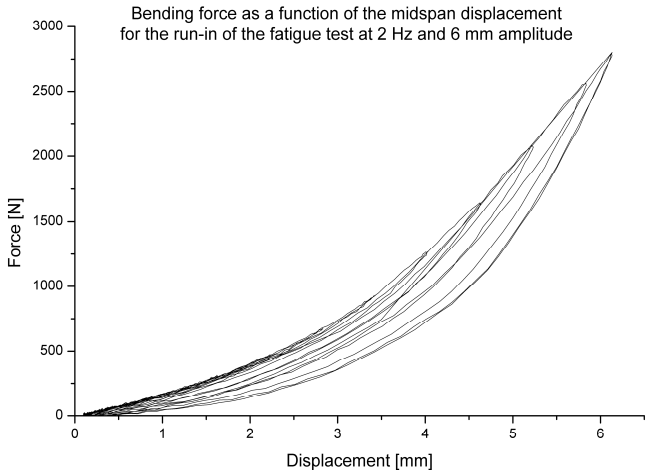

Figure 6-47 Force as a function of the displacement for the run-in of the 6 mm fatigue test.

Figure 6-48 illustrates the evolution of the maximum, minimum and average value of the bending force throughout the fatigue experiment. There is a slight decrease, but this is more likely the result of sliding in the grips than of stiffness degradation, since the uni-axial tests also did not yield any stiffness degradation.

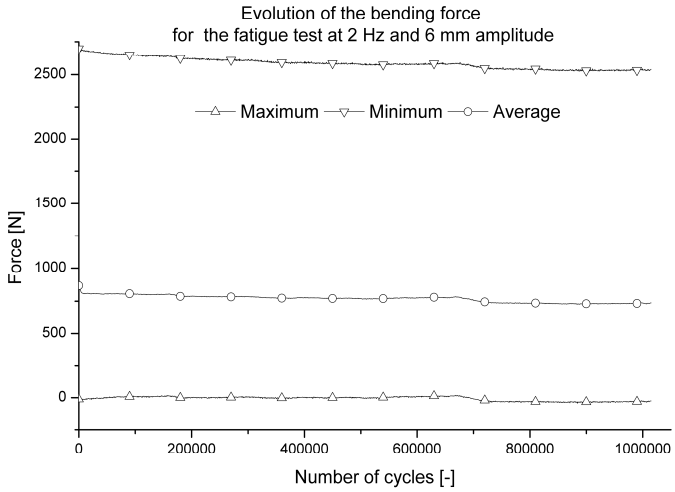

Figure 6-48 Evolution of the maximum, minimum and average value of the force during the 6 mm fatigue test.

The specimen from the fatigue test with 7 mm amplitude failed in the mid section after about 200 cycles and the 7.5 mm amplitude caused failure to occur during the run-in of the test, as is illustrated in Figure 6-49.

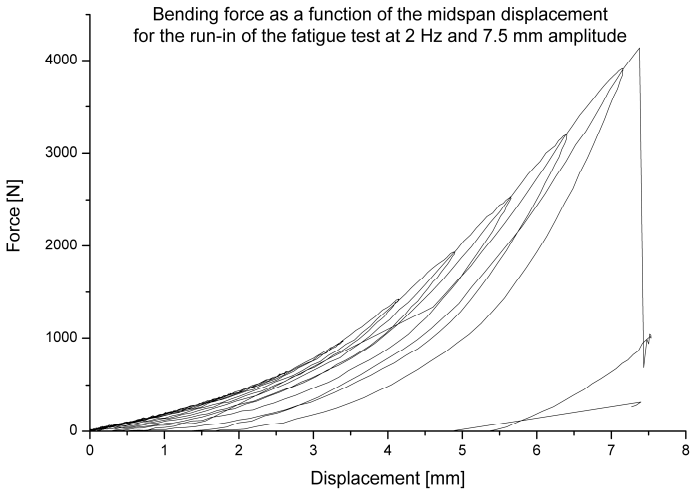

Figure 6-49 Force as a function of the displacement for the run-in of the 7.5 mm fatigue test, illustrating the failure.

As can be seen, the specimen failed right before it reached the maximum amplitude. It can also be noticed in Figure 6-49 that for displacements higher than 6 mm, the sliding gradually begins; the cycle that reaches 5.75 mm has zero force for zero displacement, but the next cycle, which reaches 6.25 mm, there is already a short moment in time where the force remains zero. This again suggests that sliding either starts after a number of cycles at low amplitude or after few cycles with large amplitudes.

Finally, it should be remarked that the amplitude range, varying from infinite lifetime to failure in a few dozen cycles is very narrow, only 1.5 mm of amplitude change is sufficient. Of course, more tests should be performed to validate this conclusion, but again, this is consistent with the results found from the uni-axial fatigue tests, where also only a narrow load range was found from infinite fatigue life to almost immediate failure.

6. 6. CONCLUSIONS

The loading conditions in three-point bending are quite interesting for validating fatigue damage models for thin composite laminates with low bending stiffness, since they combine both tensile stresses on one side and compressive stresses on the other. Single-sided bending has the advantages of being easily modelled. The disadvantage of this setup is found in the fatigue experiments. After a few thousand cycles, the permanent deflection of the specimen causes the indenter to impact on the surface and therefore corrupting the fatigue data. Furthermore, due to the friction, wear damage occurs on the specimen in the contact area between specimen and supports.

Fully-reversed (symmetrical) bending which requires rotating outer supports, does not have such a disadvantage. Furthermore, tension-compression fatigue is possible. However, the modelling in finite elements is problematic with long calculation times, due to the rotating of the supports.

The four-point bending setup has the advantage of being very easily modelled, but the experiments yield low bending forces for large midspan displacements, which only allow low testing frequencies and which make the assumptions for the easy finite element modelling (constant bending moment) invalid. Inducing membrane stresses by clamping the specimen at the ends on this four-point bending setup yields larger forces for lower displacements, but the failure always occurs next to the clamps, since that is the location of the highest bending moment.

Clamping the ends of the specimen on a three-point bending setup, yields almost four times higher bending loads for less than half the displacement when compared with the regular three-point bending setup. This makes the clamped setup preferable over the unclamped three-point bending. Fatigue tests have also been performed on the clamped setup, with good results. Again, only a narrow range was found between infinite fatigue lifetime and failure in a few cycles.

The validation of damage models can first be done with simple one-dimensional beam-theory simulations, but three-dimensional simulations still remain necessary for a complete validation of the material model. Further research must be done on how to avoid the slipping in the grips, since this phenomenon certainly has an influence on the measurement.

6. 7. REFERENCES

[1] Hansen, U. (1999). Damage development in woven fabric composites during tension-tension fatigue. JOURNAL OF COMPOSITE MATERIALS, 33(7), 614-639.

[2] Coats, T.W. and Harris, C.E. (1995). Experimental verification of a progressive damage model for IM7/5260 laminates subjected to tension-tension fatigue. JOURNAL OF COMPOSITE MATERIALS, 29(3), 280-305.

[3] Caprino, G. (2000). Predicting fatigue life of composite laminates subjected to tension-tension fatigue. JOURNAL OF COMPOSITE MATERIALS, 34(16), 1334-1355.

[4] Gamstedt, E.K. and Sjogren, B.A. (1999). Micromechanisms in tension-compression fatigue of composite laminates containing transverse plies. COMPOSITES SCIENCE AND TECHNOLOGY, 59(2), 167-178.

[5] Rotem, A. (1991). The fatigue behaviour of orthotropic laminates under tension-compression loading. International Journal of Fatigue, 13(3), 209-215.

[6] Sedrakian, A., Ben Zineb, T., Billoet, J.L., Sicot, N. and Lardeur, P. (1997). A numerical model of fatigue behaviour for composite plates: application to a three point bending test. In : Degallaix, S., Bathias, C. and Fougères, R. (eds.). International Conference on fatigue of composites. Proceedings, 3-5 June 1997, Paris, France, La Société Française de Métallurgie et de Matériaux, pp. 415-423.

[7] Sidoroff, F. and Subagio, B. (1987). Fatigue damage modelling of composite materials from bending tests. In : Matthews, F.L., Buskell, N.C.R., Hodgkinson, J.M. and Morton, J. (eds.). Sixth International Conference on Composite Materials (ICCM-VI) & Second European Conference on Composite Materials (ECCM-II) : Volume 4. Proceedings, 20-24 July 1987, London, UK, Elsevier, pp. 4.32-4.39.

[8] Caprino, G. and D'Amore, A. (1998). Flexural fatigue behaviour of random continuous-fibre-reinforced thermoplastic composites. COMPOSITES SCIENCE AND TECHNOLOGY, 58, 957-965.

[9] Van Paepegem, W., Mechanics of Materials, Faculty of Engineering, Ghent University, 2005.

[10] Quintelier J, Samyn P, De Baets P, Tuzolana T, Van Paepegem W, Van den Abeele F, Vermeulen J, Wear behaviour of carbon fibre-reinforced poly(phenylene sulphide), POLYMER COMPOSITES 27 (1): 92-98, FEB 2006.

[11] Van Paepegem, W., De Geyter, K., Vanhooymissen, P. and Degrieck, J. (2006) Effect of friction on the hysteresis loops from three-point bending fatigue tests of fibre-reinforced composites. COMPOSITE STRUCTURES, Volume 72 issue 2, 212-217.

[12] K. De Geyter and P. Vanhooymissen, Vermoeiing van Koolstofvezelversterkt Thermoplasten, Master Thesis, Faculty of Engineering, Ghent University, 2004.

[13] W. C. Young and R. G. Budynas, Roark's formulas for stress and strain, seventh edition, ISBN 0-07-121059-8, McGraw-Hill Compaines Inc. 2002.

Chapter 7

IN-PLANE SHEAR TESTING UNDER QUASI-STATIC AND FATIGUE LOADING CONDITIONS

In this chapter, the in-plane shear behaviour of the carbon fabric-reinforced PPS is investigated. First, a modified design of the standard three-rail shear test is given. Then, the shear behaviour of the material is investigated by performing quasi-static, hysteresis, fatigue and creep experiments. For each of these loading conditions, the results obtained with the modified three-rail shear setup are compared with results from a $[(+45°,-45°)]_{4s}$ tensile test. Here, only the experiments are discussed, the modelling of the material behaviour will be described in the following chapter.

7. 1. INTRODUCTION

There are various ways of inducing a state of in-plane shear [1, 2] in a composite. Examples are the Iosipescu test [1, 3-5], the 10º off-axis test [4-7], the $[+45º/-45º]_{ns}$ tensile test [7-16], the two-rail shear test [17-19], the three-rail shear test [20], torsion of a rod [21] and torsion of thin-walled tubes [22-25]. From all these tests, torsion of a thin-walled tube is practically the only universal method used for determination of both in-plane shear modulus and shear strength [1] and it produces the most desired state of shear stress, free of edge effects [20]. However, this method is rather expensive, since it requires a tension-torsion machine with specialized gripping and it cannot determine the shear characteristics of flat products, fabricated by pressing or contact moulding. Furthermore, such tubes are not easily fabricated. The $[+45º/-45º]_{ns}$ tests do not require any specialised fixtures and as such are a lot easier to perform. On the other hand, they are very sensitive to edge effects due to the [+45º/-45º] lay-up [20]. For the 10º off-axis tests, oblique end tabs are required [4-7].

The rail shear test positions itself somewhat in the middle. It does not require a sophisticated apparatus like the torsion setup and it induces a stress state which does not differ a lot from pure shear. Furthermore, it requires flat specimens with limited preparation.

If fatigue loading conditions are required, then the rail shear test is only rarely considered [20]. The favourite test setup remains the torsion of thin-walled tubes, sometimes combined with tension or bending in biaxial fatigue [22-25]. The $[+45º/-45º]_{ns}$ test is also used [9] for fatigue research.

The rail shear test, both two-rail and three-rail, as described in the "*ASTM D 4255/D 4255M standard test method for in-plane shear properties of polymer matrix composite materials by the rail shear method*" has one large disadvantage: it requires drilling holes through the specimen, so that the clamps can be bolted to the specimen. Drilling in composites should be avoided, since it nearly always causes damage to the composite and it may cause stress concentrations around the holes [18]. Furthermore, the preparation of the specimen takes more time. With this in mind, there has already been a proposal of a new design for the two-rail shear test, described by Hussain and Adams [18, 19]. This design no longer requires holes in the specimen.

In this chapter, a modification for the three-rail shear test is proposed, which no longer requires holes through the specimen, as has been proposed for the two-rail shear test in [18, 19]. Furthermore, this design should allow for fatigue loading conditions, which were not considered by Hussain et al. [18, 19]. The setup used by Lessard et al. [20] for their fatigue research was the standard three-rail setup, which requires the holes. The emphasis of their study was the use of notched specimens, in order to avoid preliminary failure of the specimens.

Finally, the rail shear test is often only considered for unidirectional reinforced or cross-ply composites, whereas for this study, a carbon fabric-reinforcement is considered.

The next section elaborates on the design of the modified three-rail shear setup. This is followed by a discussion of the performed experiments, under quasi-static, cyclic and fatigue loading conditions. All fatigue tests were performed with a stress ratio equal to zero and the influence of both the loading frequency and maximum shear stress was examined. Creep tests were also performed with both setups, to verify whether the detected permanent deformation was due to creep phenomena or to fatigue damage. All these loading conditions were also applied for a $[(+45°,-45°)]_{4s}$ tensile test. The purpose of these tests is to verify if the results obtained from the modified three-rail shear setup can also be reproduced by a different kind of experiment, which also induces an in-plane shear stress state. To the author's best knowledge, such a comparison has not been presented before for fatigue loading conditions, since no rail shear fatigue data have ever been published.

7. 2. DESIGN OF A MODIFIED THREE-RAIL SHEAR TEST

7. 2. 1. Principle of the three-rail shear test

The principle of the three-rail shear test is illustrated in Figure 7-1 (a) and (b). The specimen is gripped by three rails and during the test, the central rail has a relative vertical motion with respect to the two outer rails. This movement can be either up or down. As a result, a state of shear stress is induced in the specimen.

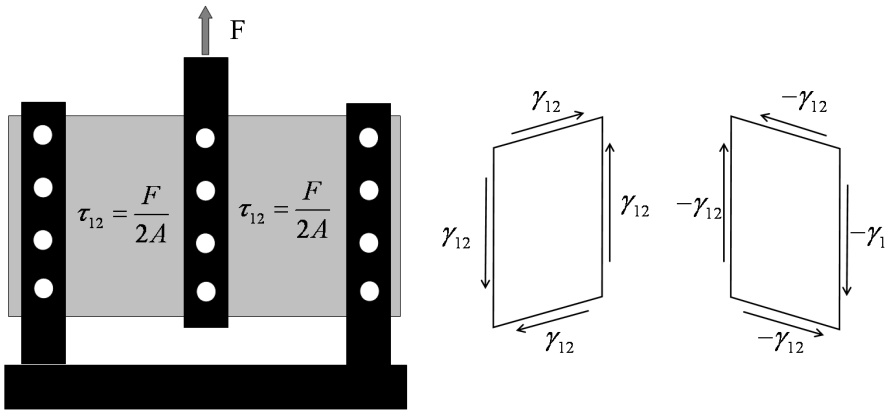

(a) The setup (b) The induced deformation

Figure 7-1 Principle of the three-rail shear test.

Figure 7-1 (b) illustrates the (theoretically) induced deformation state. Near the edges and near the clamps, the stress and deformation state will be slightly different because of the edges and corresponding edge effects.

The shear stress can be calculated by dividing half of the force (each zone carries half of the total force) by the cross section:

$$\tau = \frac{F}{2}.\frac{1}{h.t} \tag{7.1}$$

Where h is the height of the specimen, t is the thickness and F is the imposed force on the central rail.

To measure the shear strain, the ASTM D 4255/D 4255M standard prescribes to use strain rosettes, but if the loading is symmetrical and no bending of the specimen occurs, even one simple strain gauge will suffice. This can be visualised by presenting the deformation state, given in Figure 7-1 (b) on Mohr's circle, illustrated in Figure 7-2.

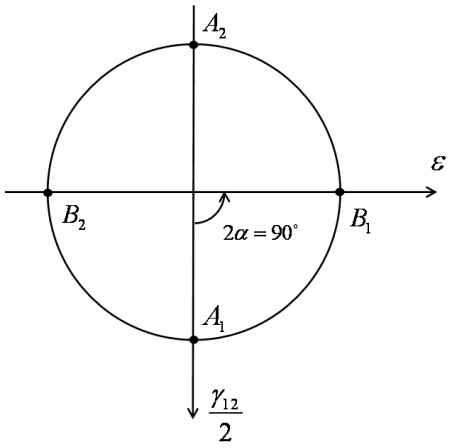

Figure 7-2 Representation of the deformation state on Mohr's circle.

Points A_1 and A_2 correspond with the occurring deformation, a state of pure shear. Rotating over $2\alpha = 90^o$ on Mohr's circle to points B_1 and B_2 yields the principal in-plane strains, which can be measured with strain gauges. This corresponds with a rotation of $\alpha = 45^o$ on the surface of the specimen for B_1 and of $\alpha = 135^o$ for B_2, meaning that the strain gauges should be mounted under an angle of +45° and -45° with respect to the fibre orientation. The shear strain is then calculated as:

$$\gamma = \left|\varepsilon_{+45} - \varepsilon_{-45}\right| \tag{7.2}$$

If only one strain gauge is mounted, then the shear strain can even be calculated as:

$$\gamma = 2\left|\varepsilon_{+45}\right| \tag{7.3}$$

The latter is also mentioned in [18], but this assumes symmetry of the loading conditions. The instrumentation of the specimens used here is discussed in paragraph 7. 3. 1. Next, the new design is commented on.

7. 2. 2. Design of the setup

Since the setup is designed for fatigue loading conditions, some modifications should be made so that the setup itself does not fail under fatigue loading. Lessard et al. had also made some modifications to the standard three-rail shear setup [20]. However, for the design presented here, the modifications are far more drastically, since there are no more bolts through the clamp, holding it together. The same principle as in [17, 18] is used, which means that the specimen is gripped by pressing a plate against the specimen. This pressure is applied by bolts which go through only one side of the clamp. However, the force required to press this load transfer plate against the specimen has a similar but opposite reaction force that pushes the two sides of the grip outwards. The latter is clarified in Figure 7-3, where the different application of the bolts is illustrated.

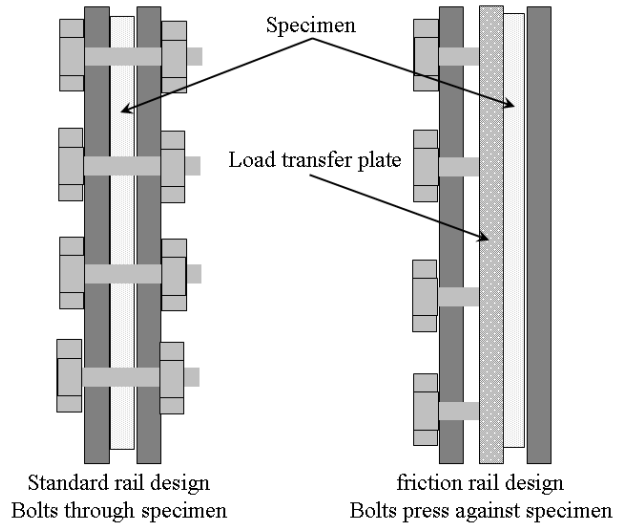

Figure 7-3 Difference between the use of bolts in the standard and the new design.

It is obvious that because of this outward force, the clamps will need to be more massive because they should withstand the fatigue loading conditions. As a starting point, the grips are designed in one piece, whereas the standard grips are two separate pieces, bolted together. In the grip, a rectangular cavity is milled away for the specimen. Since sharp corners produce unwanted stress concentrations, circular holes are drilled at the ends of this rectangular cavity, to soften the stress concentrations. This results in the grip, of which a cross section is illustrated in Figure 7-4; some general dimensions are added.

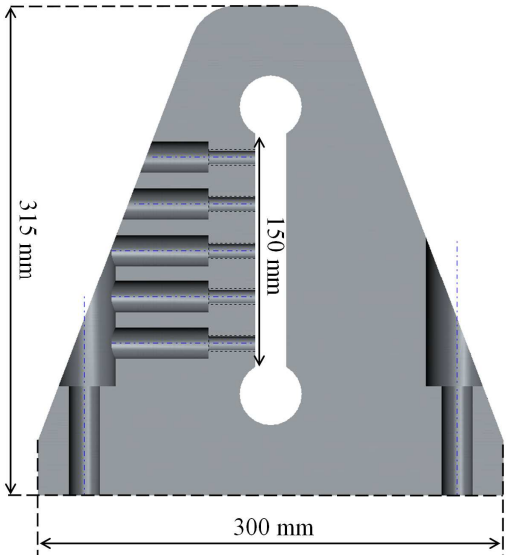

Figure 7-4 Vertical cross section of the grip, indicating some general dimensions.

The design specifications stated that the grips should be able to withstand the same dynamic load range as the servo-hydraulic tensile machine it is mounted on. This means that the grips should withstand a dynamic longitudinal force of 100 kN. Since the gripping is based on friction, a value of the friction coefficient is estimated. The assumption was made (for design purposes) that a friction coefficient of 0.5 should be feasible, with the use of additional rubber films or layers that increase the friction, should the friction between steel and composite be insufficient. After a few preliminary tests, it became obvious that for some materials, such as the carbon fabric-reinforced PPS used here, the friction coefficient of 0.5 could not be reached, even if extra layers of high frictional materials were added. In some cases the rubber film was pushed out of the grips, in other cases the film failed under the shear loads. This, however, means that the first gripping design, depicted in Figure 7-5 (a) and based on pure friction, will not suffice. Therefore, the geometrical gripping was added, which is illustrated in Figure 7-5 (b). The load transfer plate is now supported by flattened cylinders, so that the load transfer to the grip is not only achieved by friction, but also by these cylinders.

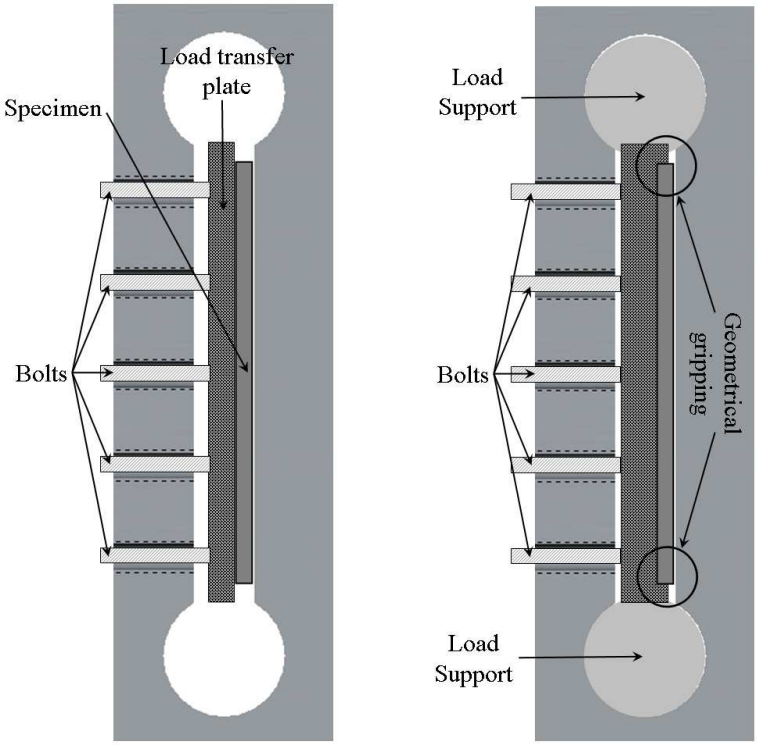

(a) Only frictional clamping (b) Friction and geometrical clamping

Figure 7-5 Illustration of the used gripping principles for the proposed design.

This final design, implementing both frictional and geometrical clamping, is illustrated in Figure 7-6, as an exploded view. This design was used for all experiments conducted in this manuscript.

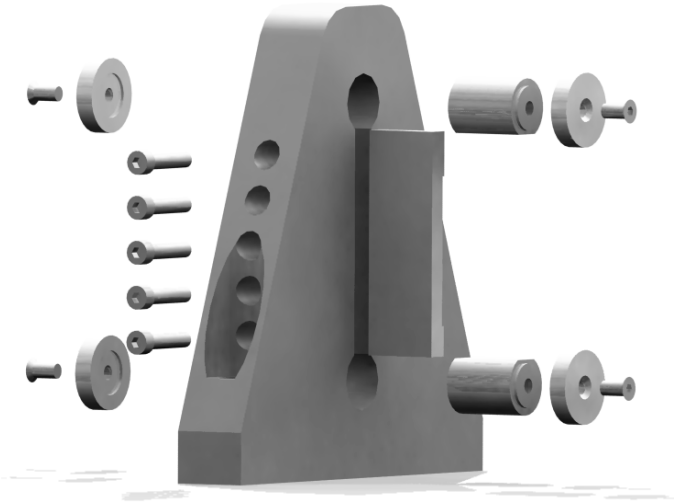

Figure 7-6 Exploded view of one clamp for the three-rail shear test.

For the design, the CAD/CAE package ‘Solidworks 2005’ was used. In this package, there is also a finite element module, ‘COSMOS Express’ which was used to determine the stress distribution in the clamp.

In order to ensure an infinite fatigue life under loading of 100 kN, a safety factor of 3 with respect to the yield stress was taken into account when designing the clamps. Because of the high loads, a high-strength steel was chosen. For the simulation, done with the COSMOS express package, the following material constants for the clamps were used:

Table 7-1 The used material constants in COSMOS express.

Elastic modulus [GPa]	210
Poisson's ratio [-]	0.28
Yield strength [MPa]	620
Mass density [kg/m^3]	7700

In this setup the central clamp carries the highest load; due to symmetry of the three-rail shear setup, each of the outer grips carries half the load of the central one. Therefore, the central grip is considered for the simulations. Furthermore, it is assumed that the vertical force of 100 kN is evenly distributed over the two vertical faces, so that each face carries 50 kN.

Using a friction coefficient of 0.5, this results in a necessary horizontal load of 100 kN by the load transfer plate on each face. These loading conditions are the worst case scenario for the grips and assume the use of only frictional gripping (Figure 7-5 (a)). If geometrical gripping is added (Figure 7-5 (b)), then the horizontal forces will be less, since part of the vertical force is transported via the cylinders to the grips. As such, the vertical load remains the same, the horizontal force will decrease.

The results of the simulation for the worst case scenario yields the stress distribution depicted in Figure 7-7, where the values of the Von Mises criterion are illustrated; the deformation is scaled with a factor of 773.2.

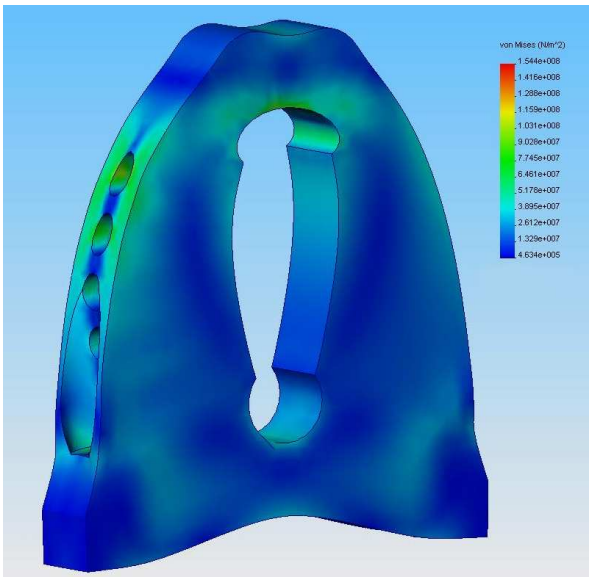

Figure 7-7 Von Mises stress distribution in the clamp under the given load conditions. Deformation factor is 773.2; maximum stress level is 154.8 MPa.

Since the maximum stress level is 154.4MPa, the minimum factor of safety is 3.86 with respect to the estimated yielding stress of 620 MPa. This should ensure infinite fatigue life.

The clamps were made out of THYROPLAST 2344 EFS steel, which is a quenched and tempered mould steel; the chemical composition is given in Table 7-2. After quenching, the material has a hardness of 54 HRC and a tensile strength of 1910 MPa. The material has no typical yield behaviour, it is linear till failure. As a result, the safety factor under fatigue loading conditions is a lot higher than 3, ensuring infinite fatigue life. This material was recommended for the highest demands and fitted the request for high strength, high yield stress and high hardness. The latter was necessary to avoid damage to the surfaces from glass or carbon fibres. The DIN material number is 1.2344 and is referred to as X 40 CrMoV 5 1.

Table 7-2 Chemical composition for the THYROPLAST 2344 EFS, typical analysis in %.

C	Si	Cr	Mo	V
0.40	1.0	5.3	1.4	1.0

After production, the clamps were nitrated for a higher surface hardness, since thermal hardening would result in large, intolerable deformations. The other parts were coated with a (black) nitrate layer with a 'niblox' treatment to avoid micro-welding of the surfaces.

Finally, two extra plates were designed in order to be able to mount this setup on a standard servo-hydraulic testing machine. The final setup, mounted on the tensile machine, is shown in Figure 7-8.

Figure 7-8 The final design, mounted on the tensile machine.

During fatigue tests, the plunger of the tensile machine may start rotating if no precautions are taken. However, this possible rotation of the plunger and therefore the bottom clamp is prevented, using a special guiding system which is mounted on the plunger. Therefore, once alignment of the clamps is achieved, this alignment is guaranteed throughout the fatigue test.

The desired stress state for this setup is to have pure and equal shear load for both of the loaded zones. However, due to misalignment of the clamps, the zones on the left and the right of the central clamp may not experience the same load.
Furthermore, buckling or bending of the specimen may occur, which means that the front and the back of one loaded zone (left or right) may have a different stress state. Hence, a few quasi-static hysteresis tests were done to assess the occurrence of buckling and whether the setup induces a symmetrical load. By performing these cyclic loadings, possible problems regarding symmetry or buckling will be more easily detected than in a quasi-static test with monotonic loading until saturation or de-bonding of the gauges, because differences in the strains will probably increase with each successive loading, due to permanent deformation of the specimen. The results of these hysteresis experiments are documented extensively in paragraph 7. 5, but it could be concluded that the setup does not induce bending and both sides are loaded symmetrically.

7. 3. SAMPLE GEOMETRY AND INSTRUMENTATION

7. 3. 1. The three-rail shear test

The dimensions of the used specimen are given in Figure 7-9.

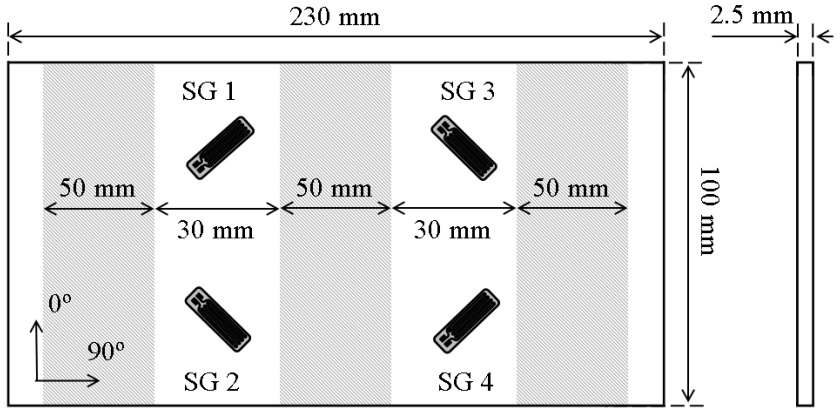

Figure 7-9 Dimensions of the used $[(0°,90°)]_{4s}$ three-rail shear specimen. The locations of the strain gauges, as well as the clamps, are also illustrated.

For all quasi-static and hysteresis tests, the force F, the strains ε_i, i = 1,2,3,4 and the temperature were recorded. With these values, the shear stress and strain can be calculated as

$$\tau_{12} = \frac{1}{2}\frac{F}{t.h} \qquad \gamma_{12} = \left|\varepsilon_i - \varepsilon_j\right| \tag{7.4}$$

Where h is the height of the specimen and t the thickness; (i,j) is either (1,2) or (3,4) with respect to the numbering of the strain gauges in Figure 7-9. For the fatigue experiments, no strain gauges were mounted since they would de-bond after a few dozen cycles due to the large deformations.

7. 3. 2. $[(+45°,-45°)]_{4s}$ Tensile test

As was mentioned in Chapter 2, the longitudinal strain ε_{xx} is measured with the extensometer and the transverse strain ε_{yy} is measured with a transverse strain gauge. When shear strains are expected, a third strain measurement can be performed on the coupon, under an angle α (see Figure 7-10, α equal to 45).
With the three strains ε_{xx}, ε_{yy} and $\varepsilon_{\alpha\alpha}$ the shear strain γ_{xy} can be calculated using a coordinate transformation:

$$\varepsilon_{\alpha\alpha} = \varepsilon_{xx}\cos^2\alpha + \varepsilon_{yy}\sin^2\alpha + 2\varepsilon_{xy}\sin\alpha\cos\alpha \tag{7.5}$$

With α = 45°, as illustrated in Figure 7-10, this becomes:

$$2\varepsilon_{xy} = \gamma_{xy} = 2\varepsilon_{\alpha\alpha} - \varepsilon_{xx} - \varepsilon_{yy} \tag{7.6}$$

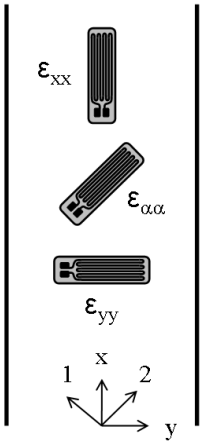

Figure 7-10 Positioning of the strain gauges ε_{yy} and $\varepsilon_{\alpha\alpha}$; ε_{xx} can be measured with either the extensometer or a strain gauge.

However, the strain gauge under 45° is not always necessary. If the strains in the xy-coordinate system are transformed to the 1,2-coordinate system for the $[(+45^o,-45^o)]_{4s}$ stacking sequence, the following expression is found for the shear strain γ_{12} [26, 27]:

$$\gamma_{12} = \varepsilon_{xx} - \varepsilon_{yy} \tag{7.7}$$

For the longitudinal and transverse strains, the following formulas can be derived for the $[(+45^o,-45^o)]_{4s}$ stacking sequence, using coordinate system transformation formulas [27]:

$$\begin{aligned} \varepsilon_{11} &= \frac{1}{2}(\varepsilon_{xx} + \varepsilon_{yy} + \gamma_{xy}) \\ \varepsilon_{22} &= \frac{1}{2}(\varepsilon_{xx} + \varepsilon_{yy} - \gamma_{xy}) \end{aligned} \tag{7.8}$$

ε_{11} being the strain along the fibre in the warp direction and ε_{22} the strain along the fibre in the weft direction.

However, for a tensile test, the following stress state is applied:

$$\sigma_{xx} = \sigma \qquad \sigma_{yy} = \sigma_{zz} = \sigma_{xy} = \sigma_{yz} = \sigma_{zx} = 0 \tag{7.9}$$

σ being the stress applied at the specimen.

$$\begin{pmatrix} \varepsilon_{xx} \\ \varepsilon_{yy} \\ \varepsilon_{zz} \\ \gamma_{yz} \\ \gamma_{xz} \\ \gamma_{xy} \end{pmatrix} = \begin{pmatrix} \frac{1}{E_{xx}} & -\frac{\nu_{xy}}{E_{xx}} & -\frac{\nu_{xz}}{E_{xx}} & 0 & 0 & 0 \\ -\frac{\nu_{yx}}{E_{yy}} & \frac{1}{E_{yy}} & -\frac{\nu_{yz}}{E_{yy}} & 0 & 0 & 0 \\ -\frac{\nu_{zx}}{E_{zz}} & -\frac{\nu_{zy}}{E_{zz}} & \frac{1}{E_{zz}} & 0 & 0 & 0 \\ 0 & 0 & 0 & \frac{1}{E_{yz}} & 0 & 0 \\ 0 & 0 & 0 & 0 & \frac{1}{G_{xz}} & 0 \\ 0 & 0 & 0 & 0 & 0 & \frac{1}{G_{xy}} \end{pmatrix} \begin{pmatrix} \sigma_{xx} \\ \sigma_{yy} \\ \sigma_{zz} \\ \tau_{yz} \\ \tau_{xz} \\ \tau_{xy} \end{pmatrix} \tag{7.10}$$

Using Hooke's law for an orthotropic material (Equation 7.10) [28], this results in $\gamma_{xy} = 0$ which combined with Equation 7.8 yields:

$$\varepsilon_{11} = \varepsilon_{22} = \frac{\varepsilon_{xx} + \varepsilon_{yy}}{2} \tag{7.11}$$

As such, for the $[(+45^o,-45^o]_{4s}$ stacking sequence, all strains in the 1,2-coordinate system can be calculated using only the longitudinal strain ε_{xx} and the transverse strain ε_{yy}. The third strain gauge, however, can be mounted to control the alignment of the test specimen in the tensile machine, since it is known that γ_{xy}, calculated using Equation 7.6 should be zero.
Finally, the dimensions of the used coupons, according the "*ASTM D3519/D3518M-94 (2001) standard test method for in-plane shear response of polymer matrix composite materials by tensile test of a ±45° laminate*", are shown in Figure 7-11.

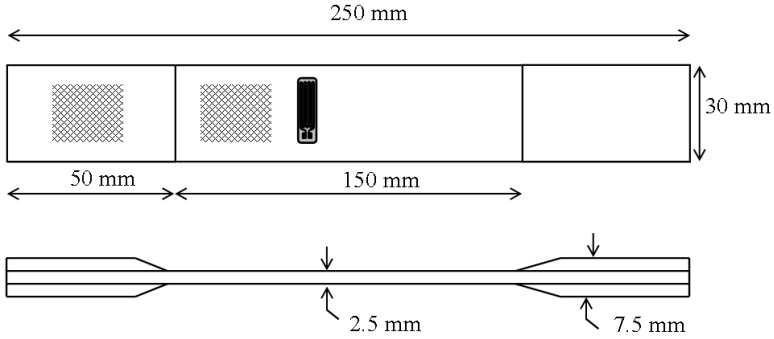

Figure 7-11 Dimensions of the used $[(+45^o,-45^o)]_{4s}$ tensile coupon, equipped with chamfered tabs of $[(+45^o,-45^o)]_{4s}$ carbon-PPS.

For every quasi-static and hysteresis experiment the force F, the longitudinal and transverse strains ε_{xx} and ε_{yy} and the temperature were recorded. With these values, the shear stress τ_{12} and shear strain γ_{12} can be calculated as

$$\tau_{12} = \frac{1}{2}\frac{F}{w.t} \qquad (7.12)$$
$$\gamma_{12} = \varepsilon_{xx} - \varepsilon_{yy}$$

Where w is the width of the specimen and t is the thickness. The transverse strain was measured using a strain gauge and the longitudinal strain was measured using the extensometer. For the fatigue experiments, no strain gauges were mounted since they would de-bond after a few dozen cycles due to the large deformations.

The following three sections will describe the quasi-static, hysteresis and fatigue experiments conducted with both the three-rail shear setup and the $[(+45°,-45°)]_{4s}$ tensile test. For each of these sections, first the experiments performed with the three-rail shear setup are discussed, after which the $[(+45°,-45°)]_{4s}$ tensile experiments are commented on and the correspondence between the results is assessed.

7. 4. QUASI-STATIC TESTS

7. 4. 1. Three-rail shear tests

All tests were done in a displacement-controlled manner with a displacement speed of 1 mm/min, during which the force F, the strains ε_i, i = 1,2,3,4 and the temperature were recorded and shear stress and strain were calculated using Equation 7.4.
A few shear stress-strain results are given in Figure 7-12. Since from each rail shear test, two curves can be derived, one from each instrumented loaded zone, there should be six curves for three specimens. However, in Figure 7-12, only the curves from the strain gauges which lasted the longest are given; the tests were stopped once all strain gauges de-bonded or saturated which means that the maximum value of the shear stress and strain in Figure 7-12 do not correspond with failure. After saturation or failure of the strain gauges, the test was stopped so the possibility for non-destructive evaluation of the specimens remained an option.

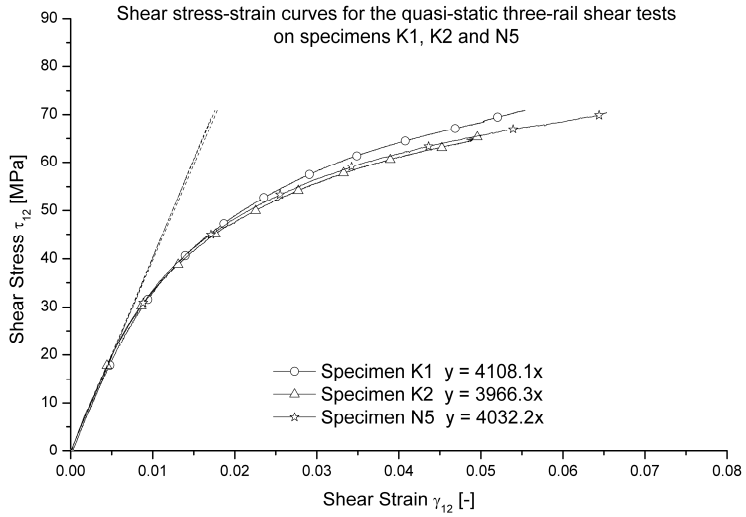

Figure 7-12 Evolution of the shear stress as a function of the shear strain for the quasi-static three-rail shear experiments.

It should be noticed that the results from these quasi-static tests are very reproducible and that the calculated stiffness corresponds very well with the value obtained with the dynamic modulus identification method (chapter 3, G_{12} = 4175 MPa). During the quasi-static rail shear tests, no temperature increase was measured.
Finally, Figure 7-13 illustrates the evolution of the measured strains and the derived shear strains for the quasi-static test on specimen N5 until saturation of the strain gauges; the numbering of the gauges corresponds with Figure 7-9.

As such, it can already be remarked that both sides of the specimen are loaded symmetrically.

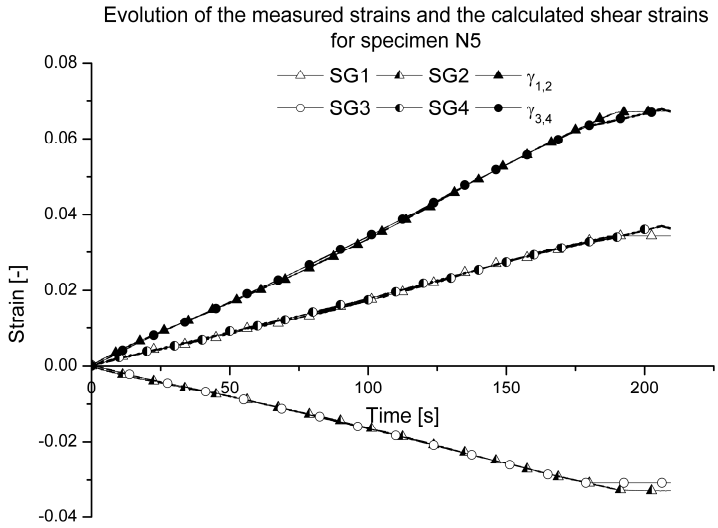

Figure 7-13 Evolution of the measured strains and calculated shear strains for specimen N5.

7. 4. 2. $[(+45°,-45°)]_{4s}$ experiments

In this paragraph, the quasi-static $[(+45°,-45°)]_{4s}$ experiments will be discussed and the results will be compared with those obtained in the previous paragraph. All tensile tests were done in a displacement-controlled manner with a displacement speed of 2 mm/min, in correspondence with the ASTM D3519/D3518M-94, during which the force F, the longitudinal and transverse strains and the temperature were recorded and shear stress and strain were calculated using Equation 7.12.

Figure 7-14 illustrates the highly nonlinear shear stress-strain evolution for two quasi-static experiments, M1 and M3. The curve is only depicted until the transverse strain gauge either saturated which was the case for M3, or de-bonded which happened for M1. The failure stresses were 105.4 MPa and 105.3 MPa for M1 and M3 respectively. These values show good correspondence with the value given in chapter 3 (S = 110 MPa). The stiffness could also be calculated from these results, as is shown in Figure 7-14. Although some scatter is present on these values, they still correspond quite well with the values given in chapter 3 (G_{12} = 4175 MPa). It should be noted that these results correspond excellently with the shear stress-strain curves from the three-rail shear tests.

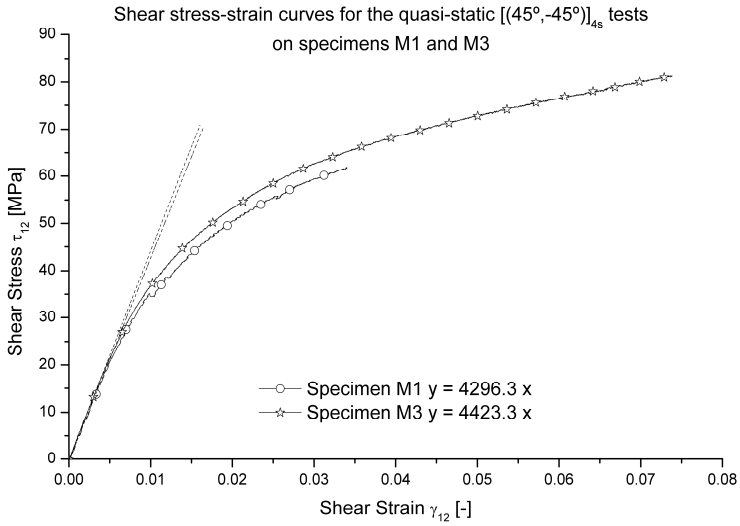

Figure 7-14 Evolution of the shear stress as a function of the shear strain for the quasi-static tensile experiments.

During these tests, no increase in temperature was recorded.

Finally, Figure 7-15 illustrates the evolution of the shear strain γ_{12} and the strains along and perpendicular to the fibre, ε_{11} and ε_{22}, both calculated using Equation 7.11 as a function of time until saturation of the strain gauges for specimen M3. It should be noted that the strains ε_{11} and ε_{22} are very low, so they will have only a very limited influence on the damage behaviour, thus the imposed stress state should correspond very well with the pure shear state in the three-rail shear test.

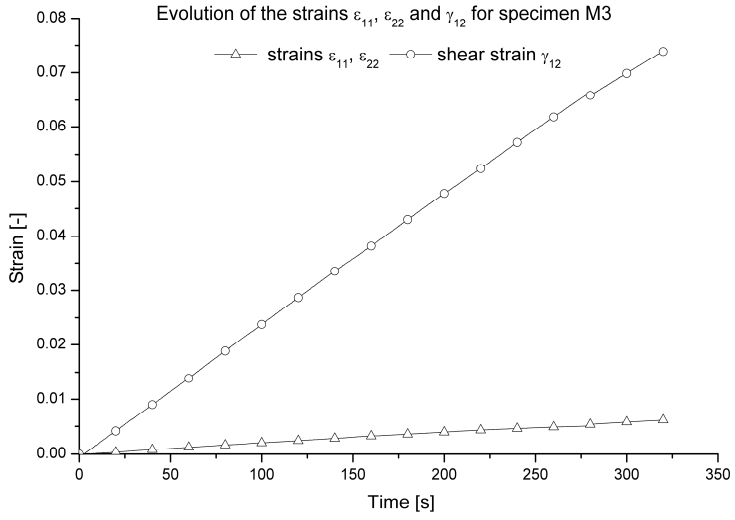

Figure 7-15 Evolution of ε_{11}, ε_{22} and γ_{12} for specimen M3.

7. 5. QUASI-STATIC HYSTERESIS TESTS

7. 5. 1. Three-rail shear tests

As was already mentioned in the design section of the chapter, the desired stress state for this setup is to have pure and equal shear load for both of the loaded zones. However, due to misalignment of the clamps, the zones on the left and the right of the central clamp may not experience the same load. Furthermore, buckling or bending of the specimen may occur, which means that the front and the back of one loaded zone (left or right) may have a different stress state. Hence, quasi-static cyclic loading (hysteresis) was applied, meaning that the specimens were loaded until a maximum shear stress of 10 MPa was reached and then completely unloaded. For each of the next cycles, the maximum shear stress was increased with 10 MPa with respect to the previous cycle. This was repeated until the strain gauge failed or de-bonded. The low starting value of 10 MPa was chosen to verify if damage already occurs for these low load levels.
All experiments were done in a displacement controlled manner with a displacement speed of 1 mm/min; the signals were sampled at 20 Hz.

By performing these cyclic loadings possible problems regarding symmetry or buckling will be more easily detected than in a quasi-static test with monotonic loading until saturation or de-bonding of the gauges, because differences in the strains will probably increase with each successive loading, due to permanent deformation of the specimen.

To verify the symmetry, four strain gauges were placed on the same side of the specimen, but distributed over the two loaded zones, as illustrated on Figure 7-9. The time evolution of the different strain gauges for such a test is given in Figure 7-16. If the setup is symmetrical, then strain gauge 1 and 3 and strain gauge 2 and 4 respectively should give the same strain. It can clearly be seen that the signals coincide almost perfectly, meaning symmetry is achieved. The de-bonding or failing of the strain gauges can also be seen: after about 350 seconds, strain gauge 3 de-bonded; after 450 s, gauge 1 failed and after 500 s, gauge 2 failed. Gauge 4 failed soon after gauge 2. As a result; the corresponding curves no longer coincide from that point on.

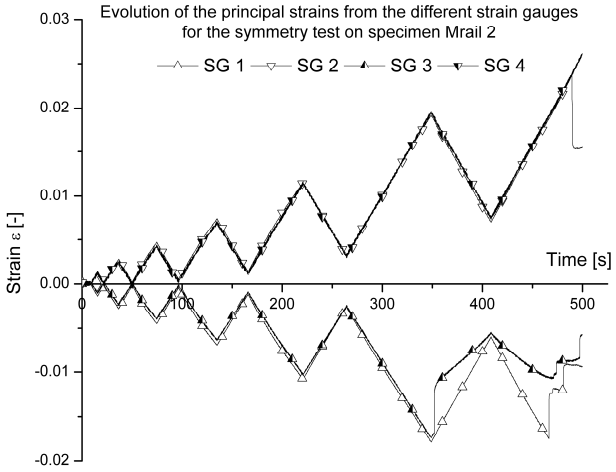

Figure 7-16 Evolution of the strain as a function of time for all four strain gauges in the symmetry test.

To assess whether buckling occurs, the four strain gauges are placed on the same loaded zone, but on front and rear surfaces. Strain gauges 1 and 2 are placed as depicted in Figure 7-9 and strain gauges 3 and 4 are placed on the same position on the opposite side of the specimen in such a way that the strains from strain gauge 1 and 2 should correspond with the signals from strain gauges 3 and 4 respectively. The result from such a test is depicted in Figure 7-17. Again, the signals coincide almost perfectly. Similar to the previous test, the curves are only shown until the strain gauges de-bonded. This happened at 470 s for gauge 3 and at 510 s for gauge 4. The other gauges failed soon after 600 s.

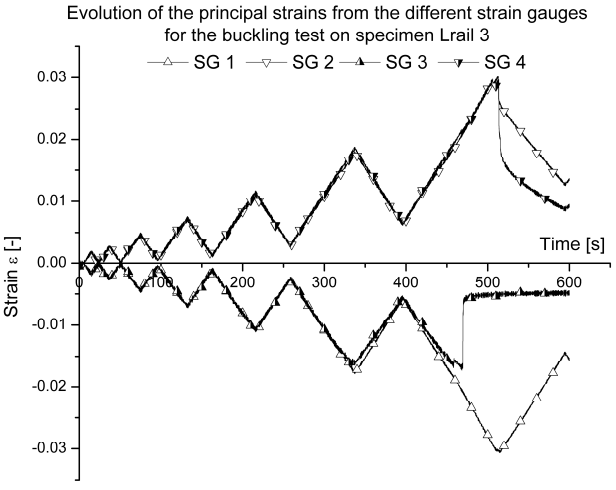

Figure 7-17 Evolution of the strains from al four strain gauges as a function of time for the buckling test.

Similar experiments have been conducted, all with corresponding results. As such, it may be concluded that the stress state induced by the clamps is symmetrical and that no buckling or bending of the specimen occurs. As a result, there is no longer need for four strain gauges. Two strain gauges, mounted on the same surface of one loaded zone under +45º and -45º suffice for the measurement.

The shear stress-strain results from these, as well as two other experiments are given in Figure 7-18 and again, only the curves from the strain gauges which lasted the longest, are plotted. The omitted curves, however, showed very good correspondence with the corresponding depicted ones. Again it should be noted that the results are very much alike and that the initial stiffness corresponds very well with the value given in chapter 3 (G_{12} = 4175 MPa).

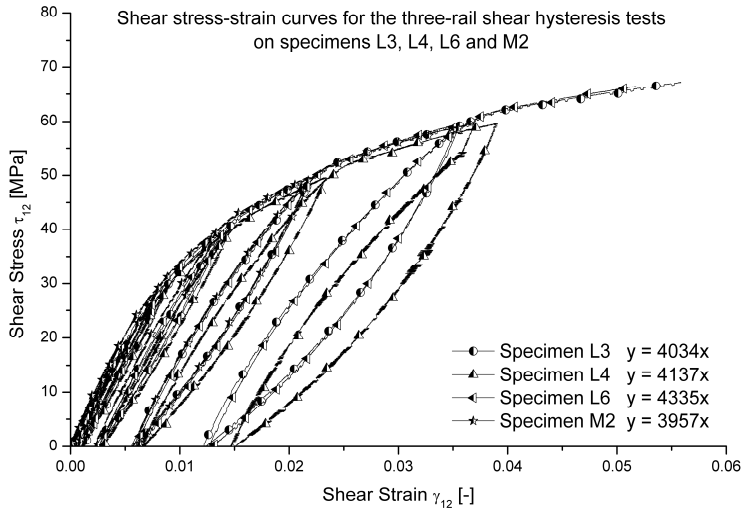

Figure 7-18 Evolution of the shear stress as a function of the shear strain for the rail shear hysteresis experiments.

For all measurements mentioned above, the temperature was also monitored, using a thermocouple. Because of the shear loads, a temperature increase is expected. However, an increase of only 1 ºC was measured.

7. 5. 2. $[(+45°,-45°)]_{4s}$ experiments

For these experiments, the specimens were loaded until a maximum shear stress of 20 MPa was reached and then completely unloaded. For each of the next cycles, the maximum shear stress was increased with 10 MPa with respect to the previous cycle, as was the case for the three-rail shear experiments. This was repeated until the strain gauge failed or de-bonded.

The value of 20 MPa was chosen because only very limited nonlinear behaviour is visible in Figure 7-14 before this value is reached and for the three-rail shear tests, very limited damage occurred at 10 MPa.

Figure 7-19 illustrates the shear stress-strain evolution for three specimens M2, M4 and M5. For M4, the cycle after 60 MPa was reversed just before the strain gauge was expected to saturate. For M2 and M5, the strain gauge de-bonded after the cycle of 60 MPa. Failure stresses were 109.8 MPa for M2, 116.3 MPa for M4 and 103.8 MPa for M5. Again these values correspond very well with the value given in chapter 3 (S = 110 MPa). The initial stiffness is also calculated and is shown in Figure 7-19. Again, there is some scatter on the results, but the values correspond quite well with those found in Figure 7-14 and with the value determined by the dynamic modulus identification method (chapter 3, G_{12} = 4175 MPa). It should be noted that the reproducibility of M2 and M4 is very high. Specimen M5 tends to behave stiffer during the entire experiment, without any apparent reason. These results show very good agreement with the cyclic shear stress-strain behaviour seen for the three-rail shear tests. This shape of the τ_{12}-γ_{12} curve was also reported in [7, 10] for a glass fibre-reinforced epoxy and in [11-14] for a carbon fibre-reinforced epoxy. The loops are the result of friction between the fibre and the matrix [12, 13].

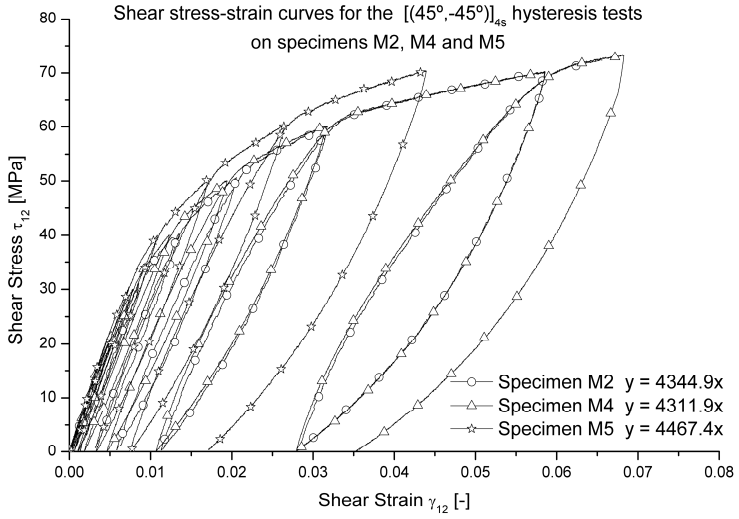

Figure 7-19 Evolution of the shear stress as a function of the shear strain for the tensile hysteresis experiments.

Figure 7-20 illustrates the evolution of the shear strain γ_{12} and the strains along and perpendicular to the fibre, ε_{11} and ε_{22}, both calculated using Equation 7.11, as a function of time until saturation of the strain gauges for specimen M4.

Again, the strains ε_{11} and ε_{22} are very low, so the behaviour should correspond well with the pure shear state from the three-rail shear test.

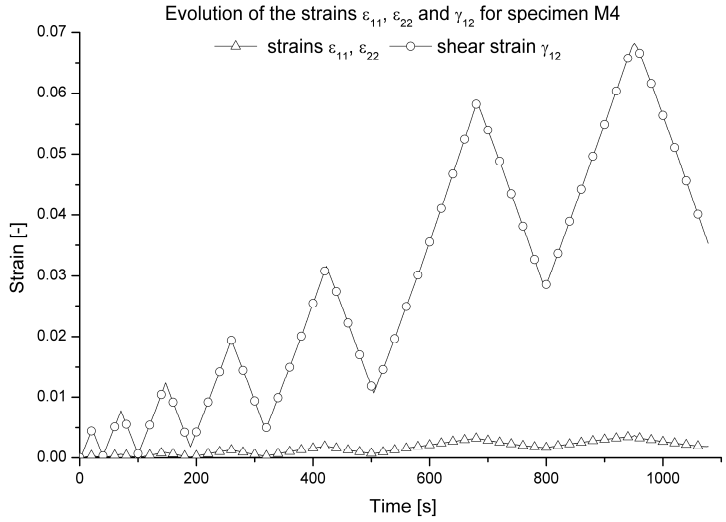

Figure 7-20 Evolution of ε_{11}, ε_{22} and γ_{12} for specimen M3

Finally, Figure 7-21 illustrates the occurring fracture for specimen M2, but this type of failure was seen for all the $[(+45°,-45°)]_{4s}$ tensile tests. The local narrowing before final failure can clearly be distinguished.

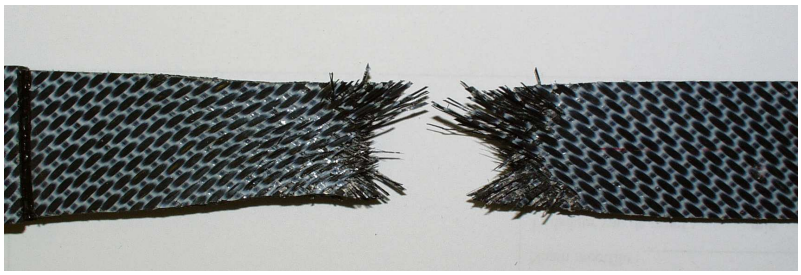

Figure 7-21 Image of the fracture of a $[(+45°,-45°)]_{4s}$ specimen.

During these experiments, a very slight increase in temperature was noted of about 1 ºC.

7. 5. 3. Shear strain-displacement correlation

Because of the combined frictional and geometrical clamping of the design, the modified three-rail shear setup has another interesting advantage. Given the definition of the shear strain γ (Figure 7-22), it can be calculated as:

$$\tan\gamma = \frac{D}{W} \tag{7.13}$$

If small displacements are assumed, the shear strain will be small and can be calculated as:

$$\tan\gamma \approx \gamma \approx \frac{D}{W} \tag{7.14}$$

This means that there should be a linear correlation between the shear strain γ and the imposed displacement from the central rail D. For the given value of W = 30 mm (see Figure 7-9), this relation becomes

$$\gamma = \frac{1}{30} D = 0.033D \tag{7.15}$$

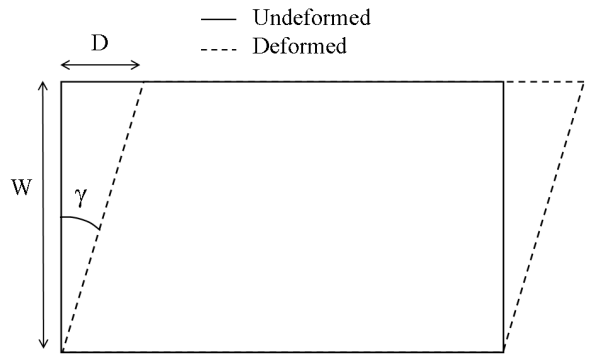

Figure 7-22 Definition of the shear strain γ.

During the quasi-static and hysteresis experiments it was noted that there is a correlation between the imposed displacement and the resulting shear strain in the specimen, but it is rather parabolic than linear. This is illustrated in Figure 7-23; the different experiments are given an offset along the x-axis for a clear image. It can be noted that for both the hysteresis tests, the curves are very reproducible.

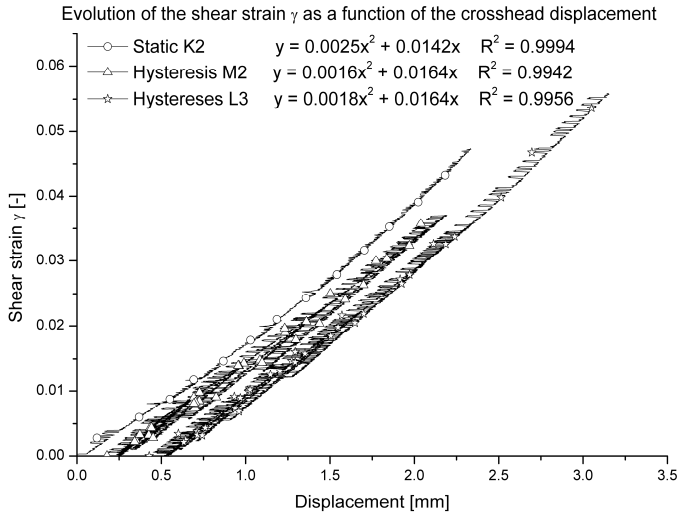

Figure 7-23 Illustration of the correlation between shear strain and displacement.

The reason for the difference between the experimental and theoretical correlation can be explained as follows. Theoretically, a displacement of 2 mm on the side edge is exactly 2 mm, whereas a displacement of 2 mm of the hydraulic actuator will be less than 2 mm displacement of the side edge of the loaded zone, because of the following reasons:

(i) The height of the specimen is not exactly equal to the height of the geometrical gripping, since then, mounting the specimen would be practically impossible. As a result, some slippage may occur.

(ii) The load transfer plates do not fit exactly in the space provided, the height is a little less since otherwise, the plates could not be mounted. Again, some slippage may occur.

(iii) The mounting mechanism on the tensile machine, as well as the tensile machine deforms under the occurring loads. Hence, the displacement of the side of the specimen will always be a little smaller than the imposed displacement by the plunger. This is the same reason why the calculated strain from the displacement in a uni-axial tensile test differs from the strain, measured with extensometer or strain gauges.

Of course, after some time, enough sliding will have occurred and all free space will be occupied, so for higher displacements, this effect should no longer be present. For instance, if the slope is calculated for specimen L3 for a displacement of 3 mm, this yields:

$$\left.\frac{df}{dx}\right|_{x=3} = 0.0036x + 0.0164\Big|_{x=3} = 0.0272 \tag{7.16}$$

which approximates the expected 0.033.

The remaining difference is due to the elastic deformation of the entire setup. This is also the reason why there is a larger difference between the curve for the quasi-static test and the hysteresis tests than between both hysteresis tests respectively. After one loading, there will still be some free space that allows sliding, whereas after a few successive loadings, this free space will no longer exist.
It is expected that a similar phenomenon is present when using the standard three-rail shear test setup. However, nothing on this matter is documented by Lessard et al. [20].

The finite element modelling of these experiments will be given in chapter 8.

7. 6. FATIGUE LOADING CONDITIONS

7. 6. 1. Three-rail shear tests

The fatigue experiments were done according to the *"ASTM D4255/D4255M standard test method for in –plane shear properties of polymer matrix composite materials by the rail shear method"* but under fatigue loading conditions.
They were done in a load-controlled manner and force, displacement and temperature were registered. Because of the large deformations, strain gauges were not considered, since they de-bond after a few dozen cycles. As such, the displacement is chosen as parameter for information about the deformed state, since there is a relationship between the shear strain and the displacement, because of the geometrical clamping of the grips.

From the quasi-static experiments, described in paragraph 7. 4, it can be derived that a maximum stress level between 30 MPa and 50 MPa for the fatigue tests should give interesting results. Lower than 30 MPa there is only very limited nonlinear behaviour and beyond 50 MPa it is expected that the specimen would fail after a few dozen cycles.

Since the objective is to compare the results of the three-rail shear test with the $[(+45°,-45°)]_{4s}$ tensile tests, all fatigue experiments were done with a shear stress ratio R equal to 0, meaning that the shear stress varies between 0 and a certain maximum value. For the $[(+45°,-45°)]_{4s}$ tensile test, it would be rather difficult to have negative shear stresses, since this would mean that compressive tests should be performed, with the corresponding difficulties with buckling.
During the fatigue experiments, every five minutes five fatigue cycles were registered and from these signals, the maximum, minimum and average value was calculated and stored.

A first experiment was done at 1 Hz with a maximum load of 40 MPa, which is halfway the range suggested in the previous paragraph. Since the test was load-controlled, an increase in the displacement amplitude corresponds with shear stiffness degradation. While monitoring the experiment, it was noticed that the permanent deformation and stiffness degradation was less than expected and no temperature increase occurred, so after 250,000 cycles, the frequency was increased to 2 Hz. The results of this experiment are shown in Figure 7-24. After 770,000 cycles, the test was stopped.

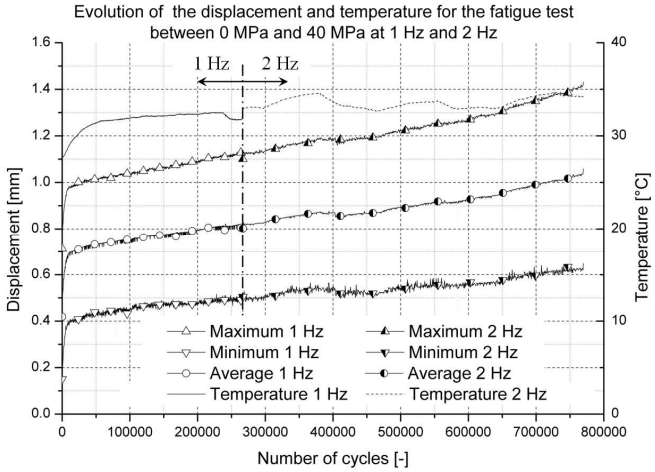

Figure 7-24 Maximum, minimum and mean value of the displacement as a function of the number of cycles for a 0-40 MPa fatigue test at a combined frequency of 1 Hz and 2 Hz.

The temperature tends to be slightly higher for 2 Hz than for 1 Hz. Therefore, a next test was done between 0 MPa and 40 MPa at 2 Hz until failure. Figure 7-25 illustrates the run-in of the experiment and Figure 7-26 shows the fatigue data. It should be noted that already some permanent deformation occurs during the run-in, followed by a steady state regime. That is also the reason why the minimum of the displacement during the fatigue test does not start at 0 in Figure 7-26. It can also be noticed that the evolution of the displacement does not have the expected sinusoidal evolution with increasing amplitude, as expected. The test was load-controlled with a sinusoidal evolution and due to stick slip, the corresponding displacement differs a little.

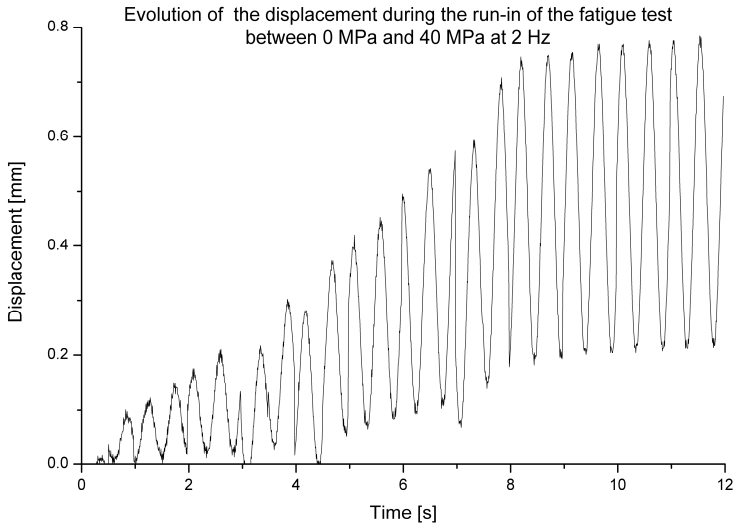

Figure 7-25 Displacement as a function of time during the run-in of the 0-40 MPa, 2 Hz fatigue test.

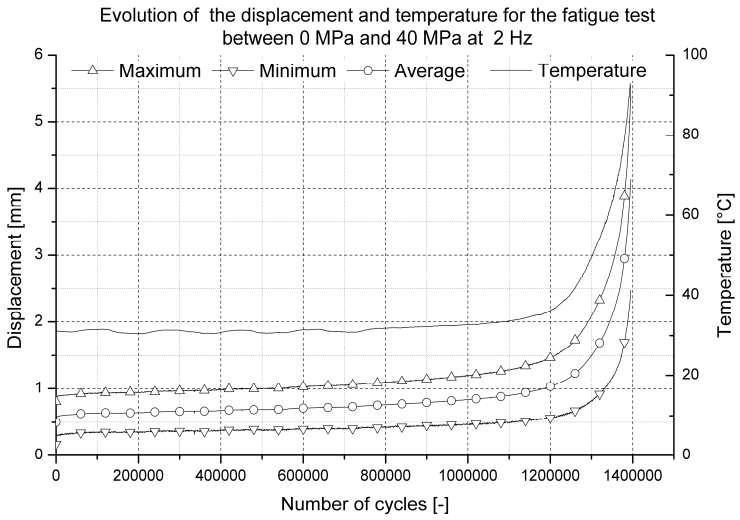

Figure 7-26 Maximum, minimum and mean value of the displacement as a function of the number of cycles for a 0-40 MPa fatigue test at 2 Hz.

The test was stopped after 1,400,000 cycles, because the temperature had already exceeded the glass transition temperature of the matrix, which is 90 °C. From Figure 7-26 it can be seen that after the run-in there is a gradual increase in permanent deformation and stiffness degradation, until about 1,200,000 cycles. Until that time, the temperature remains constant. Then, there is a sudden increase in both temperature and permanent deformation. This can be explained as follows.

During the first 1,200,000 cycles, damage grows in the material, with little effect on the stiffness. Probably the fibre-matrix interface deteriorates. Once there is sufficient damage to this interface, the fibres start to slide inside the matrix under influence of the shear load, causing heating of the matrix, with softening of the matrix as result. This, however, causes more deteriorating of the fibre-matrix interface, so that even more sliding and heating occurs. This process ends with final failure. The heating due to frictional sliding of the fibre in the matrix has also been reported in [29, 30] for fibre-reinforced ceramics and in [31] for fibre-reinforced polymers.
The following experiment was done between 0 MPa and 45 MPa at 2 Hz, to assess the influence of maximum load level. The run-in gave similar results as for the 0-40 MPa test, so it is not shown. Figure 7-27 depicts two of these experiments.

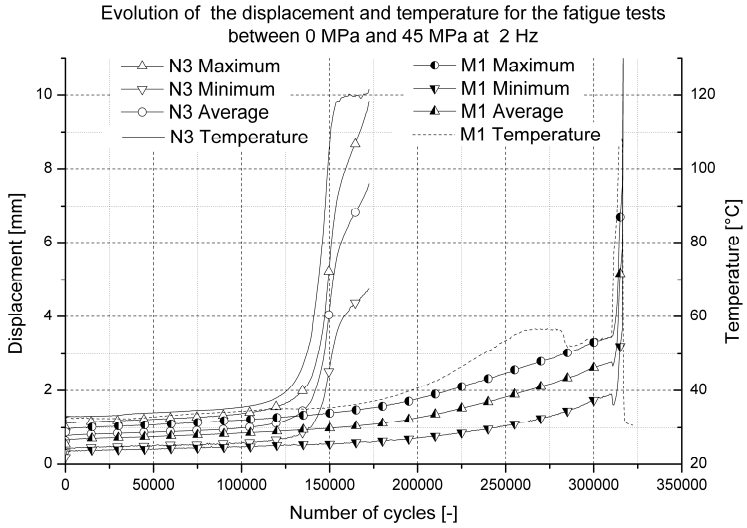

Figure 7-27 Maximum, minimum and mean value of the displacement as a function of the number of cycles for a 0-45 MPa fatigue test at 2 Hz.

Again, a similar evolution as for the 0-40 MPa test can be seen, although the initiation of the large stiffness decrease and sudden temperature increase happens a lot earlier. For these tests, the sudden jump happens around 140,000 cycles for N3 and around 310,000 cycles for M1. This is five to ten times lower than for the 0-40 MPa at the same frequency. It should, however, be noted that the increase in permanent deformation is much more sudden for N3 than for M1. For the latter, the sudden jump is preceded by a gradual increase in permanent deformation and stiffness degradation, which both start around 150,000 cycles. The latter is also the point in time where the temperature starts increasing. The sudden drop in temperature around 300,000 cycles for M1 was due to a loss of contact of the thermocouple, because of the large deformations. The thermocouple was re-attached soon afterwards.

In Figure 7-28, the fracture of this specimen is shown. Although the failure started near the clamped edges, where stress concentrations exist, final failure occurred in the centre of the specimen, under shear loading conditions.

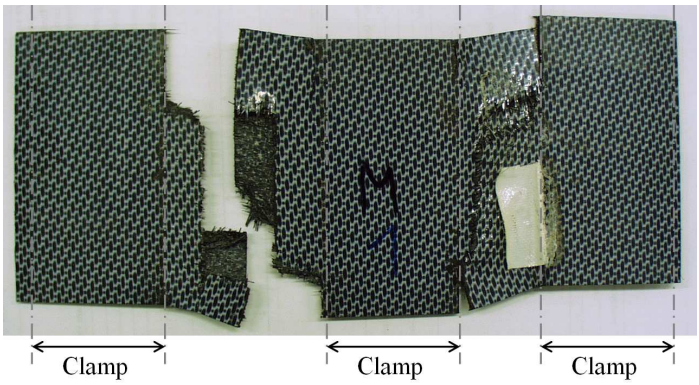

Figure 7-28 Illustration of the failure of specimen M1.

Because of this difference in lifetime, the following experiments were conducted in the same stress range, 0-45 MPa, but at 1 Hz, to assess the influence of the frequency. The results of these experiments are shown in Figure 7-29. The temperature measurement was unavailable for specimen M3, because the thermocouple de-bonded very early. Again, similar evolutions are found for the evolution of the displacement. Specimen M4 has a sudden increase in temperature and displacement after about 80,000 cycles, whereas specimen M3 has a more gradual increase, starting around 100,000, until there is a sudden increase at 160,000 cycles. Apparently, lowering the frequency tends to decrease the lifetime.

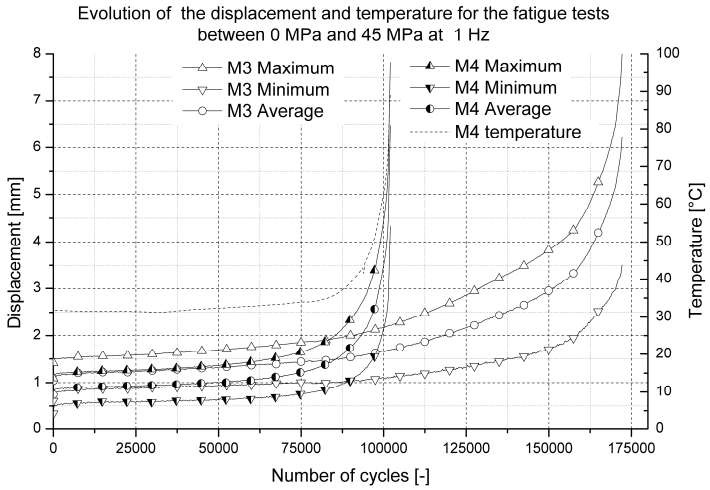

Figure 7-29 Maximum, minimum and mean value of the displacement as a function of the number of cycles for a 0-45 MPa fatigue test at 1 Hz.

To verify this behaviour, fatigue experiments were done at a load range of 0-50 MPa and again at 1 Hz and 2 Hz. Figure 7-30 shows the run-in for one of these experiments, but a similar evolution as for the 0-40 MPa@2 Hz test is found (see Figure 7-25), namely a relatively large increase, followed by a steady state regime.

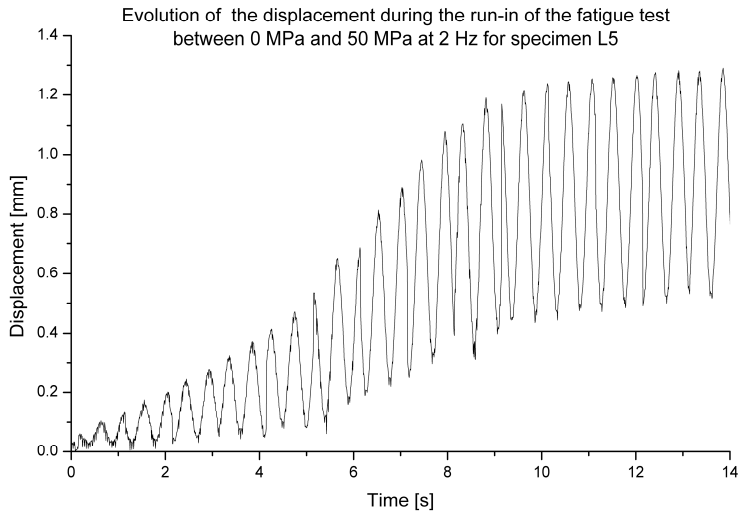

Figure 7-30 Displacement as a function of time during the run-in of a 0-50 MPa, 2 Hz fatigue test.

Figure 7-31 shows the results for the test at 2 Hz. The sudden increase for the displacement occurs around 55,000 cycles for N1 and around 45,000 cycles for L5. It should be noted that due to the large deformations, the thermocouple de-bonded after 59,000 cycles for N1, hence the sudden drop in temperature. Furthermore, the temperatures lie lower than in the previous experiments, because the thermocouple lost contact with the specimen's surface, due to the large deformations, but still remained quite close to the surface. As such, the actual temperatures would be in the same range as for the previous tests, which means higher than the softening temperature of PPS (90 °C).
Considering the lifetime, a reduction factor of about three with respect to the 0-45 MPa@2 Hz measurements is found.

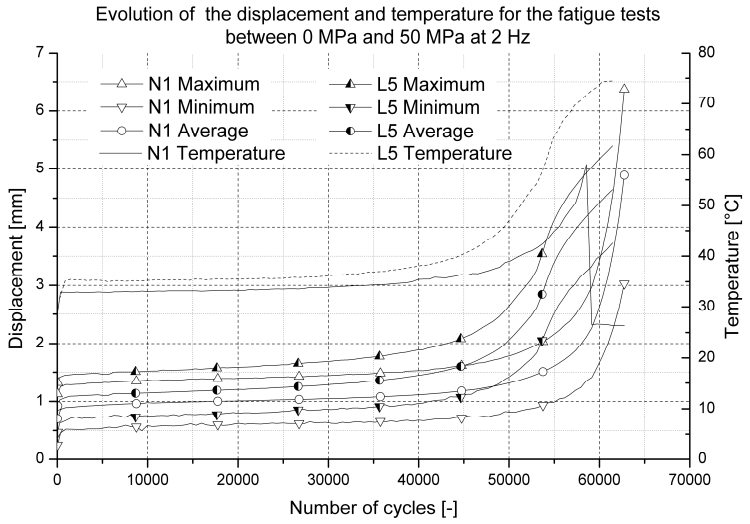

Figure 7-31 Maximum, minimum and mean value of the displacement as a function of the number of cycles for a 0-50 MPa fatigue test at 2 Hz.

Finally, Figure 7-32 illustrates the results from the 0-50 MPa@1 Hz experiment. Unfortunately, the temperature measurement was not successful, because of the de-bonding of the thermocouple. The sudden increase in displacement occurs after about 27,500 cycles, which indeed is lower than for the corresponding experiment at 2 Hz.

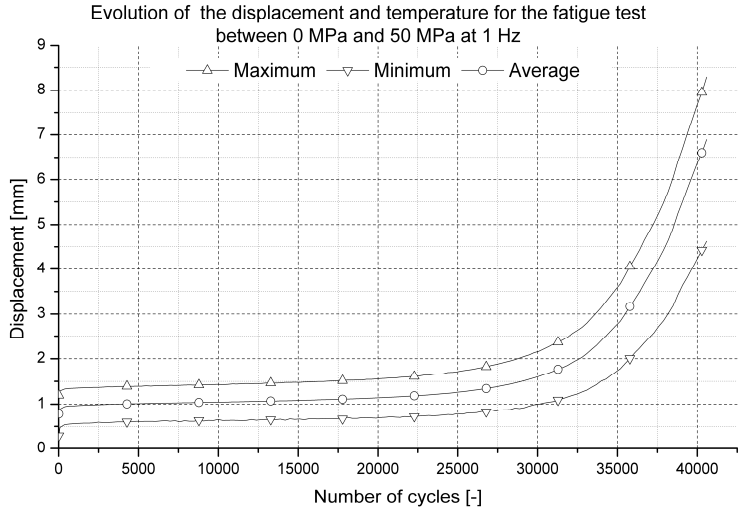

Figure 7-32 Maximum, minimum and mean value of the displacement as a function of the number of cycles for a 0-50 MPa fatigue test at 1 Hz.

In conclusion, increasing the maximum shear stress for fatigue tests with R equal to zero decreases the fatigue life, while increasing the loading frequency for a given load range seems to increase fatigue life. The fatigue life is very sensitive to the maximum shear stress at low maximum stresses; an increase from 40 MPa to 45 MPa decreased fatigue life with a factor ten. For higher stresses, the sensitivity is lower; an increase from 45 MPa to 50 MPa only reduces fatigue life with a factor of about three. During run-in, there is first a relatively large increase in displacement. Then, there is some sort of steady state with a very gradual increase and finally, a sudden large increase in both temperature and displacement occurs, before failure.

7. 6. 2. $[(+45°,-45°)]_{4s}$ experiments

These experiments were done according the *"ASTM D3479/D3479M-96 (2002) standard test method tension-tension fatigue of polymer matrix composite materials*" and the *"ASTM D3518-76 standard practice for in-plane shear stress-strain response of unidirectional reinforced plastics"*.
The fatigue experiments were done in a load-controlled manner; because of the large deformations, strain gauges were not considered since they would de-bond after a few dozen of cycles. The longitudinal strain was measured with the extensometer, but since there is no data of the transverse strain, the shear strain cannot be calculated. Of course, load, displacement and temperature were also registered.

As previously mentioned, the same experiments as were done with the three-rail shear test are repeated, with exception of the test between 0 MPa and 40 MPa, because of long duration of this experiment. For each experiment it was verified that no slipping in the grips occurred. For comparison with the three-rail shear tests, the evolution of both temperature and displacement is only considered until there is a significant temperature increase and stiffness degradation. Afterwards, a new regime reinstates itself, which is discussed at the end of this paragraph. Also, the specimens tend to deform into a 'dog-bone' like shape. This deformation was most apparent for the highest stress range and frequency, which is illustrated in Figure 7-33, where the specimen N2, on which a 0-50 MPa, 2 Hz fatigue experiment was done, can be compared with another specimen which is still to be tested, but with the same dimensions as specimen N2 had before testing.

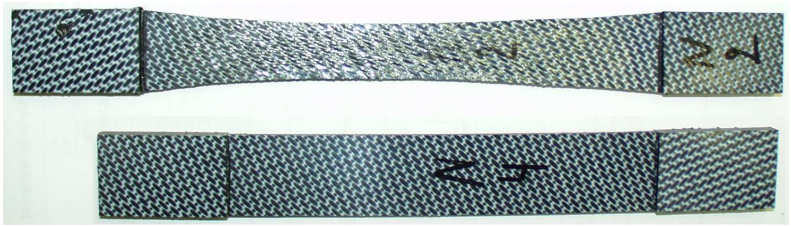

Figure 7-33 Deformed (top) and undeformed (bottom) $[(+45°,-45°)]_{4s}$ specimen.

For the discussing of the fatigue experiments, the same order with respect to test frequency and load range as used for the three-rail shear tests is followed here. Figure 7-34 shows the results from a fatigue test between 0 MPa and 45 MPa at 2 Hz. The initiation of the increase in temperature and deformation is situated around 400,000 cycles, which is higher than the 140,000 and 310,000 cycles found for the corresponding rail shear test.

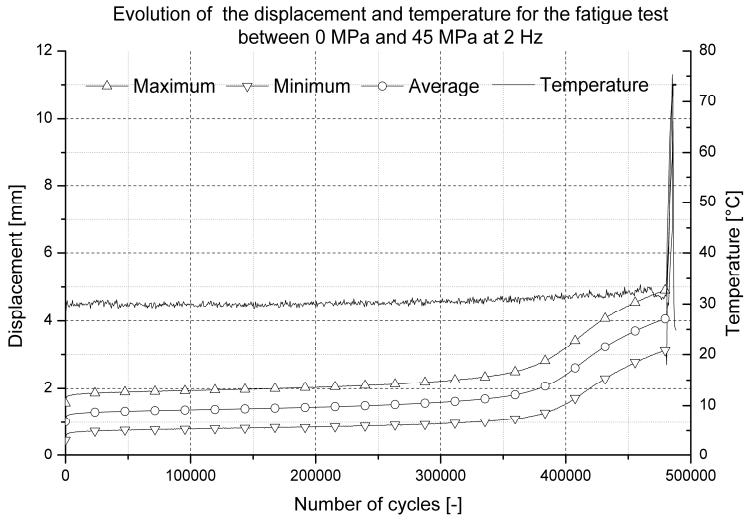

Figure 7-34 Maximum, minimum and mean value of the displacement as a function of the number of cycles for a 0-45 MPa tensile fatigue test at 2 Hz.

Figure 7-35 shows the evolution of the displacement of a fatigue test between 0 MPa and 45 MPa at 1 Hz. The initiation of both the increase in temperature and deformation growth occurs around 280,000 cycles. For the corresponding rail shear test, this happened at 80,000 and 160,000 cycles.

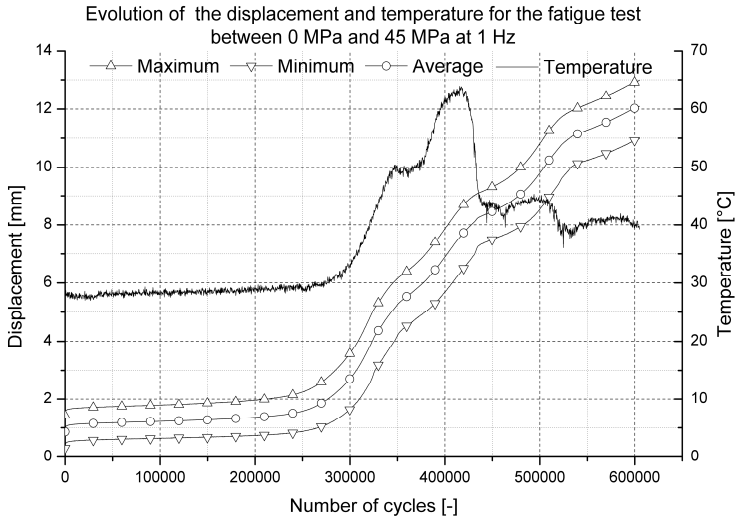

Figure 7-35 Maximum, minimum and mean value of the displacement as a function of the number of cycles for a 0-45 MPa tensile fatigue test at 1 Hz.

For the same experiment, Figure 7-36 shows the evolution of the longitudinal strain. It must be noted that the sudden increase in longitudinal strain only occurs around 400,000 cycles and stops after 510,000 cycles, whereas the temperature and displacement increase (see Figure 7-35) already started at 280,000 cycles and carried on until the test was stopped at 600,000 cycles. This illustrates that the narrowing of the specimen to a 'dog-bone' like shape, as illustrated in Figure 7-33, does not happen in a uniform manner over the entire specimen, but starts near the clamped ends and then gradually grows along the entire specimen length. Since the extensometer is mounted near the centre of the specimen, it only measures the narrowing and the resulting elongation when it occurs between the blades of the extensometer. This growing of the localization of the shear strain could clearly be seen in the experiments.

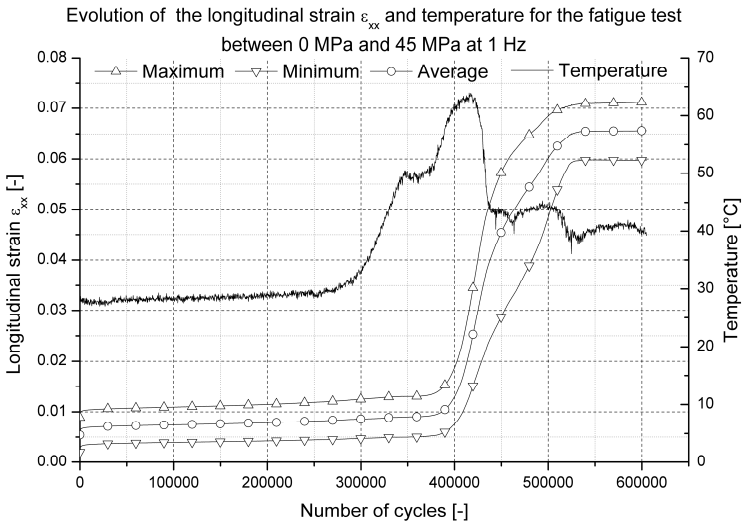

Figure 7-36 Maximum, minimum and mean value of the longitudinal strain as a function of the number of cycles for a 0-45 MPa tensile fatigue test at 1 Hz.

A similar effect occurs with the temperature measurement; the temperature is the highest in the zone of localization, but since the carbon fibres are highly conductive, this effect is not so distinct.

Figure 7-37 shows the results from a 0-50 MPa@1 Hz experiment. It can again be remarked that the behaviour is very similar to the three-rail shear tests. The initiation of the increase in temperature and deformation is situated at 45,000 cycles, which is again higher than the 27,500 cycles found for the corresponding rail shear test. However, an increase in frequency tends to yield an increase in lifetime, which corresponds with the rail shear test.

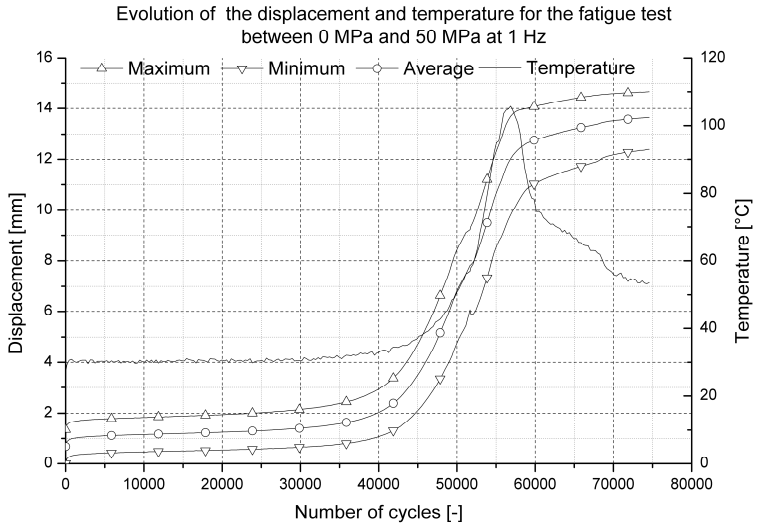

Figure 7-37 Maximum, minimum and mean value of the displacement as a function of the number of cycles for a 0-50 MPa tensile fatigue test at 1 Hz.

Figure 7-38 shows the results from two of the conducted 0-50 MPa@2 Hz experiments. It can be remarked that the behaviour is very similar to the three-rail shear tests. The sudden jump occurs at 70,000 cycles for N2 and at 125,000 cycles for N5, which is higher than the corresponding rail shear tests, where the jump occurred at 45,000 and 50,000 cycles. However, an increase in frequency again tends to yield an increase in lifetime, corresponding with the rail shear test.

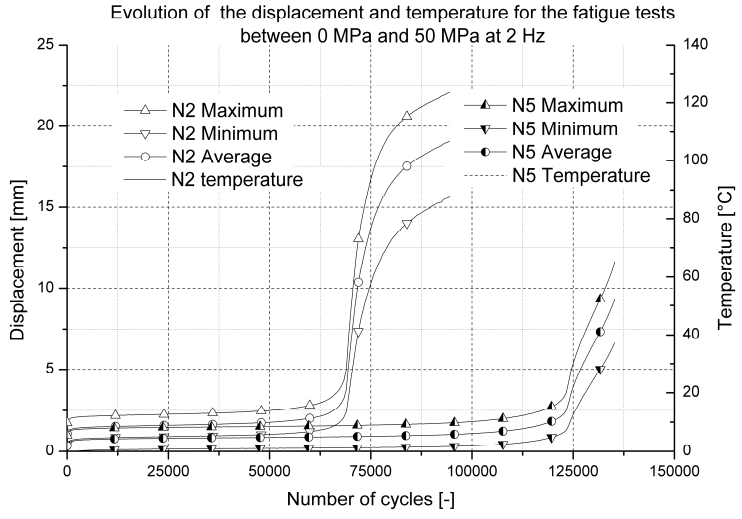

Figure 7-38 Maximum, minimum and mean value of the displacement as a function of the number of cycles for a 0-50 MPa tensile fatigue test at 2 Hz.

Finally, the entire measured evolution of the displacement for the 0-50 MPa@2 Hz from specimen N2 (see Figure 7-38) is given in Figure 7-39. As can be seen, a different behaviour manifests itself after the rise in temperature and decrease in stiffness.

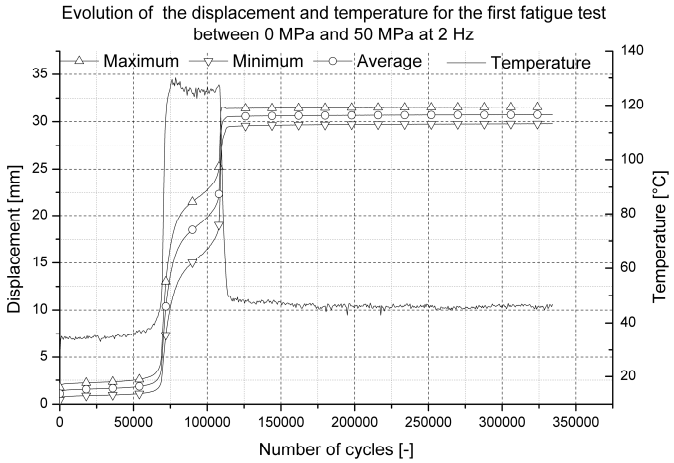

Figure 7-39 Maximum, minimum and mean value of the displacement as a function of the number of cycles for the preliminary 0-50 MPa tensile fatigue test at 2 Hz.

The evolution of both displacement and temperature is very similar to the three rail shear test until the point of the sudden rise in temperature and deformation, which occurs here at about 60,000 cycles. For the three-rail shear test, the specimen failed soon after the rise in temperature, but for the $[(+45°,-45°)]_{4s}$ tensile test, a new regime initiates. After the sudden rise in temperature, which again exceeds the softening temperature of the matrix, the specimen cools down and no further increase in displacement or stiffness degradation manifests itself. This can be explained by re-observing the images of the specimen after the test (Figure 7-33).
This 'dog-bone' like shape arose during the heating of the specimen. Because of the softening of the matrix, the fibres were able to realign considerably with respect to the loading direction. This can be seen in a detailed image of specimen N2 (see Figure 7-40).

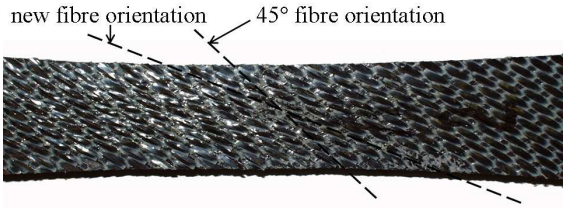

Figure 7-40 Illustration of the change in fibre orientation due to the softening of the matrix.

As such, a new load distribution occurs, with less shear load and more load along the fibres and Equation 7.12 for the shear stress and strain is no longer valid. Therefore, after the sudden rise in temperature and displacement, no more increase in stiffness degradation or deformation occurs, because the specimen is now loaded more along the fibres.

During the increase in temperature, the force-displacement hysteresis loops become much wider, as illustrated in Figure 7-41, indicating that a lot of energy is dissipated, both in damage and of course in the heating of the specimen.

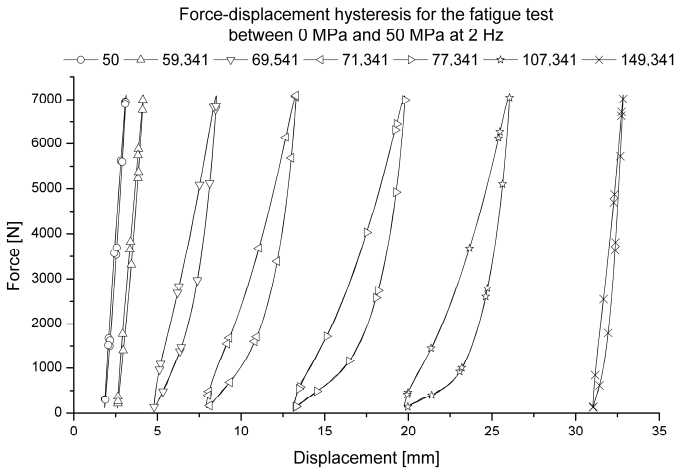

Figure 7-41 Force as a function of the displacement for a few measurements of the tensile fatigue test on specimen N2.

In conclusion, the same remarks as with the three-rail shear test could be made. Increasing the maximum load and decreasing the frequency both decrease the lifetime of the specimen. The point in time where both the sudden temperature increase as the stiffness decrease occur, is situated a little later than in the three-rail shear test, which can been seen in Figure 7-42. Also, after this increase, the specimen does not fail, but a new regime re-instates itself, due to a re-alignment of the fibres along the loading direction, because of the softening of the matrix.

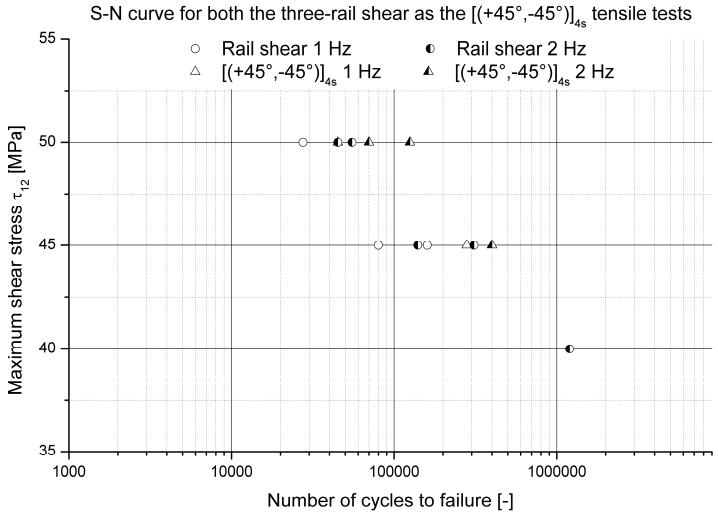

Figure 7-42 S-N curve for all fatigue experiments discussed in this chapter.

7. 7. CREEP LOADING CONDITIONS

7. 7. 1. Three-rail shear setup

Since all fatigue experiments were done with a shear stress between 0 MPa and a maximum value τ_{max} , the specimen is subjected to an average load of half of τ_{max}.
To verify whether the detected deformation during the fatigue loading originates from fatigue damage, a creep test was performed. The specimen was instrumented with two strain gauges and a constant shear stress of 25 MPa was applied. The latter corresponds with the fatigue tests with a maximum shear stress of 50 MPa, which are the highest fatigue loading conditions for this manuscript. The load was applied for about 700,000 seconds, which equals 700,000 cycles at 1 Hz or 1,400,000 cycles at 2 Hz. The evolution of the shear strain γ_{12} is depicted in Figure 7-43. As can be seen, the absolute increase in shear strain is less than 0.0008.

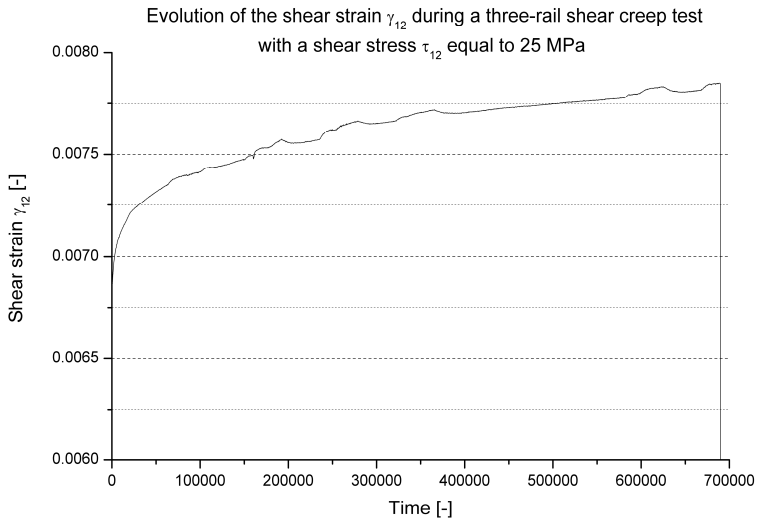

Figure 7-43 Shear strain as a function of time for the three-rail shear creep test.

Since the shear strain could not be registered during the fatigue experiments, only information about the displacement is available. For the latter, an increase of only 0.05 mm over 700,000 seconds occurred, so it may be concluded that the increase in displacement during the fatigue test is mainly caused by fatigue damage, since the measured increase is larger.

7. 7. 2. $[(+45°,-45°)]_{4s}$ experiments

Again to verify if the occurring growth in deformation is due to fatigue damage, a creep test was performed. The same constant shear stress as with the rail shear test was applied, namely 25 MPa, in order to compare the results; the test was stopped after 600,000 seconds, corresponding with 600,000 cycles for a 1 Hz test and 1,200,000 cycles for a 2 Hz test. Figure 7-44 depicts the shear strain during this experiment and again, very limited growth is measured, only 0.0008 absolute increase in shear strain, which corresponds excellently with the rail shear test.

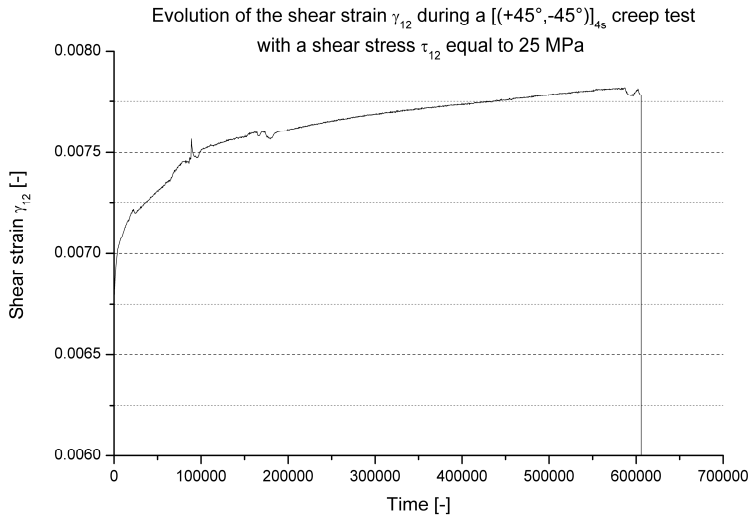

Figure 7-44 Shear strain as a function of time for the $[(+45°,-45°)]_{4s}$ tensile test.

To be able to assess the creep in the fatigue results, where the displacement was illustrated, the evolution of the occurring displacement during the creep test was also registered and an increase of 0.05 mm was measured over the 600,000 seconds, meaning that the occurring deformation during the fatigue is dominated by fatigue damage.

7. 8. CONCLUSIONS

A modified design of the standard three-rail shear setup, as described in the "*ASTM D 4255/D 4255M standard test method for in-plane shear properties of polymer matrix composite materials by the rail shear method*" has been presented. This new design uses friction and geometrical gripping, without the need of drilling holes through the composite specimen. From the performed quasi-static tests, it could be concluded that both sides of the specimen are loaded symmetrically and no buckling occurs.

The material behaviour was investigated by means of quasi-static, hysteresis, fatigue and creep tests.

For the quasi-static tests a highly nonlinear shear stress-strain relationship was found. The stress-strain data were obtained by performing both the $[(+45°,-45°)]_{4s}$ tensile test, as described in the ASTM D3519/D3518M-94 (2001) Standard and the three-rail shear test, as described in the ASTM D 4255/D 4255M Standard. Both types of experiments yielded very similar results and the shear stiffness, derived from these static tests is in good correspondence with the stiffness determined by the dynamic modulus identification method (see chapter 3).

Quasi-static cyclic loadings were applied, to derive the evolution of the permanent deformation and the stiffness degradation, which both lead to the highly nonlinear behaviour. Again, the results from both the three-rail shear test and the $[(+45°,-45°)]_{4s}$ tensile test corresponded very well.

Fatigue tests have been performed to assess the behaviour of the grips and to investigate the material behaviour under fatigue loading conditions. With respect to the grips, excellent results were achieved; the specimen fails under shear loading conditions in the loaded area.

All fatigue experiments were done with a stress ratio equal to 0, meaning that the shear stress varied between 0 MPa and a certain maximum. For both the three-rail shear test and the $[(+45°,-45°)]_{4s}$ tensile test, the same conclusions could be drawn with respect to the frequency and the maximum shear stress: (i) increasing the maximum shear stress decreases fatigue lifetime; (ii) increasing the frequency seems to increase the fatigue lifetime. To explain this frequency effect, a more profound study of the micro-mechanical behaviour of this specific material will be necessary.

The results from both types of tests show good correspondence, although the lifetime was always higher for the $[(+45°,-45°)]_{4s}$ tensile test. The main advantage of the new design of the three-rail shear test over the $[(+45°,-45°)]_{4s}$ tensile test is the absence of free-edge effects. The material under study was not very sensitive to delaminations, but for most fibre-reinforced epoxies, the damage behaviour in the $[(+45°,-45°)]_{4s}$ tensile test will be dominated by delaminations, caused by these free edges.

Due to the absence of these edge effects in the three-rail shear setup, the damage behaviour of these reinforced epoxies will be dominated by in-plane shear, also because there are no longer holes from which the delaminations can grow.

The material behaviour itself can be described in three stages: (i) run-in of the fatigue test, where a certain amount of permanent deformation occurs without an increase in temperature; (ii) a steady-state phase, where there is a gradual increase in permanent deformation, without an increase in temperature and (iii) the end-of-life phase, where there is a sudden increase in temperature, above the softening temperature of the matrix and a sudden growth in permanent deformation. It can of course be expected that the increase in temperature will accelerate the damage occurring under fatigue loading conditions, but it would be very difficult to separate both effects, since keeping the specimen at a constant temperature is more easily said than done.

One remark should be made: for the three-rail shear test, the end-of-life phase ended with failure of the specimen, whereas for the $[(+45°,-45°)]_{4s}$ test, a 'dog-bone' like shape was formed, with re-alignment of the fibres along the loading direction.

Finally, creep tests were performed to verify whether the constant growth of permanent deformation during the 'steady-state' phase in the fatigue life was due to fatigue damage. It could be concluded that the material did creep, but the main damage occurred due to the fatigue loading conditions. Yet again, the creep results corresponded excellently for both types of testing. Over 700,000 seconds, an absolute increase in shear strain of only 0.0008 at a constant load of 25 MPa was measured.

7. 9. REFERENCES

[1] Tarnopol'skii YM, Arnautov AK, Kulakov VL, Methods of determination of shear properties of textile composites. COMPOSITES PART A-APPLIED SCIENCE AND MANUFACTURING 30 (7): 879-885 1999.

[2] Whitney, J.M., Daniel, I.M. and Pipes, R.B. (1984). Experimental mechanics of fiber reinforced composite materials. Chapter 4: Composite characterization. Connecticut, The Society for Experimental Mechanics, pp. 160-202.

[3] Odom E.M., Blackketter D.M. and Suratno B.R., Experimental and analytical investigation of the modified Wyoming shear-test fixture. EXPERIMENTAL MECHANICS 34 (1): 10-15 MAR 1994.

[4] Odegard G. and Kumosa M. Determination of shear strength of unidirectional composite materials with the Iosipescu and 10º off-axis shear tests. COMPOSITES SCIENCE AND TECHNOLOGY 60 (2000) 2917-2943.

[5] Pierron, F and Vautrin A. New ideas on the measurement of the in-plane shear strength of unidirectional composites. JOURNAL OF COMPOSITE MATERIALS 31(9) pp. 889-895, 1997.

[6] Pierron, F and Vautrin A.. The 10º off-axis tensile test: a critical approach. COMPOSITES SCIENCE AND TECHNOLOGY 56 (1996) 483-488.

[7] W. Van Paepegem, I. De Baere and J. Degrieck, Modelling the nonlinear shear stress-strain response of glass fibre-reinforced composites. Part I: Experimental results, COMPOSITES SCIENCE AND TECHNOLOGY 66 (10): 1455-1464 AUG 2006.

[8] Echtermeyer, A.T. (1994). Evaluation of the [±45]s inplane shear test method for composites reinforced by multiaxial fabrics. In : Hogg, P.J., Schulte, K. and Wittich, H. (eds.). ECCM-CTS 2 : Composites testing and standardisation. European Conference on composites testing and standardisation, 13-15 September 1994, Hamburg, Germany, Woodhead Publishing Limited, pp. 305-313.

[9] Shalom S, Harel H, Marom G, Fatigue behaviour of flat filament-wound polyethylene composites. COMPOSITES SCIENCE AND TECHNOLOGY 57 (9-10): 1423-1427 1997.

[10] Thollon, Y. Hochard, C. Herman, M. And Charles J.P. Mechanical behaviour of unbalanced woven fabric composite up to first failure. 12th European Conference on Composite Materials (ECCM 12) 29 August – 2 September 2006, Biarritz, France.

[11] Payan J, Hochard C, Damage modelling of laminated carbon/epoxy composites under static and fatigue loadings. INTERNATIONAL JOURNAL OF FATIGUE 24 (2-4): 299-306 FEB-APR 2002.

[12] Hochard C., Lahellec N. and Bordreuil C. A ply scale non-local fibre rupture criterion for CFRP woven ply laminated structures. COMPOSITE STRUCTURES 80 (3): 321-326 OCT 2007.

[13] Hochard C., Aubourg P.A. and Charles J.P. Modelling of the mechanical behaviour of woven-fabric CFRP laminates up to failure. COMPOSITES SCIENCE AND TECHNOLOGY 61 (2): 221-230 2001.

[14] Thollon, Y. Hochard, C. Herman, M. And Charles JP. Mechanical behaviour of unbalanced woven fabric composite up to first failure. 12th European Conference on Composite Materials (ECCM 12) 29 August – 2 September 2006, Biarritz, France.

[15] Khashaba UA, In-plane shear properties of cross-ply composite laminates with different off-axis angles. COMPOSITE STRUCTURES 65 (2): 167-177 AUG 2004.

[16] Maeda T, Baburaj V, Koga T, Evaluation of in-plane shear modulus of composite laminates using holographic interferometry; OPTICAL ENGINEERING 36 (7): 1942-1946 JUL 1997.

[17] Hussain AK, Adams DF, The Wyoming-modified two-rail shear test fixture for composite materials. JOURNAL OF COMPOSITES TECHNOLOGY & RESEARCH 21 (4): 215-223 OCT 1999.

[18] Hussain AK, Adams DF , Experimental evaluation of the Wyoming-modified two-rail shear test method for composite materials. EXPERIMENTAL MECHANICS 44 (4): 354-364 AUG 2004.

[19] Hussain AK, Adams DF, Analytical evaluation of the two-rail shear test method for composite materials. COMPOSITES SCIENCE AND TECHNOLOGY 64 (2): 221-238 FEB 2004.

[20] Lessard, L.B., Eilers O.P., Shokrieh M.M., Testing of in plane shear properties under fatigue loading. JOURNAL OF REINFORCED PLASTICS AND COMPOSITES 14 (9): 965-987 SEP 1995.

[21] Ferry L, Perreux D, Varchon D, Sicot N, Fatigue behaviour of composite bars subjected to bending and torsion. COMPOSITES SCIENCE AND TECHNOLOGY 59 (4): 575-582 1999.

[22] El-Assal, Ahmed M., Khashaba, U. A., Fatigue analysis of unidirectional GFRP composites under combined bending and torsional loads. COMPOSITE STRUCTURES 79 (4): 599-605 AUG 2007.

[23] Qi, DT, Cheng, GX, Fatigue behavior of filament-wound glass fiber reinforced epoxy composite tension/torsion biaxial tubes under loading. POLYMER COMPOSITES 28 (1): 116-123 FEB 2007.

[24] Kawakami H, Fujii TJ, Morita Y, Fatigue degradation and life prediction of glass fabric polymer composite under tension torsion biaxial loadings. JOURNAL OF REINFORCED PLASTICS AND COMPOSITES 15 (2): 183-195 FEB 1996.

[25] Fujii T and Lin F, Fatigue behaviour of a plain-woven glass fabric laminate under tension-torsion biaxial loading. JOURNAL OF COMPOSITE MATERIALS 29 (5): 573-590 1995.

[26] ASTM D3518-76, standard practice for in-plain shear stress-strain response of unidirectional reinforced plastics, 1982.

[27] De Baere I., Studie van het Afschuifgedrag van Composieten, master thesis 2003-2004, Faculty of Engineering, Ghent University.

[28] Van Paepegem W., Mechanics of Materials, Faculty of Engineering, Ghent University, 2005.

[29] Cho C.D., Holmes J.W., Barber J.R., Estimation of interfacial shear in ceramic composites from frictional heating measurements, JOURNAL OF THE AMERICAN CERAMIC SOCIETY 74 (11): 2802-2808 NOV 1991.

[30] Jacobsen TK, Sorensen BF, Brondsted P, Measurement of uniform and localized heat dissipation induced by cyclic loading, EXPERIMENTAL MECHANICS 38 (4): 289-294 DEC 1998.

[31] Gamstedt EK, Redon O, Brondsted P, Fatigue dissipation and failure in unidirectional and angle-ply glass fibre/carbon fibre hybrid laminates, EXPERIMENTAL TECHNIQUES AND DESIGN IN COMPOSITE MATERIALS 5 KEY ENGINEERING MATERIALS 221-2: 35-47 2002.

Chapter 8

MODELLING THE SHEAR BEHAVIOUR OF THE CARBON FABRIC-REINFORCED PPS

In this chapter, the behaviour of the material under in-plane shear loading conditions is discussed. First, some explanation is given on how to use user-defined material models in ABAQUS™ and then, an existing material model is implemented in the software. After optimisation of the material constants, the quasi-static tests are simulated and a final validation is done using a standard three-point bending test on a $[(+45°,-45°)]_{4s}$ specimen.

8. 1. INTRODUCTION

In this chapter, the mechanical behaviour of the carbon fabric-reinforced polyphenylene sulphide under in-plane shear loading is modelled for the quasi-static loading conditions. During his master thesis, the author has already modelled the nonlinear shear stress-strain behaviour of a glass fibre-reinforced epoxy, by performing $[+45^o/-45^o]_{ns}$ tensile tests and 10^o off-axis tests [1-3]. The carbon fabric-reinforced PPS, which is considered here is of a totally different nature than the one used in the previous study [2, 3]: (i) carbon fabric versus unidirectional glass fibre-reinforcement and (ii) thermoplastic matrix versus thermosetting epoxy.
However, rather than developing an entirely new model, the same model as given in [1, 3] is used to prove that the developed approach may be considered applicable to a wide range of materials. Once the material constants are determined by optimising the model, the quasi-static experiments, both the three-rail shear test and the $[(+45°,-45°)]_{4s}$ tensile test, are simulated to verify whether the model can predict the nonlinear behaviour. Then, an extra validation of the model and the material constants is done using a quasi-static three-point bending test. All data necessary for the material model are derived from the experiments described in chapter 7.

Unfortunately, the in-plane fatigue behaviour was to complicated to be modelled based on the experiments that were already performed. A more extensive experimental program is required in order to obtain sufficient experimental data to model the fatigue behaviour under these loading conditions.

In the next paragraph, a general introduction is given on how to implement user defined material behaviour in the used finite element software ABAQUS™/Standard.

8. 2. IMPLEMENTING USER-DEFINED MATERIAL MODELS IN ABAQUS/STANDARD

As was mentioned in chapter 2, the finite element software ABAQUS™ was chosen for all finite element calculations in this doctoral research. This software also has the ability to implement a user-defined material model, using the UMAT routine, which requires the FORTRAN programming language.
Running a simulation with a material model can be done both from within the ABAQUS™ pre-processor as from the command line with an input file. The only requirement is that the used computer has a FORTRAN compiler. However, the author found it easiest to work from the command line, so this approach is discussed here.
The input file contains al details necessary for the simulation, such as geometries, materials, boundary conditions,… and the easiest way to generate it is by using the pre-processor of ABAQUS/Standard, which is called the CAE module.
A small remark must be made concerning the used version of ABAQUS™. The problem with CAE files is that they cannot be opened by the CAE module of a lower version of ABAQUS™ than the one they are generated with. However, the input file is not bound to a certain version of ABAQUS™. As such, this is another advantage of working from the command prompt.

Given an input file, suited for simulations with built-in material models, some alterations need to be made for the use of a user-defined material model. It should be remarked that these alterations, which are discussed in the following two paragraphs could also be done in the CAE module of ABAQUS™.

As previously mentioned, there is a section in the input file where the used materials for the simulation are defined. Here, it must be indicated that a user material will be used, rather than a built-in material model. For instance, for a built-in linear orthotropic material model, the material section could look like this:

```
** MATERIALS
**
*Material, name=PPS090
*Elastic, type=ENGINEERING CONSTANTS
38900.,13300.,13300., 0.258, 0.258, 0.258, 5130., 5130.
 5130.,
```

For a user-defined material model, this must be altered in:

```
** MATERIALS
**
*Material, name=PPS090
*USER MATERIAL, CONSTANTS=9
38900., 13300., 13300., 0.258, 0.258, 0.258, 5130., 5130.,  5130.,
```

Now, the software will use the UMAT routine with nine constants. It can already be remarked that the material model itself is not implemented in the input file. It is simply indicated that a simulation with this input file will require a user-defined model, but this model is supplied to the software in a separate file.

In the UMAT routine, it is possible to define as many extra variables as deemed necessary by the user; these variables are called solution dependent variables (SDV). However, if the information stored in these variables is needed in the next iteration, for example the damage or permanent deformation, they must be stored in user-defined variables.
Therefore, the DEPVAR command is added in the input file:

```
** MATERIALS
**
*Material, name=PPS090
*USER MATERIAL, CONSTANTS=9
38900.,13300.,13300., 0.258, 0.258, 0.258, 5130., 5130.
 5130.,
*DEPVAR
2,
```

ABAQUS™ now creates extra memory for 2 variables. However, these variables are not yet stored in the output database, which means that the user does not have access to the values stored in these variables during the post-processing. It must be defined in the input file that the values of the SDV are available in the post-processor. To achieve this, some changes must be made to the OUTPUT section of the input file. If no alterations have been made, the output section of the input file will be given by:

```
** OUTPUT REQUESTS
**
*Restart, write, frequency=1
**
** FIELD OUTPUT: F-Output-1
**
*Output, field, variable=PRESELECT
```

This means that ABAQUS™ stores pre-selected variables in the Output DataBase (ODB-file), such as displacement, force, stress, strain… and the results from this output database can be accessed and visualized in the post-processor of ABAQUS™. However, not all this information may be necessary or other information can be needed, as is the case with the user-defined variables. Thus, the output request is changed:

```
** OUTPUT REQUESTS
**
*Restart, write, frequency=1
**
** FIELD OUTPUT: F-Output-1
**
*Output, field
*ELEMENT OUTPUT, POSITION=INTEGRATION POINTS
S,  EE, SDV
*NODE OUTPUT
U, RF
```

The names of the variables are the same as can be selected in the post-processor and some of them are clarified in Table 8-1.

Table 8-1 Clarification of the abbreviations used for the output commands.

S	Stresses
EE	Elastic strains
SDV	Solution Dependent Variable
RF	Reaction Force
U	Displacement

Concerning the output, the following remarks must be made:
If there is more than one time step in the simulation, then the output section of each step must be altered in the same way as mentioned above. It is, however, not necessary that the same information is stored in each step. This could be done to save disk space.
The displacement U needs to be stored if one wants to show the deformed shape in the post-processor.
The SDV are always stored for the calculation. By adding SDV in the element output, the SDV are also stored in the ODB, so that they can be visualized.

Now, the input file is ready. To start a job with a user defined material, the following command must be entered at the command prompt:

ABAQUS job=<name of the input file> user=<name material model>.f analysis interactive

The option 'analysis interactive' can be omitted. If so, then control is immediately returned to the user. If the option is used, ABAQUS™ prompts its current task to screen, which makes follow-up a lot easier.
As previously mentioned, at this point, the material model is supplied to ABAQUS™ in a separate file. This file is written in the FORTRAN language and the general approach can be summarized as follows. Within a general programming frame, the newly updated strain state in the material, which consists of the total strains and the total strain increments, is supplied to the routine for the current time increment. The user uses these strains, or strain-increments, to calculate the new stresses or stress increments for this time increment (implicit routine) by means of the material model. The updated values of the stress (not the stress increments, they can only be used as an intermediate step to calculate the total stresses) are then exported and this is repeated until a convergent solution is obtained for this time increment. Then, the entire procedure is repeated for the next time increment.

8. 3. MODELLING THE QUASI-STATIC EXPERIMENTS

8. 3. 1. The material model

As mentioned in the introduction, the same model as used in the author's master thesis [1-3] will be used in this manuscript, to prove the wide applicability of the model. The shear stress-strain relationship is given by:

$$\begin{aligned} \tau_{12} &= G_{12}^{0}.(1-D_{12}).(\gamma^{total}-\gamma^{elast}) \\ D_{12} &= 1-\frac{G_{12}^{*}}{G_{12}^{0}} \end{aligned} \tag{8.1}$$

In this equation:

- G_{12}^{0} is the initial shear stiffness
- G_{12}^{*} is the shear stiffness of the damaged material
- D_{12} is the damage parameter, which indicates the stiffness degradation
- γ_{12}^{total} is the total shear strain, given by the sum of the elastic and the permanent shear strain
- γ_{12}^{perm} is the permanent shear strain

Modelling the shear behaviour using stiffness degradation and permanent shear strains was also done in [4-6]. Figure 8-1 shows how the values of G_{12}^{*} and γ_{12}^{perm} can be derived from the experimental data. A similar approach was used in [7-9].

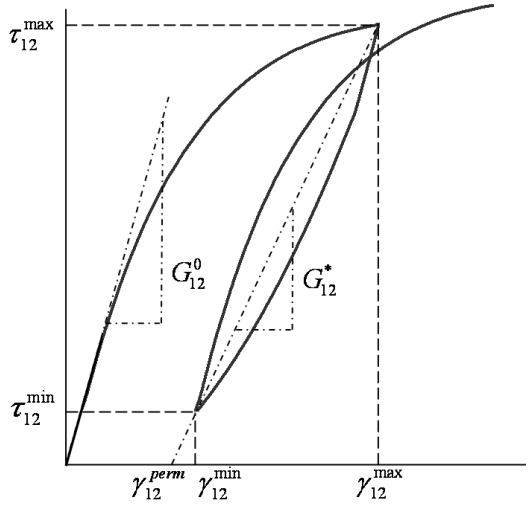

Figure 8-1 Definition of the shear modulus G_{12}^{*} and the permanent shear strain γ_{12}^{perm}.

Using these definitions, γ_{12}^{perm} and D_{12} (Figure 8-3) show the following evolutions (Figure 8-2 and Figure 8-3 respectively) for the cyclic rail shear experiments, described in chapter 7.

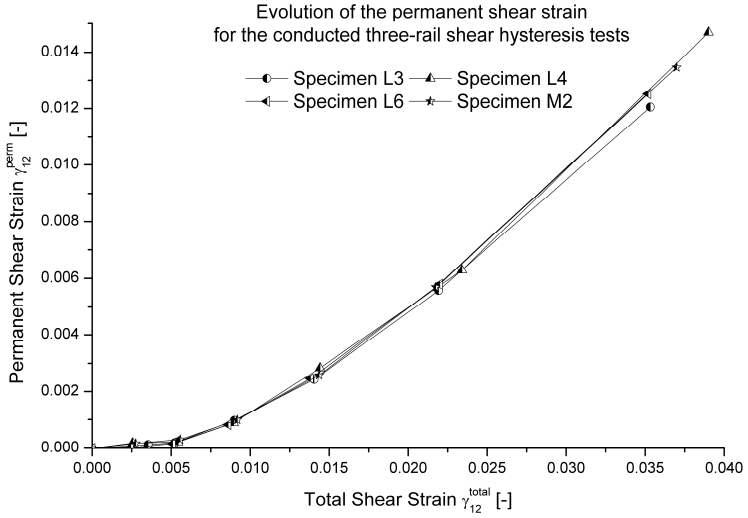

Figure 8-2 Evolution of the permanent shear strain during the three-rail shear hysteresis experiment.

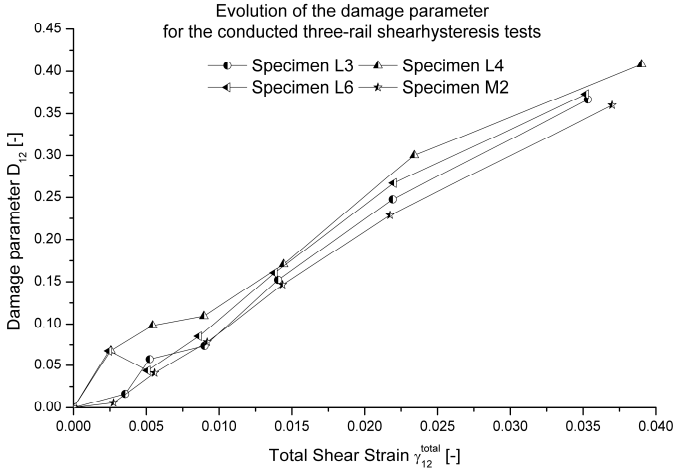

Figure 8-3 Evolution of the damage parameter during the three-rail shear hysteresis experiment.

It should be noted that there is a significant scatter on the damage parameter D_{12} for low total shear strains. This is due to the fact that the strains are very low and therefore, the determination of the slope of the hysteresis loop, as described in [2], is a lot more sensitive to noise and scatter on the strain measurement.
These data will be used for determining the material constants in paragraph 8. 3. 2.
For the $[(+45°,-45°)]_{4s}$ tensile tests, the following evolutions for permanent deformation (Figure 8-4) and stiffness degradation (Figure 8-5) are obtained from the cyclic experiments described in chapter 7.

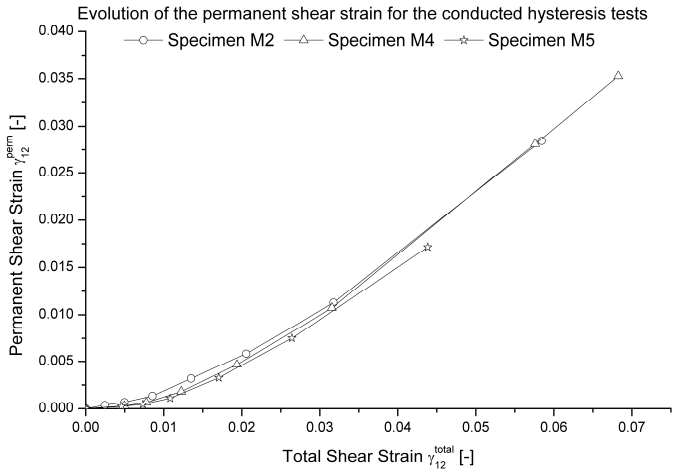

Figure 8-4 Evolution of the permanent shear strain during the tensile hysteresis experiment.

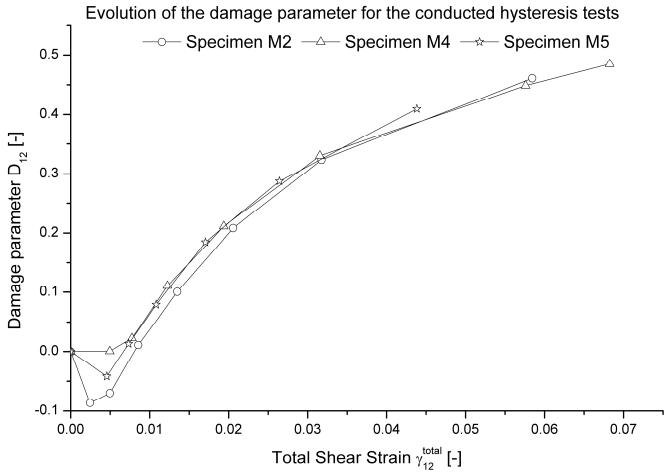

Figure 8-5 Evolution of the damage parameter during the tensile hysteresis experiment.

The results are very reproducible for both damage parameters. Again, there is some scatter on the damage parameter D_{12} for low values of the total shear strain, but as mentioned before, this is due to the fact that the strains are very low and therefore, the determination of the slope of the hysteresis loop, as described in [2] is more sensitive to scatter and noise on the measured strains. It should be noted that these evolutions show very good correspondence with the damage parameters obtained from the three-rail shear tests.

These data will also be used for determining the material constants in the following section.

8. 3. 2. Implementing the material model

Since D_{12} and γ_{12}^{perm} show a very good correspondence with respect to the shape of the evolutions found in the author's master thesis, the same material model will be considered here. For this model, the evolution of D_{12} and γ_{12}^{perm} are given by the following equations:

$$\begin{aligned} \frac{d\gamma_{12}^{perm}}{d\gamma_{12}^{total}} &= C_1.\left|\gamma_{12}^{total}\right|.\exp\left(C_2.\left|\gamma_{12}^{perm}\right|\right) \\ \frac{dD_{12}}{d\gamma_{12}^{elast}} &= C_3.\exp\left(C_4.D_{12}\right) \end{aligned} \tag{8.2}$$

Where C_1 till C_4 are material constants and still need to be determined.

The permanent shear strain is assumed to depend on the total shear strain, and the increase shows an exponential behaviour. The factor $\left|\gamma_{12}^{total}\right|$ is added so that the increase in γ_{12}^{perm} is lower for low values of the total shear strain, but higher for higher values.

The damage parameter D_{12} is assumed to depend on the elastic part of the strain and the increase also shows an exponential behaviour. Since the growth depends on the elastic part of the strain, first the permanent deformation must be determined, after which D_{12} can be calculated.
More details about the derivation of the model can be found in [1, 3].

In order to implement the material model in UMAT, it must first be written using finite differences. This yields for Equation 8.2, with $\gamma_{12}^{elast} = \gamma_{12}^{total} - \gamma_{12}^{perm}$:

$$\begin{aligned}
\gamma_{12}^{perm,new} &= \gamma_{12}^{perm,old} \\
&\quad + C_1.\left|\gamma_{12}^{total,new}\right|.\exp\left(C_2.\left|\gamma_{12}^{perm,old}\right|\right).\left(\gamma_{12}^{total,new} - \gamma_{12}^{total,old}\right) \\
D_{12}^{new} &= D_{12}^{old} \\
&\quad + C_3.\exp\left(C_4.D_{12}^{old}\right).\left[\left(\left|\gamma_{12}^{total,new}\right| - \left|\gamma_{12}^{perm,new}\right|\right)\right. \\
&\quad \left. -\left(\left|\gamma_{12}^{total,old}\right| - \left|\gamma_{12}^{perm,old}\right|\right)\right]
\end{aligned} \tag{8.3}$$

Where the superscript ‘old’ refers to the values obtained from the previous time step and the superscript ‘new’ refers to the value necessary for the current time step.
Next, Equation 8.1 can be implemented. However, after some test runs with UMAT, it became clear that a converging solution could only be found if strain increments are used rather than the total strains, meaning that the total stress is calculated using stress increments. As such, Equation 8.1 must be rewritten with finite differences. This yields:

$$\begin{aligned}
\tau_{12}^{new} &= G_{12}^0.(1 - D_{12}^{new}).(\gamma_{12}^{total,new} - \gamma_{12}^{perm,new}) \\
\tau_{12}^{old} &= G_{12}^0.(1 - D_{12}^{old}).(\gamma_{12}^{total,old} - \gamma_{12}^{perm,old})
\end{aligned} \tag{8.4}$$

Hence, the following equation is derived for the stress:

$$\begin{aligned}
\tau_{12}^{new} &= \tau_{12}^{old} \\
&\quad + G_{12}^0.(1 - D_{12}^{new}).\left[(\gamma_{12}^{total,new} - \gamma_{12}^{total,old})\right. \\
&\quad \left. -(\gamma_{12}^{perm,new} - \gamma_{12}^{perm,old})\right] \\
&\quad - G_{12}^0.(D_{12}^{new} - D_{12}^{old}).(\gamma_{12}^{total,old} - \gamma_{12}^{perm,old})
\end{aligned} \tag{8.5}$$

The sum in Equation 8.5 consists of two terms: the first is the expected one, giving a stress increment using the increment in elastic strain. The second term is the result of the use of stress increments and must not be forgotten.
Next, the modelling in ABAQUS of the two test geometries is discussed.

8. 3. 3. Modelling the three-rail shear test

For these simulations, only the loaded part of the specimen was modelled and because of symmetry, only half of the specimen was drawn, Figure 8-6 depicts the used mesh and boundary conditions.

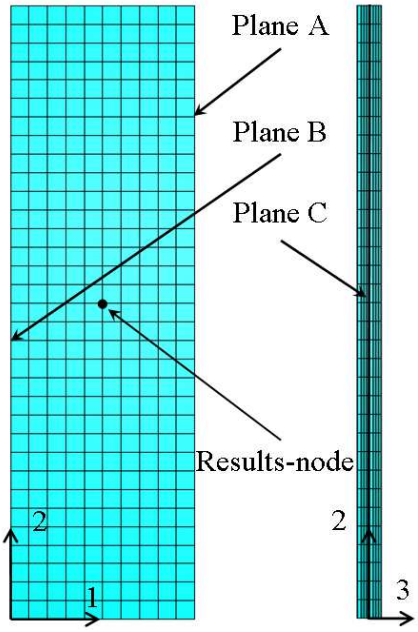

Figure 8-6 Used mesh for the finite element simulations of the three-rail shear test.

The specimen was meshed using a 3D quadratic brick element with reduced integration; the size of the mesh was 3 mm and eight elements through the thickness were used. An extra simulation was performed with a mesh size of 1 mm, also to assess the influence of the mesh size on the output of the material model. The width of the modelled specimen was 30 mm and the height 100 mm, as was the case in the experiments. The following boundary conditions were applied:

- Plane A, the right side of the loaded zone, was fixed along the 1- and 2-axis.
- Plane B, the left side of the loaded zone, was fixed along the 1-axis and given a displacement of 3 mm along the 2-axis. This value corresponds with the value at which point the strain gauges in the experiments de-bonded or saturated.
- Plane C, the central plane of the loaded zone, was fixed along the 3-axis.

Since it is a 3D analysis, there are no rotational degrees of freedom. Because of the large deformations, a geometrically nonlinear simulation was performed.

8. 3. 4. Modelling the $[(+45°,-45°)]_{4s}$ test

For these simulations, only the loaded part of the specimen was modelled, resulting in a rectangular specimen of 150 mm by 30 mm. Symmetry was not used, since this would yield images of stress distributions which are a little more difficult to interpret than if the entire specimen is modelled. Figure 8-7 depicts the used mesh and boundary conditions.

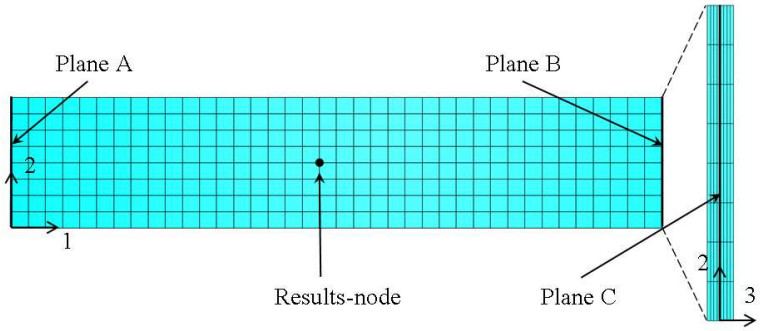

Figure 8-7 Used mesh for the finite element simulations of the $[(+45°,-45°)]_{4s}$ tensile test.

The specimen was meshed using a 3D quadratic brick element with reduced integration; the size of the mesh was 4 mm and eight elements through the thickness were used. An extra simulation was performed with a mesh size of 2 mm, to assess whether the mesh size has significant influence on the model. The following boundary conditions were applied:

- Plane A, the left side of the loaded zone, was fixed along the 1- and 2-axis, simulating the rigid grip.
- Plane B, the right side of the loaded zone, was fixed along the 1-axis and given a displacement of 10 mm along the 2-axis. This value corresponds with the value at which point the strain gauges in the experiments de-bonded or saturated.
- Plane C, the central plane of the loaded zone, was fixed along the 3-axis.

Since it is a 3D analysis, there are no rotational degrees of freedom. Because of the large deformations, a geometrically nonlinear simulation was performed.

8. 3. 5. Discussion of the simulations

Of course, first the material constants C_1 till C_4 in Equation 8.2 need to be determined. These values have been determined by the combined optimisation of the evolutions of the τ_{12}-γ_{12} curve, γ_{12}^{perm} and D_{12} on the experimental results, given in Figure 8-2 till Figure 8-5.

This yielded the following combination of material constants:

$$C_1 = 29 \qquad C_2 = -35 \qquad C_3 = 16 \qquad C_4 = -0.1 \tag{8.6}$$

For both the three-rail shear and the $[(+45°,-45°)]_{4s}$ tensile test simulation, the evolution of the shear stress, shear strain, permanent shear strain γ_{12}^{perm} and damage parameter D_{12} was plotted for a node in the centre of the specimen (Results-node in Figure 8-6 and Figure 8-7), so that the stress concentrations near the clamps did not have any influence. These results are given in Figure 8-8, Figure 8-9 and Figure 8-10 respectively.

It should be remarked that there is an excellent correspondence for all three evolutions and that refining the mesh, for both the three-rail shear as the $[(+45°,-45°)]_{4s}$ simulations does not have a significant effect.

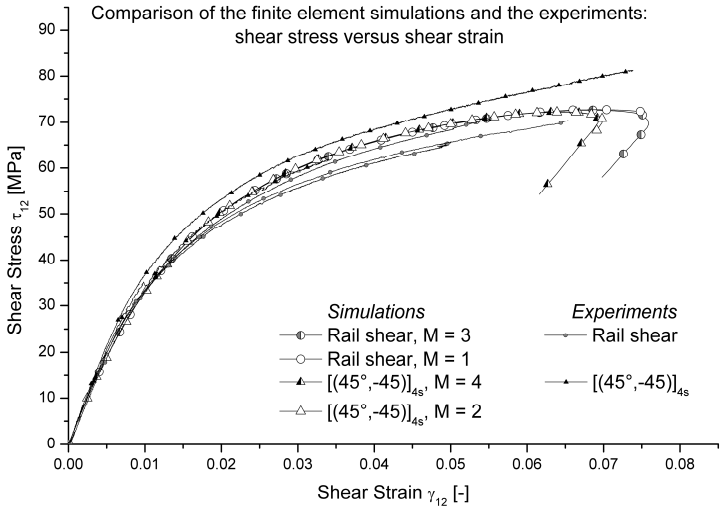

Figure 8-8 Evolution of the shear stress as a function of the shear strain for both the simulations and the experiments.

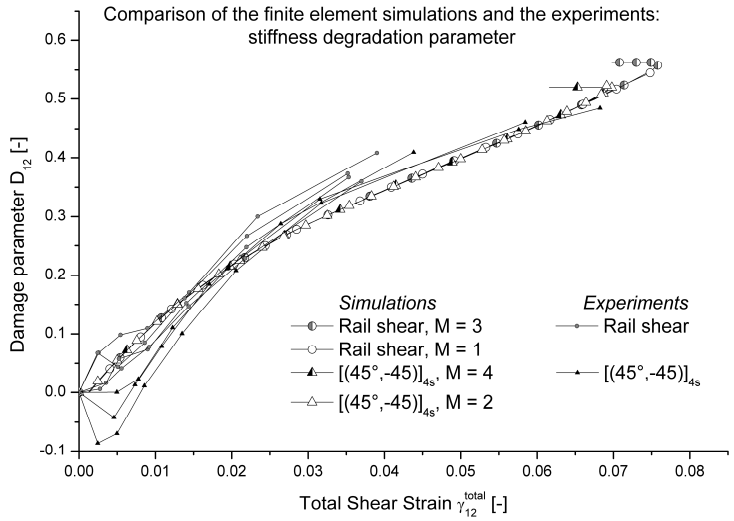

Figure 8-9 Evolution of the permanent shear strain for both the simulations and the experiments.

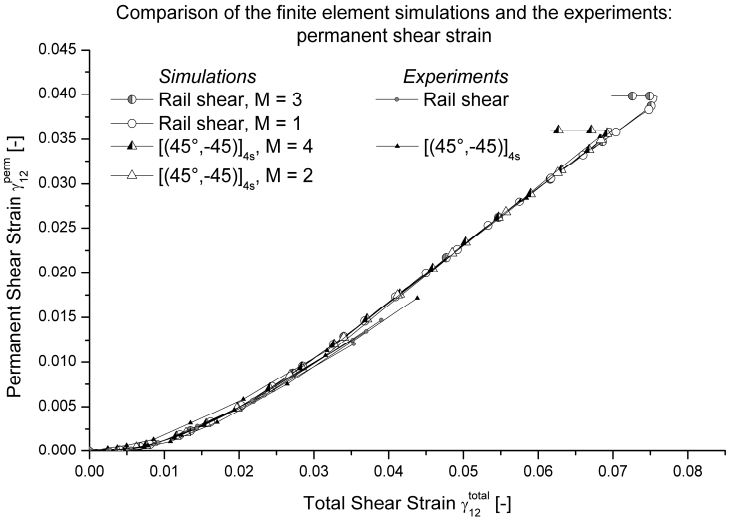

Figure 8-10 Evolution of the damage parameter for both the simulations and the experiments.

In the shear stress-strain evolution, depicted in Figure 8-8, it can be seen that after a certain strain level is reached, the total strain tends to decrease, as well as the corresponding shear stress. The corresponding damage and permanent shear strain remain constant during this decrease. This happens for both types of simulations and is the result of a stress relief in the centre of the specimen, due to localization of the total shear strain elsewhere in the specimen.

This can be easily shown in the $[(+45°,-45°)]_{4s}$ simulations. Figure 8-11 depicts the total shear strain at three well chosen time-steps. Time-step 45 represents the end of the increase in shear strain, Time step 58 is the last time-step available and time-step 51 is chosen for an intermediate distribution plot. The deformation is scaled by 2.0 to visualise the reason more clearly.

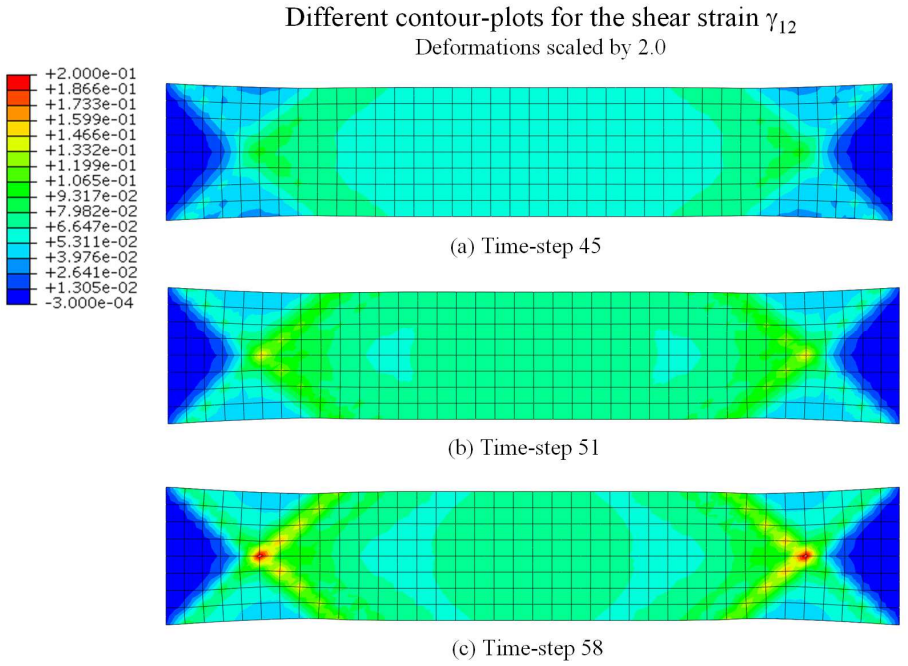

Figure 8-11 Illustration of the decrease in the shear strain in the centre of the specimen.

From these different stages in time, it can clearly be seen that the fast narrowing of the specimen near the clamped ends results in a high increase in shear strain. Since the simulation is done displacement-controlled, corresponding with the experiment, the shear strain in the centre of the specimen is allowed to relax. Given the fact that the permanent shear strain is not allowed to decrease, this renders a decrease in elastic shear strain and as a result, a decrease in shear stress. Figure 8-12 shows this localization in three stages as it could be seen in the experiment.

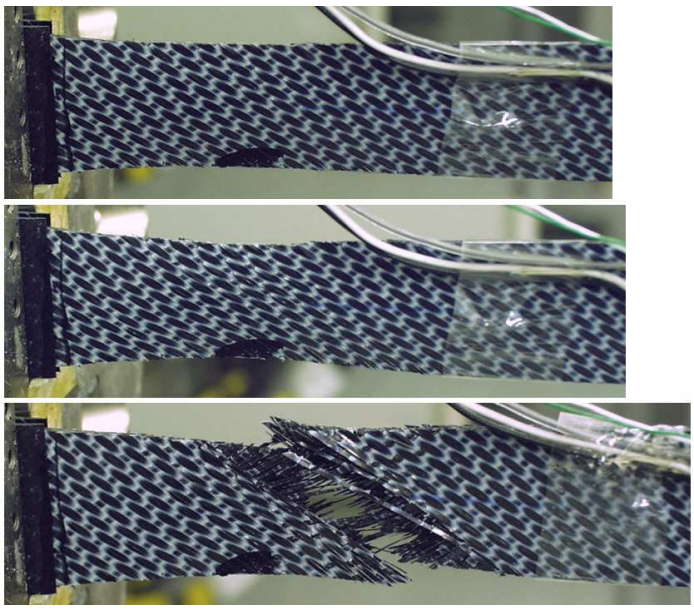

Figure 8-12 Illustration of the experimental localization of the total shear strain.

This decrease in shear stress and strain was not seen in the experiments, but the localization of the total shear strain occurred after the strain gauge saturated and the strain measurement was stopped, meaning that the material model predicts this effect too early.

Finally, in Figure 8-13 and Figure 8-14, the distributions of the shear stress and the damage model parameters are given for the time step at which maximum stress in the central area is reached. The shear stress distribution is very uniform, except near the clamped ends, where a cross-like shape can be distinguished. However, this uniform distribution is still the main reason why the $[(+45°,-45°)]_{4s}$ is chosen to characterise the shear behaviour of a composite. The permanent shear strain is also relatively uniform, although higher values are reached where the specimen is most likely to narrow. The damage parameter D_{12} also indicates where failure is most likely to occur.

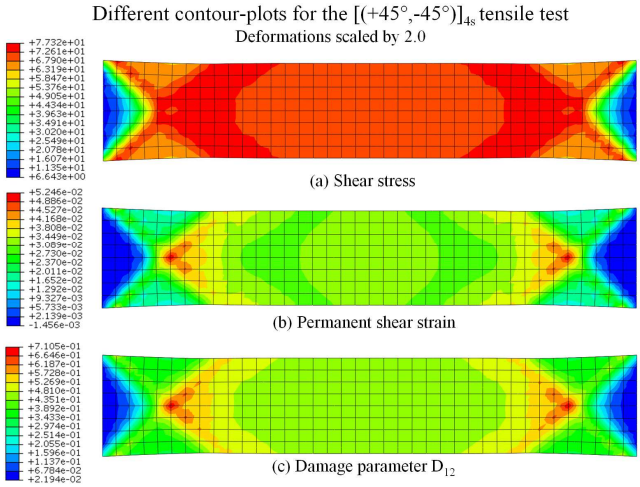

Figure 8-13 Distribution of the (a) shear stress, (b) permanent shear strain and (c) damage parameter D_{12} for the $[(+45°,-45°)]_{4s}$ simulation.

For the three-rail shear test, also a very uniform shear stress distribution can be seen. The distribution of both damage and permanent deformation clearly indicate where failure will start, namely in the vicinity of the clamps. This was also derived by Lessard et al. [10]. A possibility for future research could be to investigate whether the use of notches, as was done in [10] would have the same effects on a fabric-reinforced composite.

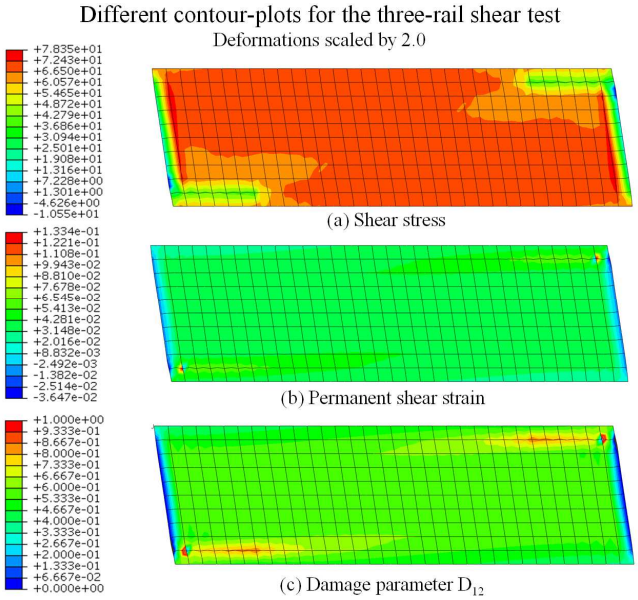

Figure 8-14 Distribution of the (a) shear stress, (b) permanent shear strain and (c) damage parameter D_{12} for the three-rail shear simulation.

Finally, in Figure 8-15, the calculated relation between shear strain and displacement is depicted for the three-rail shear test, as verification for the theoretical deduction given in chapter 7. It can be seen that there is a slight difference, possibly because in the theoretical deduction, where a factor of 0.033 was derived, small displacements were assumed, whereas this simulation has taken geometrical nonlinearities into account.
To assess the effect of the boundary condition on this factor, a second simulation was performed, using the same boundary conditions as in [10], which mean that for plane A, only zero displacement along the 2-axis was prescribed (BC2). This however does not seem to have any influence on the shear strain-displacement relationship.

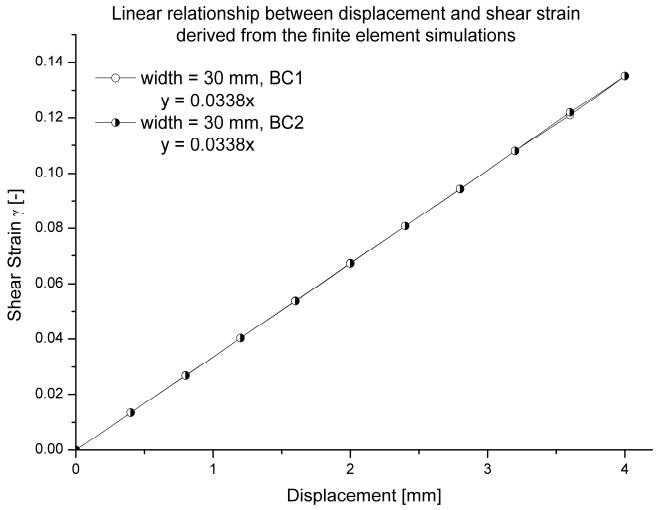

Figure 8-15 Numerical evolution of the shear strain as function of the displacement.

8. 3. 6. The bending test for final validation

Although the model has already been tested using two different types of experiments, namely the $[(+45°,-45°)]_{ns}$ tensile test and the three-rail shear test, a final validation is considered by applying the model to a quasi-static three-point bending test of a $[(+45°,-45°)]_{4s}$ specimen. In this test, also a highly nonlinear behaviour was present, as can be seen in the experimentally measured force-displacement relationship, depicted in Figure 8-16. The test was displacement-controlled using a speed of 2 mm/min; after a maximum midspan displacement of 25 mm for a span of 120 mm, the specimen was unloaded. Figure 8-17 illustrates the bending profile before loading, at maximum midspan displacement and after unloading.

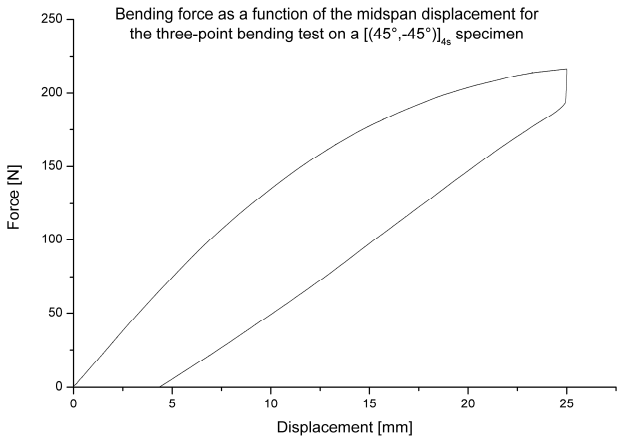

Figure 8-16 Force-displacement curve for the bending test on a $[(+45°,-45°)]_{4s}$ specimen.

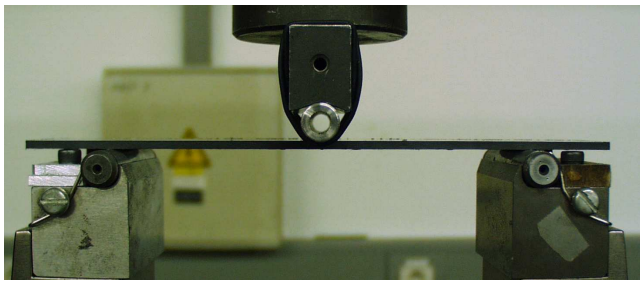

(a) At 0 mm displacement.

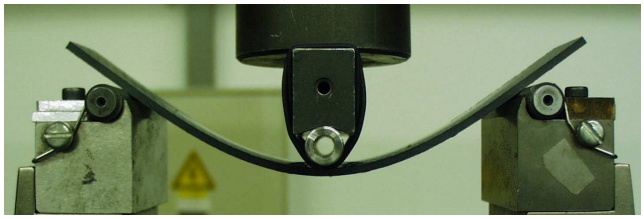

(b) At maximum displacement, 25 mm.

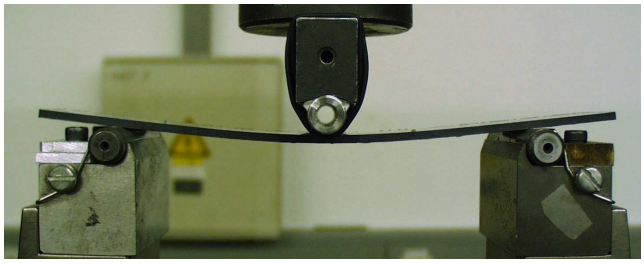

(c) After unloading, 4.8 mm displacement.

Figure 8-17 Experimental bending profiles at three stages of the bending test: before the start, at maximum displacement and after unloading.

The modelling of the standard three-point bending test in ABAQUS is already extensively documented in chapter 6, so only a brief summary is given here.
The used mesh is illustrated in Figure 8-18, the general mesh size of the specimen is 1 mm and symmetry was used. For the supporting rolls and the contact areas of the specimen, the mesh size was refined to 0.4 mm, to ensure convergence. The specimen is meshed with quadratic brick elements with reduced integration, C3D20R whereas the supports are meshed with linear brick elements with reduced integration, C3D8R. Three time steps are implemented, one for the loading, one for the change in loading direction, causing the change in frictional force as explained in chapter 6 and one for the unloading.

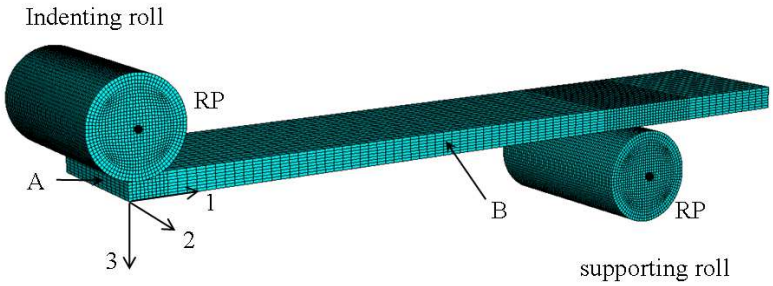

Figure 8-18 Used mesh and boundary conditions for the three-point bending simulation.

To model symmetry, the following boundary conditions are applied:
on plane A: $U_1 = 0$ and on plane B: $U_2 = 0$.
Since 3D elements do not have rotational degrees of freedom, no rotational boundary conditions are used. The reference point of the supporting roll is completely fixed and for the indenting roll, the movement along the 1-axis and 2-axis is fixed and a downward displacement of 25 mm is imposed on the reference point for the first time step followed by an upward displacement of 0.1 mm for the second time step and finally an upward displacement of the remaining 24.9 mm. Because of the large deformations, geometrical nonlinearity was always taken into account. Three simulations were done, one only taking the geometrical nonlinearity into account, one also considering the material nonlinearity for both tension and compression and one considering the material nonlinearity only for the elements loaded in tension. The last was done to see if better result can be achieved this way, since the material model was developed from tensile data.
The simulated force-displacement curves, as well as the experimental curve are shown in Figure 8-19. It can be noted that if only the geometrical nonlinearity is taken into account, the force is highly overestimated for a given displacement, which emphasises the need of a material model. It can be noted that when the material model is implemented, whether only used in tension or in both tension and compression, the bending stiffness is slightly underestimated.

This can be explained by the fact that the increase of D_{12} for the model starts slightly earlier than in the experiments (see Figure 8-9). When using the model only on the elements in tension, the force is slightly overestimated at maximum displacement, but residual midspan displacement after unloading is much lower than the experimental one. If the model is used for all elements, the bending force is slightly underestimated during the entire experiment, but the residual midspan displacement after unloading corresponds very well.
It should be remarked that the waviness of the unloading curves for both simulations with the nonlinear material model, is due to the combination of the use of a user defined model and the contact conditions on the supports. Refining the mesh or the time steps did not improve this behaviour.

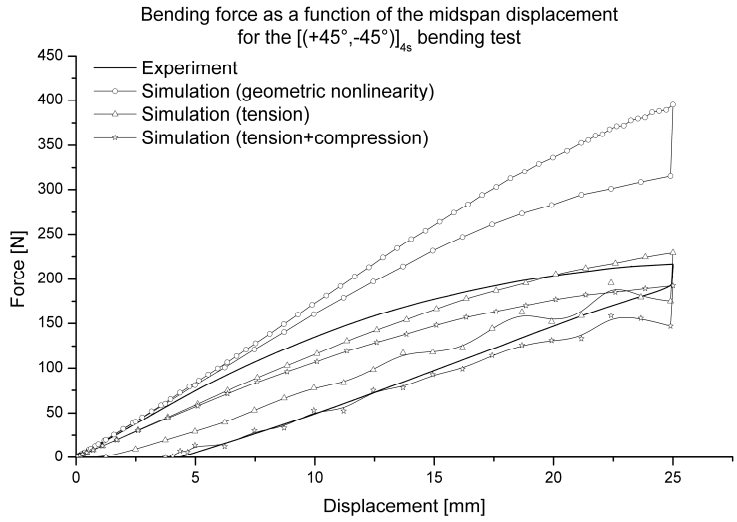

Figure 8-19 Experimental and simulated load-displacement curve for the three-point bending test.

While performing the experiment, it was noted that for larger midspan displacements, the specimen tended to have a saddle-like shape (see Figure 8-20 (a) on the left). If the model is accurate, then the simulations with the material model should also predict this shape. In order to visualize this, the simulation which implements the material model for all elements is considered. The results for a midspan displacement of 25 mm and after unloading are shown in Figure 8-20 (a) and (b) on the right. As can be seen, the finite element model predicts the deformation well. For the finite element image after unloading, the bottom roll has been removed to have a better visualization.

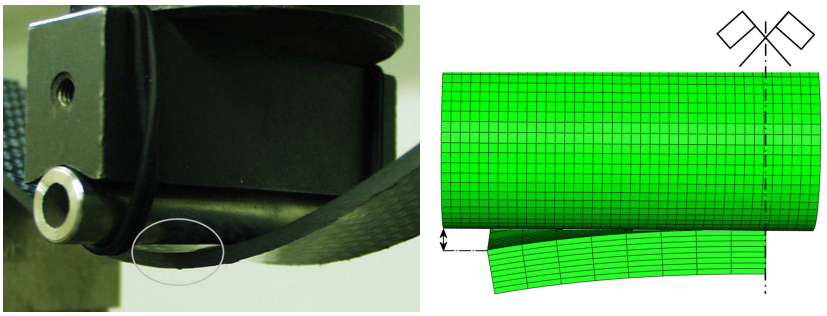

(a) Maximum midspan displacement.

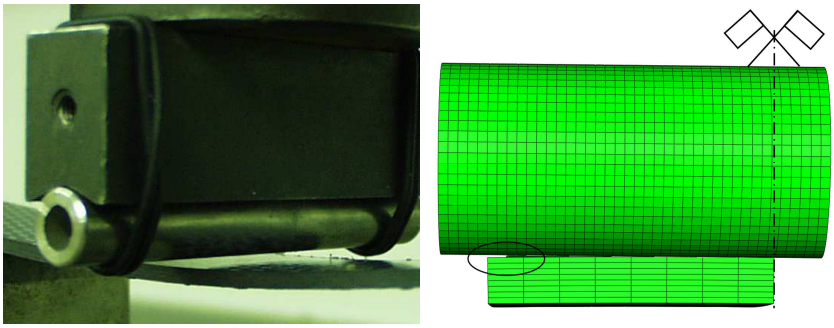

(b) After unloading.

Figure 8-20 Illustration of the saddle-like shape for experiment and finite element simulation, at maximum midspan displacement and after unloading.

It should be remarked that this effect is not entirely due to the use of the material model, but it is also a result of the $[(+45°,-45°)]_{4s}$ stacking sequence. The simulation taking only the geometrical nonlinearity into account also showed a saddle-like shape at maximum displacement, but the amount of cross-section bending was little less than for the simulation with the material model implemented for all elements. However, at the point of zero force, the geometric nonlinear simulation showed a flat specimen, whereas the simulation with the material model for tension and compression showed a slight curvature, as illustrated above (Figure 8-20 (b) on the right). The main reason is probably the large Poisson's ratio in the x,y-coordinate system ν_{xy}. The top of the specimen is loaded in compression, resulting in positive transverse strains, whereas the bottom of the specimen is loaded in tension, resulting in negative transverse strain. As a result, the cross-section will have a bent trapezoid shape, as could be seen in the images above.

Finally, Figure 8-21 shows the distribution of the damage parameter D_{12} and the permanent shear strain γ_{12}^{perm} at maximum midspan displacement. For a better visualization, ABAQUS™ offers the possibility of mirroring an image along different planes, so that when boundary conditions of symmetry are used, as is the case here, the entire specimen, with the symmetry taken into account, can be shown. This option has been used here and for a better vision on the distributions, the indenting roll has been removed.

As could be expected, both parameters have their highest value in the centre of the specimen, where fracture is most likely to occur in the three-point bending test.

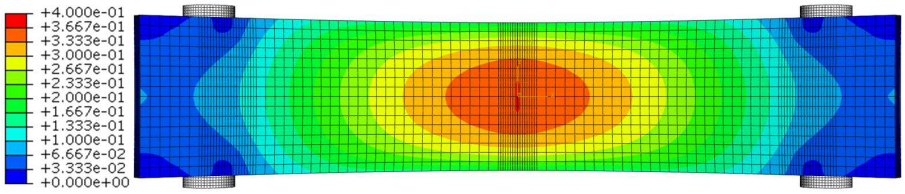

(a) Distribution of the damage parameter D_{12}

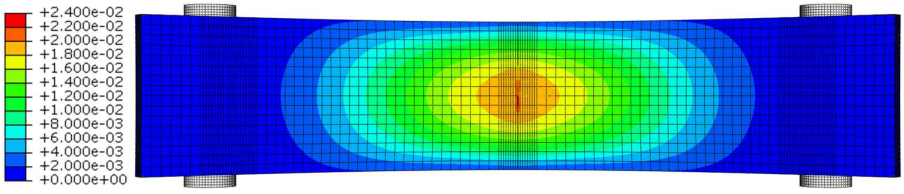

(b) Distribution of the permanent shear strain γ_{12}^{perm}

Figure 8-21 Contour plots of the damage parameter D_{12} and the permanent shear strain γ_{12}^{perm} at maximum midspan displacement.

8. 3. 7. Conclusions

Using the stress-strain data, discussed in chapter 7, the nonlinear shear stress-strain behaviour was modelled using a previously derived material model, which has two damage parameters: (i) D_{12} which represents the shear stiffness degradation and (ii) the permanent shear strain γ_{12}^{perm}, which represents the permanent shear deformation. This material model was then implemented in the finite element software ABAQUS/Standard with the UMAT routine and both test setups were modelled. The four material constants of the material model were optimised based on the experimentally derived evolutions of shear stress-strain, D_{12} and γ_{12}^{perm}. Afterwards, the results from the simulations were compared with the experimental curves and a very good agreement was achieved.

For a final validation of the material model, a three-point bending test was performed and simulated. Three simulations were performed, one taking only the geometrical nonlinearity into account, one which implements the material model for the elements loaded in tension and one which uses the model for all elements. Using a material model clearly increases the correspondence between the experiment and simulation, and although the bending force is slightly underestimated during the entire experiment, the simulation with the material model implemented for all elements provided the best correspondence, especially concerning the residual midspan displacement after unloading.

8. 4. REFERENCES

[1] De Baere I., Studie van het Afschuifgedrag van Composieten, master thesis 2003-2004, Faculty of Engineering, Ghent University.

[2] W. Van Paepegem, I. De Baere and J. Degrieck, Modelling the nonlinear shear stress-strain response of glass fibre-reinforced composites. Part I: Experimental results, COMPOSITES SCIENCE AND TECHNOLOGY 66 (10): 1455-1464 AUG 2006.

[3] Van Paepegem W., De Baere I. and Degrieck J., Modelling the nonlinear shear stress-strain response of glass fibre-reinforced composites. Part II: Model development and finite element simulations, COMPOSITES SCIENCE AND TECHNOLOGY 66 (10): 1465-1478 AUG 2006.

[4] Hochard C., Lahellec N. and Bordreuil C. A ply scale non-local fibre rupture criterion for CFRP woven ply laminated structures. COMPOSITE STRUCTURES 80 (3): 321-326 OCT 2007.

[5] Hochard C., Aubourg P.A. and Charles J.P. Modelling of the mechanical behaviour of woven-fabric CFRP laminates up to failure. COMPOSITES SCIENCE AND TECHNOLOGY 61 (2): 221-230 2001.

[6] Thollon, Y. Hochard, C. Herman, M. And Charles JP. Mechanical behaviour of unbalanced woven fabric composite up to first failure. 12th European Conference on Composite Materials (ECCM 12) 29 August – 2 September 2006, Biarritz, France.

[7] Lafarie-Frenot, M.C. and Touchard, F. Comparative in-plane shear behaviour of long-carbon-fibre composites with thermoset of thermoplastic matrix. COMPOSITES SCIENCE AND TECHNOLOGY 52 (1994) 417-425.

[8] Ladeveze, P. and Le Dantec, E. Damage modelling of the elementary ply for laminated composites. COMPOSITES SCIENCE AND TECHNOLOGY 43 (1992) 257-267.

[9] Echtermeyer, A.T. (1994). Evaluation of the [±45]s in-plane shear test method for composites reinforced by multiaxial fabrics. In : Hogg, P.J., Schulte, K. and Wittich, H. (eds.). ECCM-CTS 2 : Composites testing and standardisation. European Conference on composites testing and standardisation, 13-15 September 1994, Hamburg, Germany, Woodhead Publishing Limited, pp. 305-313.

[10] Lessard, L.B., Eilers O.P., Shokrieh M.M., Testing of in-plane shear properties under fatigue loading. JOURNAL OF REINFORCED PLASTICS AND COMPOSITES 14 (9): 965-987 SEP 1995.

[11] Van Paepegem W. Development and finite element implementation of a damage model for fatigue of fibre-reinforced polymers. Doctoral thesis at Ghent University, 2002. ISBN 90-76714-13-4.

Chapter 9

CONCLUSIONS AND FUTURE RESEARCH

In this chapter, all important facts that should be remembered after reading this dissertation are briefly summarised. With these in mind, some recommendations for future work are suggested. Furthermore, a brief introduction on the author's post-doctoral research topic is given.

9. 1. CONCLUSIONS

This doctoral research was about the conducting and monitoring of fatigue experiments on fibre-reinforced thermoplastics as well as about the development of better test setups and the accurate finite element modelling of those setups. Since the targeted family of materials is quite large, only one was chosen as a representative, namely a carbon fabric-reinforced polyphenylene sulphide.

The elastic properties of the material were determined both by quasi-static tests and by the 'resonalyser' method, which is based on determining the resonance frequencies of the test specimen. The results of both experiments corresponded very well and the low value of the Poisson's ratio, found in the static tests, was verified. During the hysteresis and fatigue loading conditions, it was noted that the material did not seem to have any stiffness degradation and only limited permanent deformation occurred. As such, it is very difficult to monitor the damage state of the material using only these two parameters. The evolution of the Poisson's ratio, however, was a lot more sensitive and clearly decreased with increasing damage. Unfortunately, it was impossible to measure the Poisson's ratio till failure for the fatigue experiments, since the transverse strain gauges de-bonded prior to failure. A peculiar shape was found for the ν_{12}-ε_{xx} curve, but eventually, it was concluded that this was due to the damage mechanics of the material, rather than to the used sensors and an analytical explanation was given.

A new design of a set of mechanical grips, suited for tension and compression fatigue was presented. During the design, some equations regarding the contact pressure between specimen and grips were derived. These formulas were then used to simulate the actual stress distribution in the specimen under and near the end tabs. Various combinations of tab material and geometry were simulated and finally, it was concluded that the best solution for the material under study was to use straight end tabs with a $[(0°,90°)]_{4s}$ stacking sequence and to mount the specimen in such a way that the tabs are completely inside the grips.

For the electrical resistance measurement, it was attempted to establish contact using rivets, with good results. Both a two-probe and a four-probe setup were investigated, and it was concluded that the four-probe setup was the best choice, since it was more sensitive and the measured resistance did not drift away in time, as was the case for the two-probe setup. In the hysteresis experiments, this technique showed quite promising results, the electrical resistance clearly followed the loading and unloading of the specimen and a slight increase, resulting from damage, could be noted. During the fatigue experiments, it was also proven that this technique works, the resistance followed the loading cycles even at 5 Hz. However, no clear increase as function of the number of cycles could be determined, meaning that the electrical resistance was not sensitive to the occurring damage in the material.

For the optical fibre sensors with Bragg gratings, both embedded and externally bonded fibres were considered. The embedded optical fibre sensors survived the harsh conditions of the production process for the carbon fabric-reinforced thermoplastic, although some fibres developed multiple peaks in their reflected spectrum, rendering them useless for strain measurement with the optical data acquisition systems considered for this research. Both embedded and externally bonded optical fibres yielded good results under quasi-static and fatigue loading conditions and the strain, derived from the wavelength shift, corresponded very well with the reference strain, measured using the extensometer. Furthermore, the embedded fibres survived over 500,000 cycles, which is significantly more than longitudinal strain gauges, which de-bond after a few dozen fatigue cycles.

Besides uni-axial loading conditions, bending and in-plane shear loads were also studied. With regards to the bending setup, various problems occur when using the standard three-point bending setup, even when rotational outer supports are used: (i) the hysteresis which is present in the force-displacement curve is mainly due to friction on the supports, (ii) the midspan displacement reached with the thin laminate under study is very large, limiting the maximum test frequency in fatigue tests and (iii) the finite element implementation is quite cumbersome and the simulation itself requires a lot of computational time. Improvement was sought in the four-point setup, but the large midspan displacement renders the assumption of a constant bending moment in the midsection invalid, meaning that the entire setup must be modelled, again with very long computation time as result. Clamping the ends of the specimen in a four-point bending setup did yield higher forces for lower midspan displacements, meaning that higher fatigue test frequencies are possible, but the specimen always fails at the clamping.

Finally, a clamped three-point bending setup proved to be the most promising: (i) high forces for low displacements are achieved, resulting in the fact that fatigue test frequencies of 5 Hz test were no problem and (ii) this setup has an easy finite element implementation. Furthermore, a one-dimensional analysis yielded very similar results to a full scale three-dimensional analysis, but it required only a few minutes of calculation time. Such a short computation time is of course a significant advantage when the bending setup is considered for validating user defined material models.

For studying the behaviour under in-plane shear loading conditions, both the three-rail shear test and the $[(+45°,-45°)]_{4s}$ tensile test were considered. Since the standard rail shear grips are only suited for quasi-static loads, a new design, adequate for fatigue loading conditions is presented. This new design is based on frictional and geometrical gripping and as such, there is no longer need for drilling holes through the specimen. First it was verified that the induced load was symmetrical and that no buckling or bending of the specimen occurs. Then, various static, cyclic and fatigue experiments were done, both with the three-rail shear setup and with the $[(+45°,-45°)]_{4s}$ tensile test, yielding very similar results. The in-plane shear behaviour can be summarised as follows: there is a gradual decrease in shear stiffness and a gradual development of permanent shear strain. For the fatigue, there is also a gradual decrease in stiffness and increase in permanent deformation until at some point near the end of fatigue life, there is a sudden increase in temperature, higher than the softening temperature of the matrix and a sudden increase in permanent deformation.

The static in-plane shear behaviour was modelled with a previously developed model based on stiffness degradation and permanent deformation. After optimising the four material constants, the static experiments were simulated and the results corresponded very well with the experiments. A final validation of the model was done using a three-point bending test on a $[(+45°,-45°)]_{4s}$ specimen and again, the experimental and numerical results showed good correspondence.

9. 2. SUGGESTIONS FOR FUTURE WORK

After finishing this research, there are still some topics worthy of further research. Since the monitoring of the Poisson's ratio proved very promising for monitoring the damage state of the material, sensors are required that can accurately register the (very small) transverse strain until failure of the specimen. As such, sufficient data can be obtained to accurately use the Poisson's ratio for damage and failure prediction.

The optical fibre sensors survived over half a million cycles, but the maximum stress levels were only about fifty percent of the static failure stress. More fatigue experiments with a higher maximum stress level should be conducted to verify whether the conclusions are still valid for higher stresses and of course, the problem of peak-splitting must be addressed. Either a way to avoid these multiple peaks or a method of deriving the strain from such a spectrum with multiple peaks should be developed.

It was proven that the electrical resistance measurement worked, even under fatigue loading conditions, but the longitudinal resistance was not sensitive to the occurring damage. It may be worthwhile to examine whether the through thickness resistance is more sensitive to the occurring damage.

For this research, only tension-tension fatigue was considered uni-axially. For a better understanding of the fatigue behaviour of the selected material, tension-compression and compression-compression fatigue should also be considered, using the tools provided in this research.

For the bending setup, great improvement was reached with the clamped three-point bending setup. This, however, still has one small problem, being the little amount of sliding that occurs inside the grips. Therefore, further research must be done on how to avoid the slipping in the grips, ensuring that the taken precautions do not advance preliminary failure.

More fatigue experiments are required with the three-rail shear test and the $[(+45°,-45°)]_{4s}$ tensile test, so that the behaviour of the material under in-plane shear fatigue loading conditions can be accurately modelled.

In order to find better explanations for some of the observed phenomena, such as the frequency effect in the in-plane shear experiments, or the evolution of the Poisson's ratio, a micro-mechanical study of the selected material should be considered.

Although the stress distribution in the specimen near the end tabs was modelled and suggestions for tab material and geometry could be made, it is still necessary to find a better way of bonding the tabs to the specimen, since insufficient bonding is one of the main reasons of premature (frictional) failure. Different adhesives which are better suited for the polyphenylene and other chemically inert thermoplastics should be developed or a different way of mounting the end tabs to the specimen could be considered. In fact, the latter lies at the origin of the topic of the author's intended post-doctoral research, which is discussed next.

9. 3. TOPIC FOR THE POST-DOCTORAL RESEARCH

As was mentioned in the previous paragraph, bonding or more generally joining thermoplastic composite materials is not as easy as bonding thermosetting composites, for which very good adhesive bonds can be achieved. Because of the thermoplastic nature, however, fusion bonding of the thermoplastic materials is possible. This option has already been briefly discussed in chapter 3, but within the extent of this doctoral research, developing a welding device and optimizing the process was not possible. However, this proved to be an ideal subject for a post-doctoral research grant.

In general, fusion bonding techniques can be categorised in three groups [1]: (i) frictional welding, including ultrasonic welding; (ii) electromagnetic welding, including resistance welding and induction welding and (iii) thermal welding, including infrared welding and hot-tool welding. While performing the literature study for the application for the post-doctoral grant, it became clear that already lot of research was done on the ultrasonic welding and the resistance welding, but very few papers were published on the hot-tool welding. Furthermore, most research is mainly focused on optimising the process parameters, such as consolidation pressure, temperature, duration of the different phases and process window. During this optimisation process, only quasi-static experiments till failure are considered to determine the quality of the bond. As stated by Stavros and Bersee [2], standard test methods for adhesive bonding are used for evaluating the strength and the quality of the welds. These methods give relevant information about the quality of the weld and are also quite useful for comparative studies. The most commonly chosen experimental setups are the single lap shear test (Figure 9-1(a)) and the Mode I double cantilever beam (Figure 9-1(b)).

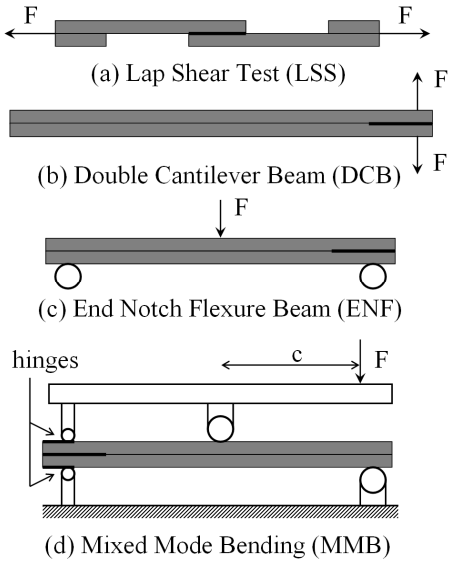

Figure 9-1 Possible experimental setups for testing welded joints.

With respect to the (finite element) modelling, a lot of attention is given on the modelling of the fusion bonding process itself [3], meaning that heat-transfer, consolidation and crystallisation of the thermoplastic are considered.

Since thermoplastic joints will occur more and more in load bearing structures, it will be necessary to have an understanding of the fatigue behaviour of these joints. However, as Stavros and Bersee state [2], there is practically no data available on the creep or fatigue behaviour of these welded joints. Indeed, while searching the open knowledge databases for articles on fatigue of composite joints, a significant number of studies of the fatigue behaviour of adhesively bonded composite joints exist, but none were found on the fatigue behaviour of welded joints in thermoplastic composites. One might expect that both types of joints will have a similar behaviour, but this has not yet been verified and therefore is a dangerous assumption for design purposes.

When studying the fatigue behaviour of adhesively bonded composite joints, usually the previously mentioned setups are used: the single lap shear test and the Mode I double cantilever beam. Topics of interest are the influence of the loading frequency [4], the influence of the geometry on the results, such as overlap length and corner geometry for the lap shear test [5-7] and the effects of creep, which is supposed to have a significant influence on the reduction in dynamic stiffness [8].

If the fatigue behaviour of adhesive bonds is described, usually a method based on Paris law is used for the crack-growth [7, 9] or simple S-N curves are derived. Also, the strain energy release rate (SERR) is considered [6].

Therefore, the subject of the intended post-doctoral grant is the experimental and numerical study of the fatigue behaviour of fusion bonded thermoplastic composites. The chosen welding technique is the 'hot-tool' process, which is illustrated in Figure 9-2. The author refers to chapter 3, paragraph 3.2.3. for more information on the principle of this fusion bonding technique

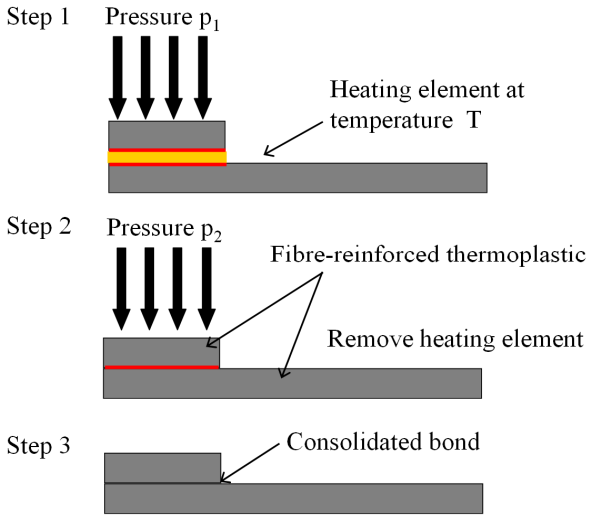

Figure 9-2 The principle of 'hot-tool' welding.

This choice is the result of an assessment of the pro's and con's of the different fusion bonding techniques during an ongoing master thesis [10]. Furthermore, this process has some interesting advantages: dissimilar thermoplastics can be welded, the temperature of the molten interfaces can be accurately controlled, surface inaccuracies can be taken into account during the process and it can handle complex geometries [1]. Moreover, it is a relatively cheap process, since it does not require expensive machinery, as is the case with friction welding and ultrasonic welding [1, 3]. The intended planning of activities is the following:

(i) Assessing which experimental setups will be considered for this research; the setups depicted in Figure 9-1, will certainly be assessed, both experimentally and numerically. Of course, should other possibilities arise during the investigation, then they will be considered as well.

(ii) Optimising the process parameters of the welding process, probably using the Mode I Double Cantilever Beam test and the Mode II End Notch Flexure test, depending on the previous assessment.

(iii) Conducting an extensive experimental program under fatigue loading conditions, to assess the influence of the frequency, load range and geometrical aspects, related to the test setup, for instance the overlap length in the LSS of the parameter c in the Mixed Mode Bending.

(iv) Modelling the fatigue behaviour, using a similar approach as used in literature [5, 6, 9], based on crack-initiation and -growth and strain energy release rate.

(v) Developing a material model which is able to predict fatigue damage and crack-growth in a geometrically nonlinear 3D analysis which updates the crack-growth pattern. With this model, it should be possible to predict the behaviour of any given joint geometry, taking the change of the Mode I to Mode II crack-growth ratio due to crack-growth and corresponding geometrical changes into account.

(vi) Validating the models using either the LSS test, which combines Mode I and Mode II crack-growth due to bending of the specimen, or the MMB test.

During the investigation, SEM and optical microscopy, ultrasonic scans and X-ray microtomography will be used to visualize both the weld and the damage.

9. 4. REFERENCES

[1] Yousefpour A, Hojjati M, Immarigeon JP, Fusion bonding/welding of thermoplastic composites. JOURNAL OF THERMOPLASTIC COMPOSITE MATERIALS 17 (4): 303-341 JUL 2004.

[2] Stavrov D, Bersee HEN. Resistance welding of thermoplastic composites - an overview. COMPOSITES PART A-APPLIED SCIENCE AND MANUFACTURING 36 (1): 39-54 2005.

[3] Ageorges C, Ye L, Hou M , Advances in fusion bonding techniques for joining thermoplastic matrix composites: a review. COMPOSITES PART A-APPLIED SCIENCE AND MANUFACTURING 32 (6): 839-857 2001.

[4] Al-Ghamdi AH, Ashcroft IA, Crocombe AD, Abdel-Wahab MM. Crack-growth in adhesively bonded joints subjected to variable frequency fatigue loading. JOURNAL OF ADHESION 79 (12): 1161-1182 DEC 2003.

[5] Quaresimin M, Ricotta M. Fatigue behaviour and damage evolution of single lap bonded joints in composite material. COMPOSITES SCIENCE AND TECHNOLOGY 66 (2): 176-187 Sp. Iss. SI, FEB 2006.

[6] Quaresimin M, Ricotta M. Stress intensity factors and strain energy release rates in single lap bonded joints in composite materials. COMPOSITES SCIENCE AND TECHNOLOGY 66 (5): 647-656 Sp. Iss. SI, MAY 2006.

[7] Ricotta, M. Meneghetti, G. Quaresimin, M. Influence of the layer orientation at the interface on the fatigue behaviour of bonded joints in composites.4th Internation Conference on Fatigue of Composites (ICFC4), 26-28 September,IVW, Kaiserslautern, Germany.

[8] Ferreira JAM, Reis PN, Costa JDM, Richardson MOW. Fatigue behaviour of composite adhesive lap joints. COMPOSITES SCIENCE AND TECHNOLOGY 62 (10-11): 1373-1379 2002.

[9] Quaresimin, M. and Ricotta, M.. Life prediction of bonded joints in composite materials. INTERNATIONAL JOURNAL OF FATIGUE 28 (10): 1166-1176 OCT 2006.

[10] Derijcke, S. Optimalisatie van het spiegellassen voor vezelversterkte thermoplasten (in Dutch) master thesis 2007-2008, Ghent University.

ABOUT THE AUTHOR

Ives De Baere was born on January 9th, 1981. After completing his secondary education science and mathematics in 1999, he started his education to obtain an engineering degree at Ghent University. After choosing the option of mechanical engineer in the third year, he became more and more interested in mechanical behaviour of materials, which led to his choice of doing a master thesis on composite materials, namely 'The study of the in-plane shear behaviour of fibre-reinforced composites'.

During this research, he became even more interested in the beauty of the fibre-reinforced polymers, which made him decide to stay a little longer and do some more research on composite materials. This led to this doctoral thesis. Even now, the hunger for composite knowledge is not satisfied and the author has applied for a post-doctoral fellowship with the FWO (Fonds Wetenschappelijk Onderzoek) in order to study the fatigue behaviour of fusion bonded joints between fibre-reinforced thermoplastics.

During his doctoral study, the author has written a number of publications and has participated in a number of national and international congresses, of which an overview is given:

Publications in international journals of the Science Citation Index (SCI)

1. W. Van Paepegem, I. De Baere and J. Degrieck, Modelling the nonlinear shear stress-strain response of glass fibre-reinforced composites. Part I: Experimental results, COMPOSITES SCIENCE AND TECHNOLOGY 66 (10): pp. 1455-1464 AUG 2006.
2. W. Van Paepegem, I. De Baere and J. Degrieck, Modelling the nonlinear shear stress-strain response of glass fibre-reinforced composites. Part II: Model development and finite element simulations, COMPOSITES SCIENCE AND TECHNOLOGY 66 (10): pp. 1465-1478 AUG 2006.
3. W. Van Paepegem, I. De Baere, E. Lamkanfi and J. Degrieck, Poisson's ratio as a sensitive indicator of (fatigue) damage in fibre-reinforced plastics, Fatigue and Fracture of Engineering Materials and Structures, 30 (4): pp. 269-276 APR 2007.
4. De Baere I. , Van Paepegem W. and Degrieck J. The use of rivets for electrical resistance measurement on carbon fibre-reinforced thermoplastics, Smart Materials and Structures 16 pp. 1821-1828, 2007.

5. De Baere I. , Van Paepegem W. and Degrieck J., Sol H., Van Hemelrijck D. and Petreli A., Comparison of different identification techniques for measurement of quasi-zero Poisson's ratio of fabric reinforced laminates, Composites part A, 38 (9) pp. 2047-2054, 2007.
6. De Baere I., Voet E., Van Paepegem W., Vlekken J., Cnudde V., Masschaele B. and Degrieck J., Strain monitoring in thermoplastic composites with optical fibre sensors: embedding process, visualization with micro-tomography and fatigue results, Journal of Thermoplastic Composite Materials (20) pp. 453-472, 2007.
7. De Baere I., Van Paepegem W. and Degrieck J., Design of a modified three-rail shear test for shear fatigue of composites. Polymer Testing, 27 (3) pp. 346-359, 2008.
8. De Baere I., Van Paepegem W. and Degrieck J. Design of mechanical clamps with extra long wedge grips for static and fatigue testing of composite materials in tension and compression, ACCEPTED for Experimental Techniques.
9. De Baere I., Van Paepegem W. and Degrieck J. On the feasibility of a three-point bending setup for the validation of (fatigue) damage models for thin composite laminates. ACCEPTED for Polymer Composites.
10. De Baere I., Van Paepegem W. and Degrieck J. On the design of end tabs for quasi-static and fatigue testing of fibre-reinforced composites. ACCEPTED for Polymer Composites.
11. De Baere I., Luyckx G., Voet E., Van Paepegem W. and Degrieck J., On the feasibility of optical fibre sensors for strain monitoring in thermoplastic composites under fatigue loading conditions, ACCEPTED for Optics and Lasers in Engineering, special issue for OPTIMESS 2007.
12. De Baere I., Van Paepegem W. and Degrieck J., Electrical resistance measurement for in-situ monitoring of fatigue of carbon fabric composites, ACCEPTED for Special Issue of International Journal of Fatigue.
13. Van Paepegem W., De Baere I., Lamkanfi E. and Degrieck J., Monitoring fatigue damage in fibre-reinforced plastics through the Poisson's ratio degradation, ACCEPTED for Special Issue of International Journal of Fatigue.
14. De Baere I., Van Paepegem W. and Degrieck J., Modelling the nonlinear shear stress-strain behaviour of a carbon fabric reinforced polyphenylene sulphide from rail shear and $[(+45°,-45°)]_{4s}$ tensile test. ACCEPTED for Polymer Composites.
15. De Baere I., Van Paepegem W. and Degrieck J., Comparison of the modified three-rail shear test and the $[(+45°,-45°)]_{ns}$ tensile test for pure shear fatigue loading of carbon fabric thermoplastics. ACCEPTED for Fatigue and Fracture of Engineering Materials & Structures.

16. De Baere I., Van Paepegem W. and Degrieck J., Comparison of different setups for fatigue testing of thin composite laminates in bending, ACCEPTED for Special Issue of International Journal of Fatigue.

Books/Chapters in books

1. Van Paepegem W., De Baere I., Lamkanfi E., Luyckx G. and Degrieck J., Numerical modelling of fatigue in textile polymer composites. Accepted chapter for Computational & Experimental Analysis of Damaged Materials, 2007; ISBN: 978-81-7895-308-3 Editor: Dimitrios G. Pavlou. Research Signpost, India.
2. Van Paepegem W., De Baere I., Lamkanfi E., Luyckx G. and Degrieck J. Research directions in the fatigue testing of polymer composites. Accepted chapter for Composite Materials Research Progress 2007; ISBN: 978-1-60021-994-8 Editor Lucas P. Durand. Nova Science Publishers, Inc., New York, United States of America.

Publications in conference proceedings

1. De Baere I., Van Paepegem W. and Degrieck J. (2004) Experimental and theoretical study of the mechanical behaviour of fibre-reinforced thermoplastics under fatigue loading conditions. 5th Ph.D. Symposium, Faculty of Engineering, 1 December 2004, Gent, Belgium.
2. De Baere I., Van Paepegem W. and Degrieck J. (2005). Modelling the nonlinear shear stress-strain response of glass fibre-reinforced composites. Third International Conference on Advanced Computational Methods in Engineering (ACOMEN), 30 May – 2 June 2005, Gent, Belgium.
3. De Baere I., Van Paepegem W. and Degrieck J. (2005) Design of a three- and four-point bending setup for fatigue testing of fibre-reinforced thermoplastics. 6th Ph.D. Symposium, Faculty of Engineering, 30 November 2005, Gent, Belgium.
4. De Baere I., Van Paepegem W. and Degrieck J. (2006). Modelling the nonlinear shear stress-strain response of glass fibre-reinforced composites. 12th European Conference on Composite Materials (ECCM 12) 29 August – 2 September 2006, Biarritz, France.
5. Degrieck, J. et al. (2006). Monitoring of Fatigue, Impact and Wear in Cetex TPC. Workshop on Cetex thermoplastic composites in honour of Willem van Dreumel. TUDelft, Delft, The Netherlands, 14 June 2006. **Invited presentation**.

6. De Baere I., Van Paepegem W. and Degrieck J., (2006) Optical fibres and electrical resistance measurement for in-situ monitoring of composite fatigue. 7th Ph.D. Symposium, Faculty of Engineering, 29 November 2006, Gent, Belgium.
7. De Baere I., Voet E., Van Paepegem W., Degrieck J. and Vlekken J. The use of optical fibres for fatigue testing of fibre-reinforced thermoplastics. 4th International Conference Emerging Technologies in Non-Destructive Testing, (ETNDT 4) 2 – 4 april 2007, Stuttgart, Germany.
8. De Baere I., Van Paepegem W. and Degrieck J., Electrical resistance measurement on carbon fibre-reinforced thermoplastics with rivets as electrodes. 4th International Conference Emerging Technologies in Non-Destructive Testing, (ETNDT 4) 2 – 4 april 2007, Stuttgart, Germany.
9. Luyckx G., Degrieck J., De Baere I., De Waele W., Van Paepegem W. and Verbeke T.. Monitoring of a curved beam test structure using Bragg sensors and acoustic emission. 4th International Conference Emerging Technologies in Non-Destructive Testing, (ETNDT 4) 2 – 4 april 2007, Stuttgart, Germany.
10. De Baere I., Voet E., Van Paepegem W., Degrieck J. and Vlekken J.. On the feasibility of optical fibre sensors for strain monitoring in thermoplastic composites under fatigue loading conditions. 3rd Workshop on Optical Measurement Techniques for Structures and Systems (OPTIMESS 2007) 28 – 30 May 2007, Leuven, Belgium.
11. Luyckx G., De Baere I., De Waele W., Degrieck J., Van Paepegem W., Vlekken J. and Verbeke T., Analysis of a curved composite test specimen zith Fibre Bragg Gratings. 3rd Workshop on Optical Measurement Techniques for Structures and Systems (OPTIMESS 2007) 28 – 30 May 2007, Leuven, Belgium.
12. De Baere I., Van Paepegem W. and Degrieck J., Comparison of different setups for fatigue testing of thin composite laminates in bending, International Conference on Damage tolerance of Aircraft Structures (DTAS), on 25-28 September 2007, Delft, The Netherlands.
13. De Baere I., Van Paepegem W. and Degrieck J., A clamped three-point bending setup for fatigue of thin composite laminates. 8th Ph.D. Symposium, Faculty of Engineering, 5 December 2007, Gent, Belgium.
14. De Baere I., Van Paepegem W., Voet E. and Degrieck J.. Fatigue testing of carbon fabric thermoplastics: different testing and instrumentation strategies. SAMPE EUROPE 28th International Conference (SEICO 08), Composites Forever, Affortable, Durable, Sustainable and Creatable. March 31st – April 2nd. 2008, Paris, France.

15. De Baere I., Van Paepegem W. and Degrieck J. A clamped three-point bending setup for fatigue of thin composite laminates, ACCEPTED for 13th European Conference on Composite Materials (ECCM-13), June 2 - 5, 2008 Stockholm, Sweden.
16. De Baere I., Van Paepegem W. and Degrieck J. A modified three-rail shear test for fatigue of composite laminates, ACCEPTED for 13th European Conference on Composite Materials (ECCM-13), June 2 - 5, 2008 Stockholm, Sweden.
17. Voet E., Luyckx G., De Baere I., Degrieck J., Bartelt H., Vlekken J. and Jacobs E., High strain measurements during fatigue cycling in fibre reinforced thermoplastic composites using imbedded draw tower fibre Bragg grating sensors. ACCEPTED for 13th European Conference on Composite Materials (ECCM-13), June 2 - 5, 2008 Stockholm, Sweden.
18. Voet E., Luyckx G., De Baere I. and Degrieck J.. High Strain monitoring during Fatigue Loading of Thermoplastic Composites using imbedded draw Tower Fibre Bragg Grating Sensors, SUBMITTED for 3rd International Conference “Smart Materials, Structures and Systems”, CIMTEC, June 8 to 13, 2008, Florence, Italy.